REVIEW

Mössbauer studies of negative-*U* tin centers in lead chalcogenides

F. S. Nasredinov, S. A. Nemov, V. F. Masterov,*) and P. P. Seregin

St. Petersburg State Technical University, 195251 St. Petersburg, Russia
(Submitted January 13, 1999)
Fiz. Tverd. Tela (St. Petersburg) **41**, 1897–1917 (November 1999)

Experimental data on identification of negative-*U* tin centers in lead chalcogenides and related solid solutions by means of ^{119}Sn Mössbauer spectroscopy are discussed. © *1999 American Institute of Physics.* [S1063-7834(99)00111-2]

1. INTRODUCTION

General concepts of the behavior of impurity atoms in semiconductors are fairly traditional, namely, substitution of an impurity for a lattice atom is believed to create in the semiconductor energy gap either a donor or an acceptor level, which is capable of donating (capturing) one electron if the Fermi level changes its position (the so-called ''one-electron centers'').

Hubbard was the first to perform a theoretical analysis of the behavior of point defects, which can donate (capture) two electrons in interaction with the lattice (the ''two-electron centers'').[1] This produces two bands of localized states in the semiconductor gap separated by the intratomic energy (the Hubbard, or correlation energy)

$$U = W - E, \tag{1}$$

where E and W are the first and second center-ionization energies.

If $U<0$, a set of levels is formed which is referred to as ''two-electron negative-correlation centers'' (negative-U, or U^- centers). The negative-U centers are characterized by the instability of their intermediate (singly ionized) charge state. Decay into one neutral and one doubly ionized center is energetically favorable for each pair of singly ionized centers. When in equilibrium, the concentration of U^- centers in the intermediate charge state is always exponentially small [i.e., proportional to $\exp(-U/2kT)$] compared to their total concentration.

The U^- center ideology in its general form was used by Anderson[2] to explain the electrical, optical, and magnetic properties of amorphous materials, and Kastner *et al.*[3] modified it to make applicable to glassy chalcogenide semiconductors. Drabkin and Moĭzhes[4] analyzed the possibility of U^- center stabilization in various semiconductors, as well as made an attempt[5] to relate the phenomenon of superconductivity to the creation of such centers in superconducting materials. The possibility of detecting two-electron localization-delocalization processes in condensed media was considered by Ionov.[6] The resonance states of the indium impurity in IV–VI crystal semiconductors are identified with the U^- centers,[7] and the question of the thallium impurity belonging to these centers is presently discussed.[8]

However despite the successful use of these concepts, two-electron centers with negative correlation energy have not been observed in semiconductors by a direct experiment.[9] The only exceptions are the tin impurity atoms in lead chalcogenides and their solid solutions (PbS, PbSe, PbTe, $PbS_{1-z}Se_z$, $PbS_{1-z}Te_z$), where such centers were identified by Mössbauer spectroscopy of the ^{119}Sn isotope.[10–21] Note that tin in lead chalcogenides is an isoelectronic impurity, which makes the electrical activity of such an impurity an interesting feature in itself.[22]

The present review discusses experimental data connected with identification of U^- tin centers in lead chalcogenides and related solid solutions, which were obtained by ^{119}Sn Mössbauer spectroscopy. Section 2 considers briefly the parameters of Mössbauer spectra used in the subsequent account. Section 3 presents results of a study of tin and lead chalcogenides by ^{119}Sn Mössbauer spectroscopy, because these results are employed in interpretation of the experimental data obtained on tin impurity atoms.

2. ^{119}Sn MÖSSBAUER SPECTROSCOPY

Mössbauer spectroscopy is an efficient method of probing impurity atoms in semiconductors. The parameters of Mössbauer spectra permit one to determine the charge state of impurity atoms, their electronic structure, the symmetry of the local environment, and the formation of various associates of impurity atoms with lattice defects.[23] The present review considers Mössbauer studies only using the ^{119}Sn isotope. The scheme by which the ^{119m}Sn Mössbauer level forms is displayed in Fig. 1. The review makes use of the following Mössbauer spectrum parameters:

(1) The natural spectral-line width G_{nat} determined by the Mössbauer level lifetime τ_0

$$G_{\text{nat}} = \hbar/\tau_0 \tag{2}$$

($\hbar$ is the Planck constant).

For ^{119}Sn, $G_{\text{nat}} = 0.324$ mm/s. The width of experimental spectra always exceeds $2G_{\text{nat}}$. One can pinpoint three main

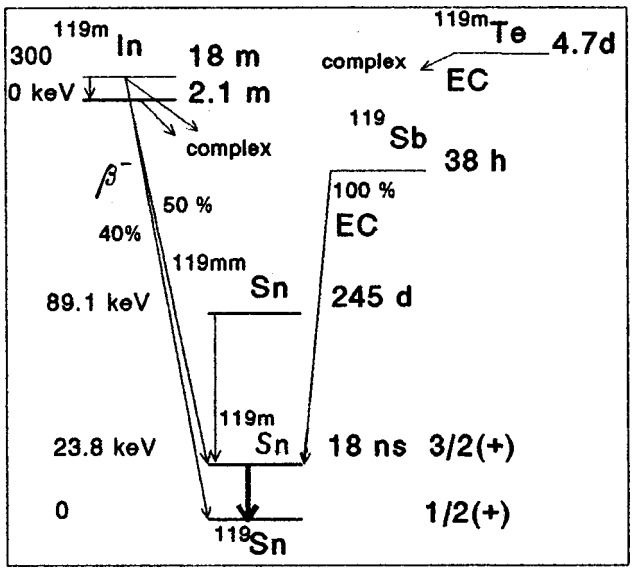

FIG. 1. Diagram of formation of the ^{119m}Sn level.

reasons for this broadening: a finite absorber surface density; unresolved quadrupole splitting; and electron exchange between the two tin charge states.

(2) The isomer shift of a spectrum

$$\delta = \alpha[|\Psi(0)_a|^2 - |\Psi(0)_s|^2], \tag{3}$$

where α is a calibration constant (for ^{119}Sn, $\alpha = 0.061\, a_0^3$ mm/s, where a_0 is the Bohr radius), $|\Psi(0)_a|^2$ and $|\Psi(0)_s|^2$ are the electronic densities at tin nuclei in the absorber and source, respectively.

The isomer shifts presented subsequently are reckoned relative to $CaSnO_3$. As follows from numerous studies of tin compounds made by ^{119}Sn Mössbauer spectroscopy, the isomer shifts of spectra of quadrivalent-tin compounds lie from -1 to 2.1 mm/s, those of divalent tin, from 2.6 to 4.2 mm/s, and those of intermetallic compounds of tin, from 2.0 to 2.7 mm/s. Thus Mössbauer spectroscopy on ^{119}Sn permits reliable determination of the valence (charge) state of tin.

(3) The quadrupole splitting of a spectrum is defined as

$$\Delta = (1/2)eQU_{zz}(1+\eta^2/3)^{1/2}, \tag{4}$$

where $Q = -0.06\, b$ is the quadrupole moment of the ^{119m}Sn nucleus, $\eta = (U_{xx} - U_{yy})/U_{zz}$ is the asymmetry parameter of the electric-field gradient (EFG) tensor at tin nuclei, and U_{xx}, U_{yy}, and U_{zz} are the EFG tensor components (for which the Laplace equation $U_{xx} + U_{yy} + U_{zz} = 0$ and the inequality $|U_{xx}| \leq |U_{yy}| \leq |U_{zz}|$ are valid).

Quadrupole splitting provides information on the symmetry of the tin environment, which is particularly useful for the case of impurity atoms, where the nearest-neighbor symmetry of an atom cannot be predicted *a priori* from the crystal structure of the host matrix.

(4) The Mössbauer coefficient f is the fraction of γ quanta emitted or absorbed without recoil. The Mössbauer coefficient is a quantity integrated over the phonon spectrum and is not very strongly dependent on the features of the latter. Therefore the f quantities are usually described in the Debye approximation; note that the Debye temperature can be derived from the temperature dependence of the Mössbauer coefficient.

The state of impurity atoms can be studied with two versions of ^{119}Sn Mössbauer spectroscopy:

(i) Mössbauer absorption spectroscopy (MAS), in which the sample under study containing the ^{119}Sn stable isotope serves as absorber, and as a source of gamma quanta one uses $Ca^{119mm}SnO_3$ with an unsplit line, whose width is close to the natural width of the spectral line. The main drawback of MAS lies in the need to employ relatively high concentrations of impurity atoms in the matrix to be investigated.

(ii) Mössbauer emission spectroscopy (MES), in which the sample to be investigated and containing a long-lived parent isotope (^{119m}Sn, ^{119}Sb, ^{119m}Te) acts as a gamma-ray source, with $Ca^{119}SnO_3$ used as absorber. The main shortcoming of MES consists in the need to take into account, in the interpretation of experimental data, the effect on the state of the daughter atom of the preceding radioactive transformation of the parent atom (the so-called post-effects of nuclear transformations).[24]

The ^{119}Sn Mössbauer spectra considered in the present review were measured within the 4.2–295-K range. For the width of the ^{119}Sn line one took that of the ^{119}Sn Mössbauer spectrum of the $Ca^{119mm}SnO_3$ source measured with a $CaSnO_3$ absorber (^{119}Sn surface density 0.1 mg/cm^2): $G_{instr} = 0.76 \pm 0.02$ mm/s.

The lead and tin chalcogenides, as well as the related solid solutions, were prepared by the ceramic technology by melting the starting components of semiconductor-grade purity in evacuated quartz ampoules, with subsequent annealing first of the ingots, and after that, of the pressed powders at 650 °C for 120 h. Metallographic and x-ray diffraction analysis of the samples of the lead chalcogenides and related solid solutions showed them to be single phase with a NaCl-type structure. Superstoichiometric lead was employed as a donor impurity, and sodium and thallium, as acceptor impurities. The starting charge was composed under the assumption that the impurity atoms of tin, sodium, and thallium substitute for lead, so that the sample composition can be written in the form $Pb_{1-x-y}Sn_xA_yS_{1-z}Se_z$ and $Pb_{1-x-y}Sn_xA_yS_{1-z}Te_z$ (Here A stands for the Na or Tl acceptor impurities, which donate one hole per atom up to concentrations $p \sim 10^{20}$ cm^{-3}).

3. STUDIES OF THE TIN AND LEAD CHALCOGENIDES

3.1. Tin chalcogenides

Information on the methods of preparation, structure, and properties of tin chalcogenides can be found in Refs. 25 and 26. Two compounds each form in the tin–sulfur and tin–selenium systems, mono- and dichalcogenides (SnS and SnSe; SnS_2 and $SnSe_2$, respectively). The existence of the Sn_2S_3, Sn_3S_4, and Sn_2Se_3 compounds cannot also be ruled out. The tin monosulfide and monoselenide crystallize in the SnS-type orthorhombic lattice, and the tin disulfide and diselenide have a CdI_2-type layered structure. Only one compound, SnTe, with a NaCl-type structure, was observed to exist in the tin–tellurium system.

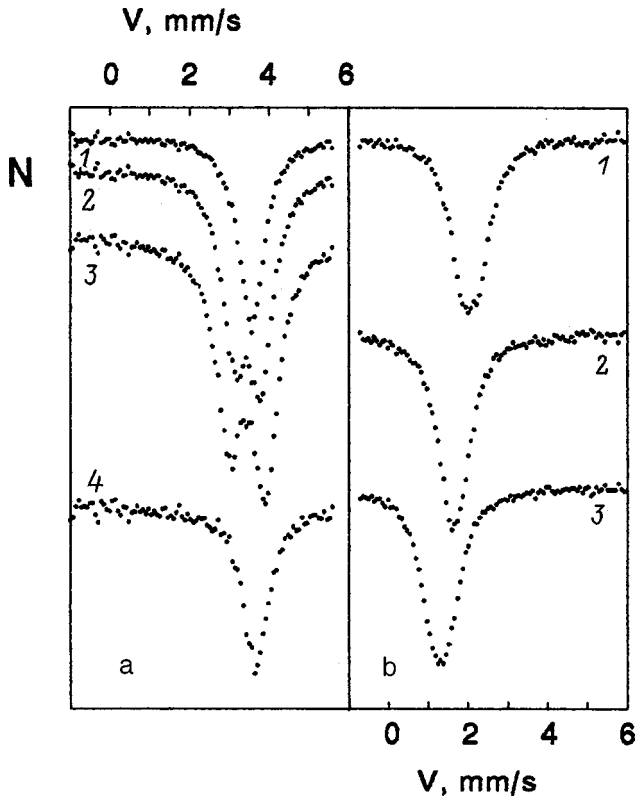

FIG. 2. 80-K ^{119}Sn Mössbauer spectra of the chalcogenides of (a) divalent and (b) quadrivalent tin. (a) *1*—SnTe (Ref. 27), *2*—SnSe (Ref. 27), *3*—SnS (Ref. 27), *4*—$Pb_{0.8}Sn_{0.2}Se$ (Ref. 11); (b) *1*—$Ge_{14.5}Sn_{0.5}Te_{85}$ glassy alloy (Ref. 28), *2*—$SnSe_2$ (Ref. 27), *3*—SnS_2 (Ref. 27).

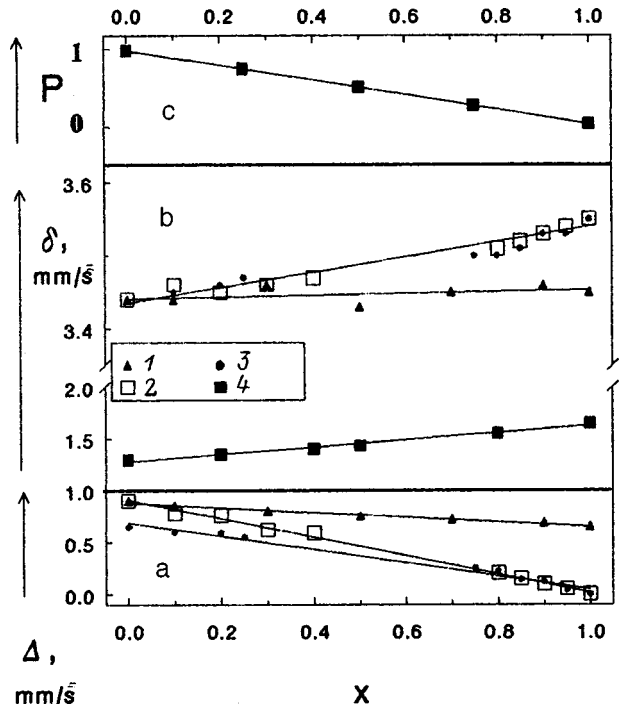

FIG. 3. (a) Dependence of the quadrupole splitting Δ of ^{119}Sn Mössbauer spectra on composition of the $SnS_{1-x}Se_x$ (Ref. 31), $SnS_{1-x}Te_x$ (Ref. 31), and $SnSe_{1-x}Te_x$ (Ref. 31) solid solutions; (b) Dependence of the isomer shift δ of ^{119}Sn Mössbauer spectra on composition of the solid solutions $SnS_{1-x}Se_x$ (Ref. 31), $SnS_{1-x}Te_x$ (Ref. 31), $SnSe_{1-x}Te_x$ (Ref. 31), and $(SnS_2)_{1-x}(SnSe_2)_x$ (Ref. 31); (c) Dependence of the fraction P of divalent tin in the ^{119}Sn Mössbauer spectra of $(SnSe)_{1-x}(SnSe_2)_x$ alloys on composition (Ref. 35). *1*—$SnS_{1-x}Se_x$, *2*—$SnS_{1-x}Te_x$, *3*—$SnSe_{1-x}Te_x$, *4*—$(SnSe)_{1-x}(SnSe_2)_x$.

The tin chalcogenides (SnS, $SnSe$, $SnTe$, SnS_2, $SnSe_2$) were subjects of numerous studies by ^{119}Sn MAS, and there is no controversy either in experimental data or in their interpretation (with the exclusion of a certain scatter in the magnitude of the isomer shift and quadrupole splitting accounted for by problems related to calibration of the spectrometer velocity scale, which are particularly characteristic of early works in this field). As an illustration, Fig. 2a and 2b presents ^{119}Sn Mössbauer spectra of the above compounds, and Table I lists their parameters.[27] The isomer shifts in ^{119}Sn spectra of tin monochalcogenides are typical of the compounds of divalent tin, and those of dichalcogenides lie in the range characteristic of quadrivalent tin compounds. The decrease of the quadrupole splitting of ^{119}Sn spectra in the SnS–SnSe–SnTe series is in accord with the structural data obtained for these compounds. An analysis of the isomer shifts and quadrupole splittings of ^{119}Sn spectra of tin monochalcogenides permitted one to establish the electronic structure of tin atoms in these compounds.[29] The spectra of SnS_2 and $SnSe_2$ represent single lines, their broadening being accounted for by the difference of the local symmetry of tin in these compounds from cubic. It was found[30] that the quadrupole splitting of a SnSe Mössbauer spectrum increases, and the isomer shift decreases, if the spectrum is measured on single-crystal samples illuminated in the optical region (with an intensity of up to 7×10^5 *lx*). It is conjectured that optical radiation initiates electronic transitions from the valence to the conduction band, which causes a change in the electron density and electric-field symmetry at the ^{119}Sn nucleus. Incidentally, the observations reported in Refs. 29 and 30 did not find confirmation.

TABLE I. Parameters of 80-K ^{119}Sn Mössbauer spectra of tin chalocgenides.

Compound	δ, mm/s	Δ, mm/s	Ref.
SnS	3.44	0.90	27
SnSe	3.45	0.65	27
SnTe	3.55	0.0	27
SnS_2	1.30	<0.40	27
$SnSe_2$	1.65	<0.30	27
$Ge_{14.5}Sn_{0.5}Te_{85}$*	2.05	<0.40	28

*In the glassy state.

Tin chalcogenides form $SnS_{1-x}Se_x$ ($0\leqslant x\leqslant 1$), $SnS_{1-x}Te_x$ ($0\leqslant x\leqslant 0.6$ and $0.8\leqslant x\leqslant 1$), $SnSe_{1-x}Te_x$ ($0\leqslant x\leqslant 0.25$ and $0.75\leqslant x\leqslant 1$), and $(SnS_2)_{1-x}(SnSe_2)_x$ ($0\leqslant x\leqslant 1$) solid solutions. It is of interest to follow the variation of the parameters of ^{119}Sn Mössbauer spectra with solid-solution composition. In particular, by Ref. 31, the quadrupole splitting of ^{119}Sn spectra of the $SnS_{1-x}Se_x$, $SnS_{1-x}Te_x$, and $SnSe_{1-x}Te_x$ solid solutions varies linearly with their composition (Fig. 3a), which evidences a statistical nature of mutual chalcogen substitution. The isomer shift of the $SnS_{1-x}Se_x$, $SnS_{1-x}Te_x$, $SnSe_{1-x}Te_x$, and $(SnS_2)_{1-x}(SnSe_2)_x$ solid solutions also varies linearly with

composition (Fig. 3b), which implies a gradual increase of electronic density at ^{119}Sn nuclei as the nearest-neighbor environment of a tin atom changes from sulfur to selenium atoms only.[31]

Attempts were made at identifying the quadrivalent-tin telluride in $SnTe_2$, SnSTe, and SnSeTe alloys by ^{119}Sn Mössbauer spectroscopy,[32] however the spectra of all these alloys were found to belong to divalent tin (i.e., SnTe, SnS, and SnSe, accordingly). One succeeded in stabilizing quadrivalent tin in a tellurium-containing system only in the $Ge_{14.5}Sn_{0.5}Te_{85}$ glassy alloy (see Fig. 2b and Table I).[28]

An attempt to identify trivalent tin in a Sn_2Se_3 compound by ^{119}Sn Mössbauer spectroscopy was also made.[33] One prepared for this purpose $(SnSe)_{1-x}(SnSe_2)_x$ alloys and measured their ^{119}Sn Mössbauer spectra, which were found to be a superposition of the quadrupole doublet (with the parameters identical to those of the SnSe spectrum) and a singlet (identical in parameters to the $SnSe_2$ spectrum). The fraction of divalent tin in this composition did not depend on the actual method of preparation used (i.e., on the melting temperature and melt cooling rate). As seen from Fig. 3c presenting the dependence of the fraction of divalent tin on composition, experimental points fall on the straight line drawn under the assumption that the $(SnSe)_{1-x}(SnSe_2)_x$ system contains no other compounds except SnSe and $SnSe_2$.

^{119}Sn Mössbauer spectra of the $(SnS)_{1-x}(SnS_2)_x$ alloys also represented a superposition of the quadrupole doublet (with the parameters identical to those of the SnS spectrum) and a singlet (identical in parameters to the SnS_2 spectrum).[34,35] It was concluded[34] that the Sn_2S_3 and Sn_3S_4 compounds were not present. However the fraction of divalent tin for this composition was found to depend on the preparation temperature and the melt cooling rate.[35] This permitted a conclusion that Mössbauer data do not rule out the existence of the Sn_2S_3 and Sn_3S_4 compounds, and that if they do exist, the tin in their structure resides in both di- and quadrivalent state.

3.2. Lead chalcogenides

Comprehensive information on the methods of preparation, structure, and properties of lead chalcogenides can be found in Refs. 25, 26, and 36. The PbS, PbSe, and PbTe compounds existing in the lead-chalcogen system have a NaCl-type cubic structure. They all are semiconductors, with a gap of 0.41, 0.29, and 0.32 eV at 300 K for PbS, PbSe, and PbTe, respectively. The materials with excess chalcogen exhibit hole, and with excess lead, electronic conduction (the carrier concentration may reach as high as 10^{18}–$10^{19}\,cm^{-3}$). To obtain a higher carrier concentration, one can dope lead chalcogenides either with halogens (donors) or with sodium and thallium (acceptors); in this way one can increase the carrier concentration to $n, p \sim 2\times10^{20}\,cm^{-3}$.

Lead chalcogenides form solid solutions with one another: $PbS_{1-z}Se_z$ $(0\leqslant z\leqslant 1)$, $PbS_{1-z}Te_z$ $(0\leqslant z\leqslant 0.1$ and $0.75\leqslant z\leqslant 1)$, and $PbSe_{1-z}Te_z$ $(0\leqslant z\leqslant 1)$, as well as solid solutions with tin monochalcogenides $Pb_{1-x}Sn_xS$ $(0\leqslant x\leqslant 0.1)$, $Pb_{1-x}Sn_xSe$ $(0\leqslant x\leqslant 0.43)$, and $Pb_{1-x}Sn_xTe$ $(0\leqslant x\leqslant 1)$ with a NaCl-type structure. The ^{119}Sn Mössbauer absorption spectra of $Pb_{1-x}Sn_xSe$ solid solutions $(x\leqslant 0.4)$ studied in Ref. 11 were found to consist of single lines (Fig. 2a) corresponding to divalent tin atoms in a cubic environment of chalcogen atoms.

The $Pb_{1-x}Sn_xTe$ solid solutions exhibit band inversion with a gapless state at $x=0.62$ and $x=0.40$ at 295 and 80 K, respectively. The Mössbauer studies carried out in a search for anomalies in the properties of these solid solutions revealed features in the composition dependences of the quadrupole splitting, isomer shift, and Mössbauer coefficient f in the region of existence of the gapless state.[37] These anomalies were interpreted[37] as due to a lowering of symmetry of the tin environment, a change in the conduction-electron concentration, and enhanced electron-phonon interaction in the gapless state. A decrease of the Mössbauer coefficient in the region of the gapless state was found also for the $(PbSe)_{1-x}(SnTe)_x$ solid solutions.[38]

One should point out here some experimental shortcomings of the study in Refs. 37 and 38. First, one used as a gamma-ray source tin dioxide, whose spectral line is broadened more than twice compared to the natural width; this obviously reduces the reliability of determining of the quadrupole splitting and the experimental linewidth. Second, f was found by comparing the areas bounded by normalized spectra, but one did not take into account the effects associated with nonresonant absorption of gamma rays by the lead and tellurium atoms.

All this stimulated an attempt to study the $Pb_{1-x}Sn_xTe$ solid solutions $(0<x<1)$ by ^{119}Sn MAS in order to detect possible changes in the local symmetry of the cation and anion sites, the electronic structure of atoms in these sites, as well as in the electron–phonon coupling in the region of the gapless state. All samples exhibited hole conduction (at 80 K, the hole concentration changed from $10^{17}\,cm^{-3}$ for PbTe to $10^{21}\,cm^{-3}$ for SnTe). The fraction of recoilless gamma-ray absorption f was determined from the relation

$$G_{\exp}=G_a+G_s+0.27G_{\text{nat}}\cdot t, \tag{5}$$

where $t=n\sigma_0 f$, n is the ^{119}Sn surface density of the absorbers, $\sigma_0=1.4\times10^{-18}\,cm^2$ is the maximum absorption cross section at resonance, $G_{\exp}$ is the width of an experimental spectrum, G_a and G_s are the widths of the absorber and source spectral lines, respectively, and G_{nat} is the natural width of the ^{119}Sn spectral line.

Because relation (5) is valid for $(G_{\text{nat}}/G_a)t<5$, this condition was met for all the solid solutions studied and absorbers used. It is essential that the above method of determination of f does not require taking into account the background gamma rays. Extrapolation of relations (5) to $t=0$ permits one to find also the experimental spectral width in the limit of an infinitely thin absorber G_0. Note that it is the dependence on composition of the G_0 quantity rather than of $G_{\exp}$ that one is interested here, because the latter is very sensitive to the chosen absorber surface density [for instance, for a SnTe absorber with a density of $1\,mg/cm^2$ $(n=5\times10^{18}\,cm^{-2})$ the transition from 295 to 80 K is accompanied by an increase of $G_{\exp}$ from 0.98 to 1.40 mm/s].

The ^{119}Sn Mössbauer spectra of all $Pb_{1-x}Sn_xTe$ samples represented single lines whose widths G_0 were close to twice

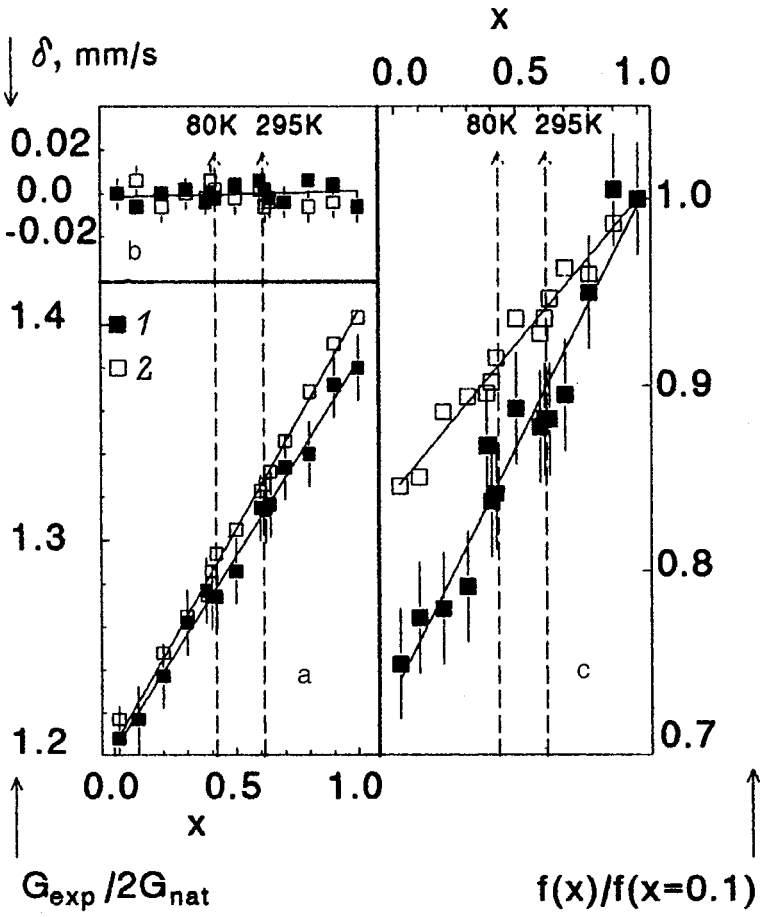

FIG. 4. (a) Dependence of the width of experimental spectra, G_{exp} (in units of double natural width $2G_{nat}$), on composition of the $Pb_{1-x}Sn_xTe$ solid solution (Ref. 39); (b) Dependence of the isomer shift δ (relative to $Pb_{0.99}Sn_{0.01}Te$ at the corresponding temperatures) on composition of the $Pb_{1-x}Sn_xTe$ solid solution (Ref. 39); (c) Dependence of the Mössbauer coefficient ratio $f(x)/f(x=1)$ on composition of the $Pb_{1-x}Sn_xTe$ solid solution (Ref. 39). *1*—295 K, *2*—80 K. The dashed lines refer to the compositions at which the gapless state forms at 80 and 295 K.

the natural width $2G_{nat}$ and increased only insignificantly with x to reach the maximum value for tin telluride (Fig. 4a). The latter is in no way unexpected, because an increase of tin content in a solid solution broadens the region of homogeneity, which gives rise to an increase of the concentration of residual structural defects and, as a consequence, to a growth of Mössbauer spectra in width. No anomalous changes in the width of spectra are observed in the region of the solid-solution gapless state both at 80 and 295 K (Fig. 4a). One may therefore conclude that the local symmetry of cation sites of the $Pb_{1-x}Sn_xTe$ solid solutions does not change throughout the region of existence of the latter.

The isomer shift of Mössbauer spectra is determined by the chemical nature of the atoms in the local environment of a Mössbauer probe. Because the local environment of tin atoms (six tellurium atoms occupying the corners of a regular octahedron) does not change with varying composition of the $Pb_{1-x}Sn_xTe$ solid solution, there is nothing strange in the constancy of the isomer shift of the ^{119}Sn Mössbauer spectra, which coincides with that of the SnTe compound for all compositions within experimental error (Fig. 4b). One observes also no anomalous changes in the electronic structure of atoms on the cation sublattice within the region of existence of the gapless state.

The transition from PbTe to SnTe is accompanied by a monotonic growth of the Mössbauer coefficient for the cation sublattice (Fig. 4c). It is such a behavior of f that should be expected based on the closeness of the Debye temperatures for PbTe (125 K) and SnTe (130 K). Significantly, no anomalous changes in the $f(x)$ relations for compositions near the gapless state are observed either.

This gives one grounds to conclude that ^{119}Sn Mössbauer spectroscopy reveals no changes either in the local site symmetry, or in the electronic structure of atoms, or again in the intensity of electron-phonon interaction in $Pb_{1-x}Sn_xTe$ solid solutions in the region of the gapless state. Note that a similar conclusion was reached in a study[11] of the $Pb_{1-x}Sn_xSe$ solid solutions by ^{119}Sn MAS.

In closing we note that the authors of Ref. 40 studied mixed tin and lead chalcogenides of the $PbSnS_2Se$ type whereas authors of Ref. 41 discovered photostructural transformations in $Pb_{0.2}Sn_{0.8}S$ single crystals.

4. NEUTRAL AND IONIZED STATES OF TIN IMPURITY ATOMS IN LEAD CHALCOGENIDES IN THE LOW-TEMPERATURE DOMAIN

Tin is an isoelectronic substitutional impurity in lead chalcogenides that should be electrically inert. However, at low concentrations, tin in PbS and PbSe was shown[42] to behave as an electrically active impurity and to act as a donor. It is this publication that initiated a number of studies of tin impurity atoms in lead chalcogenides by ^{119}Sn Mössbauer spectroscopy. The authors of Ref. 10 were probably the first to observe charge exchange of tin impurity atoms in PbS as a function of the position of the chemical poten-

TABLE II. Parameters of Mössbauer spectra of ^{119}Sn impurity atoms.

Composition		Sn^{2+}				Sn^{4+}						Carrier concentration, cm^{-3}	
		δ	G	δ	G	δ	G	δ	G	R	R		
x	y	80 K	80 K	295 K	295 K	80 K	80 K	295 K	295 K	80 K	295 K	80 K	295 K
						$Pb_{1-x-y}Sn_xA_yS$							
0.01	0.00	3.70	0.77	3.65	0.76							$n=3\times10^{18}$	$n=3\times10^{18}$
0.01	0.02					1.25	0.78	1.23	0.77			$p=6\times10^{13}$	$p=1\times10^{17}$
0.02	0.02	3.70	0.81	3.60	0.87	1.25	0.83	1.37	0.89	1.08	0.69	$p=6\times10^{13}$	$p=6\times10^{16}$
0.02	0.02	3.76	0.84	3.68	0.89	1.26	0.83	1.32	0.91	1.1	0.7	$p=6\times10^{13}$	$p=6\times10^{16}$*
0.01	0.01	3.69	0.80	3.62	0.85	1.24	0.82	1.36	0.86	1.05	0.71	$p=6\times10^{13}$	$p=6\times10^{16}$
						$Pb_{1-x-y}Sn_xA_ySe$							
0.01	0.00	3.65	0.77	3.63	0.77							$n=2\times10^{18}$	$n=2\times10^{18}$
0.005	0.02					1.52	0.76	1.50	0.77			$p=5\times10^{19}$	$p=5\times10^{19}$
0.01	0.02	3.63	0.85			1.58	0.80			0.16		$p=3\times10^{19}$	$p=3\times10^{19}$
0.017	0.02	3.53	0.92	3.13	1.56	1.58	1.05	2.05	1.37	1.38	3.52	$p=3\times10^{19}$	$p=3\times10^{19}$
0.017	0.02	3.60	0.96	3.12	1.62	1.57	1.07	1.98	1.42	1.3	3.2	$p=3\times10^{19}$	$p=3\times10^{19}$*
0.01	0.01	3.55	0.91	3.12	1.46	1.59	1.05	2.01	1.34	1.25	3.61	$p=3\times10^{19}$	$p=3\times10^{19}$

Note: The errors in determination of δ and G are ±0.02 mm/s and those for R, ±0.05. $R=J_n/J_i$, J_n and J_i are the areas bounded by the spectra of neutral and ionized tin centers.
*Data for Mössbauer emission spectra.

tial in the forbidden gap of the material. This study was followed by a comprehensive investigation of the $Pb_{1-x}Sn_xS$, $Pb_{1-x}Sn_xSe$, $Pb_{1-x}Sn_xTe$, $Pb_{1-x}Sn_xS_{1-z}Se_z$, and $Pb_{1-x}Sn_xS_{1-z}Te_z$ solid solutions.[11–21] We are presenting below the results of Mössbauer studies dealing with identification of the neutral and ionized states of tin impurity atoms in lead chalcogenides and related solid solutions at low temperatures ($T\leqslant295$ K).

4.1. The lead sulfide PbS

In degenerate n-type samples, where the chemical potential is located near the conduction-band bottom, tin centers were observed to exist only in the neutral state $[Sn]^0$ (the charges of the [Sn] centers are given relative to that of the cation sublattice, i.e., of the lead atoms). For such samples one chose the $Pb_{1-x}Sn_xS$ compositions ($x=0.01$) containing stoichiometric lead (it is believed that the energy levels in crystals with excess lead lie within the conduction band, and therefore these samples turned out to be electronic and degenerate, see Table II).[13,15,18,20] Mössbauer spectra of such samples measured at 80 K are single lines (Fig. 5a and Table II) of instrumental width with an isomer shift corresponding to divalent tin Sn^{2+}.

In compensated p-type samples, where the chemical potential lies near the valence-band top, only the ionized state of the tin centers should be observed. One chose for such samples the $Pb_{1-x-y}Sn_xA_yS$ compositions ($x=0.01, y=0.02$). The 80-K Mössbauer spectrum of such samples is a single line (Fig. 5a and Table II) of instrumental width with an isomer shift corresponding to quadrivalent tin Sn^{4+}.[13,15,18,20] Although the samples were p-type, the concentration of holes in them was found to be substantially lower than that of the introduced acceptors.[13,18]

At 80 K, Mössbauer spectra of $Pb_{1-x}Sn_xS$ and $Pb_{1-x-y}Sn_xA_yS$ samples can be explained by assuming that the impurity tin atoms substitute in the PbS cubic lattice for lead atoms to form donor states, whose ionization energy corresponds to a level in the lower half of the gap. Thus the Sn^{2+} divalent-tin line in Mössbauer spectra is produced by neutral ($[Sn]^0$), and the line of quadrivalent tin Sn^{4+}, by doubly ionized states ($[Sn]^{2+}$) of the tin donor center in PbS. By varying properly the tin to acceptor concentration ratio in PbS, one can obtain in the Mössbauer spectrum the Sn^{2+} and

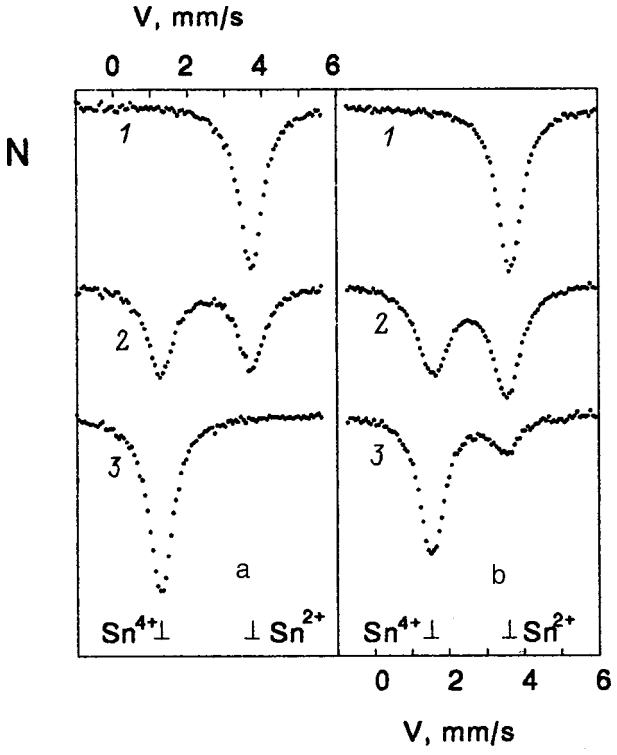

FIG. 5. Mössbauer spectra of ^{119}Sn impurity atoms in (a) $Pb_{1-x-y}Sn_xA_yS$ and (b) $Pb_{1-x-y}Sn_xA_ySe$ (Ref. 10): *1*—$x=0.01$, $y=0$; *2*—$x=0.01$, $y=0.01$, *3*—$x=0.01$, $y=0.02$.

Sn^{4+} lines with any intensity ratio.[20] In particular, Fig. 5a presents a spectrum of a partially compensated $Pb_{1-x-y}Sn_xA_yS$ sample ($x=0.01, y=0.01$), which represents a superposition of two lines, Sn^{2+} and Sn^{4+}, of about equal intensity.

Tin in PbS is an isoelectronic impurity, and therefore charge exchange of such an impurity observed with a change in position of the chemical potential in the gap is in itself an anomalous phenomenon. An additional feature is that the isomer shifts correspond to the tin charge changing by two. This suggests an interesting possibility to assign the Mössbauer line corresponding to ionized donor centers not to the quadrivalent state Sn^{4+} (in accordance with the magnitude of the isomer shift) but rather to the trivalent one, Sn^{3+} (while this state is not observed in tin compounds, its existence for impurity atoms cannot be ruled out). However this interpretation would contradict the dependence of the Sn^{2+}/Sn^{4+} line intensity ratio

$$R=J_n/J_i=f_nN_n/f_iN_i \tag{6}$$

observed in Mössbauer spectra of $Pb_{1-x-y}Sn_xA_yS$ samples on the tin (N) to acceptor (N_a) concentration ratio (here J_n and J_i are the Mössbauer line intensities corresponding to the neutral and ionized states of the tin donor center, N_n and N_i are the concentrations of these centers, and f_n and f_i are the Mössbauer coefficients for these centers).

Indeed, the expression for R can be recast in the form

$$R=k\{[f_n/f_i][N/(N_a-p)]\}-f_n/f_i, \tag{7}$$

where $k=1$ for the ionized center corresponding to Sn^{3+} (the charge neutrality equation $N_i=N_a-p$) or $k=2$ if the ionized tin center corresponds to Sn^{4+} (with this equation reading $2N_i=N_a-p$).

The experimental dependence of R on $N/(N_a-p)$ for $Pb_{1-x-y}Sn_xA_yS$ solid solutions is shown in Fig. 6a.[13,18] We readily see that the experimental data are well fitted by relation (7) with $k=2$ (here p may be neglected, because $p \ll N_a$). Hence to the ionized tin donor centers in PbS corresponds the quadrivalent state Sn^{4+}. Extrapolation of the experimental straight line to $N/(N_a-p)=0$ yields $f_n/f_i=0.93\pm0.01$.

Thus tin impurity atoms in PbS sit at regular sites of the cation sublattice and are two-electron donors. The absence in Mössbauer spectra measured at 80 K on partially compensated samples of the Sn^{3+} line indicates that tin forms in PbS two-electron donor centers with negative correlation energy, i.e. that the single-ionization energy of this center is larger than one half of its double-ionization energy. Finally, the hole nature of conduction and the absence of degeneracy in $Pb_{1-x-y}Sn_xA_yS$ samples implies that the chemical potential associated with the tin donor-level system lies in the lower half of the semiconductor gap (and, hence, that the tin donor levels are also located in its lower half).

4.2. The lead selenide PbSe

Tin donor centers in degenerate n-type PbSe samples (doped with excess lead) exhibit only the neutral state. In particular, the 80-K Mössbauer spectrum of $Pb_{1-x}Sn_xSe$ ($x=0.01$) samples consists of a single line whose isomer shift corresponds to divalent tin Sn^{2+} (Fig. 5b and Table II).[13,15,18] This spectrum relates to neutral tin donor centers $[Sn]^0$.

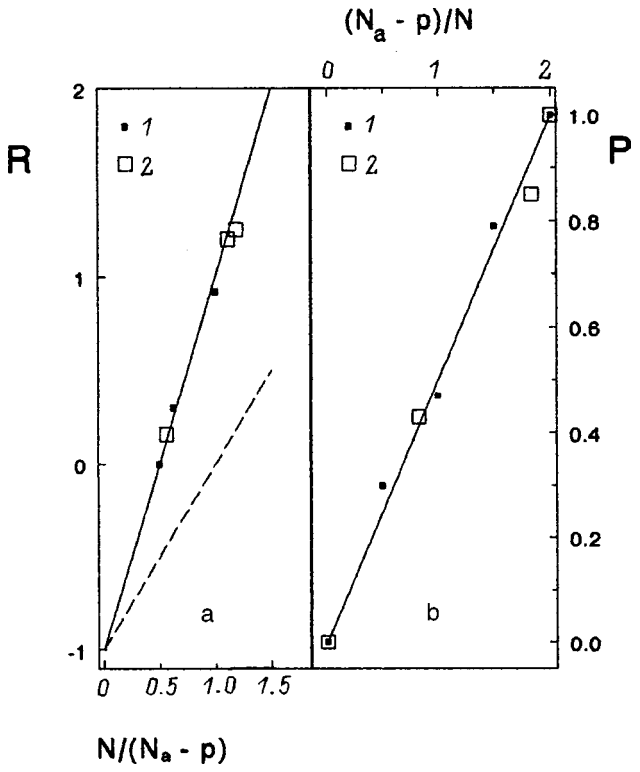

FIG. 6. (a) Dependence of $R=J_n/J_i$ on $N/(N_a-p)$ for (*1*) PbS:Sn,A and (*2*) PbSe:Sn,A (here J_n and J_i are the intensities of the lines corresponding to the neutral and ionized tin centers).[18] The solid and dashed lines are relationships calculated for the case of tin being a two- and one-electron center, respectively. (b) Dependence of $P=N_n/(N_n+N_i)$ on $(N_a-p)/N$ for (*1*) $Pb_{0.99}Sn_{0.01}A_yS$ and (*2*) $Pb_{0.99}Sn_{0.01}A_ySe$ (here N_n and N_i are the concentrations of neutral and ionized tin centers, respectively).[20] When deriving the concentrations of the Sn^{2+} and Sn^{4+} centers from Mössbauer spectra, the Mössbauer coefficient ratio for these centers was assumed to be 0.93 ± 0.01.

The experimental spectrum obtained at 80 K with a p-type $Pb_{1-x-y}Sn_xA_ySe$ compensated sample ($N_a=2N$, $x=0.01, y=0.02$) is not a single line due to Sn^{2+} but rather a superposition of the Sn^{4+} and Sn^{2+} lines, with $R=0.16\pm0.05$ (Fig. 5b and Table II).[13,15,18] Similarly, the spectrum of a partially compensated $Pb_{1-x-y}Sn_xA_ySe$ sample ($x=0.01, y=0.01$) obtained at 80 K is a superposition of two lines due to Sn^{2+} and Sn^{4+}, with the line intensity ratio $R=1.25\pm0.05$ (Fig. 5b and Table II).[20] Fully ionized tin centers can be obtained only in $Pb_{1-x-y}Sn_xA_ySe$ samples with an acceptor concentration considerably in excess of twice the donor concentration.[11,20] In particular, the Mössbauer spectrum of a sample with $x=0.005$ and $y=0.02$ contains only the Sn^{4+} line (Table II). This is accounted for by the fact that the level system in PbSe associated with the tin centers lies within the valence band. As a result, the chemical potential associated with the partially filled tin level lies also within the valence band, and the concentration of holes becomes comparable to that of acceptors. Therefore in order to describe the dependence of R on tin and acceptor concentra-

tions of the type of (7), one should include the hole concentration in the charge neutrality equation.

As seen from Fig. 6a, the experimental data for the $Pb_{1-x-y}Sn_xA_ySe$ solid solutions are well reproduced by the relation (7) with $k=2$.[13,18] Extrapolation of (7) in Fig. 6a to $N/(N_a-p)=0$ permits one to determine the ratio $f_n/f_i=0.93\pm0.01$, which was found to be the same for PbS and PbSe. Thus the Mössbauer coefficient for the quadrivalent state Sn^{4+} turns out to be larger than that for the divalent Sn^{2+} state. This does not come as a surprise, because the magnitude of f for quadrivalent tin compounds is always larger than that for the divalent ones of the same type.

4.3. The tin telluride PbTe

Besides tin, PbTe was also doped with an acceptor impurity (Na or Tl). The content of tin in the $Pb_{1-x-y}Sn_xA_yTe$ solid solutions was varied within the range $0.005<x<0.03$, and the acceptor codopant was introduced in amounts of $0<y<0.02$. All samples were p-type with a hole concentration $p\sim10^{19}-10^{20}\,cm^{-3}$.

It was found that, irrespective of the tin to acceptor concentration ratio, the Mössbauer spectra exhibit only one line corresponding to the divalent tin Sn^{2+}.[11] This means that the tin energy levels lie within the valence band deep under the level of the chemical potential, deeper than the largest attainable Fermi energies in PbTe doped with Tl or Na (i.e. they are spaced by more than 0.2 eV from the valence-band top at the L point of the Brillouin zone).

4.4. The $PbS_{1-z}Se_z$ solid solutions

As shown in the two preceding subsections, the isoelectronic tin impurity in PbS and PbSe acts as a two-electron negative-U center. The energy levels associated with the tin center change their position as one transfers from PbS to PbSe, namely, in PbS they are in the lower half of the gap, and in PbSe they are located within the valence band. A question naturally arises about the position of tin levels in the $PbS_{1-z}Se_z$ solid solutions. To answer it, $Pb_{1-x-y}Sn_xA_yS_{1-z}Se_z$ solid solutions ($z=0, 0.2, 0.4, 0.5, 0.6, 0.7, 0.8, 1.0$), with fixed tin and acceptor impurity (sodium, thallium) concentrations ($x=y=0.02$ or $x=y=0.01$), were studied.[16,17,20] All the samples were p-type, and in $z<0.6$ compositions the carrier concentration was temperature-dependent, while the compositions with $z>0.7$ were degenerate. One could expect the Mössbauer spectra obtained for a chosen tin-to-acceptor concentration ratio to contain two lines (Sn^{2+} and Sn^{4+}) of equal intensity. It was found, however, that $R\neq1.00$ for all compositions. One can conceive of two reasons for R deviating from 1.00: first, a difference between f_n and f_i and, second, the presence of holes in a substantial concentration, if the tin levels lie within the valence band. Using the $f_n/f_i=0.93$ ratio determined above, one finds $K=N_n/N_i$ for the $PbS_{1-z}Se_z$ solid solutions. As seen from Fig. 7a, for $z<0.6$ one obtains $K=1.00\pm0.01$, i.e. for the $z<0.6$ solid solutions the tin levels are located in the lower half of the gap. For $z>0.7$, $K>1.0$ (Fig. 7b), i.e., for these solid solutions the tin levels lie within the valence band. Thus Mössbauer spectroscopy permits qualitative determination of the position of the energy levels created by tin impurity atoms in the $PbS_{1-z}Se_z$ solid solutions.

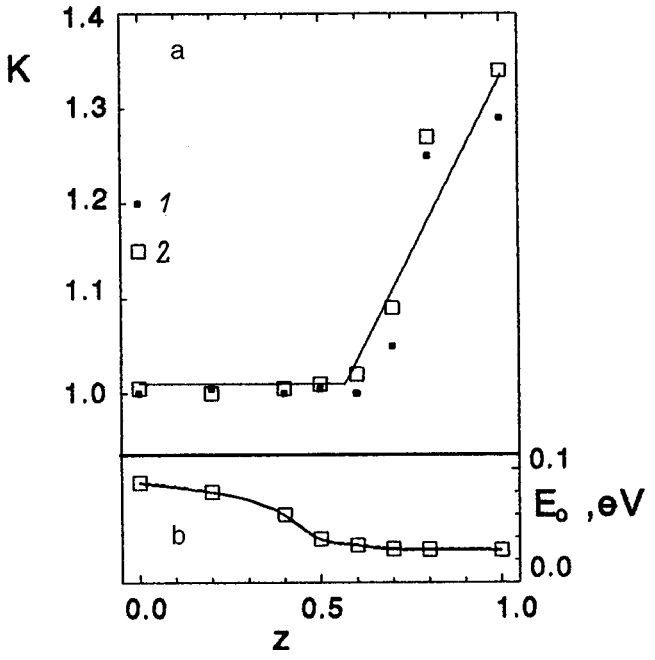

FIG. 7. (a) Dependence of $K=N_n/N_i$ on z for the $Pb_{1-x-y}Sn_xA_yS_{1-z}Se_z$ solid solutions with (*1*) $x=y=0.01$ and (*2*) $x=y=0.02$ (Ref. 20). (b) Dependence of the activation energy E_0 of electronic exchange between tin centers on z for the $Pb_{0.96}Sn_{0.02}Na_{0.01}Tl_{0.01}S_{1-z}Se_z$ solid solution.[20]

4.5. The $PbS_{1-z}Te_z$ solid solutions

$Pb_{1-x}Sn_xTe$ does not exhibit any manifestation of tin impurity states in either n- or p-type samples. If they do exist, they should lie deep in the valence band (substantially lower than the highest Fermi energy attainable by acceptor doping). In the $PbS_{1-z}Te_z$ solid solutions one may expect their shift in the vicinity of the chemical potential. To fix the position of the chemical potential, one introduced, besides tin, a Tl impurity creating a relatively narrow band of partially filled resonance states in the valence band, whose position practically does not change throughout the solid-solution compositional range studied.

It was found that Mössbauer spectra of the solid solutions with a sulfur content $1-z>0.15$ consist of two lines corresponding to di- and quadrivalent tin (for example, the Mössbauer spectrum of a $Pb_{1-x-y}Sn_xA_yS_{0.2}Te_{0.8}$ sample ($x=0.01, y=0.02$) is a superposition of the Sn^{2+} and Sn^{4+} lines, with $\delta=3.67\pm0.02$ mm/s for Sn^{2+}, $\delta=1.58\pm0.02$ mm/s for Sn^{4+}, and $R=0.67\pm0.05$.[21] Thus by increasing the PbS content in the $Pb_{1-x}Sn_xS_{1-z}Te_z$ solid solution one can raise, as it were, the tin impurity states from deep in the valence band to the level of the chemical potential and observe effects associated with a change in the charge state of tin.

4.6. Model of the two-electron tin center in lead chalcogenides

The discovery by Mössbauer spectroscopy of the dependence of the charge state of tin impurity atoms in lead chalcogenides on the position of the chemical potential stimulated intensive investigation of these materials by methods based on measuring of the electrical conductivity, Hall effect, thermopower, and optical absorption.[43–53]

For instance, measurements[43,44] of the Hall effect permitted determination of the energies of two-electron tin impurity states in $Pb_{1-x}Sn_xS$ and $Pb_{1-x}Sn_xSe$ for small x. In $Pb_{1-x}Sn_xSe$ with $x=0.02$, the tin donor states lie in the valence band (for $T=0$ K, at 0.17 eV from its top), and rise with increasing temperature at a rate of -1.6×10^{-4} eV/K. At high temperatures the impurity level acts as an acceptor. This behavior of tin is interpreted by a model in which impurity atoms residing in different charge states occupy inequivalent lattice sites at low temperatures and, as a result, they can be identified by different energies.[44] The inequivalence of atoms in different charge states decreases with increasing temperature to vanish altogether at a certain composition-dependent temperature.

A comprehensive investigation of the defect energy spectrum in $Pb_{1-x}Sn_xSe$:Na crystals was carried out by measuring the Seebeck coefficient, Hall effect, thermopower,[48,50,52] and optical absorption.[45,47,53] Attempts to explain the temperature dependences of the electrical conductivity, thermopower, and Hall effect of the $Pb_{1-x-y}Sn_xA_ySe$ solid solutions (A=Na, Tl) in terms of a single-level model did not meet with success. According to the concepts developed in Ref. 52, tin exhibits donor activity only at low temperatures (for instance, in the case of PbSe for $T<200$ K), whereas as the temperature is increased, tin transforms into an acceptor. Obviously enough, this can occur if at low temperatures the neutral (Sn^{2+}) and ionized (Sn^{4+}) tin centers in the PbSe lattice occupy different sites; for instance, the Sn^{4+} ion can distort strongly its nearest-neighbor environment to form associates with vacancies or ionized acceptors.[52] As the temperature increases, this distorted local environment of the Sn^{4+} ions becomes less stable, and the tendency to Sn^{2+} formation increases. At some critical temperature (according to Ref. 52, at $T>200$ K for PbSe), the Sn^{2+} and Sn^{4+} sites are no longer inequivalent, and this facilitates electron localization at the Sn^{4+} centers, which converts them to Sn^{2+}. An essential drawback of the concepts developed in Ref. 52 is the lack of any evidence for the existence of such associates not only in Mössbauer spectra but in the optical absorption spectra of the $Pb_{1-x-y}Sn_xA_yS$ and $Pb_{1-x-y}Sn_xA_ySe$ solid solutions as well.[49,53]

A model was proposed[21] based on Mössbauer studies[10–20] which permits one to describe the isovalent (isoelectronic) tin impurity in lead chalcogenides (PbS, PbSe) and related solid solutions ($PbS_{1-z}Se_z$) as a two-electron U^- donor. The 80-K ^{119}Sn Mössbauer spectra of the $Pb_{1-x-y}Sn_xA_yS$ solid solutions obtained on compositions with the acceptor content $0<y<2x$ were interpreted as a superposition of two lines with the isomer shifts corresponding to Sn^{2+} and Sn^{4+}, and the fraction of the Sn^{4+} centers $P=N_i/(N_n+N_i)$ (here N_n and N_i are the concentrations of the Sn^{2+} and Sn^{4+} centers, respectively) was assumed to be directly proportional to the acceptor concentration, with a coefficient of proportionality of two (Fig. 6b). Thus tin in PbS is a two-electron donor, with the Sn^{2+} and Sn^{4+} ions corresponding to the neutral, $[Sn]^0$, and doubly ionized, $[Sn]^{2+}$, tin centers, respectively. The charge neutrality condition can be written

$$2N_i=N_a-p, \tag{8}$$

and the hole concentration p may be neglected, because at 80 K $N\gg p$. Because the samples with $0<y<2x$ were p-type, and the hole concentration was temperature dependent, the chemical potential μ associated with the partially ionized tin donor level should lie in the lower half of the gap. This pattern of tin behavior accords with data on the temperature dependences of electrical conductivity, the Seebeck coefficient, and Hall effect for the $Pb_{1-x-y}Sn_xA_yS$ solid solutions.[44]

Figures 8 and 9 present the density-of-states distributions as functions of compensation ratio for the $Pb_{1-x-y}Sn_xA_yS$ solid solutions for the $U>0$ and $U<0$ cases, respectively. Also shown are the expected shapes of

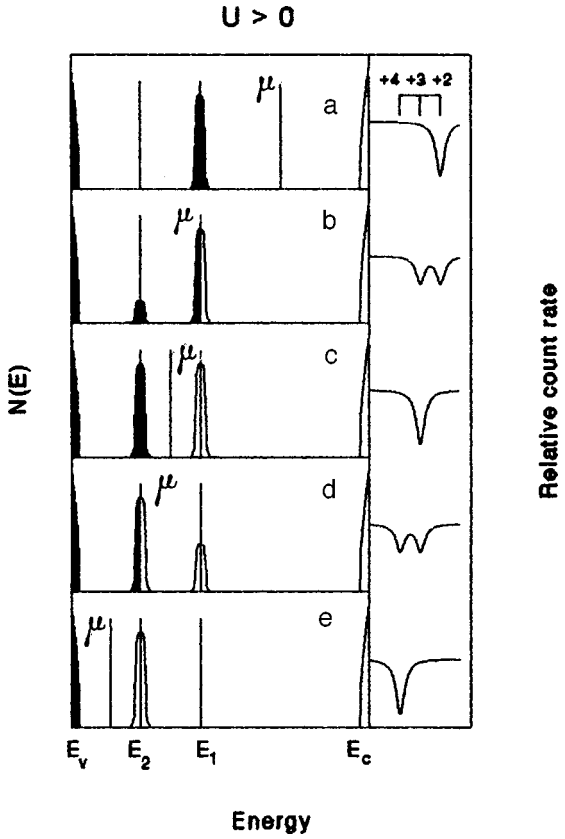

FIG. 8. Density of states for $Pb_{1-x-y}Sn_xA_yS$ ($U>0$) for the cases of $N_a=0$ (a), $0.5N$ (b), N (c), $1.5N$ (d), and $2N$ (e).[20] The dark and bright regions of the E_1 band refer to the neutral, $[Sn]^0$ (Sn^{2+}), and singly ionized, $[Sn]^+$ (Sn^{3+}), tin centers. The dark and bright regions of the E_2 band correspond to singly ionized and doubly ionized, $[Sn]^{2+}$ (Sn^{4+}), tin centers. Presented on the right are the expected ^{119}Sn Mössbauer spectra (shown on top are their positions corresponding to the Sn^{4+}, Sn^{3+}, and Sn^{2+} ions).

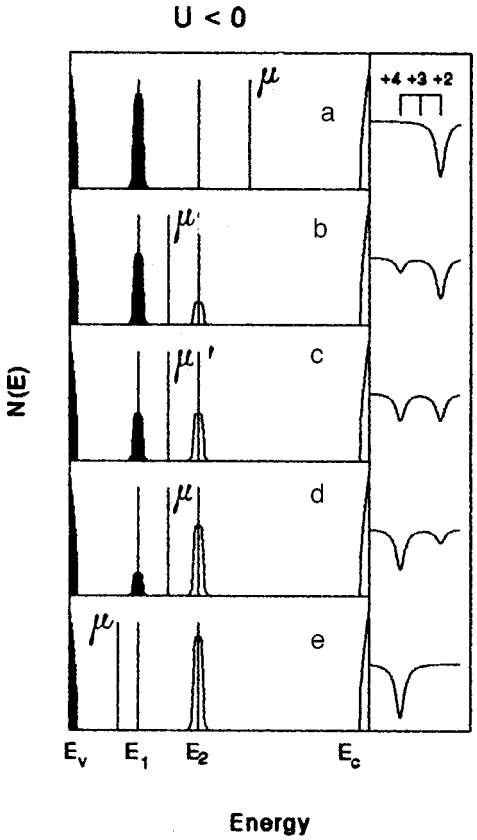

FIG. 9. Density of states for $Pb_{1-x-y}Sn_xA_yS$ ($U<0$) for the cases of $N_a=0$ (a), $0.5N$ (b), N (c), $1.5N$ (d), and $2N$ (e).[20] The dark region of the E_1 band refers to neutral, $[Sn]^0$ (Sn^{2+}), tin centers, and its bright region E_2 corresponds to doubly ionized, $[Sn]^0$ (Sn^{4+}), tin centers. Presented on the right are the expected ^{119}Sn Mössbauer spectra (shown on top are their positions corresponding to the Sn^{4+}, Sn^{3+}, and Sn^{2+} ions).

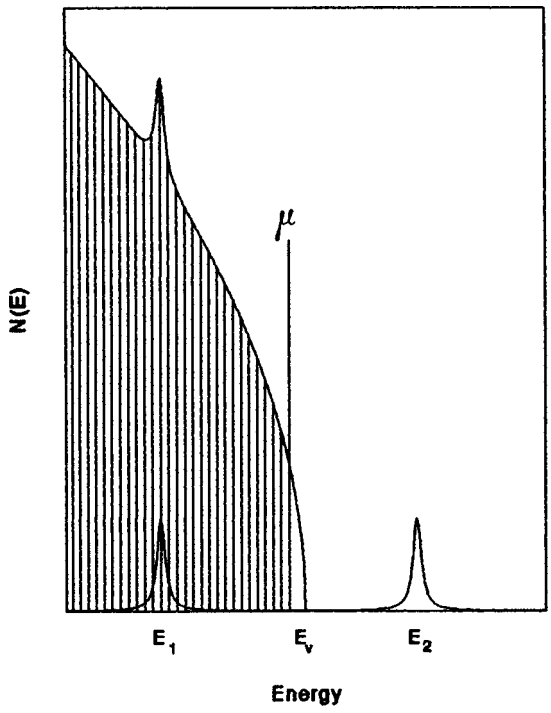

FIG. 10. Electron density of states for $Pb_{1-x-y}Sn_xA_ySe$ ($U<0$) for $x=y$.[20] For explanations see the caption to Fig. 9.

^{119}Sn Mössbauer spectra. A comparison of experimental (Fig. 5a) with theoretical (Figs. 8 and 9) Mössbauer spectra provides a convincing argument for the correlation energy for the two-electron tin centers in PbS being $U<0$.

The situation does not change radically for the $Pb_{1-x-y}Sn_xA_ySe$ solid solutions; indeed, for partially compensated samples ($0<y<2x$) the ^{119}Sn Mössbauer spectra obtained at 80 K represent a superposition of the Sn^{2+} and Sn^{4+} lines (Fig. 5b), but the fraction of the Sn^{4+} centers is proportional to $[N_a-p]$ (Fig. 6b). This is explained by the fact that the chemical potential associated with the partially ionized tin donor level in PbSe lies below the valence-band maximum [the samples with $0<y<2x$ were p-type and degenerate, so that, in the charge neutrality equation (8), one should take into account the concentration of holes, which is comparable to that of tin].

Thus the parameter $U<0$ in PbSe and the tin centers are two-electron. However the energy levels associated with tin are within the valence-band spectrum. Note that this conclusion accords with data[44,52] on the temperature dependences of the electrical conductivity and the Seebeck and Hall coefficients obtained on the $Pb_{1-x-y}Sn_xA_ySe$ solid solutions. Figure 10 displays the density-of-states distribution for partially compensated $Pb_{1-x-y}Sn_xA_ySe$.

It is essential that the width of Mössbauer spectra of $Pb_{1-x-y}Sn_xA_yS$ and $Pb_{1-x-y}Sn_xA_ySe$ containing only one tin state (Sn^{2+} for $y=0$ and Sn^{4+} for $y>2x$, see Fig. 5) is close to the instrumental width (0.77 ± 0.02 mm/s) and depends neither on the solid-solution composition nor on the measurement temperature (80–295 K).[17,20] The closeness of the width of experimental spectra of the solid solutions to the instrumental width excludes the possibility of spectral decomposition into quadrupole doublets. In other words, the search for differences in local-environment symmetry between the Sn^{2+} and Sn^{4+} centers by Mössbauer spectroscopy produced a negative result. In both cases, tin resides at the center of a regular chalcogen octahedron, and this environment depends neither on the solid-solution composition nor on temperature. Various associations of the Sn^{4+} centers with lattice defects and ionized acceptors are observed to exist only in incompletely homogenized materials, but even in this case their fraction does not exceed 0.1 of the total tin concentration.[15]

5. TWO-ELECTRON EXCHANGE BETWEEN NEUTRAL AND IONIZED TIN DONOR CENTERS IN LEAD CHALCOGENIDES

We have shown in the preceding section that Mössbauer spectroscopy is an efficient means for probing the charge state of impurity atoms in semiconductors. However Mössbauer spectroscopy also opens up possibilities for studying electronic exchange between neutral and ionized impurity centers in a partially compensated material (if the chemical potential is stabilized in the energy band formed by impurity atoms).[54] These studies were first reported for the case of tin impurity atoms in lead selenide in Ref. 12, followed by a series of similar investigations.[13–21] This Section presents the

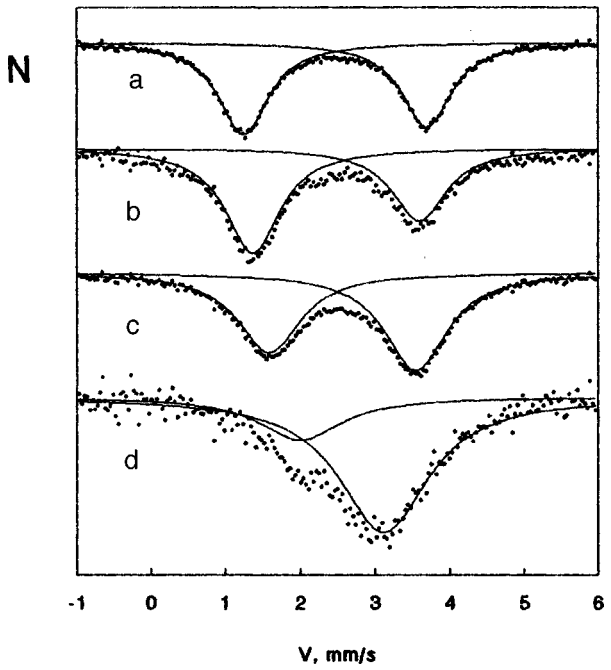

FIG. 11. Mössbauer spectra for ^{119}Sn impurity atoms in (a,b) $Pb_{0.96}Sn_{0.02}Na_{0.01}Tl_{0.01}S$ and (c,d) $Pb_{0.96}Sn_{0.02}Na_{0.01}Tl_{0.01}Se$ obtained at (a,c) 80 K and (b,d) 295 K.[20]

main experimental results and their interpretation for the case of two-electron exchange between neutral and ionized tin centers in lead chalcogenides and related solid solutions.

5.1. Lead selenide

To study electron exchange between tin centers, we chose $Pb_{1-x-y}Sn_xA_ySe$ solid solutions containing about equal amounts of the $[Sn]^{2+}$ and $[Sn]^{4+}$ centers ($x=0.017, y=0.02$ in Fig. 11).[13–15,19] Because of the electron exchange between Sn^{4+} and Sn^{4+}, each tin center resides part of the time in the neutral (τ_n), and another part, in the ionized (τ_i) state. If the lifetime of the tin centers in each of these states exceeds by far that of the ^{119}Sn Mössbauer level ($\tau_0=20$ ns), the Mössbauer spectrum will be actually a superposition of the $[Sn]^0$ and $[Sn]^{2+}$ spectra, with the ratio of the areas bounded by the corresponding lines (J_n and J_i) being defined as

$$R=J_n/J_i=f_n\tau_n/f_i\tau_i. \tag{9}$$

If, however, τ_n and τ_i become smaller than τ_0, the $[Sn]^{2+}$ and $[Sn]^0$ lines in the Mössbauer spectrum will approach one another, so that, in the limit of fast electron exchange ($\tau_n, \tau_i \ll \tau_0$), the spectrum will represent a single line corresponding to an ''averaged'' state of the tin center with an isomer shift

$$\delta=(\delta_i+R\delta_n)/(R+1). \tag{10}$$

As seen from Fig. 11, the Mössbauer spectra of the above-mentioned sample measured at 80 and 295 K represent a superposition of two single lines corresponding to Sn^{2+} and Sn^{4+}, but their isomer shifts depend substantially on temperature (see Table II). At 80 K, the isomer shifts of the Sn^{2+} and Sn^{4+} lines of this sample are close to those of the $[Sn]^0$ and $[Sn]^{2+}$ centers described above, although the Sn^{2+} and Sn^{4+} lines are observed to become slightly closer to one another. This evidences the onset of a slow electronic exchange between the $[Sn]^0$ and $[Sn]^{2+}$ centers in PbSe taking place at 80 K ($\tau_n, \tau_i > \tau_0$). An increase of temperature is accompanied by a sharp decrease of separation between the Sn^{2+} and Sn^{4+} lines; this is an unambiguous indication of electronic exchange occurring between the $[Sn]^0$ and $[Sn]^{2+}$ states, and the characteristic time of exchange between the states turns out to be of the order of τ_0, because, rather than containing one line of the ''averaged'' state, the spectrum retains the individual Sn^{2+} and Sn^{4+} lines. It should be stressed that the isomer shifts of the $[Sn]^0$ and $[Sn]^{2+}$ centers depend only weakly on temperature, and therefore the decrease in separation between the lines observed to occur in the spectrum of the above sample with increasing temperature cannot be assigned to a temperature dependence of the isomer shift of each of the $[Sn]^0$ and $[Sn]^{2+}$ states. Finally, we note that the observed electronic exchange between the $[Sn]^0$ and $[Sn]^{2+}$ centers in PbSe reflects simultaneous transfer of two electrons, because, as seen from experimental Mössbauer spectra, this exchange does not result in the formation of a singly ionized $[Sn]^+$ center (it would correspond to the trivalent tin Sn^{3+}).

In principle, one can conceive of two possible mechanisms of electronic exchange between the tin centers: tunneling electron transfer directly between tin ions and exchange between tin centers via valence-band states. In the first case, the electron transfer rate should depend on the tin concentration. To observe this effect, a $Pb_{1-x-y}Sn_xA_ySe$ sample with $x=0.01, y=0.01$ was prepared. It was found that the Sn^{2+} and Sn^{4+} Mössbauer lines of this sample coincide in width and position with those of the corresponding spectra obtained on a sample with $x=0.017, y=0.02$ (Table II).[13,15] Hence the frequency of electronic exchange is practically independent of tin concentration, and one may neglect direct exchange between the $[Sn]^0$ and $[Sn]^{2+}$ centers.

Note that the energies of the tin levels in PbSe correspond to valence-band states, but the temperature dependence of the exchange frequency ν indicates that electron transfer between the tin-center localized states and the delocalized states of the valence band requires an energy expenditure, which is equivalent to the existence of an energy barrier between them.

If neutral and ionized tin centers are present in comparable concentrations in a sample, the structure of the ^{119}Sn Mössbauer spectra depends both on the electronic exchange frequency ν between the $[Sn]^0$ and $[Sn]^{2+}$ centers and on the actual version of the Mössbauer spectroscopy employed.

1. If the electronic exchange time between $[Sn]^0$ and $[Sn]^{2+}$, $\tau=1/\nu$, is much shorter than the lifetime of the ^{119}Sn Mössbauer level ($\tau_0 \sim 10^{-8}$ s), then both the absorption and emission Mössbauer spectra will have a single line with an isomer shift described by Eq. (10).

2. If $\tau \gg \tau_0$, then the Mössbauer absorption spectrum will contain two lines corresponding to $[Sn]^0$ and $[Sn]^{2+}$, with an intensity ratio close to R. However only one line corresponding to $[Sn]^{2+}$ will be retained in the Mössbauer emission spectrum. This is because the 65-keV isomeric

transition in ^{119mm}Sn involving internal conversion, which precedes the Mössbauer transition and is accompanied by an Auger process, gives rise to formation of highly charged tin states. In times much shorter than the lifetime of the ^{119m}Sn Mössbauer level τ_0, these states transfer to Sn^{4+}. Because at 80 K the time τ it takes the $[Sn]^0$ and $[Sn]^{2+}$ states in a $Pb_{1-x-y}Sn_xA_ySe$ sample ($x=0.017, y=0.02$) to equilibrate is much longer than τ_0, the Mössbauer emission spectrum of a sample of this composition should have at 80 K only one, the Sn^{4+} line. At 295 K, $\tau \sim \tau_0$, and one should observe in the Mössbauer emission spectrum both lines ($[Sn]^0$ and $[Sn]^{2+}$), however the intensity of the $[Sn]^0$ line should be substantially lower than that in the absorption spectrum of a sample of the same composition.

To test these conclusions, a sample with $x=0.017$ and $y=0.02$ labeled with the ^{119mm}Sn radioactive isotope was prepared, and its Mössbauer emission spectra were measured at 80 and 295 K.[15,19] As seen from Table II, the structure of the emission spectra is close to that of the absorption spectra, and their processing showed them to be close in parameters too.

There can be two reasons for the anomalous behavior of Mössbauer emission spectra, namely, different local environments of the $[Sn]^0$ and $[Sn]^{2+}$ centers, and the existence of a specific mechanism of equilibration among the tin centers operating in the case of originally ionized tin atoms. Formation of associations of Sn^{4+} ions with ionized acceptors may be the natural cause of a difference in the local environments of $[Sn]^0$ and $[Sn]^{6+}$. An attempt was made to detect the existence of such associations by measuring the width of the ^{119}Sn line in samples with $x=0.01, y=0$ (they have only $[Sn]^0$ centers) and with $x=0.005, y=0.02$ (they contain only $[Sn]^{2+}$ centers); indeed, the presence of such associations should result at any rate in a broadening of the spectrum of the second sample. However, as seen from Table II, the linewidth in both spectra was found to be the same and equal to the instrumental width. Hence it is most probable that the existence of a specific mechanism of equilibration among the $[Sn]^0$ and $[Sn]^{2+}$ centers causes the neutralization of highly charged tin atoms.[20]

5.2. Lead sulfide

To study the process of electronic exchange between the tin centers in PbS, a $Pb_{1-x-y}Sn_xA_yS$ sample with $x=0.02, y=0.02$ was chosen.[13–15,19] As seen from Fig. 11 and Table II, the spectra of this sample obtained at 80 and 295 K contain only the Sn^{2+} and Sn^{4+} lines, whose isomer shifts practically coincide with those of the above $[Sn]^0$ and $[Sn]^{2+}$ centers, and only a slight decrease of their separation is observed. The decrease in the line spacing does not depend on the concentration of the impurity tin atoms (see Table II). In other words, electronic exchange between the $[Sn]^0$ and $[Sn]^{2+}$ centers in PbS occurs considerably slower than it does in PbSe. To understand this phenomenon, one has to take into account that the rate of electronic exchange is dominated by valence-band states, and in PbSe this process is obviously facilitated by the Sn 5*s* levels lying in the valence band. Finally, if one of the tin-center charge-exchange stages involves hole capture, the conditions for this in PbSe are most favorable, because the hole concentration in this material is substantially higher than that in PbS.

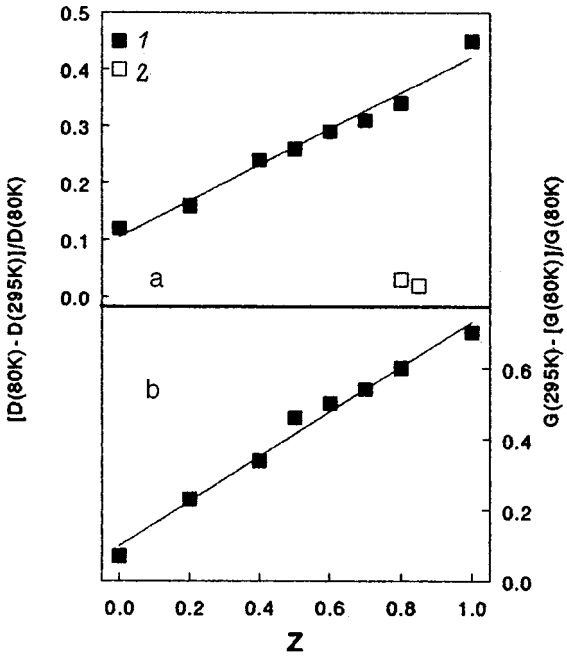

FIG. 12. Dependences on z of the relative change in the spacing between the Sn^{2+} and Sn^{4+} lines (a) and in the width of these lines (b) with the temperature increased from 80 to 295 K for the (*1*) $Pb_{0.96}Sn_{0.02}Na_{0.01}Tl_{0.01}S_{1-z}Se_z$ and (*2*) $Pb_{0.95}Sn_{0.03}Tl_{0.02}S_{0.2}Te_{0.8}$ solid solutions. Here $D(80\text{ K})$ and $D(295\text{ K})$ are the distances (in mm/s) between the Sn^{2+} and Sn^{4+} lines at 80 and 295 K, respectively; $G(80\text{ K})$ and $G(295\text{ K})$ are, accordingly, the widths (in mm/s) of the Sn^{2+} spectrum at 80 and 295 K.

We note in conclusion that the ^{119}Sn Mössbauer emission spectra of the $Pb_{1-x-y}Sn_xA_yS$ sample ($x=0.02, y=0.02$) exhibit the same features as those of the $Pb_{1-x-y}Sn_xA_ySe$ sample with $x=0.017, y=0.02$ (see Table II), and that their interpretation can be given in terms of the model[15,19] discussed above.

5.3. $Pb_{1-z}Se_z$ solid solutions

The widths of the spectra, as well as the isomer shifts of the Sn^{2+} and Sn^{4+} lines, in solid solutions containing both the Sn^{2+} and Sn^{4+} centers depend on the temperature at which the spectra were measured. Such dependences were studied for $PbS_{1-z}Se_z$ solid solutions containing tin and the acceptor in equal concentrations, $Pb_{0.96}Sn_{0.02}Na_{0.01}Tl_{0.01}S_{1-z}Se_z$ with $0<z<1$.[16,17,20] In all samples, an increase of temperature from 80 to 295 K was accompanied by a decrease in the separation between the Sn^{2+} and Sn^{4+} lines, and this decrease, as seen from Fig. 12, is the larger the larger is z. One observes simultaneously an increase of the Sn^{2+} and Sn^{4+} lines in width (Fig. 12).

Note that such temperature dependences of the isomer shifts and linewidths are characteristic of the case of electronic exchange between two charge states of a Mössbauer atom, if the lifetime of each of the states is comparable to that of the Mössbauer level (for ^{119}Sn this time is about 20 ns). One measured also the frequency of elec-

tronic exchange between the Sn^{2+} and Sn^{4+} states in the $Pb_{0.96}Sn_{0.02}Na_{0.01}Tl_{0.01}S_{1-z}Se_z$ solid solutions within the 80–295 K range, and Fig. 7b presents the dependence of the activation energy of the process, E_0, on z (Ref. 17 and 20). One readily sees that, as the selenium content z in a solid solution increases, E_0 first decreases monotonically to reach at $z=0.7$ the limiting value of 0.029 eV, after which it remains constant within the measurement error. A comparison of the $P(z)$ and $E_0(z)$ dependences (see Fig. 7b) permits a conclusion that the limiting value of E_0 is reached at the same z at which the chemical potential enters the valence band.

Two mechanisms of electronic exchange between the Sn^{2+} and Sn^{4+} centers are possible, namely, tunneling electron transfer directly among the tin ions and electron transfer via valence-band states. The electron-exchange frequency on the first model should depend on the concentration of the tin impurity atoms and be temperature independent. Because one does not observe any dependence of the rate of decrease of the separation between the Sn^{2+} and Sn^{4+} lines in the $Pb_{1-x-y}Sn_xA_ySe$ Mössbauer spectra on tin concentration ($0.01<x<0.05$), and at the same time this rate is temperature dependent, one can rule out direct exchange between the tin centers.[16,17,20]

An analysis of the density-of-states function in Figs. 9 and 10 shows that for $z<0.7$, where the donor states lie in the gap, the electron-exchange activation energy can be written

$$E_0=(\mu-E_v)+|U/2|, \tag{11}$$

and the decrease of E_0 with increasing z in this composition region evidences a decrease in the energy gap separating the chemical potential μ from the valence-band top E_v. For $z>0.7$, the conditions in which the tin donor levels lie within the valence band, the activation energy $E_0=U/2$, which permits experimental determination of the correlation energy for tin centers in $PbS_{1-z}Se_z$ ($z>0.7$), which was found to be -0.058 ± 0.005 eV.

5.4. $PbS_{1-z}Te_z$ solid solutions

The isomer shifts of the Sn^{2+} and Sn^{4+} lines in $PbS_{1-z}Te_z$ solid solutions containing both neutral and ionized tin centers depend on temperature considerably weaker than they do in the $PbS_{1-z}Se_z$ solid solutions (Fig. 12).[21] Estimation of the activation energy of the electronic exchange between neutral and ionized tin centers in $PbS_{1-z}Te_z$ yields $E_0>0.1$ eV, whence for the Hubbard energy one obtains $|U|>0.2$ eV. This figure exceeds by far the value $|U|=0.06$ eV obtained for similar centers in the $PbS_{1-z}Se_z$ solid solutions.

A comparison of the above estimates of the Hubbard energy permits certain conclusions on its nature, i.e. on the origin of the gain in energy obtained when the second electron is detached from a tin center compared to the first one. First, this gain is hardly connected with the delocalized states of the valence band, because E_0 no longer depends on z in the $PbS_{1-z}Se_z$ solid solutions after the tin levels have entered the valence band. This means that the valence-band delocalized states and the electronic states of tin atoms are separated in space, and that the Hubbard energy is determined by the nearest-neighbor environment of the latter. Second, the Hubbard energy depends on the chemical nature of the chalcogen in the tin-atom environment. Within the compositional regions where the Hubbard energy was estimated these ions are Se^{2-} for $PbS_{1-z}Se_z$ and Te^{2-} for $PbS_{1-z}Te_z$. The most probable cause of the Hubbard energy being negative may be displacement of the ligands toward the central ion (in our case, of Se^{2-} or Te^{2-} toward Sn^{4+}) after detachment of the second electron. However this effect should yield a higher gain in energy for ligands of smaller size (i.e. for Se^{2-} compared to Te^{2-}). The observed relation between the Hubbard energies suggests another origin. Such an origin could be, for example, an increase of the covalent contribution to the tin-chalcogen binding energy due to tin ionization.

5.5. Fast two-electron exchange among tin centers in $Ag_{1-y}Sn_{1+y}Se_2$ solid solutions

To measure the activation energy E_0 and to reach the temperature at which fast electronic exchange sets in ($\tau \gg \tau_0$), it would certainly be desirable to broaden the temperature range covered. However an increase in temperature is accompanied not only by an increase in the exchange rate but by a sharp growth of the ratio of the areas bounded by the Sn^{2+} and Sn^{4+} spectral lines as well (for the $Pb_{0.96}Sn_{0.02}Na_{0.01}Tl_{0.01}Se$ composition, for instance, $R=1.25\pm0.02$ at 80 K and $R=3.61\pm0.05$ at 295 K), which is associated with the increasing depth of the tin-center levels in the valence band. On the one hand, this should cause an increase of E_0 (see, e.g., Ref. 55, where the temperature range covered was increased to 373 K and, as a result, E_0 was overestimated), and on the other, interfere with observation of an ''averaged'' spectrum.

Nevertheless the trivalent tin forming in a fast two-electron exchange between the Sn^{2+} and Sn^{4+} centers was detected in solid solutions of the silver and tin selenides, $Ag_{1-y}Sn_{1+y}Se_2$, having a NaCl-type structure.[56] ^{119}Sn Mössbauer spectra of the $Ag_{1-y}Sn_{1+y}Se_2$ solid solutions represent single lines characteristic of a cubic tin- atom environment, and the isomer shifts increase with y. In the ternary compound $AgSnSe_2$, tin is formally trivalent, and its Mössbauer spectrum (*2* in Fig. 13a) corresponds to the only tin state, the isomer shift of this spectrum being intermediate between those of di- and quadrivalent-tin compounds. Variation of y in the $Ag_{1-y}Sn_{1+y}Se_2$ solid solutions from 0 to 0.2 retains the only tin state while shifting the spectra toward those of Sn^{2+}. The low paramagnetic susceptibility of the above solid solutions ($\chi\approx3\times10^{-5}$ cm^3/mol) precludes the formation of Sn^{3+} paramagnetic ions, and therefore an ionic model accounting for the properties of $Ag_{1-y}Sn_{1+y}Se_2$ was proposed. This model assumes the presence of Sn^{2+} and Sn^{4+} ions at tin sites, $[Ag^+]_{1-y}[Sn^{2+}]_{(1+3y)/2}[Sn^{4+}]_{(1-y)/2}[Se^{2-}]_2$, and the single lines observed in the spectra are assigned to the states forming in a fast electronic exchange between Sn^{2+} and Sn^{4+}. The isomer shift of such lines should be

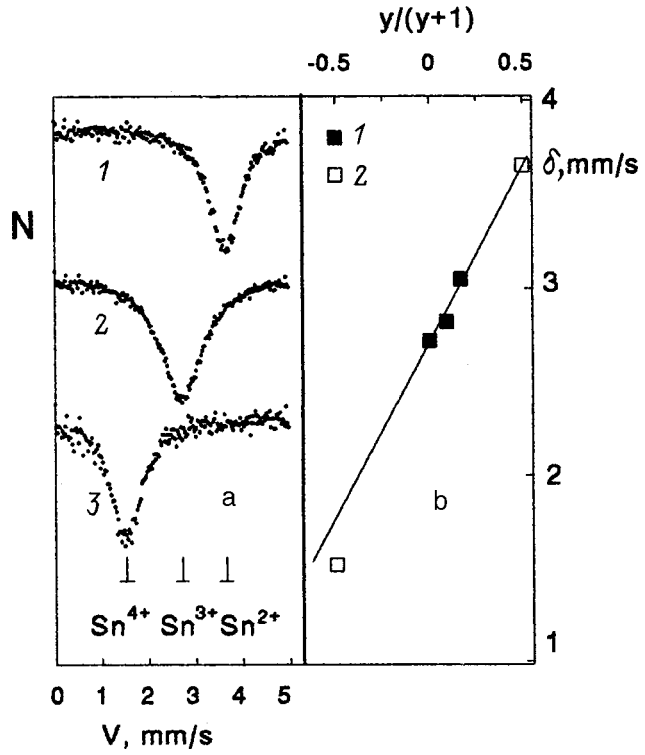

FIG. 13. (*a*) ^{119}Sn Mössbauer spectra of the solid solutions (*1*) $Pb_{0.99}Sn_{0.01}Se$, (*2*) $AgSnSe_2$, and (*3*) $Pb_{0.975}Sn_{0.005}Na_{0.01}Tl_{0.01}Se$.[56] Also shown are the isomer shifts of the Mössbauer spectra corresponding to Sn^{2+}, Sn^{3+}, and Sn^{4+}. (*b*) Dependence of the isomer shift δ of ^{119}Sn Mössbauer spectra of the $Ag_{1-y}Sn_{1+y}Se_2$ solid solutions on compositional parameter $y/(1+y)$: (*1*) $Ag_{1-y}Sn_{1+y}Se_2$, (*2*) tin impurity atoms in PbSe.[56]

$$\delta = \delta(Sn^{2+})(1+3y)/2(1+y) + \delta(Sn^{4+})(1-y)/2(1+y)$$
$$= [\delta(Sn^{2+}) + \delta(Sn^{4+})]/2 + [\delta(Sn^{2+}) - \delta(Sn^{4+})]y/(1+y), \quad (12)$$

where $\delta(Sn^{2+})$ and $\delta(Sn^{4+})$ are the isomer shifts of the assumed Sn^{2+} and Sn^{4+} states in $Ag_{1-y}Sn_{1+y}Se_2$. To estimate the latter, one used the isomer spectral shifts of the Sn^{2+} and Sn^{4+} impurity ions in PbSe (3.65 and 1.52 mm/s, respectively, spectra *1* and *3* in Fig. 13a). The tin impurity states in PbSe should simulate properly the corresponding states in $Ag_{1-y}Sn_{1+y}Se_2$, because in both matrices tin resides in a regular octahedral environment of selenium ions.

Equation (12) is a linear dependence $A + B \cdot y/(1+y)$ of the isomer shift on parameter $y/(1+y)$, where the A and B constants are explicitly related to the isomer shifts of the Sn^{2+} and Sn^{4+} states. The solid line in Fig. 13b shows the dependence of the tin isomer shift in $Ag_{1-y}Sn_{1+y}Se_2$ on the $y/(1+y)$ parameter, which can be fitted by a straight line with the parameters $A = 2.69 \pm 0.04$ mm/s and $B = 1.94 \pm 0.14$ mm/s. These parameters are in a good agreement with the values $[\delta(Sn^{2+}) + \delta(Sn^{4+})]/2 = 2.59 \pm 0.03$ mm/s and $[\delta(Sn^{2+}) - \delta(Sn^{4+})]/2 = 2.13 \pm 0.03$ mm/s, which follow from the ionic model.

Note that the authors of Ref. 57 also measured ^{119}Sn Mössbauer spectra of the $Ag_{1-y}Sn_{1+y}Se_2$ solid solutions, but their analysis of the dependence of the isomer shift on composition left the question of whether fast electronic exchange between the two tin states does exist in the system or there are no such dynamics, and all tin ions are in the same charge state, unresolved.

6. TIN ANTISITE DEFECTS IN LEAD CHALCOGENIDES

Tin impurity atoms can be introduced into lead chalcogenides both by traditional synthesis and through nuclear transformations of the corresponding parent nuclei (^{119}Sb or ^{119m}Te).[58–60]

6.1. ^{119}Sb parent nuclei

Studies of Group V impurities (As, Sb, and Bi) in lead chalcogenides are practically lacking. It is known only that these impurities are donors, although the fraction of electrically active atoms is substantially less than unity. One could put forward two explanations for this fact, namely, either a noticeable part of the impurity atoms form electrically inactive complexes in the lattice (of the type Sb_2Te_3), or the impurity is distributed between the cation sublattice (where it acts as a donor) and the anion sublattice (in which case the nature of the impurity states is unclear). One could decide between the alternate models if the positions of antimony atoms in the lead chalcogenide lattices were known. The positions of antimony impurity atoms in lead sulfide and telluride (PbS, PbTe) were determined by ^{119}Sb (^{119m}Sn) Mössbauer emission spectroscopy.[58,59] In view of the fact that the recoil energy of the ^{119m}Sn daughter atoms as a result of electron capture in ^{119}Sb and neutrino emission does not exceed 1.4 eV, one may conclude that the radioactive transformation does not displace tin atoms from the normal lattice sites. Thus the parameters of ^{119}Sb (^{119m}Sn) Mössbauer emission spectra should reflect the valence (charge) state of ^{119m}Sn atoms localized in antimony-occupied sites.

The Mössbauer sources were prepared by melting PbS or PbTe samples with carrier-free $^{119}SbCl_3$, so that the estimated concentration of antimony impurity atoms did not exceed 10^{17} cm^{-3}. The starting samples were n-type (with a lead excess, $n \sim 10^{18}$ cm^{-3}) and p-type (with a chalcogen excess, $p \sim 10^{18}$ cm^{-3}). Figure 14a presents typical spectra of PbS:^{119}Sb and PbTe:^{119}Sb.

The spectra of n-type samples [*1* and *2* in Fig. 14(a)] are superpositions of two lines. The widths of both lines (~ 1.35 mm/s) are substantially in excess of the instrumental width, which implies distortion of the cubic local-environment symmetry of the ^{119m}Sn daughter atoms. The reason for this distortion may be the difference of the replaced and substituting atoms in size. One of these lines (it is dominant in n-type samples and is referred to as spectrum I) has an isomer shift (~ 2.3 mm/s) characteristic of intermetallic tin compounds, and it should be assigned to the $^{119m}Sn^0$ centers in the anion sublattice of PbS (PbTe) (the nearest environment of these centers contains lead atoms, and the interaction of tin with the latter produces an isomer shift typical of metallic alloys of lead). $^{119m}Sn^0$ atoms form obviously of the ^{119}Sb atoms in the anion sublattice of PbS (PbTe). The second line (spectrum II) has an isomer shift (~ 3.45 mm/s) characteristic of compounds of divalent tin, and it should be assigned to $^{119m}Sn^{2+}$ centers located in the

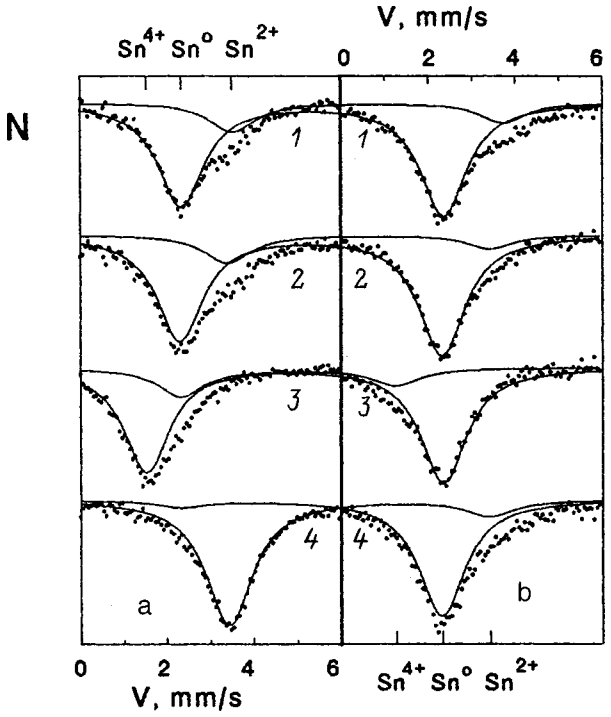

FIG. 14. Mössbauer emission spectra of (*a*) ^{119}Sb(^{119m}Sn), Refs. 58, 59, and (*b*) ^{119m}Te(^{119m}Sn), Ref. 60, obtained at 80 K on (*1*) *n*-PbS, (*2*) *n*-PbTe, (*3*) *p*-PbS, and (*4*) *p*-PbTe. Also shown is decomposition of the experimental spectra into the components corresponding to $^{119m}Sn^{0}$, $^{119m}Sn^{2+}$, and $^{119m}Sn^{4+}$.

cation sublattice of PbS (PbTe) (the nearest environment of these centers contains chalcogen atoms, and the interaction of tin with the latter produces an isomer shift close to that of the ^{119}Sn spectrum in SnS and SnTe). Obviously enough, the $^{119m}Sn^{2+}$ atoms are products of decay of the ^{119}Sb atoms residing on the PbS (PbTe) cation sublattice.

The spectra of *p*-type samples [*3* and *4* in Fig. 14(a)] likewise are superpositions of two broadened lines. One of these lines of both compounds has parameters close to those of a type-I spectrum (it was dominant in *n*-type samples, but its intensity in *p*-type samples is substantially weaker). This spectrum should be assigned to the $^{119m}Sn^{0}$ centers, which formed from the ^{119}Sb atoms on the anion sublattice of PbS (PbTe). The second line for PbS (spectrum III) has an isomer shift ($\sim$1.55 mm/s) characteristic of compounds of quadrivalent tin, and it should be assigned to the $^{119m}Sn^{4+}$ atoms produced in the decay of the ^{119}Sb atoms on the cation sublattice of PbS. The parameters of the second line of PbTe are close to those of a type-II spectrum (it had a low intensity in *n*-type samples, but in *p*-type samples its intensity increases substantially). This line should be associated with the $^{119m}Sn^{2+}$ atoms, which formed in the decay of the ^{119}Sb atoms in the PbTe cation sublattice.

Thus the position of tin impurity atoms in the lead-chalcogenide lattices depends on the nature of the deviation of the material from stoichiometric composition; indeed, in samples with a lead excess, antimony localizes primarily on the anion sublattice, and in samples with an excess of the chalcogen, predominantly on the cation sublattice (where it acts as a donor). The fraction of electrically active antimony atoms depends on the antimony distribution between the sublattices, but it is always less than unity (this follows from the fact that even in *p*-type samples a substantial fraction of antimony atoms are localized in the anion sublattice).

It should be pointed out that the ^{119m}Sn center in the anion sublattice of PbS and PbTe (it produces a type-I spectrum) represents an antisite defect, and, as follows from the independence of the isomer shift of spectrum I of the type of material conduction, the charge state of an antisite defect does not depend on the position of the chemical potential. The ^{119m}Sn center on the cation sublattice of PbS and PbTe (it accounts for the type-II and III spectra in PbS and the type-II spectrum in PbTe) is an isoelectronic substitutional impurity. As follows from Section 4, the isoelectronic tin impurity in PbS is a two-electron donor with a negative correlation energy (i.e., it is electrically active). This accounts for the observed dependence of the isomer shift of the spectrum of such centers on the conduction type of the material, namely, in *n*-type samples the spectrum corresponds to the neutral state of the donor center ($^{119m}Sn^{2+}$, spectrum II), and in *p*-type ones, to the doubly-ionized state ($^{119m}Sn^{4+}$, spectrum III). As shown in Section IV, the isoelectronic tin impurity in the PbTe lattice is electrically inert, and this is corroborated by data on the independence of the isomer shift of the spectrum corresponding to these centers of the position of the chemical potential.

6.2. ^{119m}Te parent atoms

A study was made of the tin centers in antisite defects present in PbTe and PbS.[60] The emission version of the ^{119m}Te(^{119m}Sn) Mössbauer spectroscopy used permitted one to stabilize tin impurity atoms following a chain of radioactive decays of the parent atoms in positions off their characteristic sites.

The Mössbauer sources were prepared by melting PbS or PbTe samples with carrier-free ^{119m}Te, so that the tin impurity concentration did not exceed $10^{17}\,cm^{-3}$. The starting samples were *n*-type (with a lead excess, $n\sim10^{18}\,cm^{-3}$) and *p*-type (with an excess of the chalcogen, $p\sim10^{18}\,cm^{-3}$). Typical spectra of PbS: ^{119m}Te and Pb: ^{119m}Te are shown in Fig. 14b.

As in the case of ^{119}Sb(^{119m}Sn) MES, experimental spectra of *n*-PbS and *n*-PbTe are superpositions of two lines, a strong one (spectrum I, the isomer shift characteristic of $^{119}Sn^{0}$) and a weaker one (spectrum II, the isomer shift typical of $^{119m}Sn^{2+}$). The emission spectra of *p*-PbTe and *p*-PbS are likewise superpositions of two lines. For *p*-PbTe, the experimental spectrum is similar to that of *n*-PbTe (it contains lines I and II), whereas the spectrum of *p*-PbS contains, besides a strong line I, a weaker line III as well (the isomer shift of this line corresponds to $^{119m}Sn^{4+}$).

This study[60] made use of the ^{119m}Sn Mössbauer probe formed after an electron capture first in the ^{119m}Te nucleus, and after that, in ^{119}Sb. The electron capture from an electronic shell produces a singly ionized excited daughter atom. This excitation is removed through emission of either an x-ray photon or Auger electrons to create a spectrum of tin daughter-atom charges. The ionized atom can be displaced

from the normal lattice site, and the recoil momentum imparted to it in the neutrino emission in the course of the electron capture adds to the process.

An analysis of numerous Mössbauer studies of the effects following a nuclear transformation shows that the daughter atom reaches a stable position in a time much shorter than a few ps (only in inert-gas matrices did one detect metastable states of daughter atoms).[24] In other words, in Mössbauer emission spectra one can see only the final forms of daughter-atom stabilization. The probability for an atom to be displaced depends on the relative magnitude of the daughter-atom recoil energy E_R and the threshold atom-displacement energy $E_d \sim 25$ eV. The $^{119m}\mathrm{Te} \rightarrow {}^{119}\mathrm{Sb}$ decay involves a recoil energy $E_R \sim 24$ eV. This means that one may expect to observe in $^{119m}\mathrm{Te}(^{119m}\mathrm{Sn})$ Mössbauer emission spectra of PbS and PbTe the lines corresponding both to ^{119m}Sn atoms sitting at the anion sites of the sublattice and to ^{119m}Sn atoms displaced from these sites.

Based on the magnitude of the observed isomer shifts, spectrum I corresponds to tin daughter atoms having only lead atoms in their nearest environment, so that this spectrum should be assigned to the $^{119m}\mathrm{Sn}^0$ centers formed after the decay of the $^{119m}\mathrm{Te}^{2-}$ parent atoms and residing in the anion sites of the lattice. The isomer shifts of spectra II and III are typical of chalcogenides of di- and quadrivalent tin (the nearest environment of tin in these compounds contains only chalcogen atoms) and, hence, these spectra are due to the tin daughter atoms $^{119m}\mathrm{Sn}^{2+}$ (spectrum II) and $^{119m}\mathrm{Sn}^{4+}$ (spectrum III) created after the decay of the $^{119m}\mathrm{Te}^{2-}$ parent atoms and displaced in recoil from the anion to cation lattice sites (the isoelectronic substitutional impurity).

As shown in Section IV, the tin isoelectronic impurity in PbS is a two-electron donor. This accounts for the observed dependence of the isomer spectral shift exhibited by such centers on the material conduction type. Indeed, besides spectrum I, *n*-type samples produce spectrum II, which is due to the neutral state of the donor center ($^{119m}\mathrm{Sn}^{2+}$), and samples with *p*-conduction, spectrum III corresponding to the doubly ionized state ($^{119m}\mathrm{Sn}^{4+}$). The tin impurity atoms occupying cation sites in PbTe are electrically inactive (see also Section IV), and this is supported by the data on the independence of the isomer shift of the spectrum corresponding to these centers of the position of the chemical potential.

7. ELECTRICAL ACTIVITY OF THE GERMANIUM ISOELECTRONIC IMPURITY IN LEAD CHALCOGENIDES

As already mentioned, ^{119}Sn Mössbauer spectroscopic studies showed the tin isoelectronic impurity in lead chalcogenides (PbS, PbSe) to act as a two-electron donor. Therefore one could expect the germanium isoelectronic impurity in lead chalcogenides to follow a similar behavior. The electrical activity of a germanium impurity in PbS and PbSe was studied by ^{119}Sn Mössbauer spectroscopy.[17,61] These studies were motivated by the idea that the presence of electrically active germanium donor centers in the $\mathrm{Pb}_{1-x-y}\mathrm{Sn}_{x-z}\mathrm{Ge}_z\mathrm{A}_y\mathrm{S}$ and $\mathrm{Pb}_{1-x-y}\mathrm{Sn}_{x-z}\mathrm{Ge}_z\mathrm{A}_y\mathrm{Se}$ lead chalcogenides codoped by tin, germanium, and acceptors should change under certain conditions the line intensity ratio in ^{119}Sn Mössbauer spectra between the neutral and ionized tin centers compared to samples doped only by tin and an acceptor impurity.

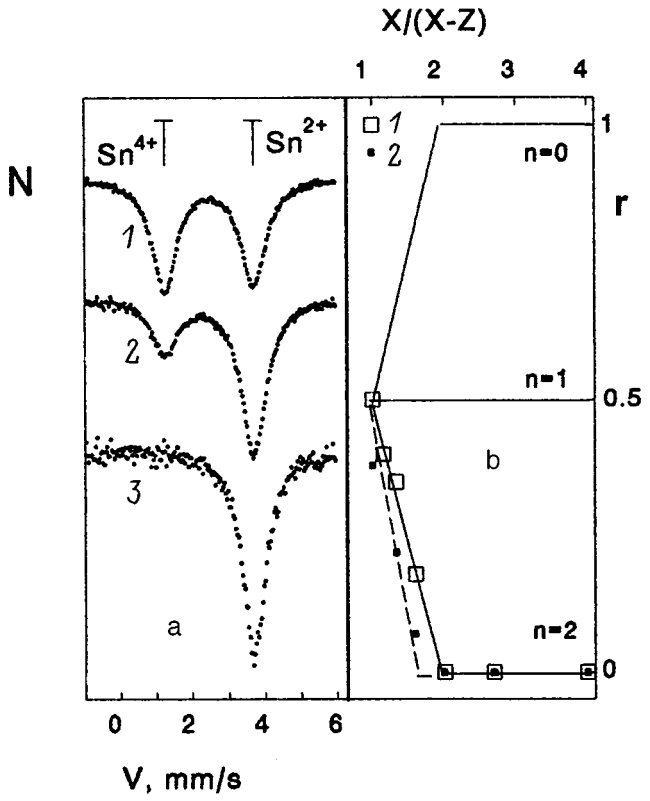

FIG. 15. (*a*) ^{119}Sn Mössbauer spectra of the $\mathrm{Pb}_{0.96}\mathrm{Sn}_{0.02-z}\mathrm{Ge}_z\mathrm{Na}_{0.01}\mathrm{Tl}_{0.01}\mathrm{S}$ solid solutions. *z*: (*1*) 0, (*2*) 0.005, (*3*) 0.01.[61] Also shown are the positions of the Sn^{2+} and Sn^{4+} spectra. (*b*) Calculated dependences of *R* on the germanium to tin concentration ratio $z/(x-z)$ (solid lines).[61] Points–experimental values of *R* for (*1*) $\mathrm{Pb}_{0.96}\mathrm{Sn}_{0.02-z}\mathrm{Ge}_z\mathrm{Na}_{0.01}\mathrm{Tl}_{0.01}\mathrm{S}$ and (*2*) $\mathrm{Pb}_{0.96}\mathrm{Sn}_{0.02-z}\mathrm{Ge}_z\mathrm{Na}_{0.01}\mathrm{Tl}_{0.01}\mathrm{Se}$.

One studied single-phase samples with $N+N_{\mathrm{Ge}}=N_a$ (here N, N_{Ge}, and N_a are the concentrations of tin, germanium, and acceptors, respectively). Typical spectra of these samples are displayed in Fig. 15a.

The Mössbauer spectrum of a PbS sample containing only lead and an acceptor is seen to be a superposition of two lines of about equal intensity corresponding to Sn^{2+} and Sn^{4+} (the neutral and doubly ionized tin donor centers, respectively) (see spectrum I in Fig. 15a). The ratio of the Sn^{2+} and Sn^{4+} concentrations ($[N_n]$ and $[N_i]$, accordingly) can be derived from the ratio of the areas bounded by the corresponding spectra, $R=[f_n/f_i]\cdot[N_n/N_i]$, with the ratio of the Mössbauer coefficients f for the Sn^{2+} and Sn^{4+} centers at 80 K being 0.93 ± 0.01. In particular, for spectrum I obtained at 80 K [Fig. 15a] $R=1.00\pm0.08$, which corresponds to ionization of one half of the tin atoms, exactly as expected for a two-electron donor.

Gradual substitution of germanium for tin impurity atoms in PbS results in a reduction of the Sn^{4+} spectrum in intensity (*2* in Fig. 15a), until the spectra of the samples with $N_{\mathrm{Ge}}>N$ contain only the Sn^{2+} line (*3* in Fig. 15a). This argues convincingly for the impurity germanium atoms exhibiting donor activity.

The charge neutrality equation for the $Pb_{1-x-y}Sn_{x-z}Ge_zA_yS$ can be written

$$2N_i + nN_{Ge} + p - N_a = 0, \quad (13)$$

where n is the germanium center charge, and p is the hole concentration. This permits us to recast the expression for R for the $x=y$ compositions studied in the form

$$R = 1/2 + (1-n)z/2(x-z) - p/2(x-z). \quad (14)$$

Figure 15(b) shows the dependences of R on the germanium to tin concentration ratio $z/(x-z)$ in PbS calculated for different germanium-center charges. It was taken into account that for $R<1$ the hole concentration may be neglected, because the chemical potential lies in the gap. If $n=0$ (germanium is electrically inactive or its energy levels are below the tin levels), a growth of germanium concentration should result in an increase of R until at $z/(x-z)=1$ all tin centers become ionized. If $n=1$ (germanium is a one-electron donor, and its levels lie above the tin levels), R should not change with varying germanium concentration. If $n=2$ (germanium, as tin, is a two-electron donor with its levels lying above those of tin), then R should decrease with increasing germanium concentration until at $N_{Ge}=N$ (i.e., at $z/(x-z)=1$) all of the tin becomes neutral, after which one will have to take into account the decrease of n because of incomplete ionization of the germanium centers. The experimental data on R in Fig. 15b obtained for the $Pb_{0.96}Sn_{0.2-z}Ge_zNa_{0.01}Tl_{0.01}S$ solid solutions suggest that the isoelectronic germanium impurity in PbS is a two-electron donor, and that its energy levels lie above those of tin.

Germanium impurity atoms in PbSe exhibit also electrical activity; indeed, substitution of germanium for tin is accompanied by a weakening of the Sn^{4+} line, and for $N_{Ge}>N$, only the Sn^{2+} line is retained in the spectrum. The experimental points plotted in Fig. 15b for the $Pb_{0.96}Sn_{0.2-z}Ge_zNa_{0.01}Tl_{0.01}Se$ solid solutions fall in the region of $N_{Ge}<N$ on the dashed curve, which passes below the curve for $Pb_{0.96}Sn_{0.2-z}Ge_zNa_{0.01}Tl_{0.01}S$ because of the hole effect, but has a similar slope. This evidently implies that the germanium isoelectronic impurity is a two-electron donor in PbSe as well, and that the energy levels of germanium lie above those of tin.

Similar to tin, germanium forms apparently both in PbS and PbSe centers with negative correlation energy, but this point requires additional investigation.

8. CONCLUSION

^{119}Sn Mössbauer spectroscopy has turned out to be an efficient method to probe tin impurity atoms in lead chalcogenides and the related solid solutions.

The tin isoelectronic impurity in $PbS_{1-z}Se_z$ solid solutions forms two-electron donor centers with negative correlation energy, the tin levels lying in the lower half of the gap for $z<0.7$ and within the valence band for $z>0.7$. The activation energy E_0 for electronic exchange between neutral and ionized tin centers decreases monotonically with increasing z, which reflects the tin-level approach to the top of the valence band and, for $z>0.7$, $E_0=|U/2|$ (U is the Hubbard energy).

The tin isoelectronic impurity in $PbS_{1-z}Te_z$ solid solutions also acts as a two-electron donor with negative correlation energy, but the levels associated with the tin centers lie within the valence band. The Hubbard energy U for tin impurity atoms in $PbS_{1-z}Te_z$ was found to be substantially higher than that of the similar tin centers in $PbS_{1-z}Se_z$.

The germanium isoelectronic impurity in PbS and PbSe is a two-electron donor, with the germanium levels lying above the levels formed in these semiconductors by the tin impurity atoms.

The tin state forming in the $Ag_{1-y}Sn_{1+y}Se_2$ variable-composition compound corresponds formally to trivalent tin and is created in a fast electron-exchange process between the Sn^{2+} and Sn^{4+} ions occupying NaCl-type lattice sites.

The position of antimony impurity atoms in the sites of PbS and PbTe is determined by deviation of the latter from stoichiometric composition, namely, in samples with excess lead the antimony resides primarily on the anion sublattice, and in samples with an excess of the chalcogen, predominantly on the cation sublattice. The charge state of the ^{119m}Sn antisite defect forming on the anion sublattice of PbS and PbSe following the radioactive transformation of ^{119}Sb does not depend on the level of the chemical potential. The ^{119m}Sn center on the cation sublattice of PbS is an electrically active substitutional impurity; in n-type samples the spectrum corresponds to the neutral state of the donor center, $^{119m}Sn^{2+}$, and in a p-type material, to its doubly ionized state, $^{119m}Sn^{4+}$. The same center on the cation sublattice of PbTe is electrically inactive.

Application of the emission version of the ^{119m}Te(^{119m}Sn) Mössbauer spectroscopy makes possible insertion of tin impurity atoms in the anion sublattices of PbTe and PbS. The charge state of the tin impurity atoms displaced from the anion sublattice was found to depend on the chemical potential.

*)Deceased.

[1] J. Hubbard, Proc. R. Soc. London, Ser. A **277**, 237 (1964).
[2] P. W. Anderson, Phys. Rev. Lett. **34**, 953 (1975).
[3] M. Kastner, D. Adler, and H. Fritzsche Phys. Rev. Lett. **37**, 1504 (1976).
[4] I. A. Drabkin and B. Ya. Moĭzhes, Fiz. Tekh. Poluprovodn. **15**, 625 (1981) [Sov. Phys. Semicond. **15**, 357 (1981)].
[5] I. A. Drabkin and B. Ya. Moĭzhes, Fiz. Tverd. Tela (Leningrad) **25**, 1974 (1983) [Sov. Phys. Solid State **25**, 1139 (1983)].
[6] S. P. Ionov, Izv. Akad. Nauk SSSR, Ser. Fiz. **49**, 310 (1985).
[7] V. I. Kaĭdanov and Yu. I. Ravich, Usp. Fiz. Nauk **145**, 51 (1985) [Sov. Phys. Usp. **28**, 31 (1985)].
[8] V. I. Kaĭdanov, S. A. Nemov, and Yu. I. Ravich, Fiz. Tekh. Poluprovodn. **26**, 201 (1992) [Sov. Phys. Semicond. **26**, 113 (1992)].
[9] N. F. Mott and E. A. Davis, *Electronic Processes in Non-Crystalline Materials* (Clarendon Press, Oxford, 1979; Mir, Moscow, 1982).
[10] L. V. Prokof'eva, S. V. Zarubo, F. S. Nasredinov, and P. P. Seregin, JETP Lett. **33**, 12 (1981).
[11] L. V. Prokof'eva, F. S. Nasredinov, Yu. A. Nikulin, and P. P. Seregin, Fiz. Tverd. Tela (Leningrad) **24**, 1630 (1982) [Sov. Phys. Solid State **24**, 931 (1982)].
[12] F. S. Nasredinov, L. V. Prokof'eva, S. V. Zarubo, A. N. Kurmantaev, and P. P. Seregin, JETP Lett. **38**, 22 (1983).

[13] F. S. Nasredinov, L. V. Prokof'eva, and P. P. Seregin, Zh. Éksp. Teor. Fiz. **87**, 951 (1984) [Sov. Phys. JETP **60**, 542 (1984)].
[14] F. S. Nasredinov, L. V. Prokof'eva, A. N. Kurmantaev, and P. P. Seregin, Fiz. Tverd. Tela (Leningrad) **26**, 862 (1984) [Sov. Phys. Solid State **26**, 522 (1984)].
[15] F. S. Nasredinov, L. V. Prokofieva, P. P. Seregin, S. V. Zarubo, A. V. Ermolaev, and A. N. Kurmantaev, Phys. Status Solidi B **130**, 727 (1985).
[16] F. S. Nasredinov, L. V. Prokof'eva, F. P. Kesamanly, A. A. Agzamov, K. T. Urazbaeva, and P. P. Seregin, Fiz. Tverd. Tela (Leningrad) **30**, 1848 (1988) [Sov. Phys. Solid State **30**, 1064 (1988)].
[17] F. S. Nasredinov, E. Yu. Turaev, P. P. Seregin, H. B. Rakhmatullaev, and M. K. Bakhadirkhanov, Phys. Status Solidi A **121**, 571 (1990).
[18] V. F. Masterov, F. S. Nasredinov, S. A. Nemov, and P. P. Seregin, Fiz. Tekh. Poluprovodn. **30**, 840 (1996) [Semiconductors **30**, 450 (1996)].
[19] V. F. Masterov, F. S. Nasredinov, S. A. Nemov, and P. P. Seregin, Fiz. Tekh. Poluprovodn. **30**, 884 (1996) [Semiconductors **30**, 472 (1996)].
[20] V. F. Masterov, F. S. Nasredinov, S. A. Nemov, and P. P. Seregin, Fiz. Tekh. Poluprovodn. **31**, 291 (1997) [Semiconductors **31**, 181 (1997)].
[21] V. F. Masterov, S. A. Nemov, F. S. Nasredinov, P. P. Seregin, and N. P. Seregin, Fiz. Tekh. Poluprovodn. **33**, 789 (1999) [Semiconductors **33**, 726 (1999)].
[22] V. K. Bazhenov and V. I. Fistul', Fiz. Tekh. Poluprovodn. **18**, 1345 (1984) [Sov. Phys. Semicond. **18**, 843 (1984)].
[23] A. R. Regel' and P. P. Seregin, Fiz. Tekh. Poluprovodn. **18**, 1153 (1984) [Sov. Phys. Semicond. **18**, 723 (1984)].
[24] P. P. Seregin, F. S. Nasredinov, and L. N. Vasilev, Phys. Status Solidi A **45**, 11 (1978).
[25] V. P. Zlomanov and A. V. Novoselova, *P-T-x Phase Diagrams of the Metal-Chalcogen Systems* (Nauka, Moscow, 1987).
[26] N. Kh. Abrikosov and L. E. Shelimova, *IV–VI-Based Semiconducting Materials* (Nauka, Moscow, 1975).
[27] B. I. Boltaks, S. I. Bondarevskiĭ, P. P. Seregin, and V. T. Shipatov, Fiz. Tverd. Tela (Leningrad) **11**, 1839 (1969) [Sov. Phys. Solid State **11**, 1483 (1969)]; B. I. Boltaks, K. V. Perepech, P. P. Seregin, and V. T. Shipatov, Izv. Akad. Nauk SSSR, Neorg. Mater. **6**, 818 (1970).
[28] P. P. Seregin, V. P. Sivkov, F. S. Nasredinov, L. N. Vasilev, Yu. V. Krylnikov, and Yu. P. Kostikov, Phys. Status Solidi A **39**, 437 (1977).
[29] I. Lefebvre, M. A. Szymanski, J. Olivier-Fourcade, and J. C. Jumas, Phys. Rev. B **58**, 1896 (1998).
[30] Sh. Sh. Bashkirov, A. B. Liberman, V. V. Parfenov, and V. I. Sinyavskiĭ, JETP Lett. **27**, 457 (1978).
[31] B. T. Melekh, P. P. Seregin, and V. T. Shipatov, Izv. Akad. Nauk SSSR, Neorg. Mater. **7**, 502 (1971); L. N. Vasil'ev, Yu. V. Kryl'nikov, B. T. Melekh, T. V. Sin'ko, and P. P. Seregin, Izv. Akad. Nauk SSSR, Neorg. Mater. **12**, 119 (1976).
[32] B. T. Melekh, P. P. Seregin, and V. T. Shipatov, Izv. Akad. Nauk SSSR, Neorg. Mater. **7**, 693 (1971).
[33] B. T. Melekh, V. T. Shipatov, and P. P. Seregin, Izv. Akad. Nauk SSSR, Neorg. Mater. **6**, 1530 (1970).
[34] G. M. Bartenev, A. D. Tsyganov, S. A. Dembovskiĭ, and V. I. Mikhaĭlov, Izv. Akad. Nauk SSSR, Neorg. Mater. **7**, 1442 (1971).
[35] P. P. Seregin, M. A. Sagatov, B. T. Melekh, Yu. P. Kostikov, and L. N. Vasil'ev, Izv. Akad. Nauk SSSR, Neorg. Mater. **9**, 134 (1973).
[36] Yu. I. Ravich, B. A. Efimov, and I. A. Smirnov, *Methods of Investigation of Semiconductors as Applied to the PbTe, PbSe, and PbS Lead Chalcogenides* (Nauka, Moscow, 1968).
[37] I. N. Nikolaev, A. P. Shotov, A. F. Volkov, and V. P. Mar'in, JETP Lett. **21**, 65 (1975); I. N. Nikolaev, V. P. Potapov, A. P. Shotov, and E. E. Yurchakevich, JETP Lett. **25**, 168 (1977).
[38] D. I. Baltrunas, S. V. Motejunas, P. M. Starik, and V. I. Mikityuk, JETP Lett. **36**, 4 (1982); D. Baltrunas, Phys. Status Solidi B **204**, 811 (1997).
[39] V. F. Masterov, F. S. Nasredinov, S. A. Nemov, and P. P. Seregin, Fiz. Tverd. Tela (St. Petersburg) **38**, 2973 (1996) [Phys. Solid State **38**, 1625 (1996)].
[40] M. Katada, T. Nakamoto, and H. Sano, Hyperfine Interact. **84**, 521 (1994).
[41] A. B. Liberman, S. S. Tsarevskiĭ, and N. A. Zyuzin, Fiz. Tverd. Tela (St. Petersburg) **38**, 1596 (1996) [Phys. Solid State **38**, 878 (1996)].
[42] L. V. Prokof'eva, M. N. Vinogradova, and S. V. Zarubo, Fiz. Tekh. Poluprovodn. **14**, 2201 (1980) [Sov. Phys. Semicond. **14**, 1304 (1980)].
[43] S. V. Zarubo, Yu. A. Nikulin, E. A. Gurieva, L. V. Prokof'eva, Yu. I. Ravich, M. N. Vinogradova, and T. B. Zhukova, Fiz. Tekh. Poluprovodn. **16**, 1892 (1982) [Sov. Phys. Semicond. **16**, 1219 (1982)].
[44] L. V. Prokof'eva, S. V. Zarubo, M. N. Vinogradova, Yu. A. Nikulin, and K. G. Gartsman, Fiz. Tekh. Poluprovodn. **16**, 2136 (1982) [Sov. Phys. Semicond. **16**, 1377 (1982)].
[45] A. N. Veĭs, E. A. Gurieva, O. G. Nefedov, and L. V. Prokof'eva, Fiz. Tekh. Poluprovodn. **18**, 1723 (1984) [Sov. Phys. Semicond. **18**, 1080 (1984)].
[46] E. A. Gurieva, L. V. Prokof'eva, Yu. I. Ravich, S. V. Zarubo, and K. G. Gartsman, Fiz. Tekh. Poluprovodn. **19**, 1746 (1985) [Sov. Phys. Semicond. **19**, 1073 (1985)].
[47] A. N. Veĭs and L. V. Prokof'eva, Fiz. Tekh. Poluprovodn. **20**, 160 (1986) [Sov. Phys. Semicond. **20**, 98 (1986)].
[48] L. V. Prokof'eva, Sh. M. Zhumaksanov, and Kh. R. Maĭlina, Fiz. Tekh. Poluprovodn. **21**, 310 (1987) [Sov. Phys. Semicond. **21**, 186 (1987)].
[49] A. N. Veĭs and L. V. Prokof'eva, Fiz. Tekh. Poluprovodn. **21**, 743 (1987) [Sov. Phys. Semicond. **21**, 455 (1987)].
[50] Yu. A. Degtyarev, P. P. Konstantinov, Kh. R. Maĭlina, and L. V. Prokof'eva, Fiz. Tekh. Poluprovodn. **23**, 1576 (1989) [Sov. Phys. Semicond. **23**, 977 (1989)].
[51] G. T. Alekseeva, B. G. Zemskov, P. P. Konstantinov, L. V. Prokof'eva, and K. T. Urazbaeva, Fiz. Tekh. Poluprovodn. **26**, 358 (1992) [Sov. Phys. Semicond. **26**, 202 (1992)].
[52] G. T. Alekseeva, E. A. Gurieva, P. P. Konstantinov, N. V. Maksimova, and L. V. Prokof'eva, Fiz. Tekh. Poluprovodn. **29**, 1388 (1995) [Semiconductors **29**, 719 (1995)].
[53] A. N. Veĭs and N. A. Suvorova, Fiz. Tekh. Poluprovodn. **29**, 278 (1995) [Semiconductors **29**, 138 (1995)]; Fiz. Tekh. Poluprovodn. **30**, 2089 (1996) [Semiconductors **30**, 1089 (1996)]; Fiz. Tekh. Poluprovodn. **32**, 445 (1998) [Semiconductors **32**, 397 (1998)].
[54] P. P. Seregin, F. S. Nasredinov, and A. Sh. Bakhtiyarov, Phys. Status Solidi B **91**, 35 (1979).
[55] B. G. Zemskov, V. S. Lyubimov, A. N. Martynyuk, A. A. Artemova, Yu. V. Permyakov, and S. P. Ionov, Fiz. Tekh. Poluprovodn. **22**, 934 (1988) [Sov. Phys. Semicond. **22**, 590 (1988)].
[56] V. F. Masterov, F. S. Nasredinov, S. A. Nemov, P. P. Seregin, S. M. Irkaev, B. T. Melekh, and N. N. Troitskaya, Fiz. Tverd. Tela (St. Petersburg) **38**, 3308 (1996) [Phys. Solid State **38**, 1805 (1996)].
[57] V. S. Lyubimov, A. N. Martynyuk, B. G. Zemskov, Yu. V. Permyakov, A. A. Artemova, and N. S. Zaugol'nikova, Sverkhprovodimost' (KIAE) **4**, 2246 (1991).
[58] V. F. Masterov, F. S. Nasredinov, S. A. Nemov, P. P. Seregin, N. N. Troitskaya, and S. I. Bondarevskiĭ, Fiz. Tekh. Poluprovodn. **31**, 1321 (1997) [Semiconductors **31**, 1138 (1997)].
[59] V. F. Masterov, F. S. Nasredinov, P. P. Seregin, N. P. Seregin, A. V. Ermolaev, and S. I. Bondarevskiĭ, Fiz. Tekh. Poluprovodn. **33**, 913 (1999) [Semiconductors **33**, 836 (1999)].
[60] V. F. Masterov, S. I. Bondarevskiĭ, F. S. Nasredinov, N. P. Seregin, and P. P. Seregin, Fiz. Tekh. Poluprovodn. **33**, 772 (1999) [Semiconductors **33**, 710 (1999)].
[61] V. F. Masterov, F. S. Nasredinov, S. A. Nemov, P. P. Seregin, A. V. Ermolaev, and S. M. Irkaev, Fiz. Tekh. Poluprovodn. **31**, 381 (1997) [Semiconductors **31**, 319 (1997)].

Translated by G. Skrebtsov

METALS. SUPERCONDUCTORS

Transport and magnetic properties of the compounds $YbNi_4In$ and $YbNiIn_4$ with valence-unstable Yb

M. D. Koterlin,*) B. S. Morokhivskiĭ, I. D. Shcherba, and Ya. M. Kalychak

Lviv State University, 290005 Lviv, Ukraine
(Submitted March 16, 1999)
Fiz. Tverd. Tela (St. Petersburg) **41**, 1918–1921 (November 1999)

The electrical resistance, thermal emf, and magnetic susceptibility of the compounds $YbNi_4In$ and $YbNiIn_4$, with valence-unstable Yb, are measured at temperatures of $4.2-300$ K. The valence state of Yb is identified by measuring the x-ray L_{III} absorption spectra at $T=300$ K. $YbNi_4In$ is shown to have a Kondo magnetic lattice and exhibit crystal-field effects. The preferred scheme is splitting of the $4f$ level of Yb^{3+} with doublet formation in the ground and first excited states. In the case of $YbNiIn_4$, a valence-unstable state of Yb is formed that makes no significant additional contributions to the transport coefficients. © *1999 American Institute of Physics.* [S1063-7834(99)00211-7]

In the physics of heavy fermion systems and Kondo lattices, questions regarding the ground state of the system and the relative roles of various interactions in its formation occupy an especially important place. In this connection, in recent years there has been a continually increasing interest in research on ternary compounds of the type RM_nX_m (R = Ce or Yb, M is a transition element, and X is a p-element in group III–V), which have a large variety of ground state properties. Heavy fermion superconductivity and band magnetism, as well as a special class of heavy fermion systems with non-Fermi liquid behavior in their basic properties (Kondo insulators, heavy-fermion systems with low charge-carrier densities, etc.), have been observed in compounds of this type.[1] In addition, the large variety in their crystal structure and the presence of a magnetoactive M element mean that compounds of the type RM_nX_m can be regarded as convenient models for studying the interaction between the Kondo and magnetic sublattices on a microscopic level.[2–4]

In this paper we present data from a study of the transport and magnetic properties of the comparatively new compounds $YbNi_4In$ and $YbNiIn_4$ with valence-unstable Yb. Preliminary data[5,6] show that, in $YbNi_4In$ ($MgSnCu_4$-type cubic structure, space group $F\bar{4}3m$),[7] Yb is in a magnetic state with additional manifestation of Kondo effects. In the crystal field, with its cubic symmetry, the degeneracy of the $^2F_{7/2}$ state of the free Yb^{3+} ion in $YbNi_4In$ is partially removed and the ground state can be a doublet or quadruplet. Recent measurements of inelastic neutron scattering[5] and of the thermodynamic and magnetic properties[6] of $YbNi_4In$ are essentially contradictory as far as the ground state of Yb is concerned. In this regard, there is some interest in a more detailed study of the peculiarities in the transport properties of $YbNi_4In$, which are more sensitive to the Kondo state of Yb. The compound $YbNiIn_4$ (rhombic $YNiAl_4$ structure, space group $Cmcm$)[8] is a new representative of a large series of compounds of the type $YbMX_4$, for which the formation of valence-unstable Yb states with maximal mixing of the $4f^{13}$ and $4f^{14}$ configurations is typical.[9,10]

These compounds were obtained by direct melting of the components nickel (99.91 % Ni), indium (99.99 % In), and the rare earth metal (main component at least 99.85 % pure) in an electric arc furnace in a pure argon atmosphere. Homogenizing annealing was performed at 900 K for 150 h. The lattice periods determined from diffraction patterns (DRON-3.0 diffractometer, Cu $K\alpha$-radiation) were in good agreement with those given elsewhere.[7,8] The stoichiometric composition of the samples was also monitored using a CAMEBAX x-ray microanalysis system. It was found that there is a slight deviation of the composition from stoichiometric owing to mutual substitution of the components Ni and Yb. Ultimately, more precise determinations of the compositions corresponded to the chemical formulas $Yb_{1-\delta}Ni_{4+\delta}In$ and $Yb_{1+\delta}Ni_{1-\delta}In_4$ with $\delta \approx 0.1$.

The preparation of the samples and the measurement techniques are similar to those described previously.[11] The valence state of the Yb was identified on the basis of measurements of the x-ray L_{III} absorption spectra at a temperature of 300 K by the method described in Ref. 12. The thermal emf was measured relative to Cu.

Figure 1 shows experimental L_{III} absorption spectra of Yb and their resolution into components (a gaussian line shape for the atomic $2p-5d$ transition and an arctangent-like curve for the band absorption edge) corresponding to the arbitrary ion configurations Yb^{3+} ($4f^{13}$) at an energy of $E=8947$ eV and Yb^{2+} ($4f^{14}$) at $E=8940$ eV. The populations of the f-shell determined from the intensity ratio of the principal lines were $\sim 0.0 \pm 0.05$ and 0.4 ± 0.02 for $YbNi_4In$ and $YbNiIn_4$, respectively. The relatively large error for $YbNi_4In$ is caused by the appearance of an additional line with a peak ~ 5 eV higher than the principal absorption line

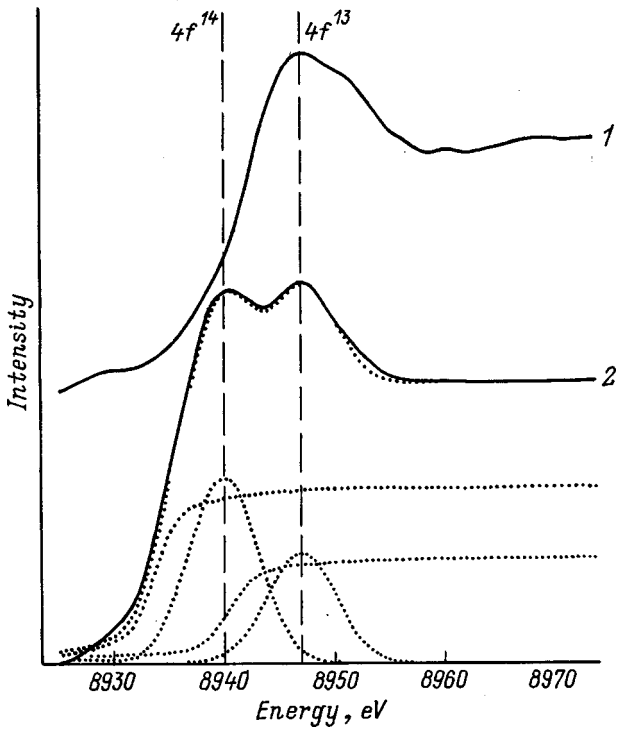

FIG. 1. X-ray L_{III} absorption spectra of Yb in $YbNi_4In$ (*1*) and $YbNiIn_4$ (*2*) and their resolutions into components (dotted curves).

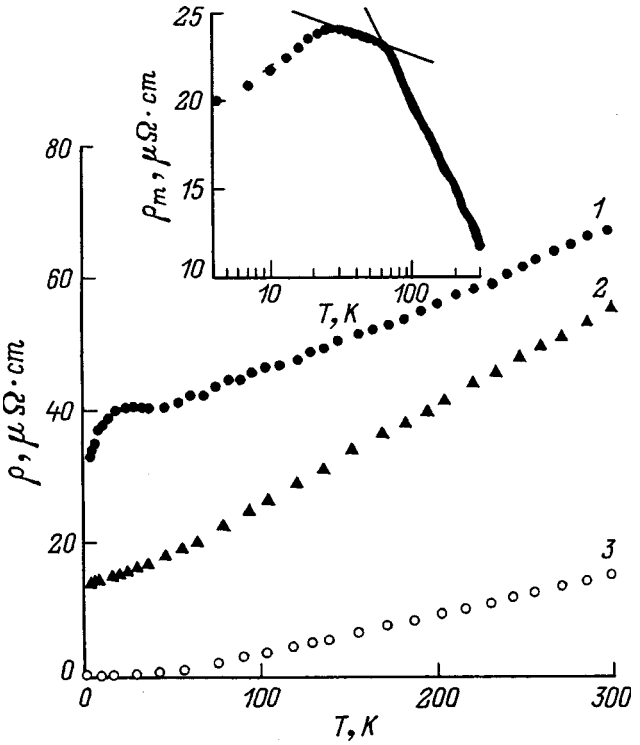

FIG. 2. Temperature dependences of the electrical resistance of RNi_4In, where $R=$ Yb (*1*), Nd (*2*), and of $YbNiIn_4$ (*3*). The inset shows the magnetic contribution to the overall electrical resistance of valence-unstable Yb on a logarithmic temperature scale.

of Yb in the $4f^{13}$ configuration. The additional line appears to be a characteristic feature of the Yb L_{III}-spectra of compounds of the type YbM_4X with trivalent Yb and may be related to structural features of the density of $5d$-states in the energy spectrum of these compounds above the Fermi level, E_F.[13]

Figures 2 and 3 show the temperature dependence of the resistivity ρ and the thermal emf S for RNi_4In ($R=$ Yb, Nd) and $YbNiIn_4$. The $\rho(T)$ curve for $YbNi_4In$ deviates substantially from linearity for $T<250$ K and has a characteristic bump at $T\sim 30$ K. At low temperatures ($T<15$ K), there is a segment with $\rho\propto T$ without saturation. The behavior of $\rho(T)$ is in good agreement with that reported[6] for a single crystal of $YbNi_4In$.

In order to evaluate the contribution of valence-unstable Yb to the total resistivity ρ, it is necessary to isolate its phonon part. To do this we have used the isostructural compound $NdNi_4In$.[7] $\rho(T)$ for $NdNi_4In$ corresponds qualitatively to the ordinary Bloch-Grüneisen law. The absence of a distinct segment with $\rho\approx$const as $T\to 0$ may be caused by scattering of charge carriers on the magnetic Nd^{3+} ions. This sort of additional scattering is not an obstacle to making a qualitative estimate of the contribution to the total ρ owing to the scattering of charge carriers by the valence-unstable Yb in $YbNi_4In$ (ρ_m). The way $\rho_m(T)$ varies can be estimated using the equation $\rho_m(T)\approx\rho(YbNi_4In)-\rho(NdNi_4In)$. It can be seen that ρ_m has two linear segments on a semilog temperature plot (inset to Fig. 2), which is characteristic of a Kondo mechanism for scattering of charge carriers by impurity Yb^{3+} ions with effects from the splitting of the $4f$ level in the crystal field.[14] According to the theory in Ref. 14, the change in the slope of the linear segments is associated with a change in the population of the sublevels formed by partial removal of the degeneracy in the ground state of the Yb^{3+} ion under the influence of the crystal field as T increases. In the limits $T\ll\Delta$ and $T\gg\Delta$ (Δ is the total splitting in the crystal field), the ratio of the slope of the linear segment at low temperatures to that at high temperatures is given by $\nu(\alpha_l^2-1)/(\alpha_h^2-1)$, where α_l and α_h denote the degeneracies at low and high temperatures, respectively. In a crystal field with cubic symmetry, the $4f$-level of the Yb^{3+} ion

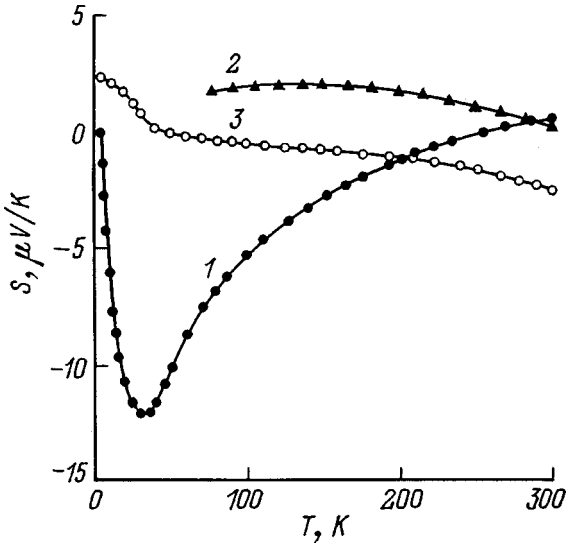

FIG. 3. Temperature dependences of the thermal emf of RNi_4In, with $R=$ Yb (*1*) and Nd (*2*), and of $YbNiIn_4$ (*3*).

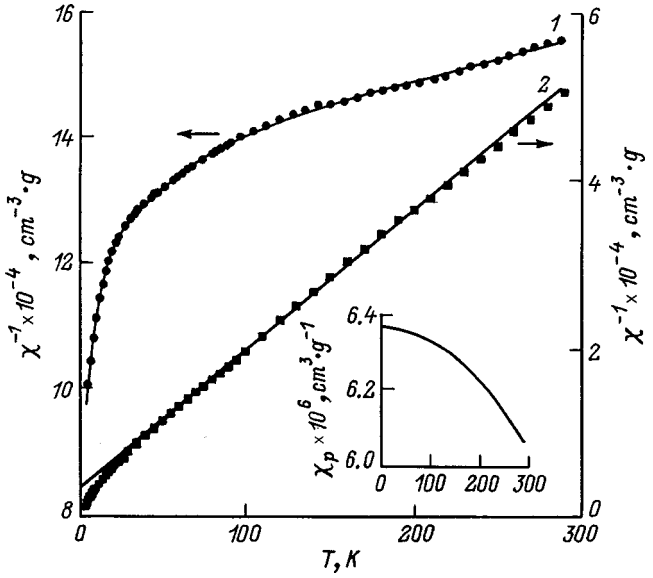

FIG. 4. The reciprocal of the magnetic susceptibility as a function of temperature for $YbNi_4In$ (*1*) and $YbNiIn_4$ (*2*). The inset shows the Pauli component of the magnetic susceptibility of $YbNiIn_4$.

splits into three sublevels with degeneracies $\alpha=2(\Gamma_6)$, $2(\Gamma_7)$ and $4(\Gamma_8)$. On examining all the possible transitions in such a crystal field, we obtain the following values for ν: 0.20 ($\alpha_l=2$, $\alpha_h=4$), 0.086 ($\alpha_l=2$, $\alpha_h=6$), 0.048 ($\alpha_l=2$, $\alpha_h=8$), 0.43 ($\alpha_l=4$, $\alpha_h=6$), and 0.24 ($\alpha_l=4$, $\alpha=8$). The experimental value $\nu=0.18$ observed in our case is closest to the value obtained in a scheme where the $4f$ level splits with doublet ground and first excited states ($\alpha_l=2$, $\alpha_h=4$). Thus, we may assume that the two linear segments in $\rho_m(\ln T)$ are related to Kondo scattering of charge carriers, predominantly in the doublet at temperatures $T<60$ K and in the fourfold degenerate $4f$ level for $T>60$ K.

The existence of crystal field effects in the Kondo scattering mechanism is confirmed by measurements of the thermal emf. A comparison of the $S(T)$ curves for $YbNi_4In$ and its analog $NdNi_4In$ shows that the Kondo centers make a characteristic negative contribution to the total S with a minimum $S_{\min}=12\,\mu$V/K at temperatures $T_{S_{\min}}\approx T_{\rho_m,\max}\propto\Delta(\Gamma_6\rightarrow\Gamma_7)$. This behavior of $S(T)$ ($S\propto T$ for $T<T_{S_{\min}}$ and $S\propto T^{-1}$ for $T>T_{S_{\min}}$) is qualitatively well described by an impurity Kondo model including the crystal field.[15] The proposed scheme, with splitting of the $4f$ level of the Yb^{3+} ion in $YbNi_4In$, agrees satisfactorily with the measured specific thermal emf and magnetization[6] but not with inelastic neutron scattering measurements.[5]

The measured ρ and S for $YbNiIn_4$ (Figs. 2 and 3) were somewhat unexpected. $\rho(T)$ is well fit by the Bloch-Grüneisen law for a Debye temperature $\theta_D=140$ K and a residual resistance $\rho_0=0.3\,\mu\Omega\cdot$cm. The absence of any additional contributions to ρ and S owing to the existence of Yb states with mixed valence in the crystal and an unusually low residual resistance for this type of compound are evidently characteristic of $YbNiIn_4$.

Figure 4 shows plots of the measured temperature variation in χ for $YbNi_4In$ and $YbNiIn_4$. Plotting the data in the form of χ^{-1} as a function of T shows that the magnetic susceptibility of $YbNi_4In$ follows the Curie–Weiss law over a wide range of temperatures. A deviation of $\chi^{-1}(T)$ from linear is observed only for $T<50$ K and appears to be related to splitting of the $4f$ level of Yb^{3+} by the crystal field and the occurrence of a magnetic transition with $T_C=3$ K.[6] Estimates of the effective localized magnetic moment and paramagnetic Curie temperature θ_P from the high temperature segment of the $\chi^{-1}(T)$ curve give $\mu_{\text{eff}}=4.6\,\mu_B$ and $\theta_P=-18$ K. The somewhat higher values of μ_{eff} and θ_P than those obtained in Ref. 6 indicate that χ may be sensitive to the $Yb\leftrightarrow Ni$ atomic substitutions observed in $YbNi_4In$. The negative paramagnetic temperature may serve as a qualitative characteristic of the energy of the Kondo interaction of an ''impurity'' f center with the electrons in the conduction band ($T_K\approx|\theta_P|/3$[16]). At temperatures $T>60$ K, where the f level can be regarded as partially degenerate ($\alpha_h=4$), an estimate of the Kondo temperature T_K for $YbNi_4In$ gives ~6 K.

For $YbNiIn_4$ the $\chi^{-1}(T)$ curve is more complicated, and resembles the case of an exchange-enhanced Pauli paramagnet with a paramagnetic impurity. Given the possibility that the impurity Yb^{3+} ions may exhibit paramagnetism ($\mu_{\text{eff}}=4.54\,\mu_B$, $\theta_P=0$) and that an impurity Yb_2O_3 phase ($\mu_{\text{eff}}=4.54\mu_B$, $\theta_P=45\pm15$ K[17]) may form during the production of this type of compound by arc melting, $\chi(T)$ for $YbNiIn_4$ is given approximately by

$$\chi(T)=C_1/T+C_2/(T+\theta_P)+\chi_P(T),$$

$$\chi_P(T)=\chi_P(0)[1+a(T/T_{sf})^2].$$

Here the first and second terms describe the paramagnetism of Yb^{3+} and Yb_2O_3 impurities, respectively. The third term describes the Fermi liquid behavior of the component of χ resulting from valence-unstable Yb.[18] The smallest error in the approximation (<2 %) occurs for the following parameter values: $C_1=1.1\times10^{-5}$ cm^{-3} g^{-1} K^{-1}, $C_2=1.2\times10^{-4}$ cm^{-3} g^{-1} K^{-1}, $\theta_P=69.6$ K, $\chi_P(0)=6.4\times10^{-6}$ cm^3 g^{-1}, $a=-1.0$ and $T_{sf}=1340$ K. This corresponds to a paramagnetic impurity in an amount ~0.3 at. % relative to the magnetic moment of the free Yb^{3+}, ~3 % Yb_2O_3, and a paramagnetic component of χ_P which decreases with rising T (inset to Fig. 4). Using the relationship between the spin fluctuation temperature T_{sf} and the paramagnetic susceptibility at $T=0$ from the paramagnetic model[18] ($T_{sf}=C/2\chi_f(0)$, where $C=2.58$ emu/mol $\cdot$ K is the Curie constant for the free Yb^{3+} ion), we can estimate the contribution to $\chi_P(0)$ from the component $\chi_f(0)$ associated with valence-unstable Yb. For $T_{sf}=1340$ K we obtain $\chi_f(0)=1.3\times10^{-6}$ cm^3 g^{-1}. By comparing the differences $\chi_P(0)-\chi_f(0)=5.1\times10^{-6}$ cm^3 g^{-1} with $\chi_f(0)$, we find that the electron density of states at the Fermi level is made up predominantly of the d-states of N, which is nonmagnetic in $YbNiIn_4$.

The above estimates of T_{sf} and $\chi_f(0)$ correlate well with the analogous formulas obtained from the Anderson impurity model in the approximation of an expansion in $1/N_f$($\chi_f(0)=Cn_f/T_K$[19]). Using the estimate for $\chi_f(0)$ and our measured population $n_f\approx0.4$, we obtain $T_K\approx1070$ K, which is comparatively close to T_{sf}. The high values of T_{sf} (or T_K)

are qualitatively consistent with the absence of a significant contribution from valence-unstable Yb to the ρ and S measured to temperatures $T \ll T_{sf}$. According to Ref. 19, in the case of strong mixing of the fluctuating configurations of Yb, a peak in the density of states of width $\sim kT_{sf}$ develops at the Fermi level with a shape that is close to symmetric Lorentzian. Thus, significant additional contributions to ρ and S may be expected for $T \sim T_{sf}$. A similar valence instability regime for Yb is apparently realized in YbM_2 ($M =$ Al, Cu).[20]

The above set of data imply that, in compounds of the type $YbNi_nIn_m$, two limiting states of valence-unstable Yb are realized, magnetic and nonmagnetic, with almost maximum mixing of the fluctuating configurations. The distinctive behavior of $YbNi_4In$ is determined by Kondo interactions with a characteristic temperature T_K that is comparable to the magnetic ordering temperature T_C (the absence of a Fermi-liquid segment in ρ and saturation in χ as $T \to 0$). The measurements of the magnetic component of the electric resistance $\rho_m(\ln T)$ and thermal emf are in good qualitative agreement with the scheme for splitting of the $4f$-level of Yb^{3+} proposed in Ref. 6 on the basis of measurements of the specific heat and magnetization. The splitting of the $4f$ level in the crystal field of $YbNi_4In$ with formation of a quadruplet in the ground state, which is based on inelastic neutron scattering measurements,[5] is less plausible.

In the case of $YbNiIn_4$, strongly mixed valency of Yb is observed which is qualitatively well described by the Anderson impurity model with the degeneracy taken into account. An unusual feature of this type of compounds is the observation of an anomalously low resistivity in $YbNiIn_4$ with a comparatively high density of states at the Fermi level. Evidently, besides features of the valence instability of Yb, some distinctive features of the crystal structure also show up in this case. According to Ref. 7, a spatial shell of In atoms is formed in the $YbNiIn_4$ structure (the interatomic distance $d(\mathrm{In}-\mathrm{In}) \approx 3.2$ Å in the shell, a distance close to the corresponding interatomic distance in metallic In); this shell can form a separate group of free charge carriers from p states which are spatially separated from the localized $4f$ states. In this situation, the contribution from the scattering of charge carriers on the f centers to the total ρ will be shunted by the high conductivity of the p band of In. The existence of such a band can also explain the observed low sensitivity of the residual electrical conductivity to the partial atomic ordering in $YbNiIn_4$ caused by mutual Yb $\leftrightarrow$ Ni substitution to within ~ 2 at.%

*)E-mail: koterlyn@wups.lviv.ua

[1] A. Amato, Rev. Mod. Phys. **69**, 1119 (1997).
[2] M. D. Koterlin, B. S. Morokhivskiĭ, N. G. Babich, and N. I. Zakharenko, Fiz. Tverd. Tela **36**, 842 (1994) [Phys. Solid State **36**, 463 (1994)].
[3] M. D. Koterlin, B. S. Morokhivskiĭ, N. G. Babich, and N. I. Zakharenko, Fiz. Tverd. Tela **36**, 1162 (1994) [Phys. Solid State **36**, 632 (1994)].
[4] G. Liang and M. Croft, Phys. Rev. B **40**, 361 (1985).
[5] A. Severling, E. Gratz, B. D. Rainford, and K. Yoshimura, Physica B **163**, 409 (1990).
[6] J. L. Sarrao, R. Modler, R. Movshovich, A. H. Lacerda, D. Hristova, A. L. Cornelius, M. F. Hundley, J. D. Thompson, C. L. Benton, C. D. Immer, M. E. Torelli, G. B. Matrins, Z. Fisk, S. B. Oseroff, Phys. Rev. B **57**, 7785 (1998).
[7] V. I. Zaremba, V. M. Baranyak, and Ya. M. Kalychak, Vestn. L'vov Un-ta. Ser. Khim **25**, 18 (1984).
[8] Ya. M. Kalychak, V. M. Baranyak, and V. I. Zaremba, Kristallografiya **33**, 1017 (1988) [Sov. Phys. Crystallogr. **33**, 602 (1988)].
[9] V. A. Romaka, Yu. N. Grin', and Ya. P. Yarmolyuk, Ukr. Fiz. Zh. **28**, 1095 (1983).
[10] V. A. Romaka, R. V. Skolozdra, R. M. Rykhal', and O. S. Koshel', in *Physics of Magnetic Materials* (Irkutsk, 1981), p. 105.
[11] M. D. Koterlin, O. I. Babich, B. S. Morokhivskiĭ, L. I. Nikolaev, and A. V. Yushchenko, Preprint No. 15 (Inst. of Materials Physics, Kiev, 1987), 28 pp.
[12] M. D. Koterlin, B. S. Morokhivskiĭ, I. D. Shcherba, and N. G. German, Ukr. Fiz. Zh. **38**, 262 (1993).
[13] J. M. Lawrence, G. H. Kwei, P. C. Canfield, J. G. DeWitt, and A. C. Lawson, Phys. Rev. B **49**, 1627 (1994).
[14] B. Cornut and B. Coqblin, Phys. Rev. **5**, 4541 (1972).
[15] A. K. Bhattacharjee and B. Coqblin, Phys. Rev. B **13**, 3441 (1976).
[16] J. M. Kawrence, Phys. Rev. B **20**, 3770 (1979).
[17] J. C. P. Klaase, F. R. deBoer, and P. F. deChatel, Physica B **106**, 178 (1981).
[18] M. T. Beal-Monod and J. M. Lawrence, Phys. Rev. B **21**, 5400 (1980).
[19] Y. Kuramoto and E. Müller-Hartmann, J. Magn. Magn. Mater. **52**, 122 (1985).
[20] A. Fujimori, T. Shimizu, and H. Yasuoka, Phys. Rev. B **35**, 8945 (1987).

Translated by D. H. McNeill

Electronic structure and lattice stability in the dihydrides of titanium, zirconium, and hafnium

S. E. Kul'kova,*) O. N. Muryzhnikova, and I. I. Naumov

Institute of Structural-Reliability Physics and Materials Science, Siberian Branch, Russian Academy of Sciences, 634021 Tomsk, Russia

(Submitted May 12, 1999)
Fiz. Tverd. Tela (St. Petersburg) **41**, 1922–1930 (November 1999)

A self-consistent linear MT-orbital method in the atomic sphere approximation (LMTO-ASA) is used to calculate the electronic structure of the dihydrides of the group IV metals in their cubic and tetragonal phases. The effect of tetragonal deformation and hydrogen vacancies on the electronic characteristics is studied. Satisfactory agreement is obtained with experimental data of photoelectron spectra. The nature of the instability in the high-temperature cubic phase is discussed. © *1999 American Institute of Physics.* [S1063-7834(99)00311-1]

The transition metals titanium, zirconium, and hafnium have nearly the largest capacity to absorb hydrogen among all metals. The hydrides based on them have a wide range of interesting physical properties and their structure and phase transformations differ from those observed in the pure metals.[1] These and other circumstances continue to attract the attention of metal physicists to these systems.

At relatively high temperatures, the dihydrides of titanium, zirconium, and hafnium exist as an interstitial phase with a fluorite (CaF_2) structure. The structure of these compounds, in which the hydrogen atoms occupy tetrahedral voids in a metallic face-centered cubic (fcc) lattice is not the same as that of the pure metals–body-centered cubic or hexagonal close packed, depending on the temperature. On cooling to temperatures on the order of room temperature, the cubic (C) structure of the dihydrides becomes unstable and transforms to tetragonal (T). Reducing the hydrogen concentration (x) stabilizes the cubic phase, and for $x<1.8$ it ceases in general to undergo this transformation to the T phase. Many physical properties of the ''incomplete'' hydrides, including their resistivity, Hall and thermal emf coefficients, magnetic susceptibility, electron specific heat, etc., have a significant dependence on x.[2–4]

Attempts to understand the physical properties and the nature of the lattice stability of the dihydrides of the group IV metals have stimulated calculations of their band structure. Most of these calculations have been done for titanium dihydride, especially for its cubic phase.[5–11] One feature of the band structure of this phase (as, by the way, of the tetrahedral phase) is the presence of two hydrogen bands below the Fermi level E_F, one of which lies immediately adjacent to E_F.[5,6] Another characteristic feature is the almost dispersionless double degeneracy of the band in the $\Gamma-L$ direction, which joins the Γ'_{25} and L_3 terms and intersects the Fermi level twice.[7–13] This feature leads to an extremely high density of electron states at the Fermi level.[7–11,13] Calculations of the cubic phase of the ZrH_2 and HfH_2 systems[14] have not yielded a high $N(E_F)$ (the degenerate band lay significantly higher than E_F, especially for ZrH_2). This led to the question of whether this feature is universal for all the group IV dihydrides.

Almost all these papers have discussed the nature of the chemical bond by analyzing the effective charge on the hydrogen atoms and various conclusions have been reached. In some papers, transfer of an additional charge to the hydrogen sphere is predicted (for example, 0.53 electrons in Ref. 10), while in others, from the hydrogen sphere (0.425 and 0.135 electrons, respectively, in Refs. 6 and 12).

Calculations of the electronic structure of the dihydrides with vacancies in the hydrogen sublattice for TiH_2[12] have shown that the growth of hydrogen vacancies leads to a rise in the density of ''vacancy'' states below the Fermi level, while including the partial ordering in the hydrogen sublattice leads to a small splitting of the hydrogenic low-energy band. In Ref. 15, on the other hand, a substantial splitting of the hydrogenic band is predicted, leading to two distinct peaks in $N(E)$ separated by a deep minimum, along with a weak change in the spectrum near the Fermi level; the first effect is related to partial ordering of the hydrogen vacancies.

The nature of the structural transformations in these systems has been discussed mainly by Kulikov *et al.*[8,16] Based on band calculations for the cubic phase of TiH_2,[6,7] it was concluded[16] that the structural transition from a cubic to a tetragonal structure is caused by Jahn–Teller splitting of the already-cited doubly degenerate band in the $\Gamma-L$ direction. This conclusion was confirmed by calculating the band structure of the T phase of titanium hydride by the model Hamiltonian method (approximate solution of the secular equation by the Korringa–Kohn–Rostocker (KKR) method):[8] when the lattice symmetry is reduced, the doubly degenerate band actually does split in a way such that E_F falls inside the resulting energy gap of width $0.03-0.05$ Ry. Doubts were raised about this picture by the results of Switendick,[13] who found that the structure of the dispersion bands for the T phases of TiH_2 and ZrH_2 differ from those obtained in Ref. 8, as well as the very character of the change in the electronic characteristics for transition from the C to the T phase. In the case of ZrH_2, for example, the peak in the electron density of states is shifted to lower energies, so that

TABLE I. Lattice parameters, radii of atomic spheres, and characteristic energy differences for the dihydrides of group IV metals for different ways of calculating the electronic structure

Compound	TiH_2			ZrH_2			HfH_2
Number of atoms per unit cell, at./unit cell	3 (I)	4 (II)	4 (III)	3 (I)	4 (II)	4 (III)	4 (II)
a, a.u.		8.3905			8.8138		8.8968
$R_s(Me)$	2.2735	2.0656	2.2120	2.3882	2.1698	2.3244	2.1903
R_s(H)	2.2735	2.0656	2.0109	2.3882	2.1698	2.1131	2.1903
E_F, Ry	0.038	0.239	0.201	0.139	0.377	0.320	0.344
$E_F - V_s$, Ry	0.809	0.943	0.851	0.893	1.067	0.940	1.069
$E_F - \Gamma_1$, Ry	0.752	0.798	0.785	0.695	0.791	0.762	0.884
$E_F - \Gamma'_{25}$, Ry	0.047	0.021	0.023	0.070	0.025	0.030	0.024
$E_F - \Gamma'_2$, Ry	−0.170	−0.070	−0.100	−0.047	0.025	0.049	0.114
$\Gamma'_2 - \Gamma_1$, Ry	0.922	0.869	0.886	0.743	0.696	0.713	0.766
$N(E_F)$, el./(Ry · unit cell)	53.408	20.20	19.96	54.72	14.49	17.17	11.68
Me	33.314	14.13	14.54	25.84	7.62	9.77	5.89
H	19.391	5.33	4.77	28.88	6.25	6.50	5.28
E	–	0.74	0.65	–	0.62	0.91	0.51
E_{tot}, Ry/unit cell	−10.1752	−9.6910	−9.8458	−9.1756	−8.3796	−8.5498	−8.4203

the Fermi level falls into a local minimum in the T phase. In the case of TiH_2, the situation is somewhat different: with the decline in the peak of the electronic density of states in the C phase, the Fermi level falls exactly into a maximum of the density of states in the T phase, leading to a rise in $N(E_F)$, which contradicts the experimentally observed tendency.[3,4,17] The disagreement with experiment was attributed[13] to factors influencing the experimental data (in particular, the presence of impurities and the effect of temperature), as well as to the computational approximations.

Therefore, despite numerous experimental and theoretical studies, the chemical bond, electronic structure, and driving forces for structural transitions in the titanium-group hydrides are still not uniquely established. In this regard, the purpose of this paper is to calculate and analyze the band structure of ideal and defective dihydrides of titanium, zirconium, and hafnium in the cubic and tetragonal phases, as well as to discuss the possible reasons for the instability in the cubic phase close to a stoichiometric composition.

1. COMPUTATIONAL TECHNIQUE

The band structure of the dihydrides was calculated in a self-consistent LMTO-ASA with a Ceperley-Alder exchange-correlation potential.[18] In order to analyze the sensitivity of the results to the choice of initial parameters, during the calculations we varied the ratio of the radii of the atomic spheres of the metal and hydrogen, R_s, from 1.0 to 1.4 by introducing supplementary ''empty'' spheres (to model the anisotropy of the crystal potential) and expanded the basis of the atomic orbitals. In the following we shall distinguish three main computational variants: (I) with 3 atoms per unit cell and a ratio of radii $R_s(Me)/R_s(\mathrm{H})=1$, (II) with 4 atoms, with the additional ''atoms'' consisting of ''empty'' spheres in the octahedral interstices ($R_s(Me)/R_s(\mathrm{H})=1$), and, finally, (III) the same as II but with a ratio $R_s(Me)/R_s(\mathrm{H})=1.1$. Self consistency was extended over 161 k points in the nonconducting part of the Brillouin zone for the fcc cell and was assumed to be achieved if the change in the eigenenergies was less than 0.003Ry, while the pressure calculated in each interaction using the Pettiford equation[19] was 1 kbar. The lattice parameters for the tetragonal phase of titanium dihydride were taken from Ref. 8 ($a=4.53$ Å, $c=4.28$ Å) and for that of zirconium dihydride from Ref. 20 ($a=4.94$ Å, $c=4.50$ Å). The calculation for the defective dihydrides was done by a model, similar to Ref. 21, based on repeating supercells with twelve atoms. A hydrogen vacancy was modelled by replacing one of the hydrogen atoms with an ''empty'' sphere with zero charge density.

2. RESULTS AND DISCUSSION

The positions of the characteristic energies in the spectrum relative to the Fermi level in the cubic structure of the dihydrides under study here are listed in Table I. Evidently, the triply degenerate hydrogen term Γ'_{25} lies below E_F, while the second hydrogen term Γ'_2 lies above it (TiH_2 (I), ZrH_2 (I)). Introducing additional empty spheres (on going to variant II) makes the Γ'_2 level fall below E_F both in ZrH_2 (Fig. 1), and in HfH_2, while in TiH_2 it remains slightly above it. Thus, the position of this level above or below E_F is established by the model for constructing the crystal potential. (This also follows from an analysis of Refs. 7–11, 14, and 20). The second hydrogen term in HfH_2 lies somewhat lower than in ZrH_2, while the width of the hydrogen band of hafnium dihydride is higher. A change in the ratio of the radii of the atomic spheres by increasing the radius of the sphere for the metal (by 20–40%) changes the results insignificantly. The total energy of titanium dihydride is less than for those of zirconium and hafnium, which, in turn, are essentially equal. The occupied portion of the d band ($E_F - \Gamma'_{25}$) varies within 4 mRy over the series of dihydrides.

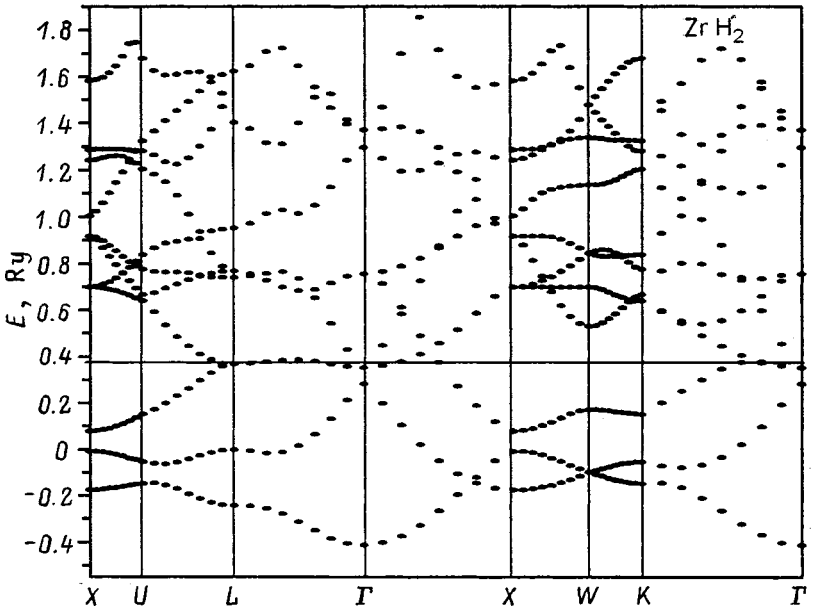

FIG. 1. Electronic energy spectrum of ZrH_2.

We now compare the results of our calculations (in variant II) with those of other authors (Table II). Many of the spectral characteristics are evidently in good agreement with one another, except for the density of states at the Fermi level: there the scatter in the values is quite large, with ours one of the smallest.

Figures 2a and 2c show the density of states for titanium and zirconium hydrides in the *C* phase for two computational variants (I and II). The new bands below the Fermi energy in the second variant show up in the form of a small bump on the electron density of states curve; there $N(E_F)$ is significantly lower. An analysis shows that the structure of this band results from a reduction in the energy of the terms genetically associated with ''antibonding'' states of hydrogen, in particular Γ_2'. The reduction in the electron density of states at the Fermi level in the sequence $TiH_2-ZrH_2-HfH_2$ correlates with the available experimental data.[3,17] Whereas the contribution of the metal to $N(E_F)$ predominates for TiH_2, in good agreement with earlier work,[9] for HfH_2 the contributions of the metal and hydrogen are essentially equal (Table I).

This calculation establishes that charge transfer takes place from the metal to the hydrogen, with titanium yielding

TABLE II. Electronic characteristics of the dihydrides, obtained by various methods.

Parameters of the band structure	TiH_2	ZrH_2	HfH_2	Computational method**
		C-phase		
$\Gamma_2'-\Gamma_1$, Ry	0.869,* 0.79 (Ref. 11),	0.696,* 0.60 (Ref. 11),	0.766,* 0.71 (Ref. 11)	APW
	0.73 (Ref. 13)	0.55 (Ref. 13), 0.54 (Ref. 27)		APW
$E_F-\Gamma_{25}'$, Ry	0.021,* 0.018 (Ref. 9)	0.025,* 0.031 (Ref. 27)	0.024*	APW
$E_F-\Gamma_1$, Ry	0.798,* 0.8 (Ref. 9)	0.791,* 0.710 (Ref. 27)	0.884*	APW
E_F-V_s, Ry	0.943,* 0.98 (Ref. 7)	1.067,* 2.030 (Ref. 27)	1.069	KKR
$N(E_F)$, el./(Ry · unit cell)	20.20*	14.49*	11.68*	LMTO-ASA
	16.85 (Ref. 12)	–	–	LCAO-CP
	23.12 (Ref. 13)	20.13 (Ref. 13)	–	APW
	25.84 (Ref. 7)	–	–	KKR
	31.28 (Ref. 11)	19.31 (Ref. 11)	15.91 (Ref. 11)	APW
	41.06 (Ref. 9)	32.92 (Ref. 27)	–	APW
	27.47 ($x=1.8$) (Ref. 3)	14.96 ($x=1.5$) (Ref. 3)	–	Experiment
		T-phase		
E_F-V_s, Ry	0.941,* 0.90 (Ref. 8)	0.987*		
$\Delta\Gamma_{25}'$, Ry	0.003,* 0.003 (Ref. 8)	0.021,* 0.029 (Ref. 13)		
ΔL_3, Ry	0.044,* 0.045 (Ref. 8)	0.063,* 0.077 (Ref. 13)		
$N(E_F)$, el./(Ry · unit cell)	16.42*	10.20*		LMTO-ASA
	23.66 (Ref. 8)	9.52 (Ref. 13)		KKR
	25.02 (Ref. 13)			APW
	17.68 ($x=2.0$) (Ref. 3)	8.98 ($x=1.96$) (Ref. 3)		Experiment

*Our calculations by the LMTO-ASA method.
**APW — associated plane wave method, LCAO-CP— Linear combinations of atomic orbitals in the coherent potential approximation.

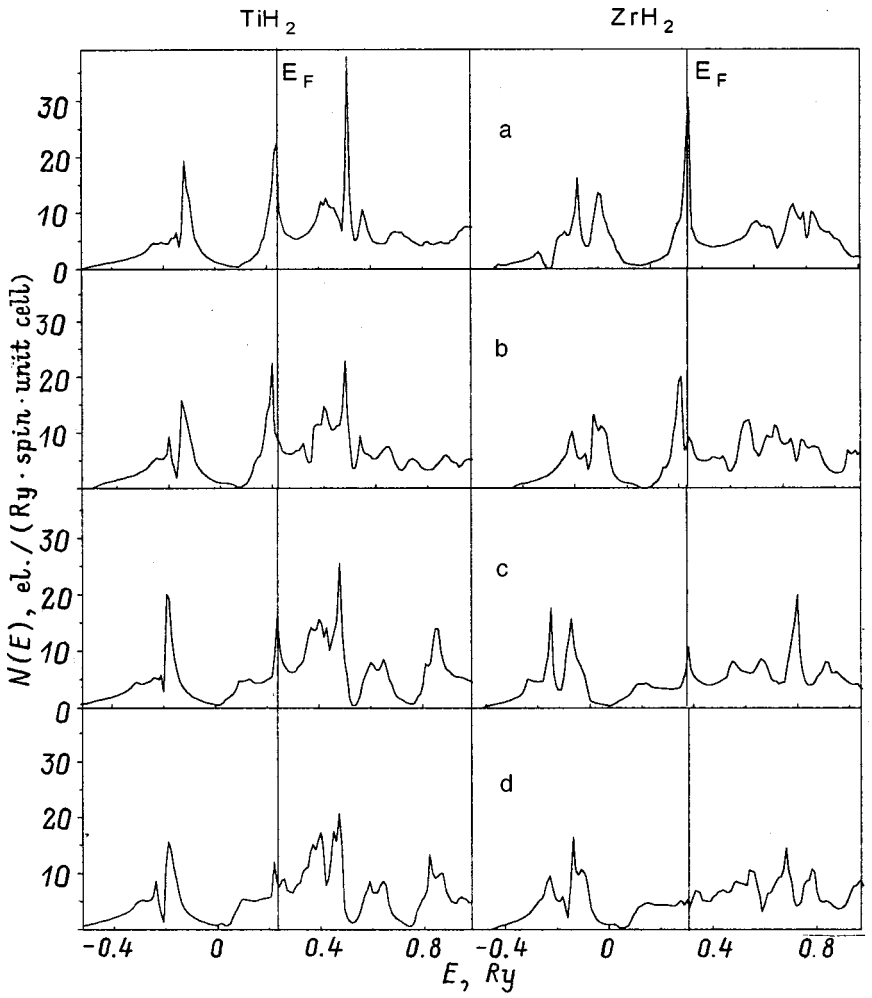

FIG. 2. Total electron density of states of TiH_2 and ZrH_2 in the *C* and *T* phases (a, c) and (b, d), respectively: a, b — calculated for three atoms per cell; c, d — calculated including an additional ''empty'' sphere.

less charge than zirconium and hafnium. The charge in an ''empty'' sphere and the charge transferred to a hydrogen sphere are practically equal: -0.73 and -0.72 electrons, respectively in TiH_2 and 0.92 and 0.93 electrons in HfH_2 (for equal atomic spheres). Note that the radius used for the hydrogen atomic sphere exceeds that for the *MT* spheres from Refs. 7 and 9; this corresponds to greater overlap of the metal and hydrogen spheres than of the spheres of nearest hydrogen atoms. This also leads to a higher charge in the hydrogen sphere than in Refs. 7 and 9. When the radius of the hydrogen sphere for TiH_2 is reduced by 10–40%, the charge in the hydrogen sphere falls to $1.63-1.36$ electrons/atom. The cross sectional areas of the Fermi surface for all the dihydrides are all extremely close, except for the size of the electron surface in the center of the Brillouin zone (the point Γ); they differ negligibly from those given in Ref. 9 for TiH_2.

It should be emphasized that the electronic structure of the cubic phase contains a dispersionless zone along the $\Gamma-K$ direction, as well as along $\Gamma-L$ (Fig. 1). The role of the former direction in the formation of the characteristic peak in the electronic density of states is just as important as that of $\Gamma-L$. In order to demonstrate this, we calculated the contributions of the third and fourth zones, both along $\Gamma-L$ and along $\Gamma-K$, to the density of states for TiH_2 and ZrH_2 (Fig. 3). Only the small regions of *k* space adjacent to the corresponding directions were included. As the figure shows, the two directions make comparable contributions to $H(E_F)$. (Given that there are more $\Gamma-K$ directions than $\Gamma-L$ directions, the total contribution from them will be roughly 4/3 times greater than that from $\Gamma-L$.)

The calculated electronic densities of states in the *T* phase of titanium and zirconium hydrides are shown in Figs. 2b and 2d. The distinctive feature of the band structure in this phase (compared to the cubic phase) is a greater splitting of the lower-lying hybrid zone (especially for TiH_2), as well as a shift of the main peak in the electron density of state to lower energies. The latter means that E_F in the *T* phase passes through a local minimum in the higher energy band of the electron density of states; the same result has been obtained elsewhere for ZrH_2.[13] Introducing additional ''empty'' spheres has practically no effect on the low energy part of the spectrum; the character of the splitting and the absolute magnitudes of the peaks in the density of states do not change. As in the case of the *C* phase, however, the largest changes occur in states near E_F; a bump develops below the Fermi energy. The latter effect brings the calculated value of $N(E_F)$ closer to the experimental value (compare 16.42 with 17.68[3] for TiH_2, and 10.20 with 8.98[3] for ZrH_2, all in units of electrons/Ry · unit cell).

The band structures of TiH_2 and ZrH_2 along the $\Gamma-L$ and $\Gamma-K$ directions in the *C*- and *T*-phases are shown in

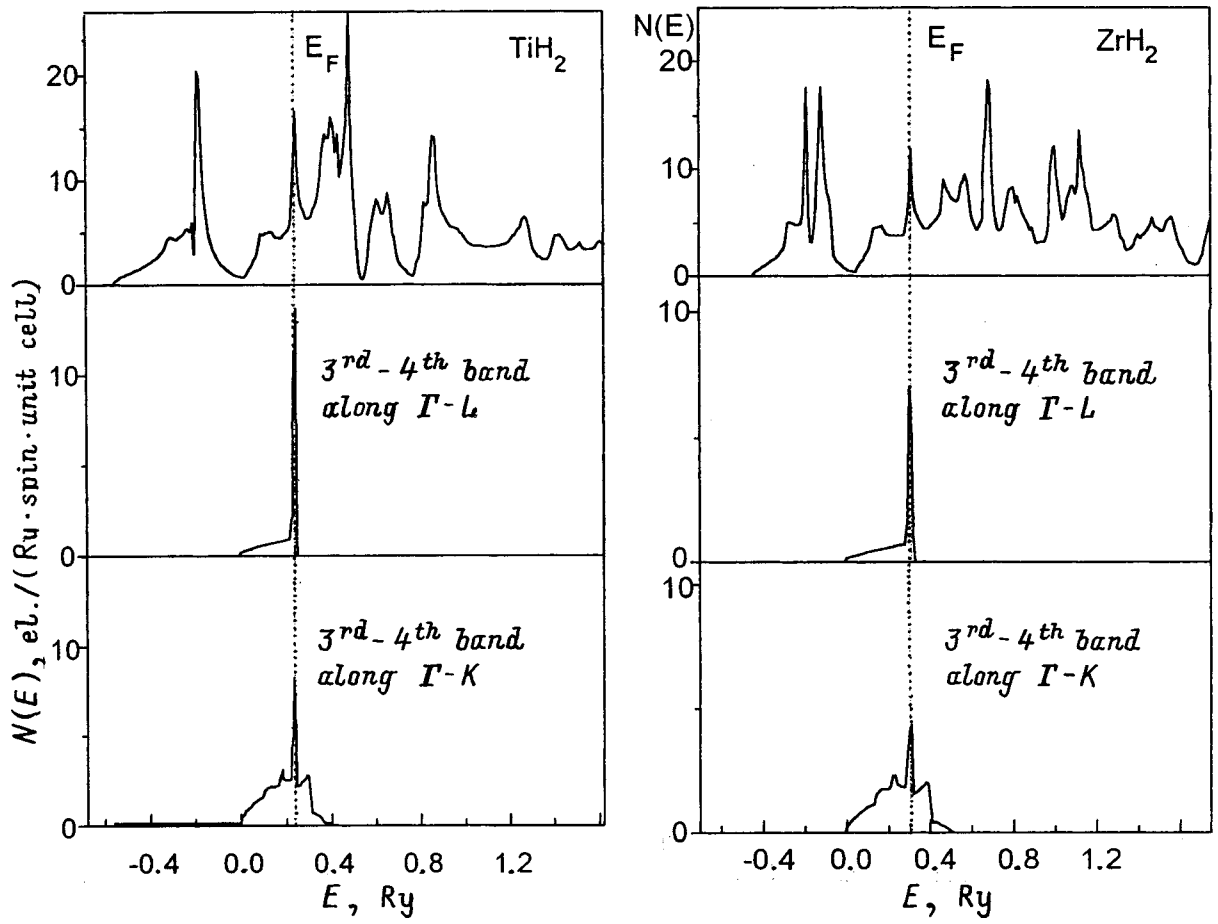

FIG. 3. Total electron density of states of TiH_2 and ZrH_2 in the C phases and the contributions to the electron density of states from the 3rd and 4th bands along the $\Gamma-K$ and $\Gamma-L$ directions.

Fig. 4. A tetragonal distortion of the cubic lattice reduces the symmetry and causes the appearance of two points, K_1 and K_2, in the nonconducting part of the Brillouin zone of the face-centered tetragonal lattice instead of a single point K in the nonconducting part of the Brillouin zone of the fcc lattice. [Since the tetragonal phase for the hydrides is obtained by a small distortion along the vertical axis of the fcc lattice (the metal atoms remain at the centers of the faces), in order to analyze the changes in the electronic structure during the $C-T$ transition it was convenient to carry out the calculation in this representation for the tetragonal lattice, although the face centered tetragonal lattice is the very same volume centered tetragonal lattice, but with transformed translation vectors in the horizontal plane.] Thus, for the T phase we introduce two directions, $\Gamma-K_1$ and $\Gamma-K_2$. Because of the distortion, the third band along $\Gamma-K$ is shifted upward and that along $\Gamma-L$ is shifted downward in energy; on the whole, this leads to a reduction in $N(E_F)$. Here both the terms formed at the point Γ lie below E_F, while at the point L the upper band lies above E_F. The splitting of the term Γ'_{25} for TiH_2 equals 0.003 Ry (cf. 0.03[8]) and for ZrH_2 it equals 0.021 (0.029[13]). The splitting at point L for TiH_2 is as high as 0.044 Ry (0.045[8]). Along the direction $\Gamma-K_1$ the third and fourth bands near E_F contain sections with a low dispersion and weak splitting (especially in TiH_2). In addition, along $\Gamma-L$ the third band falls below E_F by only 0.002 Ry, thereby keeping the dispersion low. Therefore, the main contribution to the $N(E_F)$ in the T-phase, as well as in the C phase, is from the regions of k space adjacent to the $\Gamma-K_1$, $\Gamma-K_2$, and $\Gamma-L$ directions.

A calculation without additional ''empty'' spheres yields a substantially smaller splitting of the bands, with both bands at the point L lying above E_F. This indicates that the spectrum near the Fermi energy depends significantly on the anisotropy in the potential. Thus, within the framework of the scheme used here (the atomic sphere approximation), we cannot reach an unambiguous conclusion about the behavior of the electronic states and their realignment during a structural transformation near E_F. The picture can be modified by using different approximations for the exchange-correlation potential and the magnitude of the changes may be comparable to the splitting of the degenerate bands. We believe that a more detailed discussion of the possible nature of the $C-T$ transition in terms of the electronic structure will require more precise calculations using, for example, a full potential method.

Note that the Γ'_2 level in TiH_2 lies above the Fermi energy in both the cubic and tetragonal phases (as in Ref. 8). In ZrH_2, the position of the Γ'_2 terms also does not vary relative to E_F. Varying the lattice parameters for the tetragonal phase of ZrH_2 does not reflect significantly on the results for

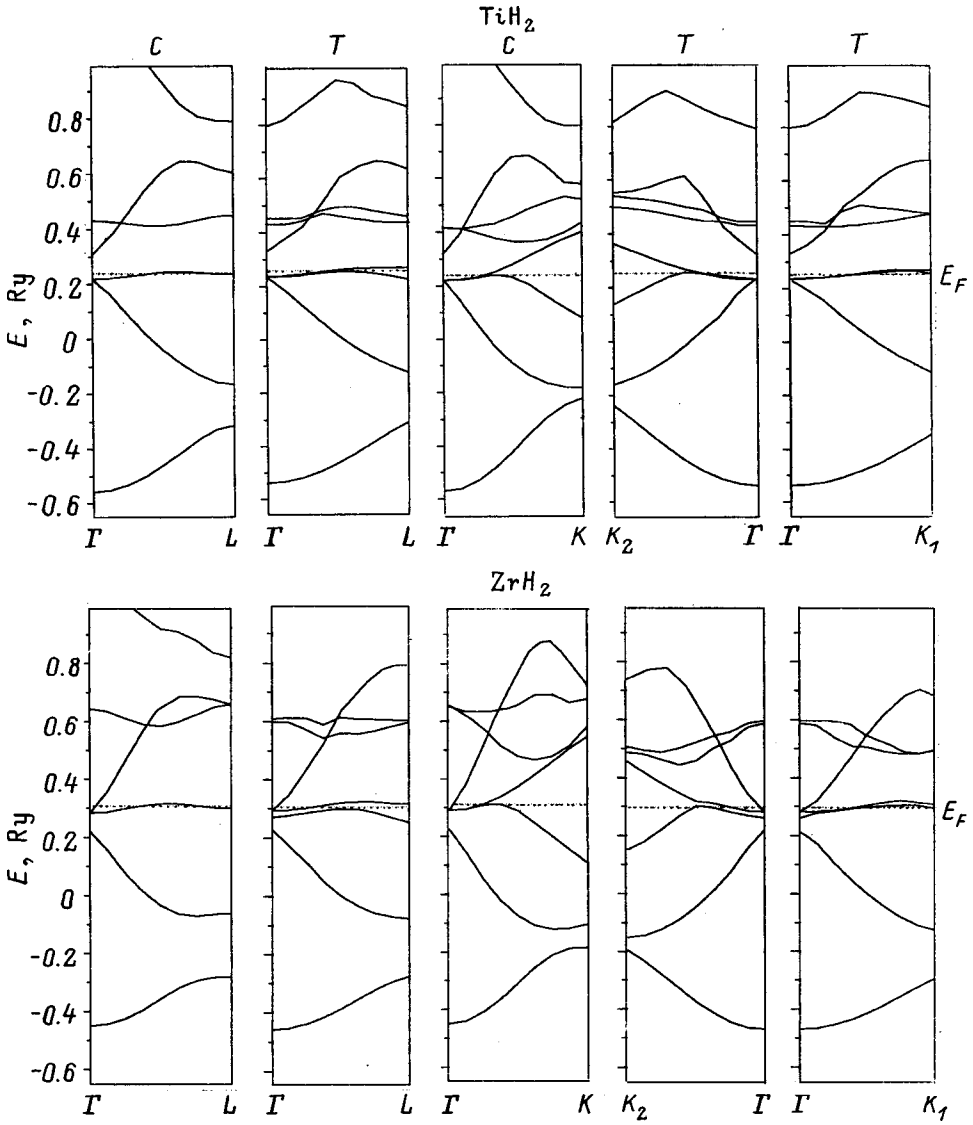

FIG. 4. Band spectra of TiH_2 and ZrH_2 in the *C*- and *T*- phases along the $\Gamma - L$ and $\Gamma - K$ directions.

the electronic characteristics. The widths of the occupied portions of the valence band in the *C* and *T* phases are similar. On going from the *C* to the *T* phase, the total energy decreases: from -1.6959 to -1.6990 Ry/electron in TiH_2 and from -1.4935 to -1.5002 in ZrH_2.

The total densities of the electronic states in the ideal and defective dihydrides are shown in Fig. 5. As the hydrogen concentration is reduced, the characteristic peak in the region of the Fermi level splits into two and $N(E_F)$ falls (from 217.51 to 145.83 electrons/(Ry · unit cell) in $ZrH_{1.75}$). The latter is consistent with Ref. 12. A shift in the Fermi level ($0.074-0.069$ Ry) and a reduction in the width of the occupied portion of the valence band ($0.696-0.668$ Ry) are observed. When there is a vacancy in the hydrogen sublattice, the metal orbitals hybridize with the additional orbitals of the vacancy; this is confirmed by a substantial transfer of density, up to 1 electron, in the metal-vacancy direction. The total energy for defective zirconium dihydride obtained here (-1.5083 and -1.5214 Ry/electron for concentrations of 1.75 and 1.5 electron, respectively) is lower than for the ideal (-1.4903). Similarly, in titanium dihydride with a hydrogen concentration of $x=1.5$, E_{tot} equals -1.7342 and -1.6959 Ry/electron for the stoichiometric composition.

Figure 5 also shows experimental x-ray photoelectron spectra,[22] which are in satisfactory agreement with the theoretical plots of the electronic density of states. The characteristic features of the photoelectron spectrum from Ref. 22 and of the calculated density of states for titanium and zirconium dihydride are listed in Table III. A numerical comparison of the data indicates good agreement between theory and experiment. Figure 6 shows theoretical plots of the electronic density of states, broadened by the instrumental resolution, for the metal dihydrides in the *C* and *T* phases and a comparison with the x-ray photoelectron spectra. We have interpreted the major features of the theoretical curves and made a detailed comparison of them with experiment for the *C* phase of the metal dihydrides.[23] In general, there is agreement in terms of the energy position of the principal maximum, the tendency of the valence band to broaden in the sequence $TiH_2-ZrH_2-HfH_2$ 1.0–1.5 eV, and the presence

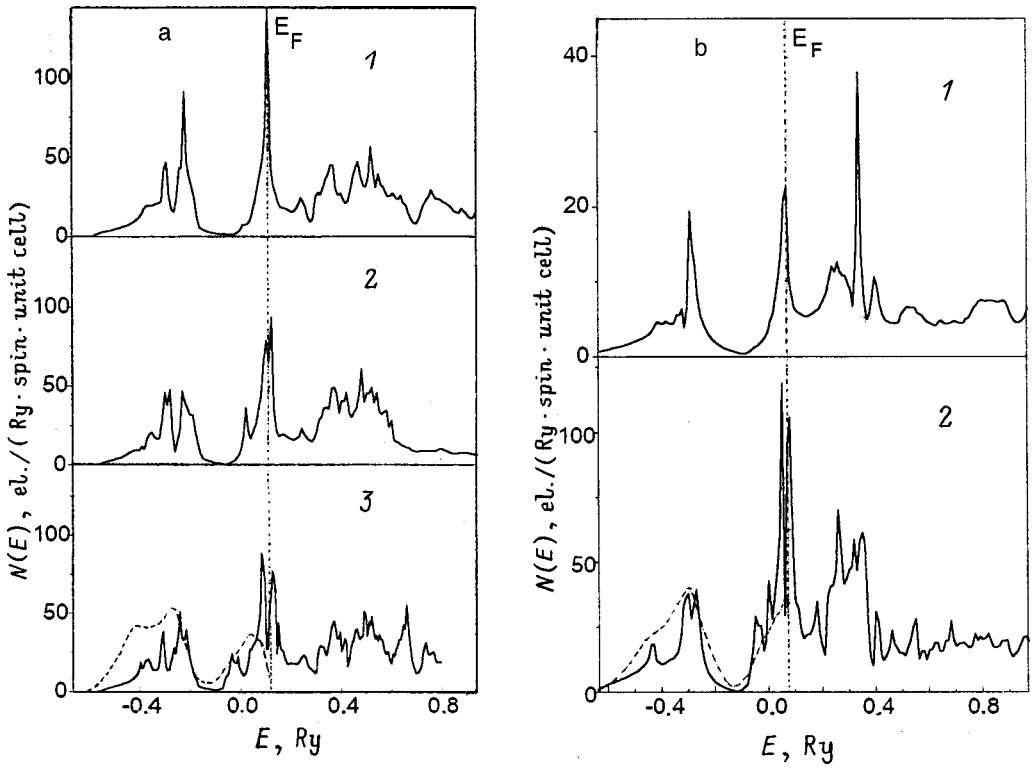

FIG. 5. Total electron densities of states in the cubic phase: ZrH_2 — *1*, $ZrH_{1.75}$ — *2*, $ZrH_{1.5}$ — *3* (a); TiH_2 — *1*, $TiH_{1.5}$ — *2* (b); the dashed curve is experimental (XPES).[22]

of a two-peaked structure for zirconium dihydride and a single-peaked structure for titanium and hafnium dihydrides.[22,24–27] The corresponding peaks for the defective dihydride are shifted toward the Fermi level by 1.0–1.5 eV. Lowering the density of electronic states causes a maximum to develop near the Fermi energy. Here a narrowing of the valence band is observed as the hydrogen concentration is lowered; this is also in satisfactory agreement with experiment.[22,24] Thus, in the experimental curve for $ZrT_{1.65}$ ($a=9.02$ a. u.) the characteristic peak lies 6 eV below E_F, while in our calculation for $ZrH_{1.75}$ ($a=9.036$ a. u.), it lies at -5.5 eV, while the theoretical peak closest to the Fermi level lies at -1.1 eV (-1 eV in the experiment[22]). In the tetragonal phase, as for the defective dihydrides, the experiments reveal a peak in the photoelectron spectrum below the Fermi energy, but in the cubic phase this peak could not be resolved, since it is separated from E_F by an amount equal to the effective resolution. The position of the principal maximum for TiH_2 lying 5.10 eV below E_F is in good agreement with the 5.02 eV obtained in Ref. 25. The theoretical curve for ZrH_2 is found to shift (less than 1 eV) toward E_F.

TABLE III. Energies for the characteristic features of the photoelectron spectrum and the calculated density of states.

	Energy relative to the Fermi level, eV			
	$TiH_{1.5}$		$ZrH_{1.5}$	
Characteristic feature	theory	experiment (Ref. 22)	theory	experiment (Ref. 22)
1	−0.94	−0.9	−1.06	−1.0
2	−1.48	−1.5	−2.04	−1.8
3	−4.88	−5.1	−4.81 −5.71	−5.3
4	−6.79	−7.3	−6.77	−7.2

As a whole, the satisfactory agreement between theory and experiment, both in the x-ray photoelectron spectra and in the electronic density of states at the Fermi level suggests that the band structure of the C and T phases for the dihydrides, and for the incomplete hydrides, obtained here is correct. In calculating the energy spectrum of the zirconium and hafnium dihydrides, of course, corrections for the spin-orbit interaction and relativistic effects should be included, but, as tests for hafnium showed, these effects are not all that big.

We now consider the stability of the high-temperature cubic phase. According to existing theory,[8] transitions from the cubic to the tetragonal phase in these systems are caused by Jahn–Teller splitting of the doubly degenerate energy band in the $\Gamma-L$ direction. It is assumed that the splitting causes the Fermi level to fall within the resulting energy gap. Our calculations of the band structure of TiH_2 and ZrH_2 are not entirely consistent with this scenario. In one variant of the calculations, a tetragonal deformation causes both split bands to fall below E_F. In the other variants, although a gap opens up at the Fermi level, it only corresponds to a small region of k space and does not cause a significant reduction in the band energy. Since there is a sharp drop in $N(E_F)$ in both cases, it is reasonable to assume that this factor, itself, is the driving force for the $C-T$ transition, and it may not even be connected with splitting of the electronic states along the $\Gamma-L$ direction. In fact, in our calculations the drop in $N(E_F)$ during a $C-T$ transition is caused mainly by a transforma-

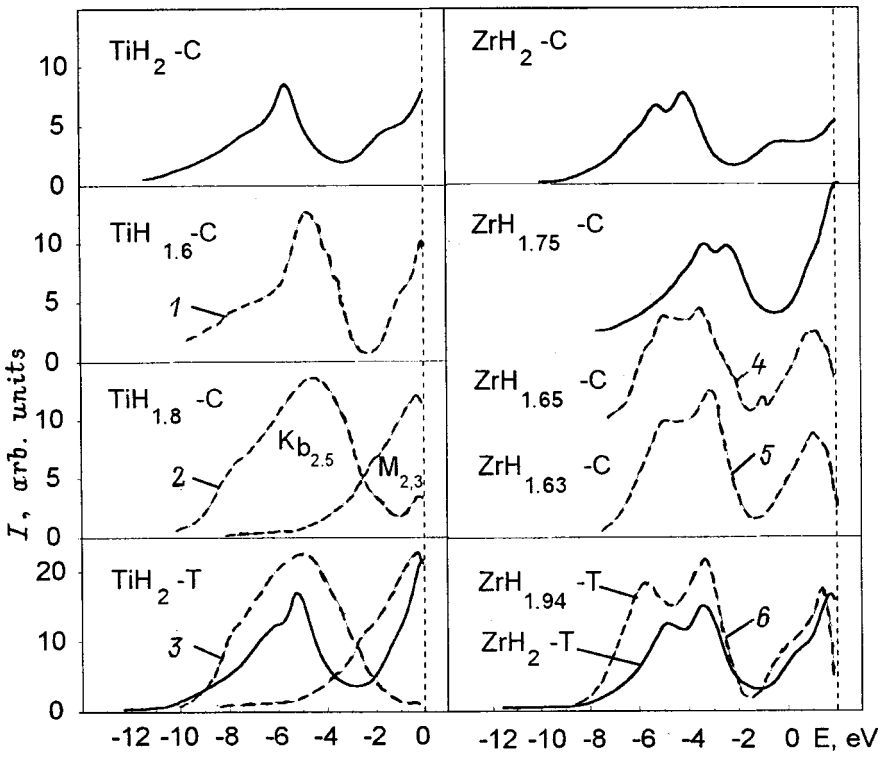

FIG. 6. Total electron density of states in the *C* and *T* phases for TiH_2 and ZrH_2 spread out by an amount equal to the instrumental resolution: smooth curve — calculation, dashed — experiment: *1* — Ref. 26, *2, 3* — Ref. 25, *4* — Ref. 24, *5* — Ref. 22, *6* — Ref. 22.

tion of the $E(k)$ curves along the $\Gamma-K$ direction, rather than along $\Gamma-L$.

If we assume that the driving force for this transition is precisely this sharp reduction in $N(E_F)$, then it is also easy to understand the reasons for the stabilization of the cubic phase by the hydrogen vacancies. In fact, the presence of hydrogen vacancies causes vacancy states to develop below the Fermi level and, thereby, reduces $N(E_F)$.

The unstable state can be eliminated, therefore, in two ways: a structural transition or a change in the composition of the hydrides. In both cases $N(E_F)$ decreases, along with the total energy. In this picture, the weakly dispersive segments of the spectrum along $\Gamma-L$ no longer have an exclusive role and they must be supplemented by the flat segments along the $\Gamma-K$ direction, which have been ignored up to now, when constructing a microscopic theory for the $C-T$ transition.

Further progress in understanding these questions can be achieved by using full-potential methods for calculating the band structure.

*)E-mail: kse74@ic.tsu.ru

[1] K. M. Mackay, *Hydrogen Compounds of the Metallic Elements* (E. & F.N. Spon LTD, London, 1966), 244 pp.
[2] K. Gesi, Y. Takagi, and T. Takeuchi, J. Phys. Soc. Jpn. **18**, 306 (1963).
[3] F. Ducastelle, R. Caudron, and P. Costa, J. de Phys. **31**, 57 (1970).
[4] V. I. Savin, R. A. Andrievskiĭ, V. V. Gorbachev, and A. D. Tsiganov, Fiz. Tverd. Tela **14**, 3320 (1972) [Sov. Phys. Solid State **14**, 2815 (1972)].
[5] A. C. Switendick, Solid State Commun. **8**, 1463 (1970).
[6] A. C. Switendick, J. Less-Common Met. **49**, 283 (1976).
[7] N. I. Kulikov, V. N. Borzunov, and A. D. Zvonkov, Phys. Status Solidi B **86**, 83 (1978).
[8] N. I. Kulikov and V. N. Borzunov, Neorgan. Materialy **14**, 1659 (1978).
[9] M. Gupta, Solid State Commun. **29**, 47 (1979).
[10] A. Fujimori and N. Tsuda, Solid State Commun. **41**, 491 (1982).
[11] D. A. Papaconstantopoulos and A. C. Switendick, J. Less-Common Met. **103**, 317 (1984).
[12] V. I. Ivashchenko, É. V. Gravit, V. V. Nemoshkalenko, and A. V. Zhalko-Titarenko, Metallofizika (Kiev) **14**, 16 (1992).
[13] A. C. Switendick, J. Less-Common Met. **101**, 191 (1984).
[14] R. S. Gupta and S. Chatterjee, J. Phys. F: Met. Phys. **14**, 631 (1984).
[15] I. A. Nechaev, V. I. Simakov, and V. S. Demidenko, Izv. Vyssh. Uchebn. Zaved. Fiz. No. 1, 40 (1997).
[16] N. I. Kulikov and V. V. Tugushev, Fiz. Tverd. Tela **23**, 2790 (1981) [Sov. Phys. Solid State **23**, 1631 (1981)].
[17] K. Bohmhammel, G. Wolf, G. Gross, and H. Madge, J. Low Temp. Phys. **43**, 521 (1981).
[18] D. M. Ceperley and B. J. Alder, Phys. Rev. Lett. **45**, 566 (1980).
[19] D. J. Pettifor, Commun. Phys. **1**, 151 (1976).
[20] M. I. Darby, M. N. Read, and K. N. Taylor, Phys. Status Solidi B **102**, 413 (1980).
[21] S. E. Kul'kova and O. N. Muryzhnikova, Izv. Vyssh. Uchebn. Zaved. Fiz. No. 9, 97 (1993).
[22] J. H. Weaver, D. J. Peterman, D. T. Peterson, and A. Franciosi, Phys. Rev. B **23**, 1692 (1981).
[23] S. E. Kulkova, O. N. Muryzhnikova, and K. A. Beketov, Int. J. Hydrogen Energy **21**, 1041 (1996).
[24] B. W. Veal, D. J. Lam, and D. G. Westlake, Phys. Rev. B **19**, 2856 (1979).
[25] V. V. Nemonshkolenko, M. M. Kindrat, V. P. Krivitskiĭ *et al.*, Neorgan. Mater. **17**, 975 (1981).
[26] D. E. Eastman, Solid State Commun. **10**, 933 (1972).
[27] M. Gupta, Phys. Rev. B **25**, 1027 (1982).

Translated by D. H. McNeill

Excess noise in $YBa_2Cu_3O_7$ epitaxial films and antenna-type microbolometers based on them

A. V. Bobyl', M. É. Gaevskiĭ, A. V. Lunev, and R. A. Suris

A. F. Ioffe Physicotechnical Institute, Russian Academy of Sciences, 194021 St. Petersburg, Russia

A. I. Dedoborets

State Agrotechnical University, 320027 Dnepropetrovsk, Ukraine

S. F. Karmanenko and A. A. Semenov

Electrotechnical University, 197376 St. Petersburg, Russia

V. N. Leonov and I. A. Khrebtov

Vavilov State Optical Institute, 199034 St. Petersburg, Russia

(Submitted March 1, 1999)
Fiz. Tverd. Tela (St. Petersburg) **41**, 1931–1935 (November 1999)

Monte Carlo modelled anneals of $YBa_2Cu_3O_7$ epitaxial films have been carried out, and the excess flicker noise in the operating frequency and temperature ranges were shown to be dominated by oxygen migration near small-angle block boundaries. Optimization of film and planar-microstructure fabrication permitted reaching a record-low Hooge noise parameter (1.8×10^{-4} at 93 K) for test structures, which can be used to prepare high-performance antenna-type strip microbolometers. Calculations show that the reduction of the microstrip size to $1\times0.7\ \mu m^2$ and of the flicker noise made possible detection of radiation within the spectral range from 3 mm to 300 μm (100–1000 GHz) at 90 K, with a nanosecond response and a noise-equivalent power of 1.5×10^{-12} W/Hz$^{1/2}$ at frequencies from 30 to 10^7 Hz, which is close to the limitations imposed by phonon noise. © *1999 American Institute of Physics.* [S1063-7834(99)00411-6]

Antenna-type microbolometers have recently been attracting considerable attention.[1–3] The noise-equivalent power (NEP) of detectors of this type in the high-frequency domain is dominated by the phonon noise associated with heat removal to the substrate, and it decreases with decreasing size of the sensor. At low frequencies, the NEP is affected substantially by excess $(1/f)$ flicker noise, which is conventionally defined by the Hooge dimensionless parameter[4] α.

The first study of the noise of antenna-type microbolometers fabricated from HTSC materials[3] reported on observation of a large α ($>10^{-3}$ at 93 K) exceeding by 2–3 orders of magnitude that of such simple metals as Ag and Au (Refs. 4–6). Besides, the comparatively large size of the sensor ($20\times3\ \mu m^2$) did not permit reaching low competitive values of NEP. It should be pointed out also that one can expect rapid degradation of these parameters at large α's, since this indicates a considerable concentration of metastable defects and their intensive low-temperature diffusion.[7]

This work reports a study of the possibility of attaining competitive NEP levels in antenna-type microbolometers based on $YBa_2Cu_3O_7$ epitaxial films. The study was started by a Monte Carlo simulation of thermal anneals of these films, which revealed dominant noise sources in the $f-T$ plane. To reduce the concentration of flicker-noise sources, various etching technologies (wet, laser, ion milling) were used to fabricate test samples measuring not more than $1\times1\ \mu m^2$. The parameters of the test samples and of a thermal model of the antenna-type microbolometer obtained were used to calculate NEP in the $1-10^9$ Hz range.

1. MONTE CARLO SIMULATION AND NOISE SOURCES IN THE $f-T$ PLANE

The oxygen atom distribution within two CuO-plane sublattices was calculated by the Monte Carlo technique using the ASYNNNI model.[7–10] The annealing process was started at a high temperature and with a random distribution of oxygen atoms within the sublattices, and completed at a low temperature with the formation of an ordered phase. As shown in Ref. 6, even the most perfect $YBa_2Cu_3O_7$ epitaxial films are made up of small-angle blocks, and oxygen migration in post-growth anneals or during storage takes place primarily through their boundaries.[11–13] The depletion of oxygen in block boundaries was taken into account in the following way. 860 atoms were generated over a 44×44 site square. As the temperature was lowered, after each four MC steps/atom the atoms, which were found in sites with coordinates from $x=0$ to -1 and from $y=-22$ to $+22$, denoted in Fig. 1a by a dark band, were excluded from subsequent calculations. Also shown in the figure is the atom distribution after the anneal. The barrier height E for atom hopping to the nearest-neighbor unoccupied site was calculated in the

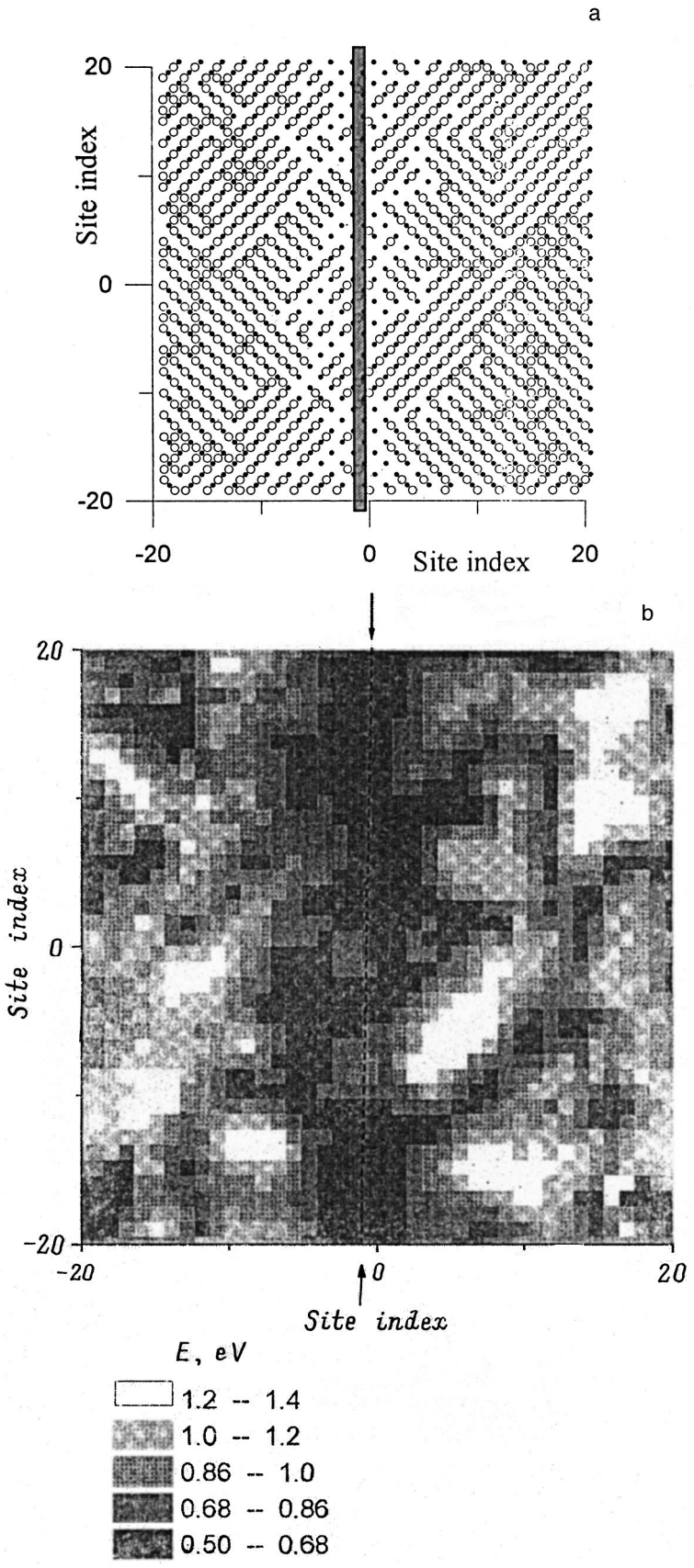

FIG. 1. Monte Carlo simulation of a block boundary in $YBa_2Cu_3O_7$ films. (a) and (b)—distributions of oxygen atoms and of barriers to their hopping among the sites on various sublattices in the CuO plane, respectively, after 10^3 MC steps/atom. The position of the block boundary is specified. The circles and points are the oxygen and copper atoms, respectively.

approximation for a harmonic potential[7] of a well at a site and averaged over 8 adjacent sites. The spatial distribution of E obtained in this way is presented in Fig. 1b. One readily sees that the oxygen atoms located near the block boundaries, chain defects, and in the ordered phase encounter barrier energies <0.5, 0.5–1.4, and >1.4 eV, respectively. Using these values, as well as the well-known relation for the energy which an atom can gain by thermal activation in a time $1/f$ at temperature T (Ref. 4)

$$E = kT \ln(2\pi f \tau_D), \tag{1}$$

where τ_D^{-1} is the Debye frequency ($\approx 10^{-13}$ s^{-1}), one can show that, the dominant noise sources in the frequency range of interest ($f>1$ Hz) in devices operating near the critical temperature T_c, are oxygen atoms located close to the block boundaries.

Thus a Monte Carlo computer simulation permits concluding that one should develop special procedures to stabilize the oxygen composition of $YBa_2Cu_3O_7$ films near block boundaries and other two-dimensional microdefects.

2. FABRICATION OF FILMS AND TEST SAMPLES AND NOISE MEASUREMENTS

$YBa_2Cu_3O_7$ epitaxial films were grown by magnetron sputtering on MgO, $LaAlO_3$, $SrTiO_3$, and $NdGaO_3$ substrates. The film orientation and the cation composition were determined by x-ray diffraction and electron-microprobe analysis, respectively. The oxygen content was derived from Seebeck coefficient measurements and from the normal-phase resistivity at 300 K. The internal micro-stresses, c-axis precessions of the blocks, and film thicknesses were extracted from the angular dependence of peak widths obtained by three-crystal x-ray diffractometry.[6] The voltage-noise spectral density S_V was measured at frequencies $f=1-10^5$ Hz. The Hooge parameter was calculated from the expression

$$\alpha(E) = fN_e \frac{S_V}{V^2}, \tag{2}$$

where $N_e = nv$ is the number of free carriers in a sample of volume v with a carrier concentration set equal to $n=10^{21}$ cm^{-3} (Refs. 6 and 7); the results obtained are shown graphically in Fig. 2.

As we shall see later, antenna-like bolometers with micron-sized sensors exhibit the best parameters. Therefore a search was made for the methods and regimes of etching assuring the micron-scale sample dimensions which would etch out the epitaxial film for edges not more than 0.1 μm. It appeared essential to monitor continuously the flicker-noise intensity of these microstrips.

The original films with deposited contacts were coated by photoresist. Ethylenediamine tetraacetate was used as a wet etchant. Laser etching made use of an ME 5551B mask retouch arrangement using an LGI 505 nitrogen laser. Ion milling was effected with a special duopigatron-type ion gun,[14] with the low-temperature plasma produced by gas-discharge emitters providing ion current densities of up to 10 A/cm^2. Ion milling enables fabrication of test samples in the form of microstrips measuring less than 1×1 μm^2 and with film-edge etchout of not more than 0.1 μm. For wet and laser etching, the film edge etchout was not more than 0.5 and 5 μm, respectively.

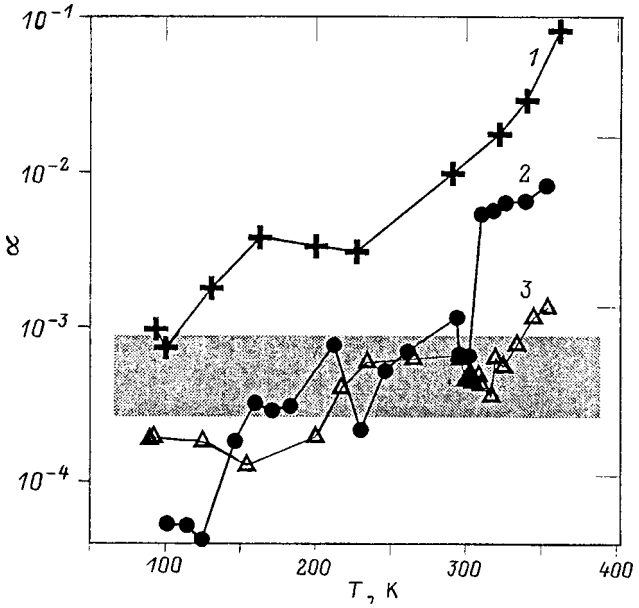

FIG. 2. Temperature dependences of the Hooge parameter of $YBa_2Cu_3O_7$ microstrips on $LaAlO_3$ substrates. Curves *1–3* refer to samples fabricated by wet and laser etching and ion milling, respectively. The dark band identifies the domain of the best results achieved prior to this work.

As seen from Fig. 2, it is near T_c, where defect fluctuators located close to block boundaries with barriers <0.5 eV are dominant noise sources, that the noise reduction achieved is the largest. While the noise level of a microstrip fabricated by wet etching was three times lower than that of an ion-milled strip, the first had uneven edges, and the value of its α increased for several days to reach 1.8×10^{-4}. This effect indicates the possibility of a further noise reduction in microstrips less than 1×1 μm^2 in size, down to $\alpha = 6\times 10^{-5}$. This can be attained by means of such anneals which reduce the number of defect fluctuators created during ion implantation.

3. ANTENNA-LIKE MICROBOLOMETER NEP

The possibility of using antenna-like microbolometers in IR measurements to increase the NEP was first considered in Ref. 1. Its original idea requires that the absorbed power of a radiation with wavelength λ is determined by the antenna area, and the heat losses, by the small area of the sensor, which has a high responsivity S (in volts per watt). It was found that, for a square antenna with side a (for optimum conditions, $a\approx\lambda$) and a square sensor with side b, the NEP of the receiver decreases λ/b times because of the antenna, for instance, 100 times for $\lambda = 100$ μm and $b=1$ μm. Neglecting the amplifier noise, the microbolometer NEP for a unit amplifier passband at a frequency f is given by the expression[2]

$$\mathrm{NEP} = (P_b^2 + P_T^2 + P_D^2 + P_{1/f}^2)^{1/2}, \tag{3}$$

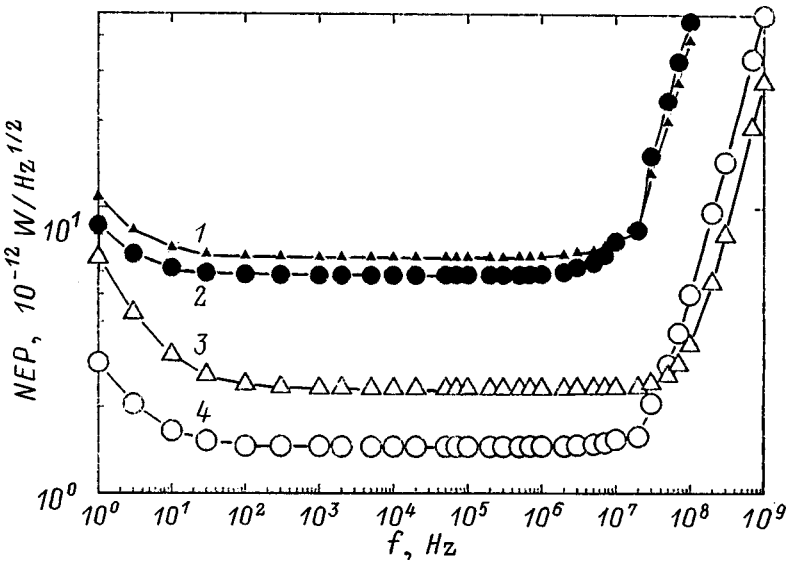

FIG. 3. Calculated NEP frequency dependences of the bolometers based on (*1,3*) Ag and (*2,4*) $YBa_2Cu_3O_7$ film sensors measuring (*1,2*) $6.0\times3.0\times0.3\ \mu m^3$ and (*3,4*) $1.0\times0.7\times0.2\ \mu m^3$. Curves *2,4* were calculated using the record-high results presented in Fig. 2.

where P_b, P_T, P_R, and $P_{1/f}$ are the power fluctuations of the background radiation, receiver heat exchange with the medium, Johnson resistance noise, and sensor flicker noise, respectively [$P_{1/f}=(\alpha/N_e f)^{1/2}IR/S$, where I and R are the current through the bolometer and its resistance, accordingly]. All the terms in Eq. (3) are proportional to the microbolometer sensor area. The $P_{1/f}$ quantity can be reduced substantially by reducing α and increasing the responsivity S. Based on the $\alpha=1.8\times10^{-4}$ level achieved, we used the thermal model[15] to calculate the NEP taking into account radial heat removal to the substrate, thermal boundary resistance, and the thermal resistance due to the film's thermal conductivity. (In these calculations, the antenna absorption coefficient is assumed to be unity.) As seen from Fig. 3, presenting the results of the calculation only at frequencies <30 Hz, the NEP increases because of the excess flicker noise of the $YBa_2Cu_3O_7$ films. At higher intermediate frequencies, up to 30 MHz, the NEP is dominated by frequency-independent phonon noise, and it is here that the 1.5×10^{-12} W/Hz$^{1/2}$ level is reached. At ultrahigh frequencies, >30 MHz, where the responsivity starts to decrease, the NEP increases because of the Johnson noise. Figure 3 shows also that one can gain a certain advantage by reducing the size of the microbolometer sensor and using $YBa_2Cu_3O_7$, rather than Ag, films. In particular, by reducing the area of the sensor by a factor of 25 one reduces the intermediate-frequency NEP five and three times for antennas made of $YBa_2Cu_3O_7$ and Ag films, respectively.

The results obtained in this work can be summarized as follows:

(1) A Monte Carlo simulation of thermal anneals of $YBa_2Cu_3O_7$ epitaxial films has revealed dominant noise sources in the $f-T$ plane. It was found that, within the operating frequency and temperature ranges of interest, these sources are related to oxygen migration near small-angle block boundaries and other two-dimensional microdefects;

(2) By properly varying the film growth regimes and using various film etching technologies (wet, laser, ion milling) to fabricate of planar microstructures, one has succeeded in reducing the defect-fluctuator concentration in the 0.2–0.6-eV range by three times;

(3) A possibility has been demonstrated of lowering considerably the noise-equivalent power of antenna-coupled microbolometers based on $YBa_2Cu_3O_7$ films by reducing the flicker noise of microstructures $1\times0.7\ \mu m^2$ in size.

Support of the Federal program ''Superconductivity'' (Grant 98031) is gratefully acknowledged.

[1] S. E. Schwarz and B. T. Ulrich, J. Appl. Phys. **48**, 1870 (1977).
[2] V. N. Leonov and I. A. Khrebtov, Prib. Tekh. Éksp. No. 4, 11 (1993).
[3] V. N. Leonov and I. A. Khrebtov, Sverkhprovodimost' (KIAE) **4**, 1371 (1991).
[4] Sh. Kogan, *Electronic Noise and Fluctuations in Solids* (Cambridge University Press, 1996).
[5] J. Pelz and J. Clarke, Phys. Rev. B **36**, 4479 (1987).
[6] A. V. Bobyl, M. E. Gaevski, S. F. Karmanenko, R. N. Kutt, R. A. Suris, I. A. Khrebtov, A. D. Tkachenko, and A. I. Morosov, J. Appl. Phys. **82**, 1274 (1997).
[7] A. A. Berzin, A. V. Bobyl', A. I. Dedoborets, A. I. Morozov, and R. A. Suris, Fiz. Tverd. Tela (St. Petersburg) **41**, 957 (1999) [Phys. Solid State **41**, 870 (1999)].
[8] D. de Fonraine, L. T. Wille, and S. C. Moss, Phys. Rev. B **36**, R5709 (1987).
[9] A. G. Khachaturyan and J. W. Morris, Jr., Phys. Rev. Lett. **61**, 215 (1988).
[10] M. Goldman, C. P. Burmester, L. T. Wille, and R. Gronsky, Phys. Rev. B **50**, R1337 (1994).
[11] D. V. Kulikov, R. A. Suris, and Yu. V. Trushin, Fiz. Tverd. Tela (St. Petersburg) **36**, 2975 (1994) [Phys. Solid State **36**, 1583 (1994)].
[12] S. J. Rothman, J. L. Routbort, U. Welp, and J. E. Baker, Phys. Rev. B **44**, 2326 (1991).
[13] A. V. Bobyl, M. E. Gaevskii, S. G. Konnikov, D. V. Shantzev, V. A. Solov'ev, and R. A. Suris, Scanning Microsc. **10**, 679 (1996).
[14] S. F. Karmanenko, A. I. Dedyk, V. T. Barchenko, R. A. Chakalov, A. V. Lunev, A. A. Semenov, and L. T. Ter-Martirosyan, Supercond. Sci. Technol. **11**, 284 (1998).
[15] V. V. Bogachev, V. N. Leonov, and I. A. Khrebtov, Pis'ma Zh. Tekh. Fiz. **20**, No. 10, 89 (1994) [Tech. Phys. Lett. **20**, 426 (1994)].

Translated by G. Skrebtsov

Triplet superconductivity in Sr_2RuO_4 in terms of the $t-J-I$-model

E. V. Kuz'min

Krasnoyarsk State University, 660062 Krasnoyarsk, Russia

S. G. Ovchinnikov*)

L. V. Kirenskii Physics Institute, Siberian Branch, Russian Academy of Sciences, 660036 Krasnoyarsk, Russia

(Submitted March 11, 1999)
Fiz. Tverd. Tela (St. Petersburg) **41**, 1936–1938 (November 1999)

A generalized $t-J-I$-model is proposed for Sr_2RuO_4 that takes the strong intra-atomic correlations of the d electrons and the features of the electronic structure of Sr_2RuO_4 into account. It is shown that, in the limit of strong correlations, there are no singlet s-type solutions for the superconducting state, but triplet solutions exist because of ferromagnetic spin correlations. For typical values of the model parameters, $T_c \sim 1$ K, consistent with the value of T_c for Sr_2RuO_4. © *1999 American Institute of Physics.* [S1063-7834(99)00511-0]

Despite its low $T_c \sim 1$ K,[1] superconductivity in Sr_2RuO_4 is of great interest for two reasons. First, this is the only superconducting oxide that is isostructural with La_2CuO_4 but does not contain copper, so that a comparison with the HTSC oxides may clarify the role of the copper. Second, the superconducting state in Sr_2RuO_4 is analogous to superfluid ^{3}He and has p-type pairing.[2,3] The triplet superconductivity in Sr_2RuO_4 has been discussed in terms of a band theory as a consequence of pairing induced by ferromagnetic spin fluctuations. It was not clear beforehand whether the triplet state would be maintained in the presence of the strong electronic correlations owing to the high effective mass of the electrons in the γ band ($12m_e$ from data on quantum mechanical oscillations[5]) and the closeness of Sr_2RuO_4 to the boundary for a Mott–Hubbard transition (the isostructural, isoelectronic crystal Sr_2FeO_4 is a Mott dielectric[6]). In this paper we propose a generalization of the $t-J$ model for strongly correlated electrons in the form of an additional ferromagnetic exchange (I) term caused by the specific features of the electronic structure and show that, with strong correlations, triplet solutions exist for the superconducting ordering parameter with $T_c \sim 1$ K for typical values of the model parameters. There are no singlet s-type solutions since they do not satisfy the sum rule.

A $(d_{x^2-y^2}-p)-\sigma$ coupling is characteristic of the copper oxides; here the interaction of neighboring copper spins only occurs through a superexchange (indirect) interaction ($t-J$-model, $J \sim t^2/U$). Sr_2RuO_4 is distinguished by the fact that bands formed by a π bond of the type $(d_{xy}-p)$ exist in the neighborhood of the Fermi level.[7,8] A simple quantum mechanical analysis shows that in this case the d_{xy} orbitals of neighboring cations overlap and this leads to a Heisenberg exchange interaction, in addition to the superexchange interaction through oxygen. For describing strongly correlated electronic states with developed ferromagnetic fluctuations, we propose a generalized $t-J-I$-model with the Hamiltonian

$$H=\sum_{\mathbf{f},\sigma}(\varepsilon-\mu)X_{\mathbf{f}}^{\sigma,\sigma}-t\sum_{\mathbf{f},\boldsymbol{\delta},\sigma}X_{\mathbf{f}}^{\sigma,0}X_{\mathbf{f}+\boldsymbol{\delta}}^{0,\sigma}$$

$$+J\sum_{\mathbf{f},\boldsymbol{\delta}}K_{\mathbf{f},\mathbf{f}+\boldsymbol{\delta}}^{(-)}-I\sum_{\mathbf{f},\boldsymbol{\delta}}K_{\mathbf{f},\mathbf{f}+\boldsymbol{\delta}}^{(+)},$$

$$K_{\mathbf{f},g}^{\pm}=\hat{\mathbf{S}}_{\mathbf{f}}\hat{\mathbf{S}}_{\mathbf{g}}\pm\frac{1}{4}\hat{n}_{\mathbf{f}}\hat{n}_{\mathbf{g}}, \tag{1}$$

where we have introduced the Hubbard operators $X_{\mathbf{f}}^{pq}=|p><q|$, which act on the intra-atomic states $|0>$ (no holes) and $|\sigma>$ (a hole with spin $\sigma=\pm 1/2$) and automatically exclude two-particle states, and $\hat{\mathbf{S}}_{\mathbf{f}}$ and $\hat{n}_{\mathbf{f}}$ are the spin- and particle-number operators at site $\mathbf{f}$. The signs in Eq. (1) have been chosen so that all the parameters (t, J, I) are positive and, for simplicity, only the sum over the nearest neighbors is retained (the vector $\boldsymbol{\delta}$). For infinitely large correlations, i.e., $U\to\infty$, the antiferromagnetic exchange $J\to 0$. We restrict ourselves to the case $I>J$. The electron concentration $n_e=N_e/N$ varies over the range $0\leqslant n_e\leqslant 1$. As $n_e\to 1$ the kinetic energy goes to zero and a dielectric state exists with a long-range ferromagnetic ordering. As the hole concentration increases, the ferromagnetism breaks up and a superconducting state can appear.

The Hamiltonian (1) describes quasiparticles in the lower Hubbard band. For comparison with Sr_2RuO_4 it is necessary to explain that the hole-α and electron-β bands in this model are a reservoir of particles and determine the chemical potential. The electron-α band, which is also responsible for the superconductivity,[9] splits into upper and lower Hubbard bands when strong electron correlations are taken into account. Calculations[8] show that the β band is half filled, the α band contains $n_\alpha=0.28$ holes, and the γ band is filled somewhat beyond half with electrons to $n_{e\gamma}=1.28$. This means that in the electron representation, the lower Hubbard γ band is completely filled, while the upper band contains 0.28 electrons. We shall work in the hole rep-

resentation, where the number of holes in the lower Hubbard band is $n_h=1-n_\alpha$, $0\leqslant n_h\leqslant 1$.

The exact equation of motion for the operator $X_{\mathbf{k}\sigma}$, the Fourier transform of the operator $X_{\mathbf{f}}^{0\sigma}$, is ($\hbar=1$)

$$i\dot{X}_{\mathbf{k}\sigma}=\xi_{\mathbf{k}}X_{\mathbf{k}\sigma}+L_{\mathbf{k}\sigma},$$

$$L_{\mathbf{k}\sigma}=-\frac{1}{\sqrt{N}}\sum_{\mathbf{p}}\gamma_{\mathbf{p}}(X^{-\sigma,\sigma}_{\mathbf{k}-\mathbf{p}}X_{\mathbf{p},-\sigma}-X^{-\sigma,-\sigma}_{\mathbf{k}-\mathbf{p}}X_{\mathbf{p},\sigma})$$

$$+\frac{1}{\sqrt{N}}\sum_{\mathbf{p}}\gamma_{\mathbf{k}-\mathbf{p}}[(g-\lambda)X^{-\sigma,\sigma}_{\mathbf{k}-\mathbf{p}}X_{\mathbf{p},-\sigma}$$

$$-gX^{-\sigma,-\sigma}_{\mathbf{k}-\mathbf{p}}X_{\mathbf{p},\sigma}-\lambda X^{\sigma,\sigma}_{\mathbf{k}-\mathbf{p}}X_{\mathbf{p},\sigma}], \tag{2}$$

where $\xi_{\mathbf{k}}=-\gamma_{\mathbf{k}}-\overline{\mu}$, $\gamma_{\mathbf{k}}=z^{-1}\Sigma_{\boldsymbol{\delta}}\exp(i\mathbf{k}\boldsymbol{\delta})$, $g=J/t$, and $\lambda=I/t$. Here all energies are expressed in units of zt (the band half-width), $\overline{\mu}=(\mu-\varepsilon)/zt$, and z is the number of nearest neighbors.

A convenient procedure for linearizing the nonlinear operator L with separation of the normal and anomalous averages is the irreducible operator method,[10]

$$L_{\mathbf{k}\sigma}=\overline{L}_{\mathbf{k}\sigma}-\frac{\langle\{L_{\mathbf{k}\sigma},X^{+}_{\mathbf{k}\sigma}\}_{+}\rangle}{\langle\{X_{\mathbf{k}\sigma},X^{+}_{\mathbf{k}\sigma}\}_{+}\rangle}X_{\mathbf{k}\sigma}$$

$$-\frac{\langle\{L_{\mathbf{k}\sigma},X^{+}_{-\mathbf{k},-\sigma}\}_{+}\rangle}{\langle\{X^{+}_{-\mathbf{k},-\sigma},X_{-\mathbf{k},-\sigma}\}_{+}\rangle}X^{+}_{-\mathbf{k},-\sigma}. \tag{3}$$

Neglecting the irreducible part $\overline{L}_{\mathbf{k}\sigma}$, we write down the equation of motion in the average field approximation

$$i\dot{X}_{\mathbf{k},\uparrow}=\tilde{\xi}_{\mathbf{k}}X_{\mathbf{k},\uparrow}-\frac{\Delta_{\mathbf{k}}}{c(n)}X^{+}_{-\mathbf{k},\downarrow},$$

$$i\dot{X}^{+}_{-\mathbf{k},\downarrow}=-\tilde{\xi}_{\mathbf{k}}X^{+}_{-\mathbf{k},\downarrow}-\frac{\Delta^{*}_{\mathbf{k}}}{c(n)}X_{\mathbf{k},\uparrow}. \tag{4}$$

Here the renormalization of the dispersion relation is taken into account in the simplest ''Hubbard 1'' form for a nonmagnetic state, $n_\uparrow=n_\downarrow=n_h/2$, $c(n)=1-n_h/2$,

$$\tilde{\xi}_{\mathbf{k}}=c(n)(-\gamma_{\mathbf{k}}-m),\quad m=[(g+\lambda)n/2+\overline{\mu}]/c(n), \tag{5}$$

and m is the effective chemical potential. The gap is given by

$$\Delta_{\mathbf{k}}=\Delta_{-\mathbf{k},\downarrow}=-\Delta_{\mathbf{k},\uparrow},$$

$$\Delta_{\mathbf{k}}=\frac{2}{N}\sum_{\mathbf{p}}\left(-\gamma_{\mathbf{p}}+\frac{1}{2}(\gamma_{\mathbf{k}+\mathbf{p}}+\gamma_{\mathbf{k}-\mathbf{p}})\right)B_{\mathbf{p}}$$

$$-\frac{\lambda}{N}\sum_{\mathbf{p}}\gamma_{\mathbf{k}+\mathbf{p}}B_{\mathbf{p}}, \tag{6}$$

where we have introduced the anomalous average $B_{\mathbf{p}}=\langle X_{-\mathbf{p}\downarrow}X_{\mathbf{p}\uparrow}\rangle$. Writing out the solution of the system of Gorkov equations for the normal and anomalous Green functions in the standard way, we obtain the following expressions for the averages in the superconducting phase:

$$n_{\mathbf{k}}=\langle X^{+}_{\mathbf{k},\uparrow}X_{\mathbf{k},\uparrow}\rangle=c(n)\frac{1}{2}\left(1-\frac{\tilde{\xi}_{\mathbf{k}}}{E_{\mathbf{k}}}\tanh\frac{E_{\mathbf{k}}}{2\tau}\right)\equiv c(n)f_{\mathbf{k}}, \tag{7}$$

$$kB^{*}_{\mathbf{k}}=\langle X^{+}_{\mathbf{k},\uparrow}X^{+}_{-\mathbf{k},\downarrow}\rangle=\frac{\Delta^{*}_{\mathbf{k}}}{2E_{\mathbf{k}}}\tanh\frac{E_{\mathbf{k}}}{2\tau}, \tag{8}$$

where $E^2_{\mathbf{k}}=\tilde{\xi}^2_{\mathbf{k}}+|\Delta_{\mathbf{k}}|^2/c^2(n)$ and $\tau=k_BT/zt$ is the dimensionless temperature. Besides the ordinary self consistent equations for the chemical potential and gap $\Delta_{\mathbf{k}}$ in the theory of strongly correlated systems, it is necessary to include the sum rules for the anomalous averages (a consequence of the algebra of X-operators that excludes two-particle states),

$$\frac{1}{N}\sum_{\mathbf{k}}B_{\mathbf{k}}=0. \tag{9}$$

Breaking up the anomalous averages into a sum of symmetric and antisymmetric components,

$$B_{\mathbf{p}}=B^{(S)}_{\mathbf{p}}+B^{(a)}_{\mathbf{p}},\quad B^{(S)}_{\mathbf{p}}=B^{(S)}_{-\mathbf{p}},\quad B^{(a)}_{-\mathbf{p}}=-B^{(a)}_{\mathbf{p}},$$

it is easy to write down an expression for the gap of the form

$$\Delta_{\mathbf{k}}=\alpha_{\mathbf{k}}\Delta_S+\lambda_{\mathbf{k}}\Delta_a,$$

$$\alpha_{\mathbf{k}}=2-(2g-\lambda)\gamma_{\mathbf{k}},\quad \lambda_{\mathbf{k}}=\lambda S_{\mathbf{k}},$$

$$S_{\mathbf{k}}=(\sin k_x+\sin k_y)/2. \tag{10}$$

The symmetric solutions $\Delta^{(S)}_{\mathbf{k}}=\alpha_{\mathbf{k}}\Delta_S$ correspond to singlet pairing and the antisymmetric solutions $\Delta^{(a)}_{\mathbf{k}}=\lambda_{\mathbf{k}}\Delta_a$, to triplet pairing. The first term in $\alpha_{\mathbf{k}}$, which equals 2, arises from a kinematic mechanism for pairing.[11] It is easy to see that the symmetric solution does not satisfy the sum rule.[12] At the same time, this rule is automatically satisfied for the antisymmetric solution. The ordering parameter Δ_α can be written in the form

$$\Delta_\alpha=\frac{i}{\sqrt{2}z}\sum_{\boldsymbol{\delta}}\frac{1}{N}\sum_{\mathbf{f}}\left\langle\frac{1}{\sqrt{2}}(X^{0,\downarrow}_{\mathbf{f}}X^{0,\uparrow}_{\mathbf{f}+\boldsymbol{\delta}}-X^{0,\downarrow}_{\mathbf{f}+\boldsymbol{\delta}}X^{0,\uparrow}_{\mathbf{f}})\right\rangle, \tag{11}$$

containing the average of the annihilation operator for a triplet pair with $S^z=0$ at neighboring lattice sites. For this solution, at $T=0$ we have the following equations for the gap

$$\frac{2-n_h}{\lambda}=\frac{1}{N}\sum_{\mathbf{p}}\frac{S^2_{\mathbf{p}}}{\sqrt{(\gamma_{\mathbf{p}}+m)^2+S^2_{\mathbf{p}}D^2_a}} \tag{12}$$

and for the chemical potential

$$\frac{n_h}{2-n_h}=\frac{1}{2N}\sum_{\mathbf{p}}\left(1+\frac{\gamma_{\mathbf{p}}+m}{\sqrt{(\gamma_{\mathbf{p}}+m)^2+S^2_{\mathbf{p}}D^2_a}}\right), \tag{13}$$

where $D^2_a=\lambda^2|\Delta_a|^2/c^4(n)$, which have solutions only for $\lambda>0$. The equations for T_c have the form

$$\frac{2-n_h}{\lambda}=\frac{1}{N}\sum_{\mathbf{p}}\frac{S^2_{\mathbf{p}}}{|\gamma_{\mathbf{p}}+m|}\tanh\left\{\frac{c(n)|\gamma_{\mathbf{p}}+m|}{2\tau_c}\right\}. \tag{14}$$

Numerical solutions of Eqs. (12)–(14) show that the gap and T_c depend nonmonotonically on the hole concentration and are nonzero within a finite interval of concentrations (n_{h1},n_{h2}) whose boundaries depend on the interaction constant λ. These dependences are characterized by a smooth maximum near populations $n_h\approx 0.7-0.8$. For Sr_2RuO_4 with $n_h=1-n_\alpha$ and $n_\alpha\approx 0.28$, this means close to optimum dop-

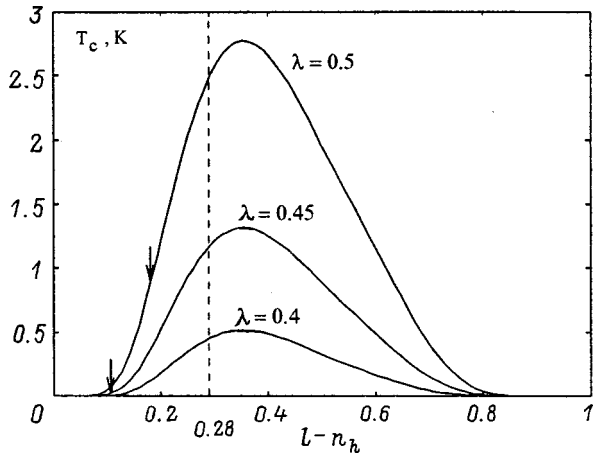

FIG. 1. T_c as a function of the hole concentration in Sr_2RuO_4 for three values of the dimensionless interaction parameter λ; the dashed curve is the hole concentration in the γ band, whose half width is 0.4 eV.

ing. $T_c \sim 1$ K for the typical model parameters. Thus, for $t=0.1$ eV, $n_\alpha = 0.28$, and $\lambda = 0.5$, we have $T_c \approx 2$ K.

As opposed to the BCS theory, the entire band is significant in Eqs. (12)–(14) and not just a narrow layer near the chemical potential. An approximate analytic solution for T_c can be written down if, when taking the integral with respect to the energy, a narrow layer of width 2δ ($\delta \approx 10^{-2}$) is selected near the chemical potential where the ordinary logarithm is obtained and, outside this, $\tanh x \approx 1$. This yields the following expression for T_c:

$$T_c = 1.14 z t c(n) \delta \exp\left\{ \frac{-c(n)}{(\lambda+\lambda_0)S^2(m)} \right\} \tag{15}$$

with values that differ from the numerical solution by a few percent. In Eq. (15) the parameter λ_0 describes the contribution from the outer part of the band,

$$\lambda_0 = \lambda^2 \frac{A(m,\delta)}{2-n_h-\lambda A(m,\delta)},$$

$$A(m,\delta) = \int_{-1}^{m-\delta} \frac{S^2(\omega)d\omega}{|\omega-m|} + \int_{m+\delta}^{1} \frac{S^2(\omega)d\omega}{|\omega-m|}, \tag{16}$$

where $S^2(\omega)$ is the average value of $S_{\mathbf{k}}^2$ on the isoenergetic surface $\omega = \gamma_{\mathbf{k}}$. T_c is plotted as a function of the hole concentration for different values of the parameter λ in Fig. 1. The arrows indicate the point where the transition to the ferromagnetic phase takes place, as defined by equality between the energies of the ferromagnetic and superconducting phases.

In conclusion, we note that generalizing the $t-J$-model by adding a ferromagnetic interaction of neighboring spins yields the $t-J-I$-model, which is a realistic model for describing the strongly correlated electrons in Sr_2RuO_4. The triplet superconductivity obtained previously[4] in terms of a band picture of Sr_2RuO_4 is also retained with strong electron correlations. An earlier attempt was made to describe a phononless mechanism for superconductivity in Sr_2RuO_4 in a strong electron correlation regime,[13] but the questions of the symmetry of the order parameter and the role of ferromagnetic fluctuations were not examined there.

This work was supported by the federal program ''State Support for the Integration of Fundamental Science and Higher Education'' (Grant No. 69) and the Krasnoyarsk Regional Science Foundation (grant 8F32).

*)E-mail: sgo@post.krascience.rssi.ru

[1] Y. Maeno, H. Hasimoto, K. Yoshida, S. Nichizaki, T. Fujita, J. G. Bednorz, and F. Lichtenberg, Nature (London) **372**, 532 (1994).
[2] T. M. Rice and M. Sigrist, J. Phys.: Condens. Matter **7**, L643 (1995).
[3] T. M. Rice, Nature (London) **396**, 627 (1998).
[4] I. I. Mazin and D. J. Singh, Phys. Rev. Lett. **79**, 733 (1997).
[5] A. P. Mackenzie, S. R. Julian, A. J. Diver, G. J. McMullan, M. P. Ray, G. G. Lonzarich, Y. Maeno, S. Nishitaki, and T. Fujita, Phys. Rev. Lett. **76**, 3786 (1996).
[6] P. Adler, A. F. Goncharov, K. Syassen, and E. Schonher, Phys. Rev. B **50**, 11396 (1994).
[7] T. Oguchi, Phys. Rev. B **51**, 1385 (1995).
[8] D. J. Singh, Phys. Rev. B **52**, 1358 (1995).
[9] T. M. Riseman, P. G. Kealey, E. M. Forgan, A. P. Mackenzie, L. M. Galvin, A. W. Tyler, S. L. Lee, C. Ager, D. Mck. Paul, C. M. Aegerter, R. Cubitt, Z. O. Mao, T. Akima, and Y. Maeno, Nature (London) **396**, 242 (1998).
[10] S. V. Tyablikov, *Methods in the Quantum Theory of Magnetism* (Nauka, Moscow, 1975).
[11] R. O. Zaĭtsev and V. A. Ivanov, Fiz. Tverd. Tela (Leningrad) **29**, 2554 (1987) [Sov. Phys. Solid State **29**, 1475 (1987)].
[12] N. M. Placida, V. Yu. Yushanhai, and I. V. Stasyk, Physica C **160**, 80 (1989).
[13] R. O. Zaitsev and Ju. V. Mihailova, Physica C **282–287**, 1677 (1997).

Translated by D. H. McNeill

SEMICONDUCTORS. DIELECTRICS

Control of quasiparticle self-fluctuations in a CuCl crystal

A. Kh. Rotaru

State University of Moldova, Kishinev, Moldova

V. Z. Tronchu

Institute of Physics, Humboldt University, Berlin, Germany;
Institute of Applied Physics, Academy of Sciences of Moldova, MD-2028 Kishinev, Moldova

(Submitted January 19, 1999)
Fiz. Tverd. Tela (St. Petersburg) **41**, 1939–1943 (November 1999)

A theory is developed for regular and chaotic self fluctuations in crystal CuCl for a ring resonator geometry. A system of nonlinear differential equations is derived for the dynamic evolution of coherent excitons, photons, and biexcitons. It is shown that, in the unstable portions of the optical bistability curves, nonlinear periodic and chaotic self fluctuations can develop with the creation of limit cycles and strange attractors in the phase space of the system. A computer simulation is used to determine the parameters for which reliable switching takes place in the system and the parameter ranges are found within which the system undergoes a transition from strange attractor to limit cycle. The possibility of experimentally observing the phenomena studied here is discussed.
[S1063-7834(99)00611-5]

The rapid development of technology and science places a premium on the problem of accumulating and rapidly processing a huge amount of information. As one of the most striking examples of optical self organization, optical bistability opens up vast prospects for practical applications in this area. The theoretical foundations of optical bistability have been discussed by Gibbs *et al.*,[1,2] who have described bistable materials and devices, discussed optical switching, and analyzed the instabilities and other phenomena. Applied research is currently directed at optimizing optically bistable devices: reducing their size, switching times, and power dissipation. As a rule, the switching times of bistable elements are on the order of the relaxation times of the dynamic characteristics of the device. The short relaxation times of the dynamic characteristics of excitons and biexcitons suggest that bistable optical elements with switching times on the order of 10^{-12} s can be constructed. Another, equally important, problem is the creation of bistable elements in which switching takes place with low energy dissipation and high reliability. However, the self fluctuations which develop in the unstable segments of the optical bistability curves can affect the operation of a bistable optical element. Thus, there is great interest in controlling the self fluctuations which develop in the system. Because of their low light losses and low intensities, quantum-well structures have recently been under active study.[3]

Optical bistability in the exciton spectral range was first studied theoretically by Elesin and Kopaev.[4] Kochelap *et al.*,[5,6] have worked in the same area. In our papers[7–10] based on the equations of Keldysh[11] we have constructed a theory of optical bistability, switching, and the development and decay of stochastic self fluctuations in high density, coherent exciton systems taking exciton-exciton interactions into account. These phenomena have been observed experimentally by Dneprovskiĭ *et al.*[12–14]

Optical bistability, switching, and self fluctuations of excitons and biexcitons have been studied before.[15–17] In Ref. 15, we studied stationary and nonstationary optical bistability and multistability and predicted the possible development of spatial turbulence in systems of coherent excitons, photons, and biexcitons in crystals. A scenario for the transition into dynamic chaos has been found and dynamic optical stability studied.[16] Crystal CuCl was chosen as a model with convincing experimental proof of the existence of biexcitons. A new class of nonlinear cooperative phenomena during light propagation in straight-band semiconductors has been studied.[17] The nonlinearity is caused by the direct bonding of two excitons into a biexciton as a result of their Coulomb interaction.[18,19]

In crystal CuCl, the exciton binding energy is on the order of 40 meV, so the exciton absorption band and the recombination M band of the biexciton are a significant distance apart. Because of the high exciton binding energy, a photon in resonance with the exciton transition frequency has a large resonance detuning relative to a transition in the region of the luminescence M band; thus, it is necessary to take into account the simultaneous effect of two independent light pulses, each of which is in resonance with a certain transition.

In this paper we construct a theory of regular and chaotic self fluctuations in a CuCl crystal involving coherent excitons and biexcitons. A system of nonlinear differential equa-

tions for the dynamic evolution of coherent excitons, photons, and biexcitons is derived for a ring resonator geometry. The stability of the stationary states is studied. It is shown that, in the unstable portions of the optical bistability curves, nonlinear periodic and chaotic self fluctuations can develop with the creation of limit cycles and strange attractors in the phase space of the system. Scenarios for the transition into dynamic chaos are found. A computer simulation is used to determine the range of parameters within which the system undergoes a transition from strange attractor to limit cycle. The parameters for which reliable switching takes place in the system are determined. We conclude by discussing the possibility of experimentally observing the phenomena studied here.

1. BASIC EQUATIONS

The complete Hamiltonian for the problem is the sum of the Hamiltonians for the free excitons, biexcitons, and fields and the interaction Hamiltonian, which has the following form in our model:

$$H_{\text{int}}=-\hbar g(E_1^- a+a^+E_1^+)-\hbar gG(a^+bE_2^-+ab^+E_2^+), \tag{1}$$

where a^+ (b^+) is the exciton (biexciton) creation operator, g is the exciton-photon interaction constant, G is the optical conversion constant for excitons into biexcitons, and $E^{+(-)}$ is the positive (negative) frequency component of the electric field of the electromagnetic wave in the jth pulse.

The equations of motion for the amplitudes of the excitons, a, and biexcitons, b, are

$$i\frac{da}{dt}=\omega_{\text{ex}}a-i\gamma_{\text{ex}}a-gE_1^+-gGbE_2^-, \tag{2}$$

and

$$i\frac{db}{dt}=\omega_{\text{biex}}b-i\gamma_{\text{biex}}b-gGE_2^+a, \tag{3}$$

where $\hbar\omega_{\text{ex}}$ and $\hbar\omega_{\text{biex}}$ are the energies of formation for the excitons and biexcitons and γ_{ex} and γ_{biex} are the damping constants for the excitons and biexcitons, which determine phenomenologically the rate at which the quasiparticles are lost from coherent into incoherent modes in the equations of motion. Note that these equations can be derived rigorously through the quantum theory of fluctuations and damping from the flux part of the corresponding Fokker–Planck equation.[20]

The equations of motion for the positive frequency component of the fields E_1^+ and E_2^+ are

$$c_1^2\frac{d^2E_1^+}{dt^2}-\frac{d^2E_1^+}{dz^2}=4\pi\hbar g\frac{d^2a}{dt^2}, \tag{4}$$

and

$$c_2^2\frac{d^2E_2^+}{dt^2}-\frac{d^2E_2^+}{dz^2}=4\pi\hbar Gg\frac{d^2(a^+b)}{dt^2}, \tag{5}$$

where c_1 and c_2 are the propagation velocities of the fields in the medium.

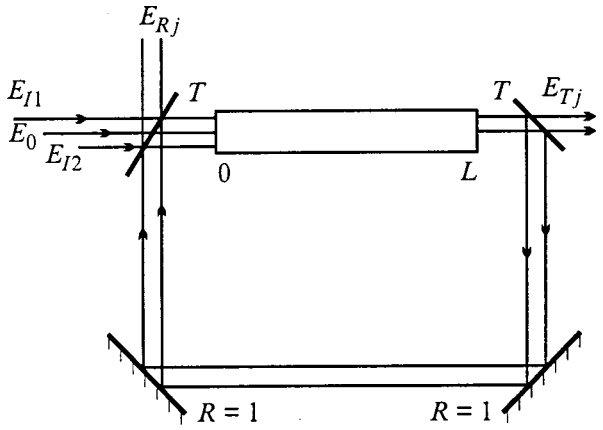

FIG. 1. A sketch of the ring cavity: E_{I1} and E_{I2} are the amplitudes of the incident fields, E_0 is an external periodic force of the form $E_0=\alpha\sin\tilde{\omega}\tau$, E_{Rj} and E_{Tj} are the amplitudes of the reflected and transmitted field, respectively, T is the transmission coefficient of the cavity mirrors, and $j=1,2$.

We write the solutions of Eqs. (2)–(5) in the form of a product of a slowly varying envelope and a rapidly oscillating component with carrier frequencies ω_1 and ω_2 and wave vectors k_1 and k_2,

$$a(z,t)=A(z,t)e^{i(k_1z-\omega_1t)},$$
$$b(z,t)=B(z,t)e^{i(k_1+k_2)z-(\omega_1+\omega_2)t},$$
$$E(z,t)=X(z,t)e^{i(k_1z-i\omega_1t)}. \tag{6}$$

In the following we shall consider the theory of optical bistability in a ring resonator geometry. Let a sample of length L be placed between the input and output mirrors of a cavity with transmission coefficients T. The other two mirrors are assumed to be ideally reflecting. (See Fig. 1.) The boundary conditions for the ring resonator are

$$E_j^+(0,t)=T^{1/2}E_{I,j}+Re^{\beta_{0,j}}E_j^+(L,t-\Delta t); \tag{7}$$
$$E_{T,j}(t)=T^{1/2}E_j^+(L,t),$$

where $E_{T,j}$ and $E_{I,j}$ are the amplitudes of the incident field at the input mirror of the cavity and of the field transmitted through the cavity, $R=1-T$ is the reflectivity of the cavity mirrors 1 and 2, $\Delta\tau$ is the delay time introduced by the feedback $\Delta t=(2l+L)/c_0$, c_0 is the speed of light in vacuum, and β_0 is the phase shift in the resonator.

On substituting Eq. (6) in Eqs. (2)–(5), in the approximation of slowly varying envelopes[1] and in the average field approximation[1,21] including the boundary conditions (7), we obtain

$$\frac{dX_1}{d\tau}=\sigma_1(-X_1+2C_1A+Y_1), \tag{8}$$

$$\frac{dX_2}{d\tau}=\sigma_2(-X_2-2C_2AB+Y_2), \tag{9}$$

$$\frac{dA}{d\tau}=-dA-d(X_1+X_2B), \tag{10}$$

and

$$\frac{dB}{d\tau} = -B + X_2 A, \tag{11}$$

where X_1, X_2, Y_1, and Y_2 are the normalized field amplitudes, τ is the dimensionless time, and C_1, C_2, σ_1, σ_2, and d are constants determined by the expressions

$$X_j = \frac{E_{Tj}}{E_s}; \quad Y_j = \frac{E_{Ij}}{E_s}; \quad A = i\frac{a}{A_s}; \quad B = \frac{b}{B_s};$$

$$E_s = \frac{\sqrt{\gamma_{ex}\gamma_{biex}}}{gG}; \quad A_s = \frac{\sqrt{\gamma_{biex}}}{\sqrt{\gamma_{ex}}}G^{-1}; \quad B_s = G^{-1};$$

$$\tau = \gamma_{biex}t; \quad d = \frac{\gamma_{ex}}{\gamma_{biex}}; \quad C_j = \frac{\alpha_j L}{4T}; \quad \sigma_j = \frac{c_j T}{\gamma_{biex} L};$$

$$\omega \approx ck; \quad \alpha_j = \frac{4\pi\hbar g^2 \omega_j}{\gamma_{ex} c_j}; \quad j = 1,2.$$

Equations (8)–(11) describe the time evolution of coherent excitons, biexcitons, and electromagnetic fields in a ring resonator and are fundamental to the following study. We shall next carry out a numerical simulation and analyze the stability of the stationary states. Note that the system of Eqs. (8)–(11) is a special case of studying the evolution of a system of the form $\dot{\mathbf{X}} = \mathbf{F}(\mathbf{X})$, where $\mathbf{X}$ is a vector in R^n $(n > 1)$ space, each component of which corresponds to a single mode. $\mathbf{F}(\mathbf{X})$ is the vector field of the system.

For dissipative systems there is a reduction in the phase space volume, since the divergence of $\dot{\mathbf{X}}$ is negative, i.e.,

$$\operatorname{div}\dot{\mathbf{X}} = \operatorname{div}\mathbf{F} = \sum_{i=1}^{n} \frac{\partial \mathbf{F}_i}{\partial \mathbf{X}_i} < 0.$$

The evolution of the solutions of Eqs. (8)–(11) depends significantly on the evolution of a small region of the phase space of this system. Regarding the motion of points in the phase space as the motion of a fluid with divergence

$$\frac{\partial \dot{X}_1}{\partial X_1} + \frac{\partial \dot{X}_2}{\partial X_2} + \frac{\partial \dot{A}_1}{\partial A_1} + \frac{\partial \dot{A}_2}{\partial A_2} + \frac{\partial \dot{B}_1}{\partial B_1} + \frac{\partial \dot{B}_2}{\partial B_2} = -[\sigma_1 + \sigma_2 + d + 1],$$

we conclude that any small volume of the phase space of the system of Eqs. (8)–(11) approaches zero as $\tau \to \infty$ at a rate $[\sigma_1 + \sigma_2 + d + 1]$. When the stationary states of the system are unstable, the attractors in phase space can be either a limiting cycle or torus, or a strange attractor. They correspond to nonlinear periodic, quasiperiodic, and stochastic self oscillations in the system.

2. CONTROLLING EXCITON AND BIEXCITON SELF FLUCTUATIONS

In the stationary case, Eqs. (8)–(11) yield coupled equations for a nonlinear optical four-terminal network with two input and two output channels.[22] Changing one of the two or both parameters can rapidly change the output characteristics of the four-terminal network, and optical bistability is possible in both channels. Figure 2 shows the nonlinear variations in the amplitudes of the output radiation, X_1 and X_2,

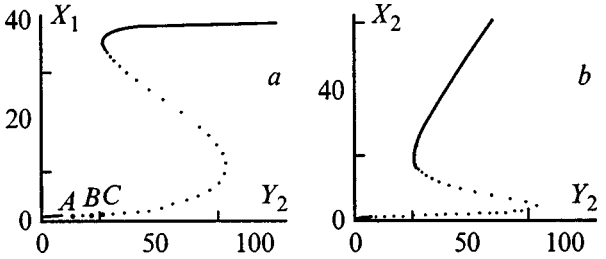

FIG. 2. Stationary dependence of the amplitudes of the transmitted field X_1 (a) and X_2 (b) on the amplitude of the incident radiation, Y_2, for $C_1 = 20$, $C_2 = 19$ and $Y_1 = 40$. (X and Y are given in units of 10 V/cm.)

with the amplitudes of the input radiation for $Y_1 = 40$, $C_1 = 20$, and $C_2 = 19$. As can be seen from the figure, clockwise optical bistability occurs in the system for these parameters.

There is further interest in studying the stability of the stationary states in connection with the possible development of self fluctuations in the unstable portions of the optical bistability curves, which will have a deleterious effect on the operation of a bistable element. The stability of the stationary optical hysteresis states with respect to small perturbations is studied using the characteristic equation for the Jacobian of the system,

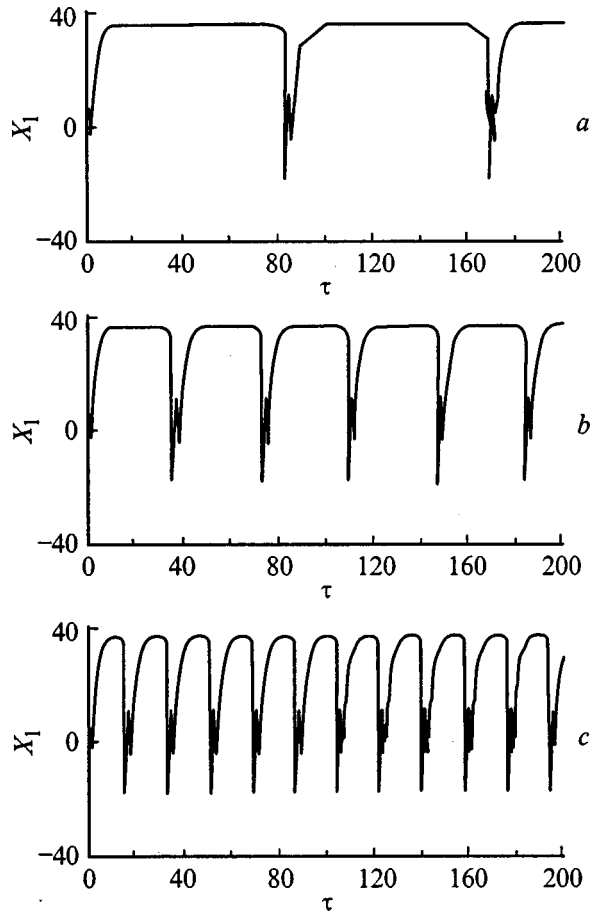

FIG. 3. Oscillations in a ring resonator with $C_1 = 20$, $C_2 = 19$, $Y_1 = 40$, $d = 0.7$, $\sigma_1 = 0.45$, $\sigma_2 = 0.55$, $T = 0.01$, and different levels of external pumping: a — $Y_2 = 10$, b — $Y_2 = 12$, and c — $Y_2 = 20$. (X is given in units of 10 V/cm, and τ in units of 10^{-12} s.)

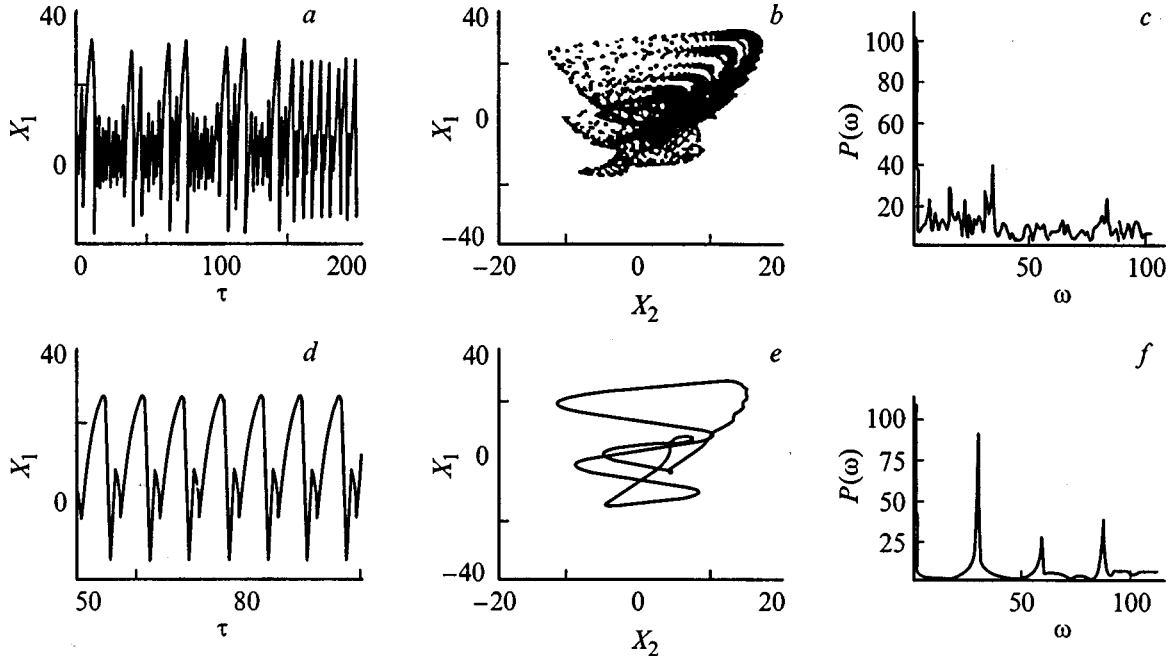

FIG. 4. The process of synchronization of stochastic self-fluctuations: a — time evolution of the radiation exiting the cavity, X_1, for constant pumping $Y_1=40$ and $Y_2=25$; b — phase portrait of the strange attractor in the X_1-X_2 plane and its power spectrum (c); d — time evolution of the radiation exiting the cavity, X_1, for $Y_1=40$ and $\tilde{Y}_2=Y_2+\alpha \sin \tilde{\omega}\tau$; e — phase portrait of the complex limit cycle in the X_1-X_2 plane and its power spectrum (f).

$$|J-\lambda E| = \begin{bmatrix} -\sigma_1-\lambda, & 0, & 2C_1\sigma_1, & 0 \\ 0, & -\sigma_2-\lambda, & -2C_2B\sigma_2, & -2C_2B\sigma_2 \\ -d, & -dB, & -d-\lambda, & -dX_2 \\ 0, & A, & X_2, & -1-\lambda \end{bmatrix},$$

where E is the unit matrix.

If the real parts of all the roots of the characteristic equation $\lambda^4+a_1\lambda^3+a_2\lambda^2+a_3\lambda+a_4=0$ are negative, then the corresponding stationary states are stable with respect to small perturbations. We have studied the stability of the stationary states using the Routh–Hurwitz criterion. For parameters $Y_1=40$, $C_1=20$, and $C_2=19$ and $\sigma_1=0.45$, $\sigma_2=0.55$, and $d=0.7$ the upper portions of the optical bistability curves are stable, while part of the lower branch becomes unstable. In this case, nonlinear self fluctuations develop in the system. On moving from point A to point B, the oscillations in the system become more complicated. New harmonics appear in their spectra (Fig. 3) and, finally, a stochastic self oscillatory regime develops in the middle of the window (point C) and optical turbulence develops. Figure 4a illustrates the stochastic self modulation process with corresponding projections of the phase trajectories and the power spectrum, which is continuous. As opposed to the well known Lorentz noise,[23–25] where stochastic oscillations and the creation of a strange attractor are associated with jumps between the corresponding equilibrium states, in our case the stochasticity is associated with the development of a chaotic attractor in the four dimensional phase space which is filled by phase trajectories in a complicated manner. When the imaging point is moved further to the right, regular nonlinear oscillations again develop in the system, and the phase trajectories leave the limit cycle; after this, the system jumps into the upper stable branches of the optical bistability curves.

There is great interest in research on the control of dynamic chaos in nonlinear systems. One control technique is to act on a self oscillating system with an external periodic force. For this purpose, we have carried out a computer simulation, assuming that an additional external periodic force of the form $E_0=\alpha \sin(\tilde{\omega}\tau)$ acts on the resonator. Here it was found that in α, $\tilde{\omega}$ parameter space, there is a region of values for which the stochastic self fluctuations in the system are broken up and the oscillations become periodic. Figures 4b illustrate the synchronization of the stochastic self fluctuations, their phase portrait, and power spectrum, in which three harmonics predominate. For $\alpha=1$ and $\tilde{\omega}=0.9$, the phase trajectory goes into a complicated limit cycle. These parameter values correspond to the synchronization regime. Reliable switching is possible in this system for these parameters and fixed intensities. Thus, an external periodic signal drives a strange attractor into a limit cycle of periodic nonlinear oscillations.

We conclude by examining the feasibility of an experimental observation of the effects predicted above. We have made some numerical estimates for crystals such as CuCl, where the binding energy of a biexciton is on the order of $40\cdot10^{-3}$ eV and $\hbar\gamma_{ex}=1.38\cdot10^{-10}$ s, $\hbar\gamma_{biex}=1.38\cdot10^{-11}$ s,[26] $G=1.25\times10^8$ cm$^{-3/2}$,[27] $L=750$ Å, $\hbar g=0.3$ eV/(cm$^{1/2}$V), and $\omega_{ex}=4\cdot10^{15}$ s^{-1}. The critical power at which these nonlinear phenomena can be observed is on the order of $P\sim10^6$ W/cm^2. Here the concentrations of excitons and biexcitons are on the order of 10^{15} and 10^{16} cm^{-3}, respectively.

We thank the Alexander Humboldt Foundation for supporting this work.

[1] H. Gibbs, *Optical Bistability. Controlling Light with Light* (Mir, Moscow, 1988).
[2] H. M. Gibbs, G. Khitrova, and N. Peghambarian *Nonlinear Photonics*, Springer Series in Electronics and Photonics, Vol. 30 (Springer, 1990).
[3] A. I. Bobrysheva, V. A. Zalozh, and A. Kh. Rotaru, Fiz. Tverd. Tela **33**, 915 (1991) [Sov. Phys. Solid State **33**, 518 (1991)].
[4] V. F. Elesin and Yu. V. Kopaev, Zh. Éksp. Teor. Fiz. **62**, 1447 (1972) [*sic*].
[5] V. A. Kochelap, L. Yu. Melnikov, and V. N. Sokolov, Fiz. Tekh. Poluprovodn. **16**, 1167 (1982) [Sov. Phys. Semicond. **16**, 746 (1982)].
[6] V. A. Kochelap, L. Yu. Melnikov, and V. N. Sokolov, Kvantovaya Élektronika (Kiev) **24**, 42 (1987).
[7] B. Sh. Parkanskiĭ and A. Kh. Rotaru, Zh. Éksp. Teor. Fiz. **99**, 899 (1991) [Sov. Phys. JETP **72**, 499 (1991)].
[8] B. Sh. Parkanskiĭ and A. Kh. Rotaru, Fiz. Tverd. Tela **33**, 2250 (1991) [Sov. Phys. Solid State **33**, 1268 (1991)].
[9] B. Sh. Parkanskiĭ and A. Kh. Rotaru, Fiz. Tverd. Tela **33**, 3378 (1991) [Sov. Phys. Solid State **33**, 1905 (1991)].
[10] A. N. Rotaru and V. Z. Tronchu, Fiz. Tverd. Tela **36**, 20 (1994) [Phys. Solid State **36**, 10 (1994)].
[11] L. V. Keldysh, *Problems in Theoretical Physics* (Nauka, Moscow, 1972), p. 433.
[12] V. N. Dneprovskiĭ, Usp. Fiz. Nauk **145**, 149 (1985) [Sov. Phys. Usp. **28**(1), 93 (1985)].
[13] V. N. Dneprovskiĭ, Izv. Akad. Nauk SSSR, Ser. Fiz. **50**, 661 (1986).
[14] A. M. Bakiev, V. N. Dneprovskiĭ, Z. D. Kovalyuk *et al.*, JETP Lett. **38**, 596 (1983).
[15] V. A. Zalozh, A. N. Rotaru, and V. Z. Tronchu, Zh. Éksp. Teor. Fiz. **103**, 994 (1993) [JETP **76**, 487 (1993)].
[16] V. A. Zalozh, A. N. Rotaru, and V. Z. Tronchu, Zh. Éksp. Teor. Fiz. **105**, 260 (1994) [JETP **78**, 138 (1994)].
[17] A. N. Rotaru and V. Z. Tronchu, Zh. Éksp. Teor. Fiz. **112**, 1778 (1997) [JETP **85**, 971 (1997)].
[18] A. L. Ivanov and P. V. Panasenko, JETP Lett. **53**, 35 (1991).
[19] A. L. Ivanov, L. V. Keldysh, and P. V. Panasenko, Zh. Éksp. Teor. Fiz. **99**, 641 (1991) [Sov. Phys. JETP **72**, 359 (1991)].
[20] S. A. Moskalenko, A. Kh. Rotaru, and Yu. M. Shvera, TMF **75**, 295 (1988).
[21] R. Bonifacio and L. Lugiato, Lett. Nuovo Cimento Soc. Ital. Fis. **21**, 510 (1978).
[22] P. I. Khadzhi, G. D. Shibarshina, and A. Kh. Rotaru, *Optical Bistability in Systems of Coherent Excitons and Biexcitons in Semiconductors* (Shtiintsa, Kishinev, 1988).
[23] E. N. Lorentz, *Strange Attractors* (Mir, Moscow, 1981), p. 88.
[24] H. Haken, *Synergetics* (Mir, Moscow, 1980).
[25] A. N. Oraevskiĭ, Kvantovaya Élektronika **8**, 130 (1981) [Sov. J. Quantum Electron. **11**, 71 (1981)].
[26] C. C. Sung, C. M. Bowden, J. M. Haus, and W. K. Chi, Phys. Rev. A **30**, 1873 (1984).
[27] P. I. Khadzhi, *Kinetics of Recombination Radiation by Excitons and Biexcitons in Semiconductors* (Shtiintsa, Kishinev, 1977).

Translated by D. H. McNeill

Effect of a magnetic field on the electroluminescence intensity of single-crystal ZnS

Yu. I. Golovin, R. B. Morgunov, and A. A. Baskakov

Tambov State University, 392622 Tambov, Russia

S. Z. Shmurak

Institute of Solid State Physics, Russian Academy of Sciences, 142432 Chernogolovka, Moscow District, Russia

(Submitted December 18, 1998)
Fiz. Tverd. Tela (St. Petersburg) **41**, 1944–1947 (November 1999)

After exposure of single-crystal ZnS with microscopic twinning to magnetic fields of 1–10 T, the integral electroluminescence brightness is found to increase by several times. It is proposed that the magnetic field facilitates relaxation of a metastable state of the structural defects. © *1999 American Institute of Physics.* [S1063-7834(99)00711-X]

Electroluminescence in II–VI compounds has been studied for a long time. It has been shown experimentally[1,2] that the motion of charged particle dislocations plays a significant role in electroluminescence in ''weak'' electric fields $\sim 10^5$ V/m and that this also explains a number of features of the electroluminescence, in particular, the degradation of the emission. Attempts have been made[3,4] to examine the effect of a magnetic field on electroluminescence, but the experiments yielded a negative result, since the field was turned on for a short time during the emission process and its induction was too low[5] to produce a significant change in the trajectories of the electrons accelerated in the pores in an electric field, as anticipated by the authors.[3,4] The results of Refs. 1 and 2 suggest that, in order to observe the influence of a magnetic field on electroluminescence, it is necessary to create experimental conditions such that the magnetic field could affect the mobility of the dislocations or the state of the point defects within the volume that participate in electroluminescence. Thus, for example, it has recently[6–8] been established that exposing type I–VII diamagnetic compounds to a magnetic field makes it easier for dislocations to move and it has been shown[9,10] that one of the reasons for plastification of crystals in magnetic fields is a change in the state of metastable point defects in the crystal volume. Similar magnetically induced changes in the subsystem of point defects has also been observed in Si.[11] Metastability in a ZnS crystal lattice with microscopic twinning[1,2] suggests that magnetic field effects on the mobility of dislocations and the state of point defects may be observable in these diamagnetic crystals and may, in turn, affect their electroluminescence.

The purpose of this paper is to study the effect of a magnetic field that is turned on before electroluminescence is excited on its integral (over the spectrum) intensity.

Samples with dimensions of $2\times2\times4$ mm with $(1\bar{2}10)$ and $(10\bar{1}1)$ faceting (hexagonal indexing) doped with 10 p.p.m. Cu were used to study the effect of preliminary exposure of single-crystal ZnS to a magnetic field on its electroluminescence. The integrated brightness I was measured at $T=293$ K using an FÉU-106 photomultiplier tube. The sample was fastened between elastic brass electrodes mounted in front of the photomultiplier and protected by a cover to eliminate stray light. Electroluminescence was excited by a sinusoidal voltage with a frequency $\nu=10^3$ Hz and an effective value of 2.2 kV applied to silver contacts deposited on the $(1\bar{2}10)$ facets of the sample. The photomultiplier was shielded from possible pickup owing to the electric fields near it. Preliminary exposure of the crystals to a constant magnetic field with an induction $B=2$ T was done in a dark space between the poles of an electromagnet at some distance from the photomultiplier. Magnetic field pulses of amplitude $B=7$ T and duration 10^{-2} s were generated by a thyristor switch and a small-turn solenoid. All of the experimental procedures were carried out in the dark, except for the contribution of phosphorescence to the measured brightness of the sample in an electric field. Special precautions were taken to prevent random mechanical loading of the crystals during the experiments. The value of I and its error were determined by averaging data from repeated removals and replacements of the sample between the electrodes under identical electroluminescence excitation conditions.

In a first series of experiments we studied the integrated brightness I as a function of the effective voltage U on the sample. First, this dependence was measured without a magnetic field. Then the sample was placed in the electromagnet, where it was exposed to a constant magnetic field for 20 min. Immediately after this, $I(U)$ was measured for a second time. It was found that after exposure to a magnetic field $I(U)$ is higher than prior to the magnetic treatment, beginning with $U>1$ kV (Fig. 1). Thus, the intensity of the emission from the sample for a given electrode voltage was higher for samples that had been exposed initially to a magnetic field than for those which had not.

A third measurement of $I(U)$ was made on the same sample after 24 h. This showed that increasing the time interval t between exposures of the crystals to the magnetic field and the measurement of the electroluminescence brightness leads to a reduction in the increment in I produced by the first exposure of the crystal to the magnetic field (Fig. 1). Note that this reduction is not related to the customary deg-

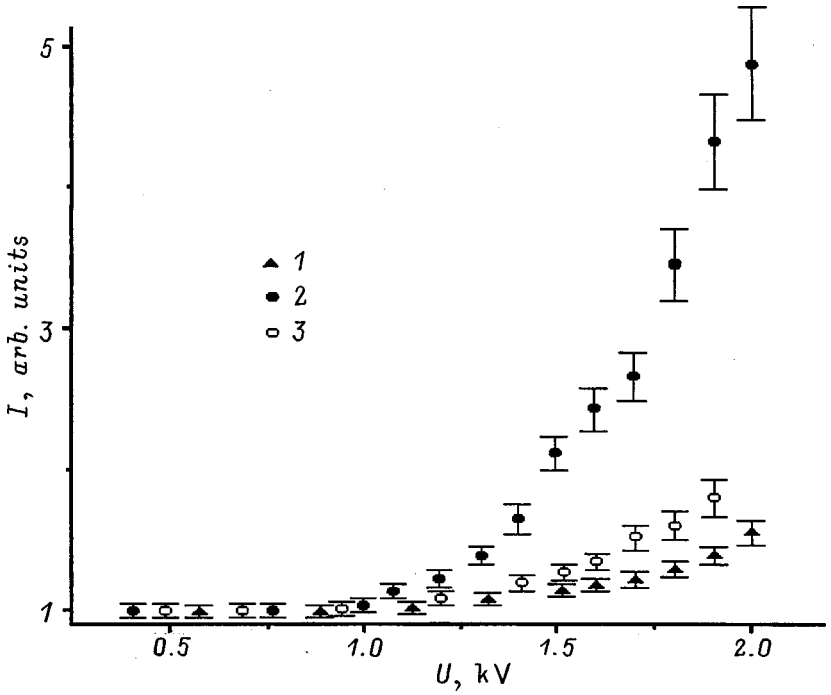

FIG. 1. Typical dependence of the electroluminescence intensity of crystal ZnS on the active voltage U, applied to the sample ($\nu = 800$ Hz): *1* — before exposure in a magnetic field; *2* — 1 min after exposure in a magnetic field ($B = 2$ T, exposure duration 20 min); *3* — 24 h after exposure in a magnetic field.

radation of electroluminescence stimulated by an electric field, since there was no voltage on the sample during the time between exposure to the magnetic field and the measurement of I, while the total duration of the tests on the sample in the electric field was ~ 1 h. At the same time, it was found in a special series of experiments that one hour's exposure of the crystal to an electric field was not enough to reduce I by even 10%.

An increase in the electroluminescence intensity could also be caused by preliminary exposure of the crystals to a 7 T magnetic field pulse lasting 10^{-2} s. With this method for processing the crystals in a magnetic field, which was used in a second series of experiments, I was also observed to decrease with increasing time between the magnetic field pulse and the application of an electric field for measuring I. It is clear, from a plot of $I(t)$ taken for one crystal (Fig. 2), that, for $t > 48$ h, the crystals ''forget'' about having being processed in the magnetic field. Applying sequential magnetic field pulses after the change ΔI_1 in the emission intensity induced by the first pulse had approached zero (for $t > 48$ h) showed that each successive magnetic field pulse leads to a smaller increment in I than the previous pulse, i.e., $\Delta I_1 > \Delta I_2 > \Delta I_3 > \Delta I_4 \ldots$ (Fig. 2).

Some experiments in which the samples were exposed to a magnetic field before the first measurement of $I(U)$ yielded the same results as those described above. The emis-

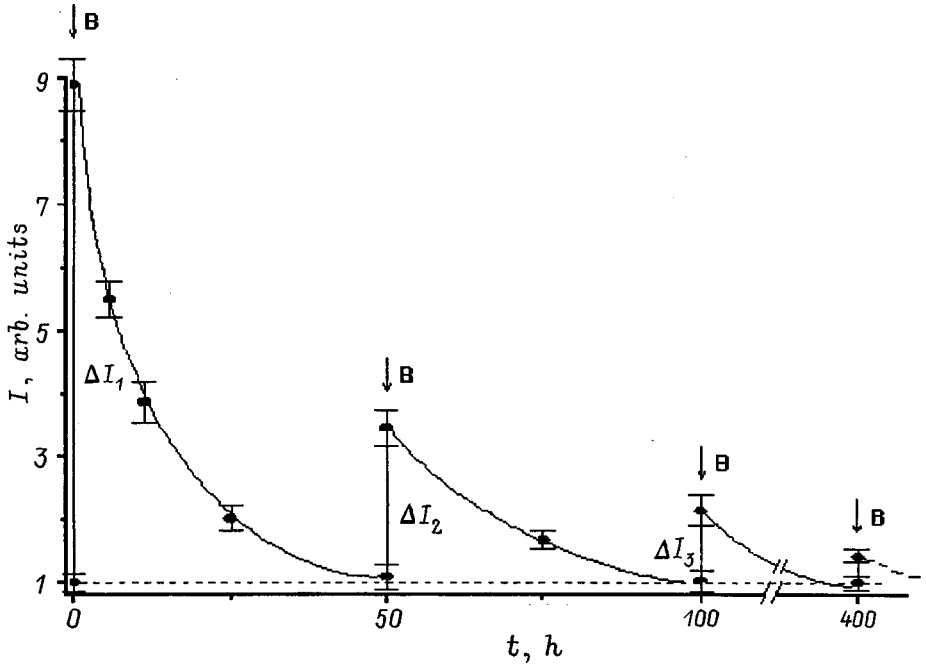

FIG. 2. Electroluminescence intensity of crystal ZnS as a function of the time t, after an electric field ($U = 1.9$ kV, $\nu = 800$ Hz) is first turned on when several successive magnetic field pulses have been applied ($B = 7$ T, pulse duration 10^{-2} s). The arrows denote the times when the crystal was subjected to magnetic field pulses. The electric field was turned on to measure I for short times 5–10 min.

sion from these samples was also significantly higher than from samples that had not been exposed to a magnetic field prior to the excitation of the electroluminescence. Therefore, a magnetic field is capable of changing the state of a crystal that has not been subjected previously to excitation in an electric field.

It was established in a special series of experiments that the absence of silver contacts on the sample had essentially no effect on the relative magnitude of the magnetic effect, $\Delta I/I$, although it did cause an absolute change in I. Therefore, the effect of a magnetic field on the electroluminescence is not associated with changes in the properties of the contacts and can be observed independently of how they are made.

These results do not permit an unambiguous interpretation of the effect of a magnetic field on electroluminescence, since it is unclear which objects in the crystal were affected by the magnetic field. It has been shown[1,2] that the most effective mechanism for electroluminescence in a prebreakdown alternating electric field of strength $\sim 10^5$ V/m in ZnS is the motion of particulate dislocations initiated by the electric field. This motion is thermodynamically favored, since it leads to relaxation of the polytypic hexagonal phase to a cubic phase. The motion of dislocations ensures transport through the crystal of electrons captured from traps and their emission into pores. In the pores the electrons are accelerated by the electric field and, as they reach the base of the luminophore, they cause it to light up. Since the mobility of dislocations in ZnS and, together with it, the intensity of the light from the crystals, depend significantly on the interaction of dislocations with point defects, we may assume that in our magnetic field experiment the following could change: the state of the point defects, the state of the dislocations, themselves, and the nature of the interaction between the dislocations and the point defects. Figure 2 implies that these changes are irreversible, i.e., a magnetic field appears to facilitate relaxation of the state of the structural defects and this eases the movement of the dislocations in the electric field. It is difficult to choose among these alternatives based on the available data. Each of them, however, has been isolated and studied in ionic crystals.[12]

It has been found[12] that a magnetic field affects the spin-dependent reactions among various types of paramagnetic structural defects. Note that the present experiments, like those described in Refs. 6–12, were done under conditions such that the energy imparted by the magnetic field to a paramagnetic defect for $B \sim 1$ T is $\sim \mu g B \sim 10^{-4}$ eV, which is two orders of magnitude below the energy of the average thermal fluctuations, $kT \sim 10^{-2}$ eV, at $T = 293$ K (μ is the Bohr magneton, $g \approx 2$ is the spectroscopic splitting factor, k is the Boltzmann constant, and T is the temperature). The effect of a constant magnetic field on electronic processes and electroluminescence in ZnS when $\mu g B \ll kT$ can change the multiplet state of intermediate short lived particle pairs (defects, under our conditions) at the time of a thermally induced decomposition or the establishment of a covalent bond between defects, thereby enabling the escape of a pair from a metastable state. A change in the multiplicity removes the spin prohibition on certain reactions among defects in ionic crystals. It becomes possible when the lifetime of the pairs is shorter than the spin-lattice relaxation time. If we assume that similar processes can occur in ZnS in a magnetic field, the ''flareup'' of electroluminescence after crystals have been exposed to a magnetic field can be explained by spin-dependent conversion of structural defects, which leads to an increase in the area covered by dislocations as they move in the electric field. This, in turn, may lead to an increase in the number of electrons emitted into pores and, therefore, to a rise in I.

We have observed, therefore, an effect of a weak magnetic field ($B \leqslant 7$ T) on the state of crystal ZnS, which causes an increase in its electroluminescence intensity. It has been found that a magnetic field initiates irreversible changes in the crystals. It has been proposed that the effect of a magnetic field involves the initiation of relaxation processes in a subsystem of metastable structural defects, which, in turn, eases the movement of dislocations.

This work was supported by the Russian Fund for Fundamental Research (Grant No. 97-02-16074).

[1] V. I. Klimenko, S. A. Omel'chenko, and S. Z. Shmurak, Fiz. Tverd. Tela **30**, 1803 (1988) [Sov. Phys. Solid State **30**, 1036 (1988)].
[2] V. I. Klimenko, A. M. Muradyan, A. V. Solov'ev, and S. Z. Shmurak, Fiz. Tverd. Tela **33**, 562 (1991) [Sov. Phys. Solid State **33**, 319 (1991)].
[3] G. Destriau, Philos. Mag. **7**, 700 (1947).
[4] A. N. Ince, Proc. Phys. Soc. London, Sect. B **67**, 870 (1954).
[5] V. Piper and F. Williams, Usp. Fiz. Nauk **70**, 621 (1960) [*sic*].
[6] V. I. Al'shits, E. V. Darinskaya, T. M. Perekalina, and A. A. Urusovskaya, Fiz. Tverd. Tela **29**, 467 (1987) [Sov. Phys. Solid State **29**, 265 (1987)].
[7] V. I. Al'shits, E. V. Darinskaya, and O. L. Kozakova, Zh. Éksp. Teor. Fiz. **111**, 615 (1997) [JETP **84**, 338 (1997)].
[8] Yu. I. Golovin and R. B. Morgunov, JETP Lett. **61**, 596 (1995)].
[9] Yu. I. Golovin and R. B. Morgunov, *Chemistry Reviews*, Vol. 24 (Harwood Academic, 1998).
[10] Yu. I. Golovin, R. B. Morgunov, and V. E. Ivanov, Izv. Vyssh. Uchebn. Zaved. Fiz., No. 4, 117 (1998).
[11] M. N. Levin and B. A. Zon, Zh. Éksp. Teor. Fiz. **111**, 1373 (1997) [JETP **84**, 760 (1997)].
[12] Yu. I. Golovin and R. B. Morgunov, Zh. Éksp. Teor. Fiz. **112**, 1232 (1998) [*sic*].

Translated by D. H. McNeill

Effect of elastic stresses on the IR spectra of lattice vibrations in epitaxial ZnSe films on (001)GaAs substrates

V. S. Vinogradov, L. K. Vodop'yanov, S. P. Kozyrev, and Yu. G. Sadof'ev

P. N. Lebedev Physics Institute, Russian Academy of Sciences, 117924 Moscow, Russia
(Submitted December 28, 1998)
Fiz. Tverd. Tela (St. Petersburg) **41**, 1948–1952 (November 1999)

The lattice IR reflection spectra of epitaxial ZnSe films are studied for different thicknesses on a (001)GaAs substrate. The frequency of the *TO* mode is found to increase for films with thicknesses of 0.8 and 1.2 μm that exceed the critical value $d_{cr} \approx 0.1\ \mu$m for ZnSe/GaAs pairs. The effect is explained by the existence of regions with residual stress in the film. © *1999 American Institute of Physics.* [S1063-7834(99)00811-4]

ZnSe and the solid solutions $Zn_{1-x}Cd_xSe$ based on it, which belong to the group of II–VI semiconductors, are promising materials for opto- and microelectronics. Various quantum sized structures are based on them: superlattices,[1] quantum dots,[2,3] and thin atomic layers.[4,5] It has been found that quantum wells and dots are efficient light emitters in the blue.[1,2] $Zn_{1-x}Cd_xSe$ quantum dots in a matrix of ZnSe can be used to control the waveguide properties of heterostructures.[3] Two-atom layers of ZnSe located at IV/IV or III–V/III–V semiconductor interfaces cause changes in the band jumps. Structural analysis and photoluminescence techniques are mostly used to study these structures based on ZnSe–$Zn_{1-x}Cd_xSe$. IR spectroscopy and optical Raman scattering have not been used on them. It is known, however, that phonons in small-sized objects can differ from those in bulk samples of the same material. The reasons for these differences may be stresses and correlation effects.

In an earlier paper[6] we made the first measurements of lattice IR reflection for films of $Zn_{1-x}Cd_xSe$ on a (001)GaAs substrate. The frequency of the transverse optical phonons for films with small x and thicknesses $d<1\ \mu$m exceeded its value for bulk samples by roughly 1 cm^{-1}. This was surprising, since the film thicknesses greatly exceeded the critical value $d_{cr} \approx 0.1\ \mu$m for ZnSe/GaAs pairs,[7] and the stresses should have vanished because of dislocations. In this paper we attempt a more detailed investigation of this phenomenon by measuring the lattice IR reflection from a series of ZnSe/GaAs films with thicknesses from $d=0.2$ to 4.2 μm. The effect was confirmed for ZnSe films with thicknesses $d=0.8$ and 1.2 μm. The changes in the frequencies of the transverse and parallel optical phonons in the directions of the films are calculated. A comparison of the theoretical and experimental frequencies of the transverse optical phonons shows that regions with residual stress exist in films with $d>d_{cr}$.

1. FILM GROWTH AND MEASUREMENTS

Heteroepitaxial layers of ZnSe were grown on GaAs by molecular-beam epitaxy on a ''Katun'' facility in which the molecular-beam formation system has been significantly improved in order to enhance the uniformity of the properties of the grown layers. The equivalent pressures of the molecular beams were monitored using an ion manometer that was also installed in the facility. The maximum pressure of the residual gases in the facility was 1×10^{-8} Pa.

Epitaxy took place on Cr-compensated (100)GaAs substrates with a misorientation of 3° to the {110} direction by evaporating high-purity (6N) elementary Zn and Se from individual molecular sources at a growth temperature of 300–320 °C. The samples were grown with a ratio of the equivalent pressures of the Se and Zn molecular beams of roughly 2, which ensured the coexistence on the surface of superstructures consisting of a mixture of the (1×2) and $c(2\times2)$ reconstructions and corresponding to stoichiometric growth conditions. The growth rate was maintained at 1 μm per hour. The growth conditions are discussed in more detail in Ref. 6.

Long-wavelength IR reflection spectra were recorded in the region of the lattice vibrations of the ZnSe films using a diffraction IR spectrometer with an optoacoustic OAP-5 sensor as an IR detector and a spectral resolution of at least 1 cm^{-1}.

2. RESULTS OF THE MEASUREMENTS

The measured lattice IR-reflection spectrum at 300 K for a ZnSe film of thickness $d=1.2\ \mu$m on a GaAs substrate is shown in Fig. 1 (curve *1*). Also shown there are the calculated spectrum (curve *2*) and the reflection spectrum of a GaAs substrate ($\omega_t=269\ cm^{-1}$, $S=2.1$) (curve *3*). It is clear from the figure that the reflection spectrum of the thin film compared to reflection spectrum of the substrate resembles the absorption curve for the film. In the long-wavelength portion of the experimental reflection curve, there are frequent oscillations associated with interference at the 400–420 μm thick GaAs substrate. The inset in Fig. 1 shows these oscillations together with the experimental points on an enlarged wave number scale. The spacing in the oscillations is roughly 2.5 cm^{-1} (or 0.8 μm). The experimental points shown in the inset also demonstrate the high spectral resolution of the apparatus (better than 1 cm^{-1}) when recording the reflection spectra.

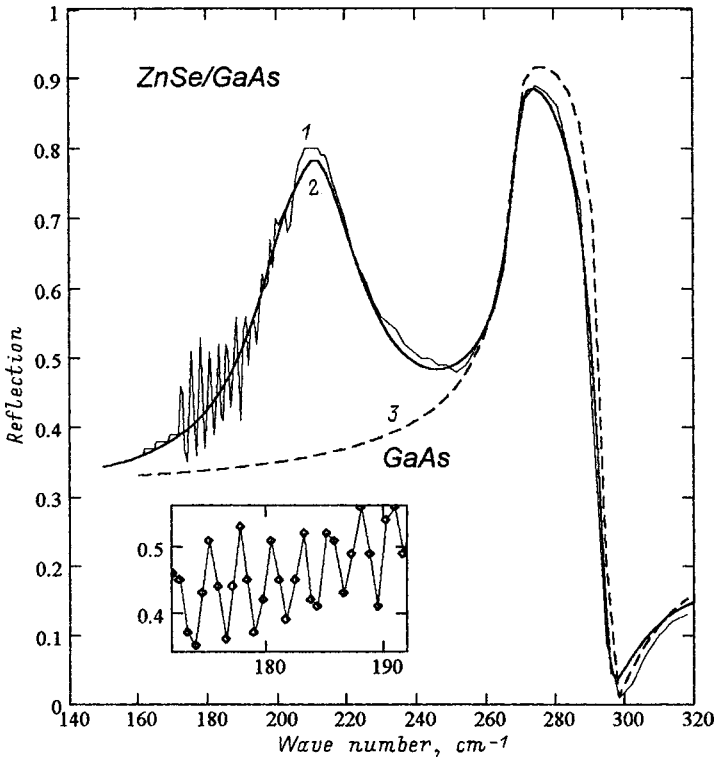

FIG. 1. Lattice IR-reflection spectrum of an epitaxial ZnSe film on a (001)GaAs substrate. *1* — Experimental spectrum, *2* — calculated, *3* — reflection spectrum of the GaAs substrate.

In order to determine the characteristics of the optically active phonons in the film (frequency, oscillator strengths, and damping parameters), the spectra were analyzed mathematically. The model structure consisted of a thin film of thickness d with a dielectric function $\varepsilon_f(\omega)$ and a semiinfinite substrate with a dielectric function $\varepsilon_s(\omega)$ and it was assumed that the film is uniform over its thickness. The amplitude reflection coefficient of this sort of model structure for normally incident light is[8]

$$r_{1fs}(\omega)=\frac{r_{1f}(\omega)+r_{fs}(\omega)\exp(i2\beta)}{1+r_{1f}(\omega)r_{fs}(\omega)\exp(i2\beta)}, \tag{1}$$

where

$$r_{1f}(\omega)=\frac{1-\sqrt{\varepsilon_f(\omega)}}{1+\sqrt{\varepsilon_f(\omega)}}, \quad r_{fs}(\omega)=\frac{\sqrt{\varepsilon_f(\omega)}-\sqrt{\varepsilon_s(\omega)}}{\sqrt{\varepsilon_f(\omega)}+\sqrt{\varepsilon_s(\omega)}}$$

and $\beta=\dfrac{2\pi d\sqrt{\varepsilon_f(\omega)}}{\lambda}$,

and λ is the wavelength ($=10000/\omega$). The reflection coefficient $R(\omega)$ is related to Eq. (1) by the formula $R(\omega)=|r_{1fs}(\omega)|^2$.

The dielectric function of the film, $\varepsilon_f(\omega)$, was written in the classical additive form

$$\varepsilon_f(\omega)=\varepsilon_\infty+\sum_j \frac{S_j\omega_{tj}^2}{\omega_{tj}^2-\omega^2-i\omega\gamma_j}. \tag{2}$$

When calculating the reflection coefficient $R(\omega)$, in the formula for $\varepsilon_f(\omega)$ the frequency of the jth TO-mode ε_{tj}, its oscillator strength S_j, and the damping parameter γ_j were varied. The calculated reflection spectrum is labeled as curve *2* in Fig. 2. The good agreement between the calculated and experimental spectra is evident.

The frequencies of the TO modes for ZnSe films with different thicknesses and for a bulk ZnSe sample are shown in Fig. 2. The bulk sample measurements were done on the same apparatus and in the same geometry as for the films. The figure shows that for samples with film thicknesses $d=0.8$ and $1.2\ \mu$m, the frequencies of the TO mode exceed those for the bulk sample. The vertical bars indicate the expected error in the measurement, which is mainly associated with the spectral resolution of the instrument and ignoring interference in Eq. (1). This error is the same for all the samples because of the almost complete identity of the substrates and measurement conditions. In this way, the excess in the frequencies of the TO mode for films with $d=0.8$ and $1.2\ \mu$m over their values in films with $d\geqslant 1.6\ \mu$m was established quite reliably. The drop in the frequency of the TO mode for very thin films ($d=0.55$ and $0.2\ \mu$m) appears to be related to an increasing error in separating the weak ZnSe-film signal from the substrate background signal.

Before reaching our final conclusions about the nature of the observed effect, we shall make some theoretical estimates.

3. CALCULATING THE CHANGES IN THE FREQUENCIES OF THE OPTICALLY ACTIVE MODES IN A FILM UNDER STRESS

In the rigid-ion model, the square of the frequency of the optically active phonons is given by

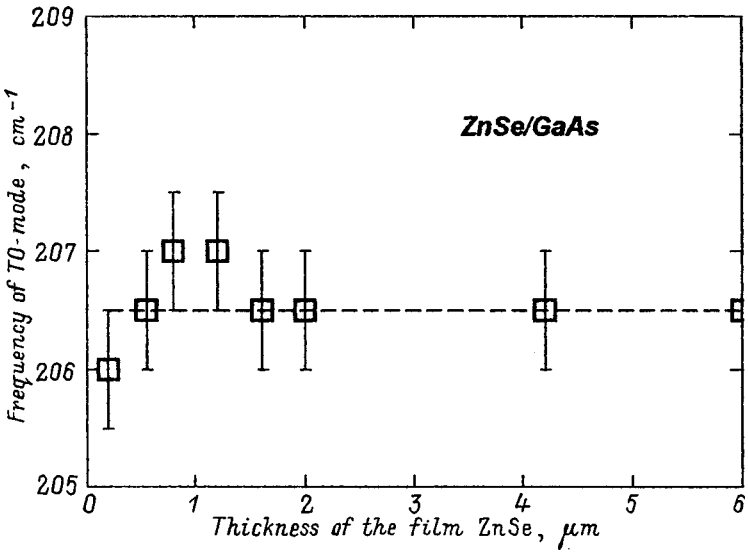

FIG. 2. The frequency of a transverse optical phonon in a ZnSe film as a function of the film thickness. The dashed line corresponds to this frequency for a bulk sample.

$$\omega_t^2=\frac{1}{\mu}\left[K_0-\frac{4\pi}{3}\frac{e^{*2}}{V_0}\right],\quad \omega_l^2=\frac{1}{\mu}\left[K_0+\frac{8\pi}{3}\frac{e^{*2}}{V_0}\right], \tag{3}$$

where μ is the reduced mass, V_0 is the volume of a unit cell, e^* is the effective charge, and K_0 is the force constant, determined by the short-range part of the interaction.

The constant K_0 and the Coulomb interaction terms in Eq. (3) change under the influence of stresses. We shall calculate these changes in the rigid-ion approximation, including just the short range interactions among nearest neighbors. We neglect angular forces, since they are an order of magnitude weaker than the central forces in ZnSe.[9] The interaction energy per ion, positive or negative, for the sphalerite crystal structure of interest to us is given by

$$U=U_k+U_c=\lambda\sum_{i=1-4}\exp(-r_{0i}/\rho)+U_c, \tag{4}$$

where $r_{0i}=|\overline{\mathbf{r}}_0-\overline{\mathbf{r}}_i|$ is the distance between an ion located at the center of the tetrahedron (0) and the ions at its corners ($i=1-4$). In the case of an undeformed structure, the Coulomb interaction energy has the form $U_c=-\alpha e^{*2}/R$, where R is the distance between nearest ions of the same type and $\alpha=1.6381$ for a sphalerite structure.

The position of the group of nearest ions in a stressed film grown on a substrate with a (001) orientation is shown in Fig. 3. Because of the difference in the lattice constants of the film and substrate, the cube in which the tetrahedron is inscribed is converted into a right prism with a square base. The sides of the prism along the x, y, and z axes have lengths $b/2$, $b/2$, $c/2$, respectively, where $b=a+\Delta b$, $c=a+\Delta c$, and a is the lattice constant of the film material in the unstressed state. Since the optically active vibrations consist of displacements of the positive and negative sublattices, the changed short range constants can be calculated by differentiating U_k with respect to the displacements $\overline{\mathbf{r}}_0$ of an ion in the center of the tetrahedron with ions $i=1-4$ fixed in their equilibrium positions. We obtain $K_0+\Delta K_t=\partial^2U_k/\partial x_0^2$ and $K_0+\Delta K_l=\partial^2U_k/\partial z_0^2$. We then expand the right hand sides of these expressions in the deformations $\Delta b/a$ and $\Delta c/a$. For a film with a free surface, the following relationship between the deformations holds[10]

$$\frac{\Delta c}{a}--=-\frac{2C_{12}}{C_{11}}\frac{\Delta b}{a}, \tag{5}$$

where C_{12} and C_{11} are elastic constants of the film. Using this relationship, we can obtain expressions for $\Delta K_t/K_0$ and $\Delta K_l/K_0$ as functions of the argument $\Delta b/a$.

The contributions of the Coulomb interaction in Eq. (3) change because of changes in the unit cell volume V_0 and the depolarization factors, as well as in the electric field of the dipoles within the Lorentz sphere. The volume V_0 changes as $V_0\rightarrow V_0+\Delta V_0=V_0(1-\delta_v)$, where

$$\delta_v=-2\left(1-\frac{C_{12}}{C_{11}}\right)\frac{\Delta b}{a}. \tag{6}$$

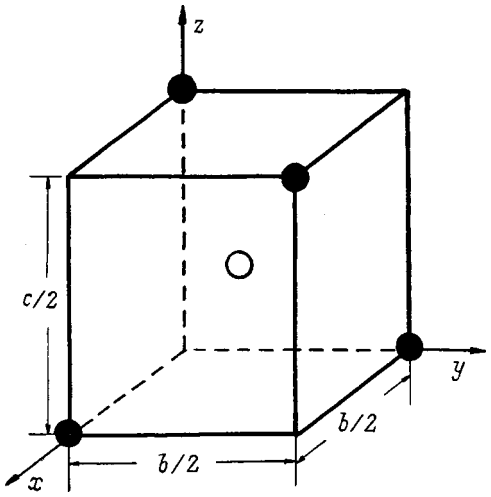

FIG. 3. Deformed tetrahedral cell of a ZnSe film on a (001)GaAs substrate. The lengths of the edges of the rectangular prism obey $b/2<a/2$ and $c/2>a/2$, where a is the lattice constant of the undeformed film.

The following must be kept in mind when calculating the changes in the depolarization factors. The depolarization (Lorentz) factor arises in the calculation of the local field, which is the field of a polarized sphere in the undeformed (cubic) crystal. The deformations in the film transform the sphere into an ellipsoid of rotation with an axis directed along the z axis. The depolarization factors then change as follows owing to the deformations:[11] $(4\pi/3)_x \rightarrow (2\pi/3)\times(1+\varepsilon^2/5)$ and $(4\pi/3)_x \rightarrow (2\pi/3)(1-2\varepsilon^2/5)$, where $\varepsilon=(1-b^2/c^2)^{1/2}$. Given these relationships and the fact that the deformations are small, we obtain the following changes associated with the depolarization factors in the terms in Eq. (3): $4\pi e^{*2}/3V_0 \rightarrow (4\pi e^{*2}/3V_0)(1+\delta_v+\delta_d)$ and $8\pi e^{*2}/3V_0 = 4\pi e^{*2}/V_0 - 4\pi e^{*2}/3V_0 \rightarrow (4\pi e^{*2}/V_0)(1+\delta_v)-(4\pi e^{*2}/3V_0)(1+\delta_v-2\delta_d)=(8\pi e^{*2}/3V_0)(1+\delta_v+\delta_d)$, where

$$\delta_d=-\frac{2}{5}\left(1+\frac{2C_{12}}{C_{11}}\right)\frac{\Delta b}{a}. \tag{7}$$

Taking the sum of these changes, we obtain

$$\frac{\Delta\omega_t}{\omega_t}=\frac{1}{2(1-\gamma)}\left[\frac{\Delta K_t}{K_0}-\gamma(\delta_v+\delta_d)\right],$$

$$\frac{\Delta\omega_l}{\omega_l}=\frac{1}{2(1+2\gamma)}\left[\frac{\Delta K_l}{K_0}+2\gamma(\delta_v+\delta_d)\right], \tag{8}$$

where

$$\gamma=[(\omega_l/\omega_t)^2-1]/[(\omega_l/\omega_t)^2+2],$$

$$\frac{\Delta K_t}{K_0}=\left(1-\frac{2\rho}{R_0}\right)^{-1}\left[\frac{2R_0}{3\rho}\left(1-\frac{C_{12}}{C_{11}}\right)-\frac{2}{3}\left(1+\frac{2C_{12}}{C_{11}}\right)-\frac{2\rho}{R_0}\right]\left(-\frac{\Delta b}{a}\right),$$

$$\frac{\Delta K_l}{K_0}=\left(1-\frac{2\rho}{R_0}\right)^{-1}\left[\frac{2R_0}{3\rho}\left(1-\frac{C_{12}}{C_{11}}\right)+\frac{4}{3}\left(1+\frac{2C_{12}}{C_{11}}\right)+\frac{2\rho}{R_0}\frac{2C_{12}}{C_{11}}\right]\left(-\frac{\Delta b}{a}\right).$$

In Eq. (8) we have left out the terms associated with the change in the dipole field inside the Lorentz sphere. Calculating them is rather complicated and their contribution is small [on the order of $\gamma(\delta_v+\delta_d)$], as are those of the remaining Coulomb terms. (See the estimates below.)

In order to use Eqs. (8), we have to know the parameter R_0/ρ, where R_0 is the distance between nearest neighbors in the undeformed material. It can be determined by relating it to the bulk rigidity modulus $B=(C_{11}+2C_{12})/3=Vd^2U/dV^2$. Given the equilibrium condition $dU/dR|_{R=R_0}=0$, as well as the relations $V_0=a^3/4$ and $R_0=\sqrt{3}a/4$, we obtain

$$\frac{R_0}{\rho}=16\sqrt{3}B\frac{R_0^4}{\alpha e^{*2}}+2. \tag{9}$$

The effective charge e^* can be calculated if the experimental difference $\omega_l^2-\omega_t^2$ is known. For estimating $\Delta\omega_t/\omega_t$ and $\Delta\omega_l/\omega_l$ we shall use the following values of the constants: for ZnSe $a=5.6687$ Å, $C_{11}=85.9\cdot10^{10}$ dyn·cm^{-2}, $C_{12}=50.6\cdot10^{10}$ dyn·cm^{-2}, $\omega_t(300\text{ K})=25.16$ meV, $\omega_l(300\text{ K})=30.49$ meV;[12] and, for GaAs $a=5.6533$ Å. We calculate the parameter R_0/ρ using $(e^*/e)^2=S=0.688$ from Ref. 9. We obtain $R_0/\rho=26$. The relative compression of the film is characterized by the quantity $\Delta b/a=-(a_{\text{ZnSe}}-a_{\text{GaAs}})/a_{\text{ZnSe}}=-0.27\%$. Substituting these values in Eq. (8), we obtain $\Delta\omega_t/\omega_t\approx0.9\%$ and $\Delta\omega_l/\omega_l\approx1.1\%$.

The main contribution to these quantities is from the terms (proportional to R_0/ρ) in $\Delta K_t/K_0$ and $\Delta K_l/K_0$ associated with the change in volume. The contributions of the remaining terms, short-range and Coulomb, are, respectively: 20 and 3% for $\Delta\omega_t/\omega_t$ and 40 and 4% for $\Delta\omega_l/\omega_l$. These numbers mean that for a different orientation of the substrate, $\Delta\omega_t/\omega_t$ and $\Delta\omega_l/\omega_l$ will differ from the maxima given here by 20 and 40%.

4. DISCUSSION OF RESULTS

The estimates of the previous section show that the change in the frequency of the *TO* mode in a stressed ZnSe film of thickness $d<d_k$ should be $\Delta\omega_t\approx2$ cm^{-1}. The observed change in $\Delta\omega_t$ in films with thicknesses $d>d_k$ ($d=0.8$ and 1.2 μm) is less than 1 cm^{-1}. This may mean that the observations result from an averaging effect over regions with residual stress and relaxed regions. As the thickness of the films is increased further below these values, $\Delta\omega_t$ decreases, both owing to a reduction in the fraction of stressed regions, and owing to stress relaxation. For thick films with $d\geqslant2$ μm, $\Delta\omega_t\rightarrow0$. Note that a similar effect has been observed previously in $In_{1-x}Ga_xSb$ films with thicknesses $d>d_k$ on GaAs substrates.[13]

This work was supported by the Russian Fund for Fundamental Research (Grant No. 97-02-16791).

[1] P. Gingo, M. De Vittorio, R. Rinald, and R. Cingolani, Phys. Rev. B **54**, 16 934 (1966).
[2] B. P. Zhang, W. X. Wang, T. Yasuda, Y. Segawa, K. Edamatsu, and T. Itoh, Appl. Phys. Lett. **71**, 3370 (1997).
[3] M. Strassburg, V. Kutzer, U. W. Pohl, A. Hoffman, I. Broser, N. N. Ledentsov, D. Bimberg, A. Rosenauer, U. Fischer, D. Gertsen, I. L. Krestikov, M. V. Maximov, P. S. Kop'ev, and Zh. I. Alferov, Appl. Phys. Lett. **72**, 942 (1998).
[4] T. Saito, Phys. Rev. B **56**, 14 933 (1997).
[5] M. Pan, S. P. Wilks, P. R. Dunstan, M. Pritchard, R. H. Williams, D. S. Cammack, and S. A. Clark, Appl. Phys. Lett. **72**, 2707 (1998).
[6] L. K. Vodop'yanov, S. P. Kozyrev, and Yu. G. Sadof'ev, Fiz. Tverd. Tela **41**, 982 (1999) [Phys. Solid State **41**, 893 (1999)].
[7] G. Horsburgh, K. A. Prior, W. Meredith, I. Galbraith, B. C. Cavenett, C. R. Whitehouse, G. Lacey, A. G. Gullis, P. J. Parbrook, P. Mock, and K. Mizumo, Appl. Phys. Lett. **72**, 3148 (1998).
[8] H. W. Verleur, J. Opt. Soc. Am. **58**, 1356 (1968).
[9] R. M. Martin, Phys. Rev. B **1**, 4005 (1970).
[10] C. Kittel, *Introduction to Solid State Physics*, 4th ed. (Mir, Moscow, 1978), 792 pp.
[11] L. D. Landau and E. M. Lifshitz, *Electrodynamics of Continuous Media*, 3rd ed. (Nauka, Moscow, 1978), 661 pp.
[12] K.-H. Hellwege, ed., *Landolt-Börnstein Numerical Data and Functional Relationships in Science and Technology* (Springer-Verlag, Berlin–Heidelberg–N. Y., 1982), Vol. 17 b, 543 pp.
[13] M. Macler, Z. C. Feng, S. Perkowitz, R. Rousina, and J. Webb, Phys. Rev. B **46**, 6902 (1992).

Translated by D. H. McNeill

Reduction of elastic strains in directly-bonded silicon structures

T. S. Argunova, R. F. Vitman, I. V. Grekhov, L. S. Kostina, and T. V. Kudryavtseva

A. F. Ioffe Physicotechnical Institute, Russian Academy of Sciences, 194021 St. Petersburg, Russia

M. Yu. Gutkin

Institute for Problems in Mechanical Engineering, Russian Academy of Sciences, 199178 St. Petersburg, Russia

A. V. Shturbin

St. Petersburg State Technical University, 195251 St. Petersburg, Russia

J. Härtwig and M. Ohler

European Synchrotron Radiation Facility, 38043 Grenoble Cedex, France

E. D. Kim and S. Ch. Kim

Power Semiconductor Research Laboratory, Korea Electrotechnology Research Institute, 641-600 Gyongnam, Republic of Korea

(Submitted February 9, 1999; resubmitted March 10, 1999)
Fiz. Tverd. Tela (St. Petersburg) **41**, 1953–1962 (November 1999)

The elastically strained state of the interface in directly-bonded silicon structures has been studied by x-ray diffraction topography and IR spectrometry. The pattern of the contrast observed in the x-ray topographs and the intensity oscillations in the IR spectra indicate a periodic strain distribution caused by the long-period surface microroughness on the plates to be bonded. The local microroughness did not exceed 2 Å, and it did not noticeably affect the interface structure. Two types of the structure were subjected to a comparative analysis, (*i*) with a smooth interface prepared by standard direct-bonding technology, and (*ii*) with an interface displaying a regular relief. The strain level in type-II structures was found to be lower by more than an order of magnitude. A model is proposed to account for the observed reduction of elastic strains at the bonded sections of the interface in terms of elastic relaxation of the free surfaces in the relief voids through their deflection and displacement. © *1999 American Institute of Physics.* [S1063-7834(99)00911-9]

Direct bonding of silicon plates is a promising technology, which has been enjoying recently wide industrial application for the fabrication of structures employed in power semiconductor devices and microelectronics.[1,2] The application of this technology to develop bipolar devices is based on connecting thermally unoxidized silicon plates, the so-called Si direct bonding.[3] According to the model proposed in Refs. 4 and 5, ideal bonding starts with a weak electrostatic contact of mirror-polished plate surfaces and is completed by an anneal to form a defect-free and stress-relieved Si–Si interface with a strength nearly equal to that of bulk silicon. However studies of the electrical characteristics of *p–n* junctions in Si–Si bicrystals,[3,6,7] as well as direct observation of the structural perfection of the interface, revealed defects in the structure, which produced a noticeable negative effect on current flow through *p–n* junctions, namely, amorphous layers,[8,9] dislocations,[3,7] and gas bubbles.[10]

Elastic strains in $Si–SiO_2–Si$ structures were investigated by a number of authors.[11,12] It was concluded[11] that a deviation from planarity of the plate surface gives rise to elastic strains and misorientation of lattice planes at the interface. It was established[11] that, in ~0.5-mm thick plates, the maximum stress in the direction normal to the bonding interface $\sigma^{\perp}_{\max} \cong 9\times10^8$ dyn/cm^2 = 0.09 GPa. A calculation was made of the elastic stresses arising from smoothing the rough plate surfaces by the relation from the contact-stress theory.[12] They were found to be $\sigma^{\perp}_{\max} \cong 1\times10^8$ dyn/cm^2 = 0.01 GPa.[12] A comparison of $\sigma^{\perp}_{\max}$ with the stress initiating spontaneous dislocation nucleation in a perfect crystal, which was taken equal to 2.5×10^{10} dyn/cm^2 = 2.5 GPa, led[12] to a conclusion that the stresses generated at the bonding interface do not affect its structural perfection. However numerous observations of dislocations near bubbles show that the elastic strain can become plastic in the most distorted interface regions. At high temperatures dislocations can glide for fairly long distances, particularly in direct Si–Si bonding, where the glide process is not impeded by the presence of an amorphous layer of thermal oxide. But even when it is still elastic, the strain nevertheless affects the carrier mobility, as pointed out in a number of publications.[13,14] Thus one may conclude that reduction of the level of elastic strains is an urgent problem for the direct-bonding technology.

The authors of the present paper have recently proposed a modified method of direct bonding.[15–17] The interface in

modified structures was intentionally fabricated in the form of a regular network of grooves of mesoscopic depth. It was shown both theoretically and experimentally that the dislocations forming in Si–Si bicrystals under misoriented bonding were attracted by the free surfaces of the grooves. A decrease in the dislocation density, an increase of the carrier lifetime, and a reduction of the charge-state density in p–n structures having a patterned interface were demonstrated.[18,19]

We are reporting in this paper a continuation of a systematic investigation of the properties of structures fabricated by direct silicon bonding by traditional[3] and by modified[15] technologies. The main attention is focused on the elastically strained state of the structure. The paper presents experimental data obtained by x-ray diffraction topography and IR spectrometry, as well as some results of a theoretical consideration, which will be analyzed in more detail separately.

1. SAMPLES AND EXPERIMENTAL TECHNIQUES

The samples used were p–n structures. The starting plates were cut from crucibleless-grown Si(111) or (100), with a resistivity $\rho = 30\,\Omega\cdot$cm, or from silicon prepared by the Czochralski method. The plates were ~ 0.5 to 1 mm thick and 20–60 mm in diameter. The quality of their surface treatment was monitored by atomic-force microscopy, and local microroughness did not exceed 2 Å.

The relief in the form of an orthogonal network of grooves used in the modified direct bonding was produced on the surface of one in each pair of plates by photolithography. The parameters of the relief were as follows: groove width 50 μm, distance between the side walls of the adjoining grooves 200 μm, groove depth $0.3-0.5\,\mu$m. Before bonding, the mirror-polished plates were subjected to standard flushing and hydrophylization, with subsequent rinsing in deionized water with a resistivity ~ 18 M$\Omega\cdot$cm. To protect the plates against dust before bonding, they were brought in contact in water. The samples were annealed at 95 °C for 5 h, at 1000 °C for 1 h, and, after that, at 1100 °C for 2 h. The plates were contacted without establishing their crystallographic registry.

The structural perfection of the plates and bicrystals was checked by x-ray diffraction topography.[20] The methods employed in the present work were projection topography with a commercial x-ray source[21] and synchrotron topography[22,23]. The synchrotron experiments were carried out at the European Synchrotron Radiation Facility (ESRF), Grenoble, France, on the ID-19 line, with the energy range covered of 8–100 keV. The ID-19 source with a focal area of 0.15×0.03 mm^2 (H×V) was located at 145 m from the sample to be studied, which provided a beam divergence of $1\times 0.2\,\mu$rad^2 (H×V). The unique parameters of the setup permit production of an x-ray beam whose parallelism and coherence depend very weakly on distance. The geometric resolution of the setup is better than 1 μm, but the resolution of the photographic material (high-resolution KODAK emulsions) limited it to ~ 1 μm. The experiments were performed in both white, 35–50 keV, and monochromatic synchrotron radiation (SR). The crystal monochromator made of high-perfection silicon was set to symmetric (111) Bragg reflection for an incident wavelength of 0.2 Å.

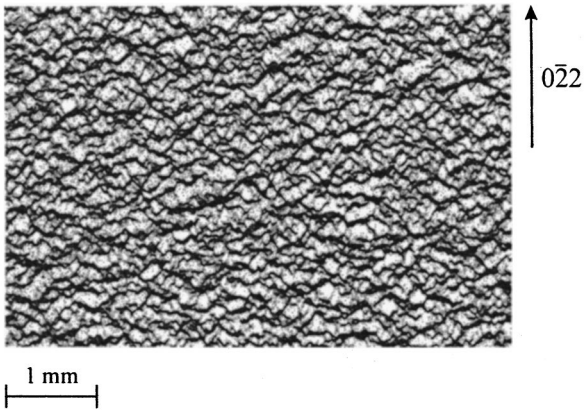

FIG. 1. Typical white-beam synchrotron-radiation topograph of a smooth-interface structure. $0\bar{2}2$ reflection, radiation wavelength $\lambda \approx 0.4$ Å.

The strained state of the interface was studied also by transmission IR spectrometry within the wavelength range of 2.5 to 25 μm.

2. EXPERIMENTAL RESULTS

2.1. X-ray diffraction study

In the course of the study, one obtained and analyzed images of smooth-interface structures, as well as of Si–Si bicrystals with a regularly-patterned interface. The smooth-structure images obtained by the synchrotron white-beam method showed similar contrasts, with noticeable differences appearing only when one crossed over to monochromatic images. Figure 1 shows an x-ray topograph of a structure with a smooth interface obtained by the white-beam method. One readily sees a wavelike enhancement and weakening in intensity with a period of about 200 μm. The high-contrast zones are extended approximately perpendicular to the scattering plane. The monochromatic images showed a totally different pattern; they consisted of narrow loops which changed in size between the slopes of its reflection curve as the sample was rotated.

When the spacing between the scattering planes d changes as a result of a sample strain, the diffraction conditions are not distorted as long as the flux contains the radiation with a wavelength λ related by the Wolf–Bragg relation to the corresponding value of d. Because λ in the white-beam method varies continuously within a broad range, the sensitivity of this arrangement to a change in the strain is low. However the low divergence of SR provides a high sensitivity of the arrangement to misorientation of the reflecting planes. Hence the contrast in Fig. 1 should be due to lattice planes that are tilted relative to their position in the unstrained material. Observation of an enhancement and weakening of the contrast as a result of focusing and defocusing of the reflected intensity may serve as one more confirmation of a local-plane curvature in the samples under examination. By properly varying the film-to-sample dis-

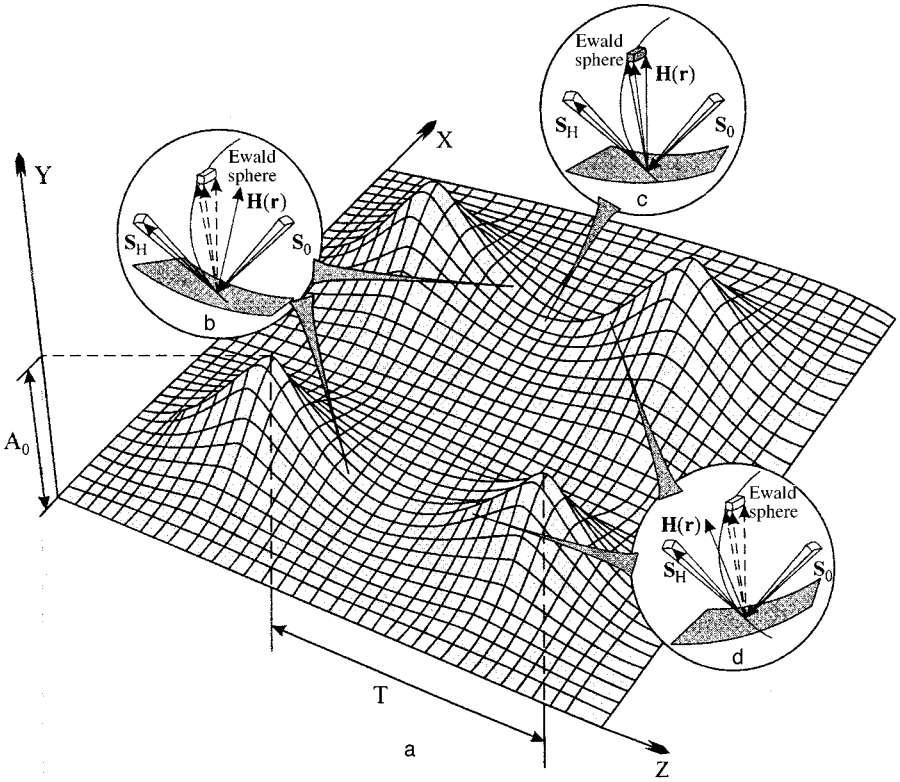

FIG. 2. Schematic illustration of x-ray image contrast in Fig. 1. a—sine-wave interface in unpatterned bicrystals; b,c,d—x-ray reflection from bent planes in reciprocal space.

tance in the synchrotron arrangement, one set the range of distances within which the best image focusing was obtained.

To explain the periodic distribution of the x-ray intensity in Fig. 1, the variation of the lattice plane curvature near the interface can be presented as a sine wave with a period T and an amplitude A_0, namely, $A(x)=A_0\sin(2\pi x/T)$ (Fig. 2a). The formation of contrast is displayed schematically in Fig. 2b–2d in reciprocal space. For a reflection to appear, the normal to the reflecting plane must be parallel to the diffraction vector $\mathbf{H}(\mathbf{r})=\mathbf{S}_H-\mathbf{S}_0$, where $\mathbf{S}_H$ and $\mathbf{S}_0$ are the directional vectors of the reflected and incident beams, respectively, and the tip of vector $\mathbf{H}(\mathbf{r})$ should lie within the node on the Ewald sphere whose dimensions are determined by the divergence of the $\mathbf{S}_0$ and $\mathbf{S}_H$ beams (Fig. 2c). The contrast depends on the relation between the angular divergence of the radiation and the extent of deviation of the reflecting plane from its position in a perfect crystal. The disappearance of a reflection is shown schematically in Fig. 2b and 2d, where the tip of the $\mathbf{H}(\mathbf{r})$ vector leaves the node on the Ewald sphere.

The plane misorientation was estimated experimentally from the focusing and defocusing of an image. By varying the film-to-sample distance in the synchrotron radiation arrangement from 10 cm to 1 m, it was established that image focusing was best within a 10–30-cm interval. When using the white x-ray beam, the planes at the maximum tilt $2\pi A_0/T_0$ focused the reflected rays at a distance $f=(T_0)^2/(8\pi^2A_0)$. For $T_0=200\,\mu$m and $f_0=30$ cm, the maximum misorientation was approximately 10 arcsec. Such weak distortions could be detected only due to the high sensitivity of the setup.

The closed-loop images observed with monochromatic radiation could not be explained by the misorientation effect. The most likely cause of their formation in the topographs is an elastic lattice strain. When viewed in Laue geometry (i.e., in transmission), the image forms by diffraction of radiation from planes perpendicular to the surface. Thus the pattern of contrast with monochromatic radiation can originate from strains in the reflecting planes perpendicular to the surfaces. One used a series of topographs recorded for different positions of the sample within its reflection curve to calculate the quantity $(\delta d/d)_\parallel$ using the relation $\delta\Theta=\Delta d/d\tan\Theta+\Delta\omega$ (where Θ is the Bragg angle and $\delta\Theta$ is the change in the Bragg angle caused by a strain perpendicular to the reflecting plane or parallel to the interface). The quantity $\Delta\omega$, where ω is the tilt angle of the reflecting planes with respect to the interface, was assumed negligible. It was found that the change in the Bragg angle $\delta\Theta$ induced by the $(\Delta d/d)_\parallel$ strain is 0.02°, which is about 70 times larger than the change of this angle corresponding to maximum misorientation. Thus the interface of the structures fabricated by traditional direct-bonding technology is characterized by a comparatively weak misorientation of crystallographic planes ($\sim 10''$) and a fairly strong relative change of interplanar spacing in the direction parallel to the interface, $(\Delta d/d)_\parallel=10^{-3}$.

$Si-SiO_2-Si$ compositions were studied by plane-wave x-ray topography and diffractometry, and the plate-surface smoothness was estimated with a profilometer. The period of alternation of the black-white contrast in x-ray topographs was shown to correlate with that of the plate-surface microroughness. It was concluded that the periodic pattern of the x-ray contrast is due to a periodically distributed microroughness on the surface of the bonded plates. It appears

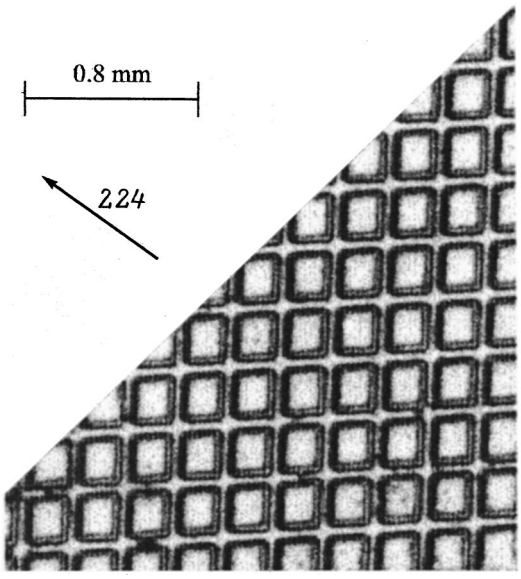

FIG. 3. X-ray projection topograph obtained by the Berg–Barrett–Newkirk method on a commercial radiation source. 224 reflection, Cu $K\alpha$ line.

reasonable to conjecture that the most probable origin of the strain and misorientation of the crystal planes near the interface is the surface microroughness. According to atomic-force microscopy, the plate microroughness did not exceed 2 Å. However these measurements were performed over a region not more than $(1\times1)\mu m^2$ in area. X-ray topography provides a substantially larger field of view and permits one to reveal a wavy pattern of the interface in Si–Si bicrystals, whose period $T\sim200\,\mu$m.

The distribution of contrast in the x-ray topographs obtained from structures with a periodically patterned interface was essentially different. Figure 3 presents a projection topograph of such a structure taken in Bragg (reflection) geometry with a commercial x-ray source. The change in intensity is seen to be maximal near the edges of the voids in the patterned relief. The contrast in the projection topograms measured in a radiation beam with a divergence substantially larger than that of the synchrotron beam cannot be attributed to the weak-misorientation and weak-strain effects described earlier. To explain the strength of the contrast and its dependence on the direction of the diffraction vector **H**, consider the relation between the integrated reflection intensity and the curvature of the reflecting planes. As follows from the dynamical scattering theory, the reflection intensity increases when $\mathbf{H}\cdot\aleph>0$ and decreases when $\mathbf{H}\cdot\aleph<0$, where $\aleph$ is the lattice-plane curvature.[24] Figure 4c shows schematically the cross section of a region in the interface where bonding between grooves occurs; the cross-sectional plane is perpendicular to the bicrystal surface. The diffracted radiation produces an image on the photographic plate (Fig. 4b). In this figure, the diffraction vector **H** in an asymmetric Bragg geometry is decomposed into two components, a larger one, $\mathbf{H}_\perp$, normal to the surface, and a smaller one, $\mathbf{H}_\parallel$, parallel to the interface. When the conditions $\mathbf{H}_\perp\cdot\aleph_1>0$ and $\mathbf{H}_\perp\cdot\aleph_2<0$ are met, a black-white contrast forms at the edges of the image of each fragment corresponding to the space between grooves. However the left-hand edge of the image of each fragment is wider than the right-hand one. This can be attributed to contributions of both components, $\mathbf{H}_\perp$ and $\mathbf{H}_\parallel$, with the latter being sensitive to the curvature $\aleph_3$ of the planes

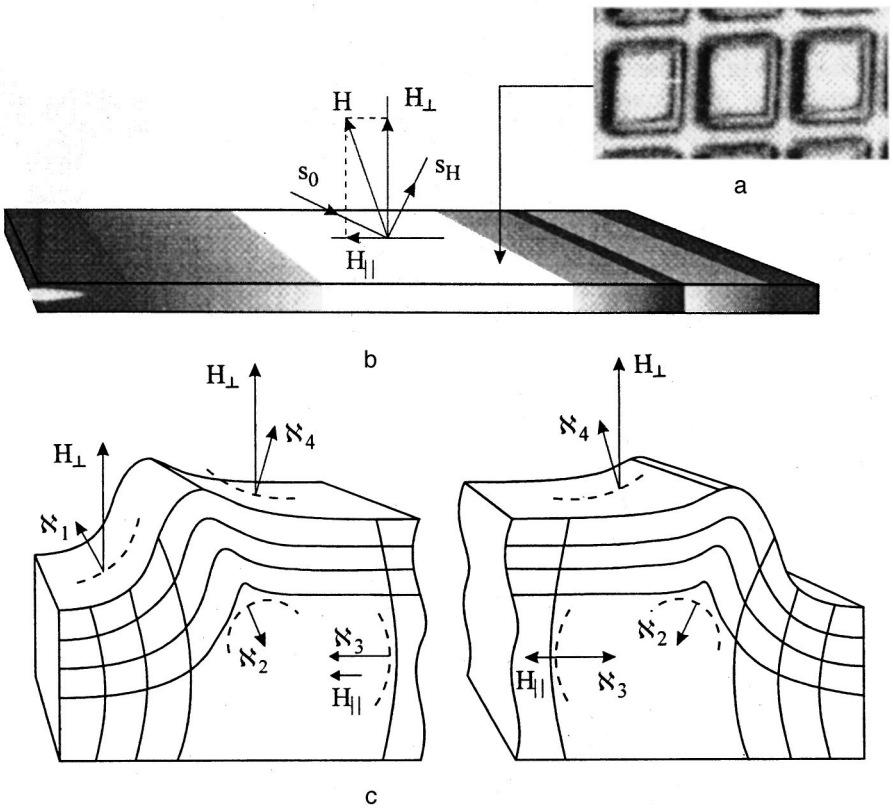

FIG. 4. Scheme illustrating the x-ray image contrast in Fig. 3. a—fragment of the topograph in Fig. 3; b—photographic plate with a schematic contrast distribution; c—cross section of one of the bicrystal plates with a patterned surface. $H_\parallel$ and $H_\perp$ are the diffraction vector components; $\aleph_i$ is the lattice plane curvature.

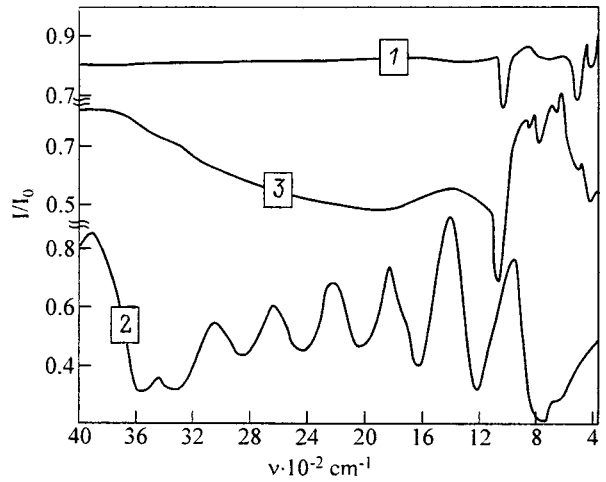

FIG. 5. Transmission (relative to a reference) of various silicon samples vs the wave number of light: *1*—starting material, *2*—smooth-interface sample, *3*—patterned-interface sample. Vertical scale coefficient: *1*—$(I/I_0)\times 0.8$, *2,3*— $(I/I_0)\times 2.2$.

normal to the surface. The right-hand edge of the image is narrower, because the $\mathbf{H}_{\|}$ component does not contribute here to contrast. The additional bright band at the right-hand edge of each fragment indicates the presence of a $\aleph_4$ curvature and that the $\mathbf{H}_{\perp}\cdot\aleph_4>0$ condition is upheld. Thus the above interpretation of the strength of the contrast permits a conclusion that, in structures having a regularly patterned interface, the free surfaces of grooves and the adjoining lattice planes are noticeably curved.

2.2. Investigation of the bonding interface quality by IR transmission spectrometry

Figure 5 presents transmission spectra of three typical samples taken within the 2.5–25-μm wavelength interval. Spectrum *1* relates to the starting material with a thickness twice that of the plates before bonding. Spectra *2* and *3* correspond to bicrystals with a smooth and a patterned interface. An analysis of the data obtained revealed the following relationships.

1. The spectra of smooth-interface samples exhibit distinct oscillations in transmission with an amplitude increasing toward low frequencies;

2. The transmission spectra of structures with a mesoscopic relief on the interface contained weakly pronounced oscillations with a period exceeding by a few times that for the smooth plates;

3. After the bonding, all samples exhibited a noticeable decrease in transmission practically throughout the wavelength range studied.

One may conclude that the structures produced by direct bonding contain an optically nonuniform layer, which gives rise to a scattering of the radiation beam propagating through the crystal. Light scattering exhibiting an oscillating pattern is called Mie scattering.[25] In a search for the reasons responsible for the transmission oscillations in the spectra of the structures under study, we considered both the stressed regions of the interface and the possible presence there of air bubbles.

In order for Mie oscillations to be pronounced in experiments with multiple scatterers, two conditions must be met:

(1) The nondimensional scattering parameter of the inhomogeneities ρ must be sufficiently large,

$$\rho = 2\pi\frac{1}{\lambda}l\frac{n-n_0}{n_0} = 2\pi\nu l\frac{\Delta n}{n_0} \gg 1\,, \tag{1}$$

where l is the ''scatterer'' size (we denote it by l_{air} and l_{strain} for the inhomogeneities of air and strain origin, respectively), n is the refractive index of the scattering region, n_0 is the matrix refractive index, $\Delta n \equiv n-n_0$, λ is the wavelength of light in vacuum, and $\nu = 1/\lambda$ is the wave number;

(2) The ''scatterer'' system must be sufficiently uniform in ρ, i.e., the total dispersion of this parameter, $\delta\rho$, must be sufficiently small

$$\delta\rho << 2\pi\,. \tag{2}$$

One can easily calculate for the silicon-air system, where $\Delta n = 2.4$ and $\delta(\Delta n)\equiv 0$, that condition (2) can be hardly satisfied even for a scatter in the microinclusion diameter $\delta l_{\text{air}} > 1$ μm. We believe such small differences between the air bubble dimensions at an interface to be highly unlikely, and no oscillations from air microinclusions in this wavelength range should be seen in our experiment.

If the change in the strain near the bonding interface is due to microroughness on the surfaces of the contacting plates, the mechanical stresses in bicrystals have alternating character, with compression arising at the contact of two projections, and tension, where two grooves face one another. The periodic pattern of the compression-tension stress distribution at the bonding interface permits one to introduce the concept of a strain nature of the scattering region, whose dimension $l^{\|}_{\text{strain}}$ in the direction parallel to the interface is one half the period of the $A(x)$ sine function (Fig. 2). Our calculations show that mechanical stresses fall off logarithmically slowly with distance from the interface. We shall assume that they extend up to the free surfaces of the bicrystal. Then one can write $l^{\perp}_{\text{strain}} = t = t_{\text{wafer 1}} + t_{\text{wafer 2}}$ for the dimension of the scattering region in the direction perpendicular to the bonding interface, where $t_{\text{wafer 1}}$ and $t_{\text{wafer 2}}$ are the respective thicknesses of the two plates. Then the effective scattering parameter (1) of such a region will take on the form $\rho = 2\pi\nu l\overline{\Delta n}/n_0$, where $\overline{\Delta n}$ is the average value of Δn in the structure, and the dispersion of the constant value of ρ vanishes. Thus condition (2) is met automatically. As follows from the above, the most probable reason for the onset of transmission oscillations is diffraction of light from the compression-tension regions, and air bubble inclusions result only in nonselective transmission losses in a sample.

The quantitative calculations were carried out in terms of a mathematical formalism developed in the theory of dispersion filters[26]. Assuming the observed transmission I of a bicrystal to result from independent action of two scattering layers of the air and strain nature, I_{air} and I_{strain}, respectively, one can write $I = I_{\text{air}}I_{\text{strain}}$. Each component was estimated from the expression[26]

$$I = \exp\left[-\frac{D}{l}4S(1-S)\sin^2(\pi\nu l\overline{\Delta n})\right], \tag{3}$$

where D is the scattering-layer thickness, and S is the volume fraction of scatterers in the layer; let S_{air} and S_{strain} describe the volume fractions of inhomogeneities of the air and strain nature, respectively.

Assuming only one scatterer layer to fit into the scattering-layer thickness, one can accept $D/l=1$ for both systems, although the values of D and l for the air and strain-induced scatterers are different. Because oscillations in the air-silicon system are not felt throughout the wavelength range covered, in recording I_{air} one can replace the phase factor $\sin^2(\pi\nu l\overline{\Delta n})$ by its mean value, which is 1/2.

Consequently, we obtain the expression

$$I(\nu)=\exp\{-[2S_{\text{air}}(1-S_{\text{air}})+4S_{\text{strain}}(1-S_{\text{strain}})\sin^2(\pi\nu I_{\text{strain}}\overline{\Delta n})]\}. \quad (4)$$

This relation describes the oscillating nature of the intensity distribution in the samples studied. By comparing curves *2* and *3* in Fig. 5 to relation (4), one can determine some of the parameters entering it, the most important of them being the strain. As follows from curve *2* in Fig. 5, the oscillation period $\Delta\nu=420\ \text{cm}^{-1}=4.2\times10^4\ \text{m}^{-1}$. Based on the character of the phase factor in Eq. (4), one can write $\overline{\Delta n}l_{\text{strain}}=1/\Delta\nu$. In view of the fact that $l_{\text{strain}}=t_{\text{wafer 1}}+t_{\text{wafer 2}}=(0.1+0.1)\ \text{cm}=2\times10^{-3}\ \text{m}$, we obtain $\overline{\Delta n}=0.012$ and $\overline{\Delta n}/n_0=0.012/3.43=3.5\times10^{-3}$.

Since the quantity Δn is linearly related to pressure P[27]

$$\frac{1}{n}\frac{dn}{dP_\nu}=(-3\pm2)\,10^3\,\text{dyn}^{-1}, \quad (5)$$

(in this expression P_ν is a type of hydrostatic compression), the quantity obtained can be considered equal to the strain in structures with a smooth interface, $(\overline{\Delta n}/n_0)^{\text{smooth}}=|\varepsilon_{yy}^{\text{smooth}}|=3.5\times10^{-3}$.

This result is in a good agreement with the x-ray data. Indeed, assuming the normal strain components along the interface to be equal, the x-ray data yield $\varepsilon_{xx}=\varepsilon_{zz}\approx10^{-3}$. In view of the fact that the normal component $\varepsilon_{yy}=-\varepsilon_{xx}/\nu$, where ν is the Poisson ratio $\nu_{\text{Si}}=0.278$,[28] we obtain $\varepsilon_{yy}^{\text{smooth}}=-3.6\times10^{-3}$.

The $\sigma_{yy}^{\text{smooth}}$ stress can be found from the expression

$$\sigma_{yy}=\frac{E}{1+\nu}\left[\frac{\nu}{1-2\nu}(\varepsilon_{xx}+\varepsilon_{yy}+\varepsilon_{zz})+\varepsilon_{yy}\right], \quad (6)$$

where $E=1.66\times10^{-12}\ \text{dyn/cm}^2=166$ GPa (Ref. 28) is Young's modulus.

Inserting the experimentally measured strain components into Eq. (6), one obtains $\sigma_{yy}^{\text{smooth}}=-6\times10^9\ \text{dyn/cm}^2=-0.6$ GPa.

The oscillation period in the IR spectra of structures with a regularly patterned interface reached the value $\Delta\nu=4500\ \text{cm}^{-1}=4.5\times10^5\ \text{m}^{-1}$. Hence the strain in the patterned structures was substantially smaller than that in the smooth ones, $(\overline{\Delta n}/n_0)^{\text{grooved}}=|\varepsilon_{yy}^{\text{grooved}}|=3.2\times10^{-4}$. For the corresponding stress one obtains $\sigma_{yy}^{\text{grooved}}=-5\times10^8\ \text{dyn/cm}^2=-0.05$ GPa. This value is less by more than an order of magnitude than the stress in the smooth-interface bicrystals studied in this work, and it is nearly one half that obtained in Ref. 11.

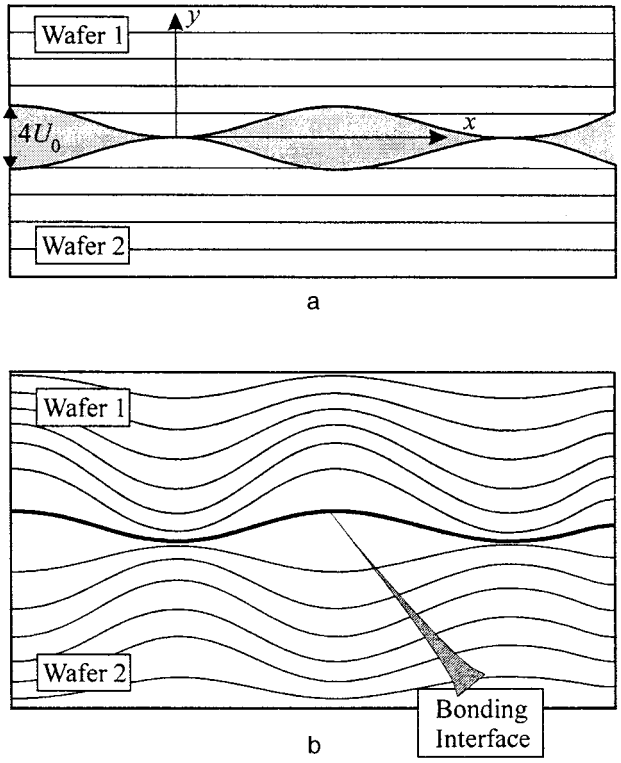

FIG. 6. (a) Schematic image of contact between two smooth plates with a surface microroughness amplitude U_0 and period T, and (b) stress distribution over the cross section of a bicrystal obtained by direct bonding of these plates.

3. DISCUSSION OF RESULTS

The experimental data obtained in this work can be explained based on the simplest geometric models of contact of rough plates, both smooth and with a periodic relief. When plates with a residual microroughness described by a sine function with a period T and amplitude U_0 are bonded, it is only natural to expect the largest strains to be generated at the points where the hillock tops meet, as this is shown in Fig. 6a. In this case the maximum distance to be overcome by the opposite surfaces in order to become bonded is $4U_0$. Bonding entails smoothing of the surface relief, and the smoothened interface described by the function $A(x)=A_0\sin(2\pi x/T)$ (Fig. 2) becomes a source of periodically distributed elastic strains (Fig. 6b).

In order to calculate the elastic-strain fields, one used special model configurations of virtual wedge disclinations, whose strength and geometric characteristics are fully determined by the relief of the starting microroughness of the surfaces to be bonded and the geometry of the resulting bonding interface. A detailed description of such models and details of elastic-field calculation of model disclination structures fall outside the scope of the present paper. We present here for illustration only the final compact expressions for the elastic dilatation fields $\varepsilon=\varepsilon_{xx}+\varepsilon_{yy}+\varepsilon_{zz}=\delta V/V$, where $\delta V/V$ is the relative difference in volume in the cases of an

originally smooth interface and a smoothened interface with an artificially patterned orthogonal system of inner voids. We shall restrict ourselves to a two-dimensional case corresponding to the case of a planar deformation of the system. In a two-dimensional case, the profile of the original microroughness depends only on the x and y coordinates, and the elastic field at the bonding interface is modeled by fields of periodic rows of positive and negative virtual disclinations forming one quadrupole disclination configuration each per period T.

Let the tops of the hillocks touch at a point $(x=0, y=0)$ lying in the interface plane XZ (Fig. 6a). It can be shown that the dilatation ε reaches its maximum value along the $x=0$ line crossing at right angles the interface at the point of contact of the hillock tops. Near the interface, for $T/|y| \gg 1$,

$$\varepsilon(x=0, |y| << T) \approx -1.2 \frac{1-2\nu}{1-\nu} \frac{U_0}{T} \ln \frac{q^2 T}{2p^2|y|}. \qquad (7)$$

Thus ε is directly proportional to the roughness amplitude U_0 and decreases with increasing period as $T^{-1} \ln T$. The logarithmic singularity at the (0,0) point can be removed by using for the elastic fields of virtual disclinations the solutions obtained not in the classical but the gradient theory of elasticity, as this was shown[29,30] to be true for dislocations.

Figure 7a presents a plot of the dilatation ε against the microroughness period T drawn for the model parameters $p=0.13$ and $q=0.37$ and the microroughness amplitude $U_0=100$ Å. Because the measurements reported in Ref. 11 covered all the characteristics governing the relation shown in Fig. 7a, namely, the period and amplitude of the wavy plate surface, as well as the stress at the interface after the bonding, one can check the validity of the constructed relation. The period corresponding to $U_0=100$ Å was found[11] to be $T=500$ μm. The graph gives for the dilatation corresponding to these characteristics $|\varepsilon|=2.3\times10^{-4}$. By converting the dilatation to normal stress σ_{yy} using Eq. (6), one obtains $|\sigma_{yy}|=9\times10^8$ dyn/cm^2 $=0.09$ GPa. This value is equal to the result of the measurement quoted in Ref. 11. In our case, the characteristic period T derived from x-ray topographs was smaller, 200 μm. As follows from the experimentally determined strain components and from the plot in Fig. 7a, the amplitude of the long-period microroughness in our case was larger than 100 Å. Thus the surface with a higher roughness gave rise to higher elastic stresses in our case compared to the data of Refs. 11 and 12.

However when one of the plates to be bonded had an artificial relief in the form of a network of grooves (with their period coinciding with that of the residual plate roughness, and the groove depth exceeding the roughness amplitude), one observed an efficient reduction of elastic strains. The main reasons for this reduction are the decrease in the effective roughness amplitude and the elastic relaxation of the free surfaces of the grooves through their elastic bending and displacement. Let's consider these reasons in more detail.

Because the surface area covered by the grooves is fairly large (in the samples under study it was about 36% of the

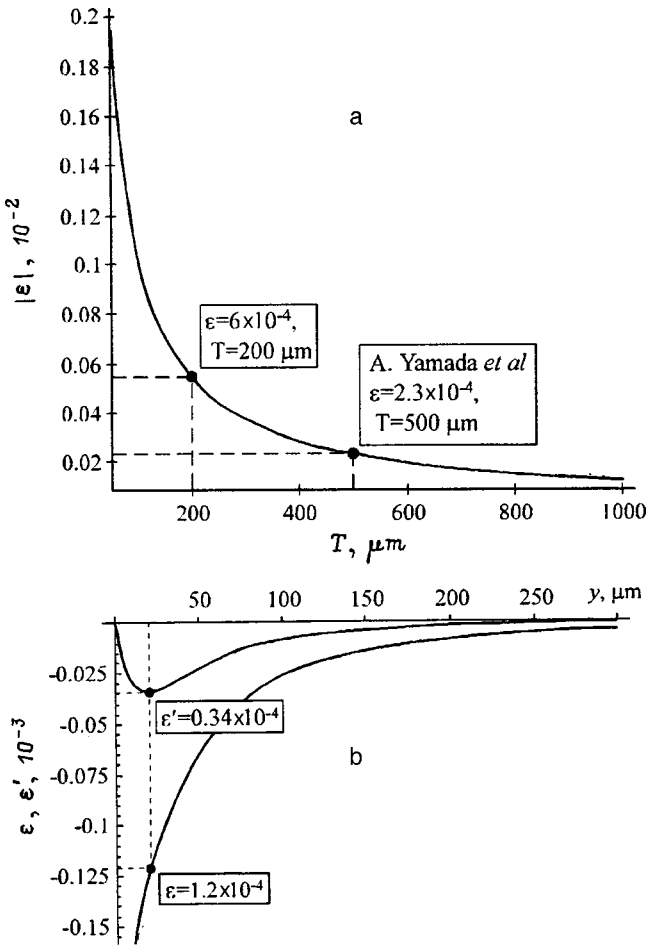

FIG. 7. Elastic dilatation near the interface: a—dependence of dilatation $|\varepsilon|$ at a point $(x=283.6, y=0.00208)$ on microroughness period T for an amplitude $U_0=100$ Å. b—dependence of dilatation along the $(x=0, y)$ line for a smooth (ε, lower curve) and patterned (ε', upper curve) interface.

total surface area of the patterned plate), the probability for a hillock top to fall into a groove is also high (Fig. 8a). This figure relates to the case of the most efficient effect of grooves on the level of residual elastic strains. Under these conditions the maximum distance between the surfaces decreases by an amount δU_0, which was about 15% of the original distance $4U_0$ in our systems. One may thus propose an effective reduction of the roughness amplitude U_0 by the same 15%. Taking into account the linear relation between U_0 and the level of residual elastic strains (7), we obtain a reduction of this level by 15%. It is not this reason, however, that is dominant in the much more substantial reduction of the strain level observed in our case.

The second and, apparently, the main reason for the reduction of residual strain is the elastic bending and displacement of the free groove surfaces. Direct bonding of plates with a regular surface relief gives rise to formation of a bonding interface, which occupies approximately 64% of the total interface area when smooth plates come in contact. This part of the interface is a source of elastic fields. At the same time free surfaces of grooves, which now became inner voids, appear in the interface region; their total area is about 53% of the total interface area. The elastic relaxation of these

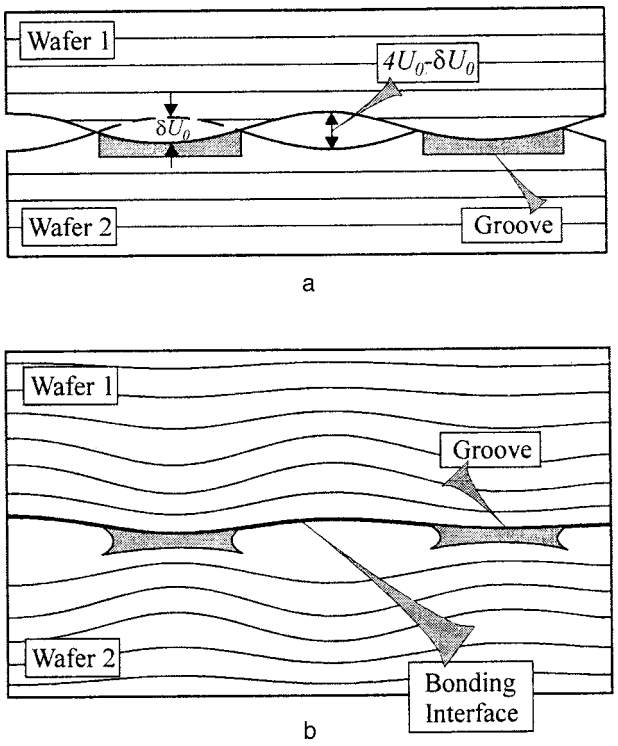

FIG. 8. Schematic representation of (a) contact between two plates, and (b) stress distribution in a bicrystal with a patterned interface.

inner free surfaces shown schematically in Fig. 8b in the form of a deflection should naturally screen efficiently the elastic fields due to the bonded regions and, as a result, reduce the total level of elastic strains in such a system.

When simulating the screening of elastic fields, secondary virtual disclinations, whose position was given by the p and s parameters, were introduced into the theoretical model. The value $s=0.38$ was chosen so as to satisfy the equality $\varepsilon'(x=0, y\to 0)=0$, where ε' is the dilatation in patterned structures. Then in the case of a hillock top facing the groove center, we obtain for the dilatation ε' along the $x=0$ line near a patterned interface

$$\varepsilon'(x=0,y)\approx \frac{1-2\nu}{2\pi(1-\nu)}\omega\left(\frac{1}{2}\ln\frac{q^2T^2+y^2}{T^2/4+y^2} + 1.66\ln\frac{(p^2T^2+y^2)[s^2T^2+(y+pT)^2]}{(q^2T^2+y^2)(y+pT)^2}\right). \quad (8)$$

Here $\omega\approx 7.57\,U_0/T$ is a parameter characterizing the strengths of virtual disclinations.

Figure 7b presents $\varepsilon(0,y)$ and $\varepsilon'(0,y)$ dependences illustrating the screening action of the free groove surfaces. The screened dilatation $\varepsilon'(0,y)$ reaches a maximum (in absolute magnitude) of about 0.34×10^{-4} close to the point $y\approx 20\,\mu$m, where the dilatation ε due to an unpatterned interface is nearly four times larger: $\varepsilon\approx 1.2\times 10^{-4}$. A more comprehensive analysis of the results obtained in this simulation of the direct-bonding interface will be given in the next publication of these authors.

Thus the main results of the above investigation into the elastically strained state of an interface under direct bonding of silicon plates can be summarized as follows.

(1) The reason for the elastic lattice distortion near the interface, which is observed in direct bonding of plates and includes lattice plane disclination and dilatation components, is the long-period microroughness of their surface. The bicrystal interface formed in the course of smoothing of the surface microroughness had a sine-wave shape $A(y)=A_0\sin(2\pi x/T)$, where $T\sim 200\,\mu$m.

(2) The normal mechanical stresses in Si–Si structures with a smooth interface, measured by x-ray diffraction topography and IR spectrometry, were found to be $|\sigma_{yy}^{\text{smooth}}|=0.6$ GPa.

(3) In structures with a patterned relief bonded by a modified technology,[15] a reduction of normal elastic stresses by more than an order of magnitude has been reached: $|\sigma_{yy}^{\text{grooved}}|=0.05$ GPa. No bending of the free surfaces of grooves and of the adjoining lattice planes was observed to occur in such structures.

(4) A semiquantitative interpretation for the reduction of elastic stresses in patterned structures has been proposed as a result of a simulation of elastic fields at the bonding interface. It assumes screening of the elastic stress fields generated by bonded interface regions by the surfaces of the grooves that underwent relaxation, i.e., elastic bending and displacement. Reducing the effective microroughness amplitude in patterned structures also favored reduction of the stress level.

Support of the Russian Fund for Fundamental Research (Grants 97-02-18331, 98-02-18250, and 98-02-18309) and of the Federal program ''Integration'' (Grant 75) is gratefully acknowledged.

E-mail: argunova@tania.ioffe.rssi.ru

[1] J. B. Lasky, Appl. Phys. Lett. **48**, 78 (1986).
[2] W. P. Maszara, G. Goetz, A. Caviglia, and J. B. McKitterick, J. Appl. Phys. **64**, 4943 (1988).
[3] M. Shimbo, K. Furukawa, K. Fukuda, and K. Tanzawa, J. Appl. Phys. **60**, 2987 (1986).
[4] R. Stengl, T. Tan, and U. Gösele, Jpn. J. Appl. Phys., Part 1 **28**, 1735 (1989).
[5] Q.-Y. Tong and U. Gösele, J. Electrochem. Soc. **143**, 1773 (1996).
[6] R. Lindner and R. Hoffman-Tikkanen, in *Springer Proceedings in Physics*, Vol. 35 (Springer, Berlin, 1989), p. 219.
[7] A. Laporte, G. Sarrabayrouse, L. Lescouzeres, A. P. Lavigne, M. Benamara, A. Rocher, and A. Claverie, *Proceedings of the 6th International Symposium on Power Semiconductor Devices & IC's* (*Davos, 1994*), p. 293.
[8] T. Abe, A. Uchiyama, K. Yoshizawa, Y. Nakazato, M. Miyawaki, and T. Ohmi, Jpn. J. Appl. Phys., Part 2 **29**, L2315 (1990).
[9] F. Widdershoven, J. Haisma, and J. Naus, J. Appl. Phys. **68**, 6253 (1990).
[10] S. Bengtsson, J. Electron. Mater. **21**, 841 (1992).
[11] A. Yamada, Bai-Ling Jiang, G. A. Rozgonyi, H. Shirotori, O. Okabayashi, and M. Kawashima, J. Electrochem. Soc. **138**, 2468 (1991).
[12] W. P. Maszara, B.-L. Jiang, A. Yamada, G. A. Rosgonyi, H. Baumgart, and A. J. R. de Kock, J. Appl. Phys. **69**, 257 (1991).
[13] M. G. Mil'vidskiĭ and V. B. Osvenskiĭ, *Structural Defects in Epitaxial Semiconducting Layers* (Metallurgiya, Moscow, 1985).
[14] B.-Y. Tsaur, J. C. C. Fan, and M. W. Geis, Appl. Phys. Lett. **40**, 322 (1982).

[15] I. V. Grekhov, T. S. Argunova, L. S. Kostina, T. V. Kudryavtseva, E. D. Kim, and S. C. Kim, Electron. Lett. **31**, 2047 (1995).
[16] T. S. Argunova, I. V. Grekhov, M. Yu. Gutkin, L. S. Kostina, E. I. Belyakova, T. V. Kudryavtseva, E. D. Kim, and D. M. Park, Fiz. Tverd. Tela (St. Petersburg) **38**, 3361 (1996) [Phys. Solid State **38**, 1832 (1996)].
[17] E. D. Kim, S. C. Kim, J. M. Park, I. V. Grekhov, T. S. Argunova, L. S. Kostina, and T. V. Kudryavtseva, J. Electrochem. Soc. **144**, 622 (1997).
[18] I. V. Grekhov, L. S. Berman, T. S. Argunova, L. S. Kostina, E. I. Belyakova, T. V. Kudryavtseva, E. D. Kim, S. C. Kim, and D. M. Park, Pisma Zh. Tekh. Fiz. **22**, No. 23, 14 (1996) [Tech. Phys. Lett. **22**, 956 (1996)].
[19] T. S. Argunova, I. V. Grekhov, L. S. Kostina, T. V. Kudryavtseva, M. I. Gutkin, J. Härtwig, E. D. Kim, S. C. Kim, and N. K. Kim, Jpn. J. Appl. Phys., Part 1 (in press).
[20] A. Authier, *Adv. X-ray Analysis*, Vol. 10 (Plenum, New York, 1967), p. 9.
[21] W. W. Webb, in *Direct Observations of Imperfections in Crystals*, edited by J. B. Newkirk and J. H. Wernick (Interscience Publishers, New York, 1962, p. 29; Mir, Moscow, 1965, p. 351).
[22] *Characterization of Crystal Growth Detected by X-Ray Methods*, edited by B. K. Tanner and D. K. Bowen (Plenum, New York, 1980).
[23] R. Barrett, J. Baruchel, J. Härtwig, and F. Zontone, J. Phys. D **28**, A250 (1995).
[24] U. Bonse and W. Graeff, Z. Naturforsch. A **28**, 558 (1973).
[25] C. F. Bohren and D. R. Huffman, *Absorption and Scattering of Light by Small Particles* (Wiley-Interscience, New York, 1983; Mir, Moscow, 1986).
[26] N. A. Borisevich, V. G. Vereshchagin, and M. A. Velidov, *Infrared Filters* (Nauka i Tekhn., Minsk, 1971).
[27] M. Cardona, W. Paul, and H. Brooks, J. Phys. Chem. Solids **8**, 204 (1959).
[28] Yu. A. Kontsevoĭ, Yu. A. Litvinov, and E. A. Fattakhov, *Plasticity and Strength of Semiconducting Materials and Structures* (Radio i Svyaz', Moscow, 1982).
[29] M. Yu. Gutkin and E. C. Aifantis, Scr. Mater. **35**, 1353 (1996).
[30] M. Yu. Gutkin and E. C. Aifantis, Scr. Mater. **36**, 129 (1997).

Translated by G. Skrebtsov

Carrier mobility contribution to the piezoresistive effect in SmS

L. N. Vasil'ev and V. V. Kaminskiĭ

A. F. Ioffe Physicotechnical Institute, Russian Academy of Sciences, 194021 St. Petersburg, Russia
(Submitted March 24, 1999)
Fiz. Tverd. Tela (St. Petersburg) **41**, 1963–1964 (November 1999)

A study is reported of the contribution to the piezoresistive effect in samarium-monosulfide-based materials by pressure-induced variation of carrier mobility. As follows from calculations and experimental data, the piezoresistance coefficient for hydrostatic pressure cannot exceed 7×10^{-3} MPa^{-1} at $T=300$ K. © *1999 American Institute of Physics.* [S1063-7834(99)01011-4]

The piezoresistive effect in samarium monosulfide is closely connected to concentration, and the pressure-induced change in carrier mobility u is small.[1] It was shown,[2] however, that the contribution to the piezoresistive effect associated with changes in the mobility increases in SMS and some related solid solutions with decreasing carrier concentration n in a sample. SmS exhibits the largest piezoresistive effect among known materials, and it appeared of interest therefore to analyze the possibility of increasing it still further by varying properly the mobility component of the piezoresistance coefficient.

Writing the electrical conductivity in the form $\sigma=enu$, the hydrostatic piezoresistance coefficient can be cast as

$$\pi=-\frac{d\ln\sigma}{dP}=-\frac{1}{n}\frac{\partial n}{\partial P}-\frac{1}{u}\frac{\partial u}{\partial P}=\pi_n+\pi_u, \tag{1}$$

where π_n and π_u are the concentration and mobility components of the piezoresistance coefficient, respectively. Taking a single-band model, the carrier mobility in the case of arbitrary degeneracy can be written in the relaxation-time approximation[3]

$$u=\frac{e}{m^*}\langle\tau\rangle=\frac{N_c}{n}\int_0^\infty\tau\left(-\frac{\partial f_0}{\partial x}\right)x^{3/2}dx, \tag{2}$$

where τ is the effective relaxation time for two simultaneously operating mechanisms of carrier scattering in SmS,[4] from acoustic phonons and charged defects

$$\tau^{-1}=\tau_A^{-1}+\tau_I^{-1}. \tag{3}$$

For the corresponding relaxation times one can write[3]

$$\tau_A=a_A(k_0T)^{-3/2}x^{-1/2}, \tag{4}$$

$$\tau_I=a_I(k_0T)^{3/2}x^{3/2}, \tag{5}$$

where $a_A=(9\pi/4\sqrt{2})(\overline{M}v_0\hbar^4/\Omega_0C^2m^{*3/2})$, $a_I=(\sqrt{2m^*}\varepsilon_0^2/\pi e^4n_I\Phi(\eta))$, v_0 is the longitudinal sound velocity ($\sim10^3$ m/s), $\overline{M}=2M_{\mathrm{Sm}}M_{\mathrm{S}}/(M_{\mathrm{Sm}}+M_{\mathrm{S}})$ is the average atomic mass characterizing acoustic vibrations ($M_{\mathrm{Sm}}=150.4$, $M_{\mathrm{S}}=32.06$, $\overline{M}\equiv53$ a.u.), m^* is the effective conduction-electron mass in SmS ($0.78\,m_0$), ε_0 is the static dielectric constant ($\varepsilon_0=18$ for SmS, Ref. 5), C is a constant which has the dimension of energy and characterizes the strength of electron coupling with lattice vibrations ($C\approx\hbar^2/(2ma^2)\approx5$ eV), n_1 is the concentration of charged defects, Ω_0 is the unit cell volume, $\Phi(\eta)=\ln(1+\eta)-\eta/(1+\eta)$ is a slowly varying function of the argument $\eta=8m^*\varepsilon/(\hbar^2q^2)$. Here $1/q=r_0=[4\sqrt{2}e^2m^{*3/2}(k_0T)^{1/2}/(\varepsilon_0\hbar^3)F'_{1/2}(\mu)]$ is the localization length of the solution to the Poisson equation $\nabla^2\varphi=(4\pi e/\varepsilon_0)(n-n')$ for the potential of the electric field generated by a point positive charge of a $+e$ ion placed at the origin and a negative excess-electron charge $-e(n'-n)$. This solution is spherically symmetric, satisfies the condition $\lim_{r\to0}(\varphi)=e/(\varepsilon_0r)$ and has the form $\varphi=(e/\varepsilon_0r)e^{-qr}$. As r_0 decreases, the screening of the scattering potential increases. For $T=$ const, r_0 decreases with increasing n.

Substituting (3)–(5) in Eq. (2) yields

$$u=\frac{3\sqrt{\pi}u_A}{4F_{3/2}}I_\lambda, \tag{6}$$

where $I_\lambda=\int_0^\infty(-\partial f_0/\partial x)(x^3/x^2+\lambda)\,dx$, $\lambda=6u_A/u_I$ is a quantity characterizing the ratio of carrier scattering intensities from acoustic phonons and charged defects, $\tau_A=(3\sqrt{\pi}/4)(m^*/e)u_Ax^{-1/2}$, and $\tau_I=(\sqrt{\pi}/8)(m^*/e)u_Ix^{3/2}$.

Using Eq. (6), as well as the Fermi integrals $F_n(\mu)=\int_0^\infty(-\partial f_0/\partial x)x^n dx$, $f_0(x,\mu)=[1+\exp(x-\mu)]^{-1}$ and their properties, the expression for the mobility-related contribution to the piezoresistance constant can be recast

$$\pi_u=-\frac{d\ln(u)}{dP}=-\frac{\partial\ln(u)}{\partial\mu}\frac{\partial\mu}{\partial P}=\left(-\frac{\partial I_\lambda}{\partial\mu}+\frac{3}{2}\frac{F_{1/2}}{F_{3/2}}\right)\frac{\partial\mu}{\partial P}. \tag{7}$$

Equation (7) was used to calculate numerically the dependence of π_u on n for $T=300$ K (Fig. 1), with no simplifications made to facilitate the computing. The quantity $\partial\mu/\partial P$ was determined, as in Ref. 1, from the relation derived by differentiation of the charge neutrality condition with respect to pressure. The number of charged defects was taken equal to that of the donor impurities at a depth of 0.0035 eV, which are completely ionized at $T=300$ K, $n_I\sim10^{20}$ cm^{-3} (Ref. 1). The experimental points *1–8* in Fig. 1 were taken from a study[2] of the dependences of the electrical resistivity and

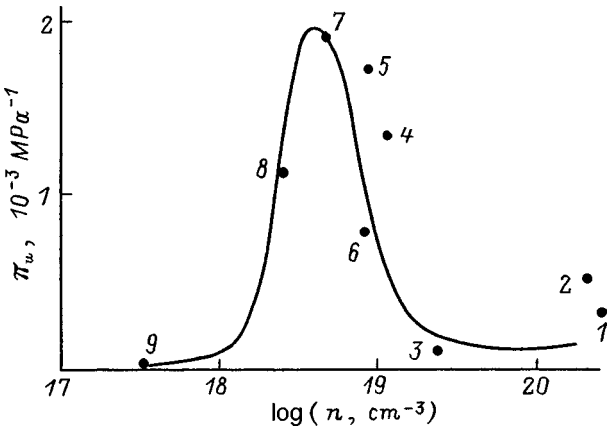

FIG. 1. Dependence of the mobility-related contribution to the hydrostatic piezoresistance coefficient on carrier concentration in SmS and SmS-based solid solutions: *1*—SmS–GdS, $n=2.56\times10^{20}$ cm^{-3}, *2*—SmS–GdS, $n=2.32\times10^{20}$ cm^{-3}, *3*—SmS, $n=2.6\times10^{19}$ cm^{-3}, *4*—SmS, $n=1.2\times10^{19}$ cm^{-3}, *5*—SmS, $n=0.95\times10^{19}$ cm^{-3}, *6*—SmS–EuS, $n=8.6\times10^{18}$ cm^{-3}, *7*—SmS–SmTe, $n=5\times10^{18}$ cm^{-3}, *8*—SmS–EuS, $n=2.75\times10^{18}$ cm^{-3}, *9*— SmS–SmSe, $n=3.5\times10^{17}$ cm^{-3}.

Hall coefficient on hydrostatic pressure, using the relation $\pi_u=\pi-\pi_n$. One observes a satisfactory agreement with the calculated curve. As n decreases, the calculated curve predicts a decrease of the mobility-related contribution to the piezoresistance coefficient. To test the validity of this prediction, we performed measurements similar to those of Ref. 2 on a sample of a SmS-based solid solution with a lower carrier concentration, $SmS_{0.75}Se_{0.25}$ with $n=3.5\times10^{17}$ cm^{-3} (point 9 in Fig. 1). The good fit of point 9, as well as of point 8 which fell out earlier from the general pattern,[2] on the calculated curve supports the correctness of the calculation.

As seen from Fig. 1, the mobility-related contribution is significant within the range $n=10^{18}-2\times10^{19}$ cm^{-3}. Besides, for $n<5\times10^{18}$ cm^{-3} the behavior of π_u is opposite to that described in Ref. 2, namely, the lower the carrier concentration in a sample, the smaller is the relative change of carrier mobility under pressure. This is so because the two competing mechanisms of scattering become dominant at different concentrations, namely, scattering by acoustic phonons predominates for $n>2\times10^{19}$ cm^{-3}, and that by charged defects, for $n<10^{18}$ cm^{-3}. Within this concentration range, pressure results not only in an increase of the concentration of conduction electrons but in an increase of their mobility as well through a stronger screening of charged defects. For $n>2\times10^{19}$ cm^{-3}, this process comes to an end, with the defects becoming screened completely by the conduction electrons.

The above analysis permits one to estimate the maximum hydrostatic piezoresistance coefficient which can be reached in SmS-based materials. Because in materials with a practically zero mobility contribution $\pi\approx\pi_n\leqslant5\times10^{-3}$ MPa^{-1} (for instance, in $SmS_{0.75}Se_{0.25}$, $\pi=5.0\times10^{-3}$ MPa^{-1}), and the maximum in the $\pi_u(n)$ curve does not exceed 2×10^{-3} MPa^{-1}, one may expect that the magnitude of π in SmS-based compounds at $T=300$ K cannot exceed 7×10^{-3} MPa^{-1}.

[1] L. N. Vasil'ev and V. V. Kaminskiĭ, Fiz. Tverd. Tela (St. Petersburg) **36**, 1172 (1994) [Phys. Solid State **36**, 640 (1994)].
[2] V. V. Kaminskiĭ, N. N. Stepanov, L. N. Vasil'ev, Yu. N. Kharchenko, and I. A. Smirnov, Fiz. Tverd. Tela (Leningrad) **27**, 77 (1985) [Sov. Phys. Solid State **27**, 44 (1985)].
[3] A. I. Ansel'm, *Introduction to the Theory of Semiconductors* (Nauka, Moscow, 1978).
[4] A. V. Golubkov, E. V. Goncharova, V. A. Kapustin, M. V. Romanova, and I. A. Smirnov, Fiz. Tverd. Tela (Leningrad) **22**, 3561 (1980) [Sov. Phys. Solid State **22**, 2086 (1980)].
[5] V. Železný, J. Petzelt, V. V. Kaminski, M. V. Romanova, and A. V. Golubkov, Solid State Commun. **72**, 43 (1989).

Translated by G. Skrebtsov

Acousto-optical effect in the luminescence excitation spectrum of HgI_2

B. K. Kardashev

A. F. Ioffe Physicotechnical Institute, Russian Academy of Sciences, 194021 St. Petersburg, Russia

V. A. Stepanov, P. A. Stepanov, and V. M. Chernov

Institute of Physics and Power Engineering, 249020 Obninsk, Kaluga District, Russia
(Submitted March 30, 1999)
Fiz. Tverd. Tela (St. Petersburg) **41**, 1965–1968 (November 1999)

A study of the photoluminescence excitation spectrum in a crystal of mercury diiodide is reported. Each of the two luminescence bands peaking at 543 and 572–575 nm investigated was found to have its own excitation spectrum. The excitation spectrum of the 575-nm line in the long-wavelength doublet band has been observed to be sensitive to strong ultrasound vibrations and preliminary irradiation of the sample by 590-nm light. This line is associated with radiative recombination of photocarriers at intrinsic point defects (vacancies or iodine and mercury interstitials) located close to dislocations. The binding energy of the photosensitive center to a dislocation was estimated from the change in the excitation spectrum. © *1999 American Institute of Physics.* [S1063-7834(99)01111-9]

The wide utilization of the HgI_2 crystal as a sensor in room-temperature detectors of ionizing (x-ray and gamma) radiation is limited to a considerable extent by the presence of various defects. As follows from available data (see reviews in Refs. 1 and 2), structural defects in mercury diiodide remain inadequately studied. This relates specifically to dislocations and to the role they play in the formation of free-carrier traps. There is experimental evidence (see, e.g., Refs. 3 and 4) for interaction of photoinduced carriers (electrons and holes) with mobile dislocations. The photoacoustic effect discovered[5,6] recently in HgI_2 shows that aged dislocations can also act as traps for photocarriers. Development of a model for the photoacoustic effect permitted first prediction, and afterwards, experimental demonstration of an acousto-optical effect in the luminescence spectrum of a HgI_2 crystal.[7]

It was found that the photoluminescence band located in the $\lambda = 565-575$-nm region consists of two distinct lines at room temperature, at 572 and 575 nm (Fig. 1). The long-wavelength part of the band exhibits a higher (compared to the short-wavelength one) sensitivity to high-intensity ultrasound. Besides the ultrasound, the 575-nm line was found also to be very sensitive to preliminary irradiation of a crystal by orange light with a wavelength of about 590 nm, at which one observes a maximum in photoconductivity[1,8] and the strongest photoacoustic effect.[5,6,9] It was conjectured[7] that the 575-nm line is due to radiative recombination of a photoelectron with a hole at intrinsic HgI_2 point defects localized near dislocations.

The acousto-optic effect observed was not very strong; indeed, a large-amplitude ultrasound reduced the intensity of the 575-nm line by about 20–25%, and that of the 572-nm line, by 10–13% only, while the intensity of the short-wavelength band peaking at close to 543 nm was not affected by ultrasonic treatment of the sample at all.

It was found[7] that each photoluminescence band of HgI_2 possesses its own excitation spectrum, which can vary depending on external conditions and sample prehistory. This publication deals primarily with an experimental investigation of excitation spectra. The main objective of the work consisted in a comprehensive study of the behavior of the excitation spectrum of the 575-nm line, which, as pointed out in Ref. 7, is produced by dislocations present in the crystal.

This work is a continuation of the studies started in Ref. 7; it is connected with an investigation of the effect of intensive ultrasound on photoluminescence spectra and deals essentially with a further development of the acousto-optic technique for probing the defect structure in HgI_2 crystals.

1. TECHNIQUE

The present study was carried out, similarly to Refs. 5–7,9, on a mercury diiodide crystal grown by static sublimation from a vapor phase. The samples measured about $10\times4\times1$ mm^3. The broad side of the plate coincided with the (001) crystallographic plane.

The sample was pasted on one of the faces of a piezoelectric oscillator in the central part of a 27-mm long quartz rod, where the vibrational mechanical stresses generated by a standing ultrasonic wave reach a maximum. The resonance ultrasonic longitudinal vibrations of the sample-quartz acoustic system were excited at close to 100 kHz. The strain amplitude could be varied within a broad range from 10^{-7} to 10^{-4}, thus permitting investigation of the behavior of optical characteristics in a strong ultrasonic field, where internal friction (ultrasound damping) became amplitude dependent. During the optical measurements (the time required to take a spectrum was about 10 min) the vibration amplitude was maintained constant automatically, as this was done in Ref. 7. All the measurements were performed in air at room temperature and atmospheric pressure.

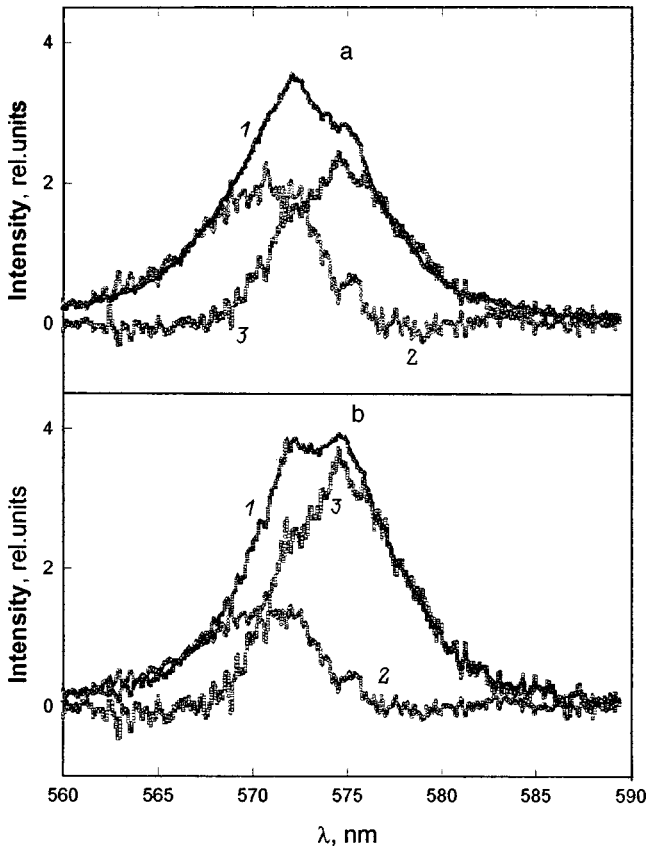

FIG. 1. (*1*) Photoluminescence doublet band of a HgI_2 crystal and its deconvolution into a (*2*) short-wavelength and (*3*) a long-wavelength component. (a) spectrum measured before illumination, and (b) after illumination at 590 nm.

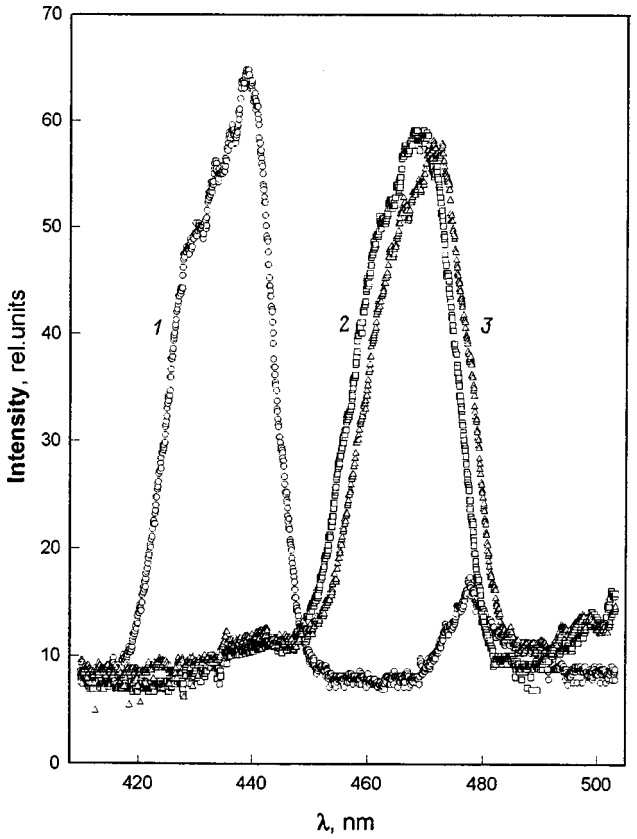

FIG. 2. Excitation spectra of HgI_2 luminescence at (*1*) 543 nm, (*2*) 572 nm, and (*3*) 575 nm.

The excitation spectra were obtained using a DRSh-250-2 high-pressure mercury lamp. The wavelength of the lamp light incident on the (001) sample face was varied by means of an MDR-4 monochromator. The luminescence intensity at the chosen wavelengths, for instance, at the wavelengths corresponding to the maxima at 543, 572, or 575 nm, or those slightly differing from them, was measured with an MDR-23 spectrometer.

Figure 1 presents the doublet band from a photoluminescence spectrum[7] of HgI_2 and its deconvolution into two components, a short-wavelength one, with the maximum at 572 nm, and a long-wavelength one, peaking at 575 nm, made by the Alentsev method[10]. It was taken into account that the intensity ratio of the two lines was affected by intensive ultrasound or preliminary illumination,[7] as already mentioned. As follows from Fig. 1, the excitation spectrum of the 577-nm luminescence can yield information on the characteristics of the long-wavelength component of this band, because the contribution of the short-wavelength, 572-nm peak at this wavelength is negligible.

2. RESULTS OF MEASUREMENTS

We are presenting here data on the excitation spectrum of HgI_2 luminescence at 543, 572, 575, and 577 nm, which were obtained on one of the samples studied.

Figure 2 presents excitation spectra of the luminescence at the wavelengths of 543, 572, and 575 nm. One readily sees that the spectrum at 543 nm differs substantially from those for the two other wavelengths. It was found (Fig. 2) that one cannot observe a sufficiently bright luminescence at 572–575 nm if the incident wavelength is either shorter than 450 nm or longer than 490 nm. As seen from the figure, the spectra for the 572- and 575-nm wavelengths are similar while being displaced by about 3 nm with respect to one another.

The excitation spectra at 577 nm, the wavelength which, according to Fig. 1, is associated with the luminescence only of the long-wavelength peak in the doublet band, could differ noticeably from one another when obtained from different regions of the same crystal (the spot illuminated by incident light was about 1 mm^2 in area). This is seen clearly from Fig. 3. It may be conjectured that nonuniform defect distribution affects considerably the 577-nm luminescence intensity when excited by light with different wavelengths.

The most interesting results of the behavior of the 577-nm luminescence are displayed in Fig. 4. Spectrum *1* in this figure was measured after preliminary illumination of the sample at 590 nm. The spectrum exhibits two clearly pronounced peaks at 454 and 493 nm. An excitation spectrum was obtained after a strong ultrasonic loading for 18 min. As seen from the figure, ultrasonic loading produced substantial changes in the long-wavelength part of the spectrum, which is evident from a comparison of spectra *1* and *2*. The maximum observed earlier at 493 nm shifted toward longer wavelengths by about 12 nm. Note that the short-

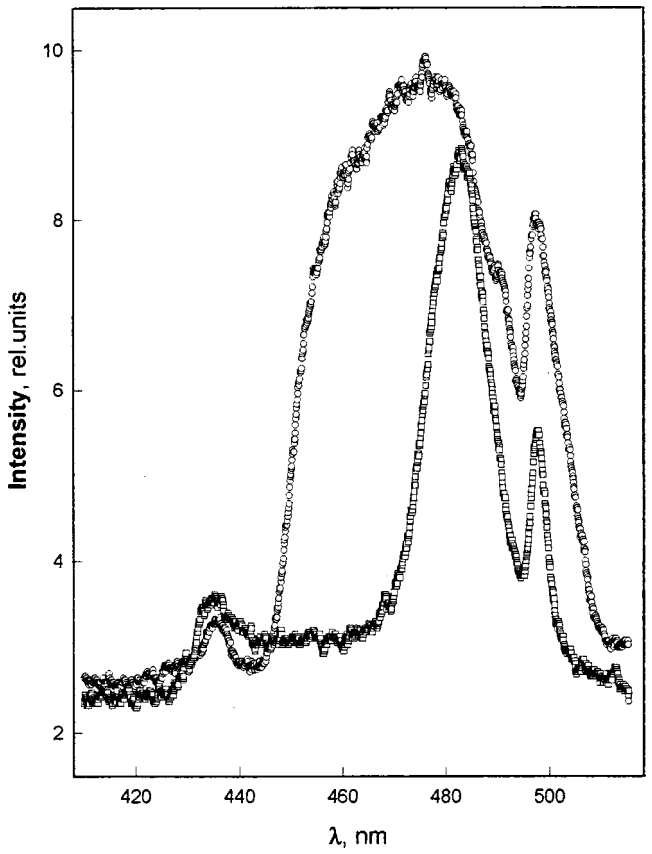

FIG. 3. Excitation spectra of HgI_2 577-nm luminescence obtained in various regions of the crystal.

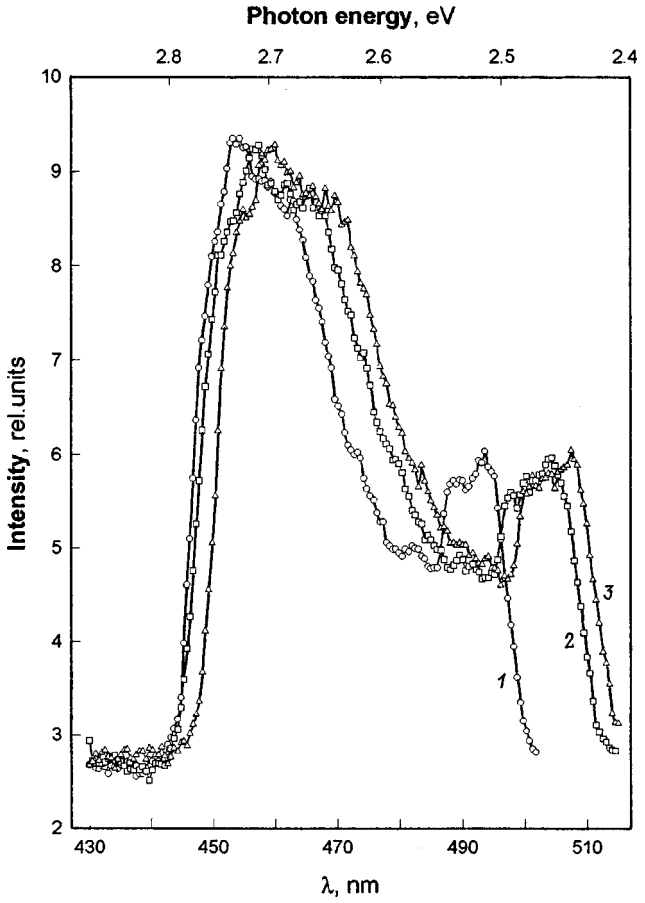

FIG. 4. Excitation spectra of HgI_2 577-nm luminescence: *1*—after sample illumination with 590-nm orange light; *2,3*—after acoustic loading with an amplitude of 1.0×10^{-5} for 18 and 31 min, respectively.

wavelength part of the spectrum shifted by not more than 3 nm. Subsequent changes induced by acoustic loading reduced to a slight longward shift of spectrum *3*.

3. DISCUSSION

Besides the luminescence spectra themselves, excitation spectra of photoluminescence can also yield information on the properties of luminescent centers. The noticeable difference in the excitation spectra of the band at 543 nm, on the one hand, and of those at 572 and 575 nm, on the other (Fig. 2), implies different nature of the luminescence centers responsible for these bands. At the same time, the small difference between the spectra for 572 and 575 nm suggests that the main properties of the centers producing luminescence at these wavelengths should differ very little from one another. A comprehensive analysis and comparison with available literature data made in Ref. 7 showed that the 543-nm band measured at room temperature is related to the low-temperature bands observed in the region of 530 nm (4.2 K) or 535 nm (77 K), and originates from exciton radiative recombination. The band at 572–575 nm (560 nm at 4.2 K and 563 nm at 77 K) is associated with radiation connected to intrinsic lattice defects, i.e., either vacancies or iodine or mercury interstitials.[2,11] The higher sensitivity of the 575-nm line in the doublet band to ultrasound and light was assigned (by a comparison of the acousto- and photo-optic with the photoacoustic effect[7]) to the same stoichiometric point defects but localized near dislocations. Our present study of the effect of intensive ultrasound on the luminescence excitation spectrum (Fig. 4) supports this assignment and makes it more revealing. It was found that one can also obtain additional information on the characteristics of the luminescence centers.

As seen from Fig. 4, the variation of luminescence intensity induced by ultrasound and preliminary illumination in the 572–575-nm band is a result of the excitation spectrum being deformed along the wavelength axis with practically no change in its intensity. This suggests that external action distorts the energy spectrum of the crystal, specifically of the levels responsible for nonradiative electron transition to a lower level corresponding to the photoelectron-hole radiative recombination.

Interestingly, the sign of the acousto-optic and photoacoustic effects observed in Ref. 7 can change, in accordance with Fig. 4, from positive (growth of the luminescence intensity) to negative, down to complete disappearance of the luminescence at a given wavelength, depending on the exciting wavelength.

In view of the fact that light (at 590 nm) creates (or strengthens) dislocation pinning centers, while intensive ultrasound destroys them, the change in position of the characteristic points in the excitation spectra presented in Fig. 4 reflects the binding energy of a dislocation to the pinning center or its increase. The properties of this center change

when it captures photocarriers.[5–7,9] The dislocation binding energy to a photosensitive center varies from 0.03 eV (a shift of the short-wavelength part of the excitation spectrum) to 0.1 eV (a shift of its long-wavelength part).

Thus we have proposed a new approach to studying dislocations in the HgI_2 crystal. The acousto-optic technique described here permits one not only to monitor qualitatively the evolution of a defect structure but also to estimate quantitatively the changes in the energy spectrum of the crystal defect subsystem under the action of external factors.

The authors are indebted to V. M. Zaletin for providing the crystals used in this work.

[1] X. J. Bao, T. E. Schlesinger, and R. B. James, Semicond. Semimet. **43**, 111 (1995).
[2] X. J. Bao, T. E. Schlesinger, and R. B. James, Semicond. Semimet. **43**, 168 (1995).
[3] J. Marshall and F. Milstein, Mater. Res. Soc. Symp. Proc. **261**, 131 (1992).
[4] J. Marshall and F. Milstein, Appl. Phys. Lett. **62**, 2784 (1993).
[5] B. K. Kardashev, S. N. Golyandin, S. B. Kustov, and V. M. Zaletin, Fiz. Tverd. Tela (Leningrad) **34**, 2148 (1992) [Sov. Phys. Solid State **34**, 1149 (1992)].
[6] B. K. Kardashev, J. Alloys Compd. **211/212**, 160 (1994).
[7] B. K. Kardashev, A. V. Rezvushkin, P. A. Stepanov, V. M. Chernov, and V. M. Zaletin, Fiz. Tverd. Tela (St. Petersburg) **38**, 1511 (1996) [Phys. Solid State **38**, 832 (1996)].
[8] P. Suryanarayana and H. N. Acharya, J. Electron. Mat. **18**, 481 (1989).
[9] B. K. Kardashev, J. Phys. IV **4**, C8-871 (1996).
[10] M. V. Fock, Trudy FIAN **59**, 3 (1972).
[11] N. N. Ovsyuk, Fiz. Tverd. Tela (Leningrad) **33**, 3436 (1991) [Sov. Phys. Solid State **33**, 1939 (1991)].

Translated by G. Skrebtsov

Electron density redistribution in Sn-doped Bi_2Te_3

I. V. Gasenkova

Institute of Electronics, Academy of Sciences of Belarus, Minsk

M. K. Zhitinskaya and S. A. Nemov

St. Petersburg State Technical University, 195251 St. Petersburg, Russia

T. E. Svechnikova

A. A. Baĭkov Institute of Metallurgy, Russian Academy of Sciences, Moscow, Russia

(Submitted December 22, 1998; resubmitted April 22, 1999)
Fiz. Tverd. Tela (St. Petersburg) **41**, 1969–1972 (November 1999)

X-ray photoelectron spectroscopy is used to investigate the redistribution of the density of electronic states in the valence band, and of the binding energies and chemical shifts of core levels in bismuth telluride caused by introduction of impurity tin atoms. A substantial increase in the density of electronic states below the valence-band top at energies $\mu \approx 15-30$ meV has been revealed. This feature in the energy spectrum accounts for the unusual behavior of the kinetic coefficients in p-Bi_2Te_3:Sn crystals. © *1999 American Institute of Physics.* [S1063-7834(99)01211-3]

Sn-doped bismuth telluride exhibits a number of features in its electrophysical properties.[1–4] Most remarkable is the falling temperature dependence of the Hall coefficient (for p-Bi_2Te_3 this is not typical), a plateau in the magnetic-field dependences in the Hall coefficient (a rarely observed effect), and a decrease of the Hall and Nernst mobilities, as well as anomalies in the temperature dependence of the Seebeck coefficient.

It is known that native lattice defects in bismuth telluride are electrically active and that the carrier concentration can differ markedly among samples of the same composition but prepared by different techniques. Therefore observation of these features depends on the actual technology used to fabricate a crystal and on relative amounts of the Sn dopant atoms and intrinsic defects.

These features find explanation in terms of a model of impurity resonance states located below the valence-band top. The depth of these states is $\varepsilon_i \approx 15-30$ meV on the hole-energy scale. This motivates an interest in studying the density of valence states and the energy distribution of the bismuth and tellurium core states in the above materials.

This paper presents the results of an investigation of the electron density redistribution in the valence band of bismuth telluride induced by doping it with Sn. The density of electron states was determined by x-ray photoelectron spectroscopy (XPS). The spectrum obtained is compared to the results of an integrated study of the kinetic coefficients, including the transverse Nernst–Ettingshausen effect.

1. XPS EXPERIMENT

The study was carried out on single-crystal samples of bismuth telluride grown by the Czochralski floating-crucible method.[5] Both stoichiometric and tin-doped samples were studied. The sample composition was represented in the form $Bi_{2-x}Sn_xTe_3$, where $x=0$; 0.01 ($x=0.01$ in Bi_2Te_3 corresponds to an atomic concentration of 6×10^{19} cm^{-3}).

The unit-cell parameters of the above compounds were determined by powder x-ray diffraction from a system of equations for the (01.26) and (30.15) planes using the standard relation for hexagonal symmetry

$$1/d^2 = 4/3(h^2+hk+k^2)/a^2 + l^2/c^2,$$

where d is the interplanar distance; h,k,l are the plane indices; and a,c are the lattice parameters. The exact position of the diffraction peaks was found by the Kukol method applicable to diffuse lines. The parameters obtained by this procedure for Bi_2Te_3 are $a=4.379$ Å, $c=30.467$ Å, and for Bi_2Te_3:Sn, $a=4.381$ Å and $c=30.490$ Å.

The XPS spectra of the valence and core states were obtained on an ÉS2401 electron spectrometer with Mg K radiation ($h\nu=1253.6$ eV). The core-level binding energies of bismuth, tellurium, and tin are given relative to the carbon $1s$ line at 284.6 eV.

2. EXPERIMENTAL XPS DATA AND THEIR DISCUSSION

Figure 1 displays XPS valence-band spectra of the compounds under study. As follows from their comparison, the density-of-states curves are, on the whole, similar in shape, although the finer structure of the spectra exhibits substantial differences. Note that most of the peaks associated with the valence band of Bi_2Te_3-based compounds and reflecting the features in the joint density of electronic states coincide in position. Maximum IV at the valence-band bottom derives from the $5s$ states of chalcogen atoms and lies at 10.5–12.5 eV, and the subband width is about 2–2.5 eV. Maximum III in the 8.5–10.2 eV region, corresponding to the bismuth $6s$ states, practically merges with the above peak to form a band about 4 eV wide. The top of the Bi_2Te_3 valence band is

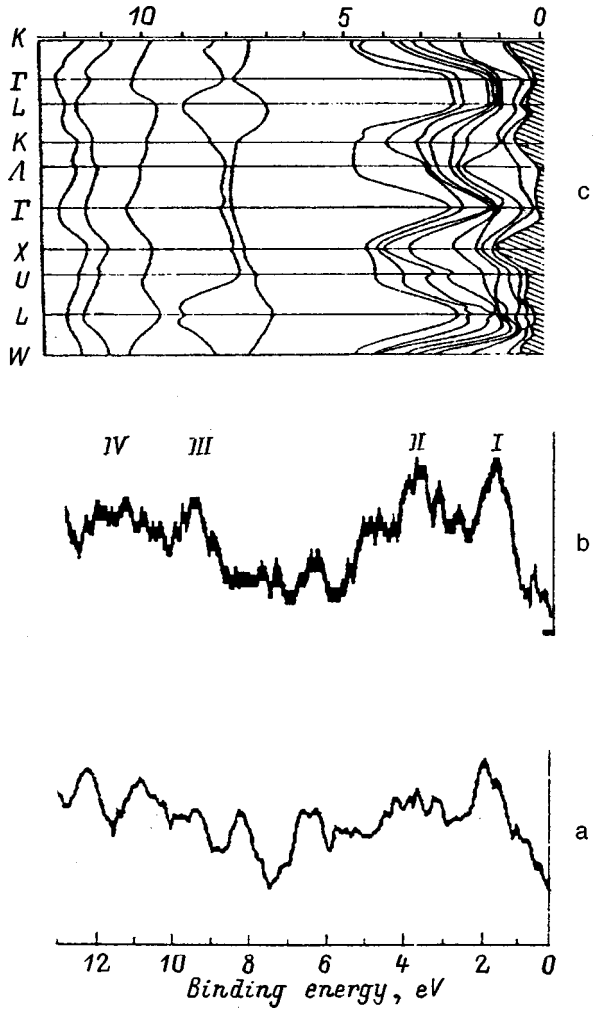

FIG. 1. Valence-band XPS spectra: (a) Bi_2Te_3, (b) Bi_2Te_3:Sn, (c) quasi-relativistic band structure of Bi_2Te_3 (Ref. 6).

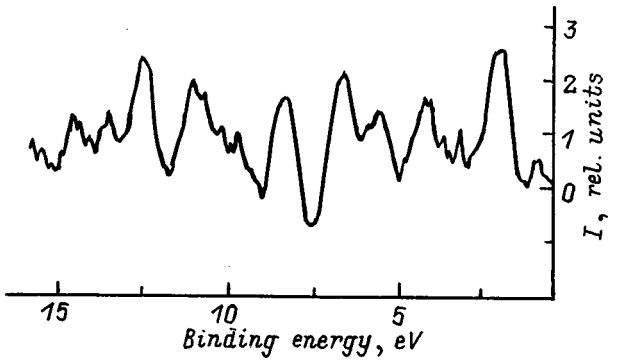

FIG. 2. Difference spectrum obtained by subtracting the spectrum of Bi_2Te_3 from that of Bi_2Te_3:Sn. Normalization against the Bi 6*s* maximum.

associated strongly with bismuth and tellurium *p* electrons. This subband is located at about 4.5 eV from the valence-band top and has a more localized maximum I at 1.5 eV, which derives predominantly from Bi $6p_{3/2}$ and Te $5p_{3/2}$, and a diffuse peak II with a maximum at 3.4 eV is due primarily to Bi $6p_{1/2}$ and Te $5p_{1/2}$. The general shape of the spectrum of undoped bismuth telluride agrees with the band structure parameters obtained by solving the Pauli equation by the pseudopotential method,[6] and the electron density-of-states distribution in the valence band is similar to what was observed in Ref. 7.

The main difference between the spectra of doped and undoped samples is observed at the valence-band top and in the central part of the spectrum. It manifests itself in different intensities of the peaks and in their shape. In the XPS spectra of tin-doped Bi_2Te_3 the more pronounced maximum II in the density of states is shifted slightly toward higher energies (by about 0.3 eV), with a shoulder appearing at $\sim$1.1 eV. One observes a tail in the density of states near the Fermi level. The relative intensities of the features in this part of the valence-band spectrum (peaks II and near $\sim$1.1 eV) are 0.49 and 0.62 for the undoped and tin-doped Bi_2Te_3, respectively. This implies a substantial increase in the density of states near the Fermi level in tin-doped samples. This is clearly seen from the difference spectrum obtained by subtracting the spectrum of Bi_2Te_3 from that of $Bi_{2-x}Sn_xTe_3$ and presented in Fig. 2. The redistribution of the density of states at the valence-band top is accompanied by changes in the density-of-states distribution in the 5–8-eV region. The broadening of the main maxima and the increased intensity of the spectrum are apparently due to the interaction of the tin 5*s* states in the valley between the maxima I, III with the bismuth and tellurium states (primarily to the superposition of the 5*s* wave functions of tin with the wave functions of tellurium and bismuth).

Besides the changes in the joint density of states, one should point out the presence of chemical shifts of the core levels induced by tin doping of bismuth telluride. Table I lists the binding energies of the core levels of bismuth, tellurium, and tin for doped and undoped samples. One readily sees a substantial change in the order of arrangement of the bismuth and tellurium core levels in $Bi_{2-x}Sn_xTe_3$, which manifests itself in a shift of Bi 4*f* toward higher energies (by 0.3 eV) and of Te 3*d* toward lower energies (by 0.2 eV). The energy separation between the Bi and Te peaks changes as one crosses over from Bi_2Te_3 to $Bi_{2-x}Sn_xTe_3$ (decreases by about 0.5 eV). In contrast to Ref. 8, we observed a chemical shift of the Te 3*d* level, which indicates the presence of two

TABLE I. Core-level binding energies for Bi_2Te_3 and $Bi_{2-x}Sn_xTe_3$ (eV).

Sample	Bi $4f_{5/2}$	Bi $4f_{7/2}$	Te $3d^*_{3/2}$	Te $3d^*_{3/2}$	ΔE_b, Te $3d_{5/2}$–C 1*s*	ΔE_b, Bi $4f_{7/2}$–C 1*s*	Sn $3d_{5/2}$
Bi_2Te_3	162.9	157.6	582.1	571.8	287.2	127.0	–
$Bi_{2-x}Sn_xTe_3$	163.2	157.9	581.9	571.6	287.0	126.7	486.5

Note: The Te 3*d* binding energies are given without taking into account line decomposition into components.

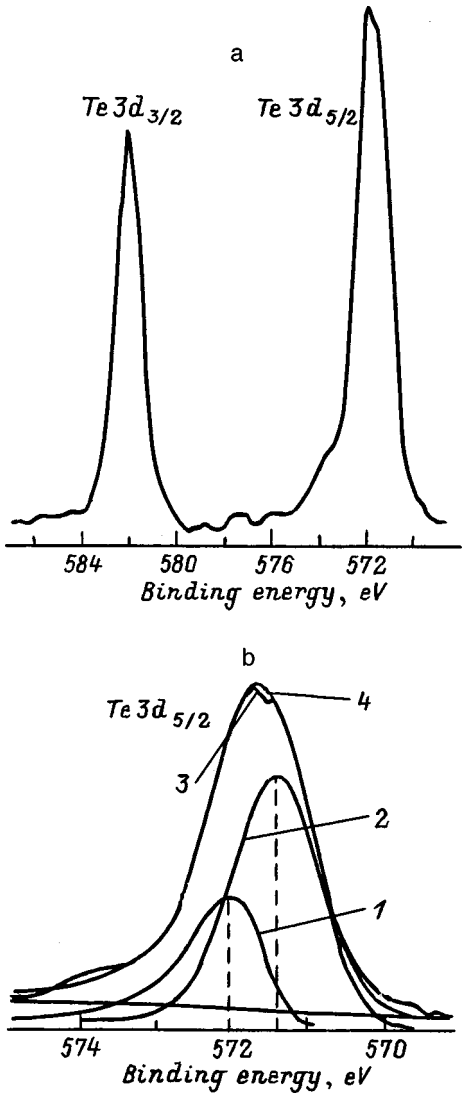

FIG. 3. (a) Te $3d$ core-level spectra of bismuth telluride, (b) unfolding the Te $3d_{5/2}$ spectrum into components: *1,2*—component peaks with E_b=571.43 and 572.01 eV, respectively; *3*—resultant experimental spectrum, *4*—resultant approximated spectrum.

types of chemical bonding. Decomposition of the spectrum by the maximum likelihood method[9] and by the fitting procedure (Fig. 3) yields 0.58 eV for the shift. The discrepancy between our results and the data of Ref. 8 on Te can be assigned to the difference in the quality (structural perfection, presence of impurities) of the crystals studied. Our crystals were grown by a unique technology developed at the IMET.[5] Besides, the cell parameter of the compound under study is somewhat smaller than the data quoted usually[10] for bismuth telluride. This may apparently result in some features in the spectrum due to increasing atomic interaction and wave-function overlap with decreasing distance between atoms. At the same time the Se $3d$ levels for two inequivalently located selenium atoms in Bi_2Se_3 were shown[7] to be shifted. The shift was found to be 0.7 eV for Se $3d_{5/2}$ and 0.8 eV for Se $3d_{3/2}$, which is close to the tellurium level shift in Bi_2Te_3 determined by us.

A comparison of the $3d_{5/2}$ binding energies of elementary tin [E_b=484.7 eV (for C $1s$, 284.6 eV, Ref. 11)] and tin in $Bi_{2-x}Sn_xTe_3$ yields $E=1.8$ eV for the chemical shift. We attempted to estimate the valence state of tin forming the chemical bond in this compound by comparing the binding energies for the compounds with di- and quadrivalent tin. The binding energy of Sn $3d_{5/2}$ in the ITO alloy (In_2O_3 + SnO_2),[12] where tin is quadrivalent, was found by us to be 486.7 eV, which is in a good agreement with the value for $Bi_{2-x}Sn_xTe_3$. The core-level binding energies quoted in the literature for SnO and SnO_2 are contradictory, which may be due, in our opinion, to possible reduction of Sn^{4+} in SnO_2 to Sn^{2+}. However Ref. 13 quotes 486.4 eV for the binding energy of Sn $3d_{5/2}$ in SnO_2 (this value is given relative to the binding energy of C $1s$ of 284.6 eV). The results obtained suggest the presence of quadrivalent tin in $Bi_{2-x}Sn_xTe_3$.

3. DETERMINATION OF THE DENSITY OF STATES $g(\varepsilon)$ FROM EXPERIMENTAL KINETIC COEFFICIENTS

The density of electronic states g at the Fermi level μ in a series of $Bi_{2-x}Sn_xTe_3$ samples with different tin contents, as well as in samples codoped with an electrically active iodine impurity to shift the chemical potential, was independently estimated by analyzing four kinetic coefficients.

As known from the theory of transport phenomena in semiconductors, in the case of degenerate carrier statistics one can write the following relation

$$S_{kk}-Q_{ikl}/R_{ikl}\sigma_{kk}=k_0/q\,\pi^2/3k_0Tg(\mu)/n\,, \qquad (1)$$

where S_{kk} and σ_{kk} are the components of the Seebeck coefficient and electrical conductivity tensors, respectively, and Q_{ikl} and R_{ikl} are the components of the transverse Nernst-Ettingshausen and Hall effect tensors, accordingly. Equation (1) was written under the assumption that the galvanomagnetic coefficients are measured with the current j flowing along the k axis, and the thermomagnetic effects, with the temperature gradient ∇T oriented along the k axis; index i denotes the direction of the Hall or Nernst–Ettingshausen emf measurement; the magnetic-field orientation is characterized by index l; q is the carrier charge taking into account the sign, so that for holes $q=+e$ (the absolute value of the electronic charge); k_0 is the Boltzmann constant; T is the temperature; $g(\mu)$ is the density of states at the Fermi level; and n is the carrier concentration.

Our calculations showed Eq. (1) to hold also in the case of intermediate degeneracy of the electron gas within both parabolic and nonparabolic (Kane type) approximations for the band spectrum of electrons (holes) in crystals.

The density of states was calculated from Eq. (1) using the experimental data of the kinetic coefficients obtained within the temperature range of 100 to 140 K, and the hole concentration was derived from the larger Hall tensor component (R_{321}) taking into account the Hall factor.

The results of the calculations for $Bi_{2-x}Sn_xTe_3$ made in this way are presented in Fig. 4 in a comparison with the data obtained for undoped Bi_2Te_3 crystals. As seen from the figure, the bismuth telluride crystals containing Sn exhibit a peak in the density of states within a narrow interval of Fermi energies, 15–30 meV (the energy is reckoned on the hole scale from the top of the main valence-band extremum).

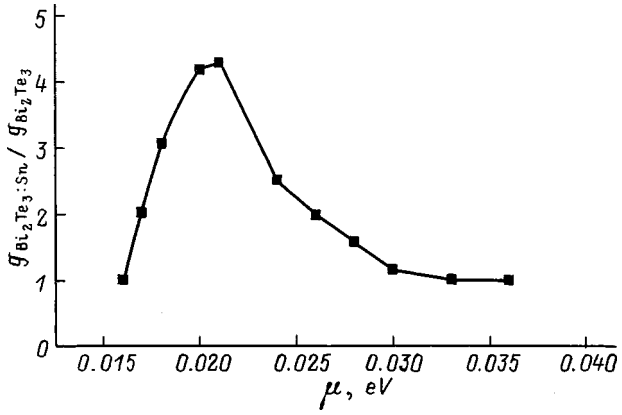

FIG. 4. Relative density of states $g_{Bi_2Te_3:Sn}/g_{Bi_2Te_3}$ as a function of Fermi level position.

Thus the data of the transport phenomena support the results obtained in the XPS study, which indicate a substantial redistribution of the electronic density of states and the appearance of a density-of-states peak within the valence band in Sn-doped Bi_2Te_3 crystals.

Thus our experimental study has established that tin impurity in bismuth telluride causes a radical rearrangement of the electron spectrum accompanied by the formation of a density-of-states peak within the valence band and by chemical shifts of the Bi $4f$ and Te $3d$ core levels of 0.3 and 0.2 eV, respectively.

[1] G. T. Alekseeva, P. P. Konstantinov, V. A, Kutasov, L. N. Luk'yanova, and Yu. I. Ravich, Fiz. Tverd. Tela (St. Petersburg) **38**, 2998 (1996) [Phys. Solid State **38**, 1639 (1996)].
[2] V. I. Kulbachinskii, M. Inoue, M. Sasaki, H. Negishi, W. X. Gao, K. Takase, Y. Giman, J. Horak, and P. Lostak, Phys. Rev. B **50**, 16921 (1994).
[3] M. K. Zhitinskaya, S. A. Nemov, T. G. Abaidulina, and T. E. Svechnikova, *Proceedings of the XIV International Conference on Thermoelectrics (ICT95)* (St. Petersburg, 1995), p. 56.
[4] M. K. Zhitinskaya, S. A. Nemov, and T. E. Svechnikova, Fiz. Tverd. Tela (St. Petersburg) **40**, 1428 (1998) [Phys. Solid State **40**, 1297 (1998)].
[5] T. E. Svechnikova, S. N. Chizhevskaya, and N. V. Polikarpova, Izv. Akad. Nauk SSSR, Neorg. Mater. **23**, 1128 (1987).
[6] E. V. Oleshko and V. N. Korolyshin, Fiz. Tverd. Tela (Leningrad) **27**, 2856 (1985) [Sov. Phys. Solid State **27**, 1723 (1985)].
[7] T. P. Debies and I. W. Rabalais, Chem. Phys. **20**, 277 (1977).
[8] M. R. Thuler, R. L. Beņbow, and Z. Hurych, Chem. Phys. **71**, 265 (1982).
[9] E. L. Kosarev, Rad. i Élektron. **35**, 68 (1990).
[10] S. N. Chizhevskaya, L. E. Shelimova, V. S. Zemskov, V. I. Kosyakov, and D. V. Malakhov, Izv. Akad. Nauk SSSR, Neorg. Mater. **30**, 3 (1994).
[11] *Practical Surface Analysis by Auger and X-Ray Photoelectron Spectroscopy*, edited by D. Briggs and M. P. Seach (Wiley, New York, 1983; Mir, Moscow, 1987).
[12] S. M. Sze, *Physics of Semiconductor Devices* (Wiley, New York, 1981; Mir, Moscow, 1987).
[13] A. W. C. Lin, N. R. Armstrong, and T. Kuwana, Anal. Chem. **49**, 1228 (1977).

Translated by G. Skrebtsov

Observation of a correlation between the dependences of the radiative decay time and intensity of the impurity core-valence luminescence on excitation energy in $K_{1-x}Cs_xCl$ and $Rb_{1-x}Cs_xCl$ mixed crystals

A. S. Voloshinovskiĭ, V. B. Mikhaĭlik, and G. B. Stryganyuk

L'vov State University, 290005 L'vov, Ukraine

P. A. Rodnyĭ

St. Petersburg State Technical University, 195251 St. Petersburg, Russia
(Submitted March 11, 1999)
Fiz. Tverd. Tela (St. Petersburg) **41**, 1973–1975 (November 1999)

A study of the spectral and kinetic parameters of impurity core-valence luminescence (CVL) excited by synchrotron radiation in $K_{1-x}Cs_xCl$ and $Rb_{1-x}Cs_xCl$ mixed crystals is reported. The dependences of the intensity and radiative decay time τ of impurity CVL on exciting photon energy $h\nu$ have been found to be correlated. It is concluded that the observed $\tau = f(h\nu)$ relation originates from nonradiative decay of core excitations near the surface, which govern also the excitation spectral features in this spectral region. © *1999 American Institute of Physics.* [S1063-7834(99)01311-8]

Starting with the very first experiments using synchrotron radiation,[1] which permitted assignment of the UV luminescence of a number of halogen compounds to radiative recombination of valence electrons with core holes, core-valence luminescence (CVL), this phenomenon has been attracting intense interest of researchers. Accumulation of new information adds to our understanding of its nature. This relates in full measure to such a CVL parameter as the radiative recombination time τ. The relative stability of this characteristic under variation of external factors pointed out in the early investigations and the independence of τ of the spectral region in which the luminescence is detected were assumed to indicate that the radiation belongs to CVL. A number of present studies, however, reveal a variation of the CVL radiative relaxation time. For instance, τ is currently known to depend on temperature. In some cases this is connected with competition between the radiative and Auger transitions (for example, in CsBr, $CsCaBr_3$, $CsSrBr_3$).[2,3] Sometimes this is associated with a change in the separation between the CVL-active cation and the nearest-neighbor anion environment, as is the case with the $RbCaF_3$ crystal at the phase transition.[4] One observed also a deviation of the CVL afterglow curves from exponential behavior[5,6] and its dependence on the excitation type[7] and energy.[8–10] It was shown[10] that the reason for such a behavior of the CVL kinetics lies in the surface losses caused by core-hole migration and dipole-dipole energy transfer to the crystal surface, where the excitations undergo nonradiative decay.

On the other hand, it is known that surface losses affect substantially the structure of luminescence excitation spectra in the absorption edge region,[11,12] which suggests the existence of a certain relation between the dependences of the CVL radiation intensity and radiative relaxation time on excitation energy. The latter point has motivated carrying out corresponding experimental studies aimed at a search for this relation. As subjects of the measurements were chosen $K_{1-x}Cs_xCl$ and $Rb_{1-x}Cs_xCl$ crystals, where one observes under high-energy excitation impurity CVL, i.e., radiative recombination of valence electrons with the holes created in the upper $5p$-core shell of the Cs impurity cation.[13,14] The choice of these subjects was governed by the main requirement that the methods of spectral and temporal selection would be capable of isolating a sufficiently strong signal due only to the impurity CVL against the background of other radiations.

The present report presents the results of measurements performed with synchrotron radiation on the SUPERLUMI setup at the HASYLAB Hamburg synchrotron laboratory. A detailed description of the characteristics of the setup, as well as of the specifics of spectral and kinetic measurements of impurity CVL, can be found in Refs. 15 and 14, respectively.

Figure 1 shows a family of impurity CVL afterglow curves obtained within the 4.5-eV emission band on a $Rb_{1-x}Cs_xCl$ crystal for different exciting photon energies $h\nu$, as well as the profile of the excitation pulse. A slight deviation from single-exponential quenching can be revealed by a thorough analysis only in the initial stage of the afterglow curves. Remarkably, the observed deviation is larger for higher exciting photon energies, which agrees with previous studies.[6,9,10] During $\sim$1.5 ns after the luminescence pulse maximum, the decay course is fitted fairly well by a single exponential within a luminescence intensity variation range of two orders of magnitude. For this reason the radiative decay time of the impurity CVL was found by a least-squares fitting of the experimental data to a single-exponential decay law. The relative error of the values of τ obtained in this way does not exceed 0.03 ns. The radiative decay times found for exciting photon energies of 15.1 and 15.3 eV, which correspond to the first peaks in the excitation

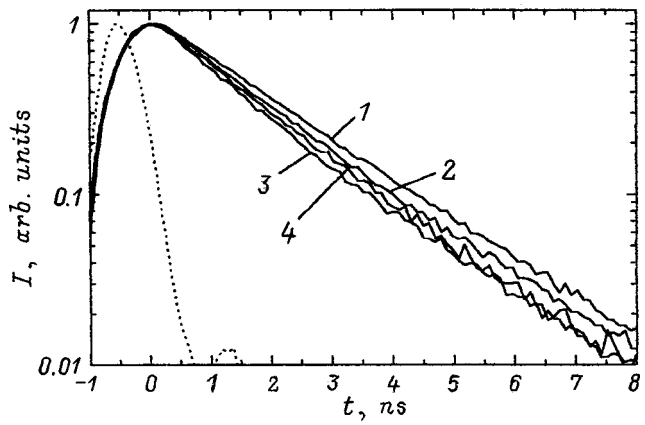

FIG. 1. Afterglow curves of the impurity CVL emission band peaking at 4.5 eV measured on a $Rb_{0.94}Cs_{0.06}Cl$ crystal excited by photons of different energies (eV): *1*—15.1, *2*—17.6, *3*—24.8, and *4*—29.5. $T=8$ K.

spectra of $Rb_{0.94}Cs_{0.06}Cl$ and $K_{0.70}Cs_{0.30}Cl$, are 2.60 and 2.46 ns, respectively.

Figure 1 exhibits a distinct difference between the afterglow curves obtained at different excitation energies. Therefore Fig. 2 shows an excitation spectrum of impurity CVL together with a $\tau=f(h\nu)$ relation. These characteristics are seen to be correlated, which is particularly evident in the region of formation of the $4p\mathrm{Rb}^+$ (16–20 eV) and $3p\mathrm{K}^+$ (19–24 eV) host cation excitons. In the energy region corresponding to excitation only of the $5p$ core states of the Cs impurity cation the change in the afterglow time is not so clearly pronounced.

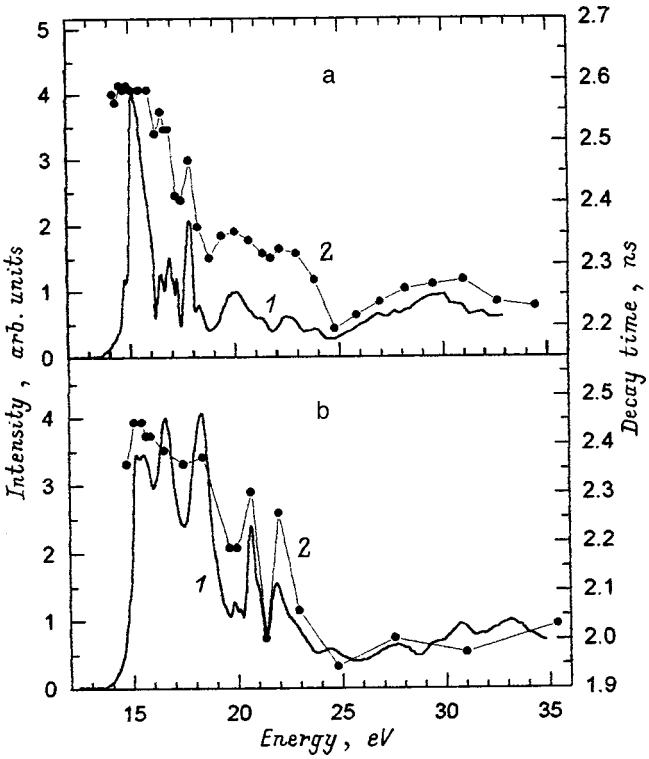

FIG. 2. Excitation spectra of impurity CVL (*1*) and dependences of radiative decay time on excitation energy obtained (*2*) on (a) $Rb_{0.94}Cs_{0.06}Cl$ and (b) $K_{0.70}Cs_{0.30}Cl$. $T=8$ K.

This effect is in full accord with the assumption of the existence of a relation between the excitation energy dependences of the luminescence intensity and radiative decay time. The reason for this is apparently the already mentioned surface losses appearing in the region of strong absorption, whose magnitude is proportional to the absorption coefficient. Indeed, the absorption coefficient in the region of host core-exciton states reaches as high as 10^6 cm^{-1}.[11,12] Hence VUV radiation penetrates only to a shallow depth (~ 10 nm), and it is here that the excited states are created. The decrease in the luminescence intensity is caused by quenching due to a high probability of multipole energy transfer and core-hole and/or exciton migration to surface states, where the concentration of defects is high, and which decay primarily nonradiatively. It should be pointed out that estimates of the core-exciton diffusion path length yield ~ 10 nm,[12] which is in a good agreement with the diffusive energy-transport model. This is also believed to be the main reason for the well-known effect of anticorrelation between the excitation spectra of luminescence, on the one hand, and of the absorption and, accordingly, reflectance spectra, on the other, which is usually observed in the region of core exciton states in crystals and luminophores.[11,12] The existence of this additional nonradiative relaxation channel results naturally in a decrease of the lifetime of excited states. Hence the observed dependence of the radiative decay time of impurity CVL on excitation energy originates from the same processes that govern the structure of its excitation spectrum.

These considerations lead one to a natural conclusion that the decrease of the absorption coefficient gives rise to an increase of the penetration depth of exciting radiation and to creation of elementary excitations at a larger distance from the crystal surface. As a result, the energy transfer processes become less efficient and, thus, nonradiative decay affects less the τ. This may account for the relatively small variation of the afterglow time with energy in the region of the $5p$ core states of the cesium impurity, where the crystal matrix absorption is substantially lower, and, accordingly, the impurity absorption proportional to the cesium concentration also remains comparatively weak.

The proposed interpretation of the observed correlation between the excitation energy dependences of the impurity CVL radiative decay intensity and time is considered as a basis for a more comprehensive theoretical analysis of the problem, whose results are planned to be published in a more general form.

The authors express their sincere gratitude to Prof. G. Zimmerer for support and interest in the work. One of the authors (V. B. M.) is indebted to Deutscher Akademischer Austauschdienst for financial support.

[1] Yu. M. Aleksandrov, V. N. Makhov, P. A. Rodnyĭ, T. I. Syreĭshchikova, and M. N. Yakimenko, Fiz. Tverd. Tela (Leningrad) **26**, 2865 (1984) [Sov. Phys. Solid State **26**, 1734 (1984)].
[2] T. Davoi, V. V. Mikhailin, S. Stizza, and A. N. Vasil'ev, J. Lumin. **51**, 275 (1992).
[3] A. S. Voloshinovskiĭ, V. B. Mikhaĭlik, P. A. Rodnyĭ, and S. N. Pidzyraĭlo, Fiz. Tverd. Tela (Leningrad) **34**, 681 (1992) [Sov. Phys. Solid State **34**, 366 (1992)].
[4] P. A. Rodnyĭ and A. S. Voloshinovskiĭ, Fiz. Tverd. Tela (Leningrad) **34**, 2543 (1992) [Sov. Phys. Solid State **34**, 1363 (1992)].

[5] I. A. Kamenskikh, M. A. MacDonald, I. H. Munro, V. V. Mikhailin, and M. A. Terekhin, Rev. Sci. Instrum. **63**, 1447 (1992).
[6] Y. Nunoya, J. Ruan, and S. Kubota, Nucl. Instrum. Methods Phys. Res. A **337**, 632 (1994).
[7] K. Kimura, J. Electron Spectrosc. Relat. Phenom. **79**, 43 (1996).
[8] S. Kubota, M. H. Macdonald, and I. H. Munro, J. Lumin. **48/49**, 589 (1991).
[9] A. N. Belskiy, I. A. Kamenskikh, V. V. Mikhailin, and A. N. Vasil'ev, J. Electron Spectrosc. Relat. Phenom. **9**, 111 (1996).
[10] M. A. Terekhin, A. N. Vasil'ev, M. Kamada, E. Nakamura, and S. Kubota, Phys. Rev. B **52**, 3117 (1995).
[11] M. Casalboni and U. M. Grassano, J. Phys. Chem. Solids **51**, 805 (1990).
[12] E. L. Benitez, D. E. Husk, S. E. Schnatterly, and C. Tarrio, J. Appl. Phys. **70**, 3256 (1991).
[13] A. S. Voloshinovskiĭ, A. G. Dmitriev, V. B. Mikhaĭlik, and P. A. Rodnyĭ, Fiz. Tverd. Tela (Leningrad) **34**, 1022 (1992) [Sov. Phys. Solid State **34**, 547 (1992)].
[14] A. S. Voloshinovskii, M. S. Mikhailik, V. B. Mikhailik, E. N. Mel'chakov, P. A. Rodnyi, C. W. E. van Eijk, and G. Zimmerer, J. Lumin. **79**, 107 (1998).
[15] G. Zimmerer, Nucl. Instrum. Methods Phys. Res. A **308**, 178 (1991).

Translated by G. Skrebtsov

Calculating the dipolon binding energy in alkaline earth metal oxides and the ground state energy of F_c^+ color centers (dipolon+electron) in MgO

G. A. Rozman

Pskov State Pedagogical Institute, 180760 Pskov, Russia
(Submitted April 5, 1999)
Fiz. Tverd. Tela (St. Petersburg) **41**, 1976–1978 (November 1999)

The binding energy of the simplest neutral crystal lattice defect, a dipolon consisting of neighboring unlike vacancies, is calculated for the alkaline earth metal oxides having an NaCl structure (MgO, CaO, SrO, BaO) using a method developed by the author. The calculated values are found to correlate with a number of physical properties of these crystals. The ground state energy of an MgO crystal with an F_c^+ color center (dipolon+electron) is calculated using two independent quantum-mechanical methods. The results of these calculations are essentially identical. © *1999 American Institute of Physics.* [S1063-7834(99)01411-2]

1. BINDING ENERGY OF DIPOLONS IN ALKALINE EARTH METAL OXIDES HAVING AN NaCl STRUCTURE

The alkaline earth metal oxides are widely used in scientific research and in technology. This is because of their high radiation resistance, mechanical durability, high melting temperature, and good transparency in the infrared and visible spectrum. In terms of their structure, they are divalent analogs of the alkali halide crystals. As opposed to the latter, however, the alkaline earth metal oxides have been little studied, either theoretically or experimentally.

It has been found[1] that in the alkaline earth metal oxides having an NaCl structure, Schottky-defect formation is energetically the most favorable. With effective electrical charges, the vacancies interact among themselves and form complexes, the simplest of which is a neutral pair– a dipolon. In alkali halide crystals, where dipolons have been studied in detail experimentally and theoretically,[2–4] the roles of these defects have been established in dielectric losses and internal friction, in electrical and diffusion processes, and in the kinetics of formation and interaction of color centers. A similar role may be assumed for dipolons in the alkaline earth metal oxides having an NaCl structure. It was noted above that these compounds have not been studied enough. In particular, the basic characteristic of the dipolons in alkaline earth metal oxides, namely their binding energy, has not been determined.

The author has developed a graphical-analytic method for determining this quantity.[5] It is based on an analysis of plots of the transcendental equation derived[6] for the concentration of all vacancies in ionic crystals (both isolated and associated in dipolons),

$$c = A \exp\left(-\frac{E-\gamma c}{2kT}\right), \tag{1}$$

where E is the energy of formation of two isolated vacancies with different signs, $\gamma = 2\alpha U \exp U/kT$, U is the dipolon binding energy, α is an orientational factor that determines the energetically equivalent positions of a dipolon in crystal, and T is the absolute temperature of the crystal. When there is no interaction among vacancies of different types, $U=0$, Eq. (1) transforms into the customary Schottky formula for the concentrations of isolated vacancies.

In the $c=c(T)$ curve of Eq. (1) there is a singular point corresponding to infinitely rapid growth of the concentration of all vacancies, $\partial c/\partial T = \infty$. Physically,[7] this process can be regarded as a melting process. Our hypothesis was developed in Ref. 8.

Equation (1) has been tabulated for each of the alkaline earth metal oxides using two approaches: for a specified defect formation energy[9] by varying U and the temperature T, values of which were chosen near the melting point of the crystal. $c=c(T)$ was plotted from the resulting tables and the temperature T_∞ at which $\partial c/\partial T = \infty$ was determined. Then, the desired dipolon binding energy U was found the graph of T_∞ as a function of U and from the experimentally determined melting point of the given crystal. Table I shows the results (second row), along with published values of the lattice constant and melting temperature,[10] which all correlate physically with one another.

2. CALCULATING THE ENERGY STATES OF AN F_c^+ CENTER IN ALKALINE EARTH METAL OXIDES BY THE MOLECULAR-ORBITAL METHOD (MO LCAO)

Since they have an electric moment, dipolons interact with other defects in the crystal lattice. In principle, various reactions leading to the formation of an F_c^+ center consisting of a dipolon that has captured an electron are possible:

$$\begin{aligned}
&\text{a)} \quad V^{+2}V^{-2} + e^{-1} \rightarrow F_c^+ ,\\
&\text{b)} \quad V^{+2}V^{-2} + e^{0} \rightarrow F_c^+ + e^{+1},\\
&\text{c)} \quad F + e^{0} \rightarrow F_c^+ + e^{+1} + Me^{+2},\\
&\text{d)} \quad F + V^{-2} \rightarrow F_c^+ , \text{ etc.},
\end{aligned} \tag{2}$$

where we have used the standard notation for doubly charged vacancies ($V^{\pm 2}$) and dipolons ($V^{+2}V^{-2}$), F color centers ($V^{+2}e^{-1}$), excitons (e^0), electrons (e^{-1}) and holes (e^{+1}), interstitial ions (Me^{+2}), and F_c^+ centers (dipolon+electron).

TABLE I. Binding energy of the dipolon (V), lattice constant (a), and melting temperature (T_{melt}) in the alkaline earth metal oxides.

Crystal	MgO	CaO	SrO	BaO
U, eV	2.197	1.818	1.420	1.238
a, Å	2.104	2.401	2.578	2.762
T_{melt}, K	3075	2860	2730	2126

The set of reactions (2) is indicative of a high formation probability of F_c^+ centers and confirms the importance of including this kind of center in the overall kinetics of color-center formation.

Without dwelling on the standard operations for applying the MO method,[11] we note only the features of an F_c^+ center: it has C_{4v} symmetry of order $g=8$. An analysis of the reduced representations shows that there are 5 energy states of an F_c^+ center, of which two belong to the one dimensional irreducible representation A_1, one to the one-dimensional irreducible representation B_1, and two to a doubly degenerate state corresponding to the second order irreducible representation E.

The energy of the various states of an F_c^+ center can be determined by solving a fifth-order secular equation in accordance with the usual scheme for solving quantum-mechanical problems of this kind.[11]

Based on the symmetry of the wave functions for the irreproducible representations,[13] we find that the representation A_1 corresponds to the lowest energy state of an F_c^+ center. For numerical estimates, we have chosen the atomic wave function whose radial part for $n=4$ and $l=0$ (a weakly bound state for our F_c^+ center) is given by[12]

$$R=(4a_0^{3/2})^{-1}\left(1-\frac{3}{2}\rho+\frac{1}{2}\rho^2-\frac{1}{24}\rho^3\right)\exp\left(-\frac{\rho}{2}\right), \qquad (3)$$

where $\rho=r/2a_0$ and a_0 is the radius of the first Bohr orbit, as a basis function.

A numerical calculation of the ground state energy gives

$$E_{A_1^{(1)}}\approx -2.52\ \text{eV} \qquad (4)$$

for the $A_1^{(1)}$ state of the F_c^+ center in MgO. The energy of the $A_1^{(2)}$ state is $E_{A_1^{(2)}}\approx -0.28\ \text{eV}$.

For the other states we obtain $E_{A_1^{(2)}}$ without overlap of the atomic orbitals. The author knows of only one publication of experimental data[14] where the F_c^+ center in crystalline MgO can be attributed to a band whose energy location is in satisfactory agreement with our value of the energy of the ground state of the F_c^+ center. The author became aware through a personal communication of yet another theoretical paper,[15] in which another method was used to determine the characteristics of the F_c^+ center that we have studied. There[15] $E=-2.42\ \text{eV}$, which is essentially the same as our calculated value of Eq. (4).

3. QUANTUM-MECHANICAL CALCULATION OF E_{MgO}

Although we have introduced two calculated values of the ground-state energy of F_c^+ centers in MgO crystals, it would not be useless to introduce yet another independent method for calculating this quantity.

Reaction (1a) is taken as a basis. The Hamiltonian of the system consists of the Hamiltonian for the electron (in a polaron state), which is supplemented by the potential energy of the interaction of the electron with the effective charges of the dipolon. The polarization energy of the crystal is not included in the Hamiltonian; the energy of the crystal's ground state without defects is taken as the origin for the energy. The interaction energies of the electron with acoustic and transverse optical vibrations are both neglected in the Hamiltonian because they are small.

As an estimating function we take the polaron wave function[16]

$$\Psi=A(1-\alpha r)\exp(-\alpha r); \quad \alpha=\frac{me^2}{2\hbar^2}\left(\frac{3}{\varepsilon}+c\right); \quad A=\frac{\alpha^{3/2}}{\sqrt{7\pi}}.$$

A numerical estimate of the ground state energy of an F_c^+ center in MgO gives

$$E_{F_c^+}\approx -2.33\ \text{eV}. \qquad (5)$$

This result is certainly an estimate in view of the simplifications that have been made. Given that a variational method always gives a numerical value that is smaller in absolute value, we may assume that this is yet another confirmation of the existence of F_c^+ color centers.

As noted above, little attention has been paid to F_c^+ centers, despite the fact that they are easily observed by their asymmetry. This means that they can be used along with optical and electrical techniques (studying the dielectric properties and polarization luminescence), as was pointed out by Frenkel'.[17]

[1] S. Vempoti Chitra and P.W.M. Jacobs, Cryst. Lattice Defects Amorphous Mater. **10**, 9 (1983).
[2] A. A. Vorob'ev, *Alkali Halide Crystals*, Books 1-4 (Izd-vo. Tomskogo Un-ta, Tomsk, 1968–1969).
[3] *Materials from the All-Union Conference on the Physics of Dielectrics and Prospects for its Development*, Vols. 1 and 2 (Leningrad, 1973).
[4] Trudy IF AN Estonii, Vols. 43–67, etc. (Tartu, 1975–1990).
[5] G. A. Rozman, Fiz. Tverd. Tela **19**, 1840 (1977) [Sov. Phys. Solid State **19**, 1075 (1977)].
[6] G. A. Rozman, Deposited in VINITI, No. 2325-76 (1976).
[7] Ya. I. Frenkel', *Introduction to the Theory of Metals* (OGIZ, Moscow–Leningrad, 1948).
[8] M. Ross, and J. Wolf, Phys. Rev. Lett. **57**, 214 (1986).
[9] V. N. Chebotin, *Physical Chemistry of Solids* (Khimiya, Moscow, 1982).
[10] *Tables of Physical Quantities*, edited by I. K. Kikoin (Atomizdat, Moscow, 1976).
[11] L. D. Landau and E. M. Lifshitz, *Quantum Mechanics* (Fizmatgiz, Moscow, 1963).
[12] D. I. Blokhintsev, *Elements of Quantum Mechanics* (Vyssh. Shkola, Moscow, 1961), p. 163.
[13] R. Knox and A. Gold, *Symmetry in the Solid State* (Nauka, Moscow, 1970).

[14] T. N. Kyarner, S. A. Dolgov, T. I. Savikhina, and B. T. Tazhigulov, Trudy IF AN Éstonii, No. 61, 139 (1987).
[15] K.C. To, A.M. Stoneham, and J. W. Henderson, Phys. Rev. **181**, 1237 (1969).
[16] S. I. Pekar, *Studies of the Electronic Theory of Crystals* (Fizmatgiz, Moscow, 1951).
[17] P. P. Feofilov, Izv. Akad. Nauk SSSR, Ser. Fiz. **31**, 788 (1967).

Translated by D. H. McNeill

Effect of lanthanides on the spectral-luminescence properties and photoresistance of organic dyes in silicate sol-gel films

G. E. Malashkevich

Institute of Molecular and Atomic Physics, Academy of Sciences of Belarus, 220072 Minsk, Belarus

V. B. Prokopenko, D. V. Dem'yanenko, and I. M. Mel'nichenko

Gomel State University 246699 Gomel, Belarus

(Submitted April 8, 1999)
Fiz. Tverd. Tela (St. Petersburg) **41**, 1979–1984 (November 1999)

A sol-gel method is used to synthesize silicate films dyed in the sol stage with rhodamine C or methylene blue and further doped with cerium or lanthanum. It is shown that this sort of doping leads to a reduction in the peak intensity and a change in the shape of the $S_1 \leftarrow S_0$ band of the dyes, as well as to a shift in this band in a direction that depends on the $H_2O : Si(OC_2H_5)_4$ ratio. At the same time, the photoresistance of the rhodamine C molecules increases. The observed spectral changes are explained by the formation of supramolecules that include organic molecules, rare earth ions, and elements from the structural grid of the film, while the enhanced photoresistance is explained mainly by strengthening of the $T_1 \rightarrow S_0$ transitions in the dye. © *1999 American Institute of Physics.* [S1063-7834(99)01511-7]

The possibility of obtaining sol-gel films doped with a high concentration of organic dyes and having acceptable wear resistance[1] has stimulated interest in these materials as potential light transformers and light filters. In both cases, additional doping of these films with rare-earth-ion compounds appears promising. These ions can interact chemically with the ionogenic groups of the organic dyes and serve as quenchants for their excited states. As a result, either the spectral-luminescence properties of the dyes can be changed or their photoresistance can be enhanced, since the photochemical decomposition reactions of the organic molecules take place in an excited state.[2,3] In this paper we attempt to explain these aspects using films dyed with rhodamine *C* (*RC*) or metheylene blue (*MB*), with further doping by lanthanum or cerium salts, as an example. The choice of these lanthanides means that we can exclude from consideration the comparatively well-studied resonant transfer of excitation to rare-earth ions from organic molecules[4] and reduce the effect on the latter of the charge carriers of both signs which develop during ultraviolet irradiation of the matrix because they are captured by cerium ions.[5]

1. EXPERIMENTAL MATERIALS AND TECHNIQUES

The process for producing the films included preparing sols by hydrolyzing tetraethyl orthosilicate in a water-alcohol solution in the presence of hydrochloric acid as a catalyst. The molar ratio $R = H_2O : Si(OC_2H_5)_4$ was varied from 2 to 10. Then the prepared sols were aged for one or two weeks and subsequently organic dyes and chlorine salts of the lanthanides were dissolved in them to the required concentration *C*. The doped (codoped) sol was then deposited on quartz and silicon substrates by centrifugation. The resulting films were annealed at 250 °C for 5 min.

The film thickness was monitored on a Talystep profilometer to within ±5%. Absorption spectra were recorded in the form of plots of the natural absorption coefficient *k* or the optical density *D* as functions of wavelength λ or wave number $\tilde{\nu}$ using Beckman-UV5270 and Perkin Elmer-180 spectrophotometers. Luminescence spectra were recorded using an SDL-2 spectrofluorometer, corrected by including the spectral sensitivity of the detection system, and presented in the form of plots of the number of luminescence photons per unit wavelength, $dn(\lambda)/d\lambda$, as a function of wavelength. The luminescence kinetics was studied using a PRA-3000 spectrofluorometer. All the measurements were done at $T = 298$ K.

2. RESULTS

Figure 1 shows absorption spectra of *RC*-, *RC*-$CeCl_3$-, and $CeCl_3$-containing films obtained for different *R* and $C(RC) = C(CeCl_3) = 2$ mass.%. Evidently, the spectrum of the *RC*-containing film with $R = 2$ has a broad band with a peak at 555 nm and a shoulder at 525 nm, as well as a series of less intense bands at $\lambda < 380$ nm (curve *1*). For the film with $R = 8$, the main band is broadened and its intensity is slightly higher (curve *2*). The spectrum of the *RC*-$CeCl_3$-containing film with $R = 2$ is characterized by a bathochromic shift of the main band and a significant drop in the integral absorption (curve *3*). The analogous film with $R = 8$, on the other hand, has a hypsochromic shift of the main band accompanied by significant broadening and a drop in the peak intensity (curve *4*). Increasing *R* to 10 causes further broadening of the main band in both films and a reduction in the hypsochromic shift with codoping. The most intense band for a $CeCl_3$-containing film with $R = 2$ lies below 200 nm and strongly overlapping bands at 260 and

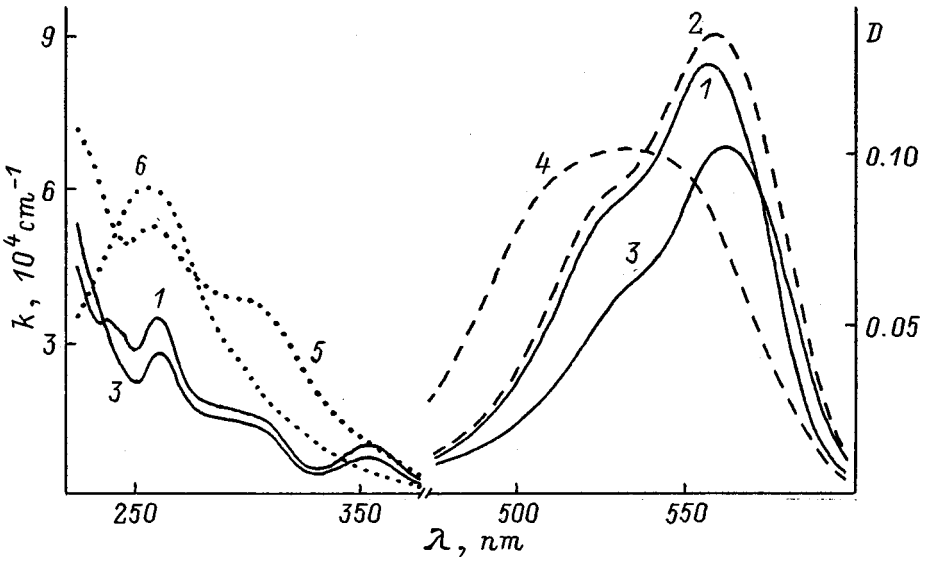

FIG. 1. Absorption spectra of *RC*-(*1, 2*), *RC*-$CeCl_3$- (*3, 4*), and $CeCl_3$-containing (*5*) films. $C(RC) = C(CeCl_3) = 2$ mass.%. $R = 2$ (*1, 3, 5*); 8 (*2, 4, 6*). The intensities in curves *1–4* and *5, 6* are given in units of *k* and *D*, respectively.

300 nm are observed on its long wavelength side (curve *5*). For $R = 8$ the absorption maximum of this kind of film lies at 260 nm (curve *6*). Substitution of Cr by La is not accompanied by any qualitative change in the ''spectroscopic behavior'' of the *RC* and codoped films. Note that no explicit dependence of the film thickness on *R* was observed, and their thickness fluctuated over 0.3 to 0.4 μm. On the other hand, it was reliably found that introducing lanthanide salts caused the thickness of the codoped films to increase by $0.02-0.07$ μm owing to the higher viscosity of the sol.

Figure 2 shows absorption spectra of undoped (curve *1*) and $CeCl_3$-containing (curve 2) films in the region where their vibrational band is most intense, $C(CeCl_3) = 2$ mass.%. For the undoped film with $R = 2$ this band (Fig. 2a) has a maximum at 1075 cm^{-1} and a ''shoulder'' at 1150 cm^{-1}. Increasing *R* to 6 (Fig. 2b) and 10 (Fig. 2c) essentially has no effect on the halfwidth and location of the peak of this band. Doping film with $R = 2$ with cerium chloride produces a small (~ 3 cm^{-1}) hypsochromic shift of this band and an intensification of its high-frequency part with a slight reduction in its integrated intensity (see the multiplier above curve *2* in Fig. 2a). For $R = 6$, the shift in this line vanishes, the increase in its high-frequency part is smaller, and there is a more substantial drop in its integrated intensity. Increasing *R* to 10 leads to a bathochromic shift in the maximum of this band by approximately 4 cm^{-1}, with no intensification of its high frequency component and a lesser drop in its integrated intensity.

Figure 3 shows luminescence spectra of *RC*-, *RC*-$LaCl_3$-, and *RC*-$CeCl_3$-containing films with $R = 10$ and $C(RC) = C(LnCl_3) = 2$ mass.%, reduced to equal numbers of absorbed exciting photons. The spectrum of the *RC*-containing film at an exciting wavelength of $\lambda_{exc} = 520$ nm is an asymmetric broad band with a peak at 600 nm (curve *1*). Note that the position and shape of this band are essentially independent of λ_{exc}. For the *RC*-$LaCl_3$- and *RC*-$CeCl_3$-containing films, the luminescence band is broadened and its integrated intensity is lower (curves *2* and *3*, respectively). At the same time, its position becomes noticeably dependent on λ_{exc} (compare curves *3* and *4*; the latter was obtained for $\lambda_{exc} = 480$ nm). For *RC*-$LnCl_3$-containing films with different *R*, the luminescence band is shifted in a direction that correlates with the direction of the displacements of the absorption bands shown in Fig. 1.

Figure 4 shows the damping kinetics of the luminescence of *RC*- (a), and *RC*-$CeCl_3$-containing (b) films with $R = 8$ and $C(RC) = C(CeCl_3) = 2$ mass.% for

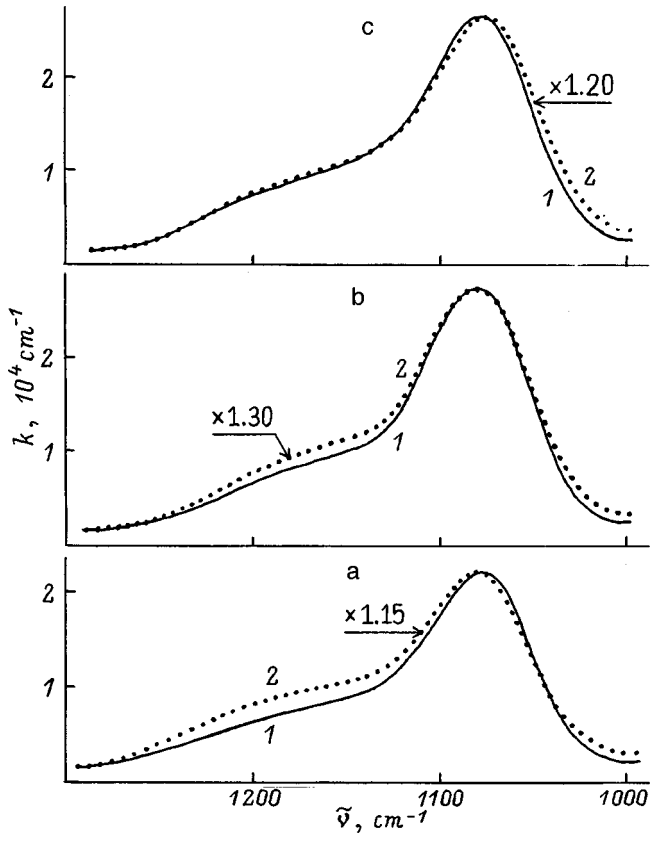

FIG. 2. Infrared absorption spectra of undoped (*1*) and $CeCl_3$-containing (*2*) films. $C(CeCl_3) = 2$ mass.%. $R = 2$ (a), 4 (b), 10 (c).

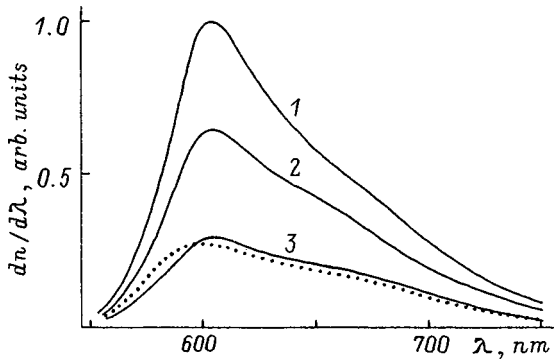

FIG. 3. Luminescence spectra of *RC*-(*1*), *RC*-$LaCl_3$-(*2*) and *RC*-$CeCl_3$-containing (*3*, *4*) films. $C(RC)=C(LaCl_3)=C(CeCl_3)=2$ mass.%. $R=10$. λ_{exc}, nm: 520 (*1*–*3*); 480 (*4*).

$\lambda_{exc}=350$ nm with a detection wavelength $\lambda_{reg}=620$ nm. It can be seen that the damping process is nonexponential for both films. Defining its average duration in terms of the relation $\bar{\tau}=(c_1\tau_1+c_2\tau_2)/(c_1+c_2)$, where c and τ are the statistical weight and damping constant of the component exponential stages, we find that doping with cerium causes $\bar{\tau}$ to increase from 0.4 to 0.8 ns. It should also be noted that the dispersion of $\bar{\tau}$ with λ_{reg} approaches 100% for an *RC*-$CeCl_3$-containing film and is several times greater than this dispersion for an *RC*-containing film. For $R=2$ and $\lambda_{reg}=620$ nm, $\bar{\tau}$ is the same for the two films to within the experimental error at approximately 0.5 ns.

Figure 5 shows absorption spectra of *RC*- and *RC*-$CeCl_3$-containing films with $R=10$ and $C(RC)=1.5C(CeCl_3)=3$ mass.% before and after irradiation for 45 min by the unfiltered light from a DKSSh-1000 xenon lamp. Also shown here is the absorption spectrum of an *RC*-containing film irradiated under identical conditions through a quartz substrate with a $CeCl_3$-containing film. The irradiance in both cases was ~ 100 W/cm^2. It can be seen that irradiating a *RC*-containing film through this substrate results in a weakening of the main band by roughly 60% (cf. curves *1* and *2*) and direct irradiation, by 80% (cf. curves *1* and *3*). At the same time, the shape of this band is deformed. When a *RC*-$CeCl_3$-containing film is irradiated, the main band is weakened by about 30% (cf. curves *4* and *5*). The weakening of the shorter wavelength bands was less for both films. Note that when Ce is replaced by La in the codoped film and irradiated through a substrate with $CeCl_3$-containing film, the intensity of the main band also decreases by about 30%. As *R* is reduced, the photoresistance of the dyes decreases, in both the *RC*- and *RC*-$LnCl_3$-containing films. Here the effect of Ln on the increased photoresistance is also less.

Figure 6 shows absorption spectra of *MB*- and *MB*-$CeCl_3$-containing films for different *R* and $2C(MB)=C(CeCl_3)=2$ mass.%. The spectra of *MB*-containing films with $R=2$ (curve *1*) and 4 (curve *2*) differ significantly. For the *MB*-$CeCl_3$-containing films, there is a significant bathochromic shift in the long wavelength absorption band for $R=2$ (curve *3*) and a hypsochromic shift for $R=4$ (curve *4*), as well as greater splitting of the individual components of this band and a redistribution of their intensities. Replacing Ce by La leads to no fundamental change in the ''spectroscopic behavior'' of the codoped films. No significant effect on the photostability of the dye owing to the presence of the rare earth elements was observed.

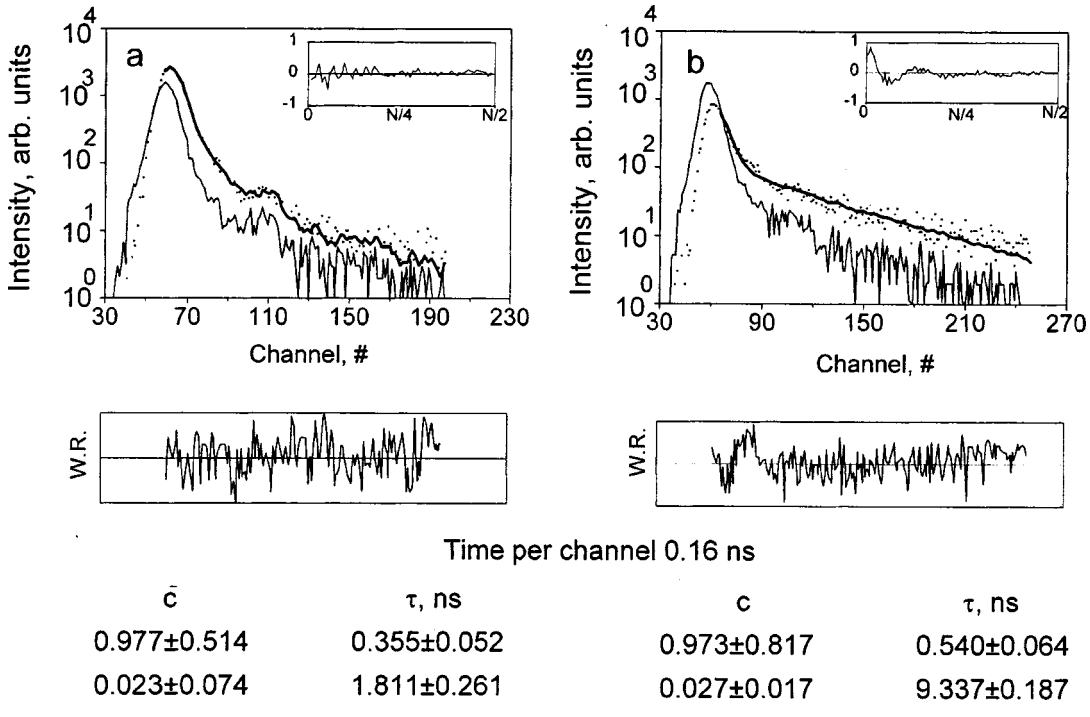

FIG. 4. Quenching kinetics of the luminescence of *RC*- (a) and *RC*-$CeCl_3$-containing (b) films with $C(RC)=C(CeCl_3)=2$ mass.%. $R=8$. $\lambda_{exc}=350$ nm. $\lambda_{reg}=620$ nm.

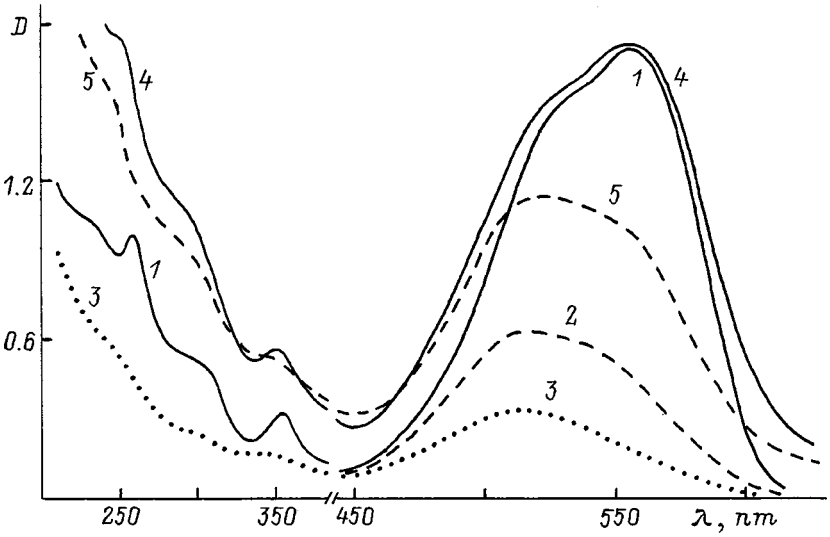

FIG. 5. Absorption spectra of *RC*- (*1–3*) and *RC*-$CeCl_3$-containing (*4, 5*) films prior to (*1, 4*) and after (*2, 3, 5*) exposure to unfiltered radiation from a xenon lamp with an irradiance of 100 W/cm^2 for 45 min. Curve *2* is for a film irradiated through a substrate with a $CeCl_3$-containing film. $C(RC) = 1.5C(CeCl_3) = 3$ mass.%. $R = 10$.

3. DISCUSSION

The broad, intense visible band in the absorption spectrum of *RC*-containing films (Fig. 1) is caused by $S_1 \leftarrow S_0$ transitions of the monomer and associated dye molecules.[1,6] The dependence of the intensity and width of this band on R for *RC*-containing films can be explained by a change in the structure of the matrix, which shows up in the hydrogen bonds of the dye molecules associated with it. It has been shown[7] that when R is increased over the range $2-10$, the structure of the polysiloxanes in the sol changes from linear to spherical. The substantial change in the spectra upon introducing the lanthanides may be caused by interactions of the ionogenic groups of organic molecules with either Ln^{3+} cations or Cl^- anions. In order to establish the true reason, films were prepared from *RC*-containing sols subjected to bubbling in chlorine gas for 30 s. It turned out that bubbling causes an entirely different change in the absorption spectra.[1)] In addition, these changes in the spectra are retained when *RC*-containing films are doped with $Ln(NO_3)_3$ salts instead of $LnCl_3$. This means that we can neglect the effect of the acid residuals of the salts on the ''spectroscopic behavior'' of the codoped films. On the other hand, the change in the direction of the shift in the $S_1 \leftarrow S_0$ band of *RC* as a function of R during codoping indicates that the dye molecules are associated with structural elements of the matrix with the aid of the rare earth ions. This conclusion is also confirmed by the substantial difference in the spectra of the Ce-containing films, which indicates a rather strong chemical interaction of the rare earth ions with the structural grid of the matrix. As for the interpretation of these spectra, the band at 260 nm is caused by charge transfer from the ligands to the Ce^{4+} ions, while the bands at 300 nm and below 200 nm are caused by interconfigurational transitions of the Ce^{3+} ions.[8]

The infrared absorption spectrum of the undoped films shown in Fig. 2 is caused by antisymmetric vibrations of Si–O bonds.[9] The slight increase in its intensity for $R = 6$ indicates that the number of these bonds is greater in the film. Here the Si–O bond strength is unchanged, given the absence of a shift in the peak of this band. The hypsochromic shift of this band owing to cerium chloride doping of a film with $R = 2$ indicates that these bonds are involved, while the greater intensity of its high-frequency shoulder indicates a reduction (according to our observations) in the stoichiometry of the matrix. On the other hand, doping at $R = 10$ leads to weakening of the Si–O bonds while retaining stoichiom-

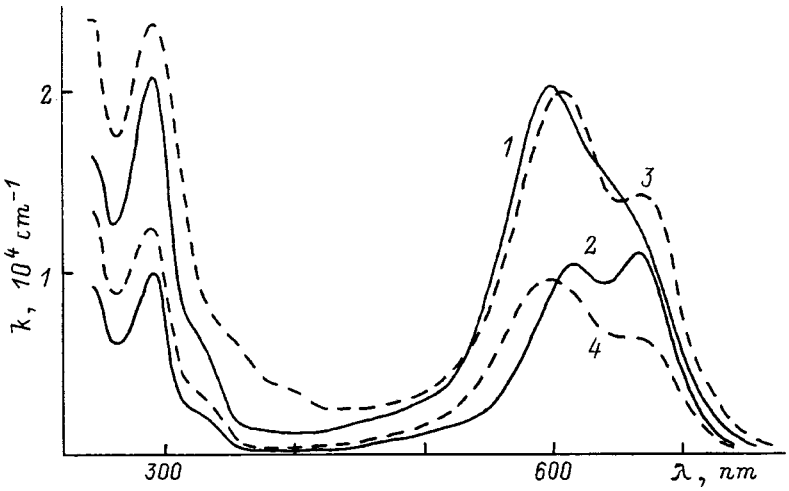

FIG. 6. Absorption spectra of *MB*- (*1, 2*) and *MB*-$CeCl_3$-containing (*3, 4*) films. $2C(MB) = C(CeCl_3) = 2$ mass.%. $R = 2$ (*1, 3*) and 4 (*2, 4*).

etry. In the intermediate case ($R=6$), there is no weakening of these bonds owing to doping, but the stoichiometry of the matrix is reduced. At the same time, for all R there is (judging from the multiplier on the curves of Fig. 2) a significant lowering of the integrated intensity of this band and, accordingly, in the number of Si–O bonds. The observed bond strengthening and reduction in stoichiometry upon doping with cerium chloride confirm the above conclusion regarding the chemical interaction of the rare-earth ions with the structural grid of the film and their possible role as a binding link between the grid and the organic molecules.

The broad luminescence band of the *RC*-containing film (Fig. 3) is caused by $S_1 \rightarrow S_0$ transitions of the dye monomers and the slight inflection in its long wavelength wing can be attributed to luminescence of complex associates.[1] The absence of changes in the location and shape of this band as λ_{exc} is shifted indicates that it is homogeneously broadened. The reduction in the luminescence intensity of the *RC*-$LaCl_3$-containing film is logically explained by more intense intercombination transitions of the *RC* molecules by heavy atoms.[10] The further weakening of the luminescence intensity of the dye when La is replaced by Ce is most likely caused by radiationless transfer of excitation from the S_1 to an absorbing transition in the visible region of the Ce-containing cluster,[8] although quenching by charge transfer is not excluded.[10] The absence of significant distortions in the luminescence band profile for the *RC*-$LnCl_3$-containing films indicates that the ratio of the monomers and associates of the dye molecules changes little. At the same time, the dependence of the position of the luminescence band on λ_{exc} for these films suggests that reorientation of the nearest surroundings of the dye molecules is impeded over the lifetime of their excited state. This impediment may be a consequence either of the formation of supramolecules or of a shortening of $\overline{\tau}$.

The nonexponential decay of the luminescence of an *RC*-containing film (Fig. 4) and its low $\overline{\tau}$ (the luminescence duration for this dye in a water solution is ~ 20 ns[11]) indicate that the luminescence of the monomer is strongly damped by dimers and more complex associates.[12] The negligible dependence of $\overline{\tau}$ on R in these films may indicate a weak change in the degree of association of the *RC* molecules with the matrix structure. Given the lowering of the luminescence intensity of the *RC*-$LnCl_3$-containing films, it would be logical to expect a reduction in $\overline{\tau}$. The contrary increase in this parameter of $R=8$ observed in the experiment suggests a rise in the radiative lifetime for luminescence in the organic molecules. This assumption is consistent with the intensity drop in the long wavelength of the main absorption band (see Fig. 1) owing to introducing $CeCl_3$, which is caused mainly by the monomers.[1] Here the increased dispersion of $\overline{\tau}$ with λ_{reg} indicates increased inhomogeneity of the luminescence centers, while the absence of a drop in $\overline{\tau}$ suggests a link between the above impediment to reordering of the local surroundings of the dye molecules and their entry into supramolecules.

The relatively weak photodecoloration of the short wavelength segment of the $S_1 \leftarrow S_0$ band of an *RC*-containing film irradiated by a xenon lamp (Fig. 5) can be explained by the high photoresistance of the associates, which ensure comparatively efficient dissipation of the excitation energy.[2] The most intense absorption band of these associates lies in the short wavelength side of the $S_1 \leftarrow S_0$ absorption band of the monomers (Ref. 13). The comparatively greater photodestruction of this film, when irradiated through a quartz substrate with a $CeCl_3$-containing film, indicates that the internal filter has relatively little effect on the increased photoresistance of the dye molecule with cerium chloride codoping. The roughly equal photodecoloration of the *RC*-$LaCl_3$-containing film irradiated through this substrate and the *RC*-$CeCl_3$-containing film, which is characterized by a substantially lower photoluminescence intensity (cf. curves *2* and *3* of Fig. 3), suggests that the main mechanism for the increased photoresistance of the dye is an intensification of the $T_1 \rightarrow S_0$ transitions by heavy atoms. In fact, these films are characterized by an extremely low luminescence quantum yield ($\eta < 1\%$[1]), even for dye concentrations which ensure a negligibly low fraction of associated molecules. This indicates a high interconversion efficiency and may be accompanied by a substantial filling of the T_1 state. Given the similarity of the shapes of the $S_1 \leftarrow S_0$ absorption bands of irradiated *RC*- and *RC*-$CeCl_3$-containing films, we may also assume that the observed rise in photoresistance is caused mainly by those associates whose organic molecules are bound with rare earth ions. Here it should be noted that this increase in the photoresistance of the *RC* is not related to a weakening of the deprotonation of the carboxyl group of this dye, which also causes its decoloration.[14] This was confirmed by a control experiment in which the photoresistance of $LnCl_3$-containing films doped with Rhodamine 6G, which is not decolored upon deprotonation, was found to increase.

The ''spectroscopic behavior'' of *MB*-containing films codoped with cerium chloride (Fig. 6) does not conflict with the analysis of Fig. 1. In addition, the substantially faster shift in the main absorption band of the *MB* than for a *RC*-containing film and the redistribution in the intensities of its individual components as R is varied indicates a stronger coupling of the matrix with the molecules of this dye. Apparently, this is caused by a difference in the alkyl groups in the ionogenic $N^+(C_2H_5)_2Cl^-$ and $N^+(CH_3)_2Cl^-$ fragments of the *RC* and *MB* molecules, respectively. The weak variation in the photoresistance of the *MB*-containing films upon doping with cerium chloride justifies the assumption that the formation of charge carriers during ultraviolet irradiation of the matrix (they can be intercepted by ions of this element[5]) has no significant effect on the dye molecules, as in the case discussed above.

Therefore, the presence of rare-earth elements in silicate gel films containing a dye leads to the formation of supramolecules which include organic molecules, rare earth ions, and elements of the grid structure. The formation of such structures makes it possible to vary the color tint of the films and leads to increased photoresistance of the luminescent dyes, primarily through enhancement of $T_1 \rightarrow S_0$-transitions.

This work was supported by the Belarus Republican Foundation for Basic Research (Grant No. F97-116).

[1)]It is planned to discuss the results of this study in a separate paper.

[1] G. E. Malashkevich, E. N. Poddenezhnyĭ, I. M. Mel'nichenko, V. B. Prokopenko, and D. B. Dem'yanenko, Fiz. Tverd. Tela **40**, 466 (1998) [Phys. Solid State **40**, 427 (1998)].
[2] A. S. Cherkasov and M. I. Snegov, in *Spectroscopy of Photoconversion in Molecules*, edited by A. A. Krasnovskiĭ (Nauka, Leningrad, 1997), p. 161.
[3] G. E. Krichevskiĭ, *Photochemical Conversion of Dyes and Photostabilization of Dyed Materials* (Khimiya, Moscow, 1986), 247 pp.
[4] V. L. Ermolaev, E. N. Bodunov, E. B. Sveshnikova, and T. A. Shakhverdov, *Radiationless Transport of the Energy of Electronic Excitation* (Nauka, Moscow, 1977), p. 161.
[5] A. A. Appen, *Glass Chemistry* (Khimiya, Leningrad, 1974), 352 pp.
[6] L. V. Levshin, E. Yu. Bekhli, T. D. Slavnova, and V. I. Yuzhakov, Optika i Spektroskopiya **36**, 503 (1974).
[7] A. H. Boonstra and C. A. M. Mulder, J. Non-Cryst. Solids **105**, 201 (1988).
[8] G. E. Malashkevich, E. N. Poddenezhny, I. M. Melnichenko, and A. A. Boiko, J. Non-Cryst. Solids **188**, 107 (1995).
[9] A. R. Silin' and A. N. Trukhin, *Point Defects and Elementary Excitations in Crystalline and Vitreous* SiO_2 (Zinatne, Riga, 1985), p. 159.
[10] A. N. Terenin, *Photonics of Dye Molecules* (Nauka, Leningrad, 1967), p. 616.
[11] A. Penzkofer and W. Falkenstein, Opt. Quantum Electron. **10**, 399 (1978).
[12] L. V. Levshin, E. Yu. Bekhli, and T. D. Slavnova, Optika i Spektroskopiya **36**, 503 (1974).
[13] A. K. Chibisov, G. A. Ketsle, L. V. Levshin, and T. D. Slavnova, Optika i Spektroskopiya **38**, 83 (1975) [Opt. Spectrosc. **38**, 45 (1975)].
[14] G. A. Korsunovskiĭ and Kh. L. Arvan, in *Molecular Photonics* (Nauka, Leningrad, 1970), p. 274.

Translated by D. H. McNeill

DEFECTS. DISLOCATIONS. PHYSICS OF STRENGTH

Influence of a weak pulsed magnetic field on grain-boundary relaxation in aluminum

O. I. Datsko, V. I. Alekseenko, and A. L. Brusova

A. A. Galkin Donetsk Physicotechnical Institute, Ukrainian Academy of Sciences, 340114 Donetsk, Ukraine
(Submitted February 3, 1999)
Fiz. Tverd. Tela (St. Petersburg) **41**, 1985–1987 (November 1999)

It is discovered that the treatment of technical-grade polycrystalline aluminum in a weak pulsed magnetic field during heating leads to displacement of the grain-boundary maximum of the low-frequency internal friction toward lower temperatures. This phenomenon is associated with a decrease in the degree of interaction of the grain boundaries with impurity atoms.
 [S1063-7834(99)01611-1]

1. According to the existing theories,[1] when materials that contain crystal-lattice defects and are in a nonequilibrium metastable state are treated in a weak pulsed magnetic field, changes occur in their properties and in the structure of the impurity-defect complexes, which cause accompanying changes in their physicomechanical properties.

As we know, the impurity-defect complexes in a material can differ in nature, structure, properties, and chemical composition, as well as with respect to the concentration of impurity atoms and the type of defects present, which may be vacancies, dislocations, phase boundaries, twins, and cracks. The influence of pulsed magnetic fields and impurity-defect complexes have scarcely been studied from the standpoint of the factors just enumerated. This problem is of current interest, because its solution may reveal the mechanisms by which pulsed magnetic treatment influences materials and their properties. To solve this problem, the characteristics of impurity-defect complexes just indicated must be established in order to understand their role and place in these mechanisms.

The present work examines the physical essence of the influence of pulsed magnetic fields on impurity-defect complexes consisting of crystallite boundaries with various degrees of blocking by impurity atoms. In particular, the dependence of the grain-boundary relaxation process in polycrystalline aluminum of different purity on pulsed magnetic treatment is investigated.

It is generally acknowledged that crystallite boundaries cause the appearance of the maximum associated with grain-boundary relaxation in the temperature dependence of low-frequency internal friction.[2] The temperature position of the maximum and the activation energy for grain-boundary relaxation are determined to a considerable degree by the impurity atoms which are adsorbed on the crystallite boundaries and block their motion. In the general case an increase in the concentration of impurity atoms in a material leads to displacement of the grain-boundary maximum toward higher temperatures and an increase in the activation energy of the process.[3] If a pulsed magnetic field has an influence on the degree of interaction of grain boundaries with impurity atoms, as we observed for dislocations pinned by impurities,[4,5] it should be manifested as changes in the parameters of the relaxation process expressed by the grain-boundary maximum of internal friction.

2. Technical grade (99.96%) polycrystalline aluminum and high-purity (99.999%) aluminum served as the objects of investigation. The samples were obtained by mechanical treatment from ingots of the material cast in the form of prisms measuring $3\times3\times60$ mm. Before the measurements, the samples were annealed at their recrystallization points. The internal friction was studied on a low-frequency apparatus of the inverted torsion pendulum type with an oscillation frequency close to 1 Hz. To reveal the influence of a pulsed magnetic field on the boundary-impurity complexes, we studied the temperature dependence of the internal friction at a relative strain amplitude of the material $\varepsilon=2\times10^{-5}$. The material was heated at the rate of ~2 °C min. The treatment of the material by a pulsed magnetic field was carried out in an OIMP-101 apparatus under the following regime: amplitude of the magnetic field, 10^5 A/m; duration of the leading edge of a pulse, 10^{-4} s; pulse repetition rate, 1 Hz. Measurements of internal friction were performed without treatment of the material by the pulsed magnetic field and with continuous treatment of the material under investigation by the pulsed magnetic field.

3. Figure 1 (curve *1*) shows the temperature dependence of the internal friction for high-purity aluminum. The plot exhibits a relaxational internal-friction peak with a maximum at 240 °C. Ke[6] observed a similar peak with a maximum at 280 °C for pure aluminum at a frequency of 1 Hz and unequivocally showed that this peak is related to grain boundaries. The conclusion that the internal-friction peak shown in Fig. 1 is a grain-boundary peak is supported by the decrease in its amplitude and displacement of its maximum toward higher temperatures (275 °C) in the technical-grade aluminum (curve *1* in Fig. 2). The temperature dependence of internal friction in the high-purity aluminum recorded in the pulsed magnetic field does not differ from the original curve (curve *2* in Fig. 1). The internal-friction peak does not shift along the temperature axis, and its amplitude remains

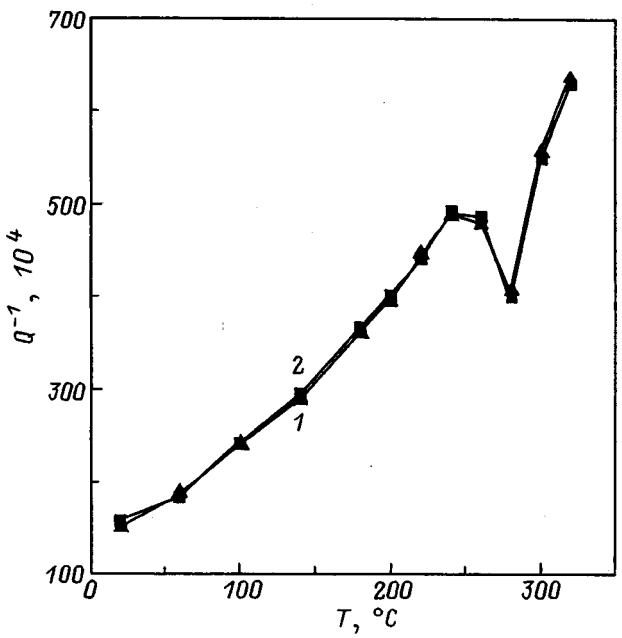

FIG. 1. Temperature dependence of the internal friction in high-purity aluminum: *1*—without a pulsed magnetic field; *2*—in a pulsed magnetic field.

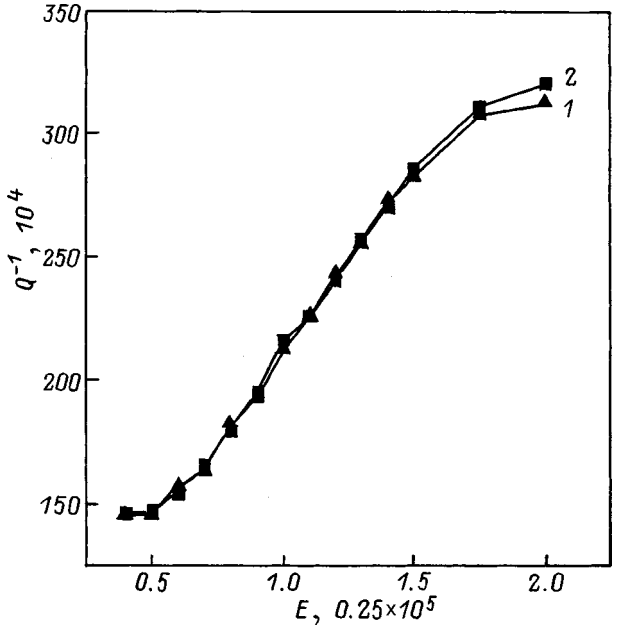

FIG. 3. Strain-amplitude dependence of the internal friction in high-purity aluminum at room temperature: *1*—without a pulsed magnetic field; *2*— in a pulsed magnetic field.

unchanged. At the same time, in the case of the technical-grade aluminum the maximum of the grain-boundary peak shifts toward lower temperatures by ~30 °C due to the pulsed magnetic treatment of the material (curve *2* in Fig. 2). Thus, the activation energy for grain-boundary relaxation at impurity-pinned boundaries decreases in the pulsed magnetic field, in contrast to the case of unpinned boundaries.

The results presented provided evidence that the pulsed magnetic field does not cause any changes in the relaxation process at unpinned boundaries. In other words, the pulsed magnetic field does not have any influence on grain-boundary relaxation. The presence of impurities in the material under investigation significantly modifies the relaxation process, blocking its development. Application of the pulsed magnetic field in the latter case has a positive effect, promoting the optimal manifestation of grain-boundary relaxation. It is now clear that the impurity atoms segregated on grain boundaries, rather than the grain boundaries themselves, react to the magnetic field. Within the dislocation model of grain-boundary relaxation,[7] impurities which block the motion of grain boundaries restrict stress relaxation. In the case where the impurities segregated on the grain boundaries are magnetically active, a pulsed magnetic field can alter their

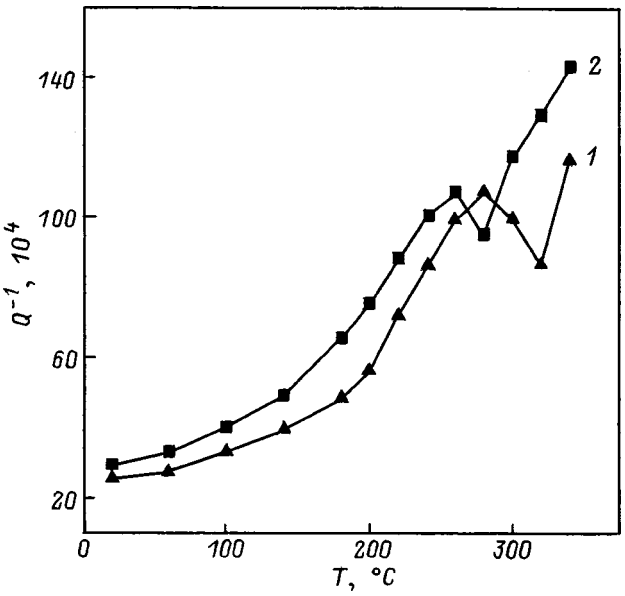

FIG. 2. Temperature dependence of the internal friction in technical-grade aluminum: *1*—without a pulsed magnetic field; *2*—in a pulsed magnetic field.

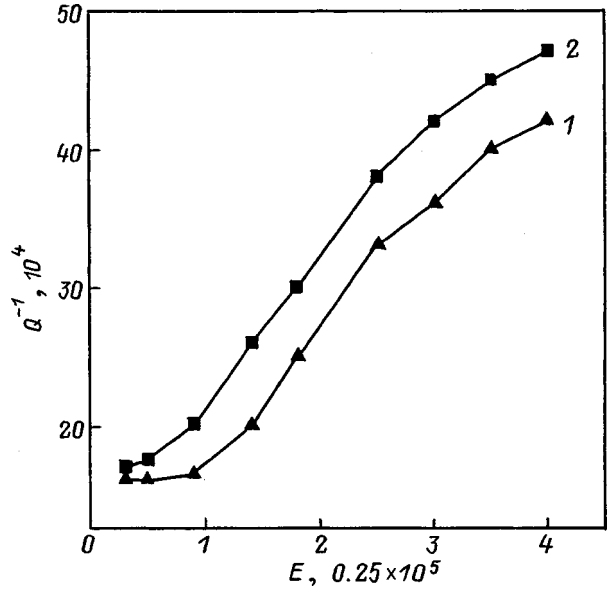

FIG. 4. Strain-amplitude dependence of the internal friction in technical-grade aluminum at room temperature: *1*—without a pulsed magnetic field; *2*—in a pulsed magnetic field.

interaction energy and raise (or lower) the degree of stress relaxation, as is observed experimentally.

To confirm this hypothesis, the strain-amplitude dependence of the internal friction in the technical-grade and high-purity aluminum was studied at room temperature with and without pulsed magnetic treatment. In this case stress relaxation took place at dislocations pinned to a greater or lesser extent by impurities.

As can be seen from Figs. 3 and 4, dislocation relaxation behaves similarly to grain-boundary relaxation: the degree of dislocation relaxation is many times greater in the high-purity aluminum than in the technical-grade aluminum. In addition, there is no magnetic-field effect in the high-purity aluminum: the plots of the strain-amplitude dependence of the internal friction with and without the pulsed magnetic field coincide (curves *2* and *1* in Fig. 3). In the technical-grade aluminum the degree of dislocation stress relaxation rises in the pulsed magnetic field (in the region of amplitude-dependent internal friction, curve *2* in Fig. 4). In the region of amplitude-independent internal friction the magnetic-field effect is reduced. It is also noteworthy that the critical amplitude (ε_1) for the transition from amplitude-independent to amplitude-dependent internal friction decreases in the technical-grade aluminum in the pulsed magnetic field (curve *2* in Fig. 4).

To analyze the strain-amplitude dependences of the internal friction within the Granato–Lücke dislocation model, we use the expression for the amplitude-independent internal friction

$$Q^{-1}=\Omega\rho L_s^4 K/\pi^2 C, \tag{1}$$

where Ω is the orientational factor, ρ is the dislocation density, L_s is the length of a free-dislocation segment, K is a coefficient which takes into account the type of length distribution of L_s, and C is the linear dislocation stress. For the first critical strain amplitude we obtain

$$\varepsilon_1 \sim [(U_b n^3)/(Gb^3)]^{1/2}, \tag{2}$$

where U_b is the binding energy of impurities to dislocations, n is the concentration of impurity atoms on a dislocation line, G is the shear modulus, and b is the Burgers vector. For the amplitude-dependent internal friction

$$Q^{-1}(\varepsilon)=C_1(C_2/\varepsilon)F(C_2/\varepsilon)\exp(-C_2/\varepsilon), \tag{3}$$

where $C_1 \sim \rho L_s^3$, $C_2=(K/L_s)\exp(U_b/kT)$, and $F(C_2/\varepsilon)$ is a function which takes into account the distribution of the stresses for different sample loading schemes.

The expressions presented faithfully describe the plots of the stress-amplitude dependence of the internal friction presented in this paper and permit accounting for the changes observed in them that are caused by the pulsed magnetic treatment. Let us analyze these changes in relationship to such parameters of dislocation internal friction as L_s and U_b, since the dislocation density in the test material does not vary in response to the pulsed magnetic field. If the pulsed magnetic treatment of the technical-grade aluminum results in a change in L_s, particularly an increase in it due to a decrease in the concentration of impurity atoms on a dislocation line, then, as can be seen from (1)–(3), it is followed by an increase in the amplitude-independent and amplitude-dependent internal friction, as well as a decrease in ε_1. In fact, an increase in the amplitude-dependent internal friction and a drop in ε_1 are observed experimentally in the technical-grade aluminum (curve *2*, Fig. 4). However, there is no significant increase in the amplitude-independent internal friction, although, as follows from (1), it is highly sensitive to changes in L_s. Thus, it is impossible to account for the experimental data in terms of L_s. Therefore, U_b is the most decisive parameter in this sense, since the binding energy does not explicitly determine the level of amplitude-independent internal friction, but it does determine the level of the amplitude-dependent internal friction and ε_1. Thus, the effect of magnetic treatment on impurity-pinned dislocations can be caused by a decrease in U_b.

Since impurities have qualitatively identical effects on dislocation and grain-boundary stress relaxation in the technical-grade aluminum, it is reasonable to assume that the changes in grain-boundary relaxation can also be associated with a decrease in U_b in the pulsed magnetic field. It should be noted that Eq. (1) is valid for resonant amplitude-independent internal friction. Therefore, if the pulsed magnetic treatment of the technical-grade aluminum would have resulted in changes in the impurity concentration at the grain boundaries (the parameter L_s), the height of the grain-boundary internal-friction peak would have also varied. No changes in the height of the grain-boundary peak are observed experimentally in the pulsed magnetic field (curve *2* in Fig. 2). However, the displacement of this peak toward lower energies can also be caused by a decrease in the interaction energy of impurities with grain boundaries, which appears as a component of the activation energy for grain-boundary relaxation (U_a). In other words, the pulsed magnetic field influences the effective grain-boundary relaxation time and, as can be seen from the expression $\tau=\tau_0\exp(U_a/kT)$, thus leads to displacement of the resonant internal friction peak.

The magnetically induced grain-boundary relaxation discovered in this work is not only of practical interest, since a real and simple possibility to plasticize a material has been demonstrated, but is also of pure scientific interest, since the use of pulsed magnetic fields in relaxation processes in grain boundaries permits a deeper approach to the study of grain-boundary relaxation mechanisms and their simulation.

[1] S. N. Postnikov, V. P. Sidorov, and A. V. Ilyakhinskiĭ, in *Applied Problems in Strength and Plasticity* (Izd. Gor'kovsk. Univ., Gor'kiĭ, 1980).
[2] V. S. Postnikov, I. M. Sharmakov, and É. M. Maslennikov, in *Relaxation Phenomena in Metals and Alloys* (Metallurgizdat, Moscow, 1963).
[3] A. V. Grin', Fiz. Met. Metalloved. **4**, 561 (1957).
[4] O. I. Datsko, V. I. Alekseenko, and A. D. Shakhova, Fiz. Tverd. Tela (St. Petersburg) **38**, 1799 (1996) [Phys. Solid State **38**, 992 (1996)].
[5] O. I. Datsko and V. I. Alekseenko, Fiz. Tverd. Tela (St. Petersburg) **39**, 1234 (1997) [Phys. Solid State **39**, 1094 (1997)].
[6] T. S. Ke, Phys. Rev. **71**, 533 (1947).
[7] A. S. Nowick and B. S. Berry, *Anelastic Relaxation in Crystalline Solids* (Academic Press, New York, 1972; Atomizdat, Moscow, 1975).

Translated by P. Shelnitz

Decay kinetics of metastable states in a disordered linear system

B. V. Petukhov

Institute of Crystallography, Russian Academy of Sciences, 117333 Moscow, Russia
(Submitted March 12, 1999)
Fiz. Tverd. Tela (St. Petersburg) **41**, 1988–1993 (November 1999)

Kolmogorov's method for describing statistical crystallization is generalized to take into account disorder in the structure and is applied to the calculation of the decay kinetics of metastable states in linear (in the sense of spatial dimensionality) systems. The theory describes the influence of defects on the dynamics of polymers and domain boundaries between phases on substrates, on crystal growth involving the movement of steps over a surface, on the plastic flow of materials due to the motion of dislocations in a Peierls–Nabarro relief, and on the kinetics of other physical systems. © *1999 American Institute of Physics.* [S1063-7834(99)01711-6]

The switching kinetics of states of linear systems determines the laws governing the course of many physical processes. As examples we can point out the dynamics of spin chains, polymers,[1] domain boundaries on two-dimensional substrates,[2] crystal growth involving the movement of steps over a surface,[3] the plastic flow of materials due to the motion of dislocations in a Peierls–Nabarro relief,[4] etc.

The laws governing the decay of metastable states of an extended linear system having many degrees of freedom differ significantly from the familiar exponential relaxation kinetics of one-dimensional systems $Q(t)=Q_0\exp(-t/\tau)$ [$Q(t)$ is the fraction in the initial state at the time t, and τ is the relaxation time]. As A. N. Kolmogorov showed back in 1937,[5] the mutual influence of different degrees of freedom leads to alteration of the temporal relaxation law even in a spatially homogeneous material.

A significant contribution to the switching kinetics of states of linear systems is made by the motion of so-called kink solitons or simply kinks (see, for example, Ref. 6), which mark the boundaries between different ''phases.'' Such boundaries can be treated as one-dimensional quasiparticles of a special kind. When the driving force is relatively weak, the process takes place under quasiequilibrium conditions, i.e., as a result of the movement of kink solitons in thermal equilibrium. We, however, shall consider fairly large driving forces and processes taking place far from equilibrium, for which the contribution of thermal kinks can be neglected.

The decay of a metastable state of a system can be described as a two-stage process. At first there is a local transition of a small segment due to a thermal fluctuation. For this transition to occur, an energy barrier equal to the formation energy of two boundaries between the phases must be overcome, and it thus takes a considerable time. Such a segment can be regarded as the ''nucleus'' of a new state bounded by two kinks separating different states. Then the kinks propagate along the linear system under the action of the applied external force until they encounter and annihilate with kinks from other nuclei formed in parallel, but statistically independent events, and the switching process is completed after all the nuclei coalesce.

The problem of the decay kinetics of a metastable state in a spatially homogeneous material (for a system of any dimensionality) was solved by A. N. Kolmogorov in his classical theory of statistical crystallization[5] (for a review of the subsequent work on this subject, see Ref. 7). If we use J to denote the frequency of the formation of nuclei per unit time on a unit length as applied to our problem and v to denote the kink propagation velocity, then the fraction of the unswitched phase $Q(t)$ at the time t after the beginning of the transition process is[5]

$$Q(t)=\exp(-Jvt^2). \tag{1}$$

In real materials kink motion is subjected to the influence of defects, which is especially strong because of the one-dimensional nature of the quasiparticles (the impossibility of going around an obstacle, in contrast to systems of higher dimensionality). An example of the anomalous properties of the mobility of one-dimensional particles in the presence of a broad spectrum of random barriers is provided by the transition to anomalous drift when the driving force F is reduced:[8]

$$x(t)\sim t^{\delta(F)}(\delta(F)<1). \tag{2}$$

Reviews of the numerous theoretical studies on this subject have been published (see, for example, Refs. 9–11). We note that the phenomenon described also has other names: ''quasilocalization'' (Ref. 9), nonlinear drift in a ''random force field'' (Refs. 10 and 12), motion in a ''creep phase'' (Ref. 13), and ''heterogeneous dynamics'' (Ref. 14). The anomalous drift of dislocation kinks was recently discovered in experiments on the mobility of dislocations in Ge.[15]

Since kink motion is an important component of the decay of metastable states of linear systems, we should expect disorder to have a significant influence on its kinetics. The purpose of the present work was to study the influence of impurities or other defects on the laws governing such a decay process. Unlike the preceding studies in Refs. 8, 13, 14, etc., which treated the coalescence of nuclei on a qualitative level, in this paper we shall employ Kolmogorov's probabilistic approach,[5] which describes this process exactly (within the model adopted) and allows generalization to a

disordered system. Such an approach permits, in particular, tracing the transition from a normal kink drift regime (the Kolmogorov case) to an anomalous regime with corresponding modification of the overall kinetics of the state of the system. In view of the microscopic nature of kinks, studying the overall kinetics of the switching between the states of a system is frequently the only presently available possibility for obtaining information on their dynamics.[15]

Significant alteration of the kinetics can be expected in the case where the time of free motion of the kinks between barriers is small compared to the delay time in the barriers. Below we shall consider just this situation, and we shall neglect the contribution of the free drift time to the total time of kink motion.

1. STATE SWITCHING KINETICS FOR AN ARBITRARY SPECTRUM OF BARRIERS TO KINK MOTION

This section is devoted to a generalization of Kolmogorov's method[5] to the case of a disordered system.

Let us trace the variation of the state of an arbitrarily selected point in the system with time. For convenience in describing the system, we divide it into intervals of length Δl, which is of the order of the typical width of a barrier (we shall refine it below). Each interval has its own kink delay time τ_i. The delay time probability density function $P(\tau)$ is assumed to be the same in all the intervals. The total delay time for the displacement of a kink by n intervals is $T_n = \sum_{i=1}^{n} \tau_i$.

An arbitrary reference point is in the new ''switched'' state at the time t, if the boundary of a nucleus of the new state created in any interval n at the moment in time t' manages to propagate to the point under consideration before the time t, or, stated differently, if the total delay time T_n accrued during passage of the kink from the site of its creation to the point under consideration is less than $t-t'$. The probability of the creation of a nucleus in the time interval $\Delta t'$ is $J\Delta l^{(n)}\Delta t$. The additional quantity $1-J\Delta l^{(n)}\Delta t'$ is the probability that a nucleus is not created in the length interval and time interval under consideration. The probability $q_n(t)$ that the n'th interval does not serve as a source of state switching at all is equal to the product of the noncreation probabilities in all the time intervals between $t'=0$ and $t'=t-T_n$, i.e.,

$$q_n(t)=\prod_{\alpha}\ (1-J\Delta l^{(n)}\Delta t'_{\alpha})\approx\exp(-J\Delta l^{(n)}(t-T_n)). \tag{3}$$

The total probability of conservation of the initial state at a given point $Q(t)$ is the product of the noncreation probabilities in all the intervals from which the time of motion of a kink to the point selected is less than t. Such sets of intervals can be found on both sides of the point under consideration. Because the barriers are independent, $Q(t)$ can be represented as the probability product $Q(t) = q_0(t)Q^+(t)Q^-(t)$. Here $q_0(t)=\exp(-J\Delta l t)$ is the nucleus noncreation probability in the interval to which the point under consideration belongs. The unilateral probability that the state does not change because of, for example, the nuclei created only to the right of the point selected $Q^+(t)$ [and $Q^-(t)$, respectively] is equal to the product of $q_n(t)$ over all the intervals $\Delta l^{(n)}$ from 1 to the maximum value of N satisfying the condition $T_N<t<T_{N+1}$:

$$Q^+(t)=\prod_{n=1}^{N}\ \exp(-J\Delta l(t-T_n))$$

$$=\exp\left(-J\Delta l\left(N(t-T_N)+\sum_{i=1}^{N}\ \tau_i\right)\right). \tag{4}$$

The mean value of $Q^+(t)$ over all the points of the system or, equivalently, over all the possible barrier configurations and the mean value of $Q(t)$, which is equal to it in the symmetric case, are written in the form

$$\langle Q^+(t)\rangle=\langle Q^-(t)\rangle=\sum_{N=1}^{\infty}\ \int\ \prod_{m=1}^{N}\ P(\tau_m)\,d\tau_m$$

$$\times Q^+(t)P_1(t-T_N). \tag{5}$$

Here $P(\tau)\,d\tau$ is the probability of having a delay time between τ and $\tau+d\tau$ in the interval under consideration, the integration is carried out over all τ_m amounting to less than t in the sum over the intervals, and $P_1(t)=\int_t^{\infty}P(\tau)\,d\tau$ is the probability of having a delay time exceeding t. The presence of the multiplier $P_1(t-T_N)$ takes into account that, according to the definition of N, the interval following the Nth interval has a delay time which exceeds t in the sum with T_N.

We calculate the characteristic function for $Q^+(t)$, which is the Laplace transform of $\langle Q^+(t)\rangle$:

$$\hat{Q}(s)=\int_0^{\infty}dt\,e^{-st}\langle Q^+(t)\rangle dt$$

$$=\int_0^{\infty}dt\,e^{-st}\sum_{N=1}^{\infty}\ \int\ e^{-J\Delta lN(t-T_N)}P_1(t-T_N)$$

$$\times\prod_{m=1}^{N}\ e^{-J\Delta l m\tau_m}P(\tau_m)\,d\tau_m$$

$$=\sum_{N=1}^{\infty}\ ((1-\hat{P}(s+J\Delta lN))/(s+J\Delta lN))$$

$$\times\prod_{m=1}^{N}\ \hat{P}(s+J\Delta lm). \tag{6}$$

Here $\hat{P}(s)$ is the Laplace transform of $P(\tau)$: $\hat{P}(s)=\int_0^{\infty}e^{-s\tau}P(\tau)\,d\tau$.

Formula (6) is the result of averaging over an arbitrary spectrum of barriers that block the motion of boundaries of nuclei of the new state. It will be used below to calculate the state switching kinetics for a concrete model of disorder characteristic of the interaction of kinks with point defects and for other cases.

2. GAUSSIAN RANDOM-FORCE FIELD

The potential under which a kink moves is the sum of the interaction energy of the system with defects $U(x)$, which varies chaotically as the state at the length x varies,

and the regular term Fx created by the applied driving force F. In the model considered below $U(x)$ is a random quantity, which undergoes ''Brownian motion'' along the energy scale with the diffusion coefficient σ as x varies. The statistical properties of such a quantity are completely assigned by the mean values $\langle U(x)\rangle = 0$ and $\langle U(x)U(x')\rangle = \sigma\delta(x-x')$. Examples of the realization of such a model of a random potential, which is termed a ''random force field,'' can be found, for example, in Refs. 8–15. Thus, for point defects randomly distributed with a mean linear density ρ, whose interaction energy with the system undergoes a change equal to $\pm u$ when its state is switched, it is not difficult to obtain $\sigma = \rho u^2$.

Let us consider a certain barrier formed by a peak of the potential $U(x)$ and calculate the kink delay time created by it. Passage across the barrier can occur as a result of a favorable thermal fluctuation. The expectation time τ of such thermal activation can be described by the formula (see, for example, Refs. 16 and 17):

$$\tau = (\Delta l/D_k)\int_0^\infty e^{(U(x)-F_x)/kT}\,dx. \tag{7}$$

Here D_k is the kink diffusion coefficient, and Δl is the characteristic kink localization length before the barrier, which is defined as the distance over which the potential varies by an order of magnitude of the thermal energy kT. We are not interested in the exact value of the preexponential factor in (7) and confine ourselves to estimating Δl on the basis of the following simple arguments. The potential appearing in (7) is the sum of the randomly ''diffusing'' component $U(x)$, whose typical amplitude increases with x as $(\sigma x)^{1/2}$, and the regular ''drift'' component Fx. The diffusive behavior of the potential dominates at small lengths, a change in the behavior occurs at $x \sim x_b = \sigma/F^2$, and the Fx contribution is dominant at $x > x_b$. In the latter case, as can easily be seen, Δl can be estimated from the relation $F\Delta l \sim kT$ as $\Delta l \sim kT/F$. The condition for its applicability is $\Delta l > x_b$, i.e., $\delta = kTF/\sigma > 1$. In the opposite case of $\delta < 1$, Δl can be estimated from the relation $(\sigma\Delta l)^{1/2} \sim kT$ as $\Delta l \sim (kT)^2/\sigma$.

The following expression was obtained in Ref. 8 (see also Ref. 10) for the distribution function $P(\tau)$ appearing in (6):

$$P(\tau) = \frac{\exp(-1/(s_0\tau))}{\Gamma(\delta)s_0^\delta \tau^{\delta+1}}, \tag{8}$$

where $s_0 = \sigma D_k/((kT)^2\Delta l)$ and $\Gamma(\delta) = \int_0^\infty x^{\delta-1}e^{-x}\,dx$. Using the explicit form of the distribution function (8), we can find the behavior of $\langle Q^+(t)\rangle$ for various values of the parameters from formula (6).

1) $\sigma > 1$. With the exception of the narrow vicinity of small $\varepsilon = \delta - 1$ (which merits a special discussion) we have

$$\hat{Q}(s) \approx \frac{1}{s_0}\sqrt{\frac{\pi}{2\lambda\varepsilon}}\exp\left(\frac{\lambda}{2\varepsilon}\left(\frac{s}{J\Delta l}\right)^2\right)\mathrm{erfc}\left(\sqrt{\frac{\lambda}{2\varepsilon}}\frac{s}{J\Delta l}\right). \tag{9}$$

Here $\lambda = J\Delta l/s_0 = J(\Delta l kT)^2/\sigma D_k$ is a parameter which is determined by the probability of the creation of a nucleus during the time $1/s_0$ in one microscopic interval Δl and is assumed to be small, and $\mathrm{erfc}(x) = (2/\sqrt{\pi})\int_x^\infty \exp(-t^2)\,dt$ is a supplementary probability integral.

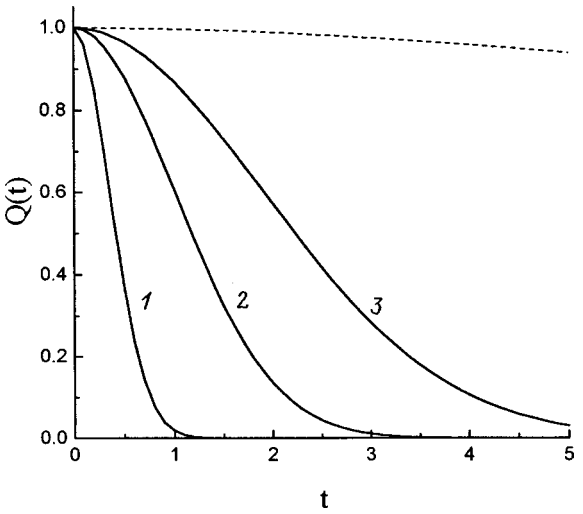

FIG. 1. Decay of the fraction in the initial state $Q(t)$ with time for various values of the driving force $F > F_c$, which is characterized by the parameter $\delta = kT/\sigma$: *1* — $\delta = 5$; *2* — 1.5; *3* — 1.1. The time is measured in units of $1/(s_0(\lambda)^{1/2})$. The switching kinetics for $\delta = 0.8$ ($F < F_c$) are shown as a dashed line for comparison.

Inverse Laplace transformation gives

$$\langle Q^\pm(t)\rangle = \exp\left(-\frac{\varepsilon}{2}s_0 J\Delta l t^2\right). \tag{10}$$

When $\Delta l = kT/F$, this expression can be rewritten in the form $\langle Q(t)\rangle = \exp\{-(1-(1/\delta))v_0 Jt^2/2\}$, where $v_0 = D_k F/(kT)$ is the free-drift velocity of the kinks. Thus, when $\delta \gg 1$, i.e., when the influence of the random addition to the potential in which a kink moves is small, the expression obtained is consistent with Kolmogorov's formula (1). [We recall that $\langle Q(t)\rangle = \langle q_0(t)Q^+(t)Q^-(t)\rangle$. In the case under consideration the characteristic switching time is small compared with the time for the formation of a nucleus in one interval, so that $q_0(t) \approx 1$ and $\langle Q(t)\rangle \approx \langle Q^\pm(t)\rangle^2$]. When $\delta \sim 1$, the equation retains the Kolmogorov form, but with renormalization of the kink velocity $v = (1-(1/\delta))v_0$. In this case the procedure for averaging the fraction in the initial state over the barrier spectrum reduces to the simple replacement of the kink velocity by its mean value.

Thus, in this region of parameters, the blocking of kinks by random barriers leads to a decrease in the mean kink velocity, which acquires a threshold type of dependence on the driving force. This is accompanied by appreciable slowing of the switching process, as is shown in Fig. 1. At a certain critical value of the driving force $F = F_c$, which is specified by the condition $\delta(F_c) = 1$, the mean kink velocity vanishes and the character of the kink motion changes. The region below the threshold calls for a special treatment.

2) $\delta < 1$. In this case the calculation gives

$$\hat{Q}(s) = t_a \exp((st_a)^{1+\delta})\Gamma\left(\frac{\delta}{1+\delta}, (st_a)^{1+\delta}\right). \tag{11}$$

Here

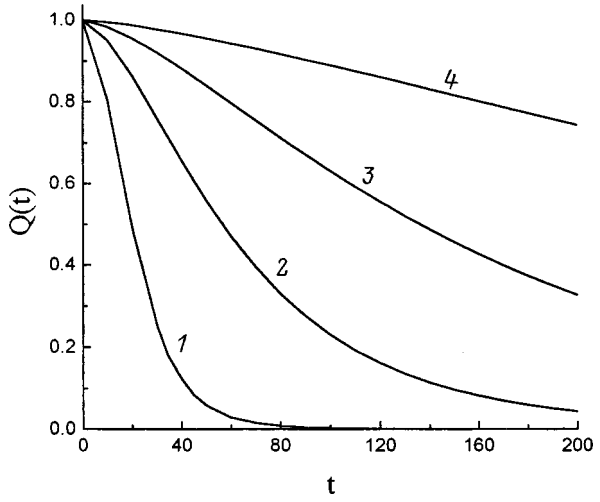

FIG. 2. State switching kinetics for a subthreshold value of the driving force: *1* — $\delta=0.8$; *2* — 0.6; *3* — 0.5; *4* — 0.4. The time is measured in units of $1/(s_0(\lambda)^{1/2})$, and $\ln(1/\lambda)=25$.

$$t_a=\frac{1}{s_0}\left[\frac{\Gamma(2-\delta)}{\Gamma(2+\delta)\lambda(1-\delta)}\right]^{\frac{1}{1+\delta}},$$

$$\Gamma(a,z)=\int_z^\infty x^{a-1}e^{-x}\,dx.$$

With consideration of the relation $\Gamma(1/2,x^2)=(\pi)^{1/2}\times\mathrm{erfc}(x)$ (Ref. 18), as $\delta\to1$, (11) takes the functional form (9), and inverse Laplace transformation leads again to the Kolmogorov dependence $\langle Q(t)\rangle=\exp(-\mathrm{const}\cdot t^2)$, but with a different coefficient in the exponential function than in the case of $\varepsilon>0$ (10) (the reason for such a jump will be discussed later on).

As can be seen from (11), the dependence of the averaged switching kinetics on λ appears only in the form of the scaling factor t_a. This will also be the case after inverse Laplace transformation: $\langle Q^{\pm}(t)\rangle=f_\delta(t/t_a)$, where $f_\delta(x)$ is a function which depends, apart from the argument, only on the single parameter δ. Using the asymptotic expansion of $\hat{Q}(s)$ (11) at small and large s, we can easily determine the explicit analytic behavior of $f_\delta(x)$ at large and small values of the argument:

$$f_\delta(x)\approx\frac{1+\delta}{\Gamma(1-\delta)}x^{-(1+\delta)},\quad x\to\infty, \tag{12}$$

$$f_\delta(x)\approx1-\frac{1}{(1+\delta)\Gamma(2+\delta)}x^{1+\delta},\quad x\to0. \tag{13}$$

Equations (12) and (13) give a fairly complete picture of the switching kinetics of the state of a linear system, which can be characterized by the mean fraction in the initial state $\langle Q(t)\rangle=\exp(-J\Delta lt)\langle Q^{\pm}(t)\rangle^2$. This behavior is illustrated in Fig. 2 (using a numerical calculation for intermediate values of $t\sim t_a$).

We see that the course of the switching process with time undergoes changes when δ drops below 1: the process slows significantly and goes over from a Kolmogorov exponential dependence like (1) to the power-law behavior described by (12) at large t.

3. SWITCHING TIME

An important integral characteristic of the kinetics of the alteration of the state of a system is the mean switching time, which can be defined by

$$\langle t\rangle=\int_0^\infty\langle Q(t)\rangle\,dt. \tag{14}$$

For $\delta>1$, using the explicit form of $\langle Q(t)\rangle$ (10) we obtain

$$\langle t\rangle=\int_0^\infty e^{-Jvt^2}\,dt=\frac{1}{2}\left(\frac{\pi}{Jv}\right)^{1/2}. \tag{15}$$

For $\delta<1$, the dependence of the mean time on t_a is isolated in an explicit form using scaling analysis, and we have

$$\langle t\rangle=C(\delta)t_a=C(\delta)\frac{1}{s_0}\left[\frac{\Gamma(2-\delta)}{\Gamma(2+\delta)\lambda(1-\delta)}\right]^{\frac{1}{1+\delta}}, \tag{16}$$

where $C(\delta)=\int_0^\infty f_0^2(x)\,dx$ is a function of δ, which varies in the relatively small range of values from 1 to $(\pi/2)^{1/2}$ as δ varies from 0 to 1. Its numerical approximation is $C(\delta)=1+((\pi/2)^{1/2}-1)x(2-x)$.

There is also definite interest in such a characteristic as t_1, i.e., the mean time for the ''unilateral blocking'' of a reference point by the boundaries of nuclei formed on one side of it. For example, because of the large difference between the mobilities of right- and left-handed kinks, the main contribution to the state switching process can be made by only the more mobile type of kinks. Such a situation is realized, in particular, in Si, where, according to the atomistic calculations in Ref. 19, the migration energies of right- and left-handed kinks are different. We have

$$t_1=\int_0^\infty\langle Q^{\pm}\rangle\,dt=\hat{Q}(s=0). \tag{17}$$

For $\delta<1$, as is seen from (11), $t_1=\Gamma(\delta/(1+\delta))t_a$. It follows from the functional Gaussian form of $\langle Q(t)\rangle$ for $\delta\to1$ that

$$\langle t\rangle=t_1/(2)^{1/2}=2^{-1/2}\hat{Q}(s=0). \tag{18}$$

The relation (18) permits a more exact description of the transition region $\delta\to1$. For $\varepsilon\ll1$ we have

$$\langle t\rangle=\frac{1}{\sqrt{2}s_0\lambda\varepsilon}\int_0^\infty dz\,(1-z^\varepsilon)\exp\left(-\frac{z^2}{2\lambda\varepsilon}(1-z^\varepsilon)\right)$$
$$\approx\left(\frac{1}{s_0}\right)\left(\frac{\pi(1-\lambda^{\varepsilon/2})}{4\lambda\varepsilon}\right)^{1/2}. \tag{19}$$

This expression describes the continuous transition from the region where $\varepsilon>0$ to the region where $\varepsilon<0$, smoothly transforming (15) into (16). It can be seen from (19) that the character of the dependence of the mean switching time on the driving force undergoes significant changes in the vicin-

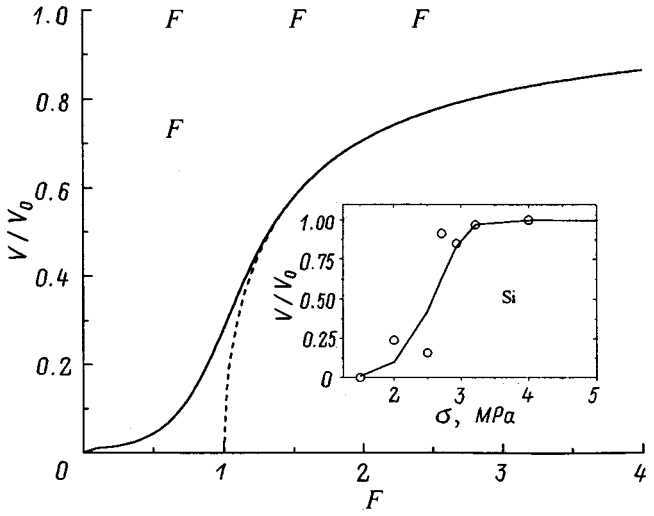

FIG. 3. Dependence of the state switching rate $V\sim 1/\langle t\rangle$ on the driving force F in the anomalous region at $F\sim F_c$. The rate V is normalized to V_0, i.e., the switching rate in the absence of blocking barriers, and F is measured in units of σ/kT.

ity of $\delta=1$ and that at $\varepsilon<0$ and $|\varepsilon|>1/\ln(1/\lambda)$ there is an exponential increase in $\langle t\rangle$ with ε: $\langle t\rangle\sim 1/\lambda^{\varepsilon/4}=\exp(|\varepsilon|\ln(1/\lambda)/4)$. The width of the transition region can be estimated as $\Delta|\varepsilon|\sim 2/\ln(1/\lambda)$, i.e., it is fairly narrow. Taking into account only the exponential Arrhenius factor $\exp(-2E_k/kT)$ in λ, where E_k is the kink energy (the energy of formation of the boundary between phases), we obtain $\Delta|\varepsilon|\sim kT/E_k\ll 1$ in a first approximation.

In problems concerning the motion of steps, domain boundaries, and dislocations, where the state of the system is multiply degenerate with a crystal-lattice period a in the absence of a driving force, $\langle t\rangle$ specifies the characteristic time for displacement by one period. This permits evaluation of the translational velocity V of the system under consideration in the presence of a driving force:

$$V\sim a/\langle t\rangle. \tag{20}$$

Figure 3 illustrates the nature of the dependence of the translational velocity on the driving force in the transition region $F\sim F_c$. This dependence has the form of a smoothed threshold. The inset presents experimental data on the mobility of individual dislocations in Si (Ref. 20).

4. DISCUSSION OF RESULTS

We have seen that the course of switching of the state of a disordered linear system changes significantly at a certain critical value of the driving force $F=F_c$. At $F>F_c$ it can be described by Kolmogorov kinetics with the kink drift velocity $v=(1-1/\delta)v_0$, which has been renormalized from the free drift velocity. This equation, which contains the threshold multiplier $1-1/\delta(F)$, already shows that the nature of kink motion changes radically when δ decreases to unity as the parameters of the problem, for example, F, are varied. As was established in Ref. 8, this is because the mean time for overcoming the barriers $\langle\tau\rangle=\int_0^\infty \tau P(\tau)\,d\tau$ goes to infinity as a result of the slow decay of the distribution function $P(\tau)$ at large τ for $\delta\leqslant 1$. As a result, the blocking of kinks begins to be determined not by the typical barriers along the entire sample, but by the few strongest barriers, which are encountered at the propagation length with a probability of order unity (heterogeneous blocking). An estimate of the variation of the kink propagation length with time can consequently be obtained from the relation $(x(t)/\Delta l)P_1(t)\sim 1$, whence, according to (8), follows formula (2) in the form $x(t)\sim t^{\delta}(\delta\leqslant 1)$ at large t.

To avoid any misunderstanding, we stress the conditional probabilistic character of this so-called nonlinear drift law. For example, if we attempt to generalize the Kolmogorov equation (1) by directly replacing the linear drift law $x(t)=vt$ by the relation (2) during the derivation, then Eq. (1) goes over to $Q(t)=\exp(-\text{const}\cdot t^{1+\delta})$, which is not confirmed by a more rigorous calculation [see Eq. (12)]. This attests to a significant contribution of the fluctuations in the distribution of the kink-blocking barriers to the switching kinetics, which requires accurate allowance for these fluctuations.

Thus, a calculation of the decay kinetics of a metastable state of a disordered linear system has revealed a transition from exponential Kolmogorov kinetics to diffuse kinetics with a power-law asymptote at large times as the driving force is lowered. This transition is caused by the change in the laws of kink soliton motion from drift which is homogeneous on the average with a finite velocity, to heterogeneous blocking by the strongest obstacles at the propagation length. The dependence of the mean state switching rate $V\sim 1/\langle t\rangle$ on the driving force F has been calculated. At $F>F_c$ this dependence has a threshold form, but in the narrow vicinity of F_c the threshold is smoothed, and at $F<F_c$ the rate V decays exponentially as the driving force decreases. Qualitatively similar behavior was observed in the experimental study of the mobility of dislocations in Si in Ref. 20 and can be associated with the influence of residual impurities.

This work was partially supported by INTAS Grant 96-363.

[1] T. Halpin-Healy and Y.-C. Zhang, Phys. Rep. **254**(4–6), 215 (1995).
[2] I. F. Lyuksyutov and V. L. Pokrovskiĭ, JETP Lett. **33**, 326 (1981)].
[3] A. A. Chernov, Usp. Fiz. Nauk **73**, 277 (1961) [Sov. Phys. Usp. **4**, 116 (1961)].
[4] J. P. Hirth and J. Lothe, *Theory of Dislocations* (McGraw-Hill, New York, 1967; Atomizdat, Moscow, 1972, 598 pp.).
[5] A. N. Kolmogorov, Izv. Akad. Nauk SSSR, Ser. Mat., No. 3, 355 (1937).
[6] R. K. Dodd, J. C. Eilbeck, J. Gibbon, and H. C. Morris, *Solitons and Nonlinear Wave Equations* (Academic Press, New York, 1982; Mir, Moscow, 1988, 694 pp.).
[7] V. Z. Belen'kiĭ, *Geometric Probability Models of Crystallization* (Nauka, Moscow, 1980), 88 pp.
[8] B. V. Petukhov, Fiz. Tverd. Tela (Leningrad) **13**, 1445 (1971) [Sov. Phys. Solid State **13**, 1204 (1971)].
[9] S. Alexander, J. Bernasconi, W. R. Schneider, and R. Orbach, Rev. Mod. Phys. **53**, 175 (1981).
[10] J.-P. Bouchaud and A. Georges, Phys. Rep. **195**(1), 127 (1990).
[11] J. W. Haus and K. W. Kerr, Phys. Rep. **150**(1), 263 (1987).
[12] V. M. Vinokur, J. Phys. (Paris) **47**, 1425 (1986).
[13] J.-P. Bouchaud and A. Georges, Comments Condens. Matter Phys. **15**(1), 125 (1991).
[14] B. V. Petukhov, Fiz. Tverd. Tela (St. Petersburg) **35**, 1121 (1993) [Phys. Solid State **35**, 575 (1993)].

[15] Yu. Iunin, V. I. Nikitenko, V. I. Orlov, and B. V. Petukhov, Phys. Rev. Lett. **78**, 3137 (1997).
[16] A. P. Kazantsev and V. L. Pokrovskiĭ, Zh. Éksp. Teor. Fiz. **58**, 677 (1970) [Sov. Phys. JETP **31**, 362 (1970)].
[17] N. G. Van Kampen, *Stochastic Processes in Physics and Chemistry* (North Holland, Amsterdam–New York–Oxford, 1981), 419 pp.
[18] *The Handbook of Mathematical Functions*, edited by M. Abramowitz and I. A. Stegun (Dover, New York, 1976; Nauka, Moscow, 1969, 830 pp.)
[19] V. V. Bulatov, in *Modelling of Structure and Mechanics of Materials from Microstructure to Product*, edited by J. N. Carstensen, T. Leffers, T. Lorentzen, O. B. Pedersen, B. F. Sorensen, and G. Winter (Riso National Laboratory, Roskilde, Denmark, 1998), p. 39.
[20] Yu. L. Iunin, V. I. Nikitenko, V. I. Orlov, and B. Ya. Farber, Zh. Éksp. Teor. Fiz. **100**, 1262 (1991) [Sov. Phys. JETP **73**, 1079 (1991)].

Translated by P. Shelnitz

Spatial correlation of impurity ions in solids

V. M. Mikheev*)

Institute of the Physics of Metals, Ural Branch, Russian Academy of Sciences, 620219 Ekaterinburg, Russia
(Submitted March 22, 1999)
Fiz. Tverd. Tela (St. Petersburg) **41**, 1994–1998 (November 1999)

A system of impurity ions in the same charge state at finite temperatures is studied. A theory describing the spatial correlations of impurity ions under conditions where the correlation radius of an impurity hole has an upper bound because of a deficiency of free impurity sites is proposed. An explicit expression for the pair-correlation function is obtained, and the influence of correlations in the positions of the impurity ions on the electron mobility in the limiting case of $T=0$ is considered. © *1999 American Institute of Physics.*
[S1063-7834(99)01811-0]

Effects associated with the spatial correlation of Fe^{3+} ions in HgSe:Fe have been studied extensively in the past 10 years.[1] In these materials ordering of the impurity ions is caused by the Coulomb interaction between the charged impurities. Nevertheless, when HgSe:Fe was studied, calculations of the correlations in the system of Fe^{3+} ions led to a short-range potential model.[2,3] The pair-correlation functions for Fe^{3+} were calculated in the hard-sphere model. Phenomenological equations containing a fitting parameter were used to determine the hard-sphere diameter. We propose a new approach to the problem of calculating correlations in a system of partially ionized impurities. In our calculation scheme the hard-sphere model is introduced on the basis of statistical arguments. Therefore, our proposed theory does not bear any relationship to the short-range potential model. The equation for determining the hard-sphere diameter does not contain a fitting parameter.

1. CORRELATION FUNCTIONS OF IMPURITY IONS

Let N be the concentration of sites (impurity centers) randomly arranged in space. The sites can be occupied by impurity holes, which can move from site to site. The concentration of impurity holes is N^+. In the case of $N/N^+=1$ the impurity holes are randomly arrayed in space. As N/N^+ increases, the holes are redistributed among the impurity sites and form a system of spatially correlated charges. Our goal is to calculate the correlation radius and to find the pair-correlation function of the impurity holes. In this study we identify the correlation radius r_c with the minimum distance between impurity holes.

We classify the states of our system in the following manner. From the system of holes we separate the subsystem of ''labeled'' sites, whose concentration equals the concentration of impurity holes N^+. We shall call any set of labeled sites comprising a subsystem a sample. There is obviously a one-to-one correspondence between the samples and the states in which a system of holes with a concentration N^+ distributed among sites with a concentration N can be found. Each sample corresponds to a possible state of the system of holes. Therefore, each sample represents a point in phase space, which is occupied by the system of impurity ions. One of the samples corresponds to the ground state of the system of holes. Such a description is complete. When we go over to an abridged description of our system, we make the following approximation. We systematically eliminate the regions of phase space which are energetically difficult to access, i.e., the regions of phase space in which the probability of finding our system is negligibly small.

In accordance with the program just described, we confine the treatment to only the samples in which the labeled sites are arranged as far from one another as possible, since holes tend to occupy just such configurations in order to minimize the repulsion energy. Let us consider the limiting case where $N^+/N\to 0$. In this limiting case we should clearly label the sites in such a manner that they would form a regular lattice. Then the nearest neighbors lie on the surface of the first coordination sphere of radius r_1. In this case the correlation radius $r_c=r_1$. The number of possible ways in which samples can be produced is equal to the number of possible types of three-dimensional lattices, and the corresponding values of the radius of the first coordination sphere r_1 allow us to distinguish between the possible sampling methods. We confine ourselves to considering only samples which lead to a regular lattice in the limit $N^+/N\to 0$.

Regular lattices of labeled sites can be organized only in the limit $N^+/N\to 0$. However, already in a small vicinity of this limiting point, only a few diffuse lattices of labeled sites can be organized, in which the nearest neighbors are arranged in a spherical layer next to the surface of the first coordination sphere at $r_c<r<r_1$. The lower boundary of the spherical layer r_c corresponds to the minimum distance between labeled sites in a sample for fixed values of N and N^+, and r_1 characterizes the way in which the sample is produced.

We use $W(N^+,r_c,r_1)$ to denote the probability of finding a site about which the nearest labeled sites lie in the spherical layer at $r_c<r<r_1$. The concentration of such sites equals $NW(N^+,r_c,r_1)$. If a label is placed only on such sites, the system of labeled sites thus obtained should satisfy the equality

$$N^+ = NW(N^+, r_c, r_1). \tag{1}$$

This equality permits the determination of the minimum distance between labeled sites r_c in a sample, if the concentrations of sites N and N^+ and the parameter r_1, which assigns the way in which the sample is produced, are fixed.

The probability $W(N^+, r_1, r_c)$ appearing in Eq. (1) can easily be calculated combinatorially. In fact, if the particles are randomly distributed, the probability W_N of finding a subsystem of N particles occupying a volume V in a system of N_0 particles occupying a volume V_0 can be obtained combinatorially and calculated from the equation[4]

$$W_N = \frac{N_0!}{N!(N_0-N)!}\left(\frac{V}{V_0}\right)^N\left(1-\frac{V}{V_0}\right)^{N_0-N}. \tag{2}$$

Setting $N=0$, $V=V_c$, $N_0=N^+V_1$, and $V_0=V_1$ (V_1 is the volume of the first coordination sphere) in this formula, we obtain the expression sought for $W(N^+, r_1, r_c)$:

$$W(N^+, r_1, r_c) = \left(1-\frac{V_c}{V_1}\right)^{N^+V_1}. \tag{3}$$

Substituting the expression obtained for $W(N^+, r_1, r_c)$ into Eq. (1), we arrive at the following expression for the correlation radius r_c:

$$(r_c/r_1)^3 = 1-(N^+/N)^{1/N^+V_1}. \tag{4}$$

Equation (4) is the result of our theory. It permits calculation of the minimum distance between labeled sites for fixed values of the concentration of sites N and the concentration of labeled sites N^+ in a sample corresponding to a fixed value of the radius of the first coordination sphere r_1. We recall that r_1 assigns the way in which the sample forms. In the case where r_1 corresponds to the close packing of hard spheres, our parameter r_c is the hard-sphere diameter, and the concentration of labeled sites N^+, which is equal to the concentration of impurity ions, is numerically equal to the concentration of hard spheres. In this special case calculations of the correlation functions describing the spatial distribution of the impurity ions in our samples at zero temperature reduce to calculations of the correlation functions describing a distribution of hard spheres.

In order to substantiate the possibility of identifying distributions of hard spheres with the spatial distributions of labeled sites in our samples, let us explore Eq. (4) in the limiting case of $N^+/N \to 1$. For this purpose we perform expansions in Eq. (4) in the parameter $(N-N^+)/N$ and write out the explicit expression for r_c

$$r_c^3 = \frac{3}{4\pi N^+}\left(1-\frac{N^+}{N}\right) \times\left[1+\frac{1}{2}\left(1-\frac{1}{N^+V_1}\right)\left(1-\frac{N^+}{N}\right)+\ldots\right]. \tag{5}$$

The first nonvanishing term in the expansion in (5) does not contain r_1. Thus, in the limit $N^+/N \to 1$ the parameter r_c does not depend on the way in which the sample is produced. Therefore, we can use any of these ways with equal success. One of them leads to the close packing of hard spheres in the limit $N/N^+ \to \infty$. Therefore, the use of the hard-sphere model to calculate the correlations of impurity ions is justified as long as variation of the parameter r_1 in Eq. (4) does not lead to a significant error in the calculation of the correlation radius r_c. Let us estimate these errors. In Eq. (4) the parameter r_1 appears in combinations which have a simple physical meaning. The ratio $(r_c/r_1)^3 = \eta/\eta_0$, where $\eta = \pi r_c^3 N^+/6$ is the packing fraction and $\eta_0 = \pi r_1^3 N^+/6$ is the value of the packing fraction for an assigned lattice with a fixed value of r_1. The product N^+V_1 characterizes the assigned lattice and is numerically equal to the number of sites within the first coordination sphere. The loosest of all the lattices, viz., the cubic lattice, has the values $\eta_0 = 0.523$ and $N^+V_1 = 4.18$ for the parameters. The most complete of all the lattices, viz., the face-centered cubic lattice, has the values $\eta_0 = 0.74$ and $N^+V_1 = 5.92$. Using these values for the parameters, we can estimate $\Delta\eta$, i.e., the spread of values taken by η as r_1 is varied. When $N/N^+ = 2\times10^2$ (when the concentration ratio is such, the iron atoms in HgSe:Fe form clusters) $\Delta\eta/\eta \approx 15\%$. All these estimates are illustrated in Fig. 1. The solutions of the fundamental equation (4) of our theory are depicted by curves *3*, *4*, and *5*, which correspond to the values of r_1 taken for fcc, bcc, and cubic structures, respectively. Curve *1* is a plot of calculated results from Ref. 2. Wilamowski *et al.* wrote down an equation for determining the hard-sphere diameter on the basis of common-sense arguments. This equation is valid only in the case of weak correlations ($\eta < 0.125$) but, even in its region of applicability, it overestimates the value of the packing fraction by roughly twofold. Kuleev[5] refrained from obtaining a microscopic description and wrote down a phenomenological equation containing a fitting parameter for calculating the

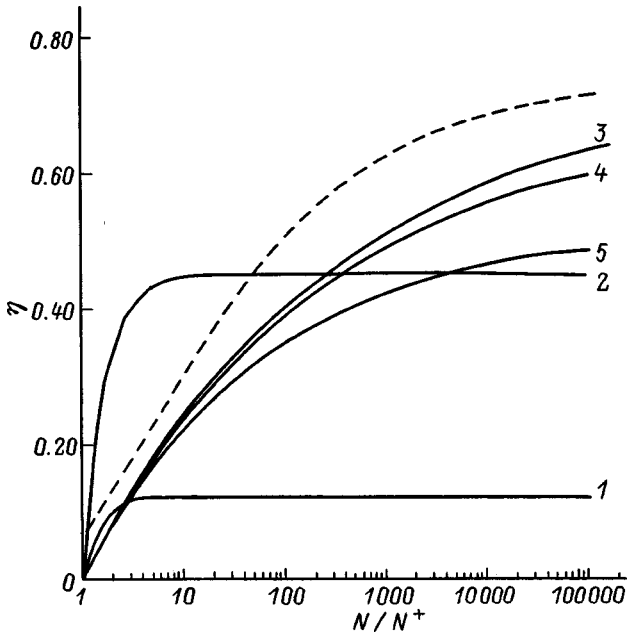

FIG. 1. Dependence of the packing fraction η on the ratio of the concentration of impurities N to the concentration of impurity ions N^+. Curves *1* and *2* depict the results of the calculations in Refs. 2 and 5. Curves *3*, *4*, and *5* were obtained from Eq. (4) with the values of η_0 and N^+V_1 taken for the fcc, bcc, and cubic structures, respectively. The dashed curve represents the upper bound for η ($N^+ = 5\times10^{18}\,\mathrm{cm}^{-3}$, η_0 was taken for the fcc structure).

packing fraction η. The value of that parameter was determined by fitting the electron mobility in specimens of HgSe:Fe (Ref. 6). The results of the calculations in Ref. 5 (curve *2*) correspond to extremely large values of the packing fraction η and are erroneous. The fact is that Eq. (3) in Ref. 6, which was used to determine the mobility, is incorrect. The expression for the interference term containing the product of the scattering amplitudes by charged and neutral centers in the form $2[(N_{Fe^{3+}}N_{Fe^{2+}})^{1/2}/N_{Fe}]|V_+(q)V_0(q)|S_{+0}(q)$ is erroneous. In the case of a random distribution of scatterers [where the structure factor $S_{+0}(q)=1$] the interference term takes the highest possible value, while the correct expression for interference[7] is equal to zero in this case. The use of an erroneous equation to determine the fitting parameter led Kuleev *et al.*[5,6] to excessively large values of η (curve *2*).

Since the calculations of the packing fraction η performed in different studies led to qualitatively different results, it would be instructive to estimate the value of η from the above and to compare the estimate with calculated results. The degree of order in a system of labeled sites is determined by the thickness of the spherical layer at $r_c<r<r_1$, within which the labeled sites are located. Since this spherical layer itself consists of impurity sites, the boundaries of this layer do not have distinct outlines, and, therefore, in our problem only the spherical layers whose thickness, in any case, is greater than the mean distance between impurity sites $\overline{r}$ have meaning. Equating the thickness of the spherical layer to the mean distance between sites, we obtain the maximum possible value of the correlation radius r_c in a system of labeled sites and, consequently, in a system of impurity ions, $\max r_c=r_1-\overline{r}$. In Fig. 1 the dashed curve is a plot of the maximum possible value of the packing fraction as a function of N/N^+. In these calculations we took the value of r_1 for the fcc structure, and the concentration of impurity ions N^+ was set equal to the concentration of impurity ions in HgSe:Fe ($N^+=5\times10^{18}\,\mathrm{cm}^{-3}$). Therefore, in this special case only situations in which the calculated values of the packing parameter η lie below the dashed curve are realized. This condition is satisfied by the results of the calculations performed in Ref. 2 (curve *1*) and the results of our calculations (curves *3–5*). As for the calculations in Ref. 5 (curve *2*), they lead to overestimated values of the packing parameter, which, in principle, cannot be realized specifically in the concentration range $1<N/N^+<20$, in which a correlation of the impurity ions is detected experimentally in HgSe:Fe. Therefore, the calculations in Refs. 5 and 6, whose results are represented by curve *2*, should be considered erroneous.

Thus, our theory was based on an abridged description of a system of impurity holes distributed among impurity sites. In the approximation that we adopted, each state of the system of impurity holes (impurity ions) is associated with a pair-correlation function $f(r_{c1},r)$, where r_{c1} is the hard-sphere diameter. In this approximation the states of the system of impurity holes are classified using r_{c1}, so that each state of our system has a corresponding value of r_{c1}. At finite temperatures the system can be found in any state which corresponds to a value of r_{c1} in the range $0<r_{c1}<r_c$. The parameter r_c is the maximum possible value of the hard-sphere diameter and is determined from the fundamental equation (4) of the theory. In each of the possible states the system has an energy $E(r_{c1})$, which is equal to the energy of a system consisting of neutral impurities, impurity ions, and conduction electrons calculated for a fixed distribution of impurity holes. This distribution of impurity holes is assigned by the pair-correlation function $f(r_{c1},r)$ with a fixed value of r_{c1}. The set of the correlation functions $f(r_{c1},r)$ and the corresponding energies $E(r_{c1})$ in the approximation which we chose contains the maximum possible amount of information on the system of impurity ions and permits calculation of the mean value of any quantity associated with the distribution of impurity ions.

At nonzero temperatures the system of impurity ions can be found in any of the possible states with a value of r_{c1} in the range $0<r_{c1}<r_c$. The probability of finding such a state is given by the Boltzmann factor $\exp(-E(r_{c1})/kT)$. Therefore, at finite temperatures, we should use the pair-correlation function $F(r_c,r,T)$ in the form

$$F(r_c,r,T)=\int_0^{r_c}dx\,f(x,r)\exp(-E(x)/kT)\times\left(\int_0^{r_c}dx\exp(-E(x)/kT)\right)^{-1}. \tag{6}$$

In the special case of $T=0$, the spatial distribution of the impurity ions is described by the pair-correlation function $f(r_c,r)$.

2. INFLUENCE OF THE SPATIAL CORRELATION OF IMPURITY IONS ON THE ELECTRON MOBILITY AT $T=0$

The differential cross section for the scattering of electrons by a system of spatially correlated scatterers $\sigma(q)$ (q is the scattering vector) is expressed in terms of the cross section for scattering by an individual center $\sigma_0(q)$ (Ref. 8):

$$\sigma(q)=\sigma_0(q)S(q). \tag{7}$$

The structure factor $S(q)$, in turn, is related to the Fourier transform of the pair-correlation function $f(r)$ describing the spatial distribution of the scatterers:

$$S(q)=1+N_r\int(f(r)-1)\exp(iqr)\,dr, \tag{8}$$

where N_r is the concentration of scatterers (in our case $N_r=N^+$). In the hard-sphere model the correlation function $f(r)$ calculated with consideration of the first two terms of the expansion in the density has the form[8]

$$f(r_c,r)=\begin{cases}0, & r^*<1,\\ 1+8\eta\left(1-\dfrac{3}{4}r^*+\dfrac{1}{16}r^{*3}\right), & 1<r^*<2,\\ 1, & r^*>2.\end{cases} \tag{9}$$

Here $r^*=r/r_c$. Let us consider the scattering of electrons by a screened Coulomb potential in the Thomas–Fermi model. In this model the electron mobility μ_0 for scattering by un-

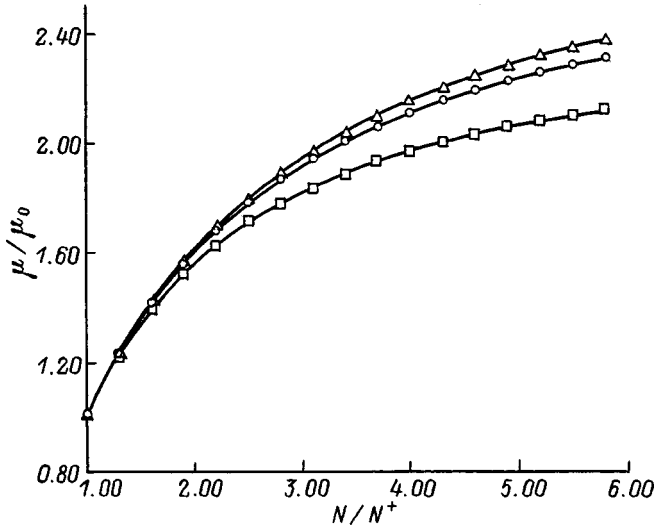

FIG. 2. Dependence of the electron mobility μ on the relative concentration of ionized impurities; μ_0 is the mobility calculated from the Brooks–Herring equation. The calculated curves were obtained for the values of r_1 corresponding to the fcc (triangles), bcc (circles), and cubic (squares) structures.

correlated centers is described by the Brooks–Herring formula.[9] The ratio of the mobility μ, for the scattering of electrons by a spatially correlated distribution of charges, to μ_0 can be written, according to (7), in the form

$$\frac{\mu}{\mu_0}=\int_0^{2k_F}\frac{q^3\,dq}{[q^2+q_s^2]^2}\Bigg/\int_0^{2k_F}\frac{S(q)q^3\,dq}{[q^2+q_s^2]^2}, \tag{10}$$

where the screening radius in the Thomas–Fermi model $r_{TF}=q_s^{-1}$.

Equations (8)–(10) permit calculation of the mobility ratio μ/μ_0, if the value of the screening parameter q_s, the hard-sphere diameter $d=r_c$, and the concentration of ions N^+ are known. Using Eq. (4) for the correlation sphere radius r_c, we can calculate the mobility ratio as a function of N/N^+. The Thomas–Fermi screening radius was calculated using the parameters characteristic of HgSe:Fe ($N^+=5\times10^{18}\,\mathrm{cm}^{-3}$, a Fermi energy $\varepsilon_F=210\,\mathrm{meV}$, and a dielectric constant $\chi=20$). The results of numerical calculations of the dependence of the electron mobility on impurity concentration are presented in Fig. 2. As follows from it, the mobility increases by 2–2.5 fold when the concentration ratio N/N^+ varies from 1 to 6. The highest mobility value (and, accordingly, the largest value of the packing fraction η) corresponds to the state of the system impurity ions in the case of the value of r_1 taken for the fcc structure. The smallest increase in mobility is obtained for the value of r_1 corresponding to the cubic structure. At relatively small values of N/N^+ the changes in mobility occurring in response to the variation of r_1 are relatively small. This circumstance renders the choice of the values of r_1 insignificant over a fairly broad range of variation of the values of N/N^+, justifying the use of Eq. (4) for determining r_c.

In conclusion, let us discuss the range of applicability of our theory. The fundamental equation (4) of the theory is valid only in the range of variation of N/N^+ where a shortage of free sites restricts the value of the correlation radius. This range can be estimated in the following manner. In a system of impurity ions the value of the correlation radius cannot be greater than the distance over which the screened Coulomb interaction is nonzero. Therefore, the estimate $\max r_c=r_s$, where r_s is the screening radius, is valid. The ensuing estimates are made for a material with the parameters of HgSe:Fe. Substituting the value of the screening radius calculated in the Thomas–Fermi model into the expression for the packing fraction instead of r_c, we obtain the maximum possible value of the packing fraction $\eta=0.45$. According to our calculations (see Fig. 1), such a value of η can be achieved only in the case of a very large number of free impurity sites $N/N^+=2\times10^2$. Correlation effects are manifested in HgSe:Fe only in the range of variation of the concentration $1<N/N^+<10$ (at higher impurity concentrations drift scattering dominates).[3] Thus, our estimate shows that, at least in the case of HgSe:Fe, under conditions for which correlation effects are observed, the value of the correlation radius is restricted by the deficiency of impurity sites and should be determined from Eq. (4) of our theory.

*)E-mail: mikheev@imp.uran.ru

[1] I. M. Tsidilkovski, *Electron Spectrum of Gapless Semiconductors*, Springer Series in Solid State Sciences, Vol. 116 (Springer, Berlin–New York, 1996).
[2] Z. Wilamowski, K. Swatek, T. Dietl, and J. Kossut, Solid State Commun. **74**, 833 (1990); Z. Wilamowski, Acta Phys. Pol. A **77**(1), 133 (1990).
[3] I. M. Tsidilkovski and I. G. Kuleev, ''Spatial correlations of impurity charges in gapless semiconductors,'' Semicond. Sci. Technol. **11**, 625 (1996).
[4] L. D. Landau and E. M. Lifshitz, *Statistical Physics, Vol. 1*, 3rd. ed. (Pergamon Press, Oxford–New York, 1980; Nauka, Moscow, 1976, Part 1, p. 378).
[5] I. G. Kuleev, Fiz. Tverd. Tela (St. Petersburg) **39**, 250 (1997) [Phys. Solid State **39**, 219 (1997)].
[6] I. G. Kuleev, I. Lyapilin, and I. M. Tsidil'kovskiĭ, Zh. Éksp. Teor. Fiz. **102**, 1652 (1992) [Sov. Phys. JETP **75**, 893 (1992)].
[7] J. M. Ziman, *Models of Disorder: the Theoretical Physics of Homogeneously Disordered Systems* (Cambridge University Press, Cambridge–New York, 1979; Mir, Moscow, 1982).
[8] R. Balescu, *Equilibrium and Nonequilibrium Statistical Mechanics*, Vol. 1 (Wiley, New York, 1975; Mir, Moscow, 1978, 405 pp.).
[9] F. J. Blatt, *Physics of Electronic Conduction in Solids* (McGraw-Hill, New York, 1968; Mir, Moscow, 1971, 470 pp.).

Translated by P. Shelnitz

Deformation of alkali-metal halide crystals by a concentrated load

Z. K. Saralidze, M. V. Galustashvili, and D. G. Driyaev

Institute of Physics, Georgian Academy of Sciences, 380077 Tbilisi, Georgia
(Submitted February 10, 1999; resubmitted April 1, 1999)
Fiz. Tverd. Tela (St. Petersburg) **41**, 1999–2003 (November 1999)

The parameters characterizing the effect of a concentrated load on crystals subjected to various preliminary treatments and their possible relationship to the mechanical characteristics manifested during ordinary (one-dimensional) deformation are investigated. The significant upward deviation of the microhardness from the values of the elastic limit and yield strength of crystals is shown to be caused not so much by the larger values of the strain under an indenter as by the larger value of the strain hardening coefficient in the case of deformation by a concentrated load. It is also shown that the types of hardening caused by uniaxial deformation and by reactor irradiation influence the microhardness of LiF crystals differently. © *1999 American Institute of Physics.* [S1063-7834(99)01911-5]

The method of applying a concentrated load to a crystal (imposing a hard indenter and then measuring the size of the impression formed) is widely employed for investigating the mechanical properties (microhardness) of solids. The conditions for deformation of a crystal under an indenter differ significantly from the conditions for deformation under a uniform load, and the mechanisms of deformation and mass transfer in the contact region between an indenter tip and a crystal, where the largest stresses are displayed, have not yet been ascertained reliably. Theories regarding the state of the material in the region of the indenter impression, where the strain amplitude should be considerably greater than in the case of uniaxial compression or elongation of crystals, have been developed. In the opinion of some investigators, the strain appearing upon indentation is caused by the development of a high-density dislocation structure under an indenter,[1–3] while others believe that mass transfer is caused by an interstitial (crowding) mechanism.[4–6] There are opinions that a finely dispersed nanocrystalline state forms under an indenter[7] or that all the processes occurring upon indentation are caused by phase transformations.[8]

Thus, we see that, since there is no unanimously accepted, fully developed theory regarding the mechanism of the formation of an impression upon indentation, it is difficult to assign a clear and unequivocal physical meaning to the microhardness, as well as to relate it to (or at least find a correlation with) any ordinary mechanical characteristic.[9,10]

The purpose of the present work is to reveal relationships between the processes occurring under an indenter and the processes accompanying deformation upon uniaxial compression and to determine the mechanical characteristics that appear in the case of ordinary deformation and are closest to the microhardness or determine it.

1. EXPERIMENTAL METHODS

Crystals of LiF were investigated. The samples were subjected to local deformation using a PMT-3 machine. The indent was made by a diamond indenter on the (001) cleavage plane. The indenter had the form of a pyramid with a square base and an angle between the faces equal to 136°. All the parameters of the dislocation rosette around the indenter impression were measured: the length of the diagonal (d) and height (h) of the impression, the lengths of the edge (l_1) and screw (l_2) dislocation rays, and the radius of the most highly strained region with the maximum dislocation density (l_3).

The minimum load on the indenter was 5×10^{-4} N, and the maximum load was 4 N.

Crystals (or regions of a crystal) with different strength and plastic characteristics were obtained by subjecting samples of LiF to the following treatments: uniaxial compression to different degrees of strain (the maximum degree of strain was 15%); irradiation in a nuclear reactor by mixed n,γ radiation with fluences up to 10^{14}, 10^{15}, and 10^{16} n/cm^2 (with respect to the fast neutrons); preliminarily formation of an indent by the indenter under a large load.

The dependences of the indenter impression and the dislocation rosette around it on the size of the load and the dependence of the parameters corresponding to an assigned load on the degree of preliminary strain of the crystal were investigated. In addition, the dependences of the dimensions of the impressions obtained with comparatively small loads (0.01, 0.05, and 0.1 N) on the distance to the center of the preliminary indent obtained upon indentation under large loads (1 and 2 N).

2. EXPERIMENTAL RESULTS AND DISCUSSION

The ratio of the load P on the indenter to the square of the length of the diagonal $d(P)^2$ of the impression relaxed after removal of the load,

$$H(P)=\frac{\alpha P}{d(P)^2}, \tag{1}$$

depends on load in the general case ($\alpha=1.854$ in SI units). At fairly large loads $d(P)^2$ is proportional to P, and $H(P)=H_m$ becomes independent of load and can serve as

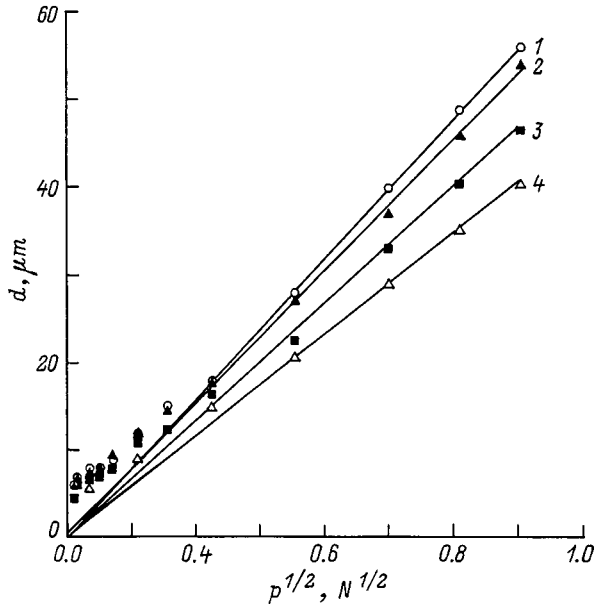

FIG. 1. Dependence of the length of the diagonal d of a relaxed impression on the load P for an untreated LiF crystal (*1*) and crystals irradiated with doses equal to 10^{14} (*2*), 10^{15} (*3*), and 10^{16} (*4*) n/cm^2.

one of the characteristics of the mechanical properties of the crystals (the microhardness). Clearly, H_m differs weakly from the ratio (1) for an unrelaxed impression and corresponds to the level of maximum strain hardening of the crystal established under the indenter σ_m.

At comparatively small loads, where $H(P)$ depends on P, the degree of strain of the material in the region directly adjacent to the indenter decreases with decreasing load. Accordingly, the level of strain hardening of the crystal achieved and the pressure developed by the indenter should decrease. In other words, $H(P)$ should decrease with decreasing P. As for the cases of an increase in the ratio (1) with decreasing load at very small loads, such increases should be associated with an increase in the relative role of elastic relaxation in diminishing the dimensions of the impression upon relaxation, rather than with features of the strain hardening process, as conjectured by Pethica *et al.*[11] In our experiments no increase in $H(P)$ was observed when the load was diminished to 5×10^{-4} N.

Figure 1 shows plots of the dependence of the length of the diagonal of relaxed impressions on the square root of the load for four LiF crystals: an untreated crystal and crystals irradiated in a reactor with doses equal to 10^{14}, 10^{15}, and 10^{16} n/cm^2. It is seen from the figure that these plots are generally nonlinear. Linearity, which corresponds to load-independent microhardness, is observed only at loads equal to 0.5 N or more.

It follows from Fig. 1 that $H(P)$ reaches a level which is independent of P at loads greater than 0.5 N, that it drops sharply with decreasing P in the range $0.5-0.01$ N, and that the rate of this drop slows at $P<0.01$ N.

The fact that $H(P)$ becomes independent of P and thus of $d(P)$ at large loads indicates that any material is characterized by a certain maximum possible strain amplitude ε_m and a maximum possible level of strain hardening $\sigma_m=H_m$ associated with it. Above these values the crystal cannot be deformed. If ε_m and σ_m have already been achieved under the indenter, only the volume of the region where the maximum values ε_m and σ_m have already been achieved can increase as the load is increased further.

In regard to the distinguishing features of the deformation process under a concentrated load as opposed to deformation under uniaxial compression, two more points should be noted. First, in the region of maximum strain under the indenter the strain is far more uniform than in the case of uniaxial compression, where dislocation glide bands, in which the bulk of the strain is concentrated, adjoin the unstrained regions and the characteristics averaged over the volume can differ strongly from the local characteristics. Second, attention should be focused on the fact that when an indenter is impressed on a crystal, deformation occurs in a restricted volume (the stresses decrease rapidly with increasing distance) even under crowded conditions. Therefore, the crystal can withstand high levels of local strains and stresses without failure.

For comparison, Table I lists all the principal mechanical characteristics which we measured for ordinary deformation (uniaxial compression) and parameters characterizing local deformation caused by an indenter under a load of $P=0.5$ N for four crystals: an untreated crystal and crystals irradiated by mixed n,γ radiation in a reactor (10^{14}, 10^{15}, and 10^{16} n/cm^2), which differ from one another with respect to their mechanical properties.

According to some data, alkali-metal halide crystals doped with divalent impurities exhibit a good correlation between the changes in the yield strength σ_0 and the micro-

TABLE I. Principal mechanical characteristics of the LiF crystals investigated.

No.	Parameter	Untreated	Irradiated by 10^{14} n/cm^2	Irradiated by 10^{15} n/cm^2	Irradiated by 10^{16} n/cm^2
1	Yield strength σ_0, MPa	7	82	130	148
2	Ultimate strength σ_n, MPa	68	98	135	150
3	Max. strain ε_c, %	15	10.2	3.5	1.6
4	Impression diagonal d, μm	28	27	23.5	20
5	Microhardness H_m, MPa	1180	1270	1710	2280
6	Length of the ''screw'' dislocation ray l_2, μm	98	63	25.0	15
7	Length of the ''edge'' dislocation ray l_1, μm	163	105	47.4	20.5

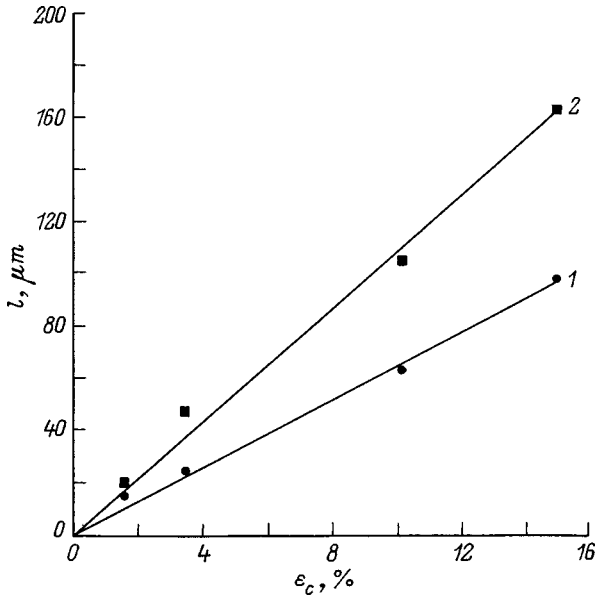

FIG. 2. Dependence of the length l of the ''screw'' (*1*) and ''edge'' (*2*) rays of the dislocation rosette on the maximum strain ε_c of a LiF crystal under uniaxial deformation.

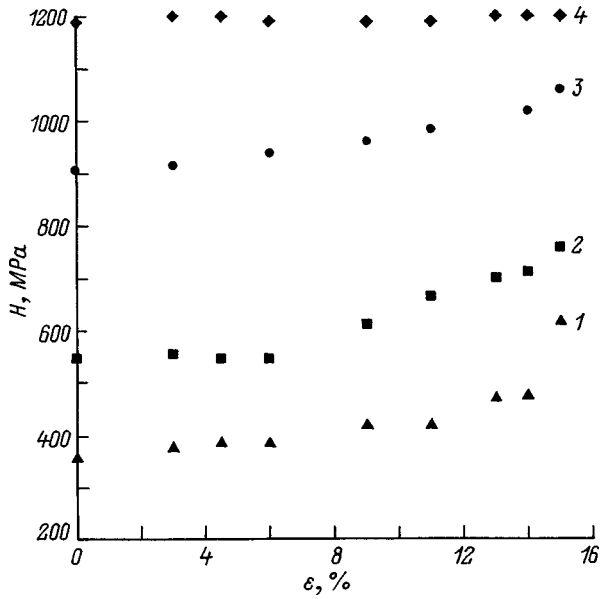

FIG. 3. Dependence of $H(P)$ on the preliminary strain ε (uniaxial compression) for loads equal to 0.03 N (*1*), 0.05 N (*2*), 0.15 N (*3*), and 0.5 N (*4*).

hardness H_m (Refs. 12–15), which can be described by the formula

$$\sigma_0 = \beta(H - H_0), \tag{2}$$

where β and H_0 are constants. Vasauskas[16] proposed relating the microhardness to the deforming stress causing a 10% strain. At first glance, it is also reasonable to assume that the microhardness, which, as was noted above, is the maximum achievable level of strain hardening, correlates with the ultimate strength, i.e., with the maximum stress which the crystal can withstand without failure during uniaxial loading. However, as can easily be verified, the data presented in Table I cannot be described by Eq. (2). The relationship between the microhardness and the stresses characterizing the uniaxial deformation of a crystal is significantly nonlinear. It seems to us that if a linear relationship would exist, it would have the form $H_m = C\sigma_m$, rather than (2), since it is totally unreasonable that it would be represented by the quantity H_0, which, accordingly to formula (2), should have the physical meaning of the microhardness for a zero ultimate strength (either the yield strength or the deforming stress). Thus, in our opinion, such correlations can only be accidental, and no importance should be attached to them. Moreover, since the microhardness significantly surpasses the strength characteristics of the crystal in all cases and the processes determining them differ radically from one another, there is most probably no sense in searching for a direct relationship between these quantities.

The only correlation which is reliably displayed and can be understood from the physical standpoint is the correlation between the lengths of the dislocation rays and the plasticity of the crystal: the more plastic the crystal is, the greater are l_1 and l_2. Moreover, this relationship can be described to fairly good accuracy by a dependence of the form $l = C\varepsilon_c$ (Fig. 2), where ε_c is the maximum strain which the crystal can withstand under uniaxial compression, and the coefficients C_1 and C_2 are equal to 11.2 and 6.8 μm/%.

As follows from Fig. 1, the values of $H(P)$ for the crystals irradiated by different doses differ significantly from one another and from the values obtained for unirradiated crystals, i.e., for any load on the indenter $H(P)$ depends strongly on the preliminary treatment of the crystal. In this connection it would interesting to investigate the function $H(P)$ for crystals subjected to preliminary uniaxial deformation to different levels of strain hardening. These investigations show (Fig. 3) that at loads $P \geqslant 0.5$ N the value of H_m does not depend at all on the strain amplitude, while $H(P)$ increases quite appreciably at $P \leqslant 0.2$ N, although it does not reach H_m even at a 15% strain (the maximum uniaxial strain which the crystals investigated can withstand without failure). It is seen from the results of these investigations that the maximum possible strain under the indenter ε_m, which corresponds to a maximum strain hardening equal to H_m, should significantly surpass the maximum achievable degree of strain for uniaxial compression ε_c (15%). However, if deformation under an indenter would take place according to the same mechanism as in the case of uniaxial compression, and, if it would have the same character and the same value of the strain hardening coefficient, the strain amplitude needed for local hardening of the crystal to the observed microhardness value ($H_m \geqslant 1200$ MPa) would be 300% or more, which by no means can correspond to reality. Therefore, the strain hardening coefficient must also be much larger in the case of deformation under an indenter than in the case of deformation of the crystal by uniaxial compression.

Stress-strain diagrams show that the crystals investigated are hardened linearly under uniaxial compression. Therefore, the yield strength of the preliminarily deformed crystals increases linearly with increasing strain amplitude. Consequently, plots of the dependence of $H(P)$ on the strain amplitude should be exact copies of the plots of its dependence

on the yield strength (the corresponding values of the deforming stress) of the preliminarily deformed crystals. It is seen from Fig. 3 that $H(P)$ exhibits a patently nonlinear dependence on the yield strength of the preliminarily deformed crystals and that H_m (curve *4*) does not depend on it. It should also be noted that, although the yield strengths of the crystals preliminarily deformed to different degrees differ quite considerably from one another (σ_0 varies from 7 to 68 MPa), the values of the microhardness H_m for them are identical, i.e., 15% preliminary strain with almost tenfold strain hardening has no effect whatsoever on the microhardness, while hardening caused by reactor irradiation leads to a significant increase in the microhardness (see Table I). Thus, strain hardening and radiation hardening are reflected in totally different ways in the microhardness of LiF crystals.

It should be specially stressed that $H(P)$ significantly exceeds the yield strength of the crystals investigated at all the values of the loads used in the experiments. For example, even at such a small load as $P=0.01$ N, we have $H_m=270$ MPa, which greatly surpasses the yield strength $\sigma_0=68$ MPa of the strain-hardened ($\varepsilon=15\%$) crystal. Therefore, it is clear that in each case the measured value of $H(P)$ is the maximum deforming stress which is achieved as a result of the strain hardening accompanying the deformation caused by the indenter forces.

When an indent is created under a large load, a strained region in which the strain hardening is maximal (the region within the impression and near it) forms under the indenter, and strain hardening should decrease fairly rapidly with increasing distance from the center of the impression.

The method described in Ref. 15 was employed to establish the nature of this dependence. A preliminary impression was created on a (001) face by a large load $P_0=1$ N. The value of $H(P)$ as a function of the distance x to the center of the preliminary impression was then measured under small loads along $\langle 110\rangle$ directions, which are perpendicular to the sides of the impression.

Figure 4 presents plots of the dependence of $H(P)$ on the distance x for three load values $P=0.01$, 0.05, and 0.10 N. As can be seen from the figure, in all three cases the value of $H(P)$ measured using the small load approaches the value of H_m corresponding to the maximum level of strain hardening σ_m as the center of the preliminary indent is approached, whereas it approaches the value in the unstrained region as the distance from the center increases. It should also be noted that, in complete agreement with the arguments presented above, if secondary indents are made under the same load P_0 that was used to make the primary indent, no dependence on the distance to the center of the preliminary indent is observed.

These results unquestionably support our conclusion that H_m is, in fact, the maximum value of the stress to which the particular crystal is capable of being hardened, and the ascending portions of the plots presented in Fig. 4 (for approach toward the center of the primary indent) should reflect the dependence of the level of the stress achieved as a result of strain hardening under the indenter on the distance to the center of the indent, i.e., $\sigma_D(x)$. It is seen from these results that the region where the maximum strain ε_m and the maximum level of strain hardening σ_m are achieved comprises a small part of the strained region and that its linear dimensions only slightly exceed the dimensions of the relaxed mark from the indenter.

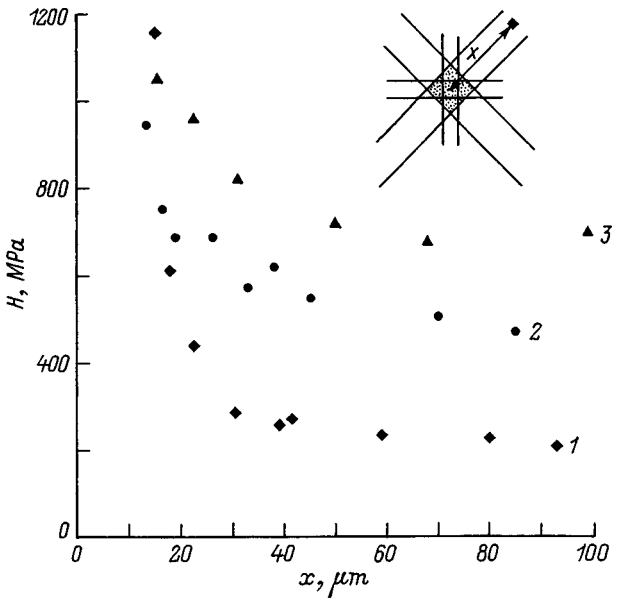

FIG. 4. Dependence of $H(P)$ on the distance x to the center of the preliminary impression formed by the load $P_0=1$ N for LiF crystals and loads equal to 0.01 N (*1*), 0.05 N (*2*), and 0.1 N (*3*).

The following steps were taken to discover the possibility of obtaining the explicit form of $\sigma_D(x)$. Secondary indents were made by the smallest possible load near indenter impressions obtained under different loads. This made it possible to obtain the dependence of the value of $H(P)$ corresponding to the small load on the values of $H(P_0)$ corresponding to the preliminary application of the indenter under different loads (i.e., on the levels of the deforming stresses achieved under the indenter). By comparing plots of $H(P)$ versus x similar to those shown in Fig. 4 with the plots of $H(P)$ versus $\sigma_D(P)$ obtained by the method just described, we can reconstruct the explicit form of $\sigma_D(x)$. Unfortunately, at the small loads suitable for reproducing this dependence, the measurement accuracy in our experiments was insufficient. Therefore, although we are confident of the fundamental soundness of this procedure, we shall not present the results obtained.

As we have already noted, the high values of the deforming stress under the indenter are caused by the high values of the strain hardening coefficient, which can greatly exceed the analogous coefficient for uniaxial deformation, rather than by the high strain amplitudes under the indenter.

In the case of uniaxial compression, strain develops in an ionic crystal according to the following scheme: narrow glide bands first form in a system which is oriented most advantageously relative to the load axis and randomly turns out to be the weakest among them. Then the crystal deforms as a result of the contraction and expansion of the bands formed until they overlap. Strain hardening occurs at this point with a not very large coefficient. By the stage in which other systems could begin to operate, the original system is

so filled and hardened that the crystal fails when other systems intersect the original system (the strain is strongly nonuniform among glide systems of different orientation).

The picture under an indenter is different. Here, because of the complexity of the stressed state and the large magnitude of the initial stresses, all the intersecting glide systems can begin to operate simultaneously, causing a high strain hardening coefficient and high levels of deforming stresses at comparatively low strain amplitudes. As has been noted previously, the ability of a crystal to withstand high stresses can be due to the restricted size of the strained volume, which is confined by the unstrained crystal surrounding that region. Knowledge of the strain amplitude (or at least its scale) of the crystal under the indenter is needed to establish the true value of the strain hardening coefficient.

This work was carried out with financial support from the Georgian Academy of Sciences (Grant No. 2.15).

[1] M. P. Shaskol'skaya, Wang Yang-Wen, and Ku Shu-Chao, Kristallografiya **6**, 277 (1961) [Sov. Phys. Crystallogr. **6**, 216 (1961)].
[2] A. A. Predvoditelev, V. N. Rozhanskiĭ, and V. M. Stepanova, Kristallografiya **7**, 418 (1962) [Sov. Phys. Crystallogr. **7**, 330 (1962)].
[3] Yu. S. Boyarskaya, *Deformation of Crystals in Microhardness Testing* (Kishinev, 1972), 235 pp.
[4] V. L. Indenbom, JETP Lett. **12**, 369 (1970).
[5] V. L. Indenbom and A. N. Orlov, Fiz. Met. Metalloved. **43**, 469 (1977).
[6] Yu. I. Golovin and A. I. Tyurin, JETP Lett. **60**, 742 (1994).
[7] M. Sh. Akchurin and V. G. Galstyan, Poverkhnost', No. 3, 119 (1983).
[8] I. V. Grindina, Yu. V. Milman, and V. I. Trefilov, Phys. Status Solidi A **14**, 177 (1972).
[9] L. G. Tsinzerling, *Advances in the Field of Microhardness Testing* (Moscow, 1974), p. 86.
[10] Yu. S. Boyarskaya, *Current Topics in the Physics of Microindentation* (Kishinev, 1989), p. 3.
[11] J. B. Pethica, R. Hutchings, and W. S. Oliver, Philos. Mag. A **48**, 593 (1983).
[12] G. Y. Chin, L. G. Van Vitert, M. L. Green, and S. Zydzik, Scr. Metall. **6**(6), 50 (1972).
[13] Yu. S. Boyarskaya, R. P. Zhitaru, M. S. Kats, M. A. Linte, and S. S. Shutova, Fiz. Khim. Obrab. Mater., No. 6, 75 (1981).
[14] Yu. S. Bojarskaja, R. P. Zhitaru, and M. A. Linte, Cryst. Res. Technol. **19**(1), 101 (1986).
[15] Yu. S. Boyarskaya, D. Z. Drabko, and M. S. Kats, *Physics of Microindentation Processes* (Kishinev, 1986), 294 pp.
[16] S. S. Vasauskas, *Research in the Field of Hardness* (Moscow–Leningrad, 1967), p. 33.

Translated by P. Shelnitz

Dislocation motion in NaCl crystals under combined loading by electron-beam-produced mechanical and electromagnetic pulses

V. I. Al'shits, E. V. Darinskaya, and M. A. Legen'kov

Institute of Crystallography, Russian Academy of Sciences, 117333 Moscow, Russia

V. A. Morozov

St. Petersburg State University, 198904 St. Petersburg, Russia
(Submitted November 4, 1999; resubmitted April 14, 1999)
Fiz. Tverd. Tela (St. Petersburg) **41**, 2004–2006 (November 1999)

A study is reported of the effect of a pulsed electromagnetic field on edge dislocation mobility in NaCl crystals under mechanical loading by an electron beam. It is shown that taking this effect into account removes the discrepancy in determination of the dislocation dynamic damping coefficient by two methods, namely, with an electron beam and by mechanical impact loading. © *1999 American Institute of Physics.* [S1063-7834(99)02011-0]

Investigation[1] of edge-dislocation mobility in LiF and NaCl crystals under a pulsed mechanical loading produced by an electron beam revealed that the corresponding dynamic damping coefficient B for NaCl crystals is 4.5 times smaller than that measured[2] under mechanical impact loading. At the same time, for LiF the damping coefficient B was found to agree within experimental error with impact experiments.

A study of the nature of this discrepancy led one to a discovery of dislocation motion in NaCl crystals in a pulsed magnetic field.[3] It appeared natural to assume that the dislocation motion in the NaCl experiments[1] was induced not only by the mechanical forces generated by electron-beam interaction with the target but also by the electromagnetic field of the beam itself.

This paper describes an experimental separation of the two above effects and demonstrates their additive nature. It was found that the dynamic component of the pathlength of dislocations associated with their cross-barrier motion under the action of a short and intense mechanical pulse results in a damping coefficient B which coincides with the value measured earlier[2] by a radically different technique. The independently measured dislocation pathlength component induced by an electromagnetic pulse in a sample is of considerably larger interest. This component is associated with the subsequent fairly slow relaxation of the dislocation structure as a result of lowering local impurity barriers in the bulk of the crystal, caused by resonance spin-dependent transitions by the mechanism described in Ref. 4.

The pulsed magnetic field of the electron beam and the dislocation motion were measured as described elsewhere[1] (Fig. 1). In studies of dislocation motion, the sample was housed in a chamber of a diamagnetic material (Al) and, thus, could be acted upon by a magnetic field. The mechanical pulse was excited by an electron beam in an aluminum plate serving as the chamber front wall and was transmitted to the sample. The sample was in an acoustic contact with the plate through a thin layer of silicone oil. When the acoustic contact with the plate was removed, one could study the effect on the crystal of the electromagnetic field only. No dislocation motion was observed in control experiments with the sample placed in a chamber made of a ferromagnetic material. A possibility was also provided of acting on the sample with a mechanical pulse only. In this case the sample was placed in a steel chamber, whose front wall was irradiated with an electron beam that generated a mechanical pulse transmitted to the sample. The duration of such a pulse in the experiments was varied within a narrow range and was about $\sim 5\times 10^{-8}$ s (curve *1* in Fig. 2). By properly controlling the beam current, the pulse amplitude could be varied within a factor of 1.5.

The magnetic field in the chamber that housed previously the NaCl sample was measured with a ferrite-core coil. The coil was loaded by a 50-Ω resistance. The coil output was fed to a C1-75 high-frequency oscillograph and photographed subsequently. An oscillogram of the signal is presented in Fig. 2 (curve *2*). To determine the field induction, the coil was calibrated properly. The 100-ns calibrating voltage pulses were supplied over a coaxial line loaded by the wave resistance. The coil was placed at a fixed distance from the line core, and it is there that the voltage induced in it was measured. In this way one established the dependence of the coil voltage on field induction $U=f(B)$. When studying the dislocation motion, the beam current was monitored, so that one could determine the magnetic component of the field induction $B=kI$, where $k=4.5\times 10^{-9}$, and all quantities are assumed to be expressed in the SI system. In our experiments, the magnetic induction varied within the range $B=(7-11)\times 10^{-6}$ T.

Figure 3 presents the dependence of the mean free path of dislocations in NaCl crystals on magnetic-field induction and electron-beam current in the absence of mechanical action. The width of the magnetic induction pulse, controlled by the beam current length, was $\sim 30\times 10^{-8}$ s (curve *2* in Fig. 2), which is substantially longer than the duration of the

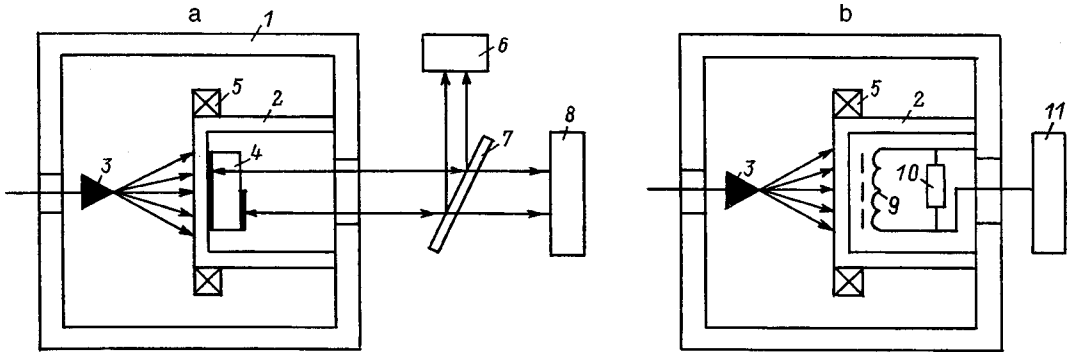

FIG. 1. Experimental arrangement: a—in measurements of the combined action of a mechanical and a magnetic pulse on a crystal, b—for measurement of electromagnetic-field induction. *1*—electron accelerator, *2*—chamber, *3*—electron beam source, *4*—sample, *5*—beam current meter, *6*—PM tube, *7*—semitransparent mirror, *8*—He–Ne laser, *9*—measuring coil, *10*—50-Ω load resistance, *11*—oscillograph.

mechanical load pulse. Such a difference in the length of these pulses acting on the NaCl sample within one exposure is accounted for by the specific features of the mechanism of mechanical pulse formation.[1]

The experimental data obtained for edge-dislocation motion in NaCl crystals under a pulsed electromagnetic field can be used to interpret the results quoted in the earlier publication.[1] In this study, one measured the electron current in each electron-beam interaction with the sample, and therefore one could readily derive the mean free paths of dislocations, which in the conditions of Ref. 1 were determined by the electromagnetic field only (straight line *4*, Fig. 4). The straight line *1* in Fig. 4 displays the dependence of the dislocation pathlength in NaCl crystals measured[1] under combined action of a mechanical and an electromagnetic field on the mechanical pressure pulse. By subtracting from the resultant pathlengths in each experiment the paths due to the electromagnetic field only one can obtain the dependence of the pathlengths on mechanical pressure pulses (straight line *3* in Fig. 4). The points in this relation refer to experimental data on the mechanical effect only. That they nicely fit a straight line *3* indicates that the two effects, mechanical and electromagnetic, act in an additive way. The dynamic damping coefficient B of edge dislocations calculated from relationship *3* was found to be $\sim 2\times 10^{-4}$ P, which agrees within experimental error with the data on dynamic mechanical loading of materials. This removes the paradox pointed out in Ref. 1.

Incidentally, physical interpretation of the observed dislocation motion induced by electromagnetic pumping appears to be of a fundamental nature and much less trivial. Actually, the above-mentioned component of dislocation mobility was detected by the present authors as far back as 1986. These data, which stimulated subsequent studies of the magnetoplastic effect, were mentioned briefly in Ref. 3 but were not published in a separate paper, because no physical hypothesis capable of explaining such a strong effect of so weak vortex magnetic fields could be put forward at the time. Concurrently, a recent publication[4] reported a resonance effect of a microwave field on dislocation mobility in NaCl crystals placed in a dc magnetic field. The condition of resonance coincides, in fact, with that observed in an EPR signal, which reduces to the equality of the energy of the microwave quantum $h\nu$ to the Zeeman splitting $g\mu_B B$, where g is the Landé factor, and μ_B is the Bohr magneton. It may be conjectured that, in our experiments of 1985–1986, we actually observed the same effect but with the geomagnetic field $B_E \approx 5\times 10^{-5}$ T playing the part of the dc field, and the microwave field of a characteristic frequency $\nu_0 \sim 1$MHz created by the electron beam (Fig. 2). One can readily see that the resonance condition $h\nu_0 \approx g\mu_B B_E$ was also met in our ex-

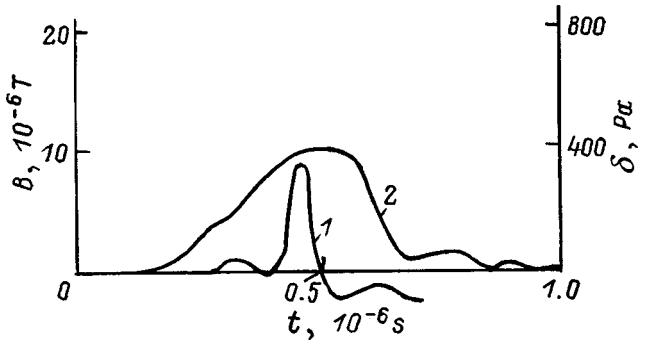

FIG. 2. Oscillographic traces of a mechanical pulse and an electromagnetic-field induction pulse.

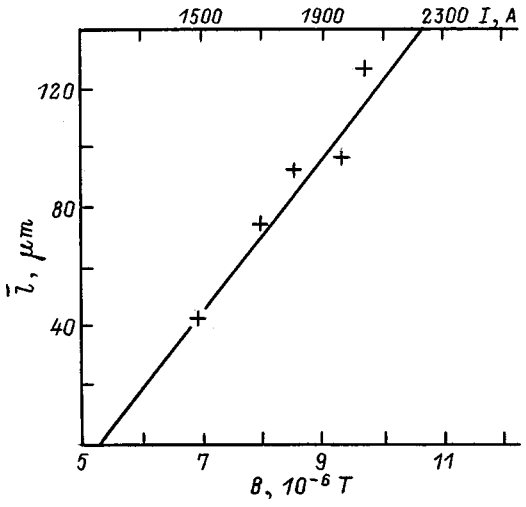

FIG. 3. Dependence of the dislocation mean-free pathlength $\bar{l}$ in NaCl crystals on electromagnetic field induction B and electron-beam current I.

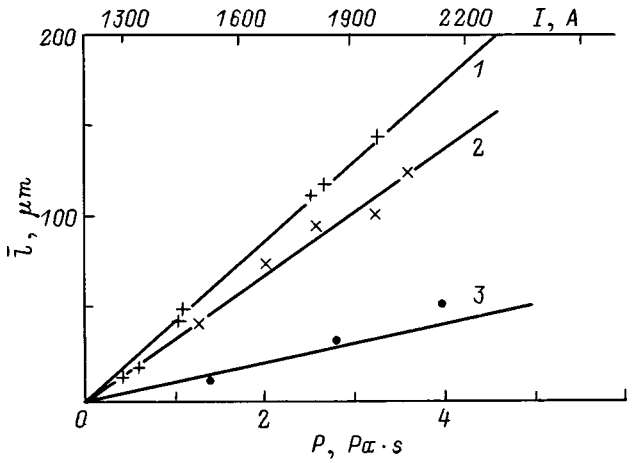

FIG. 4. Dislocation mean-free pathlength $\bar{l}$ in NaCl crystals vs mechanical pressure pulse and electron-beam current. *1*—Combined action of mechanical and magnetic pulses; *2*—electromagnetic field pulses alone; *3*—mechanical pressure pulses alone.

periments. Considered in the light of the systematic study of Ref. 4, the proposed explanation does not appear unduly extravagant and can be put forward as a working hypothesis.

It is assumed that the resonance spin transition lifts the quantum forbiddenness of some electronic transition in an impurity center at a dislocation or in the bulk of the crystal, which lowers the local barriers and initiates relaxation of the dislocation structure in the internal stress field.

It should be borne in mind that, for typical dislocation relaxation-motion velocities of a few μm/s, the time required to move to distances of the order of 100 μm is a few min. This means that dislocations continue to move a long time after the end of the pulse, which suggests that the electromagnetic pulse acts directly on point defects in the bulk of the crystal, exactly what is observed in the experiments of Ref. 4. The linear growth of this component of the pathlength with current reflects apparently the increase of the probability of the corresponding transition at the given impurity center with increasing intensity of the electromagnetic pumping of the crystal.

The authors are indebted to B. I. Smirnov for fruitful discussions and comments, and to V. P. Kisel' and V. M. Chernov for assistance in sample preparation.

Partial support of the Russian Fund for Fundamental Research (Grant 97-02-16327) is gratefully acknowledged.

[1] E. V. Darinskaya, I. P. Makarevich, Yu. I. Meshcheryakov, V. A. Morozov, and A. A. Urusovskaya, Fiz. Tverd. Tela (Leningrad) **24**, 1564 (1982) [Sov. Phys. Solid State **24**, 898 (1982)].
[2] E. V. Darinskaya, A. A. Urusovskaya, V. I. Al'shits, Yu. I. Meshcheryakov, V. A. Alekhin, and R. Voska, Fiz. Tverd. Tela (Leningrad) **25**, 3636 (1983) [Sov. Phys. Solid State **25**, 2092 (1983)].
[3] V. I. Al'shits, E. V. Darinskaya, T. M. Perekalina, and A. A. Urusovskaya, Fiz. Tverd. Tela (Leningrad) **29**, 467 (1987) [Sov. Phys. Solid State **29**, 265 (1987)].
[4] Yu. I. Golovin, R. B. Morgunov, V. E. Ivanov, S. E. Zhulikov, and A. A. Dmitrievskiĭ, JETP Lett. **68**, 426 (1998).

Translated by G. Skrebtsov

MAGNETISM AND FERROELECTRICITY

Influence of the transport current on the magnetoelectric properties of $La_{0.7}Pb_{0.3}MnO_3$ single crystals with giant magnetoresistance in the microwave region

N. V. Volkov, G. A. Petrakovskiĭ,*) K. A. Sablina, and S. V. Koval'

L. V. Kirenskiĭ Institute of Physics, Siberian Branch, Russian Academy of Sciences, 660036 Krasnoyarsk, Russia

(Submitted January 13, 1999)
Fiz. Tverd. Tela (St. Petersburg) **41**, 2007–2015 (November 1999)

The results of experiment on the influence of a direct current and a low-frequency alternating current, as well as a magnetic field, on the microwave-range conductivity σ_{MW} of $Ln_{0.7}Pb_{0.3}MnO_3$ single crystals with giant magnetoresistance are presented. The greatest sensitivity of the samples toward the effects of a current is observed in the temperature range corresponding to the dc magnetoresistance maximum. The response signal of a sample in the microwave range to the effects of an alternating current of a low frequency f_0 has a nonlinear character. As f_0 is varied in a magnetic field, the amplitude of the response signal varies with the appearance of resonance peaks. The results obtained are interpreted within an approach based on the coexistence of two phases having different conductivities in the doped manganite crystals. This two-phase interpretation is supported by data from magnetic-resonance investigations, which demonstrate the existence of two magnetic phases over a broad temperature range in $Ln_{0.7}Pb_{0.3}MnO_3$ single crystals. © *1999 American Institute of Physics.* [S1063-7834(99)02111-5]

The heightened interest in manganese oxides with a perovskite structure and the general formula $R_{1-x}A_xMnO_3$ (where R is a rare-earth ion, and A = Sr, Ba, Ca, Pb) is due to their unusual magnetic and electrical properties. This is mainly because the materials in this family have a large isotropic negative magnetoresistance, which has been termed giant magnetoresistance (GMR). At the same time, it has been established that the magnetic and electrical properties of manganites undergo significant changes as the composition, concentration, pressure, and temperature are varied. There is a hope that materials with acceptable GMR parameters for use in practical magnetic data storage devices and other microelectronics devices will be obtained. Nevertheless, the concentrated research efforts employing every possible method in recent years have not lead to a complete understanding of the mechanisms which account for the entire spectrum of observed magnetic and transport properties and the significant correlation between them.

The mechanism of electronic phase separation has been discussed as one of the possible models which accounts for GMR in substituted manganites.[1–3] In the case of such separation, a sample consists of regions with different carrier concentrations under thermodynamic equilibrium, while the sample is homogeneous from the crystallographic standpoint. The state of such a two-phase system is strongly sensitive to the effects of external factors, such as the temperature, external magnetic field, and pressure. It should probably be expected that such a system will be sensitive to the effects of direct and, especially, alternating currents of various frequencies and amplitudes (we are referring to appreciable probe currents) either without a field or in an external magnetic field. A phenomenon associated with the effect of a current pulse on the behavior of a system undergoing separation of phases has been observed in the degenerate semiconductor EuTe,[4] whose two-phase AFM–FM state is considered proved. As for the investigation of manganites, most of the data presented in the literature refer to resistance and magnetoresistance measurements in a direct current (with small probe currents), but there are scarcely any data from investigations of the magnetoresistive effect in alternating currents in different frequency ranges. The series of publications devoted to the investigation of the magnetoresistive effect at microwave frequencies[5–7] should be noted. One characteristic observation in these investigations is the existence of significant differences in the temperature and magnetic-field dependences of the samples measured in a direct current and in the microwave range.

In this communication we report the results of investigations into the influence of direct and alternating currents on the magnetic and electrical properties of manganite single crystals exhibiting GMR. The changes in the state of the materials investigated was monitored by determining the variation of their losses in the microwave frequency range.

1. EXPERIMENTAL

The investigations were performed on $Ln_{1-x}Pb_xMnO_3$ single crystals grown by spontaneous crystallization from a molten solution. One special feature of the technology was that PbO and PbF_2 served as the solvent and, at the same

time, acted as the source of Pb in the crystals. The mixture of La_2O_3, MnO_2, and the solvent was prepared in such a manner that a Pb concentration $x \sim 0.3$ would be ensured. The crystals were grown in a platinum crucible. The technological regime selected ensured the formation of crystals with the mean dimensions $5\times5\times5$ mm^3. X-ray analysis of the single crystals obtained confirmed the structure and lattice constants corresponding to $x \sim 0.3$.

The samples for the investigation were prepared in the form of wafers measuring $4\times2\times0.1$ mm^3, and the surfaces of the wafers were polished. The conductivity in the microwave range σ_{MW} was measured using a magnetic-resonance spectrometer[8] with a working frequency of 10.6 GHz. The sample was placed within a three-dimensional rectangular cavity at the maximum of the electric component of the microwave electromagnetic field. Clamped contacts in the form of thin needles were used to pass a current through the sample.

The power reflected from the cavity with the sample P_c or its variation as a function of temperature, external magnetic field, and the amplitude and frequency of the voltage applied to the sample at a constant value of the input microwave power P_{in} was measured during the experiments.

We note that, in the procedure usually used to measure the microwave conductivity σ_{MW}, a sample having a high conductivity is placed at the maximum of the magnetic component of the microwave electromagnetic field. In this case it is not difficult to obtain a dependence which directly relates σ_{MW} to the power reflected from the cavity P_c. However, if the sample is ferromagnetic, the situation is complicated to a considerable extent, because in that case it is necessary to take into account the contribution of the dynamic permeability μ, which depends on the frequency of the electromagnetic radiation, the external magnetic field, and the magnetization of the sample, to the microwave absorption.

In the case where the dimensions of the sample are much smaller than the wavelength of the electromagnetic radiation and the thickness of the skin layer δ is larger than the smallest dimension of the sample or of the same order, we can utilize the procedure for measuring σ_{MW} in which the sample is placed at the maximum of the electric component of the microwave field in the cavity.[9] Using perturbation theory, we can obtain the relationship between the complex dielectric constant of the sample $\varepsilon=\varepsilon'-i\varepsilon''$ and the parameters of the cavity. For conductive materials $\varepsilon''=\sigma_{MW}/\omega$, and, as a rule, $\varepsilon'' \gg \varepsilon'$. In the absence of depolarizing factors

$$\frac{1}{Q}-\frac{1}{Q_0}\approx(\varepsilon'' E_m^2 \Delta V)\left(\varepsilon_0 \int_{V_0} E_0^2\, dV\right)^{-1} = (\sigma_{MW} E_m^2 \Delta V)\left(\varepsilon_0 \omega \int_{V_0} E_0^2\, dV\right)^{-1},$$

where Q_0 is the Q factor of the cavity without a sample, Q is the Q factor with a sample, ΔV is the volume of the sample, V_0 is the volume of the cavity, E_m is the strength of the electric field at the antinode, E_0 is the unperturbed electric field in the cavity, and ε_0 is the dielectric constant of the cavity medium. Thus, σ_{MW} is related to the Q factor of the loaded cavity, and while measurement of the absolute value of σ_{MW} raises certain difficulties, it is simple to evaluate its variation in response to the influence of external factors from the change in the microwave power reflected from the cavity ΔP_c.

The use of such a method for measuring σ_{MW} was substantiated in our case, since the skin depth for the samples was $\delta > 0.6$ mm over the entire temperature range, and the contribution of μ to the microwave power absorbed by the sample was essentially eliminated.

The measurements were performed in comparatively weak magnetic fields up to $H=7$ kOe. The direction of H coincided with the direction of the current in the sample. The resistivity of the materials in a constant current and in a low-frequency alternating current was measured by the traditional four-point probe technique. The measurements were performed in a flow-through nitrogen cryostat in the temperature range 100–360 K.

2. RESULTS AND DISCUSSION

As was noted above, the variation of the parameters of the microwave response (the power reflected from the cavity P_c) contains information on the variation of the conductivity of the material σ_{MW}. Therefore, the magnitude of the relative change in P_c was taken as the principal parameter to be monitored.

Figure 1a presents the dependence of the power reflected from the cavity P_c on the constant voltage U_- applied to the sample in a zero magnetic field and in a field of intensity $H=7$ kOe. Our attention is drawn to the extremely nonlinear course of $P_c(U_-)$, the slight asymmetry of the dependence relative to $U_-=0$, and the increase in the relative influence of the external magnetic field with increasing U_-. Such a dependence cannot be attributed to simple heating of the sample. First, the dc current–voltage characteristic is essentially linear at the same values of U_- (Fig. 1b). Second, we directly monitored the temperature of the sample, and the maximum heating did not exceed 1 K even after prolonged passage of current. Finally, under the effect of an alternating current, in the case of heating, everything would be reduced to a change in P_c by a constant amount.

We performed experiments to determine the parameters of the microwave response ΔP_c with a low-frequency alternating voltage in the range from 20 Hz to 10 kHz acting on the sample. These results turned out to be very interesting and informative. When the sample was excited by an alternating current of frequency f_0, the microwave response signal consisted of a set of even and odd harmonic components:

$$\Delta P_c(t)=\sum_n A_n \cos(n f_0 t).$$

The component at $2f_0$ had the largest amplitude, and the even harmonics were generally more intense than the odd harmonics. The amplitudes of each harmonic component in the microwave response signal and the ratio between the amplitudes of the harmonics depended on the amplitude $U_\sim$ of the voltage applied to the sample. Figure 2 presents plots of the dependence of the amplitude of the even and odd harmonics in the microwave response on $U_\sim$ for $f_0=1$ kHz.

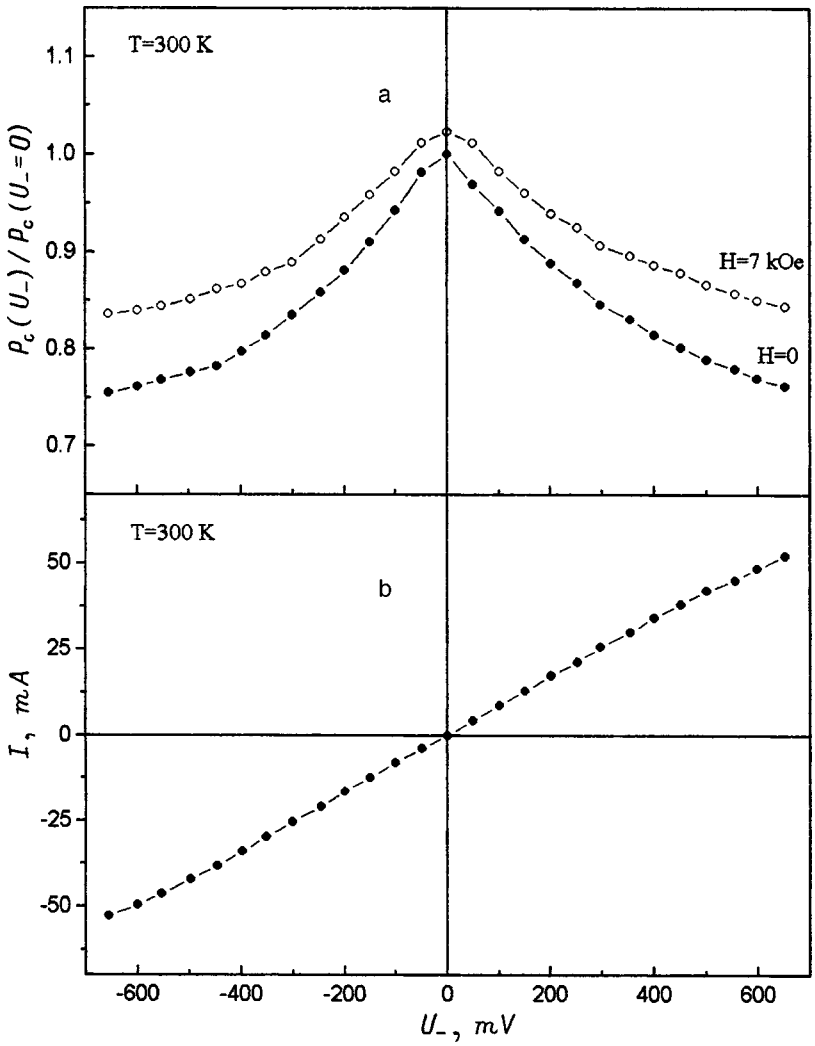

FIG. 1. a—Dependence of the power reflected from the cavity P_c on the dc voltage U_- passed through a $La_{0.7}Pb_{0.3}MnO_3$ single crystal. The value of the power is normalized to the quantity $P_c(U_-=0, H=0)$. $T=300$ K. b—Current–voltage characteristic of the sample. $T=300$ K.

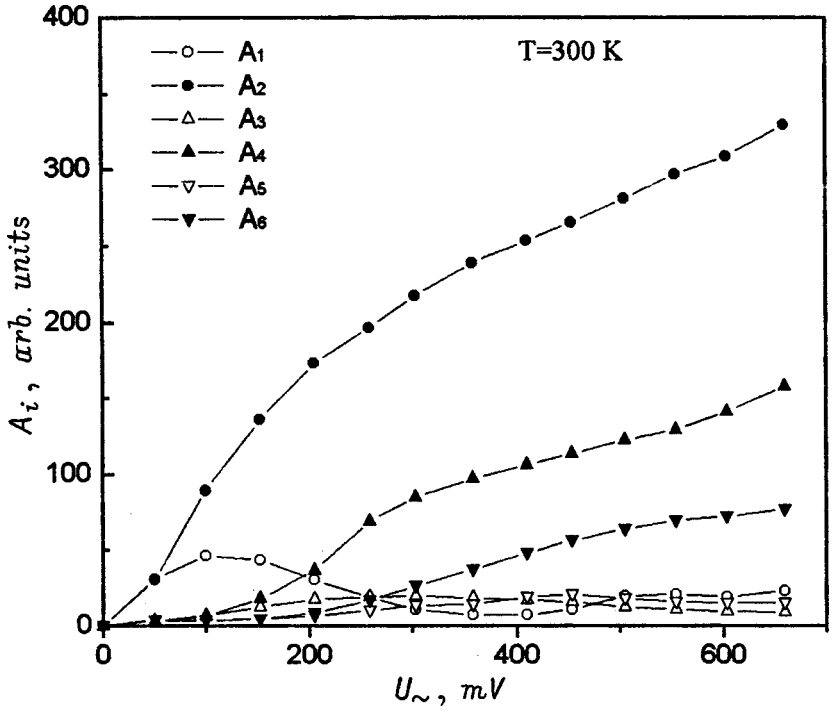

FIG. 2. Dependence of the amplitudes of the odd (A_1, A_3, and A_5) and even (A_2, A_4, and A_6) harmonics in the microwave response signal on the alternating voltage $U_\sim$ with a frequency $f_0=1$ kHz applied to the sample. $T=300$ K.

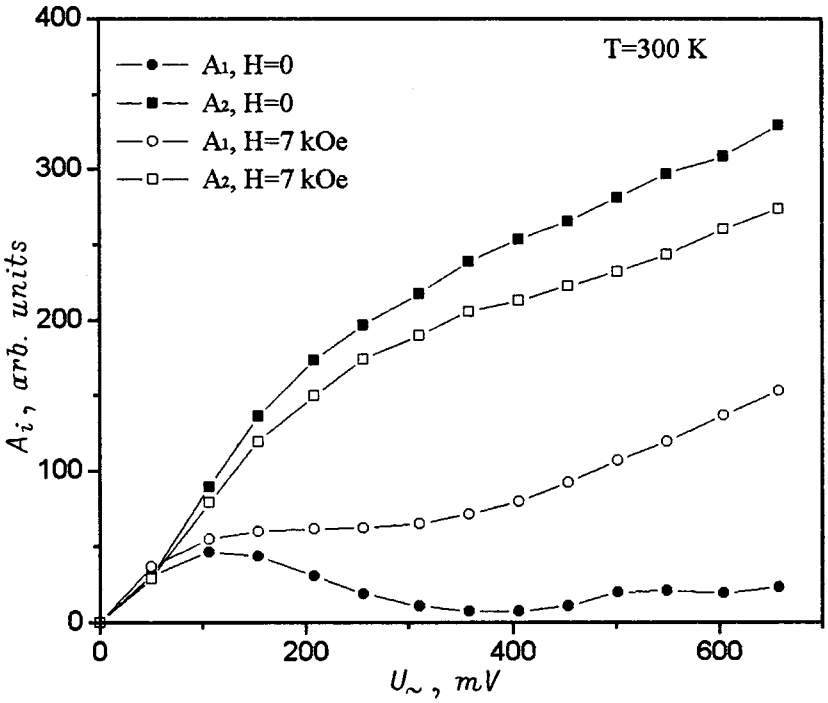

FIG. 3. Dependence of the amplitude of the first (A_1) and second (A_2) harmonics in the microwave response signal on the alternating voltage $U_\sim$ ($f_0 = 1$ kHz) applied to the sample in magnetic fields of intensity $H=0$ and $H=7$ kOe. $T=300$ K.

The harmonics from f_0 to $6f_0$ are shown, although our instrumentation allowed us to observe a component in ΔP_c with a frequency of $12f_0$. Measurements by the four-point probe technique at $f_0=1$ kHz did not reveal any nonlinear effects, and the current–voltage characteristic, as in the case of a direct current, was essentially linear. The linear current–voltage characteristic and the special additional experiments that we performed with variation of the shape and material of the electric contacts allow us to rule out any hypothesis that the effects observed are due to contact phenomena.

Next, for simplicity, let us dwell on the behavior of the first and second harmonics in the microwave response signal. Figure 3 shows the influence of the external magnetic field on the behavior of the amplitude of the first (A_1) and second (A_2) harmonics as a function of $U_\sim$ at $T=300$ K. The value of A_1 depends most strongly on the strength of the external magnetic field H (A_1 increases with increasing H), and the amplitude of the second harmonic A_2 decreases slightly. Figures 4a and b present the temperature dependences of A_1 and A_2 for $H=0$ and $H=7$ kOe. An alternating voltage of constant amplitude $U_\sim=500$ mV with a frequency $f_0=1$ kHz was maintained on the sample over the entire temperature range. For comparison, Fig. 4c presents the temperature-dependent behavior of the resistivity ρ and the magnetoresistance $\Delta\rho/\rho_0=(\rho(0)-\rho(H)/\rho(0))\cdot 100\%$ of a sample in a field of intensity $H=7$ kOe, which was obtained from dc measurements by the four-point probe method.

The temperature dependence of the amplitude of the second harmonic A_2 in the microwave response signal qualitatively mimics the behavior of the dc magnetoresistance. The maximum of A_2 and the strongest influence of the magnetic field H are observed at $T\sim 325$ K, and the maximum of $\Delta\rho/\rho_0$ corresponds to the same temperature. In the temperature range from 250 to 330 K a decrease in A_2 is observed in an external magnetic field. At $T<250$ K and $T>330$ K, A_2 rises slightly with increasing H.

The unusual temperature dependence of the amplitude of the first harmonic in the microwave signal A_1 became more understandable after we recorded the dependences of A_1 and A_2 on the frequency f_0 of the modulating voltage applied to the sample for various temperatures (Fig. 5). In general, the amplitude of the microwave response signal at a fixed temperature varied only slightly for frequencies of the alternating voltage on the sample up to 5 kHz. When f_0 was increased further, the amplitude of the signal quickly decreased, and above 10 kHz no microwave response signal was observed.

When $H=0$, the amplitude of the first harmonic A_1 depends weakly on f_0 and has a smooth curve at all temperatures. In an external magnetic field there are resonance peaks of A_1 at certain frequencies (in the range from 200 Hz to 2 kHz; see Fig. 5). The height of the peaks on the plot of A_1 versus f_0 increases with increasing H without shifts along the frequency scale. Features in the form of two peaks in the spectrum of A_1 ($H=7$ kOe) begin to be displayed at $T=355$ K (Fig. 5c). As the temperature is lowered, their height increases, and they undergo slight frequency shifts (Fig. 5b). Below $T\sim 300$ K the peaks transform into a single maximum (Fig. 5a), whose height decreases as the temperature is lowered further. The features on the plot of $A_1(f_0, H=7$ kOe) vanish at $T\sim 100$ K, and it then coincides with the $A_1(f_0, H=0)$ curve. The maximum sensitivity of A_1 toward the magnetic field is observed at $T\sim 325$ K, which corresponds to the maximum of the dc magnetoresistive effect.

Observing A_2 in the frequency range from 20 Hz to 2 kHz did not reveal any features. Increasing the external

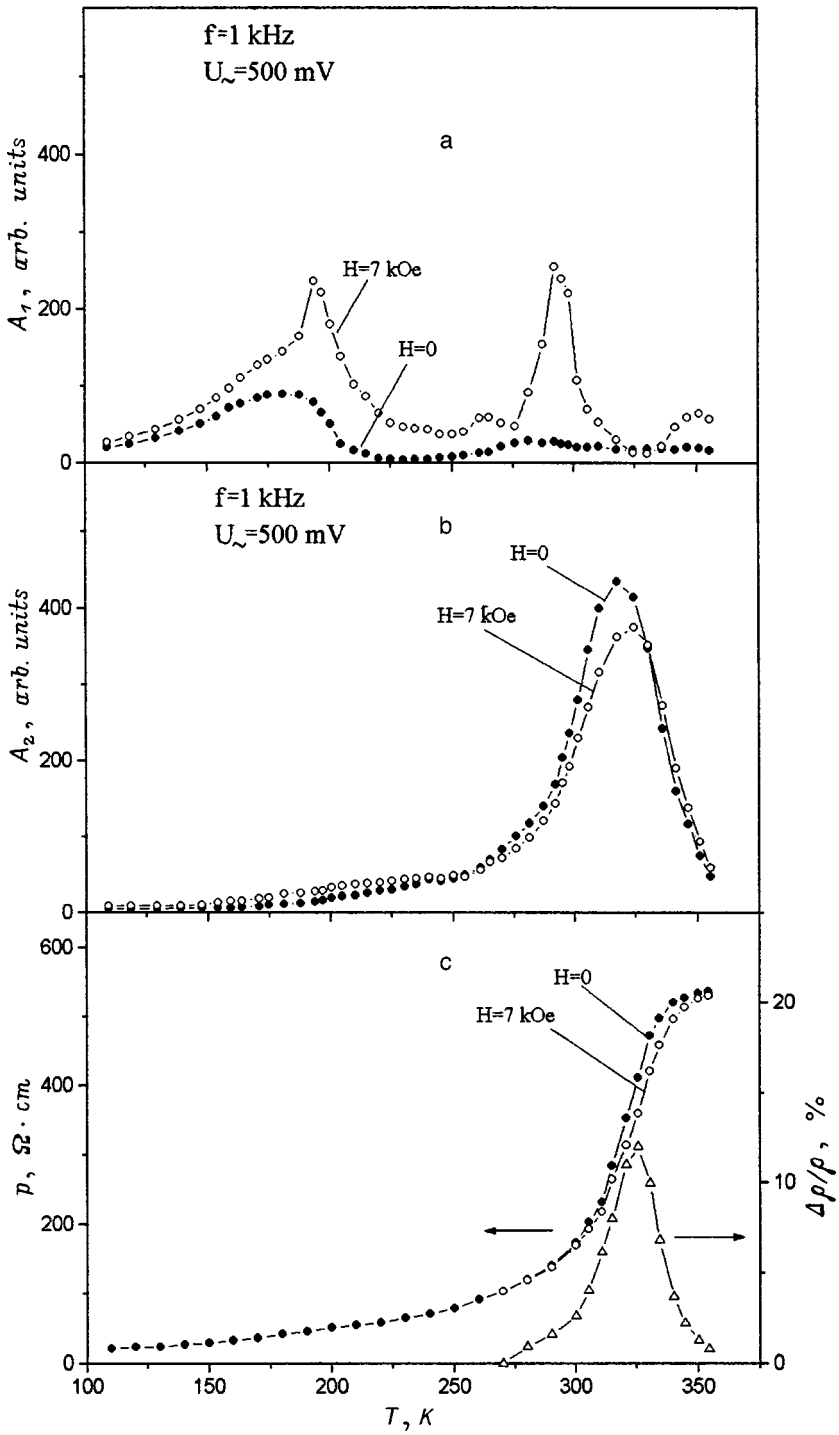

FIG. 4. Temperature dependence of the amplitude of the first A_1 (a) and second A_2 (b) harmonics in the microwave response signal with an alternating voltage $U_{\sim}=500$ mV ($f_0=1$ kHz) on the sample in magnetic fields of intensity $H=0$ and 7 kOe. Temperature dependence of the resistivity ρ and the magnetoresistance $\Delta\rho/\rho_0$ in a magnetic field of intensity $H=7$ kOe recorded under dc conditions (c).

magnetic field changed A_2 by the same amount over the entire frequency range considered.

As was shown above, the variation of the microwave response signal ΔP_c is associated with changes in the conductivity in the microwave range σ_{MW}. Our data provide evidence that the passage of a constant current through a sample of a $La_{0.7}Pb_{0.3}MnO_3$ single crystal leads to a decrease in its conductivity in the microwave range σ_{MW}. As would be expected, an external magnetic field H increases σ_{MW}, the relative influence of H being enhanced as the constant voltage on the sample U_{-} is increased. The change in σ_{MW} in response to the passage of a current does not depend on its direction in the crystal. The effect of the external magnetic field H is isotropic, i.e., there is no dependence on the relative orientation of the direction of the transport current and H.

The sharp difference between the behavior of σ_{MW} and the conductivity measured under dc conditions σ_{DC} can be understood, in our opinion, by utilizing the model of a sample in a two-phase state.[1] In this case the manganite single crystal is a thermodynamic equilibrium system of coexisting regions with different carrier concentrations. One of the phases corresponds to regions with high conductivity thus to ferromagnetic (FM) ordering, and the other phase

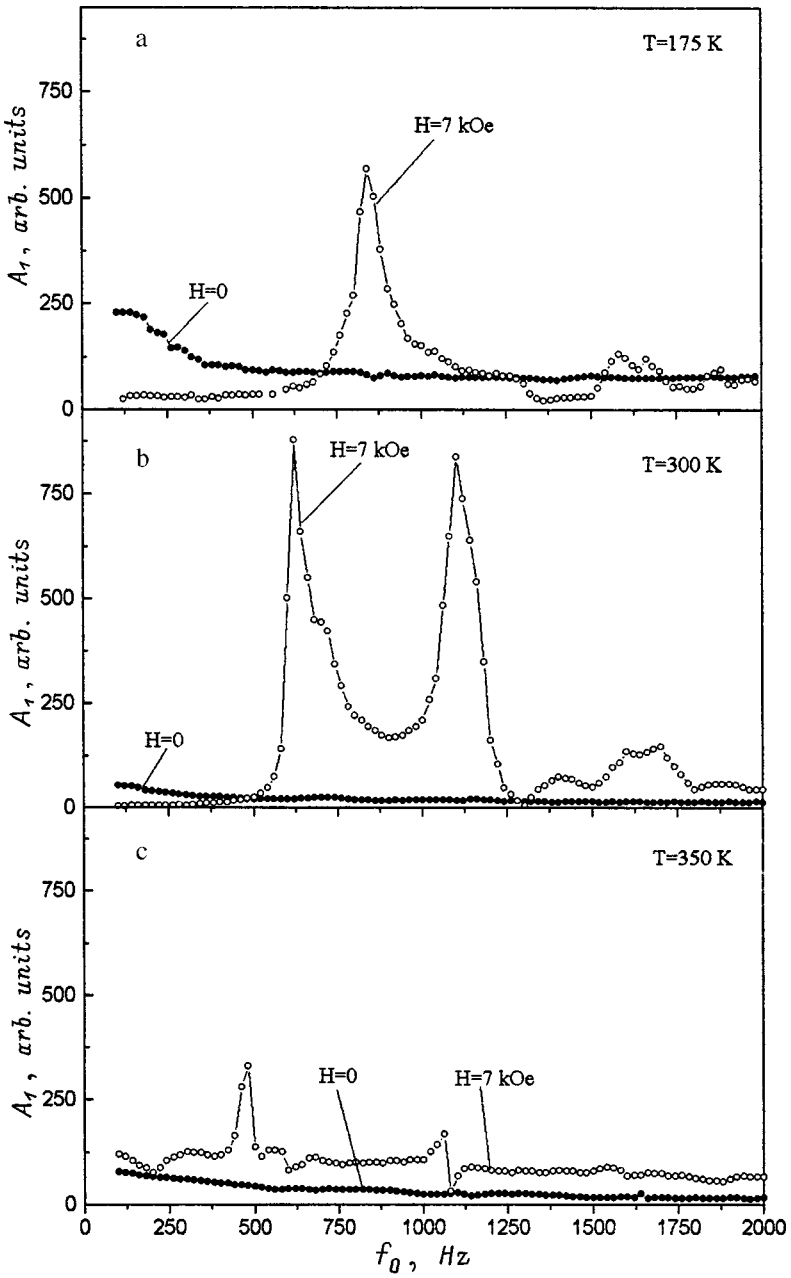

FIG. 5. Dependence of the amplitude of the first harmonic A_1 in the microwave response signal on the frequency f_0 of the alternating voltage on the sample ($U_{\sim}=500$ mV) in magnetic fields of intensity $H=0$ and 7 kOe. a — $T=175$ K, b — $T=300$ K, c — $T=350$ K.

corresponds to regions with a lower conductivity, which are in a different magnetic state, for example, a paramagnetic (PM) state. We shall refer to these phases as the ''metallic'' and ''dielectric'' phases, respectively.

To account for the behavior of the conductivity of a sample in the two-phase state we start with the classical percolation model (see, for example, Ref. 10), in which there are no specific mechanisms for conduction in each of the phases and everything is determined by the ratio between the concentrations of the regions with different conductivities and their topology. At low temperatures the sample consists of a single connected FM ''metallic'' phase, within which regions of the ''dielectric'' phase unconnected to each other can exist. As the temperature is increased, the regions of the ''dielectric'' phase grow, and the volume of the ''metallic'' phase decreases. The ratio between the volumes of the phases at a fixed doping concentration is determined not only by the temperature, but also by the external magnetic field (the magnetic field increases the volume of the FM phase) and probably, as follows from our experiments, by the value of the transport current passed through the sample.

When the conductivity is measured in the microwave range, σ_{MW} manifests itself as the effective averaged value of the conductivities of the ''metallic'' and ''dielectric'' phases. In fact, it is generally known that, if a material is an inhomogeneous mixture and the wavelength of the electromagnetic radiation is much larger than the inhomogeneity scales, such a mixture can be regarded as a homogeneous isotropic medium. However, it will be characterized by definite values of ε and, therefore, of σ_{MW} (Ref. 11). The effective value of ε for an inhomogeneous medium can be calculated exactly in a general form only for certain limiting cases.

When the measurements are performed under dc condi-

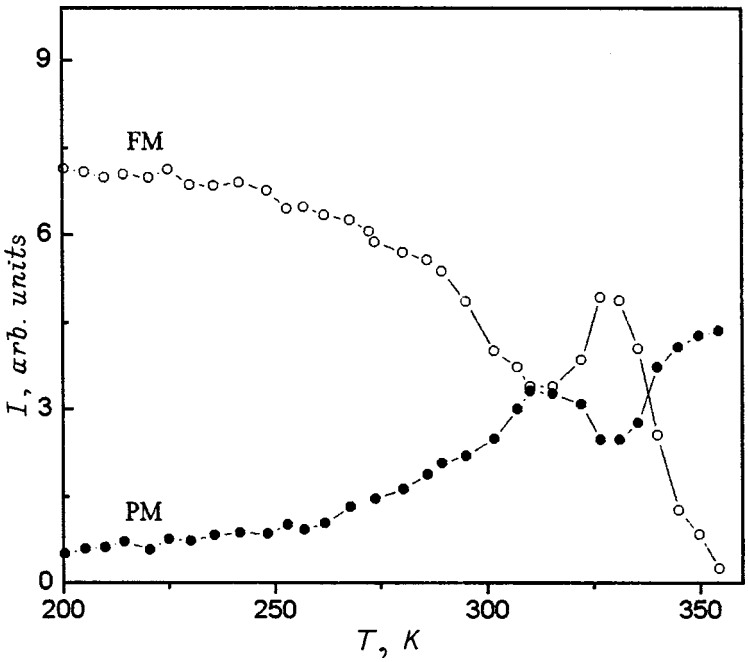

FIG. 6. Temperature behavior of the intensities of the magnetic resonance lines ($\nu = 10.6$ GHz) corresponding to the PM and FM phases in a $La_{0.7}Pb_{0.3}MnO_3$ single crystal.

tions, for which there is percolation through the ''metallic'' phase, the conductivity σ_{DC} is determined mainly by the conductivity of that phase. Therefore, small variations in the ratio between the concentrations of the phases do not have an appreciable effect on the measured value of σ_{DC}. In order to produce an appreciable change in σ_{DC}, a stronger magnetic field must be applied. The same applies to the transport current, whose influence on σ_{DC} should be appreciable at large values of the voltage applied to the sample, but in this case considerable warming of the sample will occur, and correct planning of an experiment is not possible.

As the temperature is increased, the FM order is suppressed, and the concentration of the ''dielectric'' phase increases. Above a certain temperature T_0, the quantity of the ''metallic'' phases decreases so much that it is transformed from a single connected region into numerous separate connected regions, and the flow of current in it through the entire sample ceases. Therefore, the conductivity is determined mainly by the ''dielectric'' phase. It is understood that the strongest conductivity changes and the strongest sensitivity to the magnetic field and the transport current should be manifested within the percolation model in the vicinity of T_0, which can be regarded as the threshold temperature for percolation in the ''metallic'' phase. In our case $T_0 \sim 325$ K, and the maximum of $\Delta\rho/\rho_0$ is achieved at just that temperature.

As an additional argument in support of the idea that two phases coexist in the manganites we investigated, we present the results of magnetic-resonance investigations of $Ln_{0.7}Pb_{0.3}MnO_3$ single crystals. At $T > T_c \sim 355$ K a magnetic-resonance absorption line corresponding to the PM state of the crystal is observed. Below T_c two magnetic-resonance lines were observed down to ~ 100 K. The line corresponding to the PM state underwent strong broadening as the temperature was lowered, the resonance field H_r remained unchanged, and its intensity decreased practically monotonically except in the temperature range from 315 to 340 K (Fig. 6). The intensity of the absorption line corresponding to the ferromagnetic (FM) state increased with decreasing temperature, H_r decreased most strongly at values of T ranging from 355 to 290 K and then reached a plateau. The features of the behavior of the intensities of the FM and PM resonance lines in the vicinity of $T_0 \sim 325$ K, which corresponds to the maximum magnetoresistive effect, are noteworthy. They can be attributed to the fact that the external magnetic field H most effectively increases the concentration of the FM phase in the sample at these temperatures.

The nonlinear form of the dependence of the power reflected from the cavity P_c on the value of the voltage U_- applied to the sample (Fig. 1) allows us to postulate some manifestation of this nonlinearity in the microwave response signal upon the application of an alternating voltage $U_\sim$ with a low frequency f_0 to the sample, for example, in the form of the appearance of high-order harmonic components. The essentially fully symmetric form of the characteristic allows us to expect that the principal microwave response signal will be observed at the doubled frequency of the modulating voltage $2f_0$ and that the presence of even harmonics of the response signal is possible. This is confirmed by our experiments.

According to Fig. 1, the external magnetic field H should diminish the amplitude of the microwave response, as we observed in the case of A_2 (Fig. 3). The qualitatively similar form of the temperature dependences of A_2 and $\Delta\rho/\rho_0$ corroborates the direct connection between the mechanisms responsible for the influence of the external magnetic field and the transport current on the electrical properties of the manganite single crystals, which has a reasonable explanation within the theory of the two-phase state of the samples.

The reason for the appearance of the f_0 component and the odd harmonics in the microwave response signal and especially for the resonant increase in A_1 in an external magnetic field upon variation of the frequency f_0 of the modu-

lating voltage on the sample is still unclear. This behavior can most probably be associated within the two-phase approach with the dynamics of the displacement of the boundaries of the regions of the ''metallic'' and ''dielectric'' phases or with the mobility of the regions as a whole. When the frequency of the modulating voltage acting on the sample f_0 coincides with natural vibrational frequencies of the boundaries, a resonant increase in A_1 is observed, and the external magnetic field can be regarded as the quantity which effectively influences the dissipation parameters ω_d of the system under consideration and, consequently, the intensity of the resonance lines in the spectrum. The main factor causing the diffuseness of the resonance spectrum of the boundaries is the complex geometry of a two-phase state with a distribution of the regions belonging to the different phases according to size and shape. As the temperature is varied, significant restructuring of the two-phase state of the system occurs, which is reflected in the spectra recorded at different temperatures.

We are intentionally presenting only qualitative arguments, since there are numerous questions which preclude making correct quantitative estimates. First of all, the mechanism of the separation of phases in the materials that we studied is unclear. For example, realization of a mechanism of an impurity separation of phases associated with the inhomogeneous distribution of the impurity in the crystal is possible. On the other hand, in this case, as opposed to the mechanism of an electronic separation of phases, it is difficult to expect strong sensitivity to the effects of external factors, such as the external magnetic field and the transport current. The question of the mechanism underlying the influence of the transport current on the conductivity σ_{MW} of $La_{0.7}Pb_{0.3}MnO_3$ single crystals that we discovered remains open. The topology of the two-phase state, which varies radically with temperature, is unknown. The concrete mechanisms of conduction in each of the phases must also be taken into account.

Thus, in this report we have presented the results of experiments on the influence of direct and alternating currents on the conductivity of $La_{0.7}Pb_{0.3}MnO_3$ single crystals in the microwave range σ_{MW}. The investigations have shown that a transport current leads to a decrease in σ_{MW}, while an external magnetic field, as would be expected, increases the conductivity. The strongest influence of a current is observed at the temperature where the maximum of the magnetoresistive effect recorded under dc conditions is observed. Under the effect of an alternating current the crystals display nonlinear properties, which are manifested in the generation of harmonics in the microwave response signal from the cavity containing the sample. A dependence of the microwave response on the frequency of the alternating current in the sample in an external magnetic field has been discovered, and its course has a resonance character.

The results obtained can be described directly within the theory of phase separation in crystals of doped manganites using the classical percolation approach. A separation of phases is also supported by magnetic-resonance investigations, which demonstrated directly the coexistence of FM and PM phases in the samples over a broad temperature range.

*)E-mail: gap@cc.krascience.rssi.ru

[1] É. L. Nagaev, Usp. Fiz. Nauk **166**, 833 (1996) [Phys. Usp. **39**, 781 (1996)].
[2] É. L. Nagaev, Usp. Fiz. Nauk **168**, 917 (1998) [Phys. Usp. **41**, 831 (1998)].
[3] L. G. Gor'kov, Usp. Fiz. Nauk **168**, 664 (1998) [Phys. Usp. **41**, 589 (1998)].
[4] V. V. Osipov and I. V. Kochev, Fiz. Tverd. Tela (Leningrad) **33**, 942 (1991) [Sov. Phys. Solid State **33**, 535 (1991)].
[5] M. Domingnez, S. M. Bhagat, S. E. Lofland, J. S. Ramachaudran, G. C. Xiong, H. L. Ju, T. Venkatesan, and R. L. Greene, Europhys. Lett. **32**, 349 (1995).
[6] S. E. Lofland, S. M. Bhagat, S. D. Tyagi, Y. M. Mukovskii, S. G. Karabashev, and A. M. Balbashov, J. Appl. Phys. **80**, 3592 (1997).
[7] N. I. Solin, A. A. Samokhvalov, and S. V. Naumov, Fiz. Tverd. Tela (St. Petersburg) **40**, 1881 (1998) [Phys. Solid State **40**, 1706 (1998)].
[8] N. V. Volkov and G. S. Patrin, Preprint No. 635, Institute of Physics, Academy of Sciences of the USSR, Siberian Branch, Krasnoyarsk (1990), 18 pp.
[9] L. I. Buravov and I. F. Shchegolev, Prib. Tekh. Éksp. , No. 2, 171 (1972).
[10] B. I. Shklovskii and A. L. Efros, *Electronic Properties of Doped Semiconductors* (Springer-Verlag, Berlin, 1984; Nauka, Moscow, 1979).
[11] L. D. Landau and E. M. Lifshitz, *Electrodynamics of Continuous Media* (Pergamon, Oxford, 1984; Nauka, Moscow, 1982, 620 pp.).

Translated by P. Shelnitz

Microinhomogeneities in the distribution of oxygen concentration in ferrite-garnet films

V. K. Karpasyuk and M. F. Bulatov

Astrakhan State Pedagogical University, 414056 Astrakhan, Russia
(Submitted February 19, 1998)
Fiz. Tverd. Tela (St. Petersburg) **41**, 2016–2019 (November 1999)

Artificial microinhomogeneities were created in iron-garnet $(TmBiCa)_3(FeGa)_5O_{12-\gamma}$ films with various degrees of oxygen nonstoichiometry, changes in the individual magnetic characteristics of these inhomogeneities were tracked during chemical oxidation and reduction, and the interactions of these inhomogeneities with planar domain walls and spiral domains were investigated. The resulting experimental data were interpreted by analyzing how the saturation magnetization, domain-wall surface-energy density, and uniaxial anisotropy constants depended on the concentrations of different-valency iron ions, cationic vacancies, and anionic vacancies. © *1999 American Institute of Physics.* [S1063-7834(99)02211-X]

In ferrites like in phases of variable composition, the most characteristic imperfections in their crystal structure are associated with deviations from stoichiometry with respect to oxygen and (or) the cation component.[1] The literature devoted to such imperfections in iron garnets is very extensive (see, e.g., the review Refs. 2–4). However, existing publications focus primarily on point defects, and very little information is available at this time about physically macroscopic bulk imperfections of micron and submicron size, which we refer to henceforth as microinhomogeneities.[5] Attempts to model the interactions between microinhomogeneities and domain walls usually postulate changes in various physical parameters within the inhomogeneities, e.g., their exchange-interaction and (or) anisotropy constants, saturation magnetization, and orientation of the easy-magnetization axis.[2,6–8] However, because there is very little experimental data on the intrinsic magnetic parameters of microinhomogeneities,[9] it is very difficult to establish how these parameters are related to composition and material synthesis and processing conditions (especially in the presence of nonisovalent impurities). For the most part this is due to problems in observing how individual isolated inhomogeneities evolve under external probe fields. In Refs. 10 and 11 we described techniques for creating and studying artificial microinhomogeneities in the distribution of oxygen concentration in films, techniques that make it possible to overcome these difficulties.

In previous papers[10,12] we reported identifying a sequence of transformations of the valence state of iron ions in the iron-garnet $(TmBiCa)_3(FeGa)_5O_{12-\gamma}$, and the structural formula of the latter, based on analysis of experimental data on changes in the saturation magnetization, domain-wall surface-energy density, and optical properties of the garnet films during oxidation and reduction.

The goal of this paper is to determine (for films of the same composition) how the individual magnetic characteristics of artificial microinhomogeneities depend on oxygen content, and to study their interactions with a planar domain wall and with spiral domains.

1. EXPERIMENTAL SAMPLES AND METHODS USED TO STUDY THEM

The objects of our investigation were 6.7-μm-thick films with (111) orientation grown on a $Gd_3Ga_5O_{12}$ substrate by liquid-phase epitaxy from a lead-free solution-melt. The period of the substrate lattice was 1.2383 nm. The microinhomogeneities, which differed in their oxygen content (γ) from the bulk films, were created by processing local portions of the film with solutions of $KMnO_4$ and $FeCl_2$ with varying concentrations through openings in a mask deposited on the sample surface. The openings, which were created by photolithography, had diameters from 2 to 24 μm. The magnetic dipole moments of the microinhomogeneities were determined by measuring the distortion of a planar domain wall as it interacted with them, based on the method we described in Ref. 9 and refined in Ref. 11.

In order to interpret the data on these inhomogeneities, we also investigated changes in the following overall parameters of the host material: the period of the crystal lattice a, the saturation magnetization $4\pi M_S$, the domain-wall surface-energy density σ, and the uniaxial anisotropy constant K_U. Measurements of a were made using a DRON-3 diffractometer; the remaining parameters were determined by well-known standardized methods,[13,14] involving the use of a C500.1 magnetooptic apparatus equipped with a thermocryostat.[14]

The initial film was cut into seven samples, with identical structures and parameters. One of the samples was kept as a standard. A second was subjected to processing in a solution of $KMnO_4$ with a concentration of 0.12 mol/l. at a temperature of 80 °C for 2 hours. A third sample was processed in a solution of $FeCl_2$ with a concentration of 0.2 mol/l. under the same conditions. Sample No. 4 was processed successively with stronger and stronger solutions of $KMnO_4$, while sample No. 5 was correspondingly processed with stronger and stronger solutions of $FeCl_2$, at room temperature for 36 hours.

We first fabricated masks with openings on the surfaces

TABLE I. Characteristics of a film in the original state (sample No. 1) after processing in solutions of $KMnO_4$ (2) and $FeCl_2$ (3).

Parameter	Sample No.		
	1	2	3
a, nm	1.2450	1.2436	1.2447
$4\pi M_S$, G	67	71	76
σ erg/cm^2	0.049	0.059	0.066
K_U, erg/cm^3	554	782	992

of samples Nos. 6 and 7. By using a domain wall as a probe, we then made sure that there were no inhomogeneities present in the exposed portions of the films. Then the samples were subjected to a succession of processing stages, using increasingly concentrated solutions of $KMnO_4$ for sample No. 6 and $FeCl_2$ for sample No. 7. The oxidation and reduction regimes were the same as in the processing of samples Nos. 4 and 5. In this case we assumed that the processing changed the parameters of local sections of samples Nos. 6 and 7 in the same way as it changed the overall parameters of samples Nos. 4 and 5. After each processing stage, the open portions of the films with domain walls were investigated.

Guided by literature data[15,16] on the way structural defects affect the nucleation of spiral domains, we attempted to use these domains to investigate the properties of microinhomogeneities in the films. Spiral domains were created by applying unipolar rectangular magnetic-field pulses $\mathbf{H}(t)$ to the sample, with the applied field directed orthogonal to the plane of the film. The duration τ of the pulses was varied from 0.1 to $\sim 10\mu$s, and the repetition rate f ranged from 100 to 10^4 Hz. Spiral domains appear within a certain range of amplitudes of the pulse field which becomes narrower with increasing τ. For arbitrary f, dynamic spiral domains appear, whose probability of nucleation and lifetime depends on the relations between τ, f, and H. Certain ''resonance'' values of f give rise to the most stable domain structures, which become insensitive to the field pulses $\mathbf{H}(t)$ over a rather large time interval. Applying an additional DC bias field $\mathbf{H}_0$ accelerates the process of forming these stable structures.

2. EXPERIMENTAL RESULTS AND DISCUSSION

The characteristics of the films measured before and after the oxidation-reduction processing are listed in Tables I–III.

It is clear that the saturation magnetization, domain-wall energy density, and uniaxial-anisotropy constant are increased by processing with solutions that are sufficiently high in concentration, regardless of the processing type (oxidation or reduction); likewise, the period of the crystal lattice decreases after either oxidation or reduction (Table I).

TABLE II. Saturation magnetization $4\pi M_S$ (G) of sample No. 4 after successive processing with solutions of $KMnO_4$ with increasing concentration.

Concentration of $KMnO_4$ solution, mol/l.							
0.010	0.015	0.025	0.035	0.050	0.075	0.100	0.125
65	59	64	66	68	70	73	75

TABLE III. Saturation magnetization $4\pi M_S$ (G) of sample No. 5 after successive processings with increasingly concentrated solutions of $FeCl_2$.

Concentration of $FeCl_2$ solution, mol/l.							
0.015	0.025	0.05	0.10	0.15	0.20	0.25	0.30
67	68	68	71	75	77	83	90

Our studies of the changes in properties of the films after processing by solutions with various concentrations showed that the saturation magnetization first decreases and then increases with increasing degrees of oxidation (Table II), whereas increasing reduction monotonically increases $4\pi M_S$ (Table III).

Microinhomogeneities generated by oxidation of localized regions with a solution of $KMnO_4$ at a concentration of 0.015 mol/l. repel a domain wall that approaches them, due to the decreased saturation magnetization within the inhomogeneity,as reflected in the data in Table II.

Microinhomogeneities obtained by processing exposed sections of the films with oxidizing or reducing solutions at concentrations exceeding 0.075 mol/l., regardless of the type of processing, attract an aproaching domain wall, but repel it upon direct contact. These effects are associated with the increased saturation magnetization and surface energy density of domain walls within the inhomogeneity, as reflected in the data of Tables I–III. Figure 1 shows the interaction of a planar domain wall with a inhomogeneity created by local processing of a film with a solution of $KMnO_4$ at a concentration of 0.15 mol/l. through an opening in the mask with radius 4 μm. The wall is attracted to the surface of the microinhomogeneity, but cannot penetrate inside.

Our studies of the interaction of artificial microinhomogeneities with spiral domains at various stages of formation of the latter indicate that spiral domains always start at the inhomogeneity, preferably at its surface (Fig. 2a). With increasing amplitude of the pulsed field, the ''head'' of the spiral domain penetrates into a microinhomogeneity and grows inside it (Fig. 2b).

This behavior of spiral domains was observed near inhomogeneities obtained by oxidation of local regions with di-

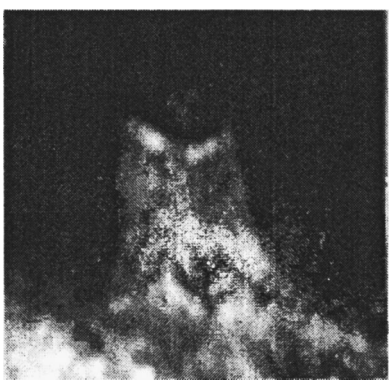

FIG. 1. Interaction of a domain wall with an artificial inhomogeneity in a gradient magnetic field.

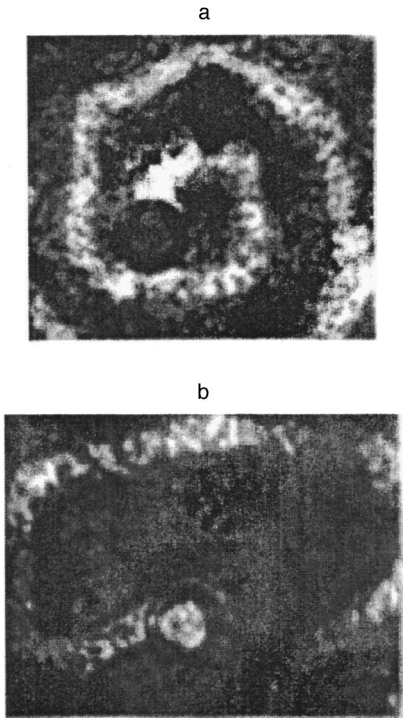

FIG. 2. a—a spiral domain starting at the surface of an artificial microinhomogeneity; b—a spiral domain growing within a inhomogeneity.

ameters of more than 6 μm. Penetration of spiral domains into smaller inhomogeneities was hindered. When spiral domains nucleate near inhomogeneities obtained by reduction of local regions of the film, penetration into the inhomogeneities was observed only for openings with diameters larger than 18 μm.

These results can be explained by the data in Ref. 12, according to which ions of Fe^{2+} and Fe^{4+} are simultaneously present in samples in their initial state (the thermodynamically stable existence of complexes of these ions was proved in Refs. 14 and 17). It has long been assumed[18] that Fe^{4+} ions are uniformly distributed among both tetrahedral and octahedral sites, while the Fe^{2+} are localized in the octahedral sublattice.

Oxidation initially decreases the concentration of divalent iron. However, if the degree of oxidation is further increased, the concentration of Fe^{4+} increases.[12] Because incorporation of O^{2-} ions at interstitial sites of the garnet structure is extremely improbable, absorption of oxygen must be accompanied by the appearance of cation vacancies in octahedral sites. During oxidation, the magnetic moment initially decreases due to the decreased concentration of divalent iron in the octahedral sublattice; the magnetization then increases as an increasing number of cation vacancies appear.[12] The slight increases in domain-wall energy density and K_U (Table I) can be connected with the disappearance of divalent iron, and with a decrease in the negative contribution to the uniaxial anisotropy from magnetoelastic energy caused by the mismatched lattice periods of the inhomogeneity and the film bulk. This happens because the lattice period of a film under compression decreases, and because the sign of the magnetostriction constant λ_{111} is negative.

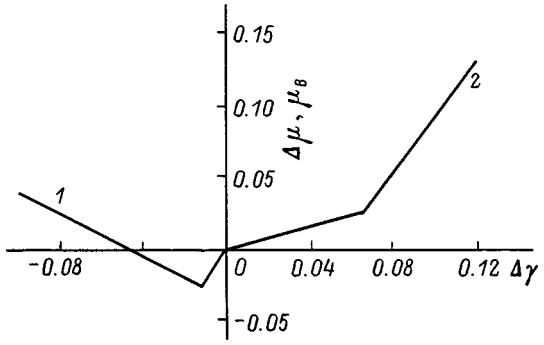

FIG. 3. Dependence of the growth rate of the magnetic moment of a garnet formula unit (in Bohr magnetons μ_B) on the change in oxygen content during oxidation (branch *1*) and reduction (branch *2*).

During reduction, the number of anion vacancies increases. In this case, the concentration of Fe^{4+} first decreases, and then an accumulation of Fe^{2+} ions takes place. This leads to an increase in the magnetic moment with respect to the initial state, and to a decrease in the lattice period. The domain-wall surface energy density (Table I) increases both because of the change in magnetoelastic energy and because of the contribution of oxygen vacancies to the uniaxial anisotropy constant.[19]

Figure 3 shows the theoretical dependence of the increase in magnetic moment of a garnet formula unit ($\Delta\mu$) as γ changes.[12] Its agreement with the experimental data listed in Tables II and III unambiguously indicates a correlation with the dependence of $4\pi M_S$ on the concentration of oxidizing and reducing solutions used to process the films.

We used the data on the increase of $4\pi M_S$ with respect to the original state to compute values of $\Delta\gamma$, and also the magnetic moment m of the artificial inhomogeneities. Our results, which relate m to $\Delta\gamma$ are shown in Fig. 4. In this figure we also show values of the magnetic moments of the inhomogeneities determined by measuring the distortion of a domain wall, which exhibit satisfactory agreement with calculated values.

The patterns we have described in the interaction of artificial inhomogeneities with spiral domains also can be in-

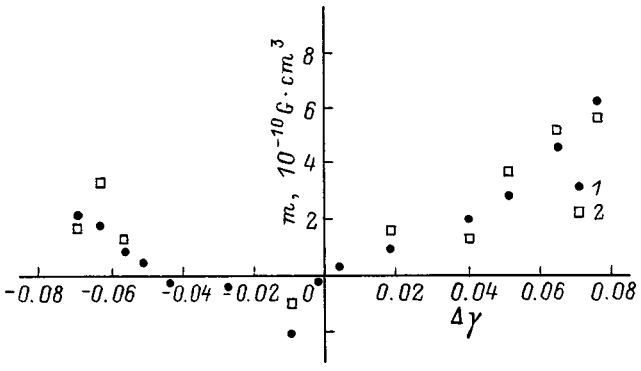

FIG. 4. Magnetic moment of an artificial inhomogeneity with radius 4 μm plotted versus the growth rate of the parameter γ with respect to the original ferrite host: *1*—calculated from data of Tables II and III, *2*—measured using a planar domain wall.

terpreted in terms of changes in the saturation magnetization and surface-energy density of the domain walls.

Thus, if the inhomogeneities have increased magnetization, they should attract a domain wall. However, since the surface energy of a wall within them is higher than it is in the host medium, crossing the boundary of the inhomogeneity can be energetically favorable only if the increase in excess surface energy is compensated by a decrease in magnetostatic energy. With increasing size of the inhomogeneity, the magnetostatic energy decreases more rapidly than the surface energy increases. Hence, penetration of a spiral domain into an inhomogeneity can take place when the dimensions of the latter are sufficiently large, and the larger these dimensions are, the higher the growth rate of the domain-wall surface-energy density and the lower the growth rate of the magnetization will be. According to the data of Table I, the growth rate of the surface-energy density prevails over the increase in its magnetostatic energy much more strongly for a reduced region than for an oxidized region. This also explains the larger critical values of the diameter for inhomogeneities obtained by reduction, i.e., for which penetration of a spiral domain is possible.

The authors are deeply grateful to G. P. Suslov for preparing the masks on the surfaces of our ferrite-garnet films.

[1] B. E. Lavin, Yu. D. Tret'yakov, and L. M. Letyuk, *Physico-Chemical Principles of the Growth, Properties, and Applications of Ferrites* (Metallurgiya, Leningrad, 1970).
[2] M. Pardavi-Horvath, Prog. Cryst. Growth Charact. **5**, 175 (1982).
[3] S. Lagomarsino and A. Tucciarone, Thin Solid Films **114**, *1–2*, 45 (1984).
[4] V. V. Randoshkin and A. Ya. Chervonenkis, *Applied Magnetooptics* (Energoatomizdat, Moscow, 1990).
[5] V. K. Karpasyuk, M. F. Bulatov, and A. A. Shchepetkin, *40th Annual Conference on Magnetism and Magnetic Materials*, Abstracts Book (Philadelphia, 1995), AS-08.
[6] A. Hubert, *Theorie der Domanenwande in Geordneten Medien* (Springer-Verlag, Berlin, 1974; Mir, Moscow, 1977).
[7] P. P. D'yachuk, E. V. Larikov, and G. O. Patrushev, Fiz. Met. Metalloved. **8**, 39 (1991).
[8] M. A. Shamsutdinov, V. G. Veselago, M. M. Farztdinov, and E. G. Ekomasov, Fiz. Tverd. Tela (Leningrad) **32**, 497 (1990) [Sov. Phys. Solid State **32**, 288 (1990)].
[9] V. K. Karpasyuk and M. F. Bulatov, IEEE Trans. Magn. **30**, 4344 (1994).
[10] V. K. Karpasyuk, M. F. Bulatov, A. A. Dmitriev, and S. V. Churzin, *Abstracts from the Proc. 15th All-Russia School-Seminar on ''New Magnetic Materials for Microelectronics''* (Moscow State Univ. Publ., Moscow, 1996), p. 197.
[11] M. F. Bulatov, Doctoral Cand. Dissertation (Ural State University, Ekaterinberg, 1998).
[12] M. F. Bulatov, V. K. Karpasyuk, R. M. Sattarov, and A. A. Shchepetkin, *Oxides: Physicochemical Properties and Technology*, Abstract from the All-Russia Conference (Ekaterinberg, 1998), p. 25.
[13] F. V. Lisovsliĭ, *Physics of Magnetic Bubbles* (Sov. Radio, Moscow, 1979; North-Holland, Amsterdam, 1975).
[14] V. G. Elemenkin, Doctoral Cand. Dissertation (Donets State University, Donets, 1985).
[15] G. S. Kandaurova, Dok. Ross. Akad. Nauk **331**(4), 428 (1993) [Phys. Dokl. **38**, 342 (1993)].
[16] V. V. Fedotova, A. P. Ges', and T. A. Gorbachevskaya, *Abstracts from the Proc. 14th All-Russia School-Seminar on ''New Magnetic Materials for Microelectronics,'' Part 3* (Moscow State Univ. Publ., Moscow, 1994), p. 16.
[17] K. Nassau, J. Cryst. Growth **2**, 215 (1968).
[18] B. Antonini, S. L. Blank, S. Lagomarsino, A. Paoletti, P. Paroli, and A. Tucciarone, IEEE Trans. Magn. **17**, *6*, 3220 (1981).
[19] L. C. Hsia, P. E. Wigen, P. DeGasperis, and C. Borghese, J. Appl. Phys. **53**, 2261 (1981).

Translated by Frank J. Crowne

Calculating coefficients for a system of moment equations used to describe the magnetization kinetics of a superparamagnetic particle in a fluctuating field

Yu. P. Kalmykov

Centre d'Etudes Fondamentales, Université de Perpignan, 52 Aveue de la Villeneuve, 66860, France

S. V. Titov

Institute of Radio Engineering and Electronics, Russian Academy of Sciences, 141120 Fryazino, Moscow District, Russia

(Submitted March 10, 1998)
Fiz. Tverd. Tela (St. Petersburg) **41**, 2020–2027 (November 1999)

A system of equations is derived for moments [averages of spherical harmonics $\langle Y_{l,m}\rangle(t)$] that determine the dynamics of the magnetization **M** of a superparamagnetic particle in a fluctuating field. The system is derived by representing the Gilbert equation in a fluctuating field, and the corresponding Fokker–Planck equation for the distribution function of **M**, in terms of angular momentum operators, which in turn makes it possible to express the coefficients of the system of moment equations in terms of Clebsch–Gordan coefficients. © *1999 American Institute of Physics.* [S1063-7834(99)02311-4]

Single-domain ferromagnetic particles are characterized by an internal anisotropy potential that can have multiple local minima, i.e., points of local equilibrium, with potential barriers between them. If the particles are small ($\sim$100 Å), which implies low potential barriers, the magnetization vector $\mathbf{M}(t)$ can be reoriented by thermal fluctuations over the barriers from one equilibrium position to another.[1] This thermal instability of the magnetization leads to superparamagnetism.[2] At present there is considerable interest in studying thermal fluctuations and relaxation of the magnetization of single-domain particles, within the context of improving the characteristics of magnetic recording media.[3]

The dynamics of the magnetization $\mathbf{M}(t)$ of a single-domain ferromagnetic particle are described by the Gilbert equation with a fluctuating field[4,5]

$$\frac{d}{dt}\mathbf{M}(t)=\gamma[\mathbf{M}(t)\times[\mathbf{H}(t)+\mathbf{h}(t)-\eta\dot{\mathbf{M}}(t)]], \tag{1}$$

where γ is the gyromagnetic ratio, η is a friction coefficient, **H** is the total magnetic field, made up of external applied fields and the magnetic anisotropy field, and $\mathbf{h}(t)$ is a random field with white-noise properties:

$$\overline{h_i(t)}=0,$$

$$\overline{h_i(t_1)h_j(t_2)}=2\eta\beta^{-1}\delta_{ij}\delta(t_1-t_2), \quad (i,j=X,Y,Z). \tag{2}$$

Here the overbar denotes statistical averaging over an ensemble of particles which at time t have the same magnetization $\mathbf{M}(t)$, $\beta=\nu/k_BT$, ν is the particle volume, k_B is the Boltzmann constant, and T is the temperature. The random field $\mathbf{h}(t)$ arises from thermal fluctuations. We estimate the amplitude of $\mathbf{h}(t)$ to be of order $kT/\nu M_s$ (where M_s is the magnetization of the particle material), which at room temperature is $\geqslant$100 Oe. Thus, the random field is comparable in size to the magnetic anisotropy field.[6]

Starting from Eq. (1), Brown derived a Fokker–Planck equation for the distribution function $W(\{\mathbf{M}\},t)$ for **M** with respect to direction:[7]

$$\frac{\partial W}{\partial t}=L_{FP}W=b\left[\frac{1}{\beta}\Delta W+W\Delta V+\left(\frac{\partial V}{\partial\theta}\frac{\partial W}{\partial\theta}-\frac{\partial V}{\partial\varphi}\frac{\partial W}{\partial\varphi}\right)+\frac{1}{\alpha\sin\theta}\left(\frac{\partial V}{\partial\theta}\frac{\partial W}{\partial\varphi}-\frac{\partial V}{\partial\varphi}\frac{\partial W}{\partial\theta}\right)\right], \tag{3}$$

where L_{FP} is the Fokker–Planck operator, Δ is the Laplace operator, V is the free energy function for unit volume, θ, φ are the polar and azimuthal angles in a spherical coordinate system, $b=\beta/2\tau_N$,

$$\tau_N=\frac{\nu M_s(1+\alpha^2)}{2k_BT\gamma\alpha} \tag{4}$$

is the characteristic time for thermal fluctuations of the magnetization, and $\alpha=\gamma\eta M_s$ is a dimensionless dissipation coefficient. Here we assume that the magnetization is uniform throughout the volume of the particle and only its orientation changes, not its magnitude. It is also assumed that the particles do not interact with each other.[8] (Discussion of the assumptions used in deriving the Gilbert and Fokker–Planck equations can be found, for example, in Refs. 6, 7, and 9).

Let us look for a solution to the Fokker–Planck equation (3) in the form of an expansion in spherical harmonics $Y_{l,m}$. This leads to an infinite system of recursive differential equations for the moments $\langle Y_{l,m}\rangle(t)$ (see Ref. 10):

$$\frac{d}{dt}\langle Y_{l,m}\rangle(t)=\sum_{l',m'} d_{l',m',l,m}\langle Y_{l',m'}\rangle(t). \tag{5}$$

Here $d_{l',m',l,m}$ are matrix elements of the Fokker–Planck operator,[10] which depend on parameters that characterize the anisotropy energy, the external field, and the dissipation. Derivations and solutions to Eq. (5) for special problems are

given, for example, in Refs. 6,10–16. Solving the Gilbert equation (1) can be reduced also to solving the system of moment equations (5).[17–20]

Although the method of moments has a long history of use in superparamagnetism theory, it can address specific kinetics problems involving single-domain particles with complicated potential anisotropies V only with difficulty. This is because calculating $d_{l',m',l,m}$ for each individual potential anisotropy potential V requires complicated transformations of the Gilbert equation, or the Fokker–Planck equation corresponding to it (see, e.g., Ref. 10). At present, there are no known general relations for $d_{l',m',l,m}$ that are correct for a particle with arbitrary anisotropy potential. The goal of this paper is to derive such relations for $d_{l',m',l,m}$.

1. THE METHOD OF THE LANGEVIN EQUATION

Equation (1) can be transformed[9] into the form of a Landau–Lifshits equation[21]

$$\frac{d}{dt}\mathbf{M}(t)=\frac{bM_s}{\alpha}\mathbf{M}(t)[\mathbf{H}(t)+\mathbf{h}(t)]-b\mathbf{M}(t)\times[\mathbf{M}(t)\times[\mathbf{H}(t)+\mathbf{h}(t)]]. \tag{6}$$

If V is the free energy per unit volume, then in a spherical coordinate basis $\{\mathbf{e}_\theta,\mathbf{e}_\varphi,\mathbf{e}_r\}$ the field $\mathbf{H}$ can be written[9,10]

$$\mathbf{H}=-\frac{1}{M_s}\left(\mathbf{e}_\theta\frac{\partial}{\partial\theta}+\mathbf{e}_\varphi\frac{1}{\sin\theta}\frac{\partial}{\partial\varphi}\right)V, \tag{7}$$

while the components of the vectors can be represented in the form

$$\mathbf{M}=\{0,0,M\},\quad \dot{\mathbf{M}}=\{M\dot{\theta},M\sin\theta\dot{\varphi},0\},$$
$$\mathbf{h}=\{h_\theta,h_\varphi,0\} \tag{8}$$

(here it is usually assumed that $\dot{M}=0$, i.e., $M=M_s$). The coefficients of the random field $h_\theta(t)$, $h_\varphi(t)$ in spherical coordinates can be expressed in terms of $h_X(t)$, $h_Y(t)$, $h_Z(t)$, i.e., its components in a Cartesian coordinate system, in the following way:

$$h_\theta(t)=h_X(t)\cos\theta(t)\cos\varphi(t)+h_Y(t)\cos\theta(t)\sin\varphi(t)-h_Z(t)\sin\theta(t), \tag{9}$$

$$h_\varphi(t)=-h_X(t)\sin\varphi(t)+h_Y(t)\cos\varphi(t). \tag{10}$$

Decomposing the vector products in Eq. (6) and taking Eqs. (7)–(10) into account, we obtain a system of stochastic differential equations in spherical coordinates:

$$\dot{\theta}(t)=-b\left(\frac{\partial V(\theta(t),\varphi(t),t)}{\partial\theta}-\frac{1}{\alpha\sin\theta(t)}\frac{\partial V(\theta(t),\varphi(t),t)}{\partial\varphi}\right)+g_{\theta X}h_X(t)+g_{\theta Y}h_Y(t)+g_{\theta Z}h_Z(t), \tag{11}$$

$$\dot{\varphi}(t)=-\frac{b}{\sin\theta(t)}\left(\frac{1}{\alpha}\frac{\partial V(\theta(t),\varphi(t),t)}{\partial\theta}+\frac{1}{\sin\theta(t)}\frac{\partial V(\theta(t),\varphi(t),t)}{\partial\varphi}\right)+g_{\varphi X}h_X(t)+g_{\varphi Y}h_Y(t)+g_{\varphi Z}h_Z(t), \tag{12}$$

where

$$g_{\theta X}=bM_s\left(\cos\theta\cos\varphi+\frac{1}{\alpha}\sin\varphi\right),$$
$$g_{\theta Y}=bM_s\left(\cos\theta\sin\varphi-\frac{1}{\alpha}\cos\varphi\right),$$
$$g_{\theta Z}=-bM_s\sin\theta,$$
$$g_{\varphi X}=\frac{bM_s}{\sin\theta}\left(-\sin\varphi+\frac{1}{\alpha}\cos\theta\cos\varphi\right),$$
$$g_{\varphi Y}=\frac{bM_s}{\sin\theta}\left(\cos\varphi+\frac{1}{\alpha}\cos\theta\sin\varphi\right),$$
$$g_{\varphi Z}=-\frac{bM_s}{\alpha}. \tag{13}$$

In order to further average and transform the stochastic differential equations (11) and (12), which contain multiplicative noise, we must use the approach of Stratonovich,[22] because the magnetic relaxation processes under study are most conveniently modeled within the framework of this approach from the physical point of view. In particular, when we use this method we do not need to first transform Eqs. (11) and (12) into the equivalent form of an Ito equation.[23] Since the rules of ordinary analysis apply when we transform stochastic differential equations within the Stratonovich approach, it is not difficult to obtain the following stochastic differential equation for the spherical harmonics:

$$\frac{d}{dt}Y_{l,m}(\theta(t),\varphi(t))=\dot{\theta}(t)\frac{\partial}{\partial\theta}Y_{l,m}(\theta(t),\varphi(t))+\dot{\varphi}(t)\frac{\partial}{\partial\varphi}Y_{l,m}(\theta(t),\varphi(t)), \tag{14}$$

where

$$Y_{l,m}(\theta,\varphi)=(-1)^m\sqrt{\frac{(2l+1)(l-m)!}{4\pi(l+m)!}}\times e^{im\varphi}(1-\cos^2\vartheta)^{m/2}\frac{d^mP_l(\cos\theta)}{d\cos^m\theta},$$
$$Y_{l,-m}=(-1)^mY^*_{l,m},\quad m>0,$$

where $P_l(x)$ are Legendre polynomials[24] and $\dot{\theta}(t)$, $\dot{\varphi}(t)$ are defined by Eqs. (11) and (12).

The procedure for averaging the stochastic differential equation (14) is analogous to that used, e.g., in Refs. 17–19. Recall that when stochastic differential equations for N variables $\{\boldsymbol{\xi}(t)\}=\{\xi_1,\xi_2,\ldots,\xi_N\}$ in the form[25,26]

$$\frac{d\xi_i(t)}{dt}=H_i(\{\xi(t)\},t)+g_{ij}(\{\xi(t)\},t)h_j(t) \tag{15}$$

with

$$\overline{h_i(t)}=0, \quad \overline{h_i(t_1)h_j(t_2)}=2D\delta_{ij}\delta(t_1-t_2),$$

are averaged according to Stratonovich's rule[22] at time t, the following expression is obtained:

$$\frac{dx_i}{dt}=\lim_{\tau\to 0}\frac{\overline{\xi_i(t+\tau)-x_i}}{\tau}$$

$$=H_i(\{\mathbf{x}\},t)+Dg_{kj}(\{\mathbf{x}\},t)\frac{\partial}{\partial x_k}g_{ij}(\{\mathbf{x}\},t). \tag{16}$$

Here $\xi_i(t+\tau)$ $(\tau>0)$ is the solution to Eq. (15) with initial condition $\xi_i(t)=x_i$ [in Eqs. (15) and (16), and in every expression that follows, we will understand summation over repeated indices j and k]. A proof of this is given, e.g., in Ref. 25. The same method was used in Ref. 17 to prove that the averaged equation for an arbitrary differentiable function $f(\{\boldsymbol{\xi}\})$ has the form

$$\frac{d}{dt}f(\{\mathbf{x}\})=H_i(\{\mathbf{x}\},t)\frac{\partial}{\partial x_i}f(\{\mathbf{x}\})$$

$$+Dg_{kj}(\{\mathbf{x}\},t)\frac{\partial}{\partial x_k}\left[g_{ij}(\{\mathbf{x}\},t)\frac{\partial}{\partial x_i}f(\{\mathbf{x}\})\right]. \tag{17}$$

In the case under discussion, the quantity $Y_{l,m}$ plays the role of the function f. Thus, carrying out the averaging in Eq. (14) we obtain

$$2\tau_N\frac{d}{dt}Y_{l,m}=\frac{1}{\sin\theta}\frac{\partial}{\partial\theta}\left(\sin\theta\frac{\partial Y_{l,m}}{\partial\theta}\right)+\frac{1}{\sin^2\theta}\frac{\partial^2 Y_{l,m}}{\partial\varphi^2}$$

$$-\beta\left[\frac{\partial V}{\partial\theta}\frac{\partial Y_{l,m}}{\partial\theta}+\frac{1}{\sin^2\theta}\frac{\partial V}{\partial\varphi}\frac{\partial Y_{l,m}}{\partial\varphi}\right]$$

$$+\frac{\beta}{\alpha\sin\theta}\left[\frac{\partial V}{\partial\varphi}\frac{\partial Y_{l,m}}{\partial\theta}-\frac{\partial V}{\partial\theta}\frac{\partial Y_{l,m}}{\partial\varphi}\right]. \tag{18}$$

It should be noted that θ and φ in Eq. (18) and $\theta(t)$ and $\varphi(t)$ in Eqs. (11), (12), and (14) have different meanings, namely: $\theta(t)$ and $\varphi(t)$ are stochastic variables (random processes), whereas θ and φ in Eq. (18) are the values of these variables at time t. Instead of using different symbols for these quantities, we will follow Refs. 25 and 26 and omit the temporal argument t from the values of the stochastic variables at time t.

In what follows, it will be convenient to express the right side of Eq. (18) in terms of the angular momentum operators L_Z, $L_\pm$, L^2, which are defined as follows[24]:

$$L^2=-\left[\frac{1}{\sin\theta}\frac{\partial}{\partial\theta}\left(\sin\theta\frac{\partial}{\partial\theta}\right)+\frac{1}{\sin^2\theta}\frac{\partial^2}{\partial\varphi^2}\right],$$

$$L_Z=-i\frac{\partial}{\partial\varphi}, \quad L_\pm=e^{\pm i\varphi}\left(\pm\frac{\partial}{\partial\theta}+i\cot\theta\frac{\partial}{\partial\varphi}\right). \tag{19}$$

Then we can transform Eq. (18) to the following form:

$$\tau_N\dot{Y}_{l,m}=\frac{\beta}{4}(L^2(VY_{l,m})-VL^2Y_{l,m}-Y_{l,m}L^2V)$$

$$-\frac{1}{2}L^2Y_{l,m}-\frac{i\beta}{4\alpha}\sqrt{\frac{3}{2\pi}}\{Y_{1,1}^{-1}[(L_ZV_+)$$

$$\times(L_+Y_{l,m})-(L_+V_+)(L_ZY_{l,m})]$$

$$+Y_{1,-1}^{-1}[(L_ZV_-)(L_-Y_{l,m})-(L_-V_-)$$

$$\times(L_ZY_{l,m})]\}, \tag{20}$$

where for V we use the following decomposition with respect to spherical harmonics:

$$V=V_++V_-,$$

$$V_+=\sum_{R=1}^{\infty}\sum_{S=0}^{R}\nu_{R,S}Y_{R,S}, \quad V_-=\sum_{R=1}^{\infty}\sum_{S=-R}^{-1}\nu_{R,S}Y_{R,S}. \tag{21}$$

This representation is convenient because the results of operators L_Z, $L_\pm$, L^2 acting on spherical harmonics are given by the well-known relations[24]

$$L_ZY_{l,m}=mY_{l,m}, \tag{22}$$

$$L_\pm Y_{l,m}=\sqrt{l(l+1)-m(m\pm1)}\,Y_{l,m\pm1}, \tag{23}$$

$$L^2Y_{l,m}=l(l+1)Y_{l,m}. \tag{24}$$

Moreover, the functions $Y_{1,1}^{-1}$ and $Y_{1,-1}^{-1}$ can also be treated as operators acting on $Y_{l,m}$ according to the rule

$$Y_{1,\pm1}^{-1}Y_{l,\pm m}=\sqrt{\frac{8\pi(2l+1)(l-m)!}{3(l+m)!}}$$

$$\times\sum_{\substack{L=m-\varepsilon_{l,m}\\ \Delta L=2}}^{l-1}\sqrt{\frac{(2L+1)(L+m-1)!}{(L-m+1)!}}$$

$$\times Y_{L,\pm(m-1)},$$

$$(m>0), \tag{25}$$

where $\varepsilon_{l,m}=1$ if the labels l and m have the same parity, and $\varepsilon_{l,m}=0$ if they have different parities. Formula (25) is a consequence of the well-known relation[24]

$$\sqrt{\frac{8\pi}{3}}\,Y_{1,\pm1}Y_{l,m}=\sqrt{\frac{(l\pm m+1)(l\pm m+2)}{(2l+1)(2l+3)}}\,Y_{l+1,m\pm1}$$

$$-\sqrt{\frac{(l\mp m-1)(l\mp m)}{(2l-1)(2l+1)}}\,Y_{l-1,m\pm1}, \tag{26}$$

which can be written in the form of a recursion relation

$$Y_{l,\pm1}^{-1}Y_{l,m}=\sqrt{\frac{8\pi}{3}}\sqrt{\frac{(2l-1)(2l+1)}{(l\pm m)(l\pm m-1)}}\,Y_{l-1,m\mp1}$$

$$+\sqrt{\frac{(2l+1)(l\mp m)(l\mp m-1)}{(2l-3)(l\pm m)(l\pm m-1)}}\,Y_{l,\pm1}^{-1}Y_{l-2,m},$$

$$(|m\mp1|\leqslant l-1), \tag{27}$$

which has the solution Eq. (25).

Taking into account the following property of the product of two spherical harmonics[24]

$$Y_{l,m}Y_{l_1,m_1}=\sqrt{\frac{(2l+1)(2l_1+1)}{4\pi}}$$

$$\times\sum_{\substack{l_2=|l-l_1|,\\ \Delta l_2=2}}^{l+l_1}\frac{\langle l,0,l_1,0|l_2,0\rangle\langle l,m,l_1,m_1|l_2,m+m_1\rangle}{\sqrt{2l_2+1}}Y_{l_2,m+m_1} \tag{28}$$

(where $\langle l_1,m_1,l_2,m_2|l,m\rangle$ are Clebsch–Gordan coefficients[24]), and Eqs. (22)–(25), we can transform Eq. (20) to the form

$$\tau_N\dot{Y}_{l,m}=\sum_{l',s}e_{l,m,l',m\pm s}Y_{l',m\pm s}, \tag{29}$$

where

$$\begin{aligned}e_{l,m,l',m\pm s}=&-\frac{1}{2}l(l+1)\delta_{l,l'}\delta_{s,0}+(-1)^m\frac{\beta}{4}\\&\times\sqrt{\frac{(2l+1)(2l'+1)}{\pi}}\sum_{r=s}^{\infty}\nu_{r,\pm s}\\&\times\left\{\frac{[l'(l'+1)-r(r+1)-l(l+1)]}{2\sqrt{2r+1}}\right.\\&\times\langle l,0,l',0|r,0\rangle\langle l,m,l',-m\mp s|r,\mp s\rangle\\&+\frac{i}{\alpha}\sqrt{\frac{(2r+1)(r-s)!}{(r+s)!}}\\&\times\sum_{\substack{L=s-\varepsilon_{r,s},\\ \Delta L=2}}^{r-1}\sqrt{\frac{(L+s-1)!}{(L-s+1)!}}\langle l,0,l',0|L,0\rangle\\&\times(m\sqrt{(L+s)(L-s+1)}\langle l,m,l',-m\mp s|L,\mp s\rangle\\&\pm s\sqrt{(l\mp m)(l\pm m+1)}\\&\left.\times\langle l,m\pm 1,l',-m\mp s|L,\mp s\pm 1\rangle\right).\end{aligned} \tag{30}$$

Here $s\geqslant 0$, and the summation ranges over all labels for which the Clebsch–Gordan coefficients are meaningful. Relation (30) allows us to calculate the coefficients $e_{l,m,l',m'}$ for any specific anisotropy potential. An example of such a calculation for a cubic anisotropy is given in the Appendix.

The quantities $Y_{l,m}$ in Eq. (29) are functions of θ and φ, which are random quantities with a corresponding distribution density W. Thus, we must also average Eq. (29) with respect to W.[26] This leads us to a system of equations for the moments (averaged spherical harmonics):

$$\tau_N\frac{d}{dt}\langle Y_{l,m}\rangle(t)=\sum_{l',m'}e_{l,m,l',m'}\langle Y_{l',m'}\rangle(t), \tag{31}$$

where the angle brackets $\langle\ \rangle$ denote averaging with respect to W, while the coefficients $e_{l,m,l'm'}$ are given by Eq. (30).

2. THE FOKKER–PLANCK EQUATION METHOD

In the previous section the coefficients $e_{l,m,l',m'}$ entering into the system of equations for the averaged spherical harmonics were obtained by the Langevin method. An analogous result can also be obtained by using the Fokker–Planck equation.

It is well known that a Fokker–Planck equation for the distribution function $W(\{\mathbf{x}\},t)$ of a set of N variables $\{x_1,\ldots,x_N\}=\{\mathbf{x}\}$ can be derived from the corresponding Langevin equation (15) and written[25]

$$\frac{\partial W}{\partial t}=\frac{\partial}{\partial x_i}\left[-D_i(\{\mathbf{x}\})W+\frac{\partial}{\partial x_j}(D_{ij}(\{\mathbf{x}\})W)\right], \tag{32}$$

where

$$D_i(\{\mathbf{x}\})=H_i(\{\mathbf{x}\},t)+Dg_{jk}(\{\mathbf{x}\},t)\frac{\partial}{\partial x_j}g_{ik}(\{\mathbf{x}\},t) \tag{33}$$

is the drift vector, and

$$D_{ij}(\{\mathbf{x}\})=Dg_{ik}(\{\mathbf{x}\},t)g_{jk}(\{\mathbf{x}\},t) \tag{34}$$

is the diffusion tensor.

Since the properties (2) of the random field $\mathbf{h}(t)$ are usually specified when discussing the dynamics of magnetization of a particle in terms of Cartesian components (e.g., $i,j=X,Y,Z$), while the equations of motion for the components of the magnetization vector $\mathbf{M}$ are conveniently written in spherical coordinates [see Eqs. (11) and (12)], the following replacement is justified[25]:

$$D_i=\frac{\partial x_i}{\partial x_{i'}}D_{i'}+\frac{\partial^2 x_i}{\partial x_{i'}\partial x_{j'}}D_{i'j'}, \tag{35}$$

$$D_{ij}=\frac{\partial x_i}{\partial x_{i'}}\frac{\partial x_j}{\partial x_{j'}}D_{i'j'}, \tag{36}$$

where $i',j'=\theta,\varphi$, $i,j,k=X,Y,Z$, and $D_{i'}$, $D_{i'j'}$ are the coefficients given in spherical coordinates in accordance with Eqs. (33) and (34), in which the coefficients $g_{i'k}(\{\mathbf{x}\},t)$, $g_{j'k}(\{\mathbf{x}\},t)$ are taken from Eq. (13). After all these substitutions, we obtain Eq. (3).[5]

Let us write the solution to Eq. (3) in the form

$$W(\theta,\varphi,t)=\Psi(\theta,\varphi,t)\Psi^*(\theta,\varphi,t), \tag{37}$$

where $\Psi(\theta,\varphi,t)$ is given as

$$\Psi(\theta,\varphi,t)=\sum_{l,m}f_{l,m}(t)Y_{l,m}(\theta,\varphi). \tag{38}$$

The conditions for normalization of the function $W(\theta,\varphi,t)$ have the form

$$\int_0^{2\pi}d\varphi\int_0^{\pi}\sin\theta\,d\theta\,W(\theta,\varphi,t)=\sum_{l,m}|f_{l,m}(t)|^2=1.$$

Our method for solving the Fokker–Planck equation differs from that used in Refs. 10–15, where the function $W(\theta,\varphi,t)$ itself was postulated to have the form of Eq. (38). Representing the function $W(\theta,\varphi,t)$ in the form of Eq. (37) has certain obvious advantages. Above all, we are not required to impose additional conditions of positiveness and reality (which follow from its physical meaning) on the function $W(\theta,\varphi,t)$. Moreover, there is a direct quantum-mechanical analogy: the function $W(\theta,\varphi,t)$ is similar to the probability density $|\Psi|^2$ (where Ψ is the wave function) for which the continuity equation holds[27]

$$\frac{\partial|\Psi|^2}{\partial t}+\operatorname{div}\mathbf{j}=0,$$

where $\mathbf{j}$ is the probability current density.

Thus, once we have expressed the Fokker–Planck operator L_{FP} in Eq. (3) in terms of the angular momentum operators L_Z, $L_\pm$, L^2 of Eq. (19), we obtain [compare with Eq. (28)]

$$\begin{aligned}L_{FP}Y^*_{l',m'}=&\frac{\beta}{4\tau_N}(VL^2Y^*_{l',m'}-Y^*_{l',m'}L^2V-L^2(Y^*_{l',m'}V))\\&-\frac{1}{2\tau_N}L^2Y^*_{l',m'}+\frac{i\beta}{4\tau_N\alpha}\sqrt{\frac{3}{2\pi}}\\&\times\{Y^{-1}_{1,1}[(L_ZV_+)(L_+Y^*_{l',m'})-(L_+V_+)\\&\times(L_ZY^*_{l',m'})]+Y^{-1}_{1,-1}[(L_ZV_-)(L_-Y^*_{l',m'})\\&-(L_-V_-)(L_ZY^*_{l',m'})]\},\end{aligned}\tag{39}$$

where $V_\pm$ are given by Eqs. (21).

By making the transformation

$$\begin{aligned}&\int_0^{2\pi}d\varphi\int_0^{\pi}\sin\theta d\theta Y_{l,m}\frac{dW}{dt}\\&=\sum_{\substack{l',l''\\m',m''}}f_{l',m'}(t)f^*_{l'',m''}(t)\\&\times\int_0^{2\pi}d\varphi\int_0^{\pi}\sin\theta d\theta Y_{l,m}L_{FP}(Y_{l',m'}Y^*_{l'',m''})\\&=\sum_{\substack{l',l'',l'''\\m',m'',m'''}}(-1)^{m'}\sqrt{\frac{(2l'+1)(2l''+1)}{4\pi(2l'''+1)}}\\&\times\langle l',0,l'',0|l''',0\rangle\langle l',-m',l'',m''|l''',m'''\rangle\\&\times f_{l',m'}(t)f^*_{l'',m''}(t)\int_0^{2\pi}d\varphi\int_0^{\pi}\sin\theta d\theta Y_{l,m}L_{FP}Y^*_{l''',m'''},\end{aligned}\tag{40}$$

we obtain the moment system (5), where

$$\begin{aligned}\langle Y_{l,m}\rangle(t)=&\int_0^{2\pi}\int_0^{\pi}Y_{l,m}(\theta,\varphi)W(\theta,\varphi,t)\sin\theta\,d\theta\,d\varphi\\=&\sum_{\substack{l',l''\\m',m''}}\sqrt{\frac{(2l+1)(2l'+1)}{4\pi(2l''+1)}}\langle l,0,l',0|l'',0\rangle\\&\times\langle l,m,l',m'|l'',m''\rangle f_{l',m'}(t)f^*_{l'',m''}(t),\end{aligned}\tag{41}$$

$$\begin{aligned}d_{l',m\pm s,l,m}=&\int_0^{2\pi}d\varphi\int_0^{\pi}\sin\theta d\,\theta Y_{l,m}L_{FP}Y^*_{l',m\pm s}\\=&-\frac{l(l+1)\delta_{l,l'}\delta_{s,0}}{2\tau_N}+(-1)^m\frac{\beta}{4\tau_N}\\&\times\sqrt{\frac{(2l+1)(2l'+1)}{\pi}}\sum_{r=s}^{\infty}\nu_{r,\pm s}\\&\times\left\{\frac{[l'(l'+1)-r(r+1)-l(l+1)]}{2\sqrt{2r+1}}\right.\\&\times\langle l,0,l',0|r,0\rangle\langle l,m,l',-m\mp s|r,\pm s\rangle+\frac{i}{\alpha}\\&\times\sqrt{\frac{(2r+1)(r-s)!}{(r+s)!}}\sum_{\substack{L=s-\varepsilon_{r,s},\\ \Delta L=2}}^{r-1}\sqrt{\frac{(L+s-1)!}{(L-s+1)!}}\\&\times\langle l,0,l',0|L,0\rangle((m\pm s)\sqrt{(L+s)(L-s+1)}\\&\times\langle l,m,l',-m\mp s|L,\mp s\rangle\\&\mp s\sqrt{(l'\pm m+s)(l'\mp m-s+1)}\langle l,m,l',-m\mp s\\&\left.\pm1|L,\mp s\pm1\rangle)\right\}\end{aligned}\tag{42}$$

are matrix elements of the Fokker–Planck operator in the spherical harmonics system. In deriving Eqs. (42) we used the well-known relation[24]

$$\begin{aligned}&\int_0^{2\pi}d\varphi\int_0^{\pi}\sin\theta d\,\theta Y_{l,m}Y_{l',m'}Y^*_{l'',m''}\\&=\sqrt{\frac{(2l+1)(2l'+1)}{4\pi(2l''+1)}}\langle l,0,l',0|l'',0\rangle\\&\times\langle l,m,l',m'|l'',m''\rangle.\end{aligned}$$

Using the equation

$$\begin{aligned}&\sqrt{(l_3\pm m_3)(l_3\mp m_3+1)}\langle l_1,m_1,l_2,m_2|l_3,m_3\mp1\rangle\\&=\sqrt{(l_1\mp m_1)(l_1\pm m_1+1)}\langle l_1,m_1\pm1,l_2,m_2|l_3,m_3\rangle\\&+\sqrt{(l_2\mp m_2)(l_2\pm m_2+1)}\langle l_1,m_1,l_2,m_2\pm1|l_3,m_3\rangle\end{aligned}$$

and comparing [Eqs. (30) and (42)], we see that

$$d_{l',m',l,m}=e_{l,m,l',m'}/\tau_N.$$

This relation shows that the systems of equations (5) and (31) are completely equivalent, and also confirms the equivalence of the the Langevin-equation and Fokker–Planck equation methods.

Thus, in this paper we have obtained analytic expressions [Eqs. (30) and (42)] for the coefficients of the system of moment equations that describe the dynamics of magnetization of superparamagnetic particles for an arbitrary anisotropy potential V. Equations (3) and (42) can be derived independently by two methods (see the Langevin and the Fokker–Planck equation), which proves the equivalence of these methods for solving problems of magnetic relaxation in systems of superparamagnetic particles. In this case, however, the use of the Langevin equation method allows us to solve the problem more simply by directly averaging the Gilbert equation with a fluctuating field, without converting to a Fokker–Planck equation.

In calculating physical quantities (susceptibilities, magnetization relaxation times, etc.), the system of moment Eqs. (5) can be solved by standard numerical methods (prolongation, etc.) once we truncate the system, i.e., use only enough equations to achieve convergence. However, for low values of dissipation[1)] (which corresponds to the experimental conditions) we must include a very large number of equations ($\sim 10^4$ or more), making a stable solution much more difficult to obtain.[16] Therefore, in solving specific problems it is preferrable to use the method of matrix continuous fractions.[25,26] In essence this method consists of transforming the moment system (5) into a matrix three-term equation of the form[25,26]

$$\tau_N\frac{d}{dt}\mathbf{C}_n(t)=\mathbf{Q}_n^-\mathbf{C}_{n-1}(t)+\mathbf{Q}_n\mathbf{C}_n(t)+\mathbf{Q}_n^+\mathbf{C}_{n+1}(t),$$

$$n=1,2,3,\ldots, \tag{43}$$

where $\mathbf{C}_n(t)$ is a column vector made up of the moments $\langle Y_{l,m}\rangle(t)$, $\mathbf{C}_0(t)=0$, and $\mathbf{Q}_n^-$, $\mathbf{Q}_n$, $\mathbf{Q}_n^+$ are matrices of the corresponding dimensionality consisting of the $d_{l',m',l,m}$. The exact solution to Eq. (43) for the Laplace transform of $\mathbf{C}_1(t)$ has the form[26]

$$\tilde{\mathbf{C}}_1(s)=\tau_N[\tau_N s\mathbf{I}-\mathbf{Q}_1-\mathbf{Q}_1^+\mathbf{S}_2(s)]^{-1}\left\{\mathbf{C}_1(0)+\sum_{n=2}^{\infty}\left[\prod_{k=2}^{n}\mathbf{Q}_{k-1}^+\mathbf{S}_k(s)(\mathbf{Q}_k^-)^{-1}\right]\mathbf{C}_n(0)\right\}, \tag{44}$$

where $\mathbf{I}$ is the unit matrix. The infinite matrix continued fraction $\mathbf{S}_n(s)$ is defined by the relation

$$\mathbf{S}_n(s)=\cfrac{\mathbf{I}}{\tau_N s\mathbf{I}-\mathbf{Q}_n-\mathbf{Q}_n^+\cfrac{\mathbf{I}}{\tau_N s\mathbf{I}-\mathbf{Q}_{n+1}-\mathbf{Q}_{n+1}^+\cfrac{\mathbf{I}}{\tau_N s\mathbf{I}-\mathbf{Q}_{n+2}-\cdots}\mathbf{Q}_{n+2}^-}\mathbf{Q}_{n+1}^-}\mathbf{Q}_n^-.$$

The initial-condition vectors $\mathbf{C}_n(0)$ can also be calculated with the help of the matrix continued fraction $\mathbf{S}_n(0)$.[25,26] As many examples have shown[25,26], the method of matrix continued fractions is considerably more convenient computationally for solving infinite systems of linear equations than standard numerical methods. This method was used in Refs. 17–20, and 29 to calculate the characteristics of superparamagnets.

This work was done with the partial support of the Russian Fund for Fundamental Research (Project No. 96-02-16762-a) and INTAS (Project No. 96-0663).

APPENDIX

Coefficients for cubic anisotropy. As an example let us consider particles with cubic anisotropy. Direct calculation of the matrix elements using the method of the Fokker–Planck equation are given, for example, in Ref. 10. Here we show how the coefficients $e_{l',m',l,m}$ follow from Eq. 30 [$d_{l',m',l,m}$ can be obtained easily from Eq. (42)]. The free-energy function for a unit volume of particles with cubic potentials is given by[9,10]

$$V=\frac{K}{4}(\sin^4\theta\sin^2 2\varphi+\sin^2 2\theta)=-\frac{2K}{15}\sqrt{\pi}Y_{4,0}-\frac{K}{15}\sqrt{\frac{10\pi}{7}}[Y_{4,4}+Y_{4,-4}]+\frac{K}{5}, \tag{A1}$$

where K is the anisotropy constant. Let us introduce a dimensionless anisotropy parameter

$$\sigma=\beta K/4.$$

Then from Eqs. (30) and (A1) we obtain 27 nonzero coefficients:

$$e_{l,m,l,m}=(-1)^m\frac{4\sigma}{9}(2l+1)\langle l,0,l,0|4,0\rangle\langle l,m,l,-m|4,0\rangle-\frac{1}{2}l(l+1)$$

$$=\sigma\frac{9(l^2-1)[(l+1)^2-1]-15m^2[6l(l+1)-5-7m^2]}{[4l^2-9][4(l+1)^2-9]}-\frac{l(l+1)}{2},$$

$$e_{l,m,l,m\pm4}=(-1)^m4\sqrt{\frac{5}{14}}\frac{\sigma}{9}(2l+1)\langle l,0,l,0|4,0\rangle\langle l,m,l,-m\mp4|4,\mp4\rangle$$

$$=\frac{15\sigma\sqrt{(l\mp m)(l\pm m+4)[l^2-(m\pm1)^2][l^2-(m\pm2)^2][l^2-(m\pm3)^2]}}{2(4l^2-9)[4(l+1)^2-9]},$$

$$e_{l,m,l-2,m}=(-1)^m\frac{2\sigma}{45}\sqrt{(2l+1)(2l-3)}(2l+9)\langle l,0,l-2,0|4,0\rangle\langle l,m,l-2,-m|4,0\rangle$$

$$=\frac{\sigma(2l+9)(l^2-l-2-7m^2)}{(2l-5)(2l-1)(2l+3)}\sqrt{\frac{(l^2-m^2)[(l-1)^2-m^2]}{(2l-3)(2l+1)}},$$

$$e_{l,m,l-2,m\pm4}=(-1)^m2\sqrt{\frac{5}{14}}\frac{\sigma}{45}\sqrt{(2l+1)(2l-3)}(2l+9)\langle l,0,l-2,0|4,0\rangle\langle l,m,l-2,-m\mp4|4,\mp4\rangle$$

$$=-\frac{\sigma(2l+9)}{2(2l-5)(2l-1)(2l+3)}\sqrt{\frac{(l\mp m-5)(l\mp m-4)(l\mp m-3)(l\mp m)[l^2-(m\pm2)^2][l^2-(m\pm1)^2]}{(2l-3)(2l+1)}},$$

$$e_{l,m,l-4,m}=(-1)^m\frac{8\sigma}{45}\sqrt{(2l+1)(2l-7)}(l+1)\langle l,0,l-4,0|4,0\rangle\langle l,m,l-4,-m|4,0\rangle$$

$$=\frac{7\sigma(l+1)}{(2l-5)(2l-3)(2l-1)}\sqrt{\frac{[(l-3)^2-m^2][(l-2)^2-m^2][(l-1)^2-m^2][l^2-m^2]}{(2l-7)(2l+1)}},$$

$$e_{l,m,l-4,m\pm4}=(-1)^m\sqrt{\frac{5}{14}}\frac{8\sigma}{45}\sqrt{(2l+1)(2l-7)}(l+1)\langle l,0,l-4,0|4,0\rangle\langle l,m,l-4,-m\mp4|4,\mp4\rangle$$

$$=\frac{\sigma(l+1)}{2(2l-5)(2l-3)(2l-1)}\sqrt{\frac{(l\mp m-7)(l\mp m-6)\ldots(l\mp m-1)(l\mp m)}{(2l-7)(2l+1)}},$$

$$e_{l,m,l-1,m}=(-1)^{m+1}\frac{2i\sigma m}{5\alpha}\sqrt{4l^2-1}[\langle l,0,l-1,0|1,0\rangle\langle l,m,l-1,-m|1,0\rangle+\langle l,0,l-1,0|3,0\rangle\langle l,m,l-1,-m|3,0\rangle]$$

$$=-\frac{3i\sigma m(3l^2-5-7m^2)}{\alpha(4l^2-9)}\sqrt{\frac{l^2-m^2}{4l^2-1}},$$

$$e_{l,m,l-1,m\pm4}=\pm(-1)^m\frac{2i\sigma}{7\sqrt{5\alpha}}$$

$$\times\sqrt{(4l^2-1)(l\pm m+3)(l\mp m-4)}\langle l,0,l-1,0|3,0\rangle\langle l,m,l-1,-m\mp3|3,\mp3\rangle$$

$$=\pm\frac{3i\sigma}{2\alpha(4l^2-9)}\sqrt{\frac{(l\mp m)(l\mp m-4)[l^2-(m\pm1)^2][l^2-(m\pm2)^2][l^2-(m\pm3)^2]}{4l^2-1}},$$

$$e_{l,m,l-3,m}=(-1)^{m+1}\frac{2i\sigma m}{5\alpha}\sqrt{4(l-1)^2-9}\langle l,0,l-3,0|3,0\rangle\langle l,m,l-3,-m|3,0\rangle$$

$$=-\frac{7i\sigma m}{\alpha[4(l-1)^2-1]}\sqrt{\frac{(l^2-m^2)[(l-1)^2-m^2][(l-2)^2-m^2]}{4(l-1)^2-9}},$$

$$e_{l,m,l-3,m\pm4}=\pm(-1)^m\frac{2i\sigma}{7\sqrt{5\alpha}}\sqrt{[4(l-1)^2-9](l\pm m+1)(l\mp m-6)}\langle l,0,l-3,0|3,0\rangle\langle l,m,l-3,-m\mp3|3,\mp3\rangle$$

$$=\mp\frac{i\sigma}{2\alpha[4(l-1)^2-1]}\sqrt{\frac{(l\mp m-6)(l\mp m-5)\ldots(l\mp m-1)(l\mp m)(l\pm m+1)}{4(l-1)^2-9}}.$$

The remaining elements are found from the relations

$$e_{l,m,l+2,m}=-\frac{2l-7}{2l+13}e_{l+2,m,l,m},$$

$$e_{l,m,l+2,m\pm4}=-\frac{2l-7}{2l+13}e_{l+2,m\pm4,l,m},$$

$$e_{l,m,l+4,m}=-\frac{l}{l+5}e_{l+4,m,l,m},$$

$$e_{l,m,l+4,m}=-\frac{l}{l+5}e_{l+4,m\pm4,l,m},$$

$$e_{l,m,l+1,m}=e_{l+1,m,l,m},\quad e_{l,m,l+1,m\pm4}=e_{l+1,m\pm4,l,m},$$

$$e_{l,m,l+3,m}=e_{l+3,m,l,m},\quad e_{l,m,l+3,m\pm4}=e_{l+3,m\pm4,l,m}.$$

The coefficients $e_{l',m'l,m,}$ coincide exactly with the expressions obtained in Refs. 10, 18, and 20.

[1)]Methods used to experimentally and theoretically estimate the dissipation parameter α are discussed, e.g., in Refs. 6, 9, and 28. These estimates give values of α of order 0.01–0.1.

[1] L. Néel, Ann. Géophys. (C.N.R.S.) **5**, 99 (1949).
[2] C. P. Bean and J. D. Livingston, Suppl. J. Appl. Phys. **30**, 1205 (1959).
[3] H. B. Braun and H. N. Bertram, J. Appl. Phys. **75**, 4609 (1994).
[4] T. L. Gilbert, Phys. Rev. **100**, 1243 (1956).
[5] W. F. Brown, Jr., Phys. Rev. **130**, 1677 (1963).
[6] Yu. L. Raikher and M. I. Shliomis, Adv. Chem. Phys. **87**, 595 (1994).
[7] W. F. Brown, Jr., IEEE Trans. Magn. **15**, 1196 (1979).
[8] I. Klik and L. Gunther, J. Appl. Phys. **67**, 4505 (1990).
[9] I. Klik and L. Gunther, J. Stat. Phys. **60**, 473 (1990).
[10] L. J. Geoghegan, W. T. Coffey, and B. Mulligan, Adv. Chem. Phys. **100**, 475 (1997).
[11] A. Aharoni, Phys. Rev. **177**, 763 (1969).
[12] Yu. L. Raĭkher and M. I. Shliomis, Zh. Éksp. Teor. Fiz. **67**, 1060 (1974) [Sov. Phys. JETP **40**, 526 (1974)].
[13] I. Eisenstein and A. Aharoni, Phys. Rev. B **16**, 1278 (1977).
[14] E. K. Sadykov and A. G. Isavnin, Fiz. Tverd. Tela (St. Petersburg) **38**, 2104 (1996) [Phys. Solid State **38**, 1160 (1996)].
[15] Yu. L. Raikher and V. I. Stepanov, Phys. Rev. B **55**, 15 005 (1997).
[16] W. T. Coffey, D. S. F. Crothers, J. L. Dormann, L. J. Geoghegan, and E. C. Kennedy, Phys. Rev. B **58**, *6*, 3249 (1998).
[17] Yu. P. Kalmykov and W. T. Coffey, Phys. Rev. B **56**, 3325 (1997).
[18] Yu. P. Kalmykov, S. V. Titov, and W. T. Coffey, Phys. Rev. B **58**, 3267 (1998).
[19] Yu. P. Kalmykov and S. V. Titov, Fiz. Tverd. Tela (St. Petersburg) **40**, 1642 (1998) [Phys. Solid State **40**, 1492 (1998)].
[20] Yu. P. Kalmykov and S. V. Titov, Zh. Éksp. Teor. Fiz. **115**, 101 (1999) [JETP **88**, 58 (1999)].
[21] L. D. Landau and E. M. Lifshitz, Phys. Z. Sowjetunion **8**, 153 (1935).
[22] R. L. Stratonovich, *Conditional Markov Processes wth Applications to the Theory of Optimal Control* (Moscow State Univ. Publ., Moscow, 1968).
[23] C. W. Gardiner, *Handbook of Stochastic Methods for Physics, Chemistry, and the Natural Sciences* (Springer-Verlag, Berlin, 1985; Mir, Moscow, 1986).
[24] R. Zar, *The Theory of Angular Momentum. Spatial Effects in Physics and Chemistry* (Mir, Moscow, 1993).
[25] H. Risken, *The Fokker–Planck Equation* (Springer, Berlin, 1989).
[26] W. T. Coffey, Yu. P. Kalmykov, and J. T. Waldron, *The Langevin Equation* (World Scientific, Singapore, 1996).
[27] L. D. Landau and E. M. Lifshits, *Quantum Mechanics: Non-Relativistic Theory* (4th edition Nauka, Moscow, 1989; Pergamon Press, Oxford, 1977).
[28] W. T. Coffey, D. S. F. Crothers, J. L. Dormann, Yu. P. Kalmykov, E. C. Kennedy, and W. Wernsdorfer, Phys. Rev. Lett. **80**, 5655 (1998).
[29] Yu. P. Kalmykov and S. V. Titov, Fiz. Tverd. Tela (St. Petersburg) **40**, 1898 (1998) [Phys. Solid State **40**, 1721 (1998)].

Translated by Frank J. Crowne

Nonequilibrium properties of re-entrant spin glasses in a magnetic field

Yu. P. Grebenyuk, A. B. Surzhenko, and G. A. Takzeĭ

Institute of Magnetism, Ukrainian Academy of Sciences, 252680 Kiev, Ukraine
(Submitted March 12, 1998)
Fiz. Tverd. Tela (St. Petersburg) **41**, 2028–2033 (November 1999)

In this paper the authors discuss how the re-entrant spin-glass state arises in the disordered alloys $Ni_{100-x}Mn_x$ $(x=19, 21, 23)$, along with the nonequilibrium magnetic properties of these alloys. It is shown that near the Gabay–Toulouse phase line the time it takes the system to reach equilibrium is comparable to times required to perform static experiments $(10^1-10^4\ \mathrm{s})$; cooling the sample into the region of crossover with the de Almeida–Thouless line causes these times to increase to astronomical values of more than 10^{16} s. A method is proposed for constructing magnetic phase diagrams of systems of this type in ''magnetic field-temperature'' coordinates. © *1999 American Institute of Physics.* [S1063-7834(99)02411-9]

Irreversible phenomena, e.g., thermomagnetic hysteresis, magnetic aging, long-time relaxation of the magnetization and correlation functions, etc., are fundamental properties of spin glasses. In systems where the spin glass arises directly from the paramagnetic state, the experimental manifestations of these properties have been rather well studied.[1] However, for a large number of systems, the state replaced by the spin-glass state during cooling is one of strongly frustrated ferromagnetism. This possibility is suggested by the calculations of Refs. 2,3, in which the molecular-field approximation is used for a frustrated ferromagnet with random domains. According to the magnetic phase diagram obtained in Refs. 2,3, cooling such systems on the Gabay–Toulouse line gives rise to components of the spin that are transverse to the spontaneous magnetization vector of the spin glass. Further cooling causes these longitudinal spin glass components to become unstable on the de Almeida–Thouless line . It is significant that, according to Refs. 2,3, the long-range frustrated-ferromagnetic order is preserved at all temperatures below the Curie temperature T_C.

In this paper, using the terminology of Ref. 4, we will refer to a state in which long-range frustrated ferromagnetic order coexists with the spin glass state as a state of asperomagnetism (ASM).

It is an established fact, however, that experimental studies of nonequilibrium magnetic properties of asperomagnets, especially in external magnetic fields, are fundamentally flawed. A partial explanation for this is the ambiguity that arises in interpreting the results when these systems are investigated by the macroscopic methods traditionally used to study spin glasses, since it is difficult to distinguish contributions from the frustrated-ferromagnet and spin-glass states.

In this paper we shall investigate the processes that give rise to the ASM state and the properties of the latter, and propose a method for constructing magnetic phase diagrams in ''magnetic field–temperature'' coordinates.

1. EXPERIMENTAL METHOD AND SAMPLES

As objects of study we chose disordered alloys from the system $Ni_{100-x}Mn_x$ $(x=19, 21, 23)$, which is characterized by competing exchange interactions. We made this choice because, in other systems that include frustrated ferromagnetic alloys, the appearance of a spin-glass state is accompanied by destruction of long-range magnetic order,[5,6] which contradicts the results of theory.[2,3] However, for the $Ni_{100-x}Mn_x$ $(x=19, 21, 23)$ system, various methods have shown that ferromagnetic alloys located in the magnetic phase diagram near the critical concentration $x_{FM} \cong 24$ at.%, at which long-range order appears, maintain the frustrated ferromagnetic order over the entire temperature interval $T<T_C$.[7] For this reason, these systems can be used to confirm experimentally the results of theory.[2,3]

A number of papers (see, e.g., the review article Ref. 8) have reported a tendency for $Ni_{100-x}Mn_x$ alloys (with $x \approx 25\%$ Mn) to form ferromagnetic regions with short-range atomic order of Ni_3Mn type, when the usual methods of sintering are used to prepare them. In light of this fact, we have arranged to accelerate the sintering by spinning from a melt in this work, so as to disorder the alloys more completely. Neutron diffraction shows that samples prepared in this way characteristically exhibit an FCC structure, and superstructure nuclear reflections (100) and (110), indicating the presence of atomically ordered regions of Ni_3Mn, are not seen on the neutron diffraction patterns.

The magnetic properties of these alloys were investigated using a standard mutual inductance bridge, allowing us to separate out the real χ' and imaginary χ'' components of the longitudinal dynamic magnetic susceptibility (DMS). The excitation sinusoidal magnetic field had a frequency 85 Hz and amplitude 0.1 Oe. Static field intensities up to 200 Oe were created using a copper solenoid.

At first glance, the fact that the Hamiltonian of a Heisenberg magnet is isotropic with respect to rotations[9] suggests that our method will be unable to record the transverse spin-glass irreversibility that appears on the GT line. However, the fact that anisotropic interactions are present in real magnets, e.g., the Dzyaloshinskiĭ–Mori anisotropy,[10] and are also very characteristic of ASM states with spin structure,[11] suggests that the longitudinal irreversibility in the magnetic response caused by strong transverse spin-glass irreversibil-

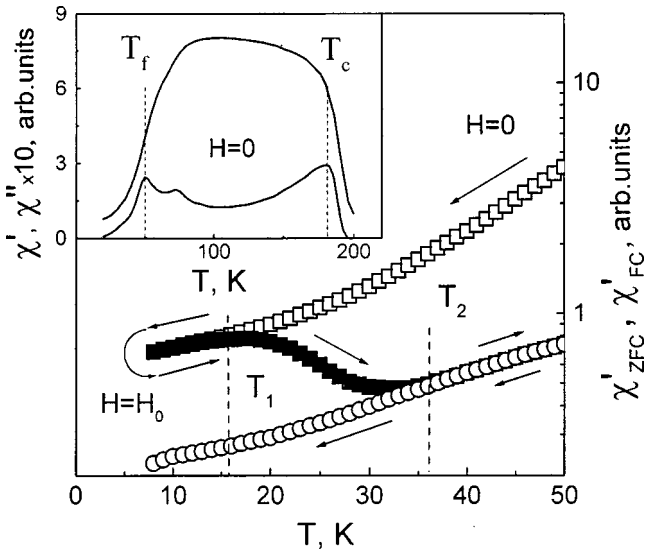

FIG. 1. Temperature dependence of the real component χ' of the dynamic magnetic susceptibility of the disordered alloy $Ni_{77}Mn_{23}$ for various regimes of thermal cycling. $H_0 = 140$ Oe. In the inset: temperature dependence of the real χ' and imaginary χ'' components of the dynamic magnetic susceptibility of the alloy $Ni_{77}Mn_{23}$ in zero magnetic field. The frequency of the magnetizing field was 85 Hz, its amplitude 0.1 Oe.

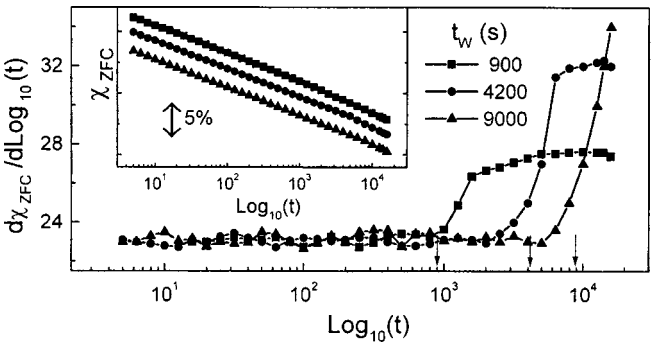

FIG. 2. Logarithmic derivative of the magnetic susceptibility $d\chi'_{ZFC}/d\ln(t)$ for the alloy $Ni_{77}Mn_{23}$ for various waiting times $t_w(s)$. The inset shows the time dependence of the relaxation of the real component of the dynamic magnetic susceptibility χ'_{ZFC}. Experimental conditions: $H_0 = 140$ Oe, $T = 16$ K.

ity may be observable. Processes that lead to braking of domain walls, which arise from viscous reorientation of the transverse spin-glass components during re-magnetization of a real sample, could provide another possible mechanism by which the transverse spin-glass irreversibility could influence the DMS.[12] It is important to note that in all the cases listed above the irreversibilities in the longitudinal DMS are due to the nonequilibrium nature of the transverse spin glass.

2. EXPERIMENTAL RESULTS AND DISCUSSION

Our studies showed that the magnetic properties of all alloys of the system $Ni_{100-x}Mn_x$ ($x = 19, 21, 23$) are similar. Therefore, we will illustrate our results with the example of the alloy $Ni_{77}Mn_{23}$. The inset in Fig. 1 shows the temperature dependences of the real χ' and imaginary χ'' components of the DMS for this alloy. Such dependences are entirely typical of frustrated ferromagnets[13]: as the sample is cooled, χ' increases strongly at the Curie temperature $T_C \approx 175$ K, then falls off abruptly at a temperature $T_f \approx 52$ K. Both of these changes correspond to peaks in χ''. Since the intermediate anomaly in χ'' noted in Ref. 14, and also other peculiarities of the ergodic phase ($T > T_f$), are irrelevant to the problems addressed in this paper, all the experimental results that follow are taken from the temperature range $T \leqslant T_f \approx 50$ K, in which the true ASM state is created.

2.1. Thermomagnetic hysteresis effects

Let us consider the results of studies of the DMS in static magnetic fields. As an example, Fig. 1 shows the temperature dependence of the DMS in a field $H_0 = 140$ Oe. Especially noteworthy is the presence of two distinct DMS curves for temperatures $T < T_f$, also observed by the authors of Ref. 15. One of these, the near-equilibrium curve $\chi'_{FC}(H_0, T)$, corresponds to cooling the alloy from $T > T_f$ in the static field H_0. In contrast, the other distinctly nonequilibrium curve $\chi'_{ZFC}(H_0, T, t)$ is obtained by cooling the sample in the absence of a static magnetic field. Since at temperatures $T < T_f$ the latter relaxes continuously towards its equilibrium value $\chi'_{FC}(H_0, T)$, the experiments were carried out at the same rates of heating (≈ 2 K/60 s).

From Fig. 1 it is clear that switching on the magnetic field H_0 at 4.2 K has almost no effect on the value of $\chi'_{ZFC}(0, T)$ obtained during the cooling process. Increasing the temperature causes the curve χ'_{FC} to depart from χ'_{ZFC} and move to smaller values; as the sample is heated, $\chi'_{ZFC}(H_0, T)$ first passes through a maximum at $T = T_1$, then decreases, and eventually becomes equal to $\chi'_{FC}(H_0, T)$ at $T = T_2$. Further study reveals that increasing the external magnetic field intensity decreases the temperatures T_1 and T_2. The authors of Ref. 15 identified these temperatures with the temperatures T_{AT} and T_{GT} associated with the appearance of longitudinal and transverse spin-glass components of the spins respectively. We will show below that it is incorrect to identify the critical temperatures in this way.

2.2. Magnetic aging effects

It is known that various physical quantities (magnetic moment, susceptibility, neutron polarization, etc.) are time-dependent in spin glass systems, with a dependence on t that is close to logarithmic.[16] It is reasonable to assume that analogous processes also take place in asperomagnets.

In order to study this phenomenon, we performed the following sequence of experiments in this work. A sample was cooled from a temperature $T > T_f = 60$ K to the measurement temperature $T < T_f = 16$ K in zero magnetic field, and kept under these conditions for various waiting times $t_w = 900$, 4200, 9000 s. Then an external magnetic field $H_0 = 140$ Oe was switched on and the value of χ'_{ZFC} was recorded as a function of time t. The results obtained are shown in the inset to Fig. 2, from which the logarithmic character of the time dependence of χ'_{ZFC} is clear.

It must be emphasized that χ'_{ZFC} exhibits logarithmic relaxation only for $t < t_w$. For longer observation times, i.e.,

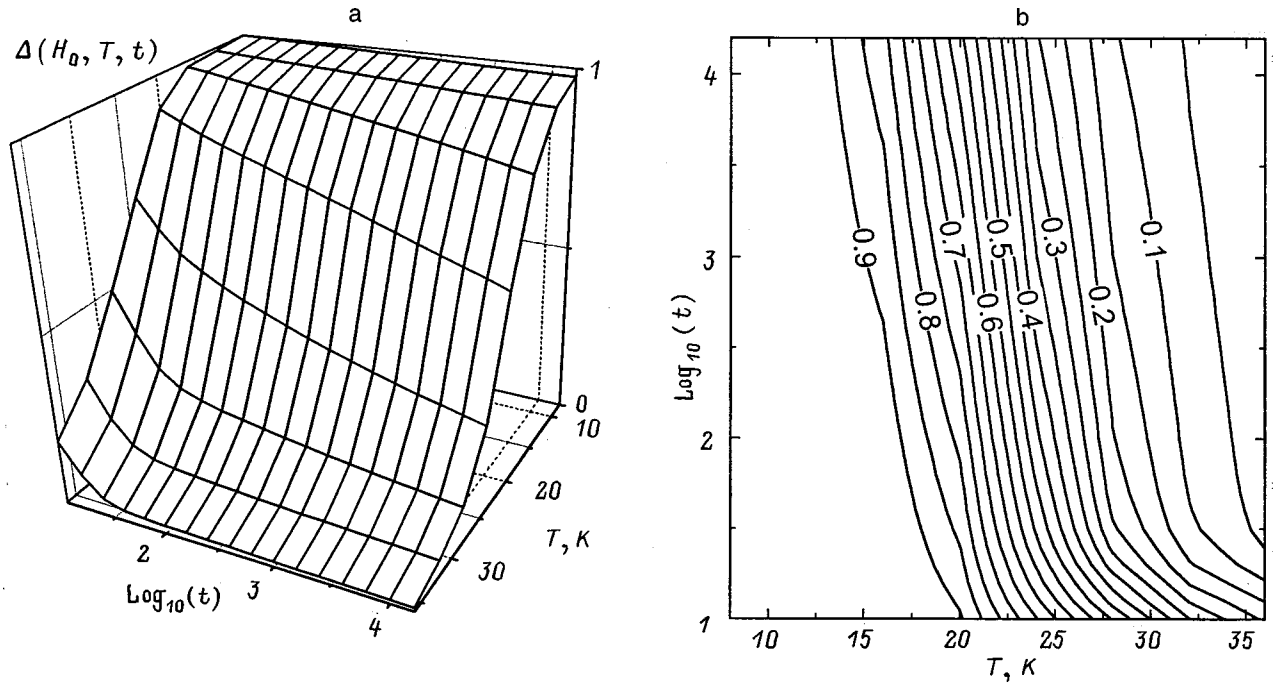

FIG. 3. Temperature and time dependence of the nonequilibrium parameter $\Delta(H_0,T,t)$ for the alloy $Ni_{77}Mn_{23}$ at a fixed value of magnetic field $H_0=140$ Oe. The data is represented in the form of a surface (a) and isolines (b).

starting from the times t_w shown in Fig. 2 by arrows, a slight ($\sim 30\%$) deviation from the logarithmic behavior is recorded.

2.3. Magnetic viscosity

Two parameters are customarily used to describe the transition to the spin glass state: the Edwards–Anderson order parameter q_{EA} and the nonergodicity parameter Δ. However, when the spins are ordered by a magnetic field, the fundamental parameter $q_{EA}=\langle\langle S^2\rangle_T\rangle_J$ is nonzero not only in the spin glass but also in the paramagnetic phase. In this case, the quantity Δ, which reflects a fundamental property of the spin glass (magnetic viscosity), becomes the only criterion for the appearance of a spin glass state. This is a property of particular interest in the presence of spontaneous ($H=0$) ordering, which is characteristic for ASM systems. According to Ref. 11, Δ corresponds to the difference between the equilibrium and nonequilibrium susceptibilities:

$$\Delta_s(t)=\chi'_{ZFC}(t)-\chi'_{FC}=\Delta_0[1-s\log(t)]. \quad (1)$$

Here $\Delta_0=\chi'_{ZFC}(t=0)-\chi'_{ZFC}(t=\infty)$, while s is the magnetic aftereffect coefficient of the spin glass. However, in practice it is more convenient to use a normalized function of the form

$$\Delta(t)|_{H,T}=\left.\frac{\chi'_{ZFC}(t)-\chi'_{ZFC}(t=\infty)}{\chi'_{ZFC}(t=0)-\chi'_{ZFC}(t=\infty)}\right|_{H,T}$$
$$=\left.\frac{\chi'_{ZFC}(t)-\chi'_{ZFC}(t=\infty)}{\Delta_0}\right|_{H,T}, \quad (2)$$

which, while retaining the previous physical meaning of Eq. (1), now takes on a more universal ($0<\Delta<1$) character. In computing the function (2), the approximations $\chi'_{ZFC}(t\to\infty)|_{H,T}=\chi'_{FC}|_{H,T}$ and $\chi'_{ZFC}(t=0)|_{H,T}=\chi'_{FC}|_{H=0,T}$ were made. In what follows we will refer to the quantity Δ as the nonequilibrium parameter. Its experimental determination requires measurement of the relaxation functions $\chi'_{ZFC}(t)$ at each fixed value of magnetic field and temperature. In order to maintain the same thermomagnetic prior history, the samples were cooled from room temperature down to the temperature of the experiment in the absence of a magnetic field and kept under these conditions for 3600 s (in order to eliminate the influence of differing cooling rates). The magnetic field $H=H_0$ was then switched on at $t=0$ and the function $\chi'_{ZFC}(t)|_{H,T}$ was recorded.

Let us discuss the results shown in Fig. 3 in the form of a surface $\Delta(T,t)$ at one value of the magnetic field $H_0=140$ Oe. First we consider the intersections of the surface with the planes $T=$ const. Their general form can be approximated by the expression

$$\Delta(t)=1-S\log(t)/\log(t_{\max})-F[1-\exp(-t/t_0)], \quad (3)$$

where $t_{\max}$ is the time it takes the system to reach equilibrium, t_0 is a time that characterizes the dynamics of the ferromagnetic components of the spins, and S and F correspond to contributions to the dynamics by the spin-glass and ferromagnetic subsystems. By using the boundary condition $\Delta(t=t_{\max})=0$, it is not difficult to show that $(S+F)=1$. The computed functions $S(T)$ and $F(T)$ (see the inset to Fig. 4) confirm the conclusions of the molecular-field theory. Actually, as the alloy is cooled from T_C to a temperature T_2 we record only the ferromagnetic component of the relaxation ($S=0$, $F=1$). Upon further cooling, the system passes from the ferromagnetic state to the ASM. Evidence of this is the coexistence in the temperature range $T_2<T<T_1$ of long-

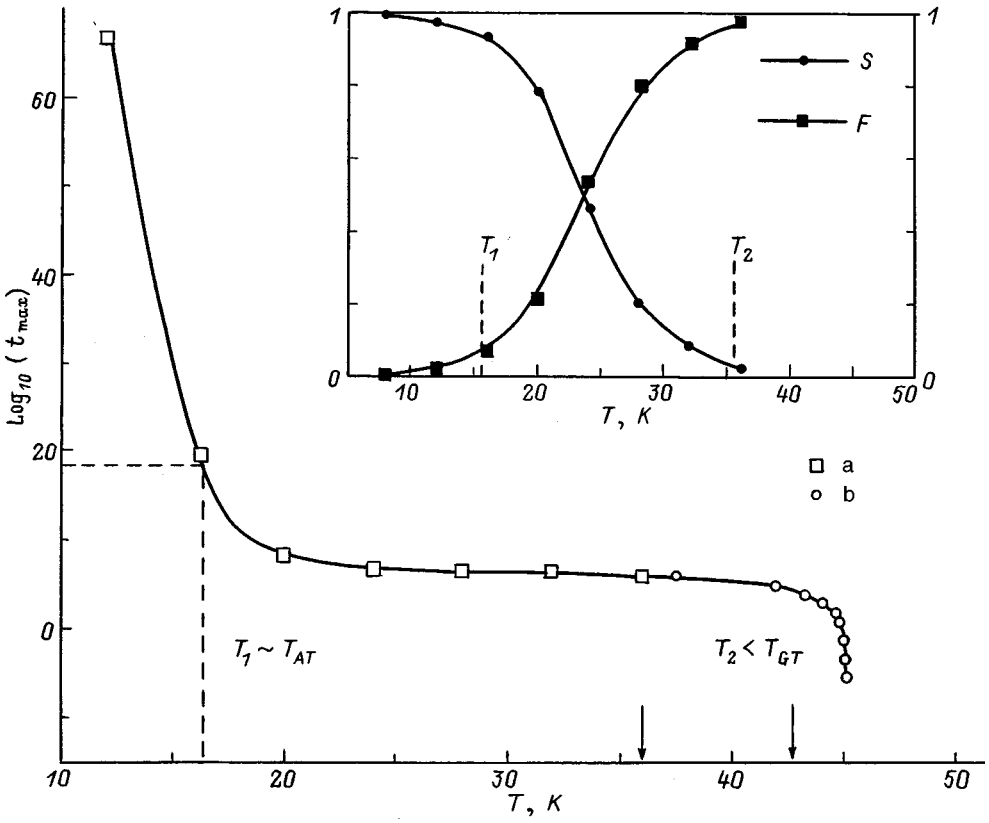

FIG. 4. Temperature dependence of time $t_{max}(s)$ for the alloy $Ni_{77}Mn_{23}$ to reach its equilibrium magnetic state. The inset shows the temperature dependence of the ferromagnetic (F) and spin glass (S) contributions to the relaxation of the quantity $\Delta(H_0,T,t)$ for the alloy $Ni_{77}Mn_{23}$.

period spin-glass and ''fast'' ferromagnetic relaxation laws ($0<S<1$, $0<F<1$). These results give us a basis for identifying the magnetic state in this temperature range with the Gabay–Toulouse phase. As the temperature decreases, when $T<T_1$ the system relaxes according to a logarithmic law ($S=1$, $F=0$) of the form Eq. (1). The fact that the parameter S equals unity indicates that its dynamics are completely described by that of the spin glass component, which is characteristic of the de Almeida–Thouless phase.

Introducing a relaxation law of the form of Eq. (3) allows us to separate both the contributions from the ferromagnetic and spin-glass states and to investigate another characteristic of the asperomagnet that is no less important—the time t_{max} it takes the system to reach its equilibrium state. Since this quantity usually exceeds the duration of a static experiment ($t_{obs}\leqslant 10^4$ s), t_{max} can be computed only by extrapolating experimental data for $\Delta(T,t)$. In this procedure it is assumed that over the entire time interval the parameters S, F, and t_0 are constants. From a physical standpoint this implies that the real spectrum of relaxation times is approximated by a sum of two terms. One of these is a ''delta'' function responsible for the exponential term in Eq. (3), while the other is a component that is continuous, uninterrupted, and uniform up to $t=t_{max}$, which provides the logarithmic relaxation law with a constant coefficient S.

At low temperatures $T<T_2$ the experimental values of $t_{max}(T)$ are computed by extrapolating the intersections of the surface $\Delta(T,t_{max})=0$ with constant-t planes (in Fig. 4 these are denoted by symbols a). However, in the neighborhood of the GT phase line ($T\cong T_2$) we used the following procedure, based on processing its temperature intersections with the planes $t_{obs}=$const. Analogous dependences for spin glasses are described by power laws of the form[17]

$$(T_E-T)\approx\Delta^{1/\beta}. \tag{4}$$

For an appropriate choice of the exponent $1/\beta$, we can perform a linear extrapolation and compute the desired temperature $T_E(t_{obs})$ at which the system reaches equilibrium. In this case, we should expect that at times t_{obs} that greatly exceed 10^{-8} s, the characteristic relaxation time of the ferromagnetic component[18] (i.e., $t_{obs}\geqslant 10^{-6}$ s), Eq. (4) must hold for the ASM as well. Unfortunately, it has been established that, when a sample is magnetized at low frequencies, as is traditionally done to study spin-glass systems, it is impossible to record such transient processes. Moreover, for reliable recording of a useful signal from the synchronous detector, the integration constant of the low-frequency filter should exceed the magnetization period by at least an order of magnitude. Since in our case ($f=85$ Hz) this period is 2 s, it is this value $t_0\approx 2$ s (independent of the magnetic field amplitude and/or temperature) that determines the true range of applicability $t_{obs}\geqslant 100\times t_0\approx 200$ s of the law (4). However, it is not difficult to reduce this region to its true size $t_{obs}\leqslant 10^{-6}$ s by artificially subtracting the contribution from the ferromagnetic component $F[1-\exp(-t/t_0)]$, $t_0\approx 2$ s. Figure

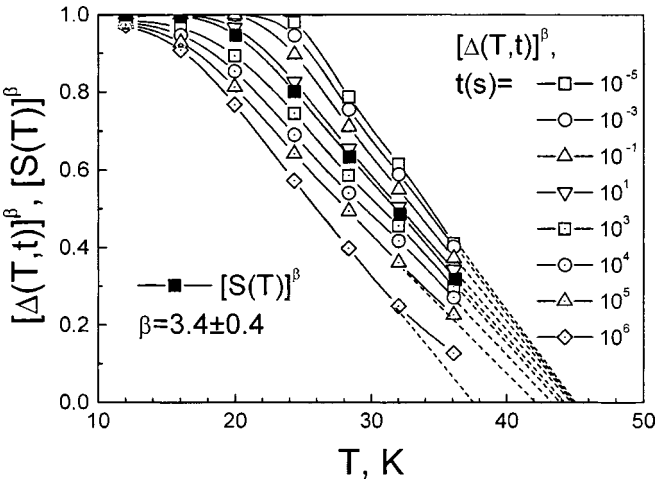

FIG. 5. Linearized temperature dependences $\Delta(T)$, obtained by intersecting the corrected surface $\Delta(H_0,T,t)$, where $H_0=140$ Oe, with various planes $t=$const, as well as linearized dependences of the spin glass component S of the dynamics (the inset in Fig. 4.

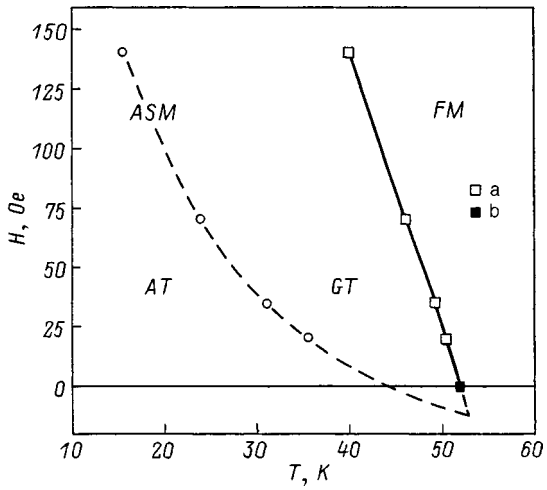

FIG. 6. Magnetic $H-T$ phase diagram of the disordered alloy $Ni_{77}Mn_{23}$. FM and ASM— ferromagnetic and asperomagnetic phases, GT and AT—Gabay–Toulouse and de Almeida–Thouless regions.

5 shows several temperature-plane intersections (10^{-5} s $\leqslant t_{\rm obs} \leqslant 10^{7}$ s) with the surface $\Delta(T,t)$ corrected in this way after carrying out the corresponding linearization ($\beta=3.4\pm0.4$). This procedure allows us to greatly extend the equilibrium curve $T_E(t_{\rm max})$ (point *b* in Fig. 4).

The results presented in Fig. 4 provide all the evidence we need to cast doubt on the validity of the widespread view that the exsolution temperature of the spin glass decreases with increasing observation time $t_{\rm obs}$. Actually, arrival at an equilibrium state for $t_{\rm obs}>t_{\rm max}(T)$ in no way implies such a disappearance of the ASM phase. Then the temperature $T_E(t_{\rm obs})$, whether it is obtained by static methods ($t_{\rm obs}=10^4-1$ s),[17] dynamic methods ($t_{\rm obs}=10^{-1}-10^{-6}$ s),[1] or resonance methods ($t_{\rm obs}=10^{-8}-10^{-12}$ s),[4,18] must be regarded not as a phase transition temperature but rather as a mere boundary between the equilibrium $T>T_E(t_{\rm obs})$ and nonequilibrium states $T<T_E(t_{\rm obs})$. The latter will coincide with the temperature and/or T_{AT} only for a suitable choice of the threshold criterion $t=t_{\rm obs}$ for weak/strong nonergodicity.

2.4. Magnetic $H-T$ phase diagram

Thus, in order to obtain the exact values $T_{GT}(H)$ and $T_{AT}(H)$, required to construct the $H-T$ magnetic phase diagram, they must first be defined using the criteria of weak and strong nonergodicity. Unfortunately, the Heisenberg model[2,3] does not provide any such concrete criteria, and experiments whose goal is to investigate relaxation-time spectra in the spin-glass phase are far from numerous. In essence, the only results available are for the dilute spin glass $Cu_{96}Mn_4$; moreover, these studies were carried out in zero magnetic field.[19]

However, the dynamics of an asperomagnet below the AT line differ little from those of a spin glass, and depend only weakly on the magnetic field intensity. Evidence of this is the closeness of the characteristic slope

$$[dT/d\,\mathrm{Log}(t_{\rm max})]/T_f=(-2.0\pm0.2)10^{-3}$$

of isolines (Fig. 3b, $H_0=140$ Oe, $16<T<8$ K) for the alloy $Ni_{77}Mn_{23}$ investigated above to the ''universal'' value -2.2×10^{-3} at $H=0$.[20] Making use of this circumstance, and also knowing that at a temperature $T=0.9T_{AT}(H=0)$ the quantity $t_{\rm max}$ is $\approx10^{20}$ s (see Ref. 19), based on the data for $t_{\rm max}(T)$ (Fig. 4) it is not difficult to recover the temperature $T_{AT}(H_0=140\ \mathrm{Oe})=17.6$ K and the nonergodicity criterion $t_{AT}(T_{AT})\approx10^{16}$ s corresponding to it. As we also should expect, due to the long-period character of the relaxation the quantity $T_1=18\pm1$ K (Fig. 1) is a rather good approximation to T_{AT}.

An entirely different situation is observed in the neighborhood of the T_{GT} line. Here the slope of the isolines

$$[dT/d\,\mathrm{Log}(t_{\rm max})]/T_f=(-2.4\pm0.2)10^{-2}$$

($H=140$ Oe, $T_2<16<T<39\ \mathrm{K}<T_1$) is approximately an order of magnitude larger, and the relaxation processes have a considerably more transient character, i.e., comparable to the times for static experiments. Consequently, formal recovery of the Gabay–Toulouse curve on the magnetic phase diagram based on results of FC and ZFC experiments, as proposed by the authors of Ref. 15, cannot be correct. In order to determine the critical temperature T_{GT} we must use the nonergodicity criterion, which should not depend on observation time. Both the time $t_{\rm max}$ for the system to reach equilibrium and the spin glass component S of the relaxation χ'_{ZFC} possess this property. The linearization of the temperature dependence $S(T)$ derived above (the inset to Fig. 3) lets us to determine that $T_{GT}(H=140\ \mathrm{Oe})=44.1\pm0.3$ K, and also that $t_{\rm max}(T_{GT})\approx10^2$ s. Analogously, we also obtain other points *a* with $0<H<200$ Oe, which make up the Gabay–Toulouse phase line in Fig. 6. However, the point *b* corresponds to a maximum in the temperature dependence of the magnetic absorption χ'' in zero magnetic field (the inset to Fig. 1). Strictly speaking, the characteristic observation time in this case $t_{\rm obs}=1/f\approx10^{-2}$ s, where $f=85$ Hz is the frequency of magnetization, was considerably less than $t_{\rm max}(T_{GT})$. However, within the time interval $t_{\rm obs}<10^3$ s this factor had only a very slight effect on the critical temperature

T_{GT} at which weak nonergodicity appears (Fig. 4). Nevertheless, it is this point that allows us to demonstrate the principal difference between the $H-T$ phase diagram of an ASM system (Fig. 6) and spin-glass phase diagrams. In the latter case, it is this point at which the Gabay–Toulouse and de Almeida-Thouless lines should intersect.[2,3] The lack of such an intersection in Fig. 6 is explained by the fact that the magnetic induction in asperomagnets $B=H\times[1+4\pi\chi]+B_s$, where χ is fully comparable to $(1/4\pi)$ and the spontaneous induction $B_S\neq 0$ no longer coincides with the external magnetic field H (in contrast to a spin glass, where $\chi \ll (1/4\pi)$ and $B_S=0$). Thus, when $H=0$, the quantity B is significantly nonzero in an ASM, which is clearly revealed in Fig. 6. However, for the alloy $Ni_{77}Mn_{23}$ under study here it is relatively small: in the temperature range $T<50$ K we find that $B_S=10-12$ G.[8]

Thus, we have shown in this paper that, when the disordered alloys $Ni_{100-x}Mn_x$ $(x=19, 21, 23)$ are cooled, the following sequence of magnetic phase transformations takes place: paramagnetic-ferromagnetic-asperomagnetic. In studying the nonequilibrium properties of the low-temperature ASM phase, we observed phenomena that are very characteristic of classical spin glasses: thermomagnetic hysteresis, magnetic aging, long-period relaxation of the susceptibility, etc. We have established that near the Gabay–Toulouse phase line the times for the system to reach equilibrium are quite comparable to the times of the static experiment $(10^1-10^4$ s), and only after cooling the sample into the region where this line intersects the de Almeida–Thouless line do these times increase to astronomical values $>10^{16}$ s. Based on our data, we conclude that constructing the Gabay–Toulouse line in an $H-T$ magnetic phase diagram requires confinement to physical criteria that do not depend on the observation time.

This work was carried out with partial financial support from the Fund for Fundamental Research of Ukraine within project No. 2.4/348.

[1] K. Binder and A. P. Young, Rev. Mod. Phys. **58**, 801 (1986).
[2] M. Gabay and G. Toulouse, Phys. Rev. Lett. **47**, 201 (1981).
[3] D. M. Gregg, D. Sherrington, and M. Gabay, Phys. Rev. Lett. **49**, 158 (1982).
[4] J. M. C. Coey, J. Appl. Phys. **49**, 1646 (1978).
[5] S. M. Shapiro, *Spin Waves and Magnetic Excitations* Vol. 22.2 (Elsevier, Amsterdam, 1988), p. 219.
[6] G. A. Takzeĭ, Yu. P. Grebenyuk, and I. I. Sych, Zh. Éksp. Teor. Fiz. **96**, 1022 (1990) [Sov. Phys. JETP **70**, 572 (1990)].
[7] I. Mirebeau, M. Hennion, S. Mitsuda, and Y. Endoh, *Recent Progress in Random Magnets* (World Scientific, Singapore, 1992), p. 41.
[8] Yu. P. Grebenyuk and G. A. Takzei, Phys. Metals **14**, 827 (1995).
[9] H. Sompolinsky, Philos. Mag. B **51**, 543 (1985).
[10] P. M. Levy and A. Fert, Phys. Rev. B **23**, 4667 (1981).
[11] G. Kotliar and H. Sompolinsky, Phys. Rev. Lett. **53**, 1751 (1984).
[12] G. A. Takzeĭ, Yu. P. Grebenyuk, A. M. Kostyshin, and I. I. Sych, Fiz. Tverd. Tela (Leningrad) **29**, 83 (1987) [Sov. Phys. Solid State **29**, 46 (1987)].
[13] G. A. Takzeĭ, A. M. Kostyshin, Yu. P. Grebenyuk, and I. I. Sych, Zh. Éksp. Teor. Fiz. **89**, 2181 (1985) [Sov. Phys. JETP **62**, 1259 (1985)].
[14] Yu. P. Grebenyuk, G. A. Takzeĭ, M. V. Gavrilenko, and A. M. Dvoeglazov, Metallofizika (Kiev) **14**, 6 (1992).
[15] H. Kunkel, R. M. Roshko, W. Ruan, and G. Williams, J. Appl. Phys. **68**, 5060 (1991).
[16] H. Sompolinsky, Phys. Rev. Lett. **47**, 951 (1981).
[17] Y. Yeshurun, Philos. Mag. B **50**, 285 (1983).
[18] G. A. Takzei, M. V. Gavrilenko, A. B. Surzhenko, and S. V. Tarapov, J. Magn. Magn. Mater. **140–144**, 221 (1995).
[19] L. Lundgren, P. Svedlindh, P. Norblad, and O. Beckman, Phys. Rev. Lett. **51**, 911 (1983).
[20] C. A. M. Mulder, A. J. van Duyneveldt, and J. A. Mydosh, Phys. Rev. B **23**, 1384 (1981).

Translated by Frank J. Crowne

Influence of induced uniaxial anisotropy on the domain structure and phase transitions of yttrium–iron garnet films

A. V. Vashkovskiĭ, É. G. Lokk, and V. I. Shcheglov

Institute of Radio Engineering and Electronics, Russian Academy of Sciences, 141120 Fryazino, Moscow District, Russia

(Submitted November 24, 1998; accepted for publication March 23, 1999)
Fiz. Tverd. Tela (St. Petersburg) **41**, 2034–2041 (November 1999)

The effect of induced uniaxial anisotropy on the properties and parameters of the domain structure and phase transitions in yttrium–iron garnet (YIG) films is investigated. Based on the measurements and the derived formulas we determine the difference between the magnetization and the uniaxial anisotropy field for each of the films. We have also measured the parameters of the domain structures and phase transitions of the films for the magnetization parallel and perpendicular to the projections of the [111] crystallographic axes onto the plane of the film. We find that films of pure YIG films grown in (111) are characterized by the existence of some critical value of the uniaxial anisotropy field. It is found that for films in which the uniaxial anisotropy field is larger than this critical value and films in which it is less than this critical value, such parameters of the domain structures as the ratio of the width of the domains to the film thickness, the orientation of the magnetization of the domains, the orientation of the domain boundaries, and the magnitudes of the phase transition fields differ substantially.
 [S1063-7834(99)02511-3]

Yttrium–iron garnet (YIG) films grown by liquid-phase epitaxy on gallium–gadolinium garnet (GGG) substrates differ from bulk single crystals of YIG by the presence of an induced (or as-grown) uniaxial anisotropy, which arises due to an insignificant lattice mismatch of YIG and GGG. As studies extending over many years[1,2] have shown, in films of pure (free of impurities) YIG magnetized to saturation, the uniaxial anisotropy field does not have a noticeable effect on the properties of the films themselves or on the physics of wave processes in the films. However, in unsaturated YIG films a completely different situation can arise: since the energy of induced uniaxial anisotropy is of the same order of magnitude as the dipole energy and the cubic anisotropy energy, even a small variation in the uniaxial anisotropy field from film to film can have a substantial effect on the formation of domain structures and on the behavior of spin waves. It was just this picture, which began to take shape after the appearance of Refs. 2–6 and became clear in Refs. 7–10, which described the different behavior of domain structures, their phase transitions, and the characteristics of spin waves, that gave the authors of Refs. 7–10 (us) grounds to hypothesize the existence of two different types of films of pure YIG. The present paper theoretically and experimentally uncovers the factors leading to the division of epitaxial films of pure YIG into two different types and investigates the influence of the magnetic parameters of YIG films on the behavior and phase transitions of different domain structures for tangential magnetization of these films.

1. DOMAIN STRUCTURE PROPERTIES OF YIG FILMS. ROLE OF UNIAXIAL ANISOTROPY

The domain structures arising in epitaxial YIG films on GGG substrates have been described in many studies that have been undertaken since the appearance of these films (see, e.g., Refs. 3–5). However, these early works used rectangular samples of small dimensions, which led to edge distortions of the domain structure (DS), the appearance in it of irregularities,[5] and an increase in its coerciveness. The orientation of the crystallographic axes in the film plane was not monitored as a rule,[5,6] and the cubic and uniaxial anisotropy fields were not measured. Thus, the overall picture of the formation of domain structures in YIG films and their behavior remained unclear, but a comparison of experiment with theory and a systematic comparison of the results of different researchers presented obstacles. Only recently, in our papers,[8,10] has a description been given of the general features of changes in the domain structure in the most common type of pure YIG films [grown in the (111) plane and free of impurities], tangentially magnetized by a uniform magnetic field $\mathbf{H}_0$. These features were revealed by a statistical analysis of results obtained with different samples, and by monitoring the orientation of the crystallographic axes in the plane of the film relative to the external magnetic field $\mathbf{H}_0$.

A general property of all the tangentially magnetized films of pure YIG described in Refs. 8 and 10 is the formation of a regular banded domain structure in them, which varies repeatedly as the magnitude of the applied field H_0 is cyclically varied from zero to a value exceeding the saturation value and then back again (the domain structure varies in this way after initial magnetization of the film to saturation, eliminating the influence of the preceding random domain structure). Another general property of all these films is a substantial difference in the behavior of the domain structure when the films are magnetized along the projections of the [111] axes onto the film plane (the hard axes h) and when magnetized in the perpendicular directions (the easy

axes s). Under these conditions, a different number of phase transitions is observed in the films, at which different types of regular or quasiregular[1)] domain structures supersede one another, differing in shape (linear or zigzag) or in the width of the banded domains (symmetrical or asymmetrical).

At the same time, it became clear (see Refs. 8 and 10) that all of the films of pure YIG can be divided into two types. In films of the first type, when observed under a microscope, the domain structure has high contrast, which is indicative of a substantial deviation from the film plane by the magnetization vectors of the domains.[2)] In films of the second type, the the domain structure has low contrast and the magnetization vectors are oriented nearly in the film plane. When the magnitude of the applied field H_0 is varied cyclically (increased and decreased in the interval from 0 to some value above the saturation value) the behavior of the domain structure in films of both types also differs substantially: in films of the first type the behavior and parameters of the domain structure are uniquely determined by the magnitude of H_0 (hysteresis is absent), while in films of the second type the variation of the domain-structure parameters exhibits hysteresis.

At first glance, the reasons for such substantial differences in the domain structure of the two types of films is unclear. Indeed, the conditions of growth of all of the films were completely identical, and their thicknesses were roughly the same ($5-20\,\mu$m). The film parameters measured in the saturated state differ only slightly—within the limits of measurement error (the methods for measuring the parameters and the values so obtained are described below). All the films have an induced uniaxial anisotropy (due to mechanical stresses in the substrate), whose axis deviates from the normal to the film plane within the limits of a few degrees. However, the effective saturation magnetizations of the films, determined by fitting the measured dispersion curves for the surface magnetostatic waves (MSW) using the Damon–Eschbach equations,[11] differed within the limits of $\cong 150$ G (we use the term ''effective magnetizations'' here since the uniaxial and cubic anisotropy fields are not taken into account in the Damon–Eschbach model).

Thus, there is practically no visible correlation between the parameters of the films in the saturated state and no division of the films into two types, distinguished by the nature of the domain structure, was observed.

At the same time, we believe that the above-described differences in the nature and behavior of the domain structures may be caused by small variations in the uniaxial anisotropy field relative to some critical value lying within the limits 50–200 Oe (this is also indicated by the small differences in the values of the effective magnetizations of the films mentioned above).

Indeed, the equilibrium orientation of the magnetization vector inside the domains in the film in the absence of an external field is due primarily to two factors: the anisotropy field and the demagnetization field. For simplicity, we restrict the discussion to uniaxial anisotropy with the easy axis perpendicular to the film plane, which is close to the actual situation in YIG films. Including cubic anisotropy, by virtue of its smallness and high degree of symmetry, leads only to small corrections having no effect on the order of magnitude of the estimated parameters. The demagnetization field in the saturated state is determined only by the shape of the film, whereas in the presence of a domain structure it also depends on the ratio of the width of the domains to the thickness of the film (it is assumed here that the domain boundaries are perpendicular to the film plane). We choose as our coordinate system one in which the yz plane coincides with the film plane, and the x axis is perpendicular to it. The expression for the energy density in this coordinate system has the form

$$W = K(M_y^2 + M_z^2)M_0^{-2} + 2\pi G M_x^2, \tag{1}$$

where K is the uniaxial anisotropy constant, $M_{x,y,z}$ are the components of the magnetization vector, M_0 is the saturation magnetization, and G is a coefficient defining the demagnetizing factor (we note at once that the use here of the concept of a demagnetizing factor is not completely correct by virtue of the inhomogeneity of the field inside a domain; however, for a rough estimate, the indicated inhomogeneity can be neglected). For films without domains $G=1$. For a film with domains, $G<1$ and is determined by the specific shape of the domains. To within a constant, the above expression can be written as

$$W = (K - 2\pi G M_0^2)(M_y^2 + M_z^2)/M_0^2. \tag{2}$$

Finding the equilibrium position of the magnetization vector, we find that the magnetization lies in the plane of the film for $H_a < H_{MG}$ and is oriented perpendicular to it for $H_a > H_{MG}$. Here $H_a = 2K/M_0$ is the uniaxial anisotropy field, and $H_{MG} = 4\pi G M_0$ is the effective demagnetizing field perpendicular to the plane of the film, obtained taking the shape of the domains into account.

Let us estimate H_{MG}. This field is created by the action of two factors: the demagnetizing field of the shape of one specific domain (it is assumed that all the domains are identical), and the fields created in this domain by neighboring domains. Obviously, in films of the second type, in which the width of a domain is on the order of the film thickness, the demagnetizing factor of a domain in the direction perpendicular to the plane of the film is large and approaches 4π (i.e., G approaches unity); therefore, the orientation of the magnetization vector in this case differs only slightly from the case of a film without domains (since the magnetization is capable of going out of the plane only in anisotropy fields on the order of or larger than $4\pi M_0 = 1750$ Oe). Let us consider now films of the first type, in which the width of a domain is less than the film thickness. The demagnetizing factor of the shape of a domain can be most simply taken into account in the approximation of an ellipsoid. For the width of a domain equal to $2-4\,\mu$m and film thickness around 12 μm, the demagnetizing factor of the shape (in units of 4π) is 0.2, giving 350 Oe for the demagnetizing factor of the shape. The effect of neighboring domains lowers this value by a factor of approximately 1.5, which gives 200 Oe. Thus, if the uniaxial anisotropy field is less than 200 Oe, the magnetization vector should lie in the film plane, and if it is greater than this value, the magnetization vector should be perpendicular to the film plane. The presence in

the YIG film of cubic anisotropy with a field of 80 Oe lowers the indicated critical value to $\cong 120$ Oe. Thus, even a small change in the anisotropy field relative to the critical value ($\cong 120$ Oe) radically alters the equilibrium orientation of the magnetization vector—from parallel to the film plane to perpendicular to it. This leads to the result that two substantially different forms of domain structure are experimentally observed for an apparent similarity of the parameters of the two types of films, determined in the saturated state.

2. CALCULATION OF THE FERROMAGNETIC RESONANCE FREQUENCY FOR DIFFERENT ORIENTATIONS OF THE FIELD

The role we have supposed for uniaxial anisotropy in the organization of the domain structures of YIG films, spelled out above is, of course, to a significant extent hypothetical and in need of a more rigorous theoretical and experimental justification. In particular, the behavior of the domain structures depends strongly on the film parameters, which can be measured with good accuracy.[1,12–19] Toward this end, the present section considers the interrelationship between the ferromagnetic resonance (FMR) frequency, which coincides with the initial frequency of the spectrum of the surface magnetostatic waves, and the remaining magnetic parameters of the ferrite films. We believe that an analysis of the experimental results (see Sec. 4) based on the equations derived in the present section justifies our hypothesis to a significant extent.

In the coordinate system chosen in Sec. 1, the uniaxial anisotropy axis and one of the [111] crystallographic axes are directed along the x axis. We direct the external field along the z axis and consider two cases.

1) The field is parallel to one of the hard axes h.

2) The field is parallel to one of the easy axes s.

Calculating as in Refs. 12–15 and 20, we obtain the resonant frequency for the first case in the form

$$f^h=\frac{\gamma}{2\pi}\{(H_0-3\sqrt{2}H_kM_x^e/M_0)[H+4\pi M_0 - H_a+H_k(1-\sqrt{2}M_x^e/M_0)]\}^{1/2}. \tag{3}$$

Here

$$\frac{M_x^e}{M_0}=-\frac{\sqrt{2}H_k/3}{H_0+4\pi M_0-H_a+H_k}, \tag{4}$$

$$H_a=2K/M_0, \tag{5}$$

$$H_k=K_1/M_0, \tag{6}$$

where γ is the gyromagnetic ratio for an electron, H_0 is the external magnetic field, M_0 is the saturation magnetization, and H_a is the uniaxial anisotropy field. Note that in our notation H_k is equal to half the cubic anisotropy field $H_{ak}=2K_1/M_0$. The above formula is approximate and is that much more exact, the larger is the field H_0 (e.g., for IYG with $4\pi M_0=1750$ G, $H_k=40$ Oe, and $H_a<200$ Oe the error does not exceed 1% for $H_0\geqslant 500$ Oe).

Similarly, for the second case we obtain

$$f^s=\frac{\gamma}{2\pi}[H_0(H_0+4\pi M_0-H_a+H_k)-2H_k^2]^{1/2}. \tag{7}$$

Within the framework of the adopted model, this relation is exact.

From the above equations it is clear that the saturation magnetization M_0 and the uniaxial anisotropy field H_a enter into them only in the combination $4\pi M_0-H_a$ and never separately. The reason is that the expressions for the energy density of the uniaxial anisotropy and for the demagnetizing field of a film (as for a thin wafer) are identical to within some constants. Measurement of the orientation dependence of the uniform FMR frequency does not allow one to measure M_0 and H_a separately. At the same time, from Eqs. (3) and (7), it is possible to obtain expressions for the difference $R=4\pi M_0-H_a$ having the form

$$R^h=\frac{(2\pi f^h/\gamma)^2}{H_0-3\sqrt{2}H_kM_x^e/M_0}-H_0-H_k(1-\sqrt{2}M_x^e/M_0), \tag{8}$$

$$R^s=[(2\pi f^s/\gamma)^2-H_0(H_0+H_k)+2H_k^2]/H_0. \tag{9}$$

Equation (8) contains the quantity M_x^e/M_0, which itself is defined in terms of R in formula (4). However, for pure IYG for $H_0>400$ Oe the value M_x^e/M_0 is small in comparison with H_0/H_k; therefore, in the initial calculation for M_x^e/M_0 it is possible to set $R=4\pi M_0-H_a=1750$ G, and then, after finding a new value of R, use it to refine the result, and so on. Such a process of successive approximation converges very fast and, as calculation shows, already at the second or third step gives an error less than 1 Oe.

3. METHODS OF VARYING THE FILM PARAMETERS. EXPERIMENTAL ARRANGEMENT

We measured experimentally the initial frequency of the spectrum of surface magnetostatic waves (SMSW), which corresponds to wave numbers k near zero. For such small values of k, the indicated frequency essentially coincides with the FMR frequency. Surface magnetostatic waves were excited in order to measure the initial frequency of the SMSW spectrum in the investigated YIG films with the help of movable antennas and the arrangement described in detail in Ref. 8. The measurements were performed at the temperature $t=20\,^\circ$C. The YIG films were magnetized in the plane of the film by a constant magnetic field $\mathbf{H}_0$, whose magnitude could be varied from 0 to 500 Oe. For the given values of H_0, surface magnetostatic waves were excited in the range 40−4000 MHz. The antenna transformers were oriented parallel to the applied field H_0. The frequencies of surface magnetostatic waves with a definite wavelength (in the interval $0<k<1000$ cm^{-1}) were measured, including the initial frequency of the SMSW spectrum with $k\cong 0$. To measure the orientation dependence of these frequencies, a capability of rotating the YIG films about the normal to the film plane was provided. A typical diagram of the dependence of the FMR frequency on the rotation angle φ for one of the films, measured in a field $H_0=457$ Oe, is shown in Fig. 1. As can be seen from this figure, in measuring the orientation dependence, six pairs of values of the FMR frequencies f^h

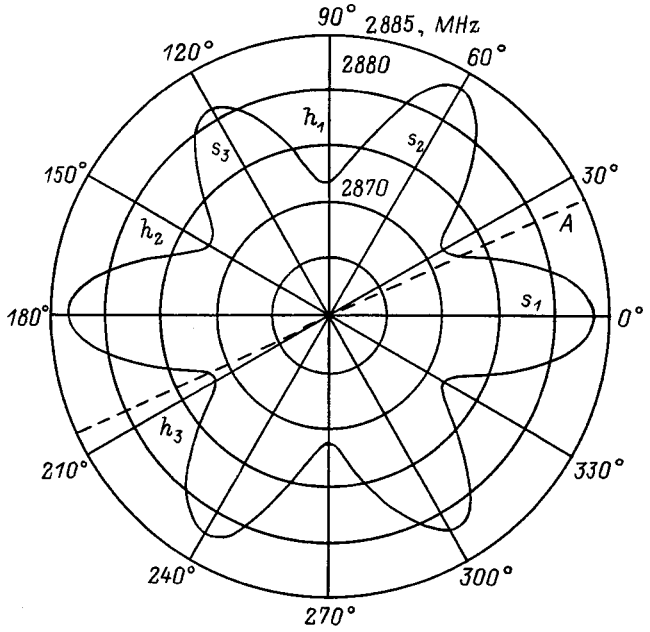

FIG. 1. Typical orientation dependence of the FMR frequency f on the direction of the external magnetic field H_0 in the plane of the film (the angle φ), measured at $H_0=457$ Oe. The diagram shows the orientations of various preferred directions in the plane of the film: h_1,h_2,h_3 — hard axes; s_1,s_2,s_3 — easy axes; the dashed line A — projection of the uniaxial anisotropy axis.

and f^s related to the magnetic parameters of the film according to Eqs. (3)–(9) were obtained for each film. All six values of f^h (and likewise, all six values of f^s) differed from one another within the limits of a few MHz, which following Ref. 16, was used to determine, using Fourier analysis, the slope angle θ of the uniaxial anisotropy axis relative to the film plane and the orientation of the projection of the uniaxial anisotropy axis in the film plane (in Fig. 1 this is the A axis). In addition to the uniaxial anisotropy parameters, we used the orientation dependences to determine the cubic anisotropy parameters: the magnitude of the field H_c, and the projection of the axes on the film plane (the hard axes h).

The domain-structure parameters in YIG films (contrast, type, period, and width of the domains) and the magnitudes of the fields H_0 in which phase transitions arose in the film were measured with the help of a microscope using the Faraday effect.[21] Near saturation, when the domain structure cannot be distinguished on the microscope, the indicated values of the field H_0 were determined from the field dependence of the SMSW frequencies (from the equiphase curves of the SMSW's).[8,10]

The value of R^h calculated according to Eq. (8) and the measured domain-structure parameters were determined for each film by magnetizing it along the same hard axis, which was then marked (the h_1 axis in Fig. 1), and the corresponding values of f^h were used in Eq. (8). Determination of R^s from Eq. (9) and measurement of the corresponding domain-structure parameters were conducted in an analogous way. For this purpose, we used the s_1 axis, perpendicular to the marked h_1 axis.

4. RESULTS OF MEASUREMENTS AND THEIR ANALYSIS

Results of magneto-optic measurements and a study of the characteristics of the magnetostatic waves (see Refs. 8 and 10) lead to the unavoidable conclusion that there are two types of YIG films, differing in the behavior of their domain structures and magnetostatic waves. As was already mentioned, we assume that the reason for the large differences described above is the induced uniaxial anisotropy field, whose magnitude in films of the first type is somewhat larger than in films of the second type. However, this assertion of ours has still not been confirmed experimentally because it is possible to determine the magnitude of the uniaxial anisotropy field H_a by the method described in Ref. 16 only very approximately. Since the problem of distinguishing the uniaxial anisotropy field from the magnetization is complicated and has so far not been worked out experimentally, we have not determined the magnitude of the uniaxial anisotropy field H_a in pure form, but on the basis of the measurements we have calculated the difference R (R^h and R^s) between the magnetization of the film $4\pi M_0$ and H_a: $R=4\pi M_0-H_a$, using Eqs. (8) and (9).

Measurements were performed on 19 films of pure YIG, nine of which belonged to the first type, and ten to the second type. All the films were grown using the same process on GGG substrates in the (111) plane. The thickness of the films w, contrast of the domain structures (high or low), and other parameters discussed below are listed in Table I. Most of the investigated films had a diameter of 60 or 76 mm (except for films No. 4, 5, and 15, which had dimensions of 20×25, 30×35, and 20×20 mm^2, respectively). Note here that we were not able to observe domain structures in films No. 15 and 18 (possibly because of their small thickness). Measurements using the method of Ref. 16 showed that the cubic anisotropy H_c in all the films varied within the limits $-85<H_c<-75$ Oe, and the angle of deviation of the uniaxial anisotropy axis from the normal to the film plane θ lay within the limits $0°<\theta<5°$. Therefore, in the calculations of R^h and R^s, the value of H_c in Eqs. (8) and (9) was taken to be equal to $\cong-80$ Oe for all the films (the error arising here is an order of magnitude less than the error determined by the accuracy of frequency measurements).

From the results of measuring the frequencies f^h and f^s we calculated the corresponding values of the difference R^h and R^s for all the films using Eqs. (8) and (9). The values of R^h and R^s for the same film differed within the limits of a few gauss, due to incompleteness of the implemented model, which did not allow for deviation of the uniaxial anisotropy axis from the normal to the film plane. Since two different values of the difference R cannot simultaneously correspond to one and the same film, the table lists the arithmetic means R_a: $R_a=(R^h+R^s)/2$. On the basis of the mean spread between R^h and R^s for the same film ($\cong10$ G), it may be concluded that the error in R_a does not exceed ±5 G. The films in the table are arranged in order of increasing R_a. Comparison of the values of R_a for different films shows that all the films with high-contrast domain structure have values of R_a ranging from 1698 to 1806 G, and the films with low-contrast domain structure have values of R_a ranging from

TABLE I. Parameters of investigated films.

Film No.	w, μm	f^h, MHz	f^s, MHz	R_a, G	Contrast of DS	T_s^h, μm	T_s^s, μm	H_{sat}^h, Oe	H_{sat}^s, Oe
1	5.2	2800	2811	1698.7	High	3.1	2.9	77	67.5
2	5.7	2810	2824	1716.7	‘‘	3.8	3.6	67	57
3	8.0	2818	2826	1724.6	’’	4.9	4.8	66	57.5
4	19.1	2823	2836	1736.4	‘‘	8.0	8.1	60	54
5	11.5	2842	2855	1766.4	’’	7.3	7.1	48	33
6	12.3	2849	2870	1783.9	‘‘	9.1	8.8	43	29.5
7	5.5	2860	2868	1791.1	’’	4.8	4.4	44	31
8	5.5	2865	2874	1799.8	‘‘	4.9	4.3	40	27
9	8.9	2867	2879	1805.4	’’	8.3	7.9	35	20
10	12.8	2867	2882	1807.8	Low	15.0	16.0	34	21
11	17.9	2870	2882	1810.2	‘‘	21.3	23.3	36	20
12	17.8	2871	2881	1810.2	’’	22.2	23.3	35	20
13	15.0	2870	2884	1811.4	‘‘	19.8	16.2	32	17
14	17.9	2871	2883	1811.8	’’	24.9	26.3	33.5	19.3
15	5.9	2874	2886	1816.3	‘‘			30	17
16	11.5	2880	2888	1823.1	’’	16.1	17.7	32.5	21
17	14.7	2878	2890	1823.1	‘‘	21.4	22.2	30	16
18	10.2	2913	2931	1884.1	’’			23	10.5
19	10.2	2924	2932	1894.3	‘‘	15.6	17.4	21.5	10

1806 to 1895 G. Thus, the value $R_a = R_a^{cr} = 1806$ G can be taken as the critical value of the difference and it may be supposed that if a film has $R_a < R_a^{cr}$ it belongs to films of the first group, and if $R_a > R_a^{cr}$ it belongs to films of the second group. The table also lists values of the periods of a regular, symmetric domain structure T_s^h and T_s^s, measured for each film for its magnetization respectively along a hard axis (h) and along an easy axis (s). Note that, before the measurement of the periods T_s^h and T_s^s, the films were magnetized to saturation, after which the external field H_0 was lowered gradually to a value $\cong 2$ Oe, at which the period of the domain structure was measured, that is to say, the period of the domain structure was measured in a field H_0 close to zero, but not so close that the regular domain structure in the film was destroyed.[10]

The ratio of the width of a domain d to the thickness of the YIG film w was determined for both cases of magnetization of the film (along a hard axis h and along an easy axis s). The ratio η^h was defined by d^h/w, and the ratio η^s was defined by d^s/w, where $d^h = T_s^h/2$ and $d^s = T_s^s/2$. The dependences $\eta^h(R_a)$ and $\eta^s(R_a)$ are plotted in Fig. 2 (curves *1* and *2*), where the experimental points are joined by smooth curves for convenience. It can be seen from Fig. 2 that, for films with minimal values of R_a (i.e., with maximal values of the uniaxial anisotropy field H_a), the ratios η^h and η^s are equal to $\cong 0.3$; for films with R_a lying near R_a^{cr}, these ratios are $\cong 0.5$, and for films with maximal values of R_a (i.e., with minimal value of H_a), these ratios have a value $\cong 0.8$. In other words, for $H_0 \cong 0$ in YIG films with a large value of H_a, the shape of the domains in cross section appears to be prolate in the direction of H_a and, in films with a small value of H_a, the domains acquire a cross section that is closer to the shape of a square.

It may be supposed that, as H_a increases from film to film simultaneously with a gradual stretching of the shape of the domains in the direction of H_a, there also takes place a gradual change in the orientation of the magnetization inside the domains: for $H_0 \cong 0$ it lies the closer to the film plane, the smaller is H_a, and deviates the more from the film plane, the larger is H_a. We also think that, for $H_0 \cong 0$ in films of the first type (with $H_a > H_a^{cr}$), the magnetization inside the domains is inclined to the film plane at an angle $\beta > \beta^{cr}$ and, in films of the second type (with $H_a < H_a^{cr}$), the magnetization is inclined to the film plane at an angle $\beta < \beta^{cr}$, where $\beta^{cr} \cong 19.5°$ is the inclination angle of the [111] axes relative to the film plane. Our reasons are as follows. On the one hand, in films with $H_a > H_a^{cr}$ a zigzag-shaped domain structure arises when the magnetization of the films is directed along

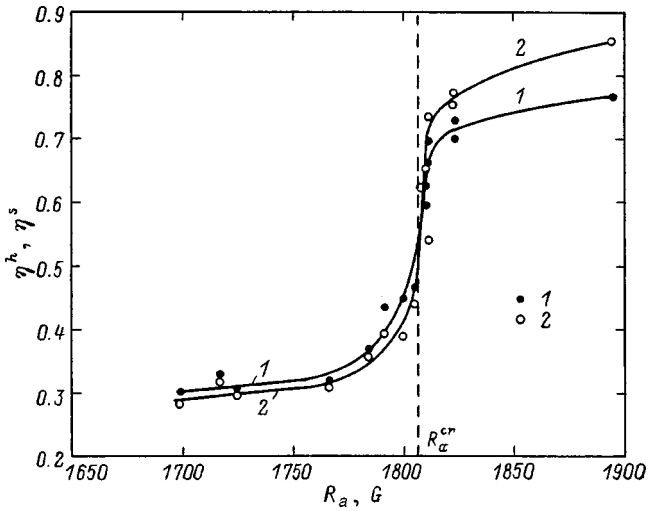

FIG. 2. Dependence of η (relative width of the domain, scaled to the film thickness) on R_a (difference between the magnetization of the film and the uniaxial anisotropy field). The points joined by smooth curves correspond to different films, for which the R_a values where determined from measurements, and the values of η were measured after the films were magnetized along the hard axis h_1 (*1*) and after being magnetized along the easy axis s_1 (*2*) for the external field $H_0 \cong 0$.

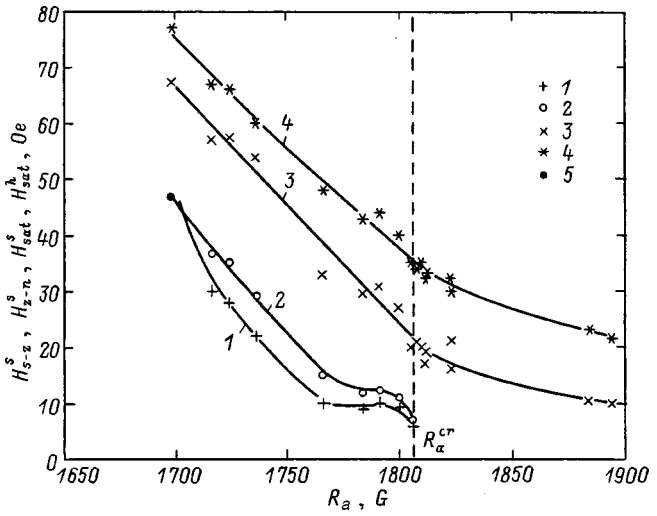

FIG. 3. Dependence of the phase transition fields H^s_{s-z} (*1*), H^s_{z-a} (*2*), H^s_{sat} (*3*), and H^h_{sat} (*4*) on the difference R_a between the magnetization and the uniaxial anisotropy field of the film (the points joined by smooth curves correspond to different films); the point *5* corresponds to the phase transition from the symmetric to the asymmetric domain structure, observed in film No. 1.

an easy axis (an *s* axis) because the magnetizations of neighboring domains become that much more inclined relative to the film plane when the external field H_0 is increased and, at a definite moment, when their directions are close to the nearest [111] axes, these magnetizations orient along these axes (at the angle β^{cr} to the film plane), leading to a simultaneous reorientation of the domain boundaries at angles $+30°$ and $-30°$ to the field H_0 (Ref. 8). On the other hand, in films with $H_a<H_a^{cr}$, a zigzag-shaped domain structure does not arise[10] since the magnetizations of neighboring domains are already inclined relative to the film plane at an angle less than β^{cr} for $H_0=0$, and, as the field is increased, this angle decreases further (i.e., the magnetizations of the domains can never orient along the [111] axes). It also follows from what has been said that the magnitude of the external field $H_0=H^s_{s-z}$ at the phase transition from a linear symmetric domain structure to a zigzag-shaped domain structure,[8] in films of the first type with values of H_a near H_a^{cr}, should be quite small (in this case a minimum external field $H_0=H^s_{s-z}$ is needed to ''knock'' the magnetizations of the domains, already so close to being aligned with the [111] axes, into alignment with these axes): the more H_a exceeds H_a^{cr}, the larger the external field $H_0=H^s_{s-z}$ that is needed to get the magnetizations of the domains into alignment with the [111] axes. The measured values of H^s_{s-z} plotted in Fig. 3 (curve *1*) confirm this trend: the larger the magnitude of H_a in the film, the larger will be the field corresponding to the phase transition H^s_{s-z}. We also found that in films with larger H_a a zigzag-shaped domain structure does not arise. For example, in film No. 1 with $R_a=1698$ G, when it is magnetized along an *s* axis, at $H_0=46.5$ Oe$=H^s_{s-n}$ a phase transition occurs in which the linear symmetric domain structure at once transforms into a linear asymmetric domain structure, bypassing the zigzag-shaped structure. This can be explained as follows. At the moment the magnetizations of the domains, progressively more and more inclined relative to the film plane with increasing H_0, become most closely aligned with the direction of the closest [111] axes, the external field H_0 is already so large that it becomes energetically more favorable for the magnetizations of the domains to remain in the *xz* plane in which the film plane normal and the external field vector H_0 lie. In films with $R_a>1705$ G, at the moment the magnetizations of the domains are most closely aligned with the nearest [111] axes, the external field H_0 is already not so large and it is energetically more favorable for the magnetizations of the domains to align with the [111] axes (reorient) with the formation of a zigzag-shaped domain structure in the film.

We also measured the fields of the phase transitions H_{z-n} at which the zigzag-shaped domain structure gives way to an asymmetric domain structure.[8] The dependence $H_{z-n}(R)$ is plotted in Fig. 3 (curve *2*). Thus, dependences *1* and *2* in Fig. 3 bound the existence region of the zigzag-shaped domain structure for the magnetization of the IYG films aligned with an *s* axis. In essence, curves *1* and *2* in Fig. 3 allow one to judge the variation of the depth of the energy minimum corresponding to the magnetization of the domains oriented along a [111] axis with variation of the uniaxial anisotropy field H_a and the external field H_0.

Table I also lists the fields H^h_{sat} and H^s_{sat} necessary for the magnetization to saturate in the directions parallel and perpendicular to the projection of a [111] axis, respectively. Values of H^h_{sat} and H^s_{sat} were measured for all the films from the salient point in the field dependences of the magnetostatic waves (equiphase curves of the surface magnetostatic waves),[8,10] since the domain structure cannot be made out in the microscope near saturation. The dependences $H^s_{sat}(R_a)$ and $H^h_{sat}(R_a)$ are plotted in Fig. 3 (curves *3* and *4*, respectively). It can be seen from Fig. 3 that the dependences $H^h_{sat}(R_a)$ and $H^s_{sat}(R_a)$ decrease monotonicly and have no distinguishing features in the vicinity of $R_a=R_a^{cr}$. This fact accords fully with our ideas about the behavior of the magnetization of the domains: features in the behavior of the magnetization of the domains arise only when it is inclined relative to the film plane at angles close to β^{cr}; for fields close to saturating, on the other hand, when the magnetization nearly lies in the film plane ($\beta\ll\beta^{cr}$), H^h_{sat} and H^s_{sat} depend only on H_a: the larger H_a is, the harder it will be to magnetize the film to saturation.

A paradoxical fact should be noted: according to our measurements the quantity $R=4\pi M_0-H_a$ for 15 of the 19 films turned out to be larger than 1750 G, which is typical for YIG bulk single crystals.[1] If we assume that the magnetization of the films, $4\pi M_0$, is determined only by their composition and that the uniaxial anisotropy field H_a is determined only by elastic stresses, which can vary from film to film, then we can estimate $4\pi M_0$ and H_a separately. Thus, the maximum of the measured values of $4\pi M_0-H_a=1894$ G. We believe that in this case $H_a\cong 0$, and $4\pi M_0$ is the same for all the films and consequently equal to the same value,

$4\pi M_0 = 1894$ G. Thus, from the fact that the quantity $4\pi M_0 - H_a$ varies from $\cong 1700$ to $\cong 1900$ G for the investigated films we obtain an estimate for the uniaxial anisotropy field H_a lying within the limits from 0 to 200 Oe, and an estimate for its critical value H_a^{cr} not less than 90 Oe.

Thus, from the results of the work presented here we can draw the following conclusions.

As is well known, epitaxial films of pure YIG have, in addition to a cubic anisotropy, an induced (as-grown) uniaxial anisotropy with axis perpendicular to the film plane (the field H_a can vary from film to film from $\cong 0$ to $\cong 250$ Oe). From our experimental observations and theoretical estimates, it follows that there exists a critical value of the uniaxial anisotropy field H_a^{cr} equal to 120 ± 30 Oe. Depending on whether the uniaxial anisotropy field H_a is greater or less than H_a^{cr}, all the YIG films can be divided into two types, distinguished in the unsaturated state by the parameters, behavior, and phase transitions of their domain structure. We have found that the domain structures of YIG films can be divided into two groups according to their appearance when viewed under a microscope: high-contrast, characteristic of films of the first type with $H_a > H_a^{cr}$, and low-contrast, characteristic of films of the second type with $H_a < H_a^{cr}$. In the high-contrast domain structures the magnetizations of the domains are inclined relative to the film plane by an angle $\beta \geqslant \beta^{cr}$, and in the low-contrast domain structures, by an angle β substantially less than β^{cr} (where $\beta^{cr} \cong 19.5°$ is the inclination angle of the [111] axes relative to the film plane). Such behavior of the domain structures arises as a result of the energy advantage of the [111] axes for orientation of the magnetizations of the domains. In this case, if the magnetization of the domains deviates from this direction toward the film plane, then the angle β decreases at once by a noticeable amount.

We found that films of the first type (with $H_a > H_a^{cr}$) for their magnetization along an easy axis *s* are characterized by saturating fields greater than 20 Oe, and for their magnetization along a hard axis *h*, the films are characterized by saturating fields greater than 35 Oe. The measured ratio of the width of the domains to the film thickness for $H_0 \cong 0$ is always less than 0.5. For the uniaxial anisotropy field of the film lying within the limits $H_a^{cr} < H_a < H_a^{cr} + \cong 100$ Oe, phase transitions are observed in the films associated with the appearance and disappearance of a banded zigzag-shaped domain structure. For cyclical variation of the external magnetic field $\mathbf{H}_0$, the parameters of all the domain structures are uniquely determined by the magnitude of $\mathbf{H}_0$ (hysteresis is absent).

We found that films of the second type (with $H_a < H_a^{cr}$) for their magnetization along an easy axis *s* are characterized by saturating fields less than 21 Oe, and for their magnetization along a hard axis *h*, they are characterized by saturating fields less than 36 Oe. The measured ratio of the width of the domains to the film thickness for $H_0 \cong 0$ is always greater than 0.5. For cyclical variation of the external field $\mathbf{H}_0$ hysteresis of the phase transition fields and the domain-structure parameters is observed in these films.

The authors are grateful to S. V. Gerus for consultation.[16]

This work was carried out with the financial support of the Russian Fund for Fundamental Research (Grant No. 96-02-17283a).

[1)] By the term quasiregular, as in Ref. 10, we mean a domain structure which differs from regular by the presence of a small number of insignificant distortions which have practically no influence on the parameters of propagating magnetostatic waves with wavelength much larger than the size of the distortion.

[2)] We would like to point out that, instead of the statement that ''the magnetization vector of the domains is oriented close to the normal to the film plane,'' used in our previous papers (Refs. 8 and 10) to characterize films of the first type, it would be more correct to say, as we do in this paper, that ''the magnetization vector of the domains deviates substantially from the film plane.''

[1] A. G. Gurevich and G. A. Melkov, *Magnetic Oscillations and Waves* (Nauka, Moscow, 1994).
[2] A. V. Vashkovskiĭ, V. S. Stal'makhov, and Yu. P. Sharaevskiĭ, *Magnetostatic Waves in Microwave Electronics* (Saratov University Press, Saratov, 1993).
[3] I. V. Zavislyak and V. V. Danilov, Pis'ma Zh. Tekh. Fiz. **8**, 72 (1982) [Sov. Tech. Phys. Lett. **8**, 31 (1982)].
[4] S. A. Vyzulin, S. A. Kirov, and N. E. Syr'ev, Vestn. Mosk. Univ., Ser. 3: Fiz., Astron. **24**, 92 (1983).
[5] P. E. Zil'berman, G. T. Kazakov, and V. V. Tikhonov, Radiotekh. Elektron. **32**, 710 (1987).
[6] G. T. Kazakov, A. G. Sukharev, and Yu. A. Filimonov, *Abstracts of the All-Union School on Spin-Wave Microwave Electronics* (Zvenigorod, 1991).
[7] A. V. Vashkovskiĭ, É. G. Lokk, and V. I. Shcheglov, JETP Lett. **63**, 572 (1996).
[8] A. V. Vashkovskiĭ, É. G. Lokk, and V. I. Shcheglov, Zh. Éksp. Teor. Fiz. **111**, 1016 (1997) [JETP **84**, 560 (1997)].
[9] A. V. Vashkovskiĭ, É. G. Lokk, and V. I. Shcheglov, Mikroelektronika **27**, 393 (1998).
[10] A. V. Vashkovskiĭ, É. G. Lokk, and V. I. Shcheglov, Zh. Éksp. Teor. Fiz. **114**, 1430 (1998) [JETP **87**, 776 (1998)].
[11] R. W. Damon and J. R. Eshbach, J. Phys. Chem. Solids **19**, 308 (1961).
[12] I. G. Avaeva, F. V. Lisovskiĭ, V. A. Osika, and V. I. Shcheglov, Fiz. Tverd. Tela (Leningrad) **17**, 3045 (1975) [Sov. Phys. Solid State **17**, 2019 (1975)].
[13] I. G. Avaeva, F. V. Lisovskiĭ, V. A. Osika, and V. I. Shcheglov, Fiz. Tverd. Tela (Leningrad) **18**, 3694 (1976) [Sov. Phys. Solid State **18**, 2152 (1976)].
[14] I. G. Avaeva, F. V. Lisovskiĭ, V. A. Osika, and V. I. Shcheglov, Radiotekh. Elektron. **21**, 1894 (1976).
[15] V. I. Shcheglov, Mikroelektronika **16**, 374 (1987).
[16] A. V. Voronenko, S. V. Gerus, and L. A. Krasnozhen, Mikroelektronika **18**, 61 (1989).
[17] V. B. Bobkov, I. V. Zavislyak, and V. F. Romanyuk, Fiz. Tverd. Tela (St. Petersburg) **35**, 431 (1993) [Phys. Solid State **35**, 222 (1993)].
[18] V. B. Bobkov and I. V. Zavislyak, Phys. Status Solidi A **164**, 791 (1997).
[19] V. I. Kozlov, *Study of Inhomogeneity and Anisotropy of Magnetic Films with the help of Gyromagnetic Effects*, Author's abstract of dissertation in pursuit of the degree of Doctor of Physical and Mathematical Sciences (000 ''ÉZhIS'' Publishing House, Moscow, 1997).
[20] A. V. Lugovskoĭ and V. I. Shcheglov, Radiotekh. Elektron. **27**, 518 (1982).
[21] A. P. Malozemoff and J. C. Slonczewski, *Magnetic Domain Walls in Bubble Materials* (Academic Press, New York, 1979).

Translated by Paul F. Schippnick

Influence of frustration on magnetization processes in the ferrite $CoFeCrO_4$

L. G. Antoshina, A. N. Goryaga, and R. R. Annaev

M. V. Lomonosov Moscow State University, 119899 Moscow, Russia
(Submitted March 31, 1999)
Fiz. Tverd. Tela (St. Petersburg) **41**, 2042–2043 (November 1999)

The behavior of isotherms of the magnetization $\sigma(H)$ and the longitudinal $\lambda_\parallel$ and transverse $\lambda_\perp$ magnetostriction of the polycrystalline ferrite $CoFeCrO_4$ with frustrated magnetic structure has been investigated for the first time in magnetic fields up to $H=50$ kOe at $T=4.2$ K. It is found that the magnetization grows with increasing field due to two different paraprocesses.
 [S1063-7834(99)02611-8]

In compounds with frustrated magnetic structure, magnetic order does not permeate the entire volume of the sample but exists only in isolated, spontaneously magnetized regions. Depending on whether the order in these regions is predominantly ferro- or ferrimagnetic, these magnetic structures are called speromagnetic or sperimagnetic. Therefore, it can be expected that the process of magnetization in a magnetic field in such magnetic structures should be different than the process of magnetization in ordinary ferro- and ferrimagnets. In compounds with frustrated magnetic structure, technical magnetization should be absent, and only a paraprocess (true magnetization) will take place.

However, it is difficult to clarify the nature of the magnetization process in such compounds only from the magnetization data, whereas a study of the behavior of longitudinal and transverse magnetostriction together with magnetization measurements can resolve the given problem.

To solve this problem, we chose the ferrite–chromite $CoFeCrO_4$. Earlier, the authors of Ref. 1 conjectured that the magnetic structure of the ferrite $CoFeCrO_4$ has a complex nature: in the temperature interval $275\,\text{K}-T_c$ it is an ''unstable ferrimagnet,'' and in the temperature interval 80–275 K it is a cluster ''spin glass.'' Later, the authors of Ref. 2 established that the magnetic structure in the given ferrite at temperatures $T<100$ K is frustrated. The presence of a frustrated magnetic structure in $CoFeCrO_4$ was also confirmed by Mössbauer studies.[3] Magnetostriction for $CoFeCrO_4$ in fields up to $H=14$ kOe was first studied in Ref. 4. They found that, in contrast to the ferrite $CoFe_2O_4$ with ferrimagnetic ordering, for which $\lambda_\parallel<0$, the longitudinal magnetostriction $\lambda_\parallel$ has a positive sign in $CoFeCrO_4$. Also, there is no saturation of the isotherms $\sigma(H)$, but the magnetostriction of $\lambda_\parallel$ and $\lambda_\perp$ has an anisotropic nature in fields up to 14 kOe.

Therefore, to elucidate the nature of the magnetization process in the ferrite $CoFeCrO_4$ with frustrated magnetic structure, it was necessary to measure the magnetization and magnetostriction in higher fields since at $T=4.2$ K the coercive force is 1300 Oe in a given sample.

As our object of study, we chose a polycrystalline sample of $CoFeCrO_4$ in which we had already measured the magnetization[2] and magnetostriction in fields up to 14 kOe (Ref. 4). In the present work we measure the magnetization σ by a ballistic method, and the magnetostriction λ, by tensometry in a superconducting solenoid in magnetic fields up to 50 kOe at 4.2 K.

Figure 1 plots isotherms of the magnetization $\sigma(H)$ and the longitudinal $\lambda_\parallel(H)$ and transverse $\lambda_\perp(H)$ magnetostriction at $T=4.2$ K. It can be seen that there is no saturation in $\sigma(H)$ all the way up to 50 kOe, and the magnetostriction $\lambda_\parallel$ has a positive sign, and $\lambda_\perp$ has a negative sign. In fields up to 15 kOe, the dependences $\lambda_\parallel(H)$ and $\lambda_\perp(H)$ are anisotropic and only in fields $H>20$ kOe do the longitudinal $\lambda_\parallel$ and transverse $\lambda_\perp$ magnetostrictions become isotropic, in which case the susceptibilities of the magnetostrictions $\Delta\lambda_\parallel/\Delta H$ and $\Delta\lambda_\perp/\Delta H$ have a negative sign.

Using the values of the longitudinal $\lambda_\parallel$ and transverse $\lambda_\perp$ magnetostrictions, we calculated isotherms of the bulk $\omega(H)$ and anisotropic $\lambda_t(H)$ magnetostrictions using the formulas $\omega=\lambda_\parallel+2\lambda_\perp$ and $\lambda_t=\lambda_\parallel-\lambda_\perp$. These isotherms are plotted in Fig. 2. It turns out that the magnetostriction λ_t in all fields has only a positive sign whereas the magnetostriction ω changes sign from positive to negative as the field is increased past $H\approx25$ kOe.

It is well known that a nonzero bulk magnetostriction ω is indicative of the presence of a paraprocess in a magnetic compound. Thus, our results on the nature of the dependence $\omega(H)$ suggest that the magnetization process in $CoFeCrO_4$ with frustrated magnetic structure consists of two paraprocesses of different nature. The first of these paraprocesses, in fields up to 25 kOe, is caused by rotation of the magnetic moments of isolated, spontaneously magnetized regions toward the direction of the external magnetic field, while the second paraprocess, in higher fields, is due to a decrease in the degree of noncollinearity of the magnetic moments of the ions in these spontaneously magnetized regions. As was shown earlier in Ref. 2, the frustrated magnetic structure in the ferrite $CoFeCrO_4$ is due to the fact that it contains three types of magnetic cations, between which there are exchange interactions which differ in sign and magnitude. It is not ruled out that the presence of a strong, direct negative exchange interaction between octahedral Cr^{3+} ions can lead to noncollinear ferrimagnetic ordering in isolated, spontaneously magnetized regions.

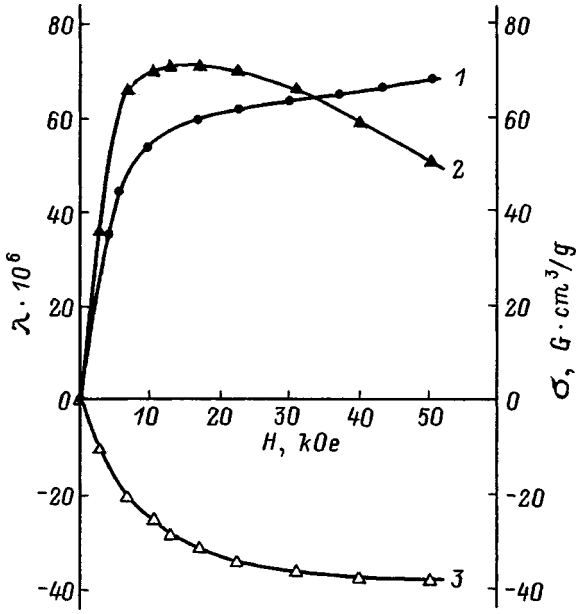

FIG. 1. Isotherms of the magnetization σ (*1*) and magnetostriction $\lambda_{\parallel}$ (*2*) and $\lambda_{\perp}$ (*3*) at $T=4.2$ K.

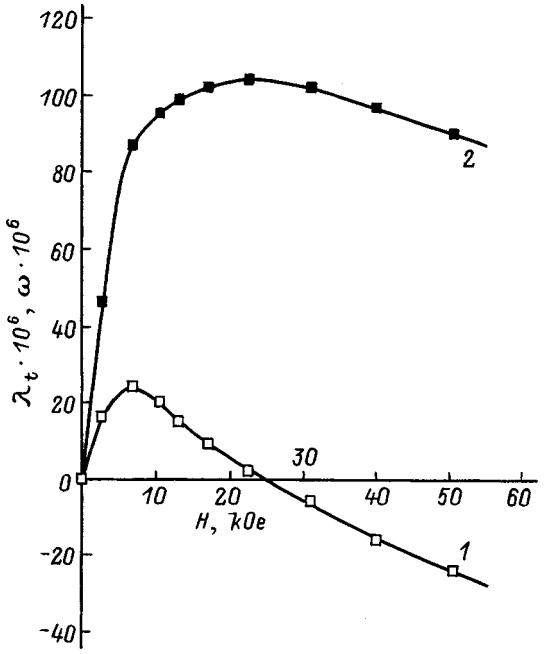

FIG. 2. Isotherms of the bulk ω (*1*) and anisotropic λ_t (*2*) magnetostriction at $T=4.2$ K.

In ordinary ferro- and ferrimagnets in the region of the technical magnetization process the behavior of the magnetostrictions $\lambda_{\parallel}$ and $\lambda_{\perp}$ obey Akulov's law: $\lambda_{\parallel}=-2\lambda_{\perp}$. In this case, the anisotropic magnetostriction λ_t, in fields greater than the magnetic anisotropy field, should saturate. However, as can be seen from Fig. 2, the magnetostriction λ_t for a ferrite with frustrated magnetic structure has an anomalous character: in fields up to ≈ 20 kOe the magnetostriction λ_t grows abruptly and is then observed to decrease with increasing field according to a linear law. Our result on the behavior of the anisotropic magnetostriction λ_t in a field also provides evidence of the absence of technical magnetization in the $CoFeCrO_4$ sample.

In this way, we have found that the process of technical magnetization is absent in the ferrite $CoFeCrO_4$ with frustrated magnetic structure, but growth of the magnetization σ with increasing field takes place on account of two paraprocesses different in nature.

[1] K. Muralledharan, J. K. Srivastava, V. R. Marathe, and R. Vijayaraghavan, J. Phys. C **18**, 5897 (1985).
[2] K. P. Belov, A. N. Goryaga, R. R. Annaev, A. I. Kokorev, and A. N. Lyamzin, Fiz. Tverd. Tela (Leningrad) **31**, 117 (1989) [Sov. Phys. Solid State **31**, 785 (1989)].
[3] H. Mohan, I. A. Shaikh, and R. G. Kulkarni, Physica B **217**, 292 (1996).
[4] A. N. Goryaga, R. R. Annaev, and A. E. Bogdanov, Vestn. Mosk. Univ., Ser. 3: Fiz., Astron. **36**, 44 (1995).

Translated by Paul F. Schippnick

Properties of phase transitions in easy-axis tetragonal antiferromagnets

G. K. Chepurnykh, V. S. Ivaniĭ, O. G. Medvedovskaya, and O. A. Nikitina

Institute of Applied Physics, Ukrainian Academy of Sciences, 244030 Sumy, Ukraine
(Submitted in final form April 12, 1999)
Fiz. Tverd. Tela (St. Petersburg) **41**, 2044–2046 (November 1999)

Properties of phase transitions in a magnetic field **H** parallel to the easy axis have been investigated, and it has been shown, in particular, that the nature of the transition of the magnetic subsystem from the antiferromagnetic phase to the angular phase depends on the ''sign'' of the Dzyaloshinskiĭ interaction. The conditions for orientation of the antiferromagnetism vector **l** in the basis plane in fields larger than the threshold field have been determined. It is shown that the transition from the angular phase to the state where the resulting magnetic moment **m** is parallel to the easy axis takes place in the field corresponding to a spin-flip transition. From an analysis of the configuration of the magnetic subsystem for arbitrary orientation of the external magnetic field, it follows that the values of the critical angle (ψ_{cr}) for which a first-order phase transition takes place satisfy the condition $\psi_{cr} \ll 1$ in the case in which the anisotropy constant f in the basis plane is of the order of the first anisotropy constant b. Usually $|f| \ll |b|$ so that the tricritical point in the phase diagram H_y, H_z satisfies the condition $H_y \sim H_z$. © *1999 American Institute of Physics.* [S1063-7834(99)02711-2]

Many papers have been dedicated to a study of orientational phase transitions induced by an external magnetic field **H** in the easy-axis tetragonal antiferromagnets (AFM) CoF_2, FeF_2, and MnF_2 (see, e.g., Refs. 1–7, Refs. 8 and 9, and Refs. 10–16, respectively). At the same time, analysis of the experimental results and theoretical studies of the indicated antiferromagnets have met with certain difficulties. In addition, a general problem[17,18] for antiferromagnets with a Dzyaloshinskiĭ interaction (DI) is the experimental determination of the ''sign'' of the Dzyaloshinskiĭ interaction, which is of fundamental interest from the point of view of a microscopic theory of the Dzyaloshinskiĭ interaction. According to Ref. 17, can be done by determining experimentally the direction of rotation of the antiferromagnetism vector **l** about the magnetic field **H** in the geometry $\mathbf{H} \perp EA \| \mathbf{d}$ (EA is the easy axis, **d** is a constant vector, whose magnitude characterizes the magnitude of the Dzyaloshinskiĭ interaction). However, as was noted in Ref. 18, a Mössbauer experiment[17] on easy-axis hematite did not give an unambiguous result (see also Ref. 19). Therefore, it is of interest to search for other experimental possibilities of resolving the indicated problem.

The present study examines peculiarities of phase transitions for $\mathbf{H} \| EA$ and shows, in particular, that the nature of the transition between the antiferromagnetic phase and the angular phase depends on the ''sign'' of the Dzyaloshinskiĭ interaction. It also examines the configuration of the magnetic moments for arbitrary orientation of **H** relative to EA.

The thermodynamic potential is utilized in the form

$$F=(2M_0)\left[\frac{E}{2}\mathbf{m}^2+\frac{b}{2}l_z^2-d(l_xm_y+l_ym_x)+\frac{a}{2}m_z^2+fl_x^2l_y^2-\mathbf{m}\cdot\mathbf{H}\right],$$

$$\mathbf{l}=(\mathbf{M}_1-\mathbf{M}_2)/2M_0, \quad \mathbf{m}=(\mathbf{M}_1+\mathbf{M}_2)/2M_0, \quad \mathbf{l}\perp\mathbf{m},$$

$$b<0, \quad f>0, \quad d>0.$$

$$E \gg |b| \gg f, \quad EA \| 0Z. \tag{1}$$

It is noteworthy that, in contrast to Refs. 7 and 12, we have chosen to put a minus sign in front of the Dzyaloshinskiĭ constant d in the thermodynamic potential (1). Considering the necessary conditions for the existence of a minimum of the thermodynamic potential (1) as a function of the variables m, φ, θ, $\varphi_\perp$ (see Fig. 1), we obtain the system of equations

$$\partial F/\partial m=0, \quad \partial F/\partial\varphi=0,$$

$$\partial F/\partial\theta=0, \quad \partial F/\partial\varphi_\perp=0 \tag{2}$$

and, initially, we shall consider the case $\mathbf{H} \| EA$.

Operating with the system of equations (2) and sufficient conditions for the existence of a minimum of (1), we find that, for fields greater than the field corresponding to a transition from the antiferromagnetic phase ($\mathbf{l} \| EA$), the angular phase ($\cos 2\varphi_\perp=0$, $\cos\theta<1$) is realized for $2d^2>fE$, and the phase $\mathbf{l} \perp EA$ ($\cos\theta=0$, $\sin 2\varphi_\perp=0$) is realized[1)] for $2d^2>fE$.

Employing sufficient conditions, we find that the largest magnetic field for which the antiferromagnetic phase occurs is given by

$$H_{cr}=H_{EA}\left(1-\frac{b}{2E}\right)+d, \quad (H_{EA}=\sqrt{|b|E}\,). \tag{3}$$

Next, determining the field H_p of the equilibrium transition between the angular phase and the antiferromagnetic phase, we find that for $\theta \ll 1$ the field difference

$$H_{cr}-H_p=\frac{1}{2}\left(d-|b|\frac{a+b}{\sqrt{|b|E}}-\sqrt{fE}\frac{\sqrt{f}}{2\sqrt{|b|}}\right)\theta^2. \tag{4}$$

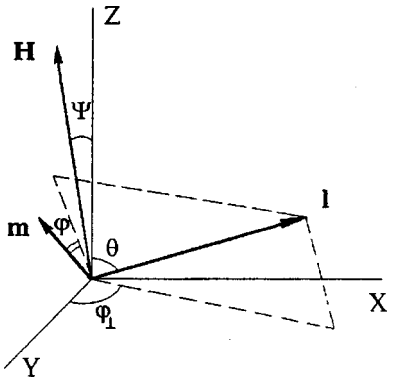

FIG. 1. Orientation of the antiferromagnetism vector **l** and the magnetization vector **m** for arbitrary orientation of the external magnetic field in the ZY plane. θ and $\varphi_\perp$ are the polar and azimuthal angles of the vector **l**, φ is the angle characterizing the direction of the vector **m** in the plane perpendicular to **l** (this angle is reckoned from the intersection line of the indicated plane with the plane passing through the Z axis and the vector **l**.

If $a+b<0$ (i.e., the usual spin-flop transition takes place in the form of a first-order transition[20]), then $H_{cr}-H_p>0$ and, consequently, the transition between the antiferromagnetic phase and the angular phase is first-order. Moreover, if $a+b>0$ (i.e., the usual spin-flop transition takes place in the form of two second-order transitions[20]), then since $d>\sqrt{fE/2}$ and ordinarily $|b|\sim\sqrt{fE}$, in this case $H_{cr}-H_p>0$.

Nevertheless, we note that, in principle, if the strict condition $[(a+b)/E]\sqrt{2|b|/f}>1$ is fulfilled, then for $d<d_{cr}=|b|(a+b)/H_{EA}$ a second-order transition takes place.

We draw attention to the following fact. In Fig. 1 the vector **m** is the rotation axis for the vector **l** (the same is true in the case of hematite[17] and, looking in the direction opposite **m**, in our case the vector **l** will be rotated clockwise from the Z axis. If we rotate the vector **l** counterclockwise, then a minus sign will appear in expression (4) in front of the Dzyaloshinskiĭ constant d and therefore the difference $H_{cr}-H_p<0$ and, consequently, the transition between the antiferromagnetic phase and the angular phase will be second-order.

Thus we see that, by determining experimentally the nature of the transition between the antiferromagnetic and angular phases, we determine the direction of rotation of the antiferromagnetism vector **l**. This statement is also valid for the case when we use the invariant $(-a_2/4)l_z^4$ instead of the invariant $(a/2)m_z^2$ in the pontential (1). However, when we rotate the vector **l** from the Z axis in the clockwise direction it is necessary to put a plus sign in front of the Dzyaloshinskiĭ constant d in Eqs. (4), (7) and (8) of Ref. 16.

Finishing up our treatment of the case $2d^2>fE$, we note that it follows from an analysis of system of equations (2) that, after the magnetic subsystem transitions to the angular phase with growth of the magnetic field, the solution $\cos\theta=0$ for $\cos 2\varphi_\perp=0$ exists if $m=1$, i.e., the spin-flop and spin-flip transition fields coincide.

Solution of the problem of finding the orientation of the vector **l** in the basis plane in fields greater than the threshold field allows us, for $d<\sqrt{fE/2}$, to obtain the following equation in the angle θ:

$$\sin 2\theta\left[\frac{2a+b}{E}H^2\sin^2\theta-\frac{b}{E}H^2\cos^2\theta-bE-H^2-d^2+\frac{2d^2H^2}{2d^2+fE}\right]=0. \tag{5}$$

The states $\mathbf{l}\parallel EA$ and $\mathbf{l}\perp EA$ follow from this equation.

Note that Eq. (5) was obtained neglecting terms $\sim(b/E)^2H^2$, and if the angular phase also exists thanks to the Dzyaloshinskiĭ interaction, then this effect is extremely insignificant.

From Eq. (5) we obtain the following expressions for the lability fields H_1 and H_2:

$$H_1=\sqrt{|b|E}\sqrt{\frac{2d^2+fE}{fE}}\left(1-\frac{d^2}{2|b|E}-\frac{2d^2+fE}{2fE}\frac{b}{E}\right), \tag{6}$$

$$H_2=\sqrt{|b|E}\sqrt{\frac{2d^2+fE}{fE}}\left(1-\frac{d^2}{2|b|E}+\frac{2d^2+fE}{2fE}\frac{2a+b}{E}\right). \tag{7}$$

The interval of metastable states for a first-order phase transition is given by

$$H_1-H_2=\sqrt{|b|E}\left(1-\frac{d^2}{2|b|E}\right)\left(\frac{2d^2+fE}{fE}\right)^{3/2}\frac{|a+b|}{E}. \tag{8}$$

The field H_{sp} of the spin-flop equilibrium transition is given by

$$H_{sp}=\sqrt{|b|E}\sqrt{\frac{2d^2+fE}{fE}}\left(1-\frac{d^2}{2|b|E}+\frac{2d^2+fE}{2fE}\frac{a}{E}\right). \tag{9}$$

It can be seen from the expressions derived for the threshold fields that they undergo substantial renormalization for $fE\sim 2d^2$.

Let us consider the configuration of the magnetic subsystem in a tilted magnetic field (see Fig. 1), following the standard approach.[15] Using the system of equations (2) and setting the angle $\theta=\pi/2-\theta_0$, we write the thermodynamic potential for $\theta_0\ll 1$ in the form

$$F=F_0+A\theta_0^2+B\theta_0^4, \tag{10}$$

where θ_0 is the order parameter.

From the equation

$$A=0 \tag{11}$$

we can determine the critical line in the phase diagram H_y, H_z on which (and above which) the state $\mathbf{l}\perp EA$ is realized.

Employing Eq. (11) and the equation

$$B=0, \tag{12}$$

it is possible to determine the tricritical point and, consequently, the critical angle ψ_{cr} (Ref. 21) within the limits of which a first-order transition between the state $\mathbf{l}\perp EA$ and the angular phase takes place. However, despite using the restriction $H_y\ll H_z$, the expressions obtained for A and B turn

out to be extraordinarily cumbersome. Therefore we give expressions for A and B for the additional restriction $H_y^2 \ll (fE+2d^2)$

$$A = H_z^2 + bE - H_z^2 \frac{2a+b}{E} + d^2 + dH_y - \frac{H_z^2(2d+H_y)^2}{2(fE+2d^2)}, \quad (13)$$

$$B = \frac{1}{3}\left[-H_z^2 - bE + H_z^2 \frac{5a+4b}{E} - d^2 - \frac{dH_y}{4} \right] + \frac{1}{3}\left[\frac{2H_z^2(2d+H_y)(d-H_y)}{2(fE+2d^2)} - \frac{3H_yH_z^4(2d+H_y)^3}{[2(fE+2d^2)]^3} \right]. \quad (14)$$

It follows from relations (11) and (13) that, as H_y grows, so does H_z. If we determine H_z from relations (11) and (13) and substitute it into (14), we discover that $B<0$ and, consequently, there exists a region in which the first-order phase transition occurs. This conclusion also follows using the restriction $H_y^2 \gg (fE+2d^2)$.

Thus we see that, if the usual condition $|b| \gg f$ is satisfied the condition for the critical angle $\psi_{cr} \ll 1$ is not satisfied.

The results obtained here are needed for experimental studies of easy-axis tetragonal antiferromagnets.

[1)] In easy-plane tetragonal antiferromagnets the angle $\theta = \pi/2$ for any orientation of the vector **l** in the basis plane, and the conditions for which $\cos 2\varphi_\perp = 0$ or $\sin 2\varphi_\perp = 0$ are given in Ref. 20.

[1] P. L. Richards, J. Appl. Phys. **35**, 850 (1964).
[2] M. E. Lines, Phys. Rev. A **137**, 982 (1965).
[3] S. J. Allen and H. J. Guggenheim, Phys. Rev. **134**, 950 (1971).
[4] V. G. Shapiro, V. I. Ozhogin, and K. G. Gurtovoĭ, Izv. Akad. Nauk SSSR, Ser. Fiz. **36**, 1556 (1972).
[5] K. N. Kocharyan and E. G. Rudashevskiĭ, Izv. Akad. Nauk SSSR, Ser. Fiz. **36**, 1556 (1972).
[6] N. F. Kharchenko, V. V. Eremenko, and L. I. Belyĭ, Zh. Éksp. Teor. Fiz. **82**, 827 (1982) [Sov. Phys. JETP **55**, 490 (1982)].
[7] K. G. Gurtovoĭ, A. S. Lagutin, and V. I. Ozhogin, Zh. Éksp. Teor. Fiz. **83**, 1941 (1982) [Sov. Phys. JETP **56**, 1122 (1982)].
[8] Yu. G. Litvinenko and V. V. Shapiro, Fiz. Nizk. Temp. **2**, 233 (1976) [Sov. J. Low Temp. Phys. **2**, 116 (1976)].
[9] A. R. King, V. Jaccarino, T. Sakakibara, M. Motokawa, and M. Date, Phys. Rev. Lett. **47**, 117 (1981).
[10] J. De Gunzbourg and J. P. Krebs, J. Phys. (Paris) **29**, *1*, 42 (1968).
[11] R. L. Melcher, Phys. Rev. B **1**, 4493 (1970).
[12] V. S. Kuleshov and V. A. Popov, Fiz. Tverd. Tela (Leningrad) **15**, 973 (1973) [Sov. Phys. Solid State **15** (1973)] [*sic*].
[13] V. V. Eremenko, N. E. Kaner, Yu. G. Litvinenko, and V. V. Shapiro, Zh. Éksp. Teor. Fiz. **89**, 1289 (1985) [Sov. Phys. JETP **62**, 746 (1985)].
[14] V. V. Eremenko and V. V. Shapiro, Fiz. Nizk. Temp. **16**, 1499 (1990) [Sov. J. Low Temp. Phys. **16**, 845 (1990)].
[15] G. K. Chepurnykh, M. I. Kolesnik, and O. G. Medvedovskaya, Fiz. Tverd. Tela (St. Petersburg) **36**, 2289 (1994) [Phys. Solid State **36**, 1247 (1994)].
[16] G. K. Chepurnykh, O. G. Medvedovskaya, and O. A. Nikitina, Fiz. Tverd. Tela (St. Petersburg) **38**, 1641 (1996) [Phys. Solid State **38**, 907 (1996)].
[17] V. I. Ozhogin, S. S. Yakimov, R. A. Voskanyan, and V. Ya. Galitskiĭ, JETP Lett. **8**, 414 (1968).
[18] V. I. Ozhogin, Author's Abstract of Dissertation, IAÉ (1974).
[19] R. Z. Levitin and V. A. Shchurov, in *Physics and Chemistry of Ferrites* (Moscow State Univ. Press, Moscow, 1973), p. 162.
[20] E. A. Turov, *Physical Properties of Magneto-Elastic Crystals* (Moscow–Leningrad, 1963).
[21] G. K. Chepurnykh, Fiz. Tverd. Tela (Leningrad) **10**, 1917 (1968) [Sov. Phys. Solid State **10**, 1517 (1968)]; M. I. Kaganov and G. K. Chepurnykh, Fiz. Tverd. Tela (Leningrad) **11**, 911 (1969) [Sov. Phys. Solid State **11**, 747 (1969)].

Translated by Paul F. Schippnick

On the nature of the Faraday effect in the rare-earth ortho-aluminate $TbAlO_3$

U. V. Valiev, M. M. Lukina, and K. S. Saidov

Tashkent State University, 700095 Tashkent, Uzbekistan
(Submitted in final form April 29, 1999)
Fiz. Tverd. Tela (St. Petersburg) **41**, 2047–2052 (November 1999)

The magnetic susceptibility χ, the absorption and luminescence spectra, and the Verde constant V along different crystallographic axes of the rhombic crystal $TbAlO_3$ have been investigated experimentally in the temperature interval 78–300 K. It is found that, in contrast to the magnetic susceptibility χ measured along the [110] axis, the Verde constant V varies in inverse proportion to the temperature in the given range. It is shown that this temperature dependence of the Verde constant measured along the [110] axis is connected with the absence of a contribution to the Faraday rotation of the van Vleck mechanism (in an external field H) of ''mixing'' of the states of the rare-earth ion Tb^{3+}. From a comparison of the optical and magnetic measurements, we have determined the wave functions and magnitudes of the Stark intervals between the lower Stark sublevels for the $^7F_6$ ground multiplet of the Tb^{3+} ion in the ortho-aluminate $TbAlO_3$. © *1999 American Institute of Physics.* [S1063-7834(99)02811-7]

It is well known that the interaction with a crystal field (CF) having C_S symmetry leads to a strong anisotropy of the magnetic moment of the rare-earth (RE) ion Tb^{3+} in the ortho-aluminate $TbAlO_3$ structure (space group D_{2h}^{16}), especially at low temperatures T (Refs. 1 and 2). The component of the magnetic moment of the rare-earth sublattice associated with the van Vleck contribution to the magnetization makes a substantial contribution to this anisotropy. This contribution, due to ''admixture'' of the excited states with the ground state upon application of an external magnetic field H, becomes very noticeable at high temperatures ($T \geqslant 100$ K) and comparable in magnitude to the mean magnetic moment of the rare-earth ion.[2] Therefore, in a study of the Faraday effect (FE) in $TbAlO_3$, along with the ''paramagnetic'' mechanism of Faraday rotation (the C term of the Faraday effect[3,4]) due to differences in the population of the lower Stark sublevels of the ground multiplet (and, consequently, proportional to the mean magnetic moment of the ion), it is necessary to take into account the contribution of the mechanism of ''mixing'' the ground state and the excited states of the magnetically active ion (the B term of the Faraday effect[3,4]) to the resulting Faraday effect. However, a correct comparison of the contributions of the different mechanisms of magneto-optical activity (MOA) requires detailed information about the energy spectrum and the symmetry of the wave functions of the electronic states of the rare-earth ion Tb^{3+} in the ortho-aluminate structure. Therefore, in the given case, a study of polarization-optical, magnetic, and magneto-optical phenomena sensitive to peculiarities of the electronic structure of the rare-earth ions in low-symmetry crystals acquires great importance.

The present paper investigates the magnetic susceptibility χ, the Faraday effect, and the absorption and luminescence spectra in single-crystal samples of $TbAlO_3$ grown from a solution–melt. The magnetic susceptibility χ was measured on a vibration-reed magnetometer in the temperature interval 80–300 K along the [110] and [001] (c axis) crystallographic directions of the rhombic $TbAlO_3$ crystal. The absorption and luminescence spectra were measured in linearly polarized light in the region of the $^7F_6 \rightarrow {}^5D_4$ absorption band (20 000–20 700 cm^{-1}) at $T = 77$ and 300 K with spectral resolution not less than 1–2 cm^{-1} in a study of the optical absorption and 10–15 cm^{-1} for the secondary luminescence spectra. In the polarization-optical experiments, light was made to propagate in the [010] (b axis) and [001] (c axis) directions of the $TbAlO_3$ crystal. The Faraday rotation was calculated from the temperature and spectral dependence of the rotation angles of the major axis of the polarization ellipse of the light, Θ, measured for remagnetization along the [110] axis of the magnetically active crystal in the wavelength range 440–750 nm and temperature interval 90–300 K. In all the experiments the measurement errors of the magnetic susceptibility χ did not exceed $\sim 2-3\%$, and of the Faraday rotation angles, $\sim 5-7\%$. The positioning of the crystal axes was within $\sim 2-3\%$.

1. EXPERIMENTAL RESULTS AND DISCUSSION

1.1. Susceptibility of $TbAlO_3$

Figure 1 shows the temperature dependence of the inverse magnetic susceptibility of $TbAlO_3$ for the crystallographic directions [110] and [001], and also the results of magnetic measurements from Ref. 2 for comparison. It is clear from Fig. 1 that the temperature dependence of $\chi_{[110]}$ agrees with the data from Ref. 2 quite closely (within the limits of measurement error) while the correspondence of the susceptibility χ_c with the data is of a more qualitative character in the investigated temperature interval.

The maximum magnetic susceptibility of $TbAlO_3$ at low temperatures ($T \leqslant 100$ K) is observed in the ab plane while the susceptibility along the c axis (χ_c) is much less than

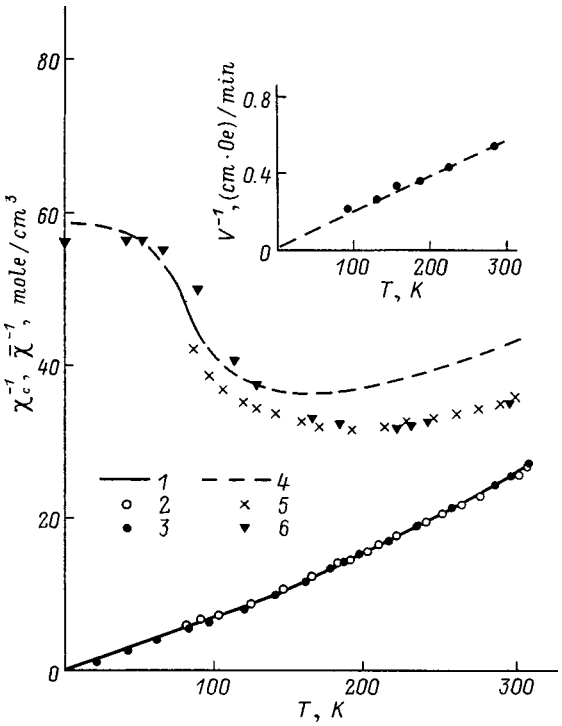

FIG. 1. Temperature dependence of the inverse magnetic susceptibility $1/\chi$, measured along the [110] and [001] axes of the rhombic crystal $TbAlO_3$: *1* — $\chi^{-1}_{[110]}$ calculated using formula (3); *2* — experimental values of $\chi^{-1}_{[110]}$ from the present work; *3* — $\bar{\chi}^{-1}$, where $\bar{\chi}=\frac{\chi_a+\chi_b}{2}$ (χ_a and χ_b are values of χ along the *a* and *b* axes according to the data of Ref. 2; *4* — χ_c^{-1} calculated using formula (2); *5, 6* — experimental values of χ_c^{-1} from the present work and Ref. 2, respectively. The inset shows a plot of the inverse Verde constant $1/V$ as a function of temperature *T*. The Verde constant *V* was determined at the wavelength $\lambda = 506$ nm for the crystallographic direction [110].

$\chi_{[110]}$ and tends to a constant limit as the temperature is lowered, indicative of its van Vleck origin (according to the data of Ref. 2). On the other hand, despite the abrupt decrease in the susceptibility $\chi_{[110]}$ with increasing temperature, the anisotropic character of the magnetic susceptibility of $TbAlO_3$ is preserved in the high-temperature region (Fig. 1). As was established in Ref. 1, such behavior of the magnetic susceptibility of $TbAlO_3$ (especially at low temperatures[2,5]) clearly indicates that the ground state of the Tb^{3+} ion in the crystal field is a quasi-doublet, formed by two close-lying Stark singlets (the magnitude of the ''gap'' is $\leqslant 10\,\mathrm{cm}^{-1}$), whose wave functions belong to different irreducible representations of the point group C_S (A and B).[1] Therefore, the Tb^{3+} ion in $TbAlO_3$ at low temperatures is treated as an ''Ising'' ion with its ''Ising'' axis being the anisotropy axis lying in the ab plane at an angle $\alpha \approx \pm 36°$ to the *a* axis of the crystal (the $\pm$ signs belong to two crystallographically nonequivalent sites differing in the orientation of the local axes). In this temperature range the susceptibility of $TbAlO_3$, measured along the [110] axis, can be represented according to Ref. 2 as

$$\chi_{[110]}=\frac{1}{2}(\chi_0^{(0)}+\chi_{V-V}^{(0)})=\frac{1}{2}\frac{N\mu_B^2}{k}\left[\frac{81}{T+\Theta_p}+\frac{13.5k}{\Delta_1}\right], \quad (1)$$

where N is the number of rare-earth ions; μ_B is the Bohr magneton; k is the Boltzmann constant; $\Theta_p \approx 5$ K is the paramagnetic Curie temperature due to the $R^{3+}-R^{3+}$ interaction; $\Delta_1 \approx 200\,\mathrm{cm}^{-1}$ is the energy interval between the ''mixing'' states of the rare-earth ion Tb^{3+} (Ref. 2). In formula (1) the contribution $\chi_0^{(0)}$ is the susceptibility along the ''Ising'' axis (the longitudinal susceptibility), corresponding to a magnetic moment parallel to the anisotropy axis: $\mu_0 \approx 9\mu_B$ (Ref. 2), and the term $\chi_{V-V}^{(0)}$ is the van Vleck contribution at low T.[1)] If we choose the ''Ising'' axis as the *z* axis of the local coordinate system of the rare-earth ion (located at one of the nonequivalent sites) and the *y* axis to be parallel to the *c* axis of the crystal, then the wave functions of the ground quasi-doublet corresponding to the maximum magnetic moment of the Tb^{3+} ion ($\mu_0 \approx 9\mu_B$) are written in the local-coordinate system as

$$|A\rangle=\frac{1}{\sqrt{2}}(|6,+6\rangle+|6,-6\rangle),$$

$$|B\rangle=\frac{1}{\sqrt{2}}(|6,+6\rangle-|6,-6\rangle).$$

At the same time, the magnitude of the van Vleck correction to the magnetic moment of the Tb^{3+} ion at low T is not hard to explain, assuming that ''pure'' $|J, \pm M_J\rangle$ states of the type $|6, \pm 5\rangle$ are represented in the expansion of the wave function of the first excited state (''admixed'' with the ground state) with significant weight (~ 1). In expression (1) the factor 1/2 appears in the summation (and subsequent averaging) over nonequivalent sites of the rare-earth ions in the ortho-aluminate structure, and the superscript (0) denotes that that quantity belongs to the ground state. As the temperature is raised, the behavior of the magnetic properties of $TbAlO_3$ become significantly more complicated and, in addition to the above-mentioned anisotropy in χ, the inverse magnetic susceptibilities begin to depend nonlinearly on T (Fig. 1). In this case, their temperature dependence can be explained by the significant contribution of the first excited state located at the energy $\sim 200\,\mathrm{cm}^{-1}$ in the spectrum of the $^7F_6$ ground multiplet of the Tb^{3+} ion in $TbAlO_3$ which becomes thermally populated as the temperature T is increased. We believe that this state is a quasidoublet, formed by excited Stark singlets whose wave functions transform according to two homotypic irreducible representations of the group C_S (A' and A'') and can be written (in the local coordinate system of the rare-earth ion) as

$$|A'\rangle \simeq \frac{1}{\sqrt{2}}(e^{-i\Psi_1}|6,+5\rangle-e^{i\Psi_1}|6,-5\rangle),$$

$$|A''\rangle \simeq -\frac{i}{\sqrt{2}}(e^{-i\Psi_2}|6,+4\rangle-e^{i\Psi_2}|6,-4\rangle),$$

where $e^{i\Psi_1}$ and $e^{i\Psi_2}$ are phase factors satisfying the condition $(\Psi_1+\Psi_2)\approx\pi/2$. Such an excited state leads to the result that the magnetic moment associated with it, μ_1, is directed along the *y* axis (*c* axis) of the local coordinate system of the ion and exhibiting ''Ising-like'' behavior. Its magni-

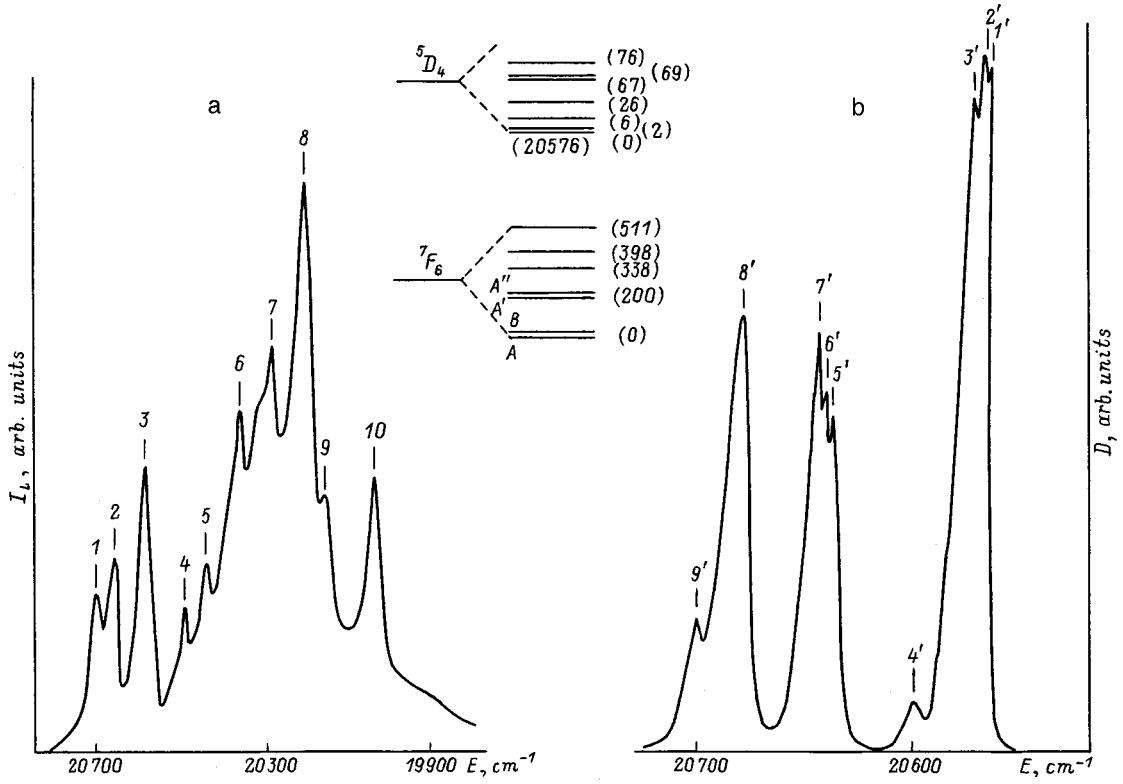

FIG. 2. Luminescence (a) and absorption (b) spectra of $TbAlO_3$, measured at $T=300$ K (a) and 78 K (b) in polarized light ($\mathbf{E}\|a$, where $\mathbf{E}$ is the electric field vector of the light wave). a — Along the c axis, b — along the b axis of the crystal. The transition energies are indicated in the table. The inset depicts the structure of the ground $^7F_6$ and excited $^5D_4$ multiplets of the Tb^{3+} ion in $TbAlO_3$. The numbers in parentheses are the energies of the Stark sublevels (in cm^{-1}).

tude is close to the maximum possible value and is $\approx 7\mu_B$. Therefore, if the external field H is along the c axis of the crystal, then both ''mixing'' of the wave functions of the states of the ground quasi-doublet (A,B) and first excited quasi-doublet (A',A'') and splitting in the field H of the sublevels of the (A',A'') quasi-doublet occurs. (These sublevels become increasingly populated as the temperature is raised.) Consequently, an expression for the transverse susceptibility χ_c valid at high temperatures has the form

$$\chi_c=\frac{N\mu_B^2}{k}\left[\frac{13.5k}{\Delta_1}(\rho_0-\rho_1)+\frac{49.5}{T}\rho_1\right], \tag{2}$$

where ρ_0 and ρ_1 are the Boltzmann populations of the states of the ground quasi-doublet and first excited quasi-doublet. At the same time, the magnetic susceptibility $\chi_{[110]}$ of $TbAlO_3$ over a wide range of temperatures ($T\geqslant 100$ K) is given by a relation similar in form to Eq. (1)

$$\chi_{[110]}=\frac{1}{2}N\mu_B^2k\left[\frac{81}{T+\Theta_p}\rho_0+\frac{13.5k}{\Delta_1}(\rho_0-\rho_1)\right]$$
$$=\frac{1}{2}(\chi_0+\chi_{V-V}), \tag{3}$$

where the contribution of the first excited quasi-doublet (A',A'') can be neglected since its ''Ising'' magnetic moment is aligned with the c axis and the states of the quasi-doublet (A',A'') do not split in an external field H lying in the symmetry plane of the crystal field—the ab plane of the crystal. Results of calculations of the temperature dependence of $\chi_{[110]}$ obtained using Eq. (3) are plotted in Fig. 1, from which it is clear that the experimental and theoretical values of the magnetic susceptibility dependence $\chi_{[110]}$ in the investigated temperature interval 80–300 K are in good agreement (within experimental error $\sim 2-3\%$). It is entirely possible that some quantitative differences in the theoretically calculated values [according to Eq. (2)] and the values measured in this work (and in Ref. 2) of the van Vleck (transverse) susceptibility χ_c in the temperature range $T>100$ K may be due to the circumstance that we neglected in deriving Eq. (2) the interaction of the states of the first excited quasi-doublet ($\sim 200\,cm^{-1}$) with the higher-lying Stark sublevels of the ground multiplet of the Tb^{3+} ion. The nature of the crystal-field induced Stark splitting of the lower sublevels of the $^7F_6$ ground multiplet of Tb^{3+} is unambiguously confirmed by the polarization-optical data. Figure 2 depicts the luminescence spectrum of the rare-earth ion Tb^{3+} in $TbAlO_3$, recorded at $T=300$ K in linearly polarized light on the radiative $4f-4f$ transition $^5D_4\rightarrow{}^7F_6$ ($20\,000-20\,700\,cm^{-1}$). A detailed comparison of the energies of the characteristic features of the secondary luminescence spectrum (see Table I) makes it possible, on the one hand, to identify them with the optical transitions occurring between Stark sublevels of the ground and excited multiplets of the Tb^{3+} ion in the ortho-aluminate structure, and, on the other, to piece together (albeit partially) a picture of Stark

TABLE I. Transition energies in $TbAlO_3$.

Luminescence of $TbAlO_3$		Absorption of $TbAlO_3$	
band	transition energy, cm^{-1}	band	transition energy, cm^{-1}
1	20699	1′	20575
2	20658	2′	20578.5
3	20588	3′	20582
4	20500	4′	20601
5	20456	5′	20642
6	20374	6′	20646.4
7	20296	7′	20651
8	20236	8′	20686.4
9	20176	9′	20702.2
10	20063		

splitting of the $^7F_6$ ground multiplet in a crystal field with C_S symmetry (inset to Fig. 2). Indeed, a comparison of the band energies (-1, -2, -3 and respectively -4, -5, -6) shows that the level or group of levels closest to the ground state are offset from it by a distance $\approx 200\,cm^{-1}$. Comparison of the energies of other bands with each other (e.g., -1 and -10, etc.) makes it possible to determine uniquely the energies of the higher-lying Stark sublevels and to establish that the total magnitude of the crystal splitting of the $^7F_6$ ground multiplet in $TbAlO_3$ is $\sim 500\,cm^{-1}$ (see inset to Fig. 2). Moreover, the high degree of ''isolation'' of the sublevels of the ground state (quasi-doublet) from the higher-lying excited states of the $^7F_6$ multiplet ($\Delta_1 \approx 200\,cm^{-1}$) also enabled us to determine the nature of the Stark splitting of the $^5D_4$ excited multiplet of the $4f^8$ ground-state configuration of the Tb^{3+} ion in the ortho-aluminate structure from the spectroscopic data on the peak energies of the polarization optical absorption on the $^7F_6 \rightarrow {}^5D_4$ transition at $T = 78\,K$ (see Table I) (Fig. 2).

1.2. The Faraday effect in $TbAlO_3$

Rare-earth compounds having ortho-aluminate structure are biaxial crystals in the optical sense, and, in their study, the problem arises of investigating linear magneto-optical effects (the Faraday effect, etc.) against the ''background'' of a large natural birefringence ($\Delta_n \sim 10^{-2}$).[5,6] Therefore, the measured dependence of the rotation angle of the major axis of the polarization ellipse, Θ, in $TbAlO_3$ on the wavelength λ and the thickness of the crystal l (and also the temperature T, see Fig. 3[2)] has an oscillatory nature, where the amplitude of the oscillations is proportional to the Faraday rotation angle α_F, and their period, to the magnitude of the natural birefringence Δ_n (Refs. 6 and 7). Reconstructing the analogous dependences for the Faraday rotation angle from the temperature (Fig. 3) and spectral dependence of the angles Θ measured along the [110] axis (by a technique described in Ref. 5), it is not hard to find the Verde constant V of $TbAlO_3$. Analysis of the spectral dependence of the Verde constant V in $TbAlO_3$ shows that it is approximated with good accuracy by the frequency dependence $V \sim \omega^2/(\omega_0^2 - \omega^2)$, where ω is the light frequency, $\omega_0 = 99 \times 10^{14}\,s^{-1}$ is the ''effective'' frequency of the (spin and parity) allowed $4f-5d$ electrical-dipole transitions at the Tb^{3+} ions in the ortho-aluminate structure. At the same time, studies of the temperature dependence of the Faraday effect in $TbAlO_3$ along the [110] axis in the temperature interval 90–300 K led to an unexpected result. It follows from Fig. 1 that in contrast to the inverse susceptibility χ^{-1} the dependence of the inverse Verde constant $1/V$ on the temperature T at the wavelength $\lambda = 506\,nm$ is linear (within the limits of experimental error $\sim 7\%$). Together with the constancy of $V \cdot T$ in the investigated temperature interval, the above aspect of the behavior of the Faraday effect indicates that the Verde constant V to first order is inversely proportional to the temperature (see the inset to Fig. 3). Thus, the Verde constant $V_{[110]}$ of the rare-earth ortho-aluminate $TbAlO_3$ along [110] is proportional to the inverse temperature ($V \sim 1/T$), which differs considerably from the dependence ($V \sim \chi$) discovered in Ref. 5 in a study of the Faraday effect along the a axis of the $TbAlO_3$ crystal. Here the absence of a slope in the temperature dependence of $V \cdot T$ (Fig. 3) is apparently due to the obvious smallness of the contribution of the temperature-independent (or weakly temperature-dependent) mechanism of van Vleck ''mixing'' (the B term of the Faraday effect[3]) to the Faraday rotation of $TbAlO_3$ measured along the [110] axis.[3)] This may be due to the following reasons. As is well known,[8,9] the temperature-dependent contribution to the magneto-optical activity of the non-Kramers rare-earth ion (Tb^{3+}, Ho^{3+}, etc.), whose energy spectrum consists of completely degenerate Stark singlet sublevels, can arise only if

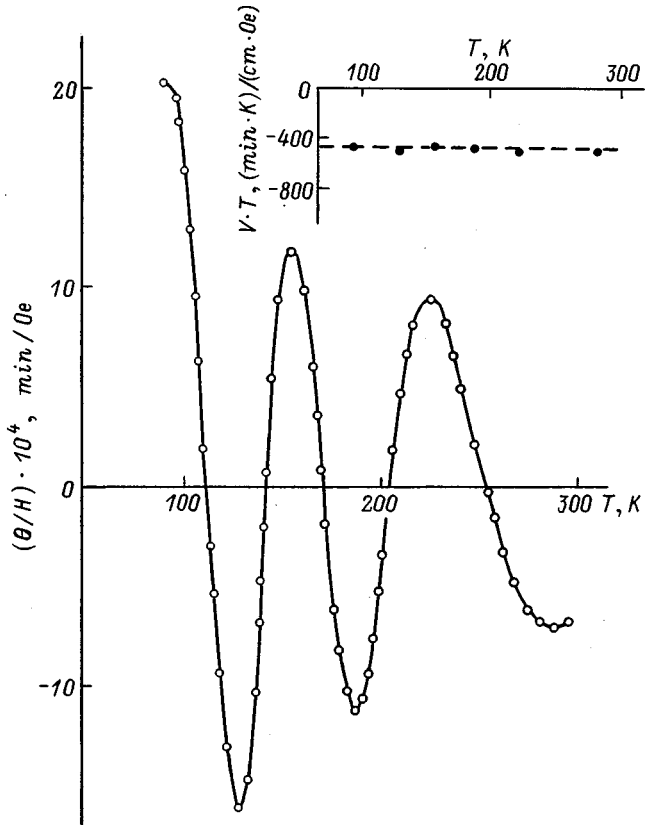

FIG. 3. Temperature dependence of the rotation angle of the major axis of the polarization ellipse Θ in $TbAlO_3$ at the wavelength $\lambda = 506\,nm$. The inset shows the $V \cdot T$ dependence on temperature at the wavelength $\lambda = 506\,nm$ for the [110] axis.

the effect of ''mixing'' in an external magnetic field H of close-lying singlets of the ground state—a quasi-doublet—is taken into account. In this case, the expression for the C term of the Faraday effect can be written as[8]

$$\alpha_F^C=\frac{2\pi N}{c\bar{n}\hbar}\left(\frac{\bar{n}^2+2}{3}\right)^2\omega^2 H\frac{1}{2}\sum_{a,b,j,r}\times\frac{\mathrm{Im}[\langle a^r|\hat{\mu}_z|b^r\rangle(\langle b^r|\hat{P}_x|j\rangle\langle j|\hat{P}_y|a^r\rangle-\langle b^r|\hat{P}_y|j\rangle\langle j|\hat{P}_x|a^r\rangle)]}{kT(\omega_{0j}^2-\omega^2)}, \tag{4}$$

where $r=1,2$ is the nonequivalent site index; $\hat{P}_x$ and $\hat{P}_y$ are the corresponding components of the dipole moment of the rare-earth ion located at the rth site; $\hat{\mu}_z$ is the magnetic moment z projection operator; $|a^r\rangle$ and $|b^r\rangle$ are the wave functions of the sublevels of the quasi-doublet, $|j\rangle$ is the wave function of the excited singlet at which the optical transition with frequency ω_{0j} takes place; $\bar{n}$ is the mean refractive index of the medium. In this approximation the expression for the temperature-independent B term of the Faraday effect due to ''admixture'' of the first excited state of the ground multiplet with the ground state (quasi-doublet) in an external field H is written, according to Ref. 10, as

$$\alpha_F^B=\frac{4\pi N}{c\bar{n}\hbar}\left(\frac{\bar{n}^2+2}{3}\right)^2\frac{\omega^2 H}{\Delta_1}\frac{1}{2}\sum_{a,b,j,r}\times\frac{\mathrm{Im}[\langle a^r|\hat{\mu}_y|d^r\rangle(\langle a^r|\hat{P}_x|j\rangle\langle j|\hat{P}_x|d^r\rangle-\langle a^r|\hat{P}_x|j\rangle\langle j|\hat{P}_z|d^r\rangle)]}{(\omega_{0j}^2-\omega^2)}, \tag{5}$$

where $|a^r\rangle$ and $|d^r\rangle$ are the wave functions of the ground state and excited state of the ground multiplet of the rare-earth ion; and $\hat{\mu}_y$ is the magnetic moment y projection operator. Neglecting level splitting (the Judd–Ofelt approximation) in the summation of Eqs. (4) and (5) over excited states $|j\rangle$ belonging to the mixed excited $4f^{n-1}5d$ configuration of the rare-earth ion, we average the obtained expressions over crystallographically nonequivalent sites of the ion in the ortho-aluminate structure. Within the framework of such a model it is not hard to convince oneself that the Verde constants V in a rare-earth ortho-aluminate along the a, b, and c axes are proportional to the corresponding magnetic susceptibilities. Indeed, calculation of the Verde constant V_a (along the a axis) in $TbAlO_3$ shows that over a wide temperature interval it can be written as

$$V_a=\left(\frac{2-g_0}{g_0}\right)A\,\chi_a\frac{\omega^2}{\omega_0^2-\omega^2}, \tag{6}$$

where $\chi_a=(\chi_0\cos^2\alpha_0+\chi_{V-V}\sin^2\alpha_0)$ is the magnetic susceptibility of $TbAlO_3$ along the a axis [see also formula (3)]; A is a constant proportional to the oscillator strength f of the allowed optical transition with mean frequency ω_0. However, for the external field H aligned with the [110] axis for the Tb^{3+} ions located in one of the nonequivalent sites in the ortho-aluminate structure, the local z axis (and for the other site the x axis) almost coincides in direction with the direction of propagation of the transverse light wave: $\mathbf{k}\|\mathbf{H}$, where $\mathbf{k}$ is the wave vector of the light. In this case, the z component of the dipole moment of the ion and the matrix elements associated with it $\langle a|\hat{P}_z|j\rangle$ (and $\langle j|\hat{P}_z|d\rangle$) in Eq. (5) will be close to zero, as a consequence of which the temperature dependence of the Verde constant $V_{[110]}$ in $TbAlO_3$ will be determined only by the longitudinal susceptibility χ_0. As can be seen from expression (3), the term χ_0, generally speaking, is proportional to the inverse temperature $1/T$ in the temperature interval 90–300 K, which agrees at least qualitatively with the results of magneto-optical experiments presented in Figs. 1 and 3.

*)E-mail: valiev@phys.silk.org

1)The choice of the [110] axis in our measurements was dictated by the fact that when the magnetic field H is applied in this direction the rare-earth ions Tb^{3+} found in one of the groups of nonequivalent sites become magnetized in the approximation linear in the field since their ''Ising'' axes are almost parallel to the [110] axis. For Tb^{3+} ions found in the other group of nonequivalent sites, this does not happen, since their ''Ising'' axes are almost perpendicular to the H field (and the [110] axis) and their contribution to the magnetic moment is the van Vleck correction to it.

2)In the case when birefringence in the crystal depends on the temperature. The natural birefringence Δ_n at the wavelength $\lambda\approx 500$ nm is equal to 1.8×10^{-2} at $T=300$ K.

3)The absence of a slope in the dependence of $V\cdot T$ also points to the negligibly small contribution to the Faraday effect of the ''diamagnetic'' (the A term of the Faraday effect[3]) of the MOA mechanism due to splitting of the excited states of the rare-earth ions Tb^{3+} in $TbAlO_3$ in an external field H (see also Ref. 5).

[1] A. K. Zvezdin, V. M. Matveev, A. A. Mukhin, and A. I. Popov, *Rare-Earth Ions in Magnetically Ordered Crystals* (Nauka, Moscow, 1985).
[2] L. Holmes, R. Sherwood, and L. G. Van Vitert, J. Appl. Phys. **39**, 1373 (1968).
[3] A. D. Buckingham and P. J. Stephens, Ann. Phys. Chem. **17**, 399 (1966).
[4] U. V. Valiev, A. I. Popov, and B. Yu. Sokolov, Opt. Spektrosk. **61**, 1156 (1986) [Opt. Spectrosc. **61**, 714 (1986)].
[5] U. V. Valiev, A. A. Klochkov, M. M. Lukina, and M. M. Turganov, Opt. Spektrosk. **63**, 543 (1987) [Opt. Spectrosc. **63**, 319 (1987)].
[6] R. V. Pisarev, in *Physics of Magnetic Insulators*, edited by G. A. Smolenskiĭ (Nauka, Leningrad, 1974), p. 356.
[7] M. V. Chetkin and Yu. I. Shcherbakov, Fiz. Tverd. Tela (Leningrad) **11**, 1620 (1969) [Sov. Phys. Solid State **11**, 1314 (1969)].
[8] P. J. Stephens, Adv. Chem. Phys. **35**, 197 (1976).
[9] U. V. Valiev, B. Yu. Sokolov, and Zh. Sh. Siranov, Opt. Spektrosk. **84**, 477 (1998) [Opt. Spectrosc. **84**, 418 (1998)].
[10] P. N. Schatz and A. D. MacCaffrey, Usp. Khim. **40**, 1698 (1971).

Translated by Paul F. Schippnick

X-ray studies of magnetic phase transitions in the intermetallic compounds RMn_2Ge_2 (R=La, Sm, Gd, Nd, Tb, and Y)

I. Yu. Gaĭdukova, Gou Guanghua, S. A. Granovskiĭ, I. S. Dubenko, R. Z. Levitin, A. S. Markosyan, and V. E. Rodimin

M. V. Lomonosov Moscow State University, 119899 Moscow, Russia
(Submitted in final form May 14, 1999)
Fiz. Tverd. Tela (St. Petersburg) **41**, 2053–2058 (November 1999)

The lattice parameters *a* and *c* of the tetragonal intermetallic compounds RMn_2Ge_2 (R=La, Sm, Gd, Nd, Tb, and Y) have been measured by x-ray diffraction in the temperature interval 10–800 K. Anomalies are observed in the temperature dependence of *a* and *c* due to phase transitions from the paramagnetic to the magnetically ordered state in the Mn subsystem, transitions between various magnetically ordered phases due to a change in the magnitude and sign of the Mn–Mn exchange interaction, and magnetic transitions caused by ordering of the rare-earth subsystem leading to a rearrangement of the magnetic structure of the Mn subsystem. It is concluded that, along with the lattice parameter *a*, the lattice parameter *c* also has an influence on the Mn–Mn exchange interaction. © *1999 American Institute of Physics.* [S1063-7834(99)02911-1]

Ternary intermetallic compounds with the formula RMn_2Ge_2 (R is a rare earth or yttrium) have tetragonal crystal structures of the type $ThCr_2Si_2$ (space group $I4/mmm$). An important feature of this structure type is the fact that it consists of alternating layers of rare earth, manganese, and germanium perpendicular to the tetragonal axis. From the magnetic point of view, intermetallics with the formula RMn_2Ge_2 contain two different subsystems, one of which is formed by the rare earth and the other by manganese. As numerous studies have shown (e.g., the review in Ref. 1), the largest interaction in these compounds is the intraplanar manganese–manganese exchange interaction, which determines the magnetic ordering temperature of these compounds (300–400 K). The interplanar exchange between neighboring manganese planes is one order of magnitude weaker; and the exchange interaction between a manganese plane and a rare-earth plane is of roughly the same magnitude. The rare earth–rare earth exchange interaction is one more order of magnitude weaker. It is important that the magnitude of the manganese–manganese interplanar exchange depends strongly on the interatomic distances (mainly on the manganese–manganese distance within a layer) and as the lattice parameter *a* is decreased changes sign from positive to negative at some critical value of the lattice parameter $a_{cr} \approx 4.045$ Å (Ref. 1).

The indicated aspects of the exchange interactions lead to the result that various spontaneous phase transitions are observed in the intermetallics RMn_2Ge_2 in the magnetically-ordered region,[1] which can be divided roughly into three different types.

One of these is connected to the transition of the manganese subsystem from a ferromagnetic to an antiferromagnetic state as the temperature is decreased, due to the change of sign of the manganese–manganese exchange interaction when the lattice parameter becomes equal to its critical value a_{cr}. Such transitions have been observed in $SmMn_2Ge_2$ and also in some mixed rare-earth compounds.[2–6]

The second type of transition is connected to a change in the state of the manganese subsystem from antiferromagnetic to ferromagnetic at low temperatures (<100 K), as a consequence of magnetic ordering of the rare-earth subsystem, and is due to the rare earth–manganese exchange interaction. Below the temperature of this transition, the resulting magnetic structure is completely ferromagnetic for light rare earths and ferrimagnetic for heavy rare earths. Such transitions were observed in compounds with Sm, Gd, Dy, Tb, and Ho, and also in a number of substituted rare-earth intermetallic compounds.[2,6–8]

Recent neutron-scattering studies have shown that in intermetallics with light rare earths, whose manganese subsystem is ferromagnetic at room temperature and below, as the temperature is raised, a transition is observed to an antiferromagnetic phase. Such transitions were observed in compounds with La, Pr, Nd, and Sm.[9–11] These same studies established that, in intermetallics with light rare earths, various types of noncollinear and, in a number of cases long-period magnetic structures are stabilized, and two different types of antiferromagnetism (collinear or noncollinear) arise in some compounds in the manganese subsystem (earlier it was assumed that each manganese plane has a ferromagnetic structure).

The nature of the third type of phase transitions is still not clear. Their study is hindered by the fact that they are sometimes not manifested or are only weakly manifested in the susceptibility and magnetization measurements and one can judge their presence in a number of cases only from neutron-scattering data.

The present study makes an attempt to detect various spontaneous magnetic transitions in some RMn_2Ge_2 com-

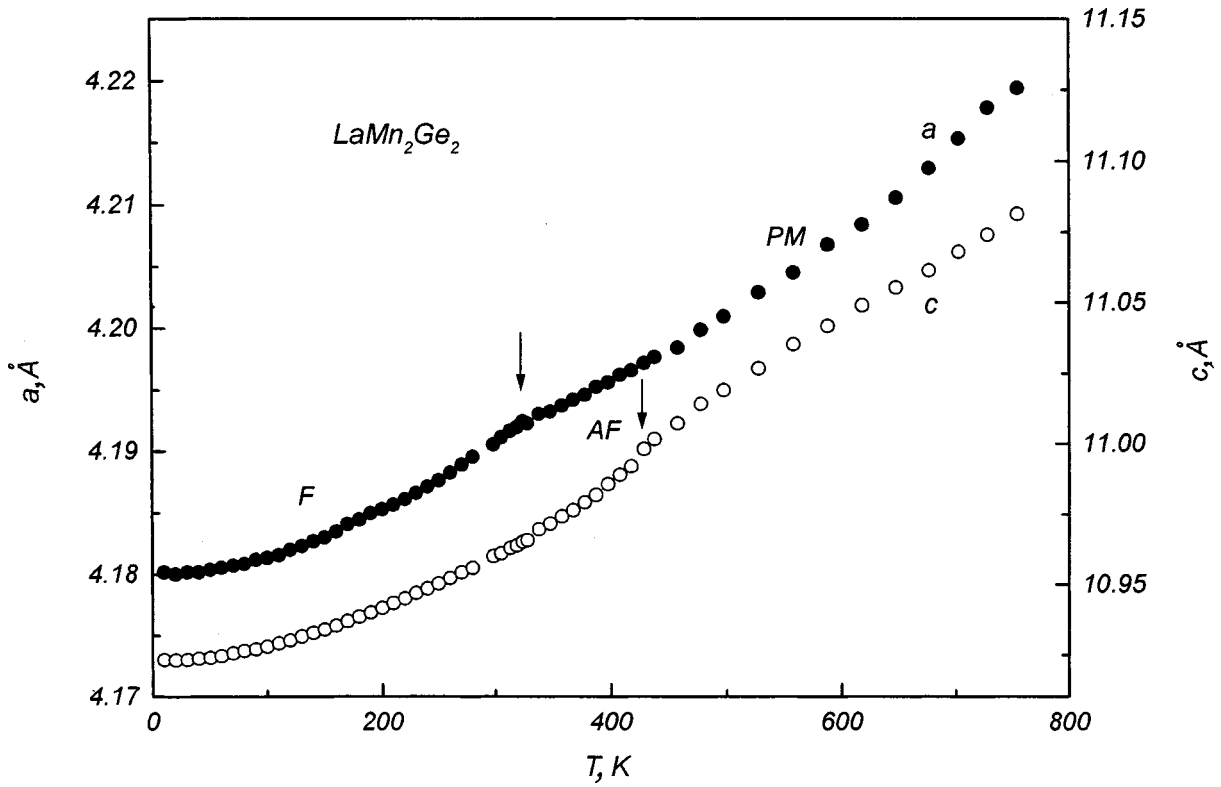

FIG. 1. Temperature dependence of the crystal-structure parameters of $LaMn_2Ge_2$. The arrows indicate the temperatures of different types of magnetic phase transitions. PM, AF, and F denote respectively the paramagnetic, antiferromagnetic, and ferromagnetic phases of the manganese subsystem.

pounds from measurements of the temperature dependence of their lattice parameters.

Intermetallics of the type RMn_2Ge_2 were synthesized in an induction furnace under quasilevitation conditions from their elements. The single-phase character of the samples was monitored by x-ray measurements. Measurements of the lattice parameter in the temperature interval 10–800 K were performed on powder samples on a Geigerflex x-ray diffractometer using Fe $K\alpha$ radiation. The lattice parameters were determined from the (008) and (220) reflections.

$LaMn_2Ge_2$. According to magnetic measurements[12] the manganese subsystem is ordered ferromagnetically below the Curie temperature $T_C = 310$ K. However, recent neutron-scattering studies[10] have revealed that T_C is the temperature of a magnetic transition from a ferromagnetic to an antiferromagnetic phase, and a transition to the paramagnetic state takes place at a higher temperature $T_N = 413$ K. Our measurements confirmed these results. As can be seen from Fig. 1, two anomalies are observed in the temperature dependence of the lattice parameters of $LaMn_2Ge_2$ at temperatures close to T_C and T_N. Note that both magnetoelastic anomalies are negative; however, the parameter c undergoes an anomaly at the point T_N, and the parameter a undergoes an anomaly at the point T_c.

$SmMn_2Ge_2$. According to numerous studies, the manganese subsystem transforms to a ferromagnetic state below $T_c \approx 340$ K (Ref. 1). Recently, on the basis of magnetic susceptibility measurements, the authors of Ref. 11 concluded that $SmMn_2Ge_2$ is found in the antiferromagnetic state above T_c while the transition to a paramagnetic phase occurs at $T_N = 389$ K. When the sample is cooled below $T_{t1} \approx 150$ K, the manganese subsystem undergoes a transition from a ferromagnetic to an antiferromagnetic state due to the change in sign of the exchange interaction caused by thermal expansion (the samarium subsystem remains in the paramagnetic state). Finally, at $T_{t2} \approx 100$ K, the manganese subsystem experiences a reverse (re-entrant) transition to the ferromagnetic state; simultaneously the samarium subsystem orders ferromagnetically.[2–4] The re-entrant transition is due to the samarium–manganese exchange interaction.

Figure 2 shows the temperature dependence of the lattice parameters of $SmMn_2Ge_2$. It can be seen that the ferromagnetic–antiferromagnetic transition at the temperature T_{t1} is accompanied by a jumplike decrease in the lattice parameter a, while the re-entrant transition at the point T_{t2} is accompanied by a jumplike increase. These data are in good agreement with the results of Refs. 2–4 and confirm that the ferromagnetic–antiferromagnetic transition is connected to the temperature dependence of the lattice parameter a. Two additional lattice parameter anomalies are observed at higher temperatures: the parameter a undergoes an anomaly at $T_C \approx 310$ K. This anomaly can be linked to the transition of the manganese subsystem from the ferromagnetic to the antiferromagnetic state (although it is somewhat lower than the temperature T_C based on magnetic measurements[1]). The second anomaly is observed in the temperature dependence of the parameter c at $T_N \approx 383$ K. This temperature is in good agreement with the temperature of the transition from the antiferromagnetic to the paramagnetic state obtained in Ref.

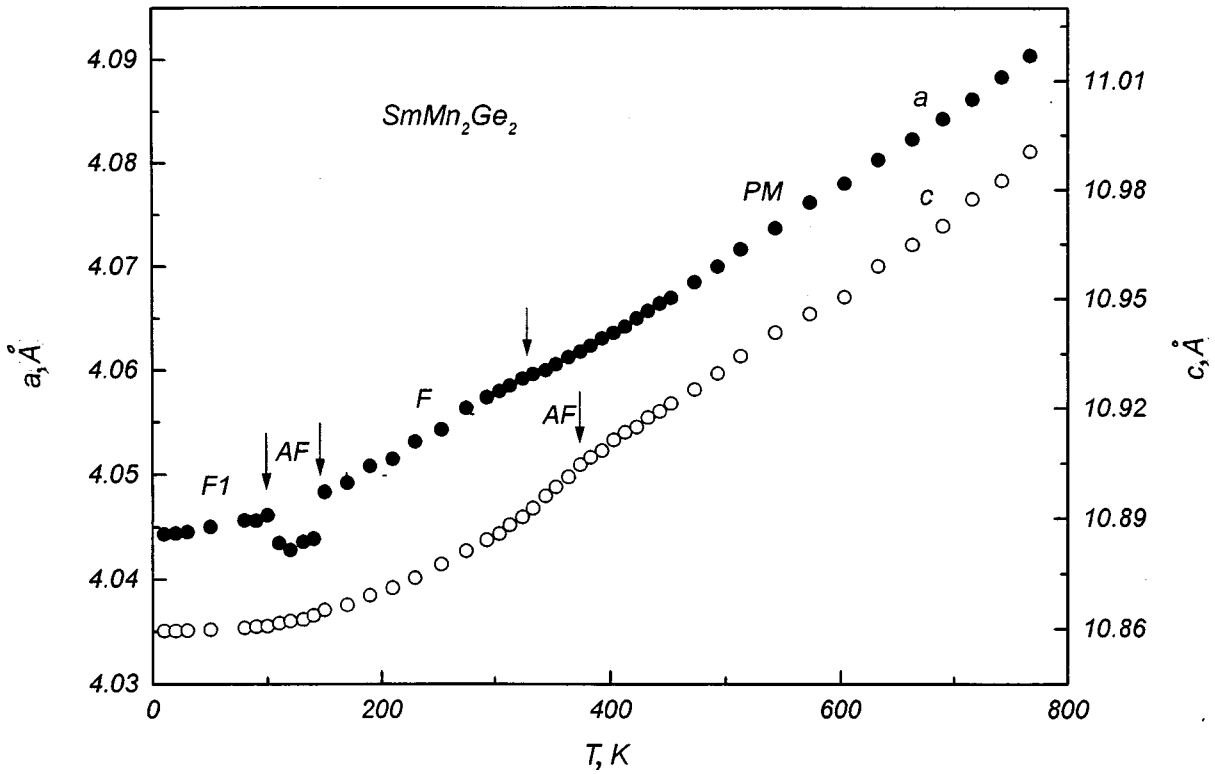

FIG. 2. Temperature dependence of the crystal-structure parameters of $SmMn_2Ge_2$. F1 denotes the region of ferromagnetic ordering of the samarium and manganese subsystems. The remaining notation is the same as in Fig. 1.

11. Unfortunately, neutron-scattering studies of $SmMn_2Ge_2$ have not been performed above 300 K; however, in $(Nd,Sm)Mn_2Si_2$, in which the the lattice parameters are similar to those of $SmMn_2Ge_2$, analogous magnetic properties were also observed, and the high-temperature antiferromagnetic–ferromagnetic transition was observed in the neutron-scattering measurements.[13]

$NdMn_2Ge_2$. In this intermetallic compound several spontaneous magnetic transitions are observed.[9,11,12] Below $T_N = 418$ K only the manganese subsystem orders, and, when the system is cooled to 330–336 K, this subsystem transforms to the ferromagnetic state as the magnetic moments become collinear to the tetragonal axis. In the temperature interval 215–250 K the manganese moments reorient into the tetragonal plane. Ferromagnetic ordering of the neodymium subsystem takes place below 40–100 K. It follows from our experiments that transitions of the manganese subsystem from the paramagnetic to the antiferromagnetic state and from the antiferromagnetic to the ferromagnetic state are accompanied by negative magnetoelastic anomalies in the lattice parameters c and a, respectively; however, magnetoelastic anomalies are not observed in the spin reorientation and ordering of the neodymium subsystem (Fig. 3).

YMn_2Ge_2. According to the results of neutron scattering[11] and magnetic[14] studies, this compound orders antiferromagnetically below 427 K (Ref. 11), 437 K (Ref. 14). No other magnetic transitions in this compound were observed. Our measurements showed that the transition to the antiferromagnetic state in YMn_2Ge_2 is accompanied by a negative magnetoelastic anomaly of the lattice parameter a (Fig. 4). Note that the value of the Néel temperature we obtained ($\sim$440 K) is in better agreement with the magnetic measurement data.

$GdMn_2Ge_2$. According to literature data,[15] the manganese subsystem in this intermetallic compound orders antiferromagnetically below $T_N \approx 365$ K, while at the temperature $T_t \approx 95$ K, the manganese subsystem undergoes a transition to a ferromagnetic state with simultaneous ferromagnetic ordering of the gadolinium subsystem so that a ferrimagnetic structure results. However, magnetization studies of single-crystal $GdMn_2Ge_2$ show that an anomalous behavior of the magnetization in weak fields is observed above T_N and below $T_{N1} \approx 480$ K. Our magnetization measurements also confirmed the existence of such an anomaly, which may be due to the second high-temperature antiferromagnetic phase. In this temperature region, a very small anomaly is also observed in the temperature dependence of the lattice parameter a of $GdMn_2Ge_2$ (it is indicated by the arrow with a question mark in Fig. 5). However, its magnitude lies near the resolution limit of our x-ray measurements and, consequently, these measurements do not allow us to confirm (or reject) the existence of a high-temperature antiferromagnetic phase in this intermetallic compound.

The first noticeable anomaly in the temperature dependence of the lattice parameter $a(T)$ in $GdMn_2Ge_2$ is observed at the temperature $T_N = 365$ K. At low temperatures, at the point $T_t \approx 95$ K, there is a jumplike change in the lattice parameter a associated with a transition from the antiferromagnetic to the ferromagnetic state in the manganese

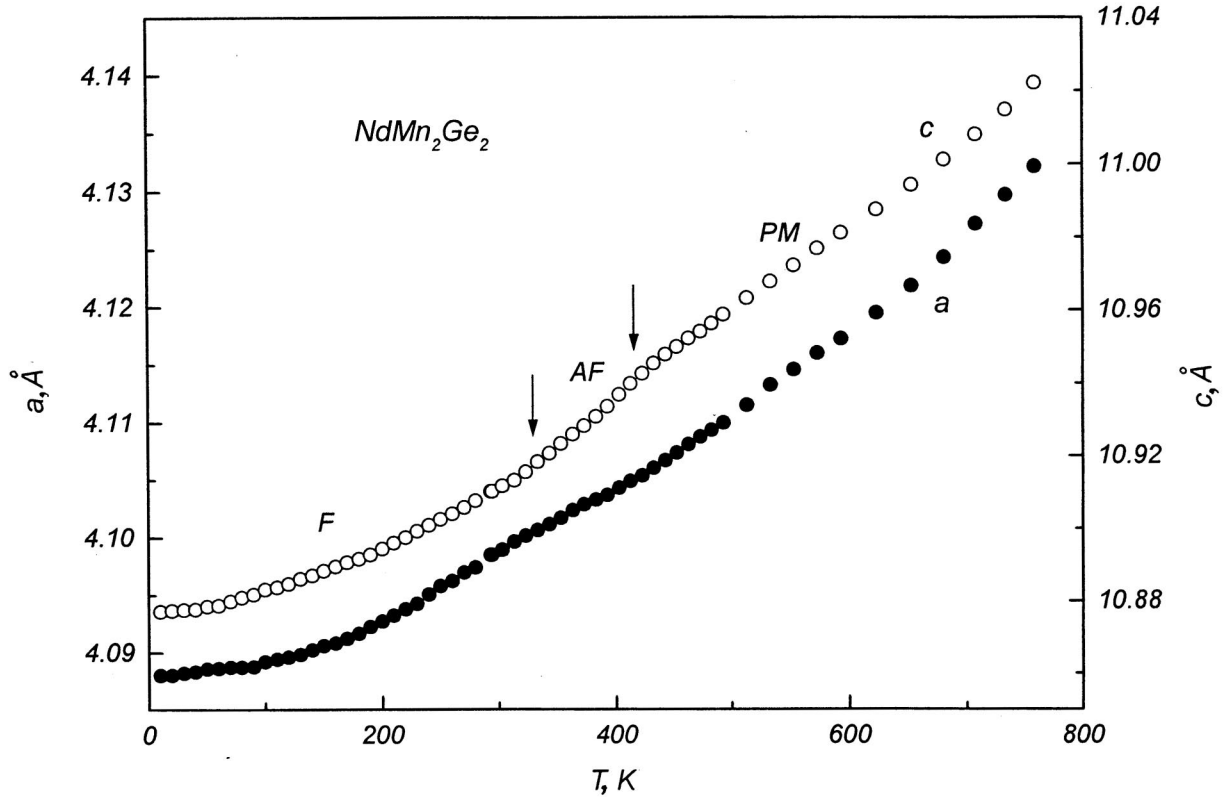

FIG. 3. Temperature dependence of the crystal-structure parameters of $NdMn_2Ge_2$. Notation the same as in Fig. 1.

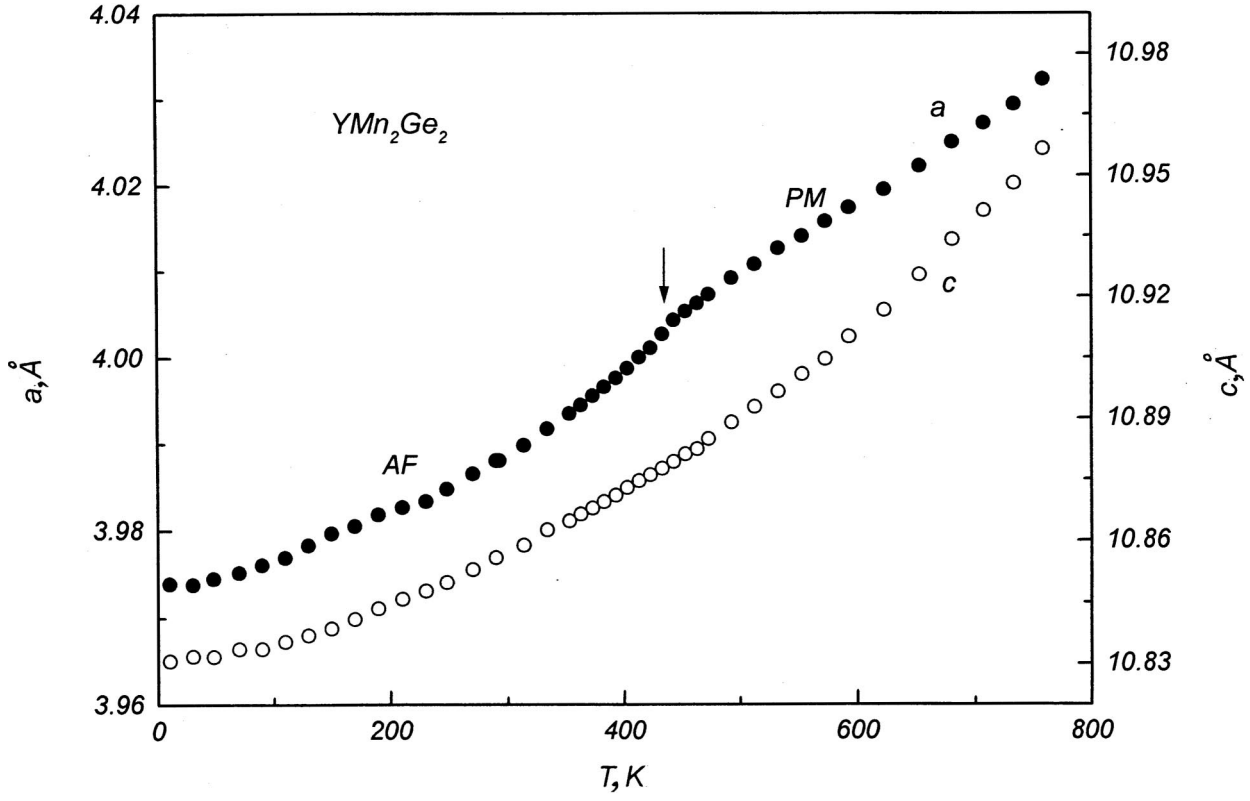

FIG. 4. Temperature dependence of the crystal-structure parameters of YMn_2Ge_2. Notation the same as in Fig. 1.

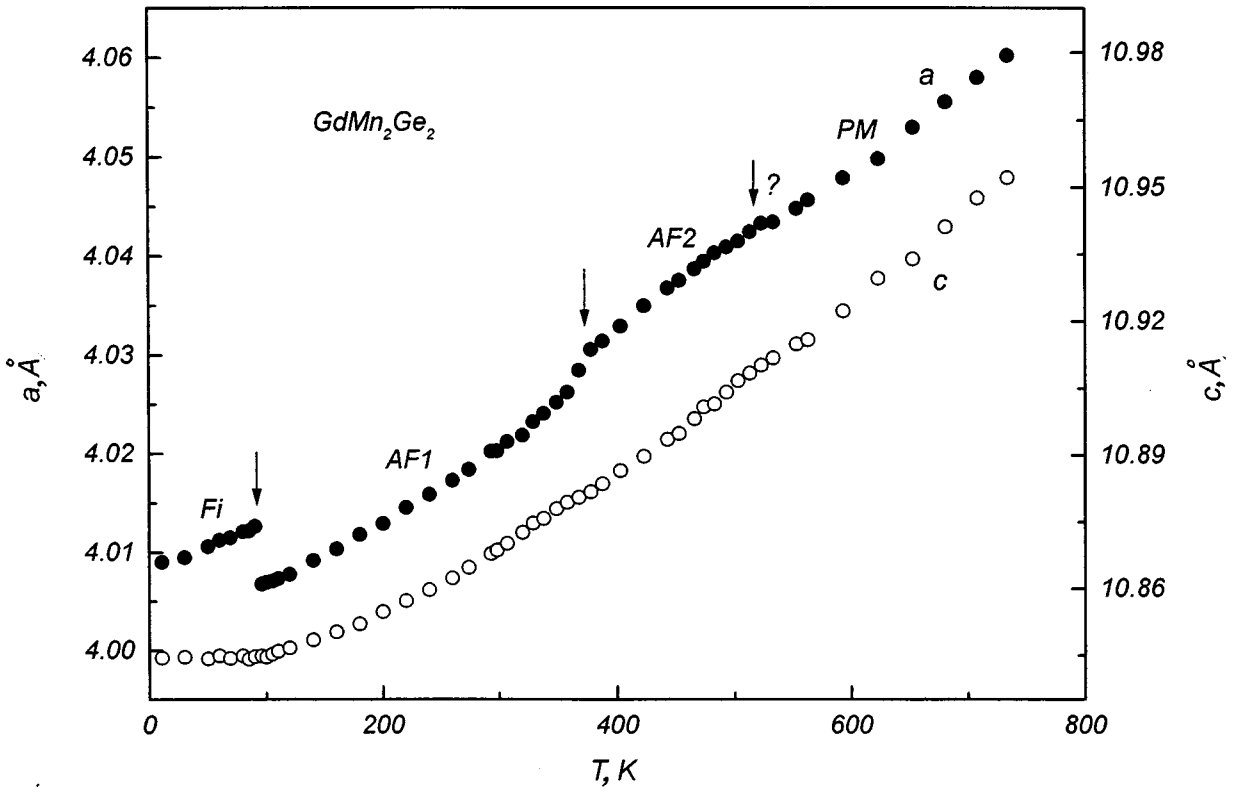

FIG. 5. Temperature dependence of the crystal-structure parameters of $GdMn_2Ge_2$. Notation the same as in Fig. 1.

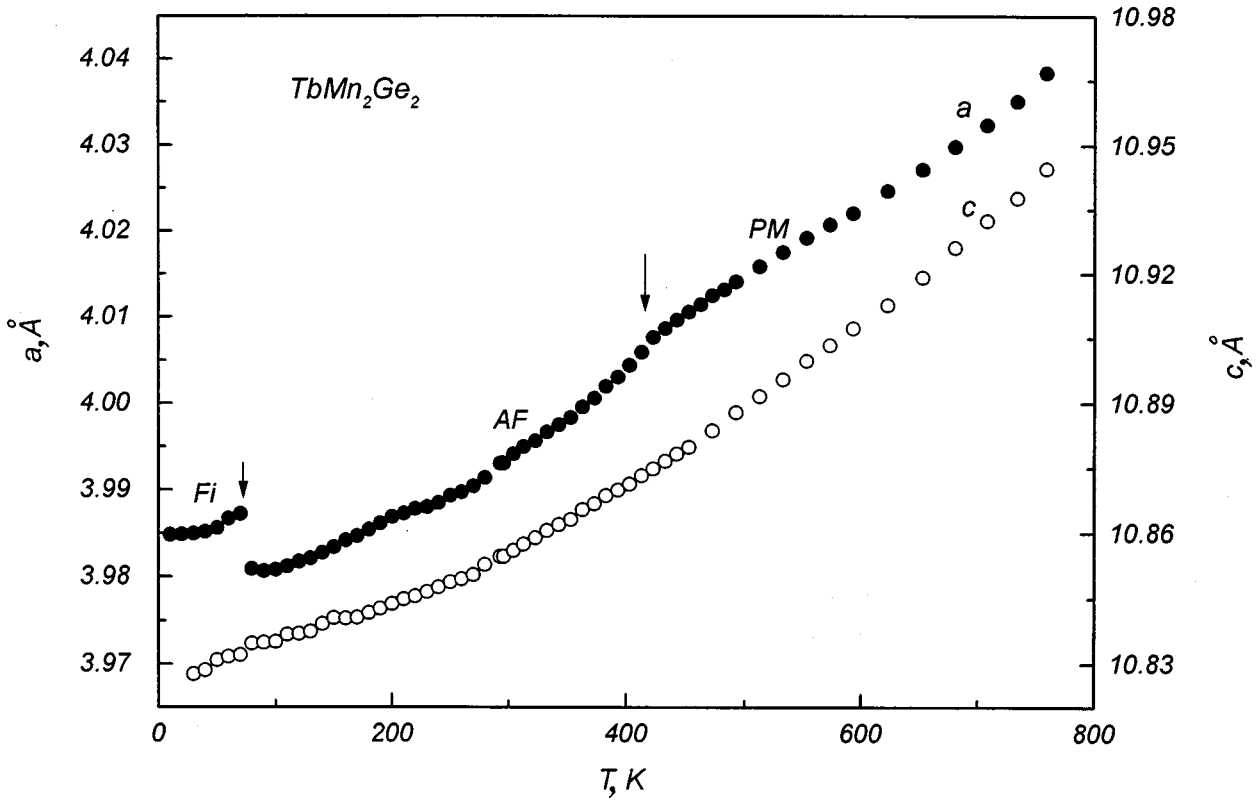

FIG. 6. Temperature dependence of the crystal-structure parameters of $TbMn_2Ge_2$. Notation the same as in Fig. 1.

subsystem under the action of the gadolinium–manganese exchange interaction.

$TbMn_2Ge_2$. Antiferromagnetic ordering of the manganese subsystem in this intermetallic compound takes place below 414 K (Ref. 1). It is accompanied by a negative magnetoelastic anomaly in the lattice parameter a (Fig. 6). At low temperatures (according to the data of different studies below 33–110 K, Ref. 1), the terbium subsystem orders ferromagnetically and the manganese subsystem also transforms to the ferromagnetic state. As can be seen from Fig. 6, this transition is accompanied by a jumplike growth in the parameter a.

To summarize, our measurements show that thermal-expansion measurements in many cases allow one to determine the temperatures of spontaneous magnetic phase transitions of various types in the intermetallic compounds RMn_2Ge_2. Most characteristic are jumplike anomalies in the lattice parameter a at low temperatures due to the transition from an antiferromagnetic to the ferromagnetic state in the manganese subsystem with simultaneous ordering of the rare-earth subsystem. At the same time, it can be seen that transitions from a paramagnetic to a magnetically ordered phase and high-temperature transitions between various magnetic phases in the manganese subsystem are also accompanied by anomalies in the lattice parameter, albeit significantly smaller in magnitude. We call attention to the fact that they are manifested in the temperature dependence of the lattice parameter c as well as the lattice parameter a.

The smooth character of the observed anomalies, expressed by a change in the slope of the temperature dependences, does not permit us to determine the critical distances a_{cr} and c_{cr} for these second-order transitions. Nevertheless, it may be remarked that transitions associated with a change in slope in the $c(T)$ dependence occur around 10.9 Å: 11.01 Å (La), 10.92 Å (Sm), and 10.95 Å (Nd). In compounds with Y, Gd, and Tb, magnetic ordering of the manganese subsystem also occurs for c roughly equal to 10.88 Å, although without a very noticeable anomaly in its temperature dependence. This circumstance indicates that, along with the intralayer distance, the interlayer distance also has an effect on the magnitude and sign of the Mn–Mn exchange interaction.

This work was supported by grants from the Russian Fund for Fundamental Research (No. 99-02-17358) and INTAS (No. 96-0630).

[1] A. Szytula and J. Leciejewicz, in *Handbook of the Physics and Chemistry of Rare Earths*, Vol. 12, edited by K. A. Gschneidner, Jr. and L. Eyring (North Holland, Amsterdam, 1989).
[2] H. Fujii, T. Okamoto, T. Shigeoka, and N. Iwata, Solid State Commun. **53**, 715 (1985).
[3] E. M. Gyorgy, B. Batlogg, J. P. Remeika, R. B. Van Dover, R. M. Fleming, H. E. Bair, G. P. Espinosa, A. S. Cooper, and R. G. Maines, J. Appl. Phys. **61**, 4237 (1987).
[4] M. Duraj and R. Duraj, J. Magn. Magn. Mater. **73**, 240 (1988).
[5] G. Venturini, R. Welter, E. Ressouehe, and B. Malaman, J. Magn. Magn. Mater. **150**, 197 (1989).
[6] M. Duraj and R. Duraj, J. Magn. Magn. Mater. **79**, 61 (1989).
[7] T. Shigeoka, J. Sci. Hiroshima Univ., Ser. A: Phys. Chem. **48**(2), 103 (1984).
[8] G. Venturini, B. Malaman, and E. Ressouche, J. Alloys Compd. **240**, 139 (1996).
[9] R. Welter, G. Venturini, E. Ressouche, and B. Malaman, J. Alloys Compd. **218**, 204 (1995).
[10] G. Venturini, B. Malaman, and E. Ressouche, J. Alloys Compd. **241**, 135 (1996).
[11] G. Venturini, J. Alloys Compd. **232**, 133 (1996).
[12] T. Shiegoka, N. Iwata, H. Fujii, and T. Okamoto, J. Magn. Magn. Mater. **53**, 58 (1985).
[13] G. Venturini, R. Welter, E. Ressouche, and B. Malaman, J. Alloys Compd. **150**, 197 (1995).
[14] Yin-gang Wang, Fuminh Yang, Changpin Chen, N. Tang, and Qidong Wang, J. Phys.: Condens. Matter **9**, 8539 (1997).
[15] T. Shigeoka, H. Fujii, H. Fujiwara, K. Yagasaki, and T. Okamoto, J. Magn. Magn. Mater. **31–34**, 209 (1983).

Translated by Paul F. Schippnick

Synthesis, structure, and dielectric properties of KH_2PO_4 fractal aggregates

I. V. Zolotukhin, S. V. Spitsina, L. I. Yanchenko, and L. N. Korotkov

Voronezh State Technical University, 394026 Voronezh, Russia
(Submitted April 8, 1999)
Fiz. Tverd. Tela (St. Petersburg) **41**, 2059–2061 (November 1999)

Macroscopic fractal aggregates of KH_2PH_4 (KDP) measuring up to 500 μm have been obtained. The fractal structure forms as a result of the precipitation of KDP particles from a supersaturated aqueous solution in the presence of a temperature gradient followed by a diffusion-controlled mechanism of aggregation. The electron-microscopic analysis performed has shown that the fractals are formed predominantly from crystallites of the tetragonal modification measuring ~ 1 μm. The dielectric constant (ε) of fractal KH_2PO_4 has been measured in the temperature range 80–300 K. A characteristic anomaly has been discovered on the $\varepsilon(T)$ curve in the vicinity of 122 K, which attests to a ferroelectric phase transition. The absolute value of ε is significantly smaller than the components ε_{11} and ε_{33} for KH_2PO_4. © *1999 American Institute of Physics.* [S1063-7834(99)03011-7]

In recent years interest has been growing in solid-state condensed media having a fractal structure. This interest is due to the fact that a solid formed under the conditions of energy dissipation and self-organization acquires a whole series of unusual properties, which are often impossible to obtain using traditional methods for forming the structure of a material. Fractal aggregates of several metals,[1–3] carbon,[4] and inorganic compounds[5,6] have already been obtained, and some of their physical properties have been investigated. The nature of surface fractal formations on ferroelectric crystals with a diffuse phase transition was discussed in Ref. 7. At the same time, the creation of fractal structures based on polar dielectrics and the study of their physical properties have not been undertaken. Therefore, the purpose of the present work was to obtain fractal aggregates based on a ferroelectric material and to investigate its structure and dielectric properties.

The starting material used to obtain the fractal aggregates was potassium dihydrogen phosphate (KH_2PO_4), which is a ferroelectric in the crystalline state and whose physical properties have been studied extensively.[8] In addition, this compound has a high solubility in water, which simplifies the obtaining of fractal aggregates. The fractals were obtained from a saturated solution of KH_2PO_4 in distilled water, which was heated to boiling (the solubility was 0.8 g/ml). A polished plate of silicon with bumps not exceeding 10 nm was placed in the heated solution. The formation of KDP fractal structures took place during cooling the solution from $T \approx 373$ K to room temperature over the course of 1–1.5 h.

The formation of a KH_2PO_4 fractal structure takes place in the following manner. The solubility of KH_2PO_4 in water increases upon heating to the boiling point; therefore, when the solution is cooled, it becomes supersaturated, and condensation of the excess quantity of KH_2PO_4 molecules begins and leads to the formation of clusters with an ordered crystal structure. Under the conditions of a temperature gradient, aggregation of the clusters with the formation of loose porous structures begins in the bulk of the liquid, and these structures are deposited on the walls of the vessel and on substrates placed in the solution. The formation of such structures is mediated by a diffusion-controlled aggregation mechanism.[9]

The structure of these formations was studied using optical and scanning electron microscopes. Dielectric measurements were performed on samples obtained from the material of the fractal aggregates by pressing it into the shape of rectangular parallelepipeds ($\sim 10 \times 10 \times 0.1$ mm^3) and affixing copper electrodes to their large sides. The samples were placed in a cryostat, where the temperature was varied from 80 to 300 K and monitored to an accuracy no poorer than ± 0.3 K. The dielectric constant (ε) of each sample was measured at a frequency of 1.59 kHz by a local method.

The maps obtained for a fragment of one of the macroscopic fractals with dimensions as high as 500 μm are presented in Fig. 1. It is seen that the fractal aggregate consists of bent spiral branches, some of which can end with branching in the form of a fan. The fractal dimension calculated by the grid method for various fractal aggregates is $D = (1.40 - 1.72) \pm 0.01$. Fractal aggregates of KH_2PO_4 of similar type and dimensions were also obtained on surfaces of freshly cleaved phlogopite and a polished aluminum foil.

The structure of the surface of the KDP fractals obtained on a silicon substrate is shown in Fig. 2. It is seen that the fractal aggregates have a columnar structure with a mean height of 13 μm. As the distance from the center of an aggregate to its edges increases, its height decreases from ~ 20 to ~ 5 μm in the peripheral portions of the fractal. Observations revealed that looser fractals with a low dimension ($D = 1.40$) and a small height form at short deposition times (up to 1 h). As the deposition time increases, each fractal aggregate becomes more developed and branched ($D = 1.72$), and its height increases accordingly. The formation of the structure of a fractal is completed at values of D close to 2.

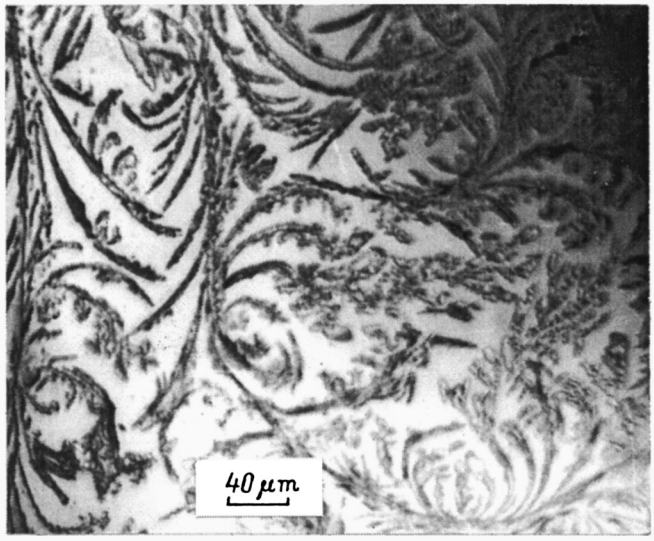

FIG. 1. KDP fractal aggregates obtained by deposition from a solution on a silicon substrate.

In order to determine the microscopic structure of the fractal aggregates obtained, fractals were grown on a copper grid of the type employed as a specimen holder in an electron microscope. The electron-microscopic investigation of KDP fractal structures revealed the presence of two crystal phases. One phase (see the electron micrograph in Fig. 3) consists of crystals of the tetragonal modification of KDP that measure $\sim 1\ \mu$m and make up roughly 95% of the entire volume. The other phase is the monoclinic modification of KDP, which is present to a small percentage (5%) as fragments. The crystallites measure $\sim 0.1\ \mu$m. Thus, the fractal structure is formed from KDP crystallites of two different types, whose dimensions differ by an order of magnitude.

The results of dielectric-constant measurements are presented in Fig. 4. It is seen that ε increases with lowering of the temperature to 122 K, at which a sharp peak of ε is observed. The position of the peak corresponds to the temperature of the ferroelectric phase transition T_C in single-crystal KDP.[8] Above T_C, between 122 and 150 K the $\varepsilon(T)$ curve is satisfactorily described by the Curie–Weiss law

$$\varepsilon = \varepsilon_\infty + \frac{C}{T-\Theta},$$

where $\varepsilon_\infty = 3$ is the temperature-independent component of ε, and $C = 180$ K and $\Theta = 50$ K are, respectively, the Curie–Weiss constant and temperature.

The results of the dielectric measurements unequivocally attest to the occurrence of a ferroelectric phase transition in the object under investigation or, at least, in individual fragments of it. The absolute value for the dielectric constant both at temperatures significantly distant from T_C and at temperatures close to it was two orders of magnitude smaller than the values of ε_{11} and ε_{33} for single-crystal KDP. Such a small value for the dielectric constant of a fractal aggregate is due to the small size and misorientation of the structural components.

Thus, fractal aggregates based on a ferroelectric have been obtained for the first time in the present work. The structural elements are crystallites of the tetragonal (95%) and monoclinic (5%) modifications of KDP measuring ~ 1

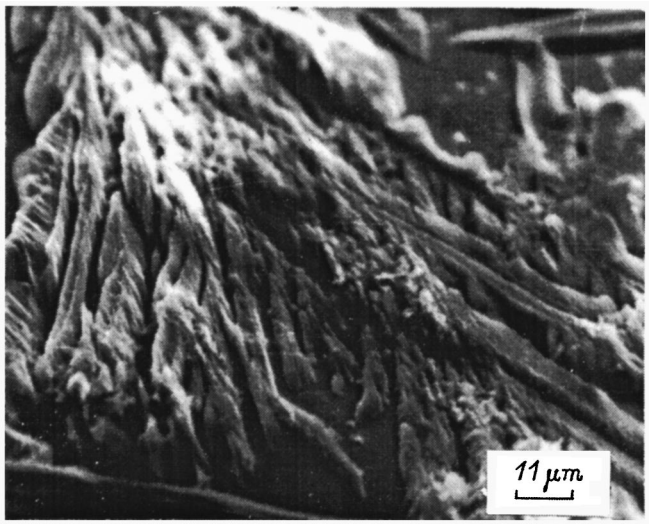

FIG. 2. Surface structure of one of the branches of a KDP fractal aggregate.

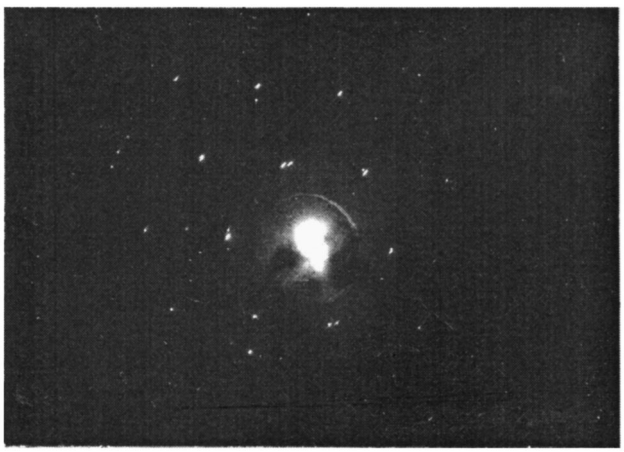

FIG. 3. Electron micrograph of KDP fractal formations.

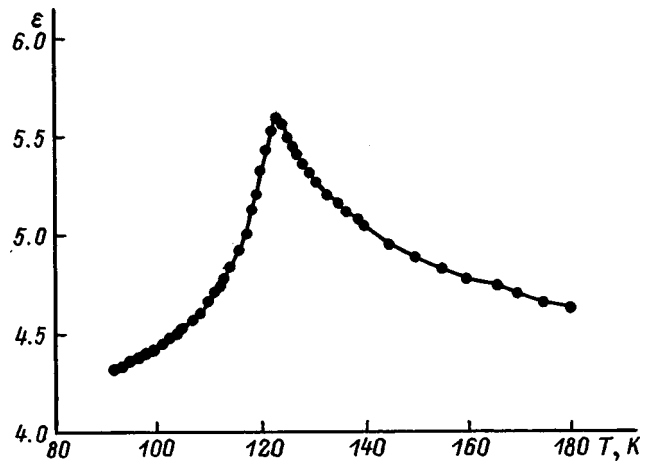

FIG. 4. Temperature dependence of the dielectric constant of KDP fractals.

and 0.1 μm, respectively. A ferroelectric phase transition takes place in the crystallites of the tetragonal modification at 122 K.

[1] J. M. Gómez-Rodríguez, A. M. Baró, L. Vázquez, R. C. Salvarezza, J. M. Vara, and A. J. Arvia, J. Phys. Chem. **96**, 347 (1992).
[2] J. Deng, Q. Y. Long, F. Ye, J. Jiang, and C. W. Lung, J. Phys. D **29**, 2671 (1996).
[3] I. V. Zolotukhin, A. B. Sukhodolov, A. S. Andreenko, and N. V. Tristan, JETP Lett. **66**, 594 (1997).
[4] I. V. Zolotukhin and Yu. V. Sokolov, Pis'ma Zh. Tekh. Fiz. **23**(13), 71 (1997) [Tech. Phys. Lett. **23**(7), 525 (1997)].
[5] J. Zhang, Phys. Rev. B **41**, 9614 (1990).
[6] J. Z. Zhang, C. H. Zhang, and H. D. Li, J. Phys.: Condens. Matter **4**(15), 245 (1992).
[7] V. A. Isupov, Fiz. Tverd. Tela (St. Petersburg) **40**, 1305 (1998) [Phys. Solid State **40**, 1188 (1998)].
[8] M. E. Lines and A. M. Glass, *Principles and Applications of Ferroelectrics and Related Materials* (Clarendon Press, Oxford, 1977; Mir, Moscow, 1981, 735 pp.).
[9] S. R. Forrest and T. A. Witten, J. Phys. A **12**(5), 109 (1979).

Translated by P. Shelnitz

LATTICE DYNAMICS. PHASE TRANSITIONS

Phase-separation kinetics of ^{3}He–^{4}He solid solutions at various degrees of supersaturation

V. A. Maĭdanov*)

Institute of Low-Temperature Physics and Engineering, Ukrainian National Academy of Sciences, 310164 Khar'kov, Ukraine

(Submitted February 1, 1999)
Fiz. Tverd. Tela (St. Petersburg) **41**, 2062–2064 (November 1999)

The phase-separation kinetics of ^{3}He$-^4$He solid solutions at various degrees of supersaturation Δx are studied using precise pressure measurements. It is found that the characteristic phase-separation times do not depend on the degree of supersaturation but are determined by the final temperature to which the crystal is cooled. The behavior of the effective diffusion coefficient, which governs the corresponding mass transfer, cannot be described within the impuriton model of the mobility of ^{3}He atoms in a ^{4}He crystal. © *1999 American Institute of Physics.* [S1063-7834(99)03111-1]

Recently performed experimental studies of the phase-separation kinetics of weak ^{3}He$-^4$He solid solutions have revealed some new features of the mobility of ^{3}He atoms during the phase transition.[1,2] It has been shown that the temperature dependence of the characteristic phase-separation time τ has a nonmonotonic character. When the sample is cooled in the phase-separation region in small steps, the value of τ at first decreases, a minimum is observed at $T \simeq 100-110$ mK, and then the phase-separation time increases as the temperature is lowered further.

Such behavior of τ does not follow from the impuriton model describing the kinetics of ^{3}He quasiparticles in a solid solution.[3] As the temperature is lowered, the concentration of ^{3}He in the ^{4}He matrix decreases exponentially, and the phase-separation times should also decrease in accordance with the $1/x$ law characteristic of quantum diffusion.[4]

Among the experimental data in Ref. 1 that were obtained when the solution was cooled in small steps, Fig. 5 in Ref. 1 also shows the result of one-step cooling from $T_i = 230$ mK to $T_f = 110$ mK. This result agrees well with the data obtained for cooling in a small step from $T_i = 125$ mK to the same temperature $T_f = 110$ mK. This finding is very unexpected, since phase separation in these cases occurred with strongly differing values of $\Delta T = T_i - T_f$ (120 and 15 mK, respectively) and degrees of supersaturation of the solution Δx (1.9 and 0.25% ^{3}He).

The purpose of the present work was to carry out a more detailed experimental study of this effect. In the experiments the time dependence of the pressure of the test crystal at a constant volume was measured after its temperature had been lowered in the phase-separation region. The experimental cell and instrumentation used were described in Ref. 1. Samples of helium solid solutions with an initial ^{3}He concentration equal to 2.05% and a molar volume equal to 20.44 cm^3/mol ($P = 33.4$ bar) were investigated.

The experimental plan is schematically represented by Fig. 1. Samples of a ^{3}He$-^4$He solid solution in an equilibrium state were rapidly cooled from various initial temperatures T_i lying on the equilibrium phase-separation line to the same fixed temperature $T_f = 100$ mK. A two-phase quantum crystal was investigated in all cases, i.e., the matrix of the dilute phase contained supercritical nuclei of the concentrated phase. After stabilization of the temperature T_f, the pressure in the sample varied in accordance with the variation of the concentration, i.e., relaxation of the system to its equilibrium state took place. The time dependence of the pressure change obtained reflected the phase-transition kinetics.

In all the cases investigated, growth of the pressure in the sample took place according to the exponential law

$$\Delta P = \Delta P_0 e^{-t/\tau}, \tag{1}$$

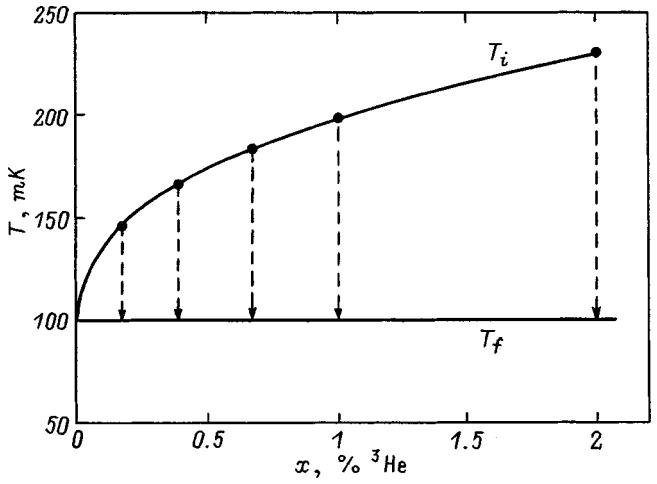

FIG. 1. Scheme for performing the experiment. Solid curve — part of the phase-separation phase diagram for $x < 2\%$ ^{3}He: T_i — initial temperature; T_f — final temperature.

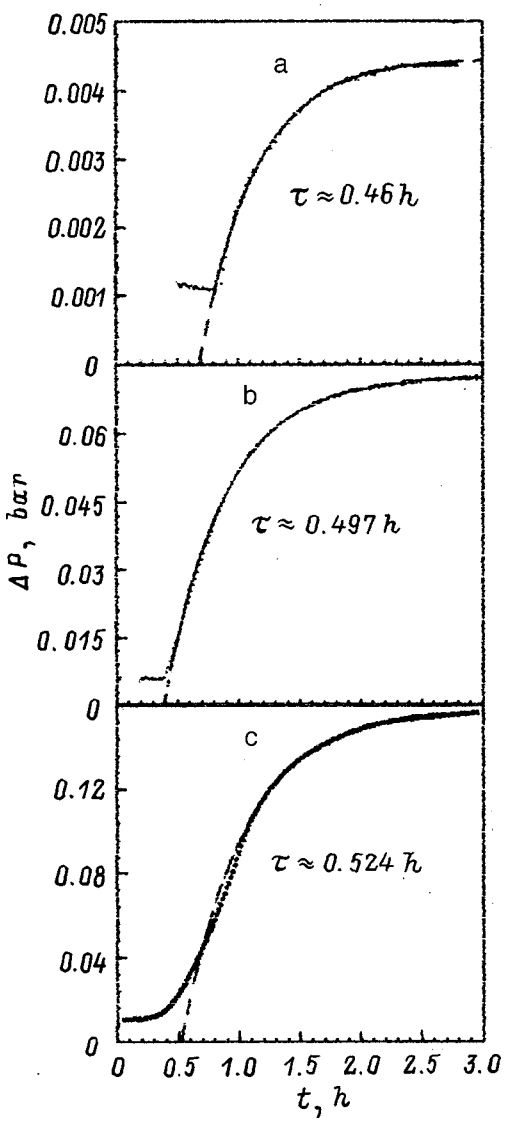

FIG. 2. Kinetics of the variation of the pressure after cooling of the sample from various initial temperatures to 100 mK: a — T_i=110 mK: b — T_i =150 mK; c — T_i=230 mK.

where τ is the characteristic phase-separation time, and ΔP_0 is the difference between the final and initial pressures. Characteristic plots of $\Delta P(t)$ for three different degrees of supersaturation ΔT are presented in Fig. 2.

An analysis of the plots using Eq. (1) shows that phase separation takes place at essentially the same rate in all cases despite the fact that the temperature difference and, consequently, the concentration difference differ significantly. The dependence of τ on the temperature difference ΔT for all the cases of cooling is shown in Fig. 3. The results presented show that the times τ do not depend on ΔT (Δx) and are, in fact, determined by the final temperature T_f after the solution was cooled.

Knowing the characteristic phase-separation time τ, the size of the inclusion of the new phase, and the original concentration of the solution, we can calculate the distance between nuclei of the new phase and the value of the effective mass diffusion coefficient D_{eff}, which governs mass transfer under phase-separation conditions. The solution of such a

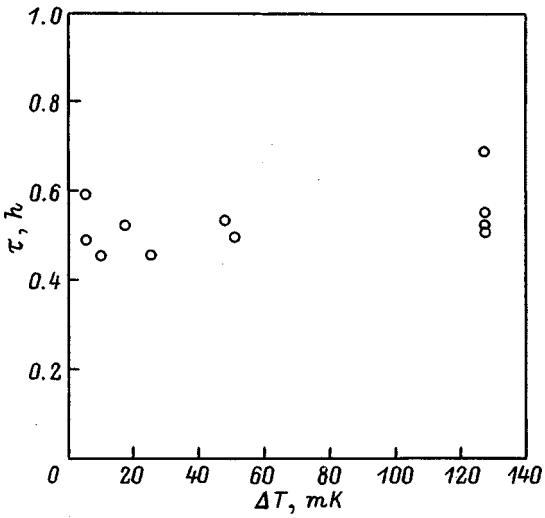

FIG. 3. Dependence of the characteristic time τ on the temperature difference ΔT.

problem was described in detail in Ref. 2. The size of the ^{3}He inclusions appearing as a result of phase separation has been established in various experiments,[5–8] which were carried out at sufficiently low temperatures, where the phase separation-process went to completion. Therefore, the data from these measurements yield the maximum size of a ^{3}He inclusion. As in Ref. 2, the value for the maximum inclusion radius $R_{\max}$=2.25 μm was used in the present calculation.

The values of D_{eff} found are presented in Fig. 4. For comparison, the dashed line in this figure is a plot of the values of the impuriton self-diffusion coefficient $D_s(x)$ found by NMR experiments.[4]

The value of the self-diffusion coefficient was averaged for each concentration interval Δx using the relation

$$D=\frac{1}{x_i-x_f}\int_{x_i}^{x_f} D_s(x)\,dx. \tag{2}$$

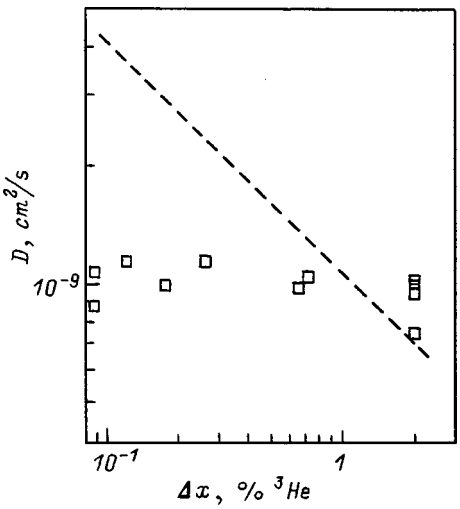

FIG. 4. Dependence of the effective diffusion coefficient on the degree of supersaturation. Dashed line — estimate of the impuriton self-diffusion coefficient according to Eq. (2).

The strong dependence of D_s on density was taken into account in the following manner:[9]

$$D_s = \frac{D_0}{x}\left(1 - \frac{x}{x_c}\right)^{1.7}, \tag{3}$$

where D_0 and x_c are quantities which depend on density. As can be seen from Fig. 4, the behavior of D_{eff} differs strongly from the concentration dependence of the impuriton self-diffusion coefficient.

During the phase-separation process, the inclusions of the new phase, which contain essentially pure ^{3}He and have a larger molar volume than the original solution, grow. This can lead to the appearance of elastic fields near the cluster boundary. Under these conditions the diffusion flux can be described in the form[2]

$$j = -\frac{Dx}{w}\left(\frac{\nabla x}{x} + \frac{\nabla U}{kT}\right), \tag{4}$$

where w is the atomic volume, ∇x is the concentration gradient, and ∇U is the potential gradient characterizing the nonuniform stress field.

As follows from the results of this study, the variation of Δx over a broad range does not cause an appreciable change in mass transfer, and the relationship between D, ∇x, x, and ∇U possibly has a more complicated nature than in (4).

Thus, the mass transfer of ^{3}He atoms under the conditions of phase separation at different degrees of supersaturation has a totally different nature than in a homogeneous solution, and further experimental and theoretical investigations are needed to account for the available facts.

We sincerely thank É. Ya. Rudavskiĭ, V. N. Grigor'ev, A. S. Rybalko, N. F. Omelaenko, A. N. Gan'shin, and A. A. Penzev for a useful discussion of the results of this study and for their assistance in performing the measurements.

*)E-mail: maidanov@ilt.kharkov.ua

[1] A. N. Gan'shin, V. A. Maĭdanov, N. F. Omelaenko, A. A. Penzev, É. Ya. Rudavskiĭ, and A. S. Rybalko, Fiz. Nizk. Temp. **24**, 815 (1998) [Low Temp. Phys. **24**, 611 (1998)].
[2] A. N. Gan'shin, V. N. Grigor'ev, V. A. Maĭdanov, N. F. Omelaenko, A. A. Penzev, É. Ya. Rudavskiĭ, and A. S. Rybalko, Fiz. Nizk. Temp. **25**, 356 (1999) [Low Temp. Phys. **25**, 259 (1999)].
[3] A. F. Andreev and I. M. Lifshits, Zh. Éksp. Teor. Fiz. **56**, 2057 (1969) [Sov. Phys. JETP **29**, 1107 (1969)].
[4] B. N. Esel'son, V. A. Mikheev, V. N. Grigor'ev, and N. P. Mikhin, Zh. Éksp. Teor. Fiz. **74**, 2311 (1978) [Sov. Phys. JETP **47**, 1200 (1978)].
[5] S. C. J. Kingsley, V. Maidanov, J. Saunders, and B. Cowan, J. Low Temp. Phys. **113**, 1017 (1998).
[6] A. E. Burgess and M. J. Crooks, Phys. Lett. A **39**, 183 (1972).
[7] A. S. Greenberg, W. C. Thomlinson, and R. C. Richardson, J. Low Temp. Phys. **8**(1), 3 (1972).
[8] A. V. Mikheev, V. A. Maĭdanov, N. P. Mikhin, S. E. Kal'noĭ, and N. F. Omelaenko, Fiz. Nizk. Temp. **14**, 563 (1988) [Sov. J. Low Temp. Phys. **14**, 309 (1988)].
[9] V. N. Grigor'ev, Fiz. Nizk. Temp. **23**, 5 (1997) [Low Temp. Phys. **23**, 1 (1997)].

Translated by P. Shelnitz

Thermal behavior of paramagnetic Gd^{3+} centers in $CsSrCl_3$

V. A. Vazhenin,*) V. B. Guseva, and M. Yu. Artemov

Scientific-Research Institute of Physics and Applied Mathematics, Ural State University, 620083 Ekaterinburg, Russia

(Submitted March 4, 1999)
Fiz. Tverd. Tela (St. Petersburg) **41**, 2065–2069 (November 1999)

The temperature dependence of the order parameters and the axial initial splitting parameter of Gd^{3+} impurity complexes is measured in the first low-symmetry phase of $CsSrCl_3$, and the relationship between these parameters is found. The parameters of the thermodynamic potential, which takes into account the interaction of the order parameter with strains, are estimated. The nature of the temperature dependence of the axial initial splitting parameter in the cubic phase is explained. © *1999 American Institute of Physics.* [S1063-7834(99)03211-6]

1. The investigations in Refs. 1–5 permitted an interpretation of the thermal behavior of $CsSrCl_3$ in the vicinity of 380 K following the sequence of three structural transformations

$$O_h^1 \overset{[00\psi]}{\rightarrow} D_{4h}^5 \overset{0\varphi\psi}{\rightarrow} D_{2h}^{17} \overset{[\varphi_2\varphi_1\psi]}{\rightarrow} C_{2h}^2, \tag{1}$$

where ψ and φ are components of the M_3 and R_{25} rotational modes, respectively. In Ref. 6 the parameters of the thermodynamic potential for two of the structural transitions were determined from thermal measurements and an investigation of the temperature dependence of the angle of rotation of the chlorine octahedron using the EPR spectrum of cubic Gd^{3+} centers (centers of type *1*) without considering the interaction of the order parameters with one another and with the strains.

The structures of two tetragonal (in the cubic phase) Gd^{3+} complexes (type *2*, which includes association with a vacancy of a nearby Sr^{2+} ion, and type *3*, which contains an O^{2-} ion at the site of a nearby chloride ion) and the relationship of their parameters to the values of the angle of rotation and strain of the chlorine octahedron were investigated in Refs. 7–10. This paper presents the results of measuring the temperature dependences of the rotation angle of the chlorine octahedron and the axial parameter b_{20}, which is related to the strain of the octahedron, in the three types of paramagnetic centers in the first low-temperature phase (the complexes of type *2* produce $2\|$ and $2\perp$ centers in this phase[8]).

2. The measurements were performed on samples which were grown by the Bridgman method in sealed quartz ampuls and have an almost monodomain structure on a 3-cm spectrometer. To obtain $b_{20}(T)$, a combination of the resonance positions for two transitions, which eliminates the contribution of the cubic parameter b_{40} of the spin Hamiltonian (the contribution of b_{60} and the off-diagonal parameters is small), was constructed at each temperature after Ref. 11: for center *1* in the case of $\mathbf{B}\|\boldsymbol{\psi}$ (B is the magnetic field induction), for center $2\|$ in the case of $\mathbf{B}\|OK\|\boldsymbol{\psi}$ (OK denotes the compensation axis), and for center $2\perp$ in the case of $\mathbf{B}\|OK\perp\boldsymbol{\psi}$. The results are presented in Figs. 1 and 2 and in Table I. The quantity $\Delta b_{20}(T)$ in Fig. 2 is the value of $b_{20}(T,\text{phase } 1)$ in the low-symmetry phase minus the jump in b_{20} and the dependence of $b_{20}(T,\text{cub})$ extrapolated from the cubic phase.

To measure the local angle of rotation of the octahedron, the polarizing magnetic field was turned from C_4 in the plane $\perp\boldsymbol{\psi}$ by the angle φ_0, and the distance Δ between the resonance positions of the EPR signals of the centers with opposite signs of rotation of the chlorine octahedron was determined. It is easy to show that the shifts of the angular dependence of the resonance position will be

$$\psi_a = 1/4 \arcsin(\Delta/(P^* \sin 4\varphi_0)) \quad \text{for centers } 1 \text{ and } 2\|, \tag{2}$$

$$\psi_a = 1/2 \arcsin(\Delta/(P^* \sin 2\varphi_0)) \quad \text{for center } 2\perp, \tag{3}$$

where P is the spread of the azimuthal (*1* and $2\|$) or polar ($2\perp$) angular dependence. The results obtained are shown in Fig. 3 and in Table I (the table also lists the data on the rotation angles from Refs. 8 and 9).

According to Ref. 8, for centers *1* and $2\|$ the angle ψ_a can be identified with the angle of rotation (upon the phase transition) of the principal axes of the fourth-rank fine-structure tensor of the paramagnetic center ψ_b and, consequently, with the angle of rotation of the chlorine octahedron ψ, while this is not true for center $2\perp$. An analysis of the shift of the angular dependence for center $2\perp$ upon the phase transition showed that the main contribution to it is made by rotation of the axes of the second-rank tensor, but neglecting the influence of the fourth-rank tensor in quantitative calculations would be erroneous.

It would be interesting to turn to the question of the relationship between the rotation angles of the second-rank tensor

$$\psi_b = 1/2 \arctan(b_{21}/b_{22} - 3b_{20}) \tag{4}$$

and the rotation angles of the octahedron for centers of type $2\perp$ at 384 and 372 K (Ref. 8) (Table I). Using the superposition model[12] for an octahedron distorted as a result of the presence of a Gd^{3+} ion and a Sr^{2+} vacancy and then turned about the direction perpendicular to the composition axis without additional distortions, we obtain for the rotation angle

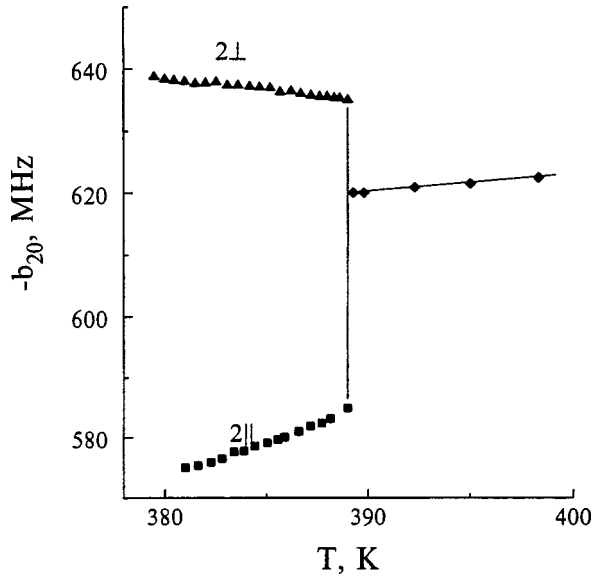

FIG. 1. Temperature dependence of b_{20} for centers of types $2\|$ and $2\perp$.

$$\delta = 1/2 \arcsin[b_{21}/3b_{20}(\text{oct})], \quad (5)$$

where $b_{20}(\text{oct})$, in contrast to (4), is the contribution to b_{20} only from the ligands of the rotating octahedron without consideration of the compensator ion. The small parameter b_{22} is not included in (5) because of the neglect of the deformation of the octahedron upon rotation.

According to the estimates in Ref. 7, $b_{20}(\text{oct})$ amounts to roughly half (in absolute value) of the observed value of b_{20}. Consideration of this estimate in (5) leads to a roughly twofold increase in the angle of rotation of the octahedron in comparison to the data in Refs. 8 and 9 for the second-rank tensor (Table I). Unfortunately, this conclusion cannot be confirmed by the behavior of the principal axis of the fourth-rank tensor (Table I), which depends weakly on the strain of the octahedron, even with consideration of the large error in the determination of b_{4m}. Nevertheless, the conclusion in Ref. 8 regarding such a strong influence of a strontium vacancy located in the rotation plane on the value of the local rotation angle can be mentioned. It should be noted that the expression (5), unlike (4), which is purely phenomenological, is a result of model representations.

TABLE I. Jump in b_{20}, the shift ψ_a of the angular dependences of the EPR signals, and the rotation angles of the axes of the rth-rank fine-structure tensor.

Center	Jump in b_{20}, MHz	ψ_a, deg	ψ_b(384 K), deg (Ref. 8)	ψ_b(372 K), deg (Ref. 9)
1	21	5.8	6.1(3) $r=4$	6.9(5) $r=4$
2∥	29	6.3	6.7(3) $r=4$	7.5(4) $r=4$
2⊥	15	3.1	3.0(3) $r=2$	4.1(2) $r=2$
			2.5(7) $r=4$	5.4(6) $r=4$

Our attention is attracted by the regular difference between the values of the local order parameter on centers *1* and *2*∥ (Fig. 3 and Table I). This finding can be explained on a qualitative level in the following manner. Since the presence of a Sr^{2+} vacancy in the neighboring octahedron causes compression of the $(GdCl_6)^{3-}$ octahedron (Ref. 7),[1)] when the *OK* and ψ directions coincide, the phase transition in this part of the crystal will take place, as it were, under the conditions of uniaxial compression, which causes, for example in $RbCaF_3$ (Ref. 11), a shift of the transition temperature, i.e., it can be expected that the structural transition near a *2*∥ center will occur at a higher temperature and, according to the data in Ref. 8, will cause further compression of the octahedron along ψ.

It is usually assumed that b_{20} (or Δb_{20}, if $b_{20} \neq 0$ in the cubic phase) is proportional to the square of the order param-

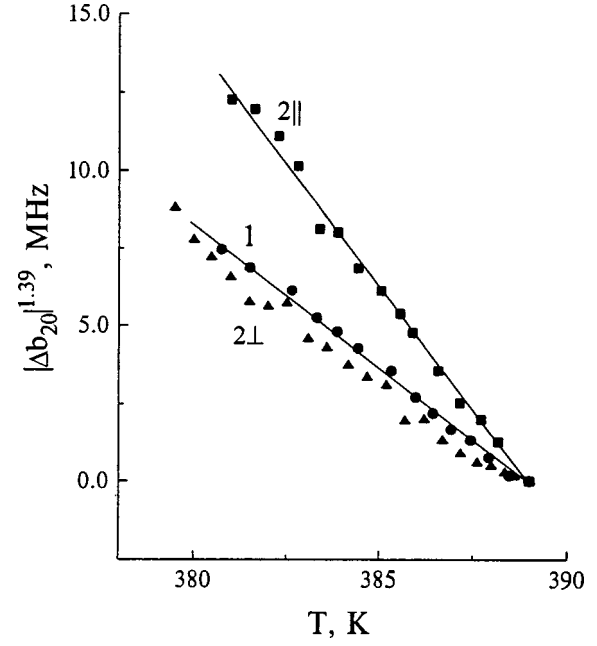

FIG. 2. Temperature dependence of the absolute value of Δb_{20} for three types of centers (*1*, *2*∥, and *2*⊥).

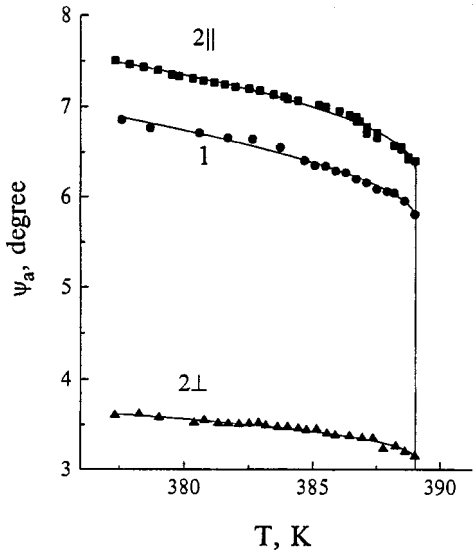

FIG. 3. Temperature dependence of the shift in the angular dependence of the resonance position for centers of types *1*, *2*∥, and *2*⊥ in the first low-symmetry phase.

eter. This relationship can be expressed more correctly in the form

$$\Delta b_{20} = \chi\psi^2 + \xi\psi^4 + \zeta\psi^{6+} \ldots .$$

Treatment of the experimental results leads to the following values: $\chi = 0.86\,\mathrm{MHz/deg^2}$, $\xi = -0.01\,\mathrm{MHz/deg^4}$, and $\zeta = 0.0002\,\mathrm{MHz/deg^6}$ for center *1* and $\chi = 1.53\,\mathrm{MHz/deg^2}$, $\xi = -0.03\,\mathrm{MHz/deg^4}$, and $\zeta = 0.003\,\mathrm{MHz/deg^6}$ for center $2\|$. Neglect of the terms with high powers markedly renormalizes the first coefficient [$\chi(1) = 0.59\,\mathrm{MHz/deg^2}$, $\chi(2\|) = 0.71\,\mathrm{MHz/deg^2}$], but the error in the description of an experiment increases by only two fold.

3. Knowing the temperature dependence of the order parameter (Fig. 3), we can estimate the ratios between the parameters of the thermodynamic potential

$$\Phi = \Phi_0 + A(T - T_c)\eta^2 + B\eta^4 + C\eta^4. \quad (6)$$

The experimental plot of $\eta(T)$ for a cubic center is satisfactorily described with the following values of the parameters in (6): $T_{cr} - T_0 = 3.06\,\mathrm{K}$, $A/B = -0.452 \times 10^{-18}\,\mathrm{cm^2/K^{-1}}$, and $B/C = -1.67 \times 10^{-17}\,\mathrm{cm^2}$, which are fairly close to the parameters determined in Ref. 6. However, the value $\eta_0 = 0.29 \times 10^{-8}\,\mathrm{cm}$ obtained in this procedure is greater than the experimentally measured value ($0.285 \times 10^{-8}\,\mathrm{cm}$).

According to Ref. 2, consideration of the elastic energy of the crystal and the interaction of the order parameter with the strains leads only to renormalization of the constant B in the potential (6):

$$B' = B - 3/2\,\frac{\alpha^2}{c_{11} + 2c_{12}} - 12\,\frac{\beta^2}{c_{11} - c_{12}}, \quad (7)$$

where c_{11} and c_{12} are the elastic moduli and α and β are parameters of the interaction η with strains. Let us try to evaluate the last term in (7). After substituting the expression for the spontaneous tetragonal strain[2]

$$x_3 - 1/2(x_1 + x_2) = -6\beta\eta^2/(c_{11} - c_{12}) \quad (8)$$

into the Hamiltonian of the spin-deformation interaction[13]

$$H_{ss} = 1/2^* G_{11} O_{20}[x_3 - 1/2(x_1 + x_2)] = 1/3^* b_{20} O_{20}, \quad (9)$$

where x_i are the components of the strain tensor, O_{20} is the Stevens spin operator, and G_{11} is a component of the fourth-rank tensor of the spin-deformation interaction, we obtain

$$\beta = -b_{20}(c_{11} - c_{12})/9G_{11}\eta^2. \quad (10)$$

Substituting the values of η and b_{20} for $T = 384\,\mathrm{K}$ from Ref. 8, the elastic constants for $CsPbCl_3$ from Ref. 2, and $G_{11} = G_{33} = 0.21\mathrm{cm^{-1}}$ (Gd^{3+} in SrO) from Ref. 14, we obtain $\beta = -0.7 \times 10^{25}\,\mathrm{erg/cm^5}$, which makes a contribution to B' through the last term in (7), which equals $0.4 \times 10^{40}\,\mathrm{erg/cm^7}$. Since the value of G_{11} for CaO obtained in Ref. 14 is two times smaller than the value for SrO, we can expect an appreciably larger addition to B (in Ref. 6 $B = -1.85 \times 10^{40}\,\mathrm{erg/cm^7}$).

The corrections to B due to the interaction η with strains can also be estimated without evoking the spin-deformation interaction by employing the data in Ref. 2 on the changes in the unit-cell parameters accompanying the phase transition as components of the strain tensor, the expression (8), and

$$\alpha = -(c_{11} + 2c_{12})(x_1 + x_2 + x_3)/3\eta^2$$
$$= -(c_{11} + 2c_{12})[(c + 2a)/a_0 - 3]/3\eta^2. \quad (11)$$

The values $\alpha = 0.78 \times 10^{25}\,\mathrm{erg/cm^5}$ and $\beta = -1.4 \times 10^{25}\,\mathrm{erg/cm^5}$ obtained from (11) and (8) lead to $\Delta B(\alpha) = 0.015 \times 10^{40}\,\mathrm{erg/cm^7}$ and $\Delta B(\beta) = 1.57 \times 10^{40}\,\mathrm{erg/cm^7}$. As we see, both estimation methods give values of the corrections to B that are comparable to the experimentally obtained values and can lead to alteration of the character of the transition when the observation conditions are altered.

4. As follows from Fig. 1, the absolute value of the axial parameter b_{20} for centers of type *2* in the cubic phase increases with increasing temperature ($\delta b_{20}/\delta T \sim 7 \times 10^{-6}\,\mathrm{cm^{-1}/K}$), while for centers of type *3* (Gd^{3+} with an O^{2-} or S^{2-} ion in a position of a nearby halogen) in $CsSrCl_3$ (Ref. 7), $CsCaCl_3$ (Ref. 15), and $RbCaF_3$ (Ref. 16) the magnitude of the initial splitting decreases. The thermal behavior of tetragonal and trigonal Gd^{3+} centers in crystals with fluorite structure, whose axial parameters are governed exclusively by the presence of fluorine atoms in the local environment of the interstitial ions,[17–19] is similar to the behavior of the three centers in perovskites and can be associated with thermal expansion of the crystals. The value of $\delta b_{20}/\delta T$ for Gd^{3+} centers with a large initial splitting (centers of type *3* and tetragonal centers in fluorites) is equal to $\sim 3 \times 10^{-5}(\mathrm{cm^{-1}/K})$. It turns out that $CsSrCl_3$ is not the only material in which the Gd^3 centers of type *2* exhibit an unusual temperature dependence of b_{20} (Tables II and III). Estimation of $\delta b_{20}/\delta T$ for centers of type *2* in the superposition approximation using the data in Ref. 23 regarding the thermal splitting of $RbCdF_3$ and $CsCdF_3$ gives a value of the order of $+3 \times 10^{-6}\,(\mathrm{cm^{-1}/K})$, which is comparatively close to the value obtained experimentally for $CsCdF_3$.

Apart from thermal expansion of the crystal, an appreciable contribution to the temperature dependence of the initial splitting can be made by the spin-phonon interaction if we take into account the anharmonicity of the lattice[13,24]

TABLE II. Initial splitting parameters of tetragonal Gd^{3+} centers associated with a nearby vacancy of a *B* ion in the cubic phase.

ABX_3	*T*, K	b_{20}, $10^{-4}\,\mathrm{cm^{-1}}$	$\delta b_{20}/\delta T$, $\mathrm{cm^{-1}/K}$	Ref.
$CsSrCl_3$	393	−206.8(10)	-7×10^{-6}	7
$KCdF_3$	487	−249.3(10)	-5×10^{-6}	20,21
$RbCdF_3$	295	−291.3(5)	-1.4×10^{-6}	21
$CsCaF_3$	298	−314.3(3)	-0.4×10^{-6}	21
$CsCdF_3$	291	−315.3(3)	$+1.4 \times 10^{-6}$	21

TABLE III. Initial splitting parameters of tetragonal Gd^{3+} centers associated with Li^+ at the site of a nearby *B* ion in the cubic phase.

ABX_3	*T*, K	b_{20}, $10^{-4}\,\mathrm{cm^{-1}}$	$\delta b_{20}/\delta T$, $\mathrm{cm^{-1}/K}$	Ref.
$CsCaF_3$	298	−388.3	$+2.2 \times 10^{-6}$	22
$CsCdF_3$	300	−379.8	$+3.4 \times 10^{-6}$	22

$$\Delta b_{20}(T) = KT^4 \int_0^{\Theta/T} (e^x - 1)^{-1} x^3 \, dx, \tag{12}$$

where Θ is the Debye temperature, as well as the interaction with localized vibrations[25–27]

$$\Delta b_{20}(T) = K_0 \left(\coth \frac{h\nu}{kT} - 1 \right), \tag{13}$$

where ν is the frequency of the localized vibration. It was shown, however, in Ref. 28 that if $K_0/K\Theta^4 = h\nu/3k\Theta$, the expressions (12) and (13) give essentially identical dependences. Since it is not simple to separate these contributions in an experiment, we say that there is a single dynamic mechanism underlying the temperature dependence of the initial splitting.

In Refs. 29–32 crystal-chemical analyses of the types of looseness in the perovskite structure revealed regions for the existence of real crystals of perovskites in the coordinates of the relative ionic radii. Appearance in a definite region presumes the existence in the crystal of stiff extended objects, which may be one-dimensional (shifting of ions in a chain) or two-dimensional (tilting of octahedrons with extension in the rotation plane), vibrate coherently in a highly anharmonic potential, and are precursors of stable low-symmetry phases.

The absence of structural phase transitions in $CsCdF_3$ and $CsCaF_3$ correlates well with the appearance of the former on the boundary and the latter near the boundary of the tilting and shifting regions. The location of the sequence of crystals consisting of $RbCdF_3$ (one structural transition), $KCdF_3$ (two transitions), and $CsSrCl_3$ (three transitions) at increasing depths in the tilting zone is probably evidence of an increase in the anharmonicity of the lattice.

Consequently, it can be expected that, in the series of crystals listed in Table II, the dynamic contribution to the temperature dependence of the initial splitting will increase from $CsCdF_3$ to $CsSrCl_3$. Then, if the signs of $\delta b_{20}/\delta T$ for the static and dynamic contributions to b_{20} are different, a change in the sign of $\delta b_{20}/\delta T$ for the experimental dependence of the axial parameter should occur in this series, in agreement with the data in Table II.

To obtain a concentration of Gd^{3+} complexes associated with Li^+ ions sufficient for observation (Table III), gadolinium and lithium doping levels much greater (~ 1 mol %) than the levels characteristic of single-ion doping (<0.1 mol%) must be employed. As a result, crystals are obtained with integral parameters which are dramatically altered by the defects and are difficult to compare with the properties of lightly doped crystals. Nevertheless, the value of $\delta b_{20}/\delta T$ for $Ge^{3+} - Li^+$ centers is closer to the value obtained with allowance for thermal expansion of the crystal in the superposition approximation than is the value for $Gd^{3+} - V_{Sr}$ centers, attesting to a decrease in the dynamic contribution.

We sincerely thank A. E. Usachev for supplying the samples, A. E. Nikiforov and E. L. Rumyantsev for participating in discussions, and A. P. Potapov for assisting in the treatment of the results.

*)E-mail: vladimir.vazhenin@usu.ru

1)The conclusion in Ref. 7 regarding compression of the octahedron as a result of the displacement of a Cl^- ion from the strontium vacancy to Gd^{3+} can be corroborated by an analysis of the data in Tables II and III. The presence of a Li^+ ion with a small ionic radius at the site of a Sr^{2+} vacancy should lead to displacement of a chlorine atom toward the lithium atom and, consequently, to a decrease in its possible contribution to b_{20}. As a result, the absolute value of b_{20} for lithium centers is greater than the value for center *2* (Tables II and III).

[1] L. A. Pozdnyakova, B. V. Beznosikov, I. T. Kokov, and K. S. Aleksandrov, Fiz. Tverd. Tela (Leningrad) **15**, 3586 (1973) [Sov. Phys. Solid State **15**, 2393 (1974)].
[2] K. S. Aleksandrov, A. T. Anistratov, B. V. Beznosikov, and N. V. Fedoseeva, *Phase Transitions in Crystals of ABX_3 Compounds of Gadolinium* (Novosibirsk, Nauka 1981), 266 pp.
[3] M. Midorikawa, Y. Ishibashi, and Yu. Takagi, J. Phys. Soc. Jpn. **41**, 2001 (1976).
[4] A. E. Usachev, Yu. V. Yablokov, L. A. Pozdnyakova, and K. S. Aleksandrov, Fiz. Tverd. Tela (Leningrad) **19**, 2156 (1977) [Sov. Phys. Solid State **19**, 1263 (1977)].
[5] M. V. Chernitskiĭ, V. A. Vazhenin, A. E. Nikiforov, A. E. Usachev, A. I. Krotkiĭ, and M. Yu. Artemov, Fiz. Tverd. Tela (Leningrad) **33**, 3577 (1991) [Sov. Phys. Solid State **33**, 2011 (1991)].
[6] A. E. Usachev, Yu. V. Yablokov, and S. G. L'vov, Fiz. Tverd. Tela (Leningrad) **23**, 1439 (1981) [Sov. Phys. Solid State **23**, 838 (1981)].
[7] V. A. Vazhenin, K. M. Starichenko, M. Yu. Artemov, and M. V. Chernitskiĭ, Fiz. Tverd. Tela (Leningrad) **34**, 1633 (1992) [Sov. Phys. Solid State **34**, 866 (1992)].
[8] V. A. Vazhenin, K. M. Starichenko, M. Yu. Artemov, and A. E. Nikiforov, Fiz. Tverd. Tela (St. Petersburg) **36**, 2695 (1994) [Phys. Solid State **36**, 1470 (1994)].
[9] V. A. Vazhenin and M. Yu. Artemov, Fiz. Tverd. Tela (St. Petersburg) **39**, 370 (1997) [Phys. Solid State **39**, 323 (1997)].
[10] V. A. Vazhenin, M. Yu. Artemov, and V. B. Guseva, Fiz. Tverd. Tela (St. Petersburg) **41**, 247 (1999) [Phys. Solid State **41**, 219 (1999)].
[11] J. Y. Buzare, J. C. Fayet, W. Berlinger, and K. A. Müller, Phys. Rev. Lett. **42**, 465 (1979).
[12] L. I. Levin, Phys. Status Solidi B **134**, 275 (1986).
[13] C. A. Bates and H. Szymczak, Phys. Status Solidi B **74**, 225 (1976).
[14] S. B. Oseroff and R. J. Calvo, Phys. Chem. Solids **33**, 2275 (1972).
[15] Y. Vaills and J. Y. Buzare, J. Phys. C **20**, 2149 (1987).
[16] J. Y. Buzare and P. Simon, J. Phys. C **17**, 2681 (1984).
[17] H. A. Buckmaster and Y. H. Shing, Phys. Status Solidi A **12**, 325 (1972).
[18] L. A. Boatner, R. W. Reynolds, and M. M. Abraham, J. Chem. Phys. **52**, 1248 (1976).
[19] A. D. Gorlov, A. P. Potapov, L. I. Levin, and V. A. Ulanov, Fiz. Tverd. Tela (Leningrad) **33**, 1422 (1991) [Sov. Phys. Solid State **33**, 801 (1991)].
[20] M. Arakawa and H. Ebisu, J. Phys. Soc. Jpn. **51**, 191 (1982).
[21] M. Arakawa, H. Aoki, H. Takeuchi, T. Yosida, and K. Horai, J. Phys. Soc. Jpn. **51**, 2459 (1982).
[22] M. Arakawa, H. Ebisu, and H. Takeuchi, J. Phys. Soc. Jpn. **54**, 3577 (1985).
[23] M. Rousseau, J. Y. Gesland, J. Julliard, J. Nouet, J. Zarembowitch, and A. Zarembowitch, Phys. Rev. B **12**, 1579 (1975).
[24] K. N. Shrivastava, Phys. Rep., Phys. Lett. **20**, *3*, 137 (1975).
[25] W. M. Walsh, J. Jeener, and N. Bloembergen, Phys. Rev. **139**, A1338 (1965).
[26] G. Pfister, W. Dreybrodt, and W. Assmus, Phys. Status Solidi **36**, 351 (1969).
[27] A. A. Mirzakhanyan and K. N. Kocharyan, Fiz. Tverd. Tela (Leningrad) **23**, 90 (1981) [Sov. Phys. Solid State **23**, 49 (1981)].
[28] H. Bill, Phys. Status Solidi B **89**, K49 (1978).
[29] F. A. Kassan-Ogly and V. E. Naish, Acta Crystallogr. B **42**, 297 (1986).
[30] F. A. Kassan-Ogly and V. E. Naish, Acta Crystallogr. B **42**, 307 (1986).
[31] F. A. Kassan-Ogly and V. E. Naish, Acta Crystallogr. B **42**, 314 (1986).
[32] F. A. Kassan-Ogly and V. E. Naish, Acta Crystallogr. B **42**, 325 (1986).

Translated by P. Shelnitz

LOW-DIMENSIONAL SYSTEMS AND SURFACE PHYSICS

Electron scattering in a point contact of one-dimensional conductors

I. A. Ryzhkin*)

Institute of Solid-State Physics, Russian Academy of Sciences, 142432 Chernogolovka, Moscow District, Russia

(Submitted November 24, 1998)
Fiz. Tverd. Tela (St. Petersburg) **41**, 2070–2074 (November 1999)

The scattering matrix of a point contact between one-dimensional coherent conductors is considered. It is shown that the flux conservation law, time-reversal symmetry, and an hypothesis of continuity of the wave function lead to parametrization of the scattering matrix by a single real parameter, regardless of the number of conductors connected by the contact. The condition of maximum transmission fixes this parameter and thereby uniquely defines the scattering matrix. The condition of flux conservation then reduces to the condition that the sum of the derivatives of the wave function with respect to the directions of the conductors vanish. Possible applications of the model considered to experimentally feasible arrays of one-dimensional elements are discussed. © *1999 American Institute of Physics.* [S1063-7834(99)03311-0]

The achievements of nanotechnology in the last 10 years have lead to the creation of semiconductor structures whose transverse dimensions are so small that only one propagating mode exists in them due to transverse quantization. Owing to the absence of impurities, the electron mean free path in such systems can be considerably greater than the longitudinal dimensions. The propagation of electrons under these conditions is a ballistic, quantum process and is completely described by a one-dimensional Schrödinger equation that is similar to the equation describing the propagation of electromagnetic waves in single-mode waveguides. For many problems (scattering on a random potential, interactions between electrons) the possibility of describing the motion of electrons by only the longitudinal part of the wave function, which depends only on the one-dimensional coordinate, is a decisive simplification and permits obtaining exact solutions for them.

The next systems in order of complexity are arrays of one-dimensional conductors containing branch points and junctions of purely one-dimensional conductors. From the theoretical standpoint it would be interesting to investigate the influence of the non-one-dimensionality introduced by contacts on the result of the purely one-dimensional problem. In addition, experimental realizations of structures containing branch points and junctions are possible, and this accounts for the practical importance of these systems. Various models used to describe the Aharonov–Bohm effect,[1] persistent currents,[2] and electron propagation in quantum wire arrays,[3,4] as well as models for investigating non-one-dimensional localization by renormalization-group analysis,[5] can be noted as examples. The main question which arises in going from one-dimensional models to arrays of such elements is the question of matching the wave functions at the connection sites; however, it has simply been ignored in many studies. The purpose of this paper is to discuss the possible form of the boundary conditions imposed on the longitudinal one-dimensional wave functions of electrons in point contacts for the special class of contacts which preserve the continuity of a one-dimensional wave function.

The most general and widely used approach to this problem was first formulated in Ref. 6 and involves introducing a contact scattering matrix which satisfies the flux conservation law and time-reversal symmetry. The latter means that the complex scattering matrix must be a unitary symmetric matrix of order $n\times n$ and can be parametrized by $n(n+1)/2$ real parameters (n is the number of wires converging at the contact). The values of these parameters are determined by the specific realization of the contact as a waveguide system, which is generally known. Such an approach is undoubtedly correct, but is excessively general and relatively uninformative. In fact, using this parametrization even for the simplest nontrivial case of $n=3$, we obtain solutions which depend in an unknown manner on six real parameters. Therefore, the values of the unknown parameters must be established using additional nonphysical arguments (the real nature of the matrix elements of the scattering matrix,[1,7] the especially small values of certain matrix elements,[7,8] etc.).

In the present paper, a hypothesis of continuity of the wave function is used to obtain a more definite form of the scattering matrix. Let us discuss its meaning in somewhat greater detail. Actually, the tenable requirement is continuity of the total wave function. For regions far from a contact in single-channel conductors, the total wave function is equal to the product of the longitudinal wave function and the fundamental transverse mode. The other terms containing higher damped transverse modes become small as the distance from the contact increases. However, they can be significant in the region adjacent to the contact. For this reason it is not en-

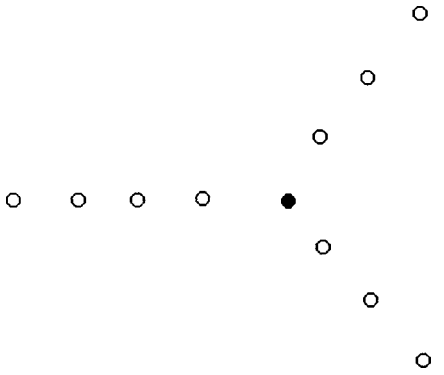

FIG. 1. Ideal model of a point contact between one-dimensional conductors. Each atom, including the central atom, has one *s* orbital. In the continuous model the chains of atoms are replaced by narrow channels with infinitely high potential walls.

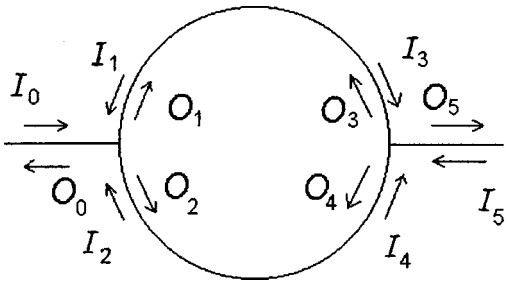

FIG. 2. Aharonov–Bohm ring with two contacts (branch points). The arrows show waves propagating in the elements of the circuit. The length of a semicircle is l, and the magnetic flux through the ring is Φ.

tirely clear that the boundary condition stipulating continuity of the total wave function can be extended to the longitudinal part of the propagating fundamental mode. Unfortunately, systematic estimation of the role of the damped modes is possible only for specific contacts and only by numerical methods (see, for example, Ref. 9). On the other hand, a sequence of limiting transitions (the tendency of the transverse dimensions of the conductors toward zero and the tendency of the particle energy toward infinity), for which the contribution of the damped modes can be neglected, unquestionably exists. In this case the continuity of the longitudinal part, i.e., the one-dimensional function, follows from the continuity of the total wave function. An example of a system with a wave function that is continuous at a contact is provided by the model depicted in Fig. 1. The chains of atoms have one common contact atom. Each atom corresponds to one electronic state (for example, an *s* orbital). Clearly, the wave function in the tight-binding approach for this problem, which is defined as

$$\Psi(\mathbf{r})=\sum_i e^{i\mathbf{k}\cdot\mathbf{r}_i}\phi(\mathbf{r}-\mathbf{r}_i), \tag{1}$$

where $\mathbf{r}$ denotes the coordinates of the atoms, will be continuous. It is easy to see that there are no analogs of damped modes in such a model. This alone ensures continuity. Summarizing the foregoing statements, we claim that the one-dimensional wave function is continuous for a definite special class of one-dimensional conductors and point contacts. In this paper we shall consider only this type of model.

It should be noted that there have been numerous publications in which the continuity of wave functions was postulated. In addition, such continuity is supplemented by the condition of equality to zero of the sum of derivatives with respect to directions of the conductors

$$\sum_{i=1}^{n}\psi_i'=0, \tag{2}$$

which is interpreted as the particle flux conservation condition. These conditions taken together are called Griffith's conditions.[10] It is easy to see, however, that the condition (2) does not coincide with the flux conservation condition, which, unlike, (2) is bilinear with respect to the wave functions. As will be shown below, Griffith's conditions are stricter and uniquely specify the scattering matrix, while flux conservation, time-reversal symmetry, and continuity of the wave functions leave one real parameter free.

Below, in Sec. 1, we shall examine the possible parametrization of the scattering matrix for our model and show that all the elements of the scattering matrix are determined by a single real parameter. The correspondence of our results to Griffith's boundary conditions, as well as to the known solutions of several quantum-mechanical problems, is also explored. In Sec. 2 we use the results to investigate the form of the conductance oscillations of an Aharonov–Bohm ring as an example (Fig. 2). In the concluding paragraph we summarize the main results of this study.

1. SCATTERING MATRIX

Moving on to the treatment of a specific model, we introduce the one-dimensional coordinates x_i, which are defined on the half-lines $[0,\infty)$. All the points $x_i=0$ are identical. The potential energies are constant along the entire length of the conductors up to the contact at $x=0$, but they can have a discontinuity in the contact itself. We represent the wave functions in the wires in the form

$$\Psi_i(x)=\frac{O_i}{\sqrt{k_i}}\exp(ik_ix)+\frac{I_i}{\sqrt{k_i}}\exp(-ik_ix), \tag{3}$$

where $k_i=\sqrt{2m(E-U_i)/\hbar^2}$ is the wave vector in the ith channel (the wave vectors in identical channels are identical), E is the energy, U_i are the constant potential energies in the conductors, and x is the coordinate measured from the contact along a conductor. We stress that, according to our assumption regarding the insignificance of the damped modes, the representation (3) is valid along an entire conductor up to the contact. The continuity of the wave functions in the contact is expressed by the equations

$$\frac{O_i+I_i}{\sqrt{k_i}}=\frac{O_{i+1}+I_{i+1}}{\sqrt{k_{i+1}}} \tag{4}$$

for $i=1,2,\ldots,n-1$. The scattering matrix expresses the scattered waves in terms of the incident waves:

$$\mathbf{O}=\hat{S}\cdot\mathbf{I}, \tag{5}$$

where the n-component vectors **O** and **I** are composed of scattered and incident amplitudes. Flux conservation and time-reversal symmetry lead to the unitarity and symmetry of the scattering matrix in the usual manner. To study the consequences of the continuity of the wave functions, let us consider the case of identical conductors first and then the general case of different U_i. We, first of all, show that the scattering matrix has only two unequal elements. Let there be an incident wave of unit amplitude only in the first conductor. Then, from Eqs. (4) and (5) we have

$$S_{11}+1=S_{12}=S_{13}=\ldots S_{1n}. \tag{6}$$

Similarly, considering the second conductor, we arrive at the relations

$$S_{12}=S_{22}+1=S_{23}=\ldots S_{2n}. \tag{7}$$

The first equalities in (6) and (7) give $S_{11}=S_{22}$, and the last ones lead to equality of the off-diagonal elements. Continuing this process, we arrive at the conclusion that the matrix has the form

$$\begin{Bmatrix} S_1 & S_2 & \ldots & S_2 \\ S_2 & S_1 & \ldots & S_2 \\ \vdots & \vdots & \ddots & \vdots \\ S_2 & S_2 & \ldots & S_1 \end{Bmatrix}, \tag{8}$$

where S_1 and S_2 satisfy the equations

$$S_1+1=S_2, \tag{9}$$

$$S_1^*S_1+(n-1)S_2^*S_2=1, \tag{10}$$

the former of which is a consequence of (6) and (7), while the latter is a consequence of the unitarity condition. We note that Eqs. (9) and (10) ensure satisfaction of the second of the unitarity conditions, which calls for the orthogonality of different columns. However, the inverse statement is incorrect: the two unitarity conditions do not ensure satisfaction of Eq. (9). From Eqs. (9) and (10) we find

$$S=\frac{2}{n}\cos\varphi,$$

$$\mathrm{Re}\,S_1=\frac{2}{n}\cos^2\varphi-1, \quad \mathrm{Im}\,S_1=\frac{\sin 2\varphi}{n}, \tag{11}$$

where S and φ are the amplitude and phase of S_2. Equations (11) show that the phase of the off-diagonal elements, which are all identical for identical channels, is the only free parameter. The value of φ is determined by the energy and the geometric properties of the contact.

Of course, the existence of contacts having different values of φ is possible. Contacts with the maximum transmission coefficient correspond to the value $\varphi=0$. In this case the elements of the scattering matrix depend only on the number of conductors connected: $S_1=(2-n)/n$, $S_2=2/n$. The same result can be attained by assuming fulfillment of the linear condition (2), instead of the flux conservation condition, which is bilinear with respect to the amplitudes. In fact, this means that the use of the linear condition (2) is possible only for contacts of a fairly special form, viz., those with the highest conducting properties.

The method used above is also applicable to the case of channels having unequal potential energies: the entire difference is confined to the unequal values of the wave vectors. An analysis of the continuity and unitarity conditions in this case leads to parametrization of the scattering matrix in the following form:

$$\begin{Bmatrix} k_1t-1 & \sqrt{k_1k_2}t & \ldots & \sqrt{k_1k_n}t \\ \sqrt{k_1k_2}t & k_2t-1 & \ldots & \sqrt{k_2k_n}t \\ \vdots & \vdots & \ddots & \vdots \\ \sqrt{k_1k_n}t & \sqrt{k_2k_n}t & \ldots & k_nt-1 \end{Bmatrix}, \tag{12}$$

where the complex parameter t is defined by the equations

$$|t|=\frac{2\cos\varphi}{\Sigma_{i=1}^{n}k_i}, \quad \varphi=\arg(t). \tag{13}$$

As in the preceding case, the value $\varphi=0$ corresponds to free propagation.

We note that the transmission probability for $n=3$ and $\varphi=0$ is equal to 4/9, which coincides with the result for the tight-binding model[11] for energies near the center of the band in the range $|E|\ll 6$ (where the overlap integral determining the width of the one-dimensional band was set equal to unity). This conclusion can easily be generalized to arbitrary n. In fact, for the transmission and reflection coefficients (t and r) we have the system of equations

$$1+r=t, \tag{14}$$

$$(E-E_0)t=\exp(-ik)+r\exp(ik)+t(n-1)\exp(ik), \tag{15}$$

where the first equality is the continuity condition, the second equality is the tight-binding equation for the contact atom, and the interatomic distance is set equal to unity. From this system we have

$$t=\frac{-2i\sin k}{(2-n)\cos k-in\sin k}, \tag{16}$$

where we used the expression $E-E_0=2\cos k$. Hence for $|E|\ll 2n/|2-n|$ it follows that the transmission probability coincides with the result (11) when $\varphi=0$.

When $n=2$ and $\varphi=0$, Eq. (11) corresponds to free one-dimensional propagation. When $n=2$ and $\varphi=0$, Eqs. (12) and (13) describe the scattering of a one-dimensional particle on a step (in agreement with Ref. 12). When $n=2$ and $\varphi=\arctan(\Omega/k)$, formula (11) describes scattering on a one-dimensional δ-function potential: $U(x)=\hbar^2\Omega\,\delta(x)/m$ (Ref. 13).

We should also mention several unusual properties of the results obtained, which are a consequence of the one-dimensional character of the conductors and the point-like character of the contact. First of all, as $n\to\infty$, the probability of reflection from the contact tends to unity: the more conductors are connected to the contact, the higher is the probability of reflection from it! Another paradoxical property is the lack of a dependence of the scattering matrix on the

angles between the conductors, which is a direct consequence of assuming continuity for the one-dimensional wave functions. Moreover, numerical calculations for the special case of a *T*-shaped (patently asymmetric) contact directly point to a lack of a dependence of the transmission coefficients on direction in the limit $ka \ll 1$ (Ref. 9), which can be regarded as confirmation of the continuity of the wave function in the contact in this limit. We also note that, in this limit the numerical results give $|r|=1$ and $t=0$, which correspond to Eqs. (11) with $n=3$ and $\varphi=\pi/2$. The latter means that Griffith's conditions are not satisfied in this limit. The lack of a dependence of the scattering matrix on the angles for a contact joining chains of atoms with *s* orbitals is obvious from the solution procedure itself.

2. AHARONOV–BOHM OSCILLATIONS

Let us consider the system of conductors that is depicted in Fig. 2 and is usually used to account for the occurrence of the Aharonov–Bohm effect. In the usual explanation it is assumed that the output wave function ψ_5 is proportional to the sum of the wave functions before entry into the contact, i.e., $\psi_3+\psi_4$. The source of this erroneous assumption is the incorrect use of the Feynman rule for summing amplitudes corresponding to different trajectories (only the two trajectories, one along the upper arm and one along the lower arm, are used). In fact, an infinite number of topologically different trajectories with different speeds around the ring should be used. This can be effectively accomplished by writing equations for the amplitudes of the waves in the conductors and then solving them. The latter permits finding the transmission coefficient of electrons through a ring with an enclosed magnetic flux Φ and then, using Landauer's formula, the conductance and its dependence on the magnetic flux.

Using the notation in Fig. 2 and a relation of the type (8), we obtain the following system of equations for the amplitudes:

$$\begin{pmatrix} O_0 \\ O_1 \\ O_2 \end{pmatrix} = \begin{Bmatrix} r & t & t \\ t & r & t \\ t & t & r \end{Bmatrix} \begin{pmatrix} I_0 \\ I_1 \\ I_2 \end{pmatrix}, \tag{17}$$

$$\begin{pmatrix} O_3 \\ O_4 \\ O_5 \end{pmatrix} = \begin{Bmatrix} r & t & t \\ t & r & t \\ t & t & r \end{Bmatrix} \begin{pmatrix} I_3 \\ I_4 \\ I_5 \end{pmatrix}, \tag{18}$$

$$\begin{pmatrix} I_1 \\ I_3 \end{pmatrix} = \begin{Bmatrix} 0 & \exp(ikl-i\alpha) \\ \exp(ikl+i\alpha) & 0 \end{Bmatrix} \begin{pmatrix} O_1 \\ O_3 \end{pmatrix}, \tag{19}$$

$$\begin{pmatrix} I_2 \\ I_4 \end{pmatrix} = \begin{Bmatrix} 0 & \exp(ikl+i\alpha) \\ \exp(ikl-i\alpha) & 0 \end{Bmatrix} \begin{pmatrix} O_2 \\ O_4 \end{pmatrix}. \tag{20}$$

Here r and t are the complex reflection and transition coefficients for branching, which is assumed to be symmetric with respect to the arms. In Eqs. (19) and (20) we regard the arms of the ring as ballistic conductors of length l (kl is the phase trajectory along a half-ring, $\alpha=(\Phi/\Phi_0)\pi$, Φ is the magnetic flux passing through the ring, and $\Phi_0=hc/e$ is the magnetic flux quantum).

Taking the amplitude of the wave incident from the left as unity ($I_0=1$) and the amplitude of the wave incident from the right as zero ($I_5=0$), we arrive at an inhomogeneous system of equations, which can easily be solved. The amplitude of the transmitted wave $O_5=t(I_3+I_4)$ specifies the complex transmission coefficient f:

$$f=2t^2\cos\alpha\,\frac{e^{-ikl}-e^{ikl}(t-r)^2}{e^{-2ikl}+e^{2ikl}(t-r)^2(t+r)^2-2r^2-2t^2\cos 2\alpha}. \tag{21}$$

Taking into account that the conductance of the system is proportional to $|f|^2$, we can account for its dependence on magnetic field (on α). It can be seen from (21) that the multiplier $\cos\alpha$ in front of the fraction leads to ordinary Aharonov–Bohm oscillations with a period Φ_0 (a $1+\cos 2\alpha$ dependence). The square of the modulus of the fraction from (21) gives the additional modulation of the conductance with the magnetic field owing to the last term in the denominator. Just this dependence is also a consequence of taking into account the trajectories with nonzero speeds around the ring.

We have hitherto utilized only the branching symmetry, but not the continuity of the wave function. This continuity can be expressed by Eq. (8): $t-r=1$. Substituting this equality into (21), we obtain the following expression for the transmission coefficient:

$$f=\frac{-4it^2\cos\alpha\sin kl}{e^{-2ikl}+e^{2ikl}(2t-1)^2-2(t-1)^2-2t^2\cos 2\alpha}. \tag{22}$$

It can be seen from (22) that f and, therefore, the conductance tend to zero as $kl\to 0$ in this case. The latter takes place near the threshold where the fundamental mode is converted from a damped mode to a propagating mode. It is important to stress that the conductance vanishes at the threshold for the appearance of the first allowed channel only if $t-r=1$, i.e., only if the one-dimensional wave function is continuous. Otherwise, a finite conductance appears abruptly in the system. Thus, the different behaviors of the conductance at the threshold can be used to experimentally test the hypothesis of continuity of the wave function.

In conclusion, let us recount the main results of this study. The scattering matrix of a point contact between one-dimensional conductors is parametrized by a single real parameter φ. The concrete values of this parameter are determined both by the geometry of the contact and by the energy of the incident particles. The most conductive contacts have $\varphi=0$. The linear condition (2), i.e., Griffith's condition, can be used instead of the bilinear flux conservation condition only in this case. When the correct boundary conditions at the sites of connection of the conductors are used, the Aharonov–Bohm oscillations exhibit a complicated magnetic-field dependence: there are multiple harmonics in addition to the fundamental harmonic with a period Φ_0. The energy dependence of the conductance at the threshold for the appearance of the first conducting channel can be used to test the hypothesis of continuity of the wave function.

We express our thanks to V. M. Édel'shteĭn for some fruitful discussions and for turning our attention to Ref. 9.

This work was supported by the Russian Fund for Fundamental Research (Grant No. 98-02-16640).

*)E-mail: Ryzhkin@issp.ac.ru

[1] Y. Gefen, Y. Imry, and M. Ya. Azbel, Phys. Rev. Lett. **52**, 139 (1984).
[2] N. Buttiker, Y. Imry, and R. Landauer, Phys. Lett. A **96**, 365 (1983).
[3] Y. Avishai and J. M. Luck, Phys. Rev. B **45**, 1074 (1992).
[4] M. Kohmoto, Preprint, Technical Report of ISSP, Tokyo, Japan (1993).
[5] P. M. Bell and A. MacKinnon, Phys. Rev. B **51**, 9544 (1995).
[6] B. Shapiro, Phys. Rev. Lett. **50**, 747 (1983).
[7] M. Buttiker, Y. Imry, and M. Ya. Azbel, Phys. Rev. A **30**, 1983 (1984).
[8] D. Takai and K. Ohta, Phys. Rev. B **48**, 14 318 (1993).
[9] J. L. Bohn, Phys. Rev. B **56**, 4132 (1997).
[10] S. Griffith, Trans. Faraday Soc. **49**, 345 (1953); **49**, 650 (1953).
[11] J. L. D'Amato, H. M. Pastawski, and J. F. Weisz, Phys. Rev. B **39**, 3554 (1989).
[12] L. D. Landau and E. M. Lifshitz, *Quantum Mechanics: Non-Relativistic Theory*, 2nd ed. (Pergamon Press, Oxford–New York, 1965; Fizmatgiz, Moscow, 1963).
[13] S. Flügge, *Practical Quantum Mechanics* (Springer-Verlag, Berlin, 1971; Mir, Moscow, 1974).

Translated by P. Shelnitz

Electronic structure and spectral properties of nickel disilicide films

N. S. Pereslavtseva and S. I. Kurganskiĭ

Voronezh State University, 394693 Voronezh, Russia
(Submitted November 16, 1998; resubmitted March 2, 1999)
Fiz. Tverd. Tela (St. Petersburg) **41**, 2075–2080 (November 1999)

The film version of the linearized augmented plane-wave method is used to calculate the electronic structure, total and local partial electron densities of state, and photoelectron and x-ray emission spectra of various series for all the inequivalent atoms in a nickel disilicide film. Comparison of the results obtained with known experimental data permits interpretation of the special features of the spectral properties of this material. © *1999 American Institute of Physics.* [S1063-7834(99)03411-5]

Transition-metal silicides are interesting because of their use in integrated circuits to create Schottky barriers and ohmic contacts, in heterostructures on single-crystal silicon, and in epitaxial silicide films.[1,2] Consequently, silicides have been actively studied by both experimental and theoretical methods. Interesting, sometimes contradictory results have been obtained, and some of them have not been heretofore properly explained.

The experimental investigation of nickel disilicide $NiSi_2$ in Ref. 3 revealed significant differences in the Si $L_{2,3}$ spectra for bulk and film samples, particularly a strong increase in the intensity of the peak near the Fermi level (E_F) for a $NiSi_2$ film in comparison to a bulk sample. This phenomenon was subsequently confirmed by a whole series of experimental studies.[4–9] However, the attempts to account for the observed effect on the basis of theoretical calculations of the electronic structure of a bulk crystal of nickel disilicide[4,6,7,9–17] cannot be considered satisfactory as a whole, since, although these calculations gave qualitatively correct results for a bulk crystal, they did not answer the main question regarding the transformation of the spectrum upon the transition to a film sample, and the electronic structure of $NiSi_2$ films has not previously been studied by theoretical methods.

In this paper we describe the first theoretical investigation of the electronic structure of nickel disilicide films and interpret empirical results on its basis.

1. CALCULATION METHOD

The linearized augmented plane-wave method, whose formalism was described in detail in Ref. 18 was used to calculate the electronic structure of the films. The eigenfunctions $\Psi_{i,k}(r)$ and the energy eigenvalues $E_i(\mathbf{k})$ obtained as result of a band calculation were used to calculate such characteristics as the density of states

$$n(E)=\frac{2}{S_{\mathrm{BZ}}}\sum_i \int_{S_{\mathrm{BZ}}} \delta(E-E_i(\mathbf{k}))\, d\mathbf{k} \tag{1}$$

(i is the number of the energy band, and S_{BZ} is the area of the two-dimensional Brillouin zone), the x-ray emission spectra, whose intensity has the form

$$I(E)=\frac{2}{S_{\mathrm{BZ}}}\sum_i \int_{S_{\mathrm{BZ}},E_i(\mathbf{k})\leqslant E_F} M_i^2(\mathbf{k})\,\delta(E-E_i(\mathbf{k})+E_c)\, d\mathbf{k} \tag{2}$$

[$M_i^2(\mathbf{k})$ is the matrix element of the probability of an x-ray transition, and E_c is the energy of the ground state to which the transition goes], and the photoelectron spectra, whose intensity can be represented in the form

$$I(E,\omega)=\frac{2}{\pi}\mathcal{K}\left|\frac{A}{\omega c}\right|^2\sum_{s,l}\sigma_l^s(E,\omega)n_{sl}(E) \tag{3}$$

[$\hbar\omega$ is the excitation energy, σ_l^s is the photoionization cross section, n_{sl} is the local partial electron density of states, and A is the vector potential].

The integration over the two-dimensional Brillouin zone in these expressions was carried out by a combined triangle integration scheme,[19] the calculation of the x-ray emission spectra was described in detail in Ref. 20, and the calculation of the photoelectron spectra in Ref. 21.

In films the presence of a surface leads to disappearance of the periodicity of the structure in the z direction, perpendicular to the surface. Thus, translational symmetry is maintained only in the XY plane, which is parallel to the film surface. Consequently, the Bravais lattice for a film becomes two-dimensional (there are only 5 kinds of two-dimensional Bravais lattices, as compared to the 14 three-dimensional counterparts[22]). Therefore, the unit cell of a film, which can be defined, as for crystals, as the volume of space that, after being subjected to all the translations of the Bravais lattice, fills all space without ever overlapping itself or leaving gaps, becomes infinite in the z direction, i.e., along a normal to the film surface.

A (001) $NiSi_2$ film, for which we performed the calculation of the spectral characteristics, has a cubic structure of the fluorite (CaF_2) type with the lattice constant $a_0=5.4066$ Å (Refs. 23 and 24). The calculation was performed for two variants of the film structure: with a surface consisting of Si atoms (the film of type I) and with a surface consisting of Ni atoms (the film of type II). The thickness of the film of type I without allowance for the vacuum regions is 13.5165 Å, which corresponds to two unit cells of the bulk crystal plus two additional silicon surface layers, and the

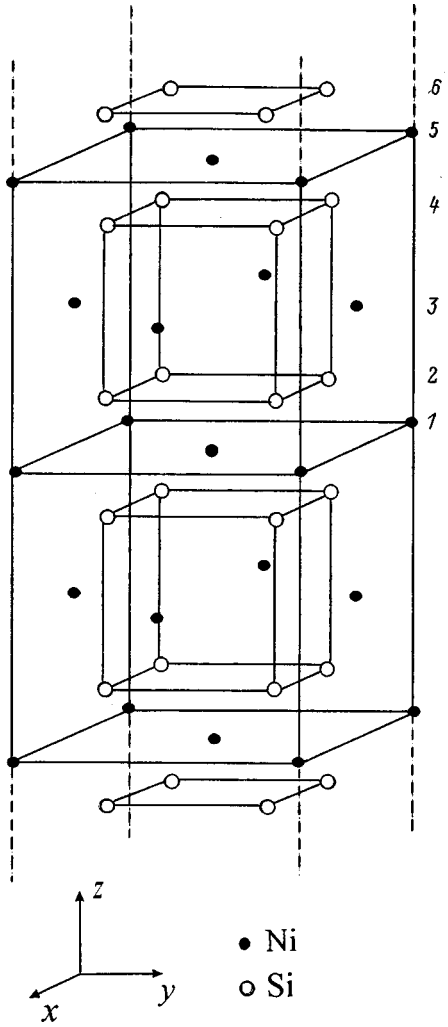

FIG. 1. Unit cell of a (001) nickel disilicide film. Film of type I: *1*, *3*, and *5* — central, intermediate, and near-surface nickel layers; *2*, *4*, and *6* — internal, intermediate, and surface silicon layers. Film of type II: *1*, *3*, and *5* — central, intermediate, and surface nickel layer; *2* and *4* — internal and near-surface silicon layers.

thickness of the film of type II is 10.8132 Å, which corresponds to two unit cells of the bulk sample. Figure 1 presents the unit cell of the film of type I, and the unit cell of the film of type II is obtained from it by removing the silicon surface layers (the symbols used to represent the atoms are shown in the caption to the figure).

2. RESULTS AND DISCUSSION

Figures 2 and 3 present the local partial electron density of states on the Ni and Si atoms, respectively, in the film of type I. As can be seen from Fig. 2, the *s* and *p* partial densities of states at the Ni atoms are distributed over the entire valence band, and their contribution to the total local electron density of states at the Ni atoms is significantly smaller than the contribution from the energetically more localized *d* density of states, whose principal peak is 3.2 eV below E_F. The Si *s* states are concentrated in two energy ranges: 6–12 and 0–2 eV below E_F; as the surface is approached, the principal maximum in the former range shifts toward E_F due to the decrease in the depth of the potential well for electrons in the surface layers, and the *s* density of states increases in the latter range. As the surface is approached, the principal maximum of the local Si *p* partial density of states also shifts slightly toward E_F and decreases in height, and the *p* density of states near E_F simultaneously increases somewhat.

Figure 4 presents the photoelectron spectra of a $NiSi_2$ film that we calculated for various values of the excitation energy $\hbar\omega$ and compares them with the experimentally obtained spectra,[10,12,25] and Table I indicates the position of the principal peak in these spectra. As follows from the calculation, the principal peak in these spectra is caused by the Ni *d* states, and its distance from E_F increases from 3.19 to 3.3 eV as the excitation energy is increased from 12 to 120 eV. At small values for the energy of the incident photons (12–17 eV), small humps can be identified in the spectra at 0–2 and 7–8 eV below E_F, which correspond to the Si *s* states. As $\hbar\omega$ is increased from 21 to 30 eV, these humps gradually vanish, since the photoionization cross section for the Ni *d* states increases more rapidly with increasing excitation energy than does the photoionization cross section for the Si *s* states, and the contribution of the Ni *d* states is thus significantly greater. Already at $\hbar\omega = 40$ eV the spectra obtained correspond only to the Ni *d* states.

We calculated the x-ray emission spectra of various series for all the atoms in the films of both types. Figures 5–7 compare them with the available experimental spectra.[5,6,8,9] The Si $L_{2,3}$ spectra shown in Fig. 5 arouse the greatest interest. In accordance with the dipole selection rules, these spectra reflect the distribution of the Si *s* and *d* states in the valence band. As follows from the calculation, the maxima at $\sim 8-10$ and 1 eV below E_F are caused by the *s* states, and the peak near 3.2 eV is caused by the *d* states, the relative intensity of the latter being small, since the transition probability matrix element for the *s* states is approximately an order of magnitude greater than the matrix element for the *d* states. In other words, the Si $L_{2,3}$ spectra are caused predominantly by the *s* states. However, a comparison of these spectra with the corresponding local *s* partial density of states shows that the intensity of the maximum near the Fermi level relative to the maximum at $\sim 8-10$ eV in the x-ray spectrum is greater than the value for the corresponding *s* partial density of states. This is because the transition probability matrix element increases monotonically with increasing energy. Therefore, the features of the electron density of states in the emission spectrum are displayed more strongly near the Fermi level than far from E_F.

The changes occurring in the peak at ~ 1 eV merit special attention. According to our calculations, as the surface is approached, its relative intensity increases considerably in the film of type I, while it decreases in the film of type II. This fact can be explained in the following manner. The Si–Ni interatomic distances in nickel disilicide [2.3411 Å (Refs. 23 and 24)] are smaller than the Ni–Ni distances in a crystalline film [2.48 Å (Refs. 26 and 27)] and the Si–Si distances in both crystalline silicon [2.68 Å (Refs. 26 and 27)] and nickel disilicide [2.7033 Å (Refs. 23 and 24)]. The sum of the atomic radii of Si and Ni [2.58 Å (Refs. 23 and 24)] is also somewhat greater than the Si–Ni interatomic distance in $NiSi_2$. Therefore, when the silicon and nickel

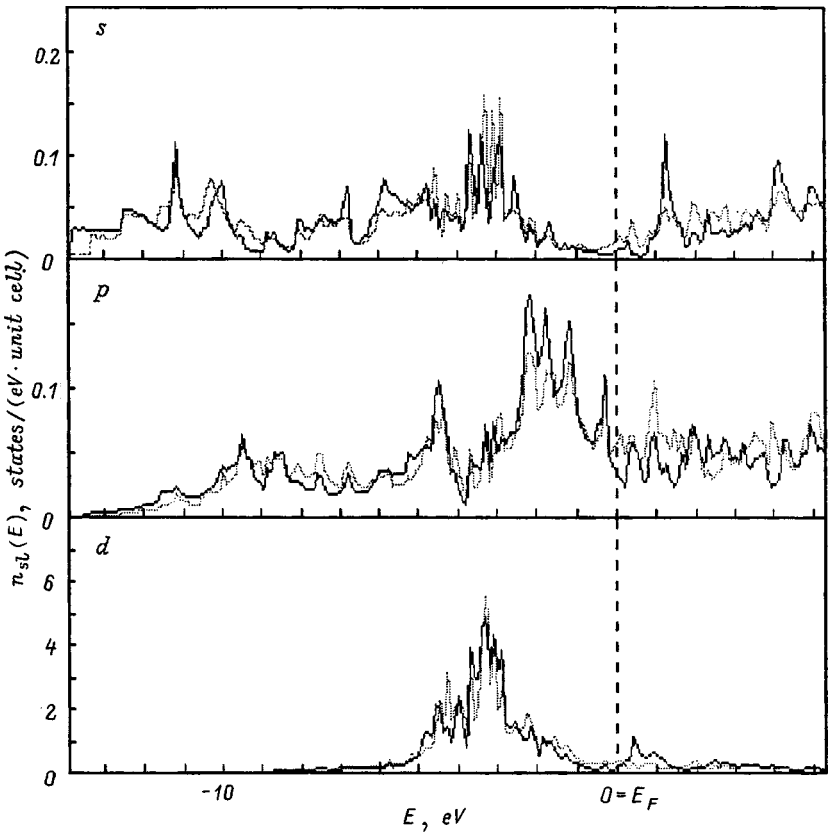

FIG. 2. Local *s*, *p*, and *d* partial densities of states at Ni atoms in a film of type I: solid line — density of states at atoms in the central layer, dashed line — density of states at the near-surface layer.

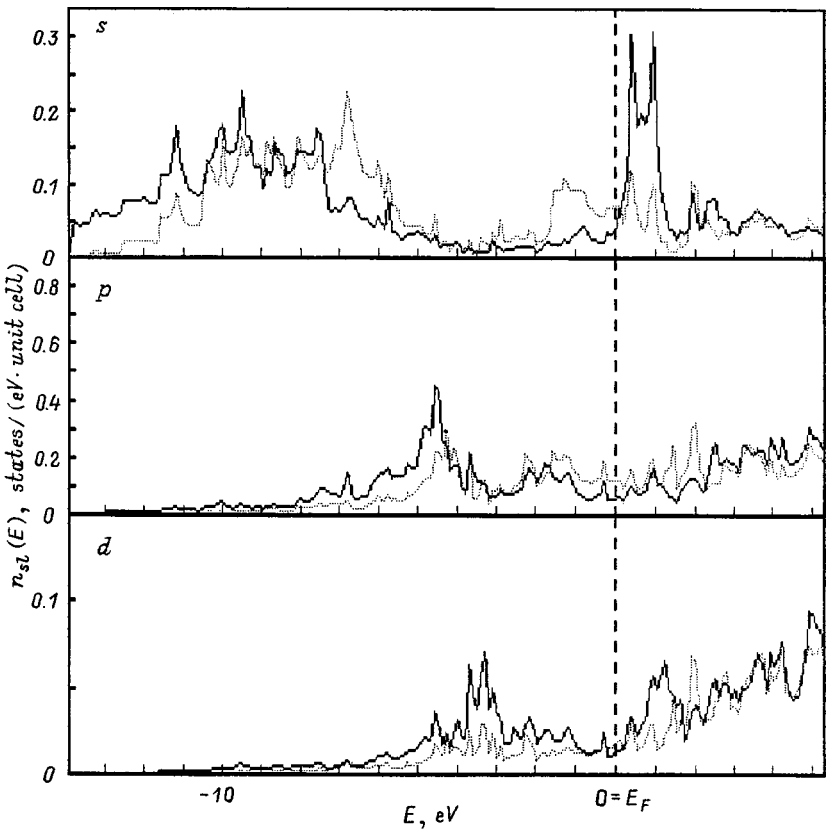

FIG. 3. Local *s*, *p*, and *d* partial densities of states on Si atoms in a film of type I: solid line — density of states at atoms in an internal layer, dashed line — density of states at the surface layer.

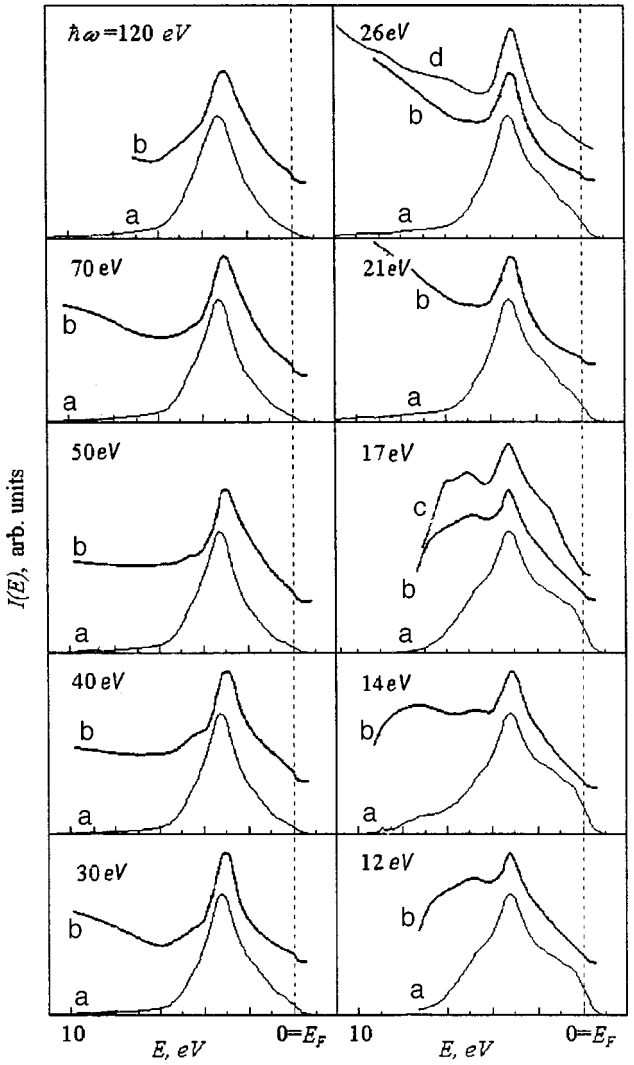

FIG. 4. Photoelectron spectra of $NiSi_2$ for various values of the energy of the incident photons $\hbar\omega$: a — present calculation; b, c, d — experiments in Refs. 10,12, and 24, respectively.

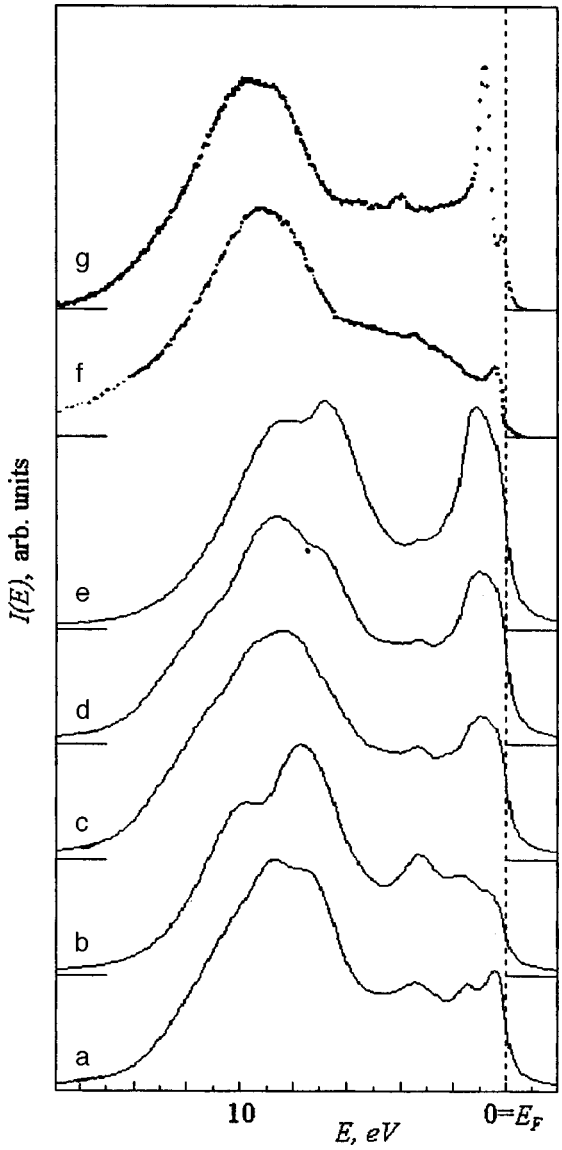

FIG. 5. Si $L_{2,3}$ x-ray emission spectra: a, b — atoms of internal and near-surface layers in a film of type II; c, d, e — atoms of internal, intermediate, and surface layers in a film of type I; f, g — experiments in Refs. 5 and 9 for bulk and film samples of $NiSi_2$, respectively.

atoms are joined in a nickel disilicide crystal, the wave functions of the valence electrons of the Si atoms ''overlap'' the Ni atoms, and an effective positive charge forms on the Si atoms, while an effective negative charge forms on the Ni atoms, as is confirmed by the experiment in Ref. 4. Thus, experiment and theory show that the transfer of electronic charge from Si atoms to Ni atoms occurs in a bulk crystal. In the film of type I, whose surface consists of Si atoms, the situation is somewhat different. While the internal Si atoms coordinated by Ni atoms are exactly the same as in a bulk

TABLE I. Position (eV) of the principal peak in the photoelectron spectra for various values of the excitation energy $\hbar\omega$ (eV).

$\hbar\omega$	12	17	26	120
Present calculation	3.19	3.19	3.24	3.30
Ref. 10	3.09	3.10	–	–
Ref. 12	2.88±0.5	2.94±0.5	2.91±0.5	–
Ref. 24	3.15	3.15	3.15	3.15

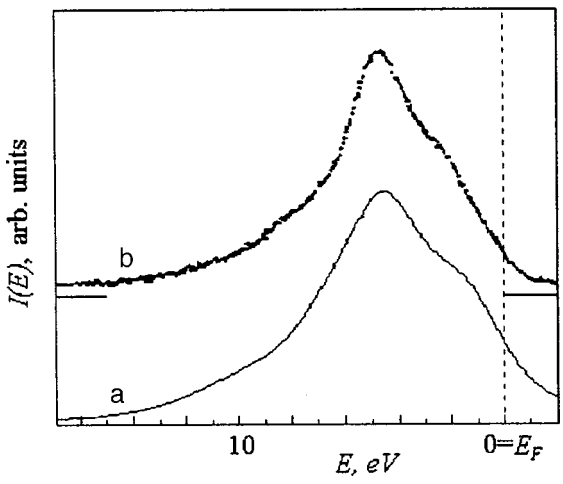

FIG. 6. Si $K\beta$ x-ray emission spectra of $NiSi_2$: a — present calculation, b — experiment in Ref. 6.

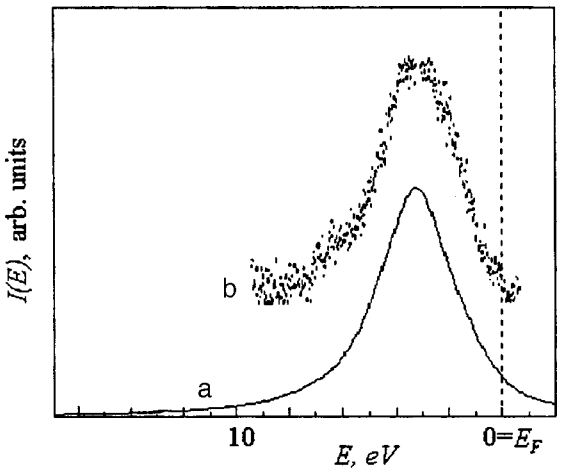

FIG. 7. Ni $M_{2,3}$ x-ray emission spectra of $NiSi_2$: a — present calculation, b — experiment in Ref. 8.

crystal, the surface Si atoms come into contact with Ni atoms only on one side (Fig. 1), and, therefore, a smaller number of electrons passes from Si to Ni in this case. Thus, we can now understand why the surface Si atoms have a larger effective electronic charge than do the bulk counterparts, i.e., why the electron density of states at Si near E_F increases as the surface is approached. These qualitative arguments explain the increase in the density of *s* states in the near-Fermi region for surface Si atoms in comparison to the bulk atoms, which is clearly displayed in Fig. 3. As a result, the intensity of the $L_{2,3}$ spectra near E_F for the surface Si atoms increases in comparison to the intensity for the internal atoms, as can be seen from Figs. 5c–e.

The results of the calculations of the $L_{2,3}$ x-ray spectra for Si atoms in the film of type II provide one more qualitative argument in support of our arguments. In this case we are dealing with a diametrically opposite situation: each surface Ni atom, being surrounded by Si atoms on only one side, draw off a larger number of electrons from an Si atom than do the bulk counterparts. Thus, as the surface is approached, the *s* density of states below the Fermi level for the Si atoms decreases, and the intensity of the peak near E_F consequently drops, as can be seen clearly in Figs. 5a and 5b.

We also note that no appreciable change in the shape of the spectra of the other series of Si and Ni atoms is observed as the surface is approached. This is reflected in Figs. 6 and 7 and occurs because the Si *s* states and thus any variations in their density are manifested only in the $L_{2,3}$ spectra. In addition, the comparatively small change in the *s* density of states near E_F is enhanced in these spectra because of the relatively large value of the transition probability matrix element in this region.

The films of types I and II that we considered are models of the two possible variants for realization of the structure of $NiSi_2$: with an excess or deficiency of Si atoms in comparison to Ni, respectively. As follows from our calculations, the relatively low intensity of the Si $L_{2,3}$ spectra of the bulk crystals in the vicinity of E_F is caused by the fact that bulk nickel disilicide crystals always have some deficiency of silicon.[28] The increase in the intensity of this peak for the film samples is attributed to an increase in the percentage content of Si relative to Ni and the appearance of superstoichiometric silicon.

[1] E. L. Sakovich, V. P. Lesnikova, L. Ya. Portnov, T. V. Makarevich, and V. V. Baranov, Poverkhnost', No. 3, 44 (1994).
[2] V. N. Chernyaev, *Technology and Manufacture of Integrated Microcircuits and Microprocessors*, Radio i Svyaz', Moscow (1987), 464 pp.
[3] É. P. Domashevskaya, Yu. A. Yurakov, V. M. Andreeshchev, and S. M. Karal'nik, Metallofizika (Kiev) **2**(5), 24 (1980).
[4] S. V. Vlasov, É. P. Domashevskaya, A. G. Narmonev, G. G. Popov, O. V. Farberovich, and Yu. A. Yurakov, Metallofizika (Kiev) **9**(3), 97 (1987).
[5] H. Nakamura, M. Iwami, M. Hirai, M. Kusaka, F. Akao, and H. Watabe, Phys. Rev. B **41**, 12 092 (1990).
[6] P. J. W. Weijs, G. Wiech, W. Zahorowski, and K. H. J. Buschow, Phys. Scr. **41**, 629 (1990).
[7] P. J. W. Weijs, M. T. Czyzyk, J. F. van Acker, W. Speier, J. B. Goedkoop, H. van Leuken, H. J. M. Hendrix, R. A. de Groot, G. van der Laan, K. J. H. Buschov, G. Wiech, and J. C. Fuggle, Phys. Rev. B **41**, 11 899 (1990).
[8] J. J. Jia, T. A. Callcott, W. L. O'Brien, Q. Y. Dong, J.-E. Rubensson, D. R. Mueller, D. L. Ederer, and J. E. Rowe, Phys. Rev. B **43**, 4863 (1991).
[9] P. J. W. Weijs, H. van Leuken, R. A. de Groot, J. C. Fuggle, S. Reiter, G. Wiech, and K. H. J. Buschov, Phys. Rev. B **44**, 8195 (1991).
[10] Y. I. Chabal, D. R. Hamann, I. E. Rowe, and M. Schluter, Phys. Rev. B **25**, 7598 (1982).
[11] D. M. Bylander, L. Kleinman, K. Mednick, and W. R. Grise, Phys. Rev. B **26**, 6379 (1982).
[12] Yu.-J. Chang and J. L. Erskine, Phys. Rev. B **26**, 7031 (1982).
[13] J. Tersoff and D. R. Hamann, Phys. Rev. B **28**, 1168 (1983).
[14] J. H. Weaver, A. Franciosi, and V. L. Moruzz, Phys. Rev. B **29**, 3293 (1984).
[15] O. Bisi, L. W. Chano, and K. N. Tu, Phys. Rev. B **30**, 6009 (1984).
[16] O. Bisi, Mater. Res. Soc. Symp. Proc. **54**, 13 (1986).
[17] W. Speier, E. van Leuken, J. C. Fuggle, D. D. Sarma, L. Kumar, B. Dauth, and K. H. J. Buschov, Phys. Rev. B **39**, 3293 (1989).
[18] H. Krakauer, M. Posternak, and A. J. Freeman, Phys. Rev. B **19**, 1706 (1979).
[19] S. I. Kurganskii, O. I. Dubrovskii, and E. P. Domashevskaya, Phys. Status Solidi B **129**, 293 (1985).
[20] S. I. Kurganskii, M. A. Kharchenko, O. I. Dubrovskii, A. M. Bugakov, and E. P. Domashevskaya, Phys. Status Solidi B **185**, 179 (1994).
[21] E. R. Likhachev and S. I. Kurganskiĭ, Izv. Akad. Nauk, Ser. Fiz. **61**, 996 (1997).
[22] M. P. Shaskol'skaya, *Crystal Chemistry*, 2nd edn. (Vysshskaya Shkola, Moscow, 1984), 376 pp.
[23] E. I. Gladyshevskiĭ, *Crystal Chemistry of Silicides and Germanides* (Metallurgiya, Moscow, 1971), 296 pp.
[24] P. V. Gel'd and F. A. Sidorenko, *Transition Metal Silicides* (Metallurgiya, Moscow, 1972), 574 pp.
[25] A. Franciosi, J. H. Weaver, and F. A. Schmidt, Phys. Rev. B **26**, 546 (1982).
[26] *A Chemist's Handbook*, 2nd edn., Vol. 1, edited by B. P. Nikol'skiĭ (Khimiya, Leningrad, 1966), 1071 pp.
[27] V. G. Ormont, *Introduction to the Physical Chemistry and Crystal Chemistry of Semiconductors* (Vysshskaya Shkola, Moscow, 1982), 528 pp.
[28] G. V. Samsonov, L. A. Dvorina, and B. M. Rud', *Silicides* (Metallurgiya, Moscow, 1979), 271 pp.

Translated by P. Shelnitz

Quasistationary states of an electron in a spherical β-HgS/β-CdS/β-HgS nanoheterosystem

N. V. Tkach and V. A. Golovatskiĭ

Chernovtsy State University, 274012 Chernovtsy, Ukraine
(Submitted March 12, 1999)
Fiz. Tverd. Tela (St. Petersburg) **41**, 2081–2083 (November 1999)

The electron scattering matrix for spherically symmetric states in a spherical β-HgS/β-CdS/β-HgS nanoheterosystem is calculated. The positions of the energy levels and the lifetimes of an electron in the corresponding states are found as functions of the geometric parameters of the system and analyzed. © *1999 American Institute of Physics.* [S1063-7834(99)03511-X]

The interest in ''artificial atoms,'' i.e., nanoheterosystems of complex spherical (and other) shapes, is due both to the possibilities of their practical application[1,2] (precision-frequency lasers operating at high temperatures) and the possibilities of investigating new fundamental physical phenomena.

Spherically symmetric β-CdS/β-HgS/H_2O and β-CdS/β-HgS/β-CdS/H_2O nanoheterosystems were created experimentally not so long ago by ion substitution under pressure.[3,4] The electron and exciton spectra were investigated experimentally and theoretically as functions of the geometric parameters of the system in the same studies. A theory describing the electron (hole) spectrum in multilayer spherical nanoheterosystems within the effective-mass approximation without consideration of the interaction with phonons was presented in Ref. 5. The influence of polarization phonons (confined and interface) on the electron spectrum was taken into account in Ref. 6, and their influence on the exciton spectrum in complex quantum wells was treated in Ref. 7.

In all of these and other studies the respective nanoheterosystem was assumed explicitly or implicitly to be such that it was enclosed in an external macroscopic medium, whose potential creates a very high barrier to an electron or a hole. As a result, bound stationary electron states of an ''artificial atom'' form at energies below the barrier height of the external medium, and a continuous spectrum forms at energies above the potential barrier.

As far as we know, the electron spectrum in spherical nanoheterosystems of another type, viz., systems in which the external medium is a potential well with respect to a spherical quantum well separated from the external medium by a potential barrier, has not been investigated as yet. It is clear from physical arguments that quasistationary electron and hole states for such quasiparticles having finite lifetimes should appear in these nanoheterosystems. Since the synthesis of such systems does not present any fundamental difficulties, and since they can have interesting practical applications, it would be interesting to investigate the electronic states in one of these systems.

In this paper we shall investigate the spherically symmetric quasistationary states of an electron in a β-HgS/β-CdS/β-HgS nanoheterosystem, since this system probably can be created experimentally by ion substitution, if the external β-HgS sphere is made so thick that it can be treated as an external medium.

We shall study the electronic spectrum of a spherical nanoheterosystem consisting of a β-HgS core (a quantum well) and a β-CdS layer (a potential barrier) enclosed in a macroscopic medium of β-HgS. The geometric scheme and the potential energy of an electron are shown in Fig. 1. The potential energy of the electron depends only on the distance to the center of the system; therefore it is convenient to solve the Schrödinger equation in a spherical coordinate system with its origin at the center of the heterosystem, where

$$U(r)=\begin{cases} 0, & r\leqslant R_0,\ r\geqslant R_1 \\ U, & R_0<r<R_1 \end{cases}. \tag{1}$$

The electron effective mass in each medium is known, and for the system as a whole it can be written in the form

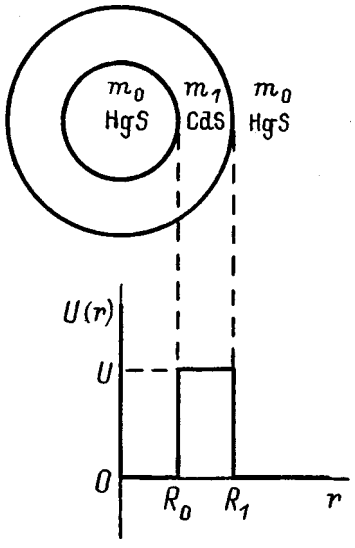

FIG. 1. Geometric scheme and potential of a multilayer spherical β-HgS/β-CdS/β-HgS nanoheterosystem.

$$m(r)=\begin{cases} m_0, & r\leqslant R_0,\ r\geqslant R_1 \\ m_1, & R_0<r<R_1 \end{cases}. \tag{2}$$

The Schrödinger equation for an electron in the system under consideration has the following form:

$$\left\{\frac{\hbar^2}{2}\nabla\frac{1}{m(r)}\nabla-U(r)\right\}\Psi(\mathbf{r})=E\Psi(\mathbf{r}). \tag{3}$$

With consideration of the spherical symmetry, the solution of this equation is sought in the form

$$\Psi(\mathbf{r})=R(r)Y_{lm}(\theta,\varphi), \tag{4}$$

where $Y_{lm}(\theta,\varphi)$ are spherical functions, and the radial functions $R(r)$, which are related to the functions $X(r)$ by the expression

$$R(r)=rX(r), \tag{5}$$

lead to a Bessel-type equation. As a result, one of the solutions for spherically symmetric states ($l=0$) has the form

$$X_k^{(+)}(r)=\begin{cases} ae^{ikr}+be^{-ikr}, & r\leqslant R_0 \\ \alpha e^{\chi r}+\beta e^{-\chi r}, & R_0<r<R_1, \\ e^{ikr}, & r\geqslant R_1 \end{cases} \tag{6}$$

where

$$\chi=\sqrt{\chi_0^2-\frac{m_1}{m_0}k^2},\quad \chi_0=\sqrt{\frac{2m_1U}{\hbar}},\quad k=\sqrt{\frac{2m_0E}{\hbar}}.$$

The coefficients α, β, a, and b are determined from the conditions for continuity of the wave function and the probability flux density on the boundaries between the regions

$$\alpha=e^{-R_1(\chi-ik)}\frac{\Delta m+g_1^+}{2m_0R_1\chi},\quad \beta=-e^{R_1(\chi+ik)}\frac{\Delta m+g_1^-}{2m_0R_1\chi},$$

$$a=e^{(\chi+ik)\rho}\frac{e^{-2\rho\chi}(\Delta m+g_1^+)(-\Delta m+g_0^+)-(\Delta m+g_0^-)(-\Delta m+g_1^-)}{4im_0m_1R_0R_1k\chi},$$

$$b=-e^{ik(R_0+R_1)\rho}\frac{e^{-2\rho\chi}(\Delta m+g_1^+)(-\Delta m+g_0^-)-(\Delta m+g_1^+)(-\Delta m+g_0^-)}{4im_0m_1R_0R_1k\chi}, \tag{7}$$

where

$$\rho=R_1-R_0,\quad \Delta m=m_0-m_1,$$

$$g_0^+=(m_0\chi+ikm_1)R_0,\quad g_1^+=(m_0\chi+ikm_1)R_1,$$

$$g_0^-=(m_0\chi-ikm_1)R_0,\quad g_1^-=(m_0\chi-ikm_1)R_1.$$

Another independent solution $X_k^{(-)}(r)$ is obtained by complex conjugation:

$$X_k^{(-)}(r)=X_k^{(+)*}(r). \tag{8}$$

Therefore, the general solution has the form

$$X_k(r)=\sqrt{\frac{2}{\pi}}S(k)^{-1/2}\frac{1}{2i}[-X_k^{(-)}(r)+S(k)X_k^{(+)}(r)], \tag{9}$$

where $S(k)$ is the scattering matrix.

The analytical calculation of the S matrix is performed exactly according to a modified (for the case of $m_1\neq m_0$) general theory.[8] The result is as follows:

$$S(k)=e^{-2ikR_1}\frac{g_1^-+\Delta m}{g_1^++\Delta m}\frac{e^{-2\chi\rho}+\dfrac{g_1^+-\Delta m}{g_1^-+\Delta m}\xi(k)}{e^{-2\chi\rho}+\dfrac{g_1^--\Delta m}{g_1^++\Delta m}\xi(k)}, \tag{10}$$

where

$$\xi(k)=\frac{m_1kR_0\cot(kR_0)+m_0R_0\chi+\Delta m}{m_1kR_0\cot(kR_0)-m_0R_0\chi+\Delta m}. \tag{11}$$

The band of the S matrix in the lower complex half-plane ($k=k_1-ik_2$) is specified by the spectrum of energies (E_n) and the lifetimes (τ_n) of an electron in the quasistationary states. These quantities can be calculated by numerical methods. Because of the large difference between the orders of magnitude of k_1 and k_2 (6–10 orders), the accuracy of the calculation of τ_n can be insufficient, especially for large values of the width and height of the potential barrier. Therefore, we should analyze formula (10). In the case where $\chi\rho\gg1$ (the barrier is fairly broad and high), the term $\exp(-2\chi\rho)$ can be neglected everywhere, except at the points $k=k_n$, where $\xi(k)=0$. Therefore, (10) will have the form of the function

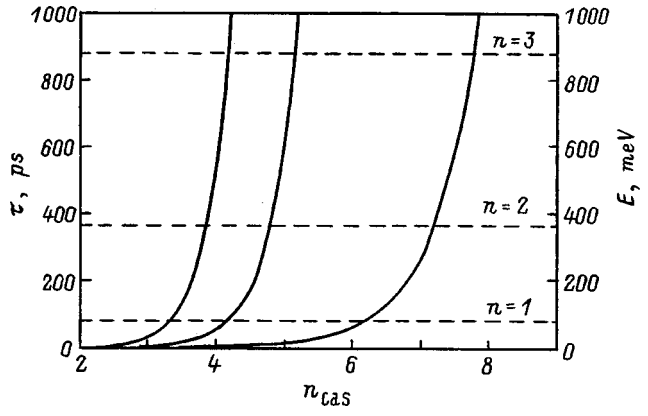

FIG. 2. Dependence of E_n (dashed lines) and τ_n (solid lines) on the width of the potential barrier $n_{\mathrm{CdS}}=\rho/a_{\mathrm{CdS}}$.

$$S(k)=e^{-2ikR_1}\frac{m_0\chi-(m_0-m_1)/R_0+ikm_1}{m_0\chi-(m_0-m_1)/R_1-ikm_1}, \tag{12}$$

which does not have poles. Thus, the S matrix can have poles only in the vicinity of $k=k_n$. The value of k_n, which is a solution of the dispersion equation

$$m_1kR_0\cot(kR_0)+m_0R_0\chi+\Delta m=0, \tag{13}$$

determines the energies of the stationary electron states in the limiting case $\rho\to\infty$. To determine the analytical expressions for the approximate values of k_1 and k_2 in the equation

$$e^{-2\chi\rho}+\frac{g_1^-+\Delta m}{g_1^++\Delta m}\xi(k)=0, \tag{14}$$

which specifies the poles of the S matrix (8), we expand $\xi(k)$ in a series in powers of $(k-k_n)$, retaining the linear term

$$\xi(k)=\frac{(k-k_n)}{2k_n}(1+R_0\chi_n)\left(\frac{m_1k_n^2}{m_0\chi_n^2}+\frac{m_0-m_1}{m_1R_0\chi_n}+\frac{m_0}{m_1}\right), \tag{15}$$

where $\chi_n=\sqrt{\chi_0^2-\frac{m_1}{m_0}k_n^2}$.

Now substituting (15) into (14), we obtain the approximate values of k_1 and k_2 and consequently the energies of the quasistationary states

$$E_n=\frac{2\hbar^2}{m_0}(k_1^2-k_2^2)\approx\frac{2\hbar^2}{m_0}k_n^2, \tag{16}$$

and the lifetimes of an electron in these states

$$\tau_n=\frac{m_0}{2\hbar^2k_1k_2}\approx\frac{\hbar e^{2\chi_n\rho}}{16E_n}\frac{\left[m_1^2k_n^2+\left(m_0\chi_n+\frac{\Delta m}{R_1}\right)^2\right]\left(m_0^2\chi_n^2+m_1^2k_n^2+m_0\Delta m\frac{\chi_n}{R_1}\right)(\chi_nR_0+1)}{m_1^2\chi_n^3k_n}. \tag{17}$$

A specific calculation of the characteristics of the electron spectrum was performed for the β-HgS/β-CdS/β-HgS system with the parameters $m_0=0.036m_e$, $m_1=0.2m_e$, $U=1.2$ eV, $a_{\mathrm{HgS}}=5.851$ Å, and $a_{\mathrm{CdS}}=5.818$ Å. The results of calculating the dependences of E_n and τ_n for the first three levels on the width of the barrier (β-CdS) for a fixed width of the β-HgS well $R_0=15a_{\mathrm{HgS}}$ are presented in Fig. 2. The calculation was performed using both the exact Eq. (10) and the approximate Eqs. (16)–(17). The deviations in the results obtained did not exceed 1% even for the smallest barrier width. As is seen from the figure, all the energy levels are essentially independent of the barrier width, and the lifetime of an electron in these states increases exponentially with increasing ρ.

Figure 3 presents plots of the dependence of E_n and τ_n on the well width R_0 for the fixed barrier width $\rho=5a_{\mathrm{CdS}}$. It is seen from Fig. 3 that, as ρ is increased, all the energy levels shift toward lower energies according to a quadratic law, while the lifetimes of an electron in these states increase rapidly with increasing well width. The latter can be understood on the basis of physical arguments, since an increase in the well width lowers each energy level and thereby increases the ''strength'' of the barrier, i.e., prevents escape of the electron into the region of free space from the bound state and thus increases the lifetime in that state.

Thus, it can be concluded that the lifetime of an electron in a spherical nanoheterosystem with quasistationary states is very sensitive to the geometric characteristics of the nanosystem.

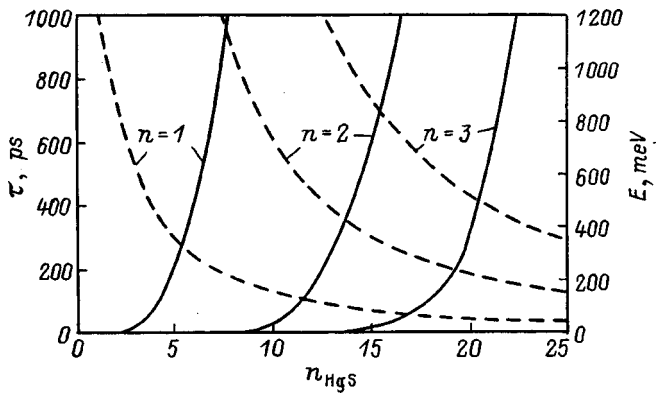

FIG. 3. Dependence of E_n (dashed lines) and τ_n (solid lines) on the width of the potential well $n_{\mathrm{HgS}}=R_0/a_{\mathrm{HgS}}$.

[1] Zh. I. Alferov, Fiz. Tekh. Poluprovodn. **32**, 3 (1998) [Semiconductors **32**, 1 (1998)].
[2] N. N. Ledentsov, V. M. Ustinov, V. A. Shchukin, P. S. Kop'ev, Zh. I. Alferov, and D. Bimberg, Fiz. Tekh. Poluprovodn. **32**, 385 (1998) [Semiconductors **32**, 343 (1998)].
[3] D. Schooss, A. Mews, A. Eychmuller, and H. Weller, Phys. Rev. B **49**, 17 072 (1994).
[4] A. Mews, A. V. Kadavanich, U. Banin, and A. P. Alivasatos, Phys. Rev. B **53**, 13 242 (1996).
[5] N. V. Tkach, V. A. Golovatskiĭ, O. N. Voĭtsekhovskaya, and M. Ya. Min'kova, Ukr. Fiz. Zh. (Russ. Ed.) **43**, 745 (1998).
[6] N. V. Tkach, Fiz. Tverd. Tela (St. Petersburg) **39**, 1109 (1997) [Phys. Solid State **39**, 995 (1997)].
[7] M. Tkach, V. Holowatsky, O. Voitsekhivska, and M. Min'kova, Phys. Status Solidi **203**, 578 (1997).
[8] A. I. Baz', Ya. B. Zel'dovich, and A. M. Perelomov, *Scattering, Reactions and Decay in Nonrelativistic Quantum Mechanics* (Israel Program for Scientific Translations, Jerusalem, 1966; Nauka, Moscow, 1971, 2nd edn., 463 pp.).

Translated by P. Shelnitz

POLYMERS. LIQUID CRYSTALS

Second-order nonlinear optical susceptibility in chalcone-group crystalline molecular compounds

N. V. Agrinskaya and V. A. Lukoshkin

A. F. Ioffe Physicotechnical Institute, Russian Academy of Sciences, 194021 St. Petersburg, Russia

V. V. Kudryavtsev, G. I. Nosova, N. A. Solovskaya, and A. V. Yakimanskiĭ

Institute of High-Molecular Compounds, Russian Academy of Sciences, 199004 St. Petersburg, Russia
(Submitted April 13, 1999)
Fiz. Tverd. Tela (St. Petersburg) **41**, 2084–2087 (November 1999)

A study is reported of the second-order nonlinear optical susceptibility in polycrystalline molecular materials of the chalcone group made by second-harmonic generation at a wavelength of 1.06 μm. Some of the compounds studied exhibit a high nonlinear activity and are transparent in the blue region of the spectrum. The measured macroscopic nonlinear polarizability χ^2 was compared with the calculated values of β, the second-order molecular polarizability tensor. The high nonlinear optical polarizability observed in some chalcone compounds is shown to be related to crystal symmetry type. © *1999 American Institute of Physics.* [S1063-7834(99)03611-4]

Considerable attention has been focused recently on investigation of organic compounds, crystals as well as polymers, exhibiting nonlinear optical properties which are necessary for development of various opto-electronics devices (electro-optical modulators, optical switches, optical-frequency converters, etc.).[1] However there is still no clear understanding of the extent to which the chemical structure of a molecule contributes to the efficiency of second-order nonlinear optical polarizability χ^2. This, in its turn, makes difficult a purposeful synthesis of new materials with optimum molecular and supermolecular structures for use in nonlinear-optics devices. It is known that high values of β, the second-order molecular polarizability tensor, can be observed in molecules with a delocalized π-electron system, and having donor and acceptor substituents. Additionally, in order for volume polarizability χ^2 to occur, the system must have an noncentrosymmetric supermolecular organization, i.e., one should either have acentric crystals or molecules polarized in a strong electric field in some polymer matrix. However, organic molecules tend to crystallize mostly in ways inimical for a high volume polarizability χ^2 to occur; indeed, polar molecules with a large dipole moment tend to form antiparallel structures, and noncentrosymmetric crystallization can be disrupted by dipole aggregation. Therefore the second way, namely, polarization in an electric field of molecules embedded in a polymer matrix moment and a high second-order molecular polarizability, and having a large dipole appears more promising. In this case the volume and molecular polarizabilities are related in the following way

$$\chi^{(2)} \approx CN(\beta\mu E/kT),$$

where N is the concentration of chromophore molecules, μ is the dipole moment, E is the applied electric field, and C is a local-field factor. On the other hand, β depends on the chemical structure of a molecule, namely, on the capability of the donor and acceptor substituents to donate or accept electrons, on the conjugation length (the π-electron delocalization length and the corresponding absorption-edge energy $\hbar\omega_0$), and on the difference between the dipole moments of the molecule in the ground and excited states $\Delta\mu$

$$\beta \approx f\frac{\Delta\mu}{\hbar\omega_0^2},$$

where f is the oscillator strength. These parameters, together with the quadratic polarizability tensors, can be estimated for various molecules by quantumchemical calculations.

The main interest of researchers was earlier focused on nitroaniline derivatives (MNA), (NPP), (MAP), and (DAN).[2] However, the fundamental absorption band of these compounds lies in the blue region and, therefore, when one attempts SHG from semiconductor-laser radiation (800 nm), the conversion efficiency is observed to drop because of the onset of two-photon absorption. Recently attention shifted to derivatives of benzal acetophenone (chalcone)

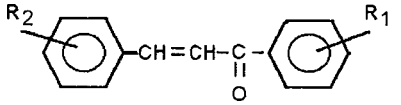

where R_1 and R_2 are substituents. A few tens of substituted chalcones exhibiting second-harmonic generation in crystalline powdered form have already been described in the literature.[3,4] The main idea behind the above studies was to introduce various substituents [OCH_3, $N(CH_3)_2$, NH_2, F, Cl, Br, I, CH_3, NO_2, $COCH_3$] leaving a fixed donor group, SCH_3, for R_1 or R_2. The C=O group was always the accep-

tor. One synthesized in this way a number of acentric organic crystals exhibiting nonlinear optical susceptibilities and transparent in the blue spectral region.

It appeared to us of interest to synthesize chalcones with the NH_2 (amine) group as a substituent and to study their nonlinear optical properties. The presence of an amine group would permit one to cross over subsequently to polymers (in order to obtain nonlinear optical polymer films by polymerization in a strong electric field). Of particular interest to us was to modify the chromophore chalcone group by substituting a furane or thiophene cycle for the benzene ring in the styryl part of the molecule.

This work reports a study of the second-order nonlinear optical susceptibility in polycrystalline molecular materials belonging to this group of chalcones by SHG at a wavelength of 1.06 μm. The values obtained were compared to the calculated values of β, the second-order molecular polarizability.

The substituted chalcones were prepared by the well-known reaction of condensation of the corresponding acetophenones and aldehydes in methanol, with NaOH used as a base. The aminochalcones were produced by reduction of nitrochalcones in hydrochloric acid. The synthesized compounds were recrystallized from alcohol or dioxane or DMPA. One measured absorption spectra and melting temperatures for all the polycrystalline chalcones obtained (see Table I). This publication reports the first measurements of the nonlinear optical properties of these compounds.

The second-order nonlinear susceptibilities χ^2 were measured on powder samples by the second-harmonic generation technique in backscattering geometry. The YAG:Nd^{3+} master laser operated in a Q-switched regime on a zero-transverse mode TEM_{00} at a repetition frequency of 14 Hz. A pulse of radiation of wavelength $\lambda = 1.064\,\mu$m, lasting $\tau = 20$ ns, and average pulse energy of 1 mJ, was fed into a single-pass YAG amplifier and amplified to 10 mJ. The exciting pulse from the amplifier output was focused on the sample under study at an angle of 45°. The second-harmonic radiation ($\lambda = 532$ nm) exiting the sample was collected by an optical system, focused on the entrance slit of a MDR-2 monochromator (this enabled spectral separation of the monochromatic SHG signal from the luminescence radiation), and detected by a PhEU-97 PM tube. To monitor the exciting pulse intensity at the sample, part of the radiation (about 5%) was split off the main beam (before the focusing lens) and directed onto a preliminarily calibrated FD-24K photodiode. Because of technical difficulties associated with determining the exciting intensity incident on the sample with sufficiently high accuracy, the quadratic susceptibility was measured by comparison with a reference sample. In this work, urea powder was used as a reference. The corresponding relative values of the SHG signal are listed in Table I. The signals obtained on the chalcone compounds in the series under study are seen to vary within a broad range (from 0.1 to 800).

To establish the extent to which the molecular characteristics of the compounds studied correlate with the measured SHG intensities, quantumchemical calculations of the quadratic polarizability of these molecules were carried out. The calculations were performed by the semiempirical RM-3 method (Ref. 5). This method proved its merits in calculating the quadratic polarizabilities of a number of organic molecules.[6,7] The results of the calculations are listed in Table I. The data presented in Table I permit the following conclusions.

(1) A comparison of molecules 1–9 (Table I) shows that their molecular nonlinearities characterized by parameter β_μ are close in magnitude. This is apparently due to these molecules having the same conjugation chain length (from the –NH– electron-donor group at one end to the –CO– electron-acceptor group at the other).

(2) As a result of the presence in the chalcone of a carbonyl group with a dipole moment perpendicular to the long axis of the molecule, the electron density of the molecule is polarized not only in the direction x of the long, π-conjugation axis, but in the perpendicular direction y as well. Therefore, the quadratic polarizability tensors β of molecules 1–14 contain, in addition to the principal component β_{xxx}, essentially nonzero components β_{xyy} and β_{yxx}. Thus these molecules are two-dimensional nonlinear optical chromophores unlike the purely one-dimensional ones (for instance, of the stilbene or azabenzene types), whose β_{xyy} and β_{yxx} components are negligible compared to β_{xxx}. Two-dimensional contributions are dominant for molecules 11–13.

(3) Interestingly, as one crosses over from amines to the corresponding benzamides (compare the molecule pairs 3–4, 5-6, and 7-8), β_μ does not decrease in magnitude, as this could be expected based on the decrease of the electron-donor character of the –NH– group involved in such a transition. Note, however, that the nonlinear optical chromophores 4 and 6 become practically one-dimensional in this cross-over (with β_{xxx} being far in excess of β_{xyy} and β_{yxx}). This is associated with the C=O bonds in the chalcone and amide groups being directed oppositely with respect to the x axis in the benzamide molecule.

(4) Molecules 10–14 have shorter conjugated fragments between the –NH– and –CO– groups than molecules 1–9, which results in smaller β_μ. An exclusion to this is molecule 14, whose relatively large value of β_μ (comparable to that for molecules 1–9) is apparently accounted for by the 3,5-dinitro-benzamide fragment which is not conjugated with the remaining part of the molecule because of the metastructure of the central phenylene ring. The largest value of β_μ obtained for molecule 9 is connected with the effect of the dimethyl aminogroup in the R_2 fragment, the strongest of the electron donors used here.

(5) By our calculations, introduction of the H_3CS substituent into the R_2 fragment results in an unfavorable mutual orientation of the dipole moment and the vector part of the quadratic polarizability tensor. For molecules 11–13, these vectors make a nearly right angle. Fairly large values of this angle were obtained also for the amines 3 and 5, which decrease, however, noticeably as one crosses over to the corresponding benzamides (4 and 6).

A comparison of the calculated nonlinearities to those derived from the observed SHG signal permits a conclusion that there is no correlation whatsoever between the molecular

TABLE I. Principal components of the quadratic polarizability tensor β of the chalcones

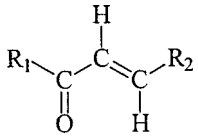

and the projections β_u of the vector part β of this tensor on the direction of dipole moment μ calculated by the RM-3 method, as well as the ratios of the measured SHG signal intensites (I) from crystalline powder samples to the SHG signal intensity (I_M) from crystalline area.

№	R_1	R_2	Angle between $\tilde{\beta}$ and μ, vectors, deg.	β_{xxx}, 10^{-30} esu	β_{xyy}, 10^{-30} esu	β_{yxx}, 10^{-30} esu	β_{μ}, 10^{-30} esu	I/I_M	T_{melt}, °C	λ_{max}, nm
1		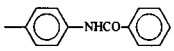	10.1	27.4	3.5	2.6	14.1	7	189	349
2		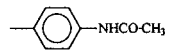	11.6	21.9	2.7	4.2	11.3	–		
3		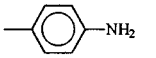	39.8	23.1	0.6	10.0	11.6	40	142	392
4		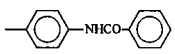	15.7	29.5	4.6	3.0	14.4	130	213	353
5		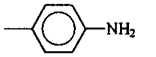	46.9	24.0	0.5	9.3	11.1	1	175	392
6		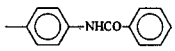	19.2	30.2	3.2	2.5	15.3	0.02	216	354
7	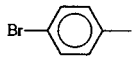	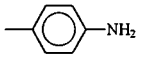	21.2	15.2	4.5	13.3	14.2	800	155	398
8	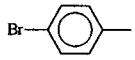	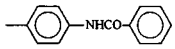	24.0	27.0	2.6	9.1	14.0	6	203	354
9	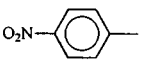	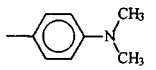					20.7	–	166	445
10	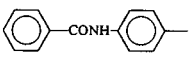		29.3	14.0	3.5	7.2	6.4	21	197	327
11	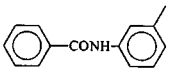	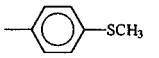	120.1	0.5	6.1	17.2	−6.0	1	180	355
12	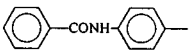	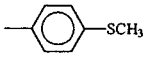	100.7	17.7	1.9	7.7	−2.3	0.1	168	356
13	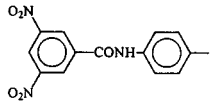	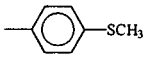	67.1	4.7	6.5	15.9	5.5	0.6	313	364
14	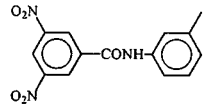	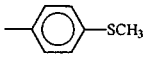	28.4	21.4	2.1	7.5	13.6	10	216	356

Note: T_{melt} is the melting temperature, and λ_{max} is the wavelength of the fundamental absorption band. The components of vector β are defined by the expression $(\beta)_i=(3/5)(\beta_{ixx}+\beta_{iyy}+\beta_{izz})$, $i=x,y,z$.

(microscopic) and crystalline (macroscopic) nonlinearities. This observation can be explained if one assumes that macroscopic nonlinearity is determined primarily by the crystal structure and the type of molecular packing in the cell. Investigation of the crystal structure of the new organic compounds is time-consuming and could be a subject of a separate study. We have succeeded in studying the crystal structure of compound 3 and found it to belong to biaxial crystals with $mm2$ point-group symmetry, which is an optimum symmetry for observing the SHG effect (note that, in

the case of molecular dipoles oriented in an optimum way with respect to the optic axis of a crystal, up to 38% of molecular nonlinearity may contribute to its macroscopic nonlinearity). A more promising approach appears to be introduction of optically nonlinear molecules into a polymer matrix, their orientational ordering in an electric field, and preservation of this order after field removal below the glass-formation temperature.

Thus our studies have demonstrated a potential of certain derivatives of organic compounds of the chalcone group for development of crystalline electro-optical devices. Estimation of the nonlinear optical properties of polymers with chalcones in the side chains will be the subject of a separate paper.

Support of the Russian Fund for Fundamental Research (Grant 98-03-33289) is gratefully acknowledged.

[1] *Nonlinear Optical Properties of Organic Molecules and Crystals*, edited by D. S. Chemla and J. Zyss (AT&T, 1987; Mir, Moscow, 1989).
[2] A. V. Vannikov, A. D. Grishina, R. V. Rivol'skaya, and A. T. Ponomarenko, Usp. Khim. **67**, 507 (1998).
[3] Y. Goto, A. Hayashi, M. Nakayama, T. Watanabe, S. Miyata, K. Honda, and M. Goto, J. Chem. Soc. Jpn. **9**, 968 (1990).
[4] C. K. Tripathy, B. H. Kim, and B. Bihari, Synth. Met. **71**, 1705 (1995).
[5] J. J. P. Stewart, J. Comput. Chem. **10**, 209 (1989).
[6] H. A. Kurtz, Int. J. Quantum Chem. **24**, 791 (1990).
[7] H. A. Kurtz, J. J. P. Stewart, and K. M. Dieter, J. Comput. Chem. **11**, 82 (1990).

Translated by G. Skrebtsov

FULLERENES AND ATOMIC CLUSTERS

The structure of copper-doped amorphous hydrogenated carbon films

T. N. Vasilevskaya, N. S. Andreev, I. A. Drozdova, and V. N. Filipovich

I. V. Grebenshchikov Institute of Silicate Chemistry, Russian Academy of Sciences, 199155 St. Petersburg, Russia

S. G. Yastrebov and T. K. Zvonareva

A. F. Ioffe Physicotechnical Institute, Russian Academy of Sciences, 194021 St. Petersburg, Russia
(Submitted November 18, 1998; resubmitted March 2, 1999)
Fiz. Tverd. Tela (St. Petersburg) **41**, 2088–2096 (November 1999)

A study of the nanostructure of *a*-C:H:Cu films by x-ray small-angle scattering, x-ray diffraction, TEM, and visible and UV spectroscopy is reported. It has been established that introduction of 9–16 at. % Cu not only decorates the original carbon fragments but produces extended (up to 4 μm in length) formations of copper-decorated strongly elongated ellipses as well. At 14–16 at. % Cu, these linear clusters represent copper nanotubes with a core made up of the original ellipses drawn in a line. It is these conducting copper formations that account primarily for the strong increase in conductivity at 12–16 at. % Cu contents in *a*-C:H films. © *1999 American Institute of Physics.* [S1063-7834(99)03711-9]

Amorphous hydrogenated carbon *a*-C:H possesses such unique properties as optical transmission in the visible and IR ranges, chemical and radiation strength, high electrical resistivity, and wear resistance. These characteristics of the material are due to specific features of its structure, which is made up of nanosized blocks (nanoclusters) of two principal carbon modifications, graphite and diamond.[1] By doping the material one can modify substantially its nanostructure and, thus, vary the electrophysical and spectral properties of *a*-C:H. It is known that introduction into the material of metals which do not form carbides creates regions containing metal-based clusters. The conductivity of such media varies over a broad range, from that of the insulating matrix to that of the bulk metal. Alongside the diversity of experimental data available for various composites,[2] this is supported by observation[3] of a nonlinear dependence on the copper concentration of the electrical conductivity of copper-doped *a*-C:H, and of indications of high-T_c superconductivity at nitrogen temperatures for a composition corresponding to the maximum of electrical conductivity. It was subsequently shown that copper forms in *a*-C:H:Cu nanoclusters of conductors of two types, which differ both in physicochemical characteristics and in shape. We have in mind here graphite-like clusters doped by copper to make an intercalate-like phase (cluster size 1.5–2 nm) and copper nanoclusters ranging from a few nm to a few tens of nm.[4] These media containing nm-sized conducting clusters are promising for the development of one-electron electronics devices.[5]

On the way to this goal, one has to study not only the properties of single nanosized clusters contained in *a*-C:H:Cu but also the specific features of their geometry, as well as the characteristics of the current percolation network on meso- and microscales. One can cite a number of works dealing with investigation of the structure of such films by x-ray diffraction, in particular, by small-angle scattering.[6,7] Note that such results describing properties of scatterers in *a*-C:H:Cu should be considered only as preliminary.

To fill this gap, the present work makes use of complementing methods of x-ray phase analysis (XPA) and x-ray small-angle scattering (XSAS) to probe the structure of the material. To increase the reliability of the results, we present also TEM data and establish correlation between the structural characteristics of a substance and the high-frequency (optical) electrical conductivity in order to reveal the effect of surface and geometric characteristics of the copper nanoclusters on the physicochemical properties of *a*-C:H:Cu films.

1. EXPERIMENTAL

The x-ray SAS measurements were carried out with Cu $K\alpha$ radiation ($\lambda = 1.54$ Å) for wave-vector moduli $s = 4\pi(\sin\theta)/\lambda$ ranging from 0.0083 to 0.65 Å^{-1}. When used at scattering angles 2θ from 0.1 to 10°, small-angle scattering provides information on inhomogeneities with linear sizes from 1 to 75 nm.[8–10] The experimental curves were obtained on an x-ray SAS instrument with a Kratki collimation system. Collimation corrections for the beam height and width were introduced. The intensities are expressed in absolute electronic units. The reference was a particularly clean quartz glass characterized by a scattering intensity from thermal density fluctuations $I_\rho(0) = 0.552$ e.u./Å^3. The XSAS intensities were measured to within $\pm 0.1\%$.

The XPA was recorded on a Philips diffractometer with Cu $K\alpha$ radiation for the scattering angle range 2θ of 5 to 180°. The TEM and electron diffraction studies were

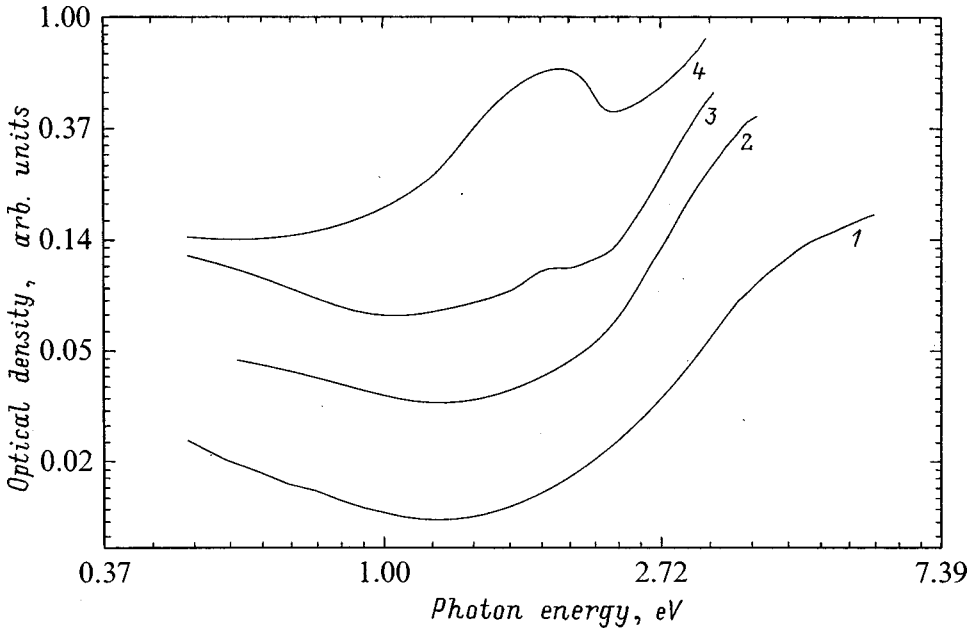

FIG. 1. Optical-density spectra of amorphous hydrogenated carbon doped with copper to concentrations (at. %): *1*—0. *2*—9, *3*—14, *4*—24.

made with an ÉM-100. The transmission spectra of *a*-C:H:Cu samples were measured with a Hitachi-U3410 spectrophotometer.

1.1. Preparation of *a*-C:H and *a*-C:H:Cu films

Copper-doped *a*-C:H films were prepared by magnetron cosputtering of a pyrolytic graphite and a copper target in an argon-hydrogen (4:1) plasma mixture.[11] The substrate temperature before film deposition was 200 °C. The layer growth rate was 250–350 nm/h. The layer composition and thickness were monitored by SIMS and ellipsometry.

This work reports a study of starting copper-free *a*-C:H films and of *a*-C:H:Cu films with copper contents of 9, 12, 14, 15, 16, 17, 18, and 24 at. % Cu. The thickness of the films used in XPA and XSAS measurements varied from 2 to 4.5 μm, and that intended for TEM and optical studies, from 30 to 100 nm. To investigate the film structure by XSAS, 100-μm thick single-crystal Si polished plane-parallel plates were prepared, on which *a*-C:H and *a*-C:H:Cu films were deposited. The choice of Si for the substrate was motivated by the absence of scattering (other than background) by silicon within the angular range covered by XSAS.

2. RESULTS AND DISCUSSION

2.1. Spectroscopic data for excitation of surface plasma oscillations

Figure 1 presents a typical optical-density pattern of an amorphous *a*-C:H:Cu film. The dependence of optical density of an undoped sample on frequency exhibits a smear at high frequencies, which is characteristic of an amorphous material. Fitting the Tautz relation to the dependence of absorption edge on wavelength yields 2–2.1 eV for the gap energy. One sees also that, as the copper concentration increases, the edge becomes modified by an absorption band, which results in an increase of the slope of the dependence under study with increasing concentration in the high-frequency region. As the copper concentration increases, this phenomenon is accompanied by the formation of another absorption band in the central region of the spectrum. The absence of absorption bands in the intermediate spectral region indicates that the optical properties of copper-doped amorphous hydrogenated carbon are due to two types of nanosized particles and that there are in the sample no optically active metallic particles with dimensions in excess of the wavelength of the radiation employed in the measurements. An analysis of the experimental data in the Lorentz oscillator formalism[12] shows that the appearance of the absorption band centered near 2 eV (1.8 eV) can be assigned to surface-plasmon excitation in spherical particles (form factor 1/3), and the variation of absorption in the high-frequency tail (the absorption band peaking near 3.5 eV), to surface plasmon excitation in nonspherical conducting inclusions, such as two-dimensional formations or their aggregates (with form factors of 1/2, 1/2, and 0 corresponding to excitation of surface plasmons in prolate cylindrical particles, with the electric field of the electromagnetic wave directed across the cylinder axis). Note that because the latter resonance frequencies are close to the copper surface plasmon frequency (3.5 eV),[13] this also permits one to associate the presence of such resonances with excitation of the surface plasmon in planar conducting nanosized copper-based inclusions (form factor 1.0). Using a theory restricting the electron mean free path to cluster dimensions[12] enabled determining the average size of copper-containing clusters of various shapes from the position of absorption maxima in the spectra. To find the dimensions, one used the value of the host-matrix dielectric permittivity $\epsilon_m = 4.62$ derived ellipsometrically for an undoped film at 1.96 eV. The bulk copper parameters $\omega_p = 1.35\times10^{16}$ s^{-1}, $\tau_{\text{inf}} = 6.9\times10^{-15}$ s, and $l_{\text{inf}} = 11$ nm were taken from Ref. 14. It was found that the relaxation times for nonspherical conducting particles vary over a broad range, from $(3.4-4)\times10^{-16}$ s for an energy of 3.5–3.6 eV to close to the bulk copper relaxation time, and the corresponding geometric dimensions, from 0.57–0.72 nm to 10 nm. For

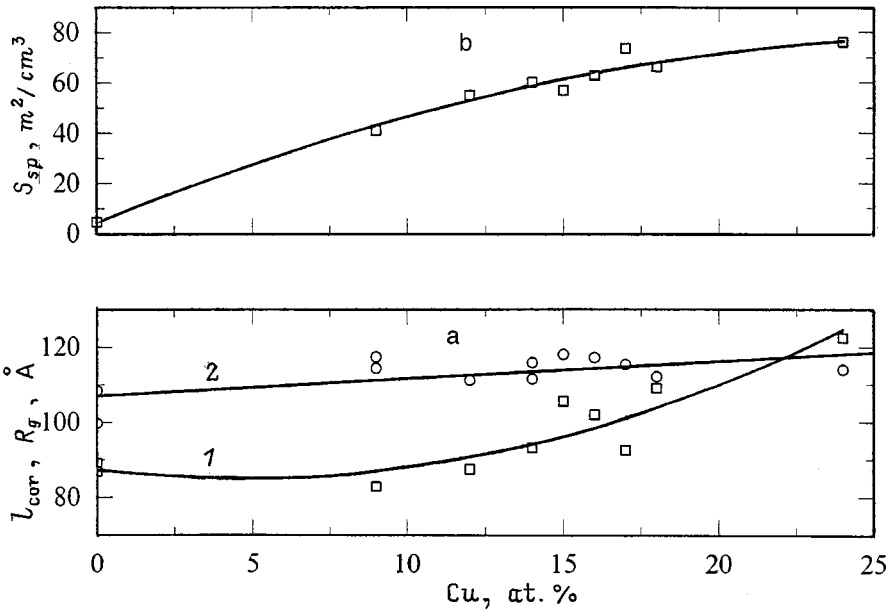

FIG. 2. Concentration dependences: (a) correlation length l_{cor}, curve *1* and integrated gyration radius R_g, curve *2*; (b) specific interface area S_{sp}.

spherical particles the situation is similar, the relaxation time at the resonance frequency being 3×10^{-16} s and particle dimensions, 0.52–10 nm.

2.2. XPA and electron diffraction data

X-ray diffraction patterns of copper-containing films exhibit broad diffraction maxima corresponding to interplanar distances of 2.08, 1.808, 1.278, and 1.090 Å. This set of data suggests the presence in the films under study of certain amounts of metallic copper (ASTM N4-836) belonging to cubic symmetry. Estimates of average Cu crystal size from the reflection halfwidth ($\sim1.5°$) made for the first and second peaks yields 6, 5, and 6.4 nm for a Cu content of 9, 14, and 24 at. % Cu, respectively. Hence magnetron cosputtering of a copper and a graphite target leads to formation of copper nanoclusters embedded in *a*-C:H. Their sizes, 5–6 nm, vary very little with increasing copper concentration, which correlates with the above optical data and Ref. 4. However judging from the intensity of the first peak (158:293:1449), their number increases substantially with copper concentration. (It should be pointed out that the thickness of the films studied was far from the optimum value to permit high-precision quantitative XPA.)

An electron diffraction study of starting copper-free films revealed only two diffuse reflections characteristic of amorphous graphite with a density of 2.265 g/cm^3.[15] In contrast to this work, an electron diffraction analysis reported in Ref. 12 demonstrated the presence in these starting films of a certain amount of nanocrystalline diamond- and graphite-like formations.

2.3. Integrated characteristics of the XSAS method

Estimation of integrated characteristics, such as the correlation length

$$l_{\rm cor}=2\int_0^\infty \gamma(r)dr=\pi\left(\int_0^\infty sI(s)ds\right)\Big/\left(\int_0^\infty s^2I(s)ds\right)$$

and the scatterer gyration radius

$$R_g^2=\left(\int_0^L p(r)r^2dr\right)\Big/\left(2\int_0^L p(r)dr\right)$$

[where $\gamma(r)$ is the correlation function, $p(r)=r^2\gamma(r)$, and L is the maximum distance in a particle] made for films with 0–24 at. % Cu permits a conclusion that the integrated dimensions of the scattering particles practically do not change. Figure 2a displays the concentration dependences of the integrated gyration radius R_g and of the correlation length $l_{\rm cor}$.

The correlation length first varies very little. Only for 24 at. % Cu does it exceed somewhat the corresponding gyration radius. This may indicate both that the scattering particles are substantially nonuniform and far from being spherical (for a uniform sphere with this gyration radius the correlation length should be nearly two times larger), and that the scattering particles are noticeably polydisperse.

An approximate estimate of the specific interface area made from Porod's relation $S_{sp}=4\omega/l_{\rm cor}$ is presented graphically in Fig. 2b. The specific interface area in a copper-free film is 4.5 m^2/cm^3. In copper-doped films, S_{sp} is an order of magnitude larger and varies from 40 to 76 m^2/cm^3, increasing proportionally to the copper content. Such high specific areas are observed usually only in the presence of clusters made up of nanosized particles.[10] However the interface morphology and the shape and geometric parameters of the particles making up this surface vary considerably depending on copper content in a film.

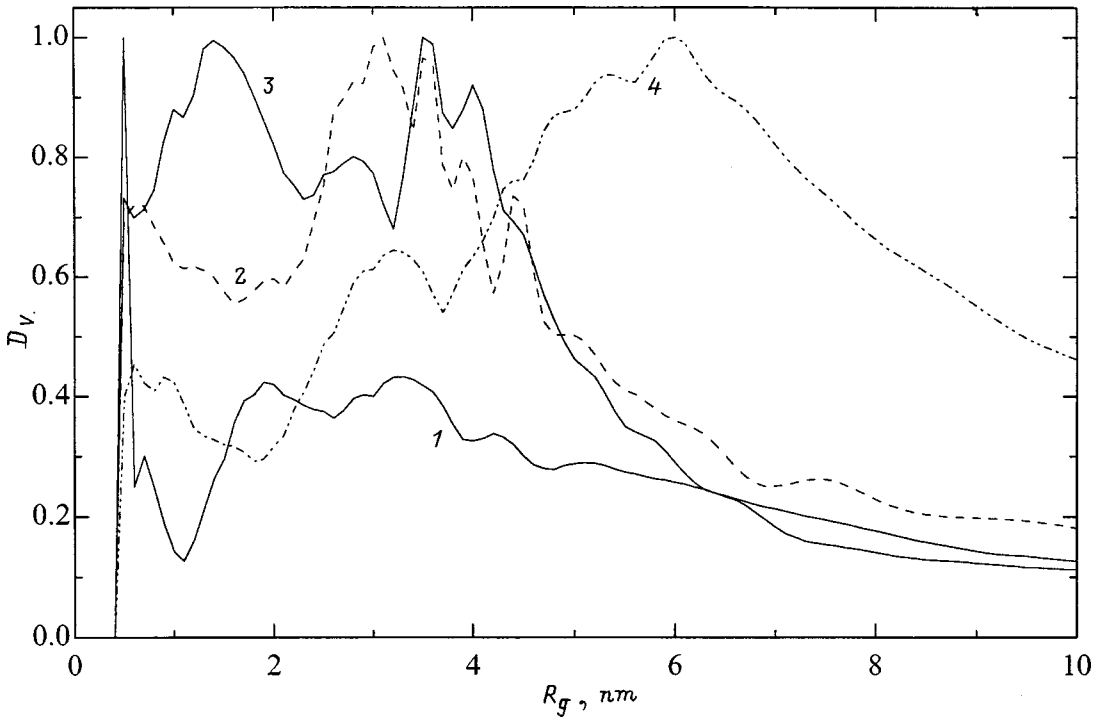

FIG. 3. Scatterer distribution function for various copper concentrations (at. % Cu): *1*—0, *2*—9, *3*—14, *4*—24. (The dispersity estimated by Plavnik.[16,17] R_g is the particle gyration radius.)

2.4. Size distribution of particles

Most methods of determination of the scatterer distribution function in size start by postulating the scatterer shape (and internal structure). As follows from the analysis of optical data, our material contains scatterers of various shapes, namely, plane particles, spherical copper particles, and their aggregates. A method for approximate estimation of the scatterer-size distribution function in gyration radius was proposed for polydisperse systems.[16,17] Figure 3 shows the distribution function of the scatterers present in *a*-C:H:Cu. This distribution correlates fairly well with the data derived both from the optical spectra and from the XPA and TEM measurements. The presence of a maximum in the distribution function for the 0.5-nm size can be associated with the scattering of x-rays from the graphite-like component of the *a*-C:H framework.

As seen from the figure, introduction of 9 at. % Cu mainly decorates the features of the original, undoped film. Copper becomes manifest in a strongly dispersed state (one sees a series of maxima corresponding to dimensions smaller than 5 nm). Doping to 14 at. % Cu gives rise to the appearance of a strong maximum at 1.5 nm. Besides, there is a trend to coagulation (or crystallization), which manifests itself in a decrease of the peak at 2.8 nm and an increase of the 4-nm peak. Note that the ordinate at 6 nm is larger at 9 at. % Cu, which correlates with the XPA data.

The presence in the graph of a broad maximum corresponding to 6 nm for 24 at. % Cu indicates predominant transfer of copper from the finely dispersed state in which it resides at low concentrations to crystalline state with 5–7 nm sizes at 24%.

2.5. Fractal dimensions and TEM

The XSAS method offers a unique possibility of determining the fractal dimension of aggregates (mass distribution in space),[10,18] which can be estimated from the slope of the $I(s)$ *vs* s plot in log coordinates, because $I(s)=As^{-D}$, where D is the fractal dimension. Consider the $\log[I(s)]$ *vs* $\log[s]$ dependence (Fig. 4). To make the graph more revealing, another axis corresponding to direct-space resolution $R=\pi/s$ is given on top. One sees clearly four characteristic regions in units of R. The first of them extends down to 9.5 nm, the second covers the sizes from 9.5 to 4 nm, the third, from 4 to 2.6 nm, and the fourth, below 3 nm, which provides information on scattering by the surface of the smallest particles, and it is of them that the aggregates consist. Note that the features in the curves vary in phase with the regions in the scattering intensity distribution for the undoped sample, whereas the doped samples reveal only a considerable increase in scattering intensity from 250 to 10^5 e.u./Å^3 as the doping increases to 24 at. % Cu.

A comparison of the dependences for the copper-free and the 9 at. % Cu films shows an exact coincidence of the fractal values practically throughout the s range covered. The main differences in the course of the curves are seen to occur in the 9.5–4 nm interval. Where the undoped film exhibits ''steps,'' the 9 at. % Cu films reveal three distinct oscillations with a period of 0.007 Å^{-1}. While in the TEM images of the original films one sees only rare rectangular formations 10 nm in width and up to 1 μm long (Fig. 5a), the images of the 9 at. % Cu films (Fig. 5b) exhibit a large number of whiskers and multi-ray stars. As a rule, the stars have 5 to 6 rays. Viewed under a 120,000 magnification (Fig. 5c),

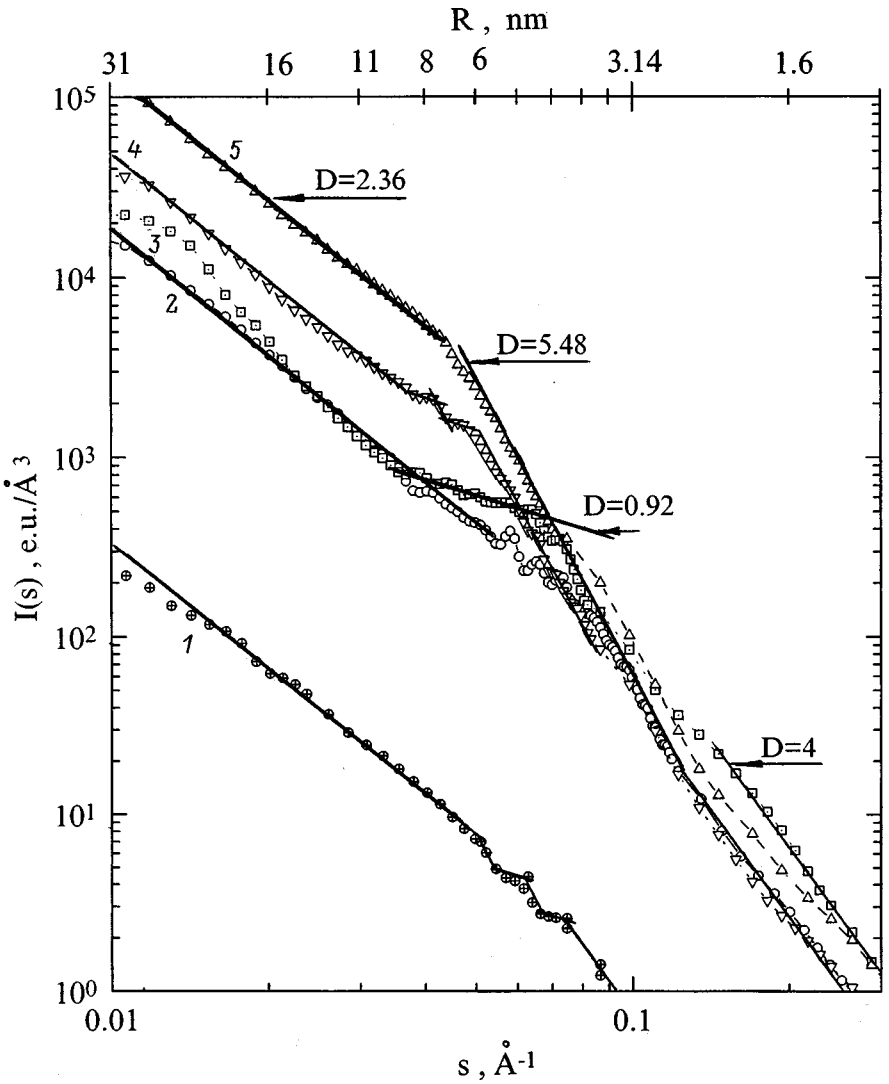

FIG. 4. Dependence of scattering intensity $I(s)$ on wave vector s drawn on a log-log scale (with s plotted on the lower axis, and $R=\pi/s$, on the upper axis) for various copper concentrations (at. % Cu): *1*—0, *2*—9, *3*—14, *4*—18, *5*—24. The fractal dimension D is specified.

the ray structure is seen to be nonuniform. The rays represent chains of elongated ellipses or edge-sharing rhombs drawn in a line. At rhomb center one perceives a bright carbon core. The average distance between these cores (45 nm) corresponds to the above-mentioned oscillation period.

One readily sees that an increase in copper content to 14% results in qualitatively new features within the 8.6–4.9-nm interval. Within this interval, the relation has a slope $D=0.92$. The oscillations are smoothened out to a certain extent, which suggests the growth at this concentration of a thicker copper layer decorating these chains than in the case of 9 at. % Cu. Indeed, internal structure of the whiskers cannot be resolved in the TEM images of the 14 at. % Cu-films because they are coated now by a solid copper layer. The width of the whiskers also remained practically unchanged. Besides, a region with dimension $D=3.78$ has appeared at small angles, which apparently can be associated with copper crystallizing into larger faceted particle, which are observed at ray ends (Fig. 5d). The space between the ellipses is filled with copper, the roughness smoothed to form metallic conducting tubes which house carbon cores. It is probably the numerous aggregates of such tubes that result in a considerable increase of the conductivity of such films, which opens up a new application potential for these films in electronics.

At 18 at. % Cu, the region with dimension $D=0.92$ contracts noticeably, to vanish altogether as one approaches 24 at. % Cu.

At 24 at. % Cu, the relation within regions *1* and *3* is generally similar in shape to the original curve. However at the center one observes an extended (7.3–2.1 nm) section with dimension $D=5.48$. This correlates well with both the average size of the crystal phase from XPA measurements, 6.4 nm, and the broad maximum at 6–10 nm in the particle-size distribution function. These clusters are uniformly distributed in the volume, which is in accord with the standard fractal dimension $D=2.36$ nm. Indeed, TEM images (Fig. 5f) show against a general background of small (3 nm) spherical particles a large number of denser, practically spherical clusters 11 nm in diameter. These clusters consist of a central sphere surrounded by five to six spheres.

These data argue for the intercalation hypothesis of copper doping of *a*-C:H at relatively low concentrations and of copper coagulation in drops at high ones. Coagulation of copper to form drops favors destruction of the electric current percolation paths and a decrease in electrical conductiv-

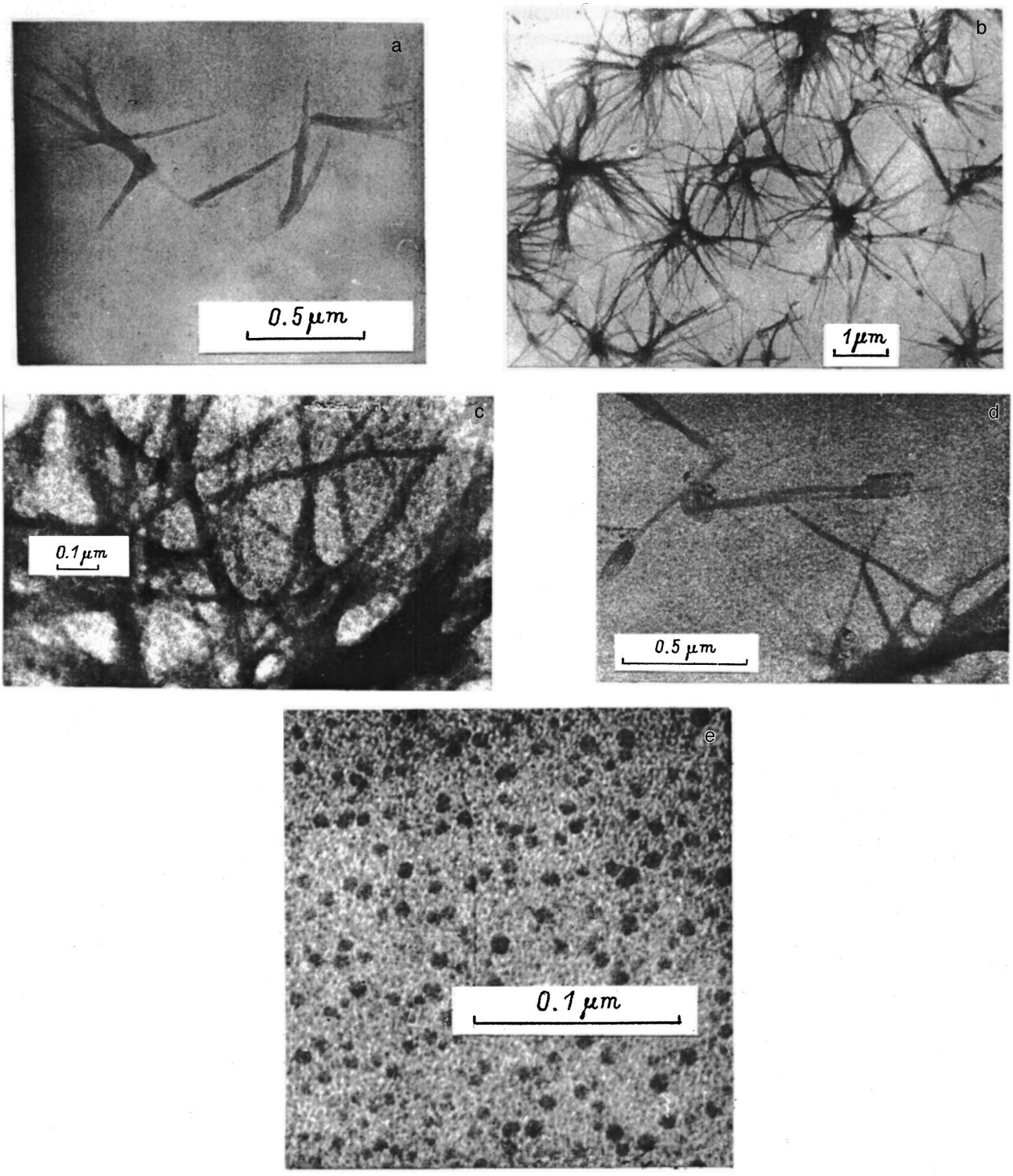

FIG. 5. TEM images of amorphous hydrogenated copper-doped carbon. a—undoped sample (magnification 60,000); b—9 and 14 at. % Cu (magnification 12,000). General view for 14 at. % reveals formations at ray extremities, and for 9 at. % no such formations are seen; c—9 at. % Cu (magnification 120,000), whisker structure resolved, individual ellipse chains seen; d—14 at. % Cu (magnification 60,000), individual fragment, whisker structure unresolved, initial crystalline formations at tube ends seen; e—24 at%Cu (magnification 480,000). Radially symmetric nanoclusters seen against the background of individual spherical formations.

ity, as well as modification of the optical properties described above through light absorption by surface plasmons in spherical and nonspherical copper nanoclusters.

2.6. Analysis of the $f(r)$ and $p(r)$ functions

The $\gamma(r)$ function, as well as the function $p(r)$ derived from it, are related both to the geometry of the particle shape (they describe quantitatively the set of sections connecting elements of particle volume) and to the distribution of intraparticle inhomogeneities. For instance, for a uniform sphere of radius R the $p(r)$ function reaches a maximum at r_m, with $r_m/2R=0.525$. For $r>2R=L$, $p(r)=0$. The value of r_m/L can serve as a criterion of particle shape anisometry. For oblate particles one can conveniently use the $f(r)=r\gamma(r)$

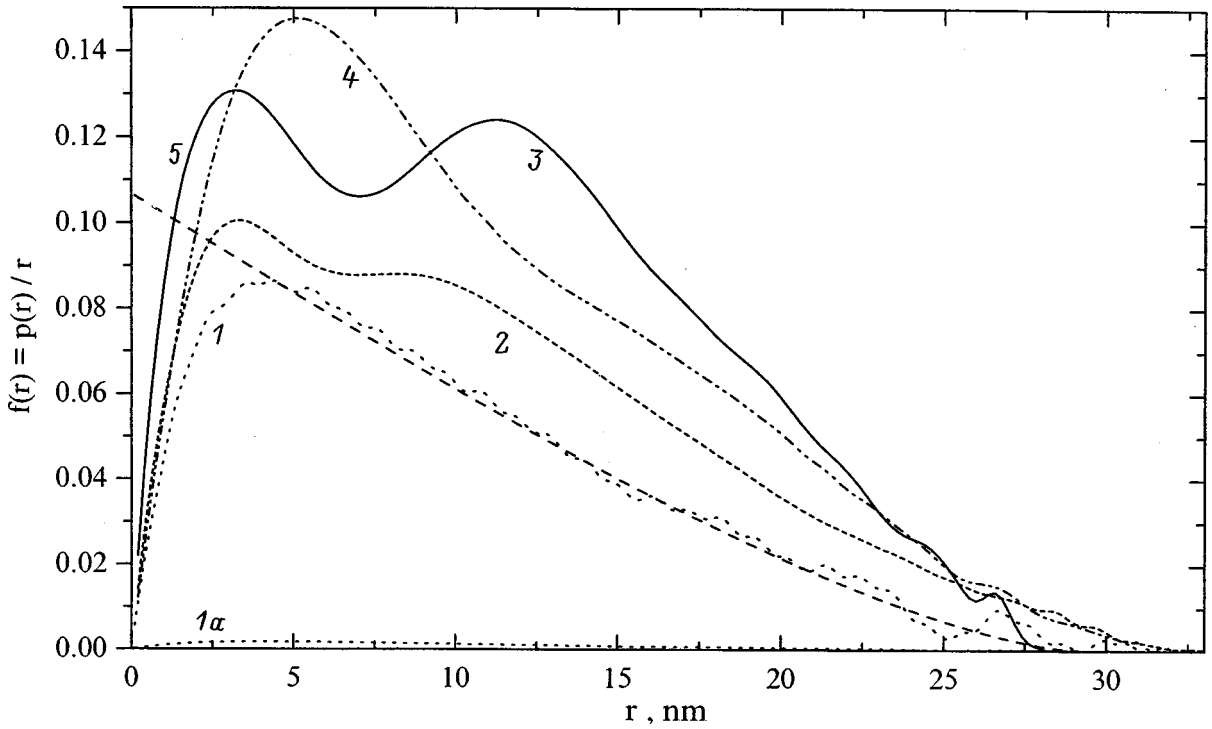

FIG. 6. $f(r)=p(r)/r$ function for amorphous hydrogenated carbon doped by copper to concentrations (at. % Cu): *1*a—0 (starting relation), *1*—0 (ordinate magnified 50 times), *2*—9, *3*—14, *4*—24 (ordinate reduced 50 times), *5*—calculation for a plane disc 29.2 nm in diameter and 3.6 nm thick.

function, because in the case of lamellar particles the number of in-plane distances $2\pi r\gamma(r)=2\pi p(r)/r$ (Ref. 19).

To analyze the shape and sizes of the scatterer aggregates estimated above, consider the function $f(r)$ (Fig. 6). Note that the ordinate of line *1* in Fig. 6 is increased five times compared to the original one (line *1a*), and that for 24%, 50 times (line *4*).

An analysis of the dependence of function $f(r)$ for the starting film and its comparison with available data[19], as well as our calculations, permit a conclusion that the aggregates of nanoparticles present in *a*-C:H are close in shape to an oblate triaxial ellipsoid with the axes $a:b:c=3.6:10.7:29.2$ nm.[20] Even a preliminary calculation of scattering from an aggregate shaped as a planar disc 29.2 nm in diameter and 3.6 nm thick demonstrates a satisfactory agreement of experimental (curve *1*) with calculated (curve *5*) data.

It is seen also that introduction of 9 and 14 at. % Cu practically does not affect the position of the first maximum (3.4 and 3.2 nm), but it results in the appearance of another maximum in $f(r)$ at approximately 8.8 and 11.2 nm, respectively. Note that, as shown by calculations, the maximum distance in the particle estimated from the tail in the function, $f(32\,\text{nm})=0$, increased compared to the undoped sample by 3 nm. This increase of the distance to 32 nm implies that introduction already of 9 at. % Cu gives rise to a growth of a 1.5-nm thick copper-containing shell around the aggregate.

The appearance of a second maximum in the $f(r)$ relation for 9 and 14 at. % Cu reflects the growth of a copper layer over two planes of the ellipse first to 2.7 nm, and after that, to 3.8 nm on both sides.

The shape of the $f(r)$ relation for 24 at. % Cu permits concluding that the particles have acquired the shape of a prolate ellipsoid of revolution with the axes 11:11:33 nm. The maximum in $f(r)$ for this ellipsoid should lie at 5.5 nm, exactly what is observed in the figure.

An analysis of the r_m/L ratio of the $f(r)$ function made for 0, 9, 14, and 24 at. % Cu yields the values of 0.3, 0.4, 0.48, and 0.5, respectively, thus giving one grounds to assume that the particles are progressively rounding off by growing a shell over the planes. This makes their shape approach a sphere, because $r_m/L=0.525$ for a uniform sphere (Ref. 20).

One also cannot rule out the possibility that these features in the aggregate structure exist already in an undoped film, and an increase in copper concentration results only in their decoration (e.g., by the intercalation mechanism) by atomic copper or larger copper nanoclusters. As the copper concentration increases to reach 24%, the $f(r)$ function again takes on the shape characteristic of scattering from a uniform ellipsoid of revolution.[20]

Thus when copper, which is not a carbide-forming material, becomes embedded in the matrix of amorphous hydrogenated carbon, it occupies in it the positions of minimum energy, i.e., formation of a film entails ordering which results both in absorption of single copper atoms by fragments of graphite-like structures with dimensions (correlation length) typically of a few nm[9] and, in the absence of unoccupied fragments in the nearest environment of thermalizing copper atoms, in a growth of copper nanocrystals. As the matrix absorbs copper atoms, the nanosized graphite-like aggregates containing absorbed copper atoms reproduce spatially the geometric features of the larger structural elements contained in the original matrix. These formations were seen by

us in TEM images and studied by means of XSAS. The mechanism by which nanoclusters of both types form results in an increase of both the interface surface and of the specific surface of the ensembles of copper-containing nanoclusters. The latter, in its turn, gives rise to a sharp increase in the x-ray scattering cross section from both bulk copper nanoclusters and the graphite-like clusters containing absorbed copper, as well as to excitation of surface-plasma waves localized on the nm scale and detected spectroscopically, which are unique for the objects under study. The interaction among surface layers results in a change of the states of the nanophases forming during synthesis of the material and in their becoming interrelated, which brings about a structural rearrangement of the copper-containing cluster network and a substantial modification of both high- and low-frequency properties of layers at dopant concentrations corresponding to the percolation threshold.

The conclusions of this work can be formulated in the following way.

A correlation has been observed to exist between the spectral, electrical, and structural properties of *a*-C:H:Cu.

The results obtained in our study of the optical properties of amorphous hydrogenated copper-doped carbon imply the existence of two types of optically active conducting copper-based nanosized inclusions, namely, spherical drops and oblate cylindrical copper-containing clusters. The presence in the material under study of copper structures with characteristic sizes close to the dimensions derived from an optical analysis is supported by XPA and XSAS measurements.

A well-developed interface formed primarily by nanoparticles 0.5 nm in size is present in the films, which follows from both the particle-size distribution function and an analysis of XSAS intensity curves.

When becoming embedded in *a*-C:H, copper decorates the carbon formations (aggregates) growing in the course of synthesis. Copper also enters the aggregates in the form of nanoclusters with characteristic sizes of a few nm.

Support of the Russian R&D program ''Fullerenes and Atomic Clusters'' and of the Russian Fund for Fundamental Research (Grant 97-03-32273a) is gratefully acknowledged.

[1] J. C. Angus and C. C. Hayman, Science **241**, 913 (1988).
[2] C. Laurent and E. Kay, J. Appl. Phys. **65**, 1717 (1989).
[3] N. E. Bazieva, S. G. Yastrebov, V. F. Masterov, and A. V. Prichodko, Mol. Mater. **4**, 143 (1994).
[4] V. I. Ivanov-Omskii, A. V. Tolmatchev, and S. G. Yastrebov, Philos. Mag. B **73**, 715 (1996).
[5] E. S. Soldatov, V. V. Khanin, A. S. Trifonov, S. P. Gubin, V. V. Kolesov, D. E. Presnov, S. A. Yakovenko, G. B. Khomutov, and A. M. Korotkov, Usp. Fiz. Nauk **168**, 217 (1998).
[6] V. I. Ivanov-Omskiĭ, V. I. Siklitskiĭ, and S. G. Yastrebov, Fiz. Tverd. Tela (St. Petersburg) **40**, 568 (1998) [Phys. Solid State **40**, 524 (1998)].
[7] M. V. Baidakova, V. I. Ivanov-Omskii, A. A. Suvorova, A. A. Sitnikova, V. I. Siklitsky, A. V. Tolmatchev, and S. G. Yastrebov, in: *Proceedings of the International Symposium on Nanostructures: Physics and Technology-97* (St. Petersburg, 1997), p. 383.
[8] D. I. Svergun and L. F. Feĭgin, *X-Ray and Neutron Small-Angle Scattering* (Nauka, Moscow, 1986).
[9] T. N. Vasilevskaya and R. I. Zakharchenya, Izv. Akad. Nauk SSSR, Neorg. Mater. **31**, 754 (1995).
[10] T. N. Vasilevskaya and R. I. Zakharchenya, Fiz. Tverd. Tela (St. Petersburg) **38**, 3129 (1996) [Phys. Solid State **38**, 1711 (1996)].
[11] V. I. Ivanov-Omskiĭ, A. B. Lodygin, and S. G. Yastrebov, Fiz. Tverd. Tela (St. Petersburg) **37**, 1693 (1995) [Phys. Solid State **37**, 920 (1995)].
[12] V. I. Ivanov-Omskii, V. I. Siklitsky, A. A. Sitnikova, A. A. Suvorova, A. V. Tolmatchev, T. K. Zvonariova, and S. G. Yastrebov, Philos. Mag. B **76**, 973 (1997).
[13] C. F. Bohren and D. R. Huffman, *Absorption and Scattering of Light by Small Particles* (Wiley-Interscience, New York, 1983; Mir, Moscow, 1986).
[14] P. B. Johnson and R. W. Christy, Phys. Rev. B **6**, 4370 (1972).
[15] R. D. Heidenreich, *Fundamentals of Transmission Electron Microscopy* (Interscience Publishers, New York, 1964; Mir, Moscow, 1966).
[16] G. M. Plavnik, Kristallografiya **24**, 737 (1979) [Sov. Phys. Crystallogr. **24**, 422 (1979)].
[17] G. M. Plavnik, Kristallografiya **29**, 210 (1984) [Sov. Phys. Crystallogr. **29**, 125 (1984)].
[18] R. Jullien, Comm. Mod. Phys., Pt. B, **13**, 177 (1987).
[19] A. Guinier, *Small-Angle Scattering of X-Rays* (Wiley, New York, 1955).
[20] O. Glatter, J. Appl. Crystallogr. **12**, 166 (1979).

Translated by G. Skrebtsov

Effect of a constant magnetic field on the photoconductivity of single-crystal C_{60}

Yu. A. Osip'yan, R. K. Nikolaev, and S. Z. Shmurak

Institute of Solid State Physics, Russian Academy of Sciences, 142432 Chernogolovka, Moscow District, Russia

Yu. I. Golovin, D. V. Lopatin, and R. B. Morgunov

G. R. Derzhavin Tambov State University, 392622 Tambov, Russia
(Submitted April 13, 1999)
Fiz. Tverd. Tela (St. Petersburg) **41**, 2097–2099 (November 1999)

Magnetic fields with induction $B<1$ T are found to affect the photocurrent in single-crystal C_{60}. This effect does not reduce to the Hall effect. The effect of the field on the multiplicity of short-lived pairs consisting of mobile carriers and their traps is proposed as a possible explanation for the observed phenomenon. [S1063-7834(99)03811-3]

Studies of the conductivity of solids provide important information on their electronic subsystems and on the interaction of current carriers with the atoms of the material. Studies of jump conductivity, which make it possible to evaluate the short lived intermediate states of the charge carriers, are of special interest. It has been found[1] that a constant magnetic field affects the photoconductivity of films of anthracene and tetracene at room temperature. Similar effects have been observed in single-crystal naphthalene and anthracene,[2] complex anthracene-dimethyl-pyromellithimide crystals,[3] polycrystalline samples based on anthracene and tetracyanbenzene,[4] doped carbosolyl-containing polmers,[5] rubrene films,[6] and other organic materials. Magnetic fields have also been found to affect the dark conductivity of polyacetylene in strong electric fields.[7] It should be noted specially that the change in conductivity under the influence of a magnetic field in these cases cannot be explained by galvanomagnetic effects, in particular the Hall effect. The possibility of a resonant change in the photocurrent in these materials in crossed direct and microwave magnetic fields provides unique evidence that magnetic fields affect the spin state of intermediate electron-hole pairs $(e \ldots h)$.[8,9] It has been reliably established by now that magnetospin effects in electrical conductivity at room temperature are observed in a whole series of molecular crystals that are characterized by jump conductivity.[10,11]

The systems having jump conductivity appear to include the fullerites C_{60}, in which athermal behavior is observed in the photocurrent relaxation time at temperatures of 150 -450 K.[12] In addition, the electronic subsystem of the fullerites has a number of properties close to the electronic properties of the polyacenes. Here we mean not only the type of conductivity, but also the polyaromaticity attributable to the fullerites in accordance with quantum-mechanical criteria, a band gap $E_G \approx 1.5-1.9$ eV, which means that the fullerites are semiconductors, and a number of other properties.[13] We may expect, therefore, that the electrical properties of crystal C_{60}, like those of the hydrocarbon systems mentioned above, may depend on the spin state of intermediate pairs $(e \ldots h)$. Thus, studies of the photoconductivity of C_{60} in magnetic fields are of interest for establishing the role of the multiplicity of these pairs in forming the electrical and optical properties of fullerites.

Our purpose here is to create experimental conditions for observing the effect of a magnetic field on the photoconductivity of C_{60} and to isolate that part of this effect that is not attributable to galvanomagnetic phenomena.

For studying the sensitivity of the photoconductivity to magnetic fields we used single-crystal samples of high purity C_{60} (99.95% C_{60}), grown from the vapor phase with the natural faceting for face-centered cubic crystals and an average linear size of $\sim 3-5$ mm. A crystal was pressed elastically to silver contacts located on opposite facets. A constant voltage $U=3-5$ V was applied to the contacts. The current was measured using a V7-30 electrometer amplifier, whose signal was delivered to a personal computer capable of processing 250 measurements per second. The resistance of the external circuit in all the measurements was much lower than that of the sample, which was $\sim 10^9\ \Omega$ in the dark. The ohmic character of the contacts was specially verified both in the dark current regime and when a photocurrent was flowing. For voltages $U=1-7$ V, the current-voltage characteristic was linear with an accuracy of 0.99, while changing the polarity of the voltage on the electrodes did not change the absolute magnitude of the current.

A photocurrent excited using light from a 30 W incandescent lamp after passage through a water filter was focussed by a lens (photon energy $1.9-3$ eV$\geqslant E_G$). A magnetic field with an induction B up to 0.6 T was created by smoothly positioning a C-shaped magnet with a variable gap. It was specially verified that the photocurrent excited in additively colored KBr crystals placed in the measurement cell was not sensitive to the magnetic field, i.e., the field did not affect the elements of the measurement cell.

Turning the light on during tests of the C_{60} crystals produced a tenfold increase in the current in the circuit. After photoexposure times longer than 100 s, there was a significant drop in the photocurrent (Fig. 1) caused by photoinduced oxidation of the surface layers of the sample.[14] Creating a magnetic field with $B=0.6$ T at the site of the crystal

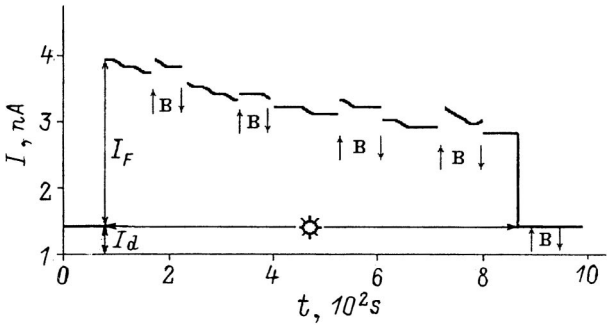

FIG. 1. The current I as a function of elapsed time t. The arrows denote the times a magnetic field is switched on and off, I_F is the photocurrent, and I_d is the dark current.

during photoexposure increased the photocurrent by $\Delta I_F \approx 5-10\%$. After the field was switched off, the photocurrent I_F decreased, recovering the value which it would have attained in the light without a magnetic field (Fig. 1). The dark current was essentially unchanged by applying a magnetic field (Fig. 1).

In order to measure the photocurrent as a function of the magnetic induction, bursts of light lasting 3 s were used to illuminate a crystal that was alternately in and out of the magnetic field. The duration of the bursts was chosen so that, during a series of bursts, the drop in I_F owing to photooxidation would be linear to within $\sim 0.1\%$. It was found that the photocurrent, averaged over the duration of a burst that was excited in the crystals while they were in the magnetic field, was $5-10\%$ higher than the expected value in the absence of a field (Fig. 2).

The increase in the photocurrent ΔI_F when a magnetic field was applied did not depend on the orientation of the magnetic induction vector relative to the direction of current flow or on the material from which the contacts were made (Fig. 2).

By comparing a series of photocurrent pulses in the absence of a magnetic field with a series of pulses initiated for different magnetic fields, it was possible to subtract the effect owing to photooxidation and obtain a plot of $\Delta I_F(B)$ in its ''pure form'' (Fig. 3). This curve is characterized by saturation with respect to the field at $B \approx 0.2$ T.

Proceeding to a discussion of the results, we note that the recovery of I_F after the magnetic field is removed (Fig. 1) indicates that it affects the photoconductivity of the fullerite C_{60}, rather than the photooxidation reaction, since, in the latter case, the irreversibility of the chemical reaction would lead us to expect only a reduction in the rate of change of I_F, rather than a sudden recovery of the absolute magnitude of the photocurrent after the field is removed.

The absence of a dependence of ΔI_F on the mutual orientation of the magnetic induction and the direction of the photocurrent, the saturation in the increment ΔI_F at $B \approx 0.2$ T (Fig. 2), and the absence of a magnetic field effect on the magnitude of the dark current suggest that the observed effect does not reduce to the Hall effect.

The sign and magnitude of the magnetic-field effect on the photocurrent, as well as the saturation with respect to the field at $B \approx 0.2$ T bring our results closer to those in a study[1–3] of the magnetic-field effect on the photoconductivity of polyacenes. This suggests that the magnetic field sensitivity of the photocurrent in the polyacenes and in C_{60} can be explained by similar causes.

In this case one of the possible mechanisms through which a magnetic field affects the photocurrent may be the following. Under the influence of light, pairs of mobile, paramagnetic particles, i.e., electrons (e) and holes (h), are generated. If the Coulomb interaction radius in the short lived intermediate pairs ($e \ldots h$) is shorter than the radius of the exchange interaction, then the relationship between the recombination and dissociation probabilities for a pair may depend on its multiplicity.[15] As a rule, recombination from a

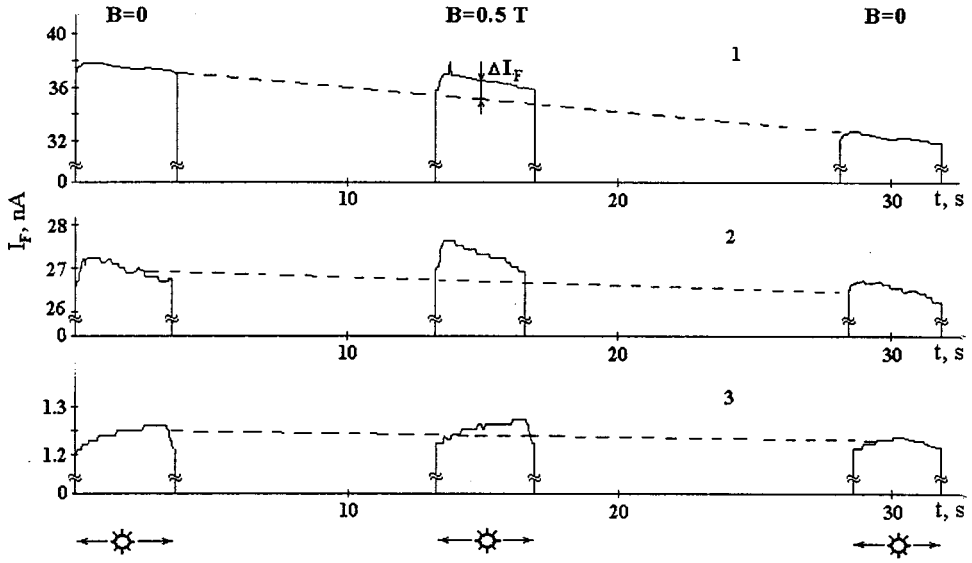

FIG. 2. Fragments of I_F as a function of elapsed time t in the course of repeated light pulses. The dashed lines denote the values of I_F that would be observed in the intermediate current pulse in the absence of a magnetic field. *1* is the current **I** perpendicular to the magnetic induction **B**, with Ag electrodes; *2* is the current **I** parallel to the magnetic induction **B**, with Ag electrodes;*3* is the current **I** perpendicular to the magnetic induction **B**, with brass electrodes.

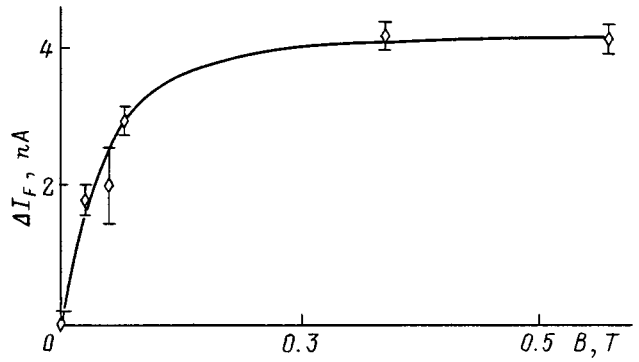

FIG. 3. The increment in the photocurrent, ΔI_F, produced by applying a magnetic field as a function of the magnetic induction B.

single state S is more efficient than from a triplet state T. If we assume that light generates pairs that are predominantly in a single state, then the role of the magnetic field may reduce to increasing the population of the triplet states over the lifetime τ of a pair. This, in turn, leads to a reduction in the carrier recombination probability, an increase in the rate of $(e \ldots h)$ pair dissociation, and, thereby, to an increase in the photoconductivity. A necessary condition for an efficient effect of the magnetic field on the photocurrent in terms of this and other, similar mechanisms is $\tau_{S-T} < \tau < \tau_r$, where τ_r is the spin relaxation time and τ_{S-T} is the spin conversion time. This ensures that thermalization of the spin system cannot take place over its lifetime and, simultaneously, it ensures a sufficiently high rate of $S-T$ transitions.[10] One of the reasons for $S-T$ transitions in a magnetic field may be a difference in the g factors of the electrons and holes, Δg, which ensures periodic transitions between the S and T states with a period $\tau_{S-T} = h/\mu \Delta g B$ (μ is the Bohr magneton). Another reason may be Zeeman splitting of the spin sublevels of a pair, which weakens the intercombination transitions induced by the hyperfine interaction at $B=0$.[10] Similar mechanisms for the effect of magnetic fields on the photoconductivity at room temperature have been successfully verified for a group of crystals in the aromatic series [1-11]. A test of their suitability for explaining the observed effect of magnetic fields on the photoconductivity of C_{60} requires further study.

This work was supported by the Russian Fund for Fundamental Research (Grant No. 97-02-16074) and the ''Universities of Russia'' Program.

[1] E. L. Frankevich and E. I. Balabanov, JETP Lett. **1**, 53 (1965).
[2] E. L. Frankevich and E. I. Balabanov, Fiz. Tverd. Tela **8**, 855 (1966) [Sov. Phys. Solid State **8**, 682 (1966)].
[3] E. L. Frankevich, M. M. Tribel, I. A. Sokolik, and B. V. Kotov, Phys. Status Solidi A **40**, 655 (1977).
[4] E. L. Frankevich, M. M. Tribel, I. A. Sokolik, and A. I. Pristupa, Phys. Status Solidi A **87**, 373 (1978).
[5] K. Okamoto, N. Oda, A. Itaya, and Sh. Kusabayashi, Chem. Phys. Lett. **35**, 1173 (1975).
[6] E. L. Frankevich, M. M. Tribel, and I. A. Sokolik, Phys. Status Solidi B **77**, 265 (1976).
[7] E. L. Frankevich, I. A. Sokolik, D. I. Kadyrov, and V. M. Kobryanskiĭ, JETP Lett. **36**, 486 (1982).
[8] E. L. Frankevich, A. I. Pristupa, M. M. Tribel', and I. A. Sokolik, DAN SSSR **236**, 1173 (1977) [*sic*].
[9] E. L. Frankevich and A. I. Pristupa, Izv. AN SSSR **50**, *2*, 220 (1986).
[10] Ya. B. Zel'dovich, A. L. Buchachenko, and E. L. Frankevich, Usp. Fiz. Nauk **155**, 3 (1988) [Sov. Phys. Usp. **31**(5), 385 (1988)].
[11] A. P. Tyutnev, A. V. Vannikov, G. S. Mingaleev, and V. S. Saenko, *Electrical Phenomena in Irradiated Polymers* [in Russian], Energoatomizdat, Moscow (1985), 176 pp.
[12] R. A. Cheville and N. J. Halas, Phys. Rev. B **45**, 4548 (1992).
[13] V. I. Sokolov and I. V. Stankevich, Uspekhi Khimii **62**, 455 (1993).
[14] V. F. Masterov, A. V. Prikhod'ko, N. I. Nemchuk, A. A. Shaklanov, and O. I. Kon'kov, Fiz. Tverd. Tela **39**, 1703 (1997) [Phys. Solid State **39**, 1522 (1997)].
[15] E. L. Frankevich, A. A. Limarev, and I. A. Sokolik, Chem. Phys. **162**, 1 (1992).

Translated by D. H. McNeill